Final report of IEA AnnexXVIII: 'Enhanced Field Rotor Aerodynamics Database'

J.G. Schepers (Netherlands Energy Research Foundation)
A.J. Brand (Netherlands Energy Research Foundation)
A. Bruining (Delft University of Technology)
J.M.R. Graham (Imperial College)
M.M. Hand (National Renewable Energy Laboratory)
D.G. Infield (Rutherford Appleton Laboratory)
H.A. Madsen (Risø National Laboratory)
T. Maeda (Mie University)
J.H. Paynter (Imperial College, Rutherford Appleton Laboratory)
R. van Rooij (Delft University of Technology)
Y. Shimizu (Mie University)
D.A. Simms (National Renewable Energy Laboratory)
N. Stefanatos (Centre for Renewable Energy Sources)

Acknowledgement

The support of the IEA R&D Wind Executive Committee which made it possible to cooperate in the Annexes XIV and XVIII is highly appreciated.

The measurement programme on the experimental facility of the Netherlands Energy Research Foundation was made possible by financial support from the Dutch Ministry of Economic Affairs (Energy R&D Targeted Funding 1991-1995). In addition support has been obtained by the Dutch Organisation for the Energy and Environment, NOVEM, within the EGIB project (NOVEM project number 224.720.9640) and through NOVEM project number 224.750.9858

The contribution from Risø to the IEA Annex XIV project has been funded by the Danish Ministry of Energy under contract: ENS 1364/94-0001 which is gratefully acknowledged.

The U. S. Department of Energy is credited for its funding of the Unsteady Aerodynamics test program through the National Renewable Energy Laboratory under contract number DE-AC36-98-GO10337.

The measurement programme from Imperial College/Rutherford Appleton Laboratories was funded by the Department of Trade and Industry, Energy Technology Support Unit and Engineering and Physical Sciences Research Council.

The measurement programme from Mie University has been supported by the Japanese Ministry of Education.

Furthermore the European experimental programmes were funded through several JOULE projects. These JOULE projects are partly funded by the EU and partly by the participating organisations and/or their national agencies.

Abstract

This report describes the work performed within the IEA Annex XIV 'Field Rotor Aerodynamics' and its successor IEA Annex XVIII 'Enhanced Field Rotor Aerodynamics Database'.

In these Annexes 7 organisations from 6 different countries collaborated in performing aerodynamic experimental programs on full scale horizontal axis wind turbines at field conditions. In such experimental programs local aerodynamic quantities (forces, velocities) are measured at several locations along a rotor blade.

The following organisations (and persons) cooperated in the projects:

- Netherlands Energy Research Foundation (ECN, NL) (Operating Agent) J.G. Schepers, A.J. Brand;
- Centre for Renewable Energy Systems, (CRES, Gr, N. Stefanatos; Only participant in IEA Annex XVIII);
- Delft University of Technology (DUT, NL): A. Bruining
- Imperial College (IC, UK), together with Rutherford Appleton Laboratory (RAL, UK): J.M.R. Graham, D.G. Infield, R.J.H Paynter (only participant in Annex XIV);
- Mie University (Mie, Jp, Y. Shimizu and T. Maeda; Only participant in IEA Annex XVIII);
- National Renewable Energy Laboratory (NREL, USA): D.A. Simms, M.M. Hand
- Risø National Laboratory (Risø, DK): H.A. Madsen

As a result of the international collaboration within the IEA Annexes it has been possible to coordinate data processing and to create and maintain a database of measured data from all participants in a common file format. The database is stored on CD-ROM or accessible through Internet. In principle the database is available for outside parties.

The detailed aerodynamic measurements obtained on very different turbines, give a unique opportunity to better understand the aerodynamic behaviour of a wind turbine. This may result in the development and validation of more accurate aerodynamic models.

Keywords

Horizontal Axis Wind Turbine Aerodynamics

Full scale aerodynamic experiments

SUMMARY

This report describes the work and the results of 'IEA Annex XIV: Field Rotor Aerodynamics' and its successor IEA Annex XVIII: Enhanced Field Rotor Aerodynamics Database'

The objective of Annex XIV was defined as the coordination of full scale aerodynamic test programs on wind turbines, in order to acquire the maximum of experimental data at minimum costs. In these full scale aerodynamic test programs local aerodynamic quantities (forces, inflow velocities, inflow angles) are measured at several radial positions along the blade. The supply of local aerodynamic data, is a major step forward in understanding the very complicated aerodynamic behaviour of a wind turbine. In conventional test programs only blade (or rotor) quantities are measured. Usually these quantities are integrated over the rotor blade(s) and they are not only influenced by aerodynamic effects, but also by mass effects. Then the local aerodynamic properties of the blade can only be derived indirectly, introducing an uncertainty.

In Annex XIV, a total of five full scale aerodynamic test programs were coordinated. The programs were carried out by:

1. Delft University of Technology, DUT Netherlands: The DUT experiments are carried out on a 2 bladed, 10 m diameter turbine. The blades are untwisted and untapered.
2. Imperial College, IC and Rutherford Appleton Laboratory, RAL, United Kingdom: The IC/RAL experiments are carried out on a 3 bladed, 16.9 m diameter turbine. The blades are twisted and tapered.
3. Netherlands Energy Research Foundation, ECN, Netherlands (Operating Agent): The ECN experiments are carried out on a 2 bladed, 27.4 m diameter turbine. The blades are twisted and tapered.
4. National Renewable Energy Laboratory, NREL, USA: The NREL experiments are carried out on a 3 bladed, 10 m diameter turbine. Measurements on two types of blades have been supplied:
   - An untwisted and untapered blade;
   - A similar blade, without taper, but with twist.
5. RISØ National Laboratory, Denmark: The RISØ experiments are carried out on a 3 bladed, 19 m diameter turbine. The blades are twisted and tapered.

By the coordination of these test programs it has been possible to create a well documented base of experimental data.

In the successor project IEA Annex XVIII the same institures as mentioned above participated, however without Imperial College, IC and Rutherford Appleton Laboratory, RAL. In addition the Japanese Mie University and the Greek Centre of Renewable Energy Systems, CRES participated. The Mie University experiments were carried out on a 3 bladed, 10 m rotor. Note that the CRES experiments were delayed and as a results no measurements could be supplied within the project period.

Annex XVIII was focussed on the storage of new measurements, in particular the measurements from Mie University and on maintenance of the existing Annex XIV database.

In order to create the IEA Annex XIV/XVIII database, a joint measurement program was agreed upon. It was agreed that time series measurements should be supplied in which the angle of attack ranges from negative values to deep stall values. Also measurements at yaw misalignment and at stand still have been supplied. Also sectional profile coefficients under rotating and 2D conditions are stored. The data file formats and the conventions have been harmonized in order to make the database easy accessible. Some selection programs are available to extract the most popular signals from the database. To aid in the interpretation of the data, an aeroelastic model description is made of all facilities.

The resulting database and documentation has been provided to several outside parties under the condition that feedback about the experiences is given to the Annex XIV/XVIII group. On basis of experiences given by users of the database it appeared that the database has led to a better understanding of the aerodynamic behaviour of a wind turbine. As a result more accurate aerodynamic models can be developed and validated.

Some recommendations were defined at the end of the project:

- The largest turbine in the project has a diameter of 27.4 m. Although at the start of the project, this was considered to be a medium sized turbine, it was regarded a small turbine at the end of the project. Aerodynamic measurements on larger turbines would be very useful;
- The mutual comparison of the measurements in the database is complicated by the fact that the angle of attack and dynamic pressure were manipulated differently by the participants. These properties are defined less straightforwardly than in the case of wind tunnel measurements. Although the project results indicate that the mean angle of attack and dynamic pressure which result from the different methods yield a reasonable mutual agreement, the differences in standard deviations are considerable;
- The experimental data are collected in the (turbulent) free air. As such the conditions cannot be controlled. Furthermore the inflow 'felt' by the turbine is only partly known. By performing aerodynamic measurements in a wind tunnel these problems can be overcome;
- The emphasis in IEA Annex XIV/XVIII was on the creation of a database. Analysis of the measurements was not a part of the project. Although some effort was spent on the analysis of the measurements, both inside and outside the IEA Annex XIV/XVIII consortium a large part of the database is still unexplored. Analysis of full scale aerodynamic measurements is considered to be an essential follow-up of the IEA Annexes.

CONTENTS

SUMMARY 5

1. INTRODUCTION 13

2. OBJECTIVES OF IEA ANNEX XIV/IEA ANNEX XVIII 15
   - 2.1 IEA Annex XIV . . . 15
   - 2.2 IEA Annex XVIII . . . 15

3. PARTICIPANTS 16

4. WORK PROCEDURE 17
   - 4.1 Definition of test matrix . . . 17
   - 4.2 Conventions and notations . . . 17
     - 4.2.1 Format of the files, filetypes, filenames . . . 18
   - 4.3 Selection of campaigns . . . 18
   - 4.4 Supply, storage and documentation of data files . . . 18
     - 4.4.1 Machine data report . . . 18
   - 4.5 Angle of attack report . . . 18
   - 4.6 Meetings . . . 19
   - 4.7 IEA Annex XVIII: Storage of the database and access to the database 19

5. DESCRIPTION OF EXPERIMENTAL FACILITES 21
   - 5.1 ECN test turbine . . . 21
     - 5.1.1 Introduction . . . 21
     - 5.1.2 Global characteristics of facility . . . 21
     - 5.1.3 Instrumentation . . . 21
     - 5.1.4 Measurement speed . . . 28
     - 5.1.5 Data reduction . . . 28
   - 5.2 IC/RAL test turbine . . . 32
     - 5.2.1 Global characteristics of facility . . . 32
     - 5.2.2 Instrumentation . . . 33
     - 5.2.3 Data reduction . . . 35
   - 5.3 NREL test turbine . . . 38
     - 5.3.1 Global characteristics of facility . . . 38
     - 5.3.2 Instrumentation . . . 43
     - 5.3.3 Measuring procedure . . . 54
   - 5.4 RISØ test turbine . . . 63
     - 5.4.1 Global characteristics of facility . . . 63
     - 5.4.2 Instrumentation . . . 65
     - 5.4.3 Measuring speed . . . 68
     - 5.4.4 Data reduction . . . 70
   - 5.5 DUT test turbine . . . 72
     - 5.5.1 Global characteristics of facility . . . 72
     - 5.5.2 Instrumentation . . . 73
     - 5.5.3 Measurement Speed . . . 76
     - 5.5.4 Calibration procedures . . . 77
     - 5.5.5 Data Reduction . . . 77
   - 5.6 Mie test turbine . . . 80
     - 5.6.1 Global characteristics of facility . . . 80

5.6.2 Instrumentation 81
5.6.3 Measurement speed 83
5.6.4 Calibration procedure 84
5.6.5 Data reduction 85
5.7 Discussion of differences between facilities 87

6. ANGLE OF ATTACK IN FIELD EXPERIMENTS 89
6.1 General 89
6.2 Methods available 90
6.2.1 IEA Annex XIV investigation 91
6.2.2 DUT investigation 92
6.2.3 NREL investigations 92
6.2.4 ECN and RISØ investigations 93
6.3 Evaluation of methods 93
6.3.1 IEA Annex XIV investigation 93
6.3.2 NREL investigation 93
6.3.3 DUT investigation 94
6.3.4 ECN investigation 95
6.3.5 RISØ investigation 95
6.4 Angles of attack in final IEA Annex XVIII database 96
6.5 Conclusion on angle of attack methods 97

7. DYNAMIC PRESSURE AND NON-DIMENSIONALISATION IN FIELD EXPERIMENTS 99
7.1 General 99
7.2 Methods available to determine the dynamic pressure 100
7.3 Evaluation of methods 101
7.4 Conclusion on non-dimensionalisation of coefficients 101

8. DESCRIPTION OF DATABASE 103
8.1 Conventions and notations 103
8.2 Format of the files, filetypes 103
8.2.1 Time series 103
8.2.2 Airfoil coefficients measured under rotating conditions . 104
8.2.3 Profile and pressure coefficients measured under 2D conditions 105
8.2.4 Power curves 105
8.3 Filenames 105
8.3.1 Time series 105
8.3.2 Airfoil coefficients measured under rotating conditions . 106
8.3.3 Profile and pressure coefficients measured under 2D conditions 106
8.3.4 Power curve 106

9. USE OF THE DATABASE, EXPERIENCES FROM USERS 109
9.1 Users 109
9.2 Comments from users 109
9.3 Use of the database 109

10. FIELD MEASUREMENTS VS. WIND TUNNEL MEASUREMENTS 111

11. CONCLUSIONS, LIMITATIONS AND RECOMMENDATIONS 113
11.1 Conclusions from IEA Annex XIV/XVIII 113
11.2 Benefits from IEA Annex XIV and Annex XVIII 114
11.3 Limitations of measurements in IEA Annex XIV/XVIII database 114
11.4 Recommendations from IEA Annex XIV/XVIII 115

REFERENCES 117

APPENDIX A. CONVENTIONS, REFERENCE SYSTEMS AND NOTATIONS 121
A.1 Introduction 121
A.2 Definitions 121
A.2.1 (Blade) azimuth angle ($\phi_{\mathrm{r,b}}$ and ϕ_{r}) 121
A.2.2 Blade numbering (1, 2 and 3) 121
A.2.3 Turbine angle (ϕ_{turb}) 121
A.2.4 Ambient wind conditions 122
A.2.5 Yaw angle (ϕ_{y}) 122
A.2.6 Pitch angle (θ) and twist (ϵ) 123
A.2.7 Angle of attack and inflow conditions 123
A.2.8 Aerodynamic forces, moments and coefficients 125
A.2.9 Unsteady conditions 126
A.3 Reference systems 126
A.3.1 Fixed $(\mathrm{xyz})_{\mathrm{N}}$ coordinate system 127
A.3.2 Fixed $(\mathrm{xyz})_{\mathrm{H}}$ coordinate system 128
A.3.3 Rotating $(\mathrm{xyz})_{\mathrm{rot}}$ coordinate system 128
A.4 Abbreviations, symbols and units 131

APPENDIX B. MEETINGS 135
B.1 IEA Annex XIV meetings 135
B.2 IEA Annex XVIII meetings 135

APPENDIX C. CONTENT OF IEA ANNEX XIV DATABASE 137
C.1 Global description of the content of the database 137
C.2 Directory tree 137
C.3 NREL time series 139
C.3.1 NREL time series: Non-rotating campaigns, twisted configuration 139
C.3.2 NREL time series: Non-yawed campaigns, untwisted configuration, phase II data 141
C.3.3 NREL time series: Non-yawed campaigns, twisted configuration 141
C.3.4 NREL non-yawed campaigns, plots of time series 143
C.3.5 NREL time series: Yawed campaigns, untwisted configuration, phase II data 152
C.3.6 NREL time series: Yawed campaigns, twisted configuration 152
C.3.7 NREL yawed campaigns, plots of time series 154
C.4 NREL turbine and sectional coefficients 166
C.4.1 NREL, 2D profile coefficients and pressure distributions 166
C.4.2 NREL rotating profile coefficients, untwisted configuration, phase II data 166
C.4.3 NREL rotating profile coefficients, twisted configuration, phase III data) 166

C.4.4 NREL rotating profile coefficients, twisted configuration, phase IV data . . . 167
C.5 IC/RAL time series . . . 168
C.5.1 IC/RAL time series: Non-yawed campaign . . . 168
C.5.2 IC/RAL non-yawed campaigns, plots of time series . . . 168
C.6 RISØ time series . . . 169
C.6.1 RISØ time series: Non-yawed campaigns . . . 169
C.6.2 RISØ non-yawed campaigns, plots of time series . . . 169
C.6.3 RISØ time series: Yawed campaigns . . . 172
C.6.4 RISØ yawed campaigns, plots of time series . . . 172
C.7 RISØ turbine and sectional coefficients . . . 173
C.7.1 RISØ, 2D profile coefficients . . . 173
C.7.2 RISØ, rotating profile coefficients . . . 174
C.8 ECN time series . . . 175
C.8.1 ECN time series: Non-rotating campaigns . . . 175
C.8.2 ECN non-rotating campaigns, plots of time series . . . 175
C.8.3 ECN time series: Non-yawed campaigns . . . 177
C.8.4 ECN non-yawed campaigns, plots of time series . . . 179
C.8.5 ECN time series: Yawed campaigns . . . 191
C.8.6 ECN yawed campaigns, plots of time series . . . 192
C.9 ECN turbine and sectional coefficients . . . 203
C.9.1 ECN, 2D profile coefficients . . . 203
C.9.2 ECN, rotating profile coefficients . . . 203
C.10 DUT time series . . . 207
C.10.1 DUT time series: Non-rotating campaigns . . . 207
C.10.2 DUT non-rotating campaign, plots of time series . . . 207
C.10.3 DUT time series: Non-yawed campaigns . . . 209
C.10.4 DUT non-yawed campaigns, plots of time series . . . 211
C.10.5 DUT time series: Yawed campaigns . . . 223
C.10.6 DUT yawed campaigns, plots of time series . . . 229
C.11 DUT turbine and sectional coefficients . . . 241
C.11.1 DUT, 2D profile coefficients . . . 241
C.12 Mie University time series . . . 242
C.12.1 Mie time series: Non-yawed campaigns . . . 242
C.12.2 Mie non-yawed campaigns, plots of time series . . . 243
C.12.3 Mie time series: Yawed campaigns . . . 244
C.12.4 Mie yawed campaigns, plots of time series . . . 245
C.13 Mie University turbine and sectional coefficients . . . 249
C.13.1 Mie University, rotating coefficients . . . 249
C.13.2 Mie University, 2D coefficients . . . 249

APPENDIX D. MODEL DESCRIPTION OF ECN TURBINE 251
D.1 Basic machine parameters . . . 251
D.2 Rotor . . . 251
D.2.1 Geometry . . . 251
D.2.2 Aerodynamics . . . 259
D.2.3 Structural properties . . . 259
D.3 Power train . . . 262
D.3.1 Layout . . . 262
D.3.2 Characteristics . . . 262
D.4 Tower . . . 262
D.4.1 Main characteristics . . . 262

D.5 Control systems . . . 263
D.5.1 Power control . . . 263
D.6 Measurements at turbine operation . . . 263
D.6.1 Profile data . . . 263

APPENDIX E. MODEL DESCRIPTION OF IC/RAL TURBINE 267
E.1 Basic machine parameters . . . 267
E.2 Rotor . . . 267
E.2.1 Geometry . . . 267
E.2.2 Aerodynamics . . . 271
E.2.3 Structural properties . . . 272
E.3 Power trains . . . 272
E.3.1 Layout . . . 272
E.3.2 Characteristics . . . 272
E.4 Tower . . . 273
E.4.1 Main characteristics . . . 273
E.5 Control systems . . . 273
E.5.1 Power control . . . 273
E.5.2 Yaw control . . . 273

APPENDIX F. MODEL DESCRIPTION OF NREL TURBINE 275
F.1 Site data . . . 275
F.2 Basic machine parameters . . . 275
F.3 Rotor . . . 275
F.3.1 Aerodynamics . . . 276
F.3.2 Structural properties: . . . 276
F.4 Power train . . . 278
F.4.1 Layout . . . 278
F.4.2 Characteristics . . . 278
F.5 Tower . . . 281
F.5.1 Main characteristics . . . 281
F.6 Control systems . . . 281
F.6.1 Power control . . . 281
F.6.2 Yaw control . . . 281
F.6.3 Remaining control systems . . . 281
F.7 Modal Analysis . . . 281
F.8 Measurements at turbine operation . . . 281
F.8.1 Power curve . . . 281
F.8.2 Profile data . . . 282

APPENDIX G. MODEL DESCRIPTION OF RISØ TURBINE 293
G.1 Basic machine parameters . . . 293
G.2 Rotor . . . 293
G.2.1 Geometry . . . 293
G.2.2 Aerodynamics . . . 293
G.2.3 Structural properties . . . 297
G.3 Power train . . . 297
G.4 Tower . . . 298
G.4.1 Main characteristics . . . 298
G.5 Control Systems . . . 298
G.5.1 Power control . . . 298
G.5.2 Yaw control . . . 298

G.6 Measurements at turbine operation . . . 298
G.6.1 Power curve . . . 298
G.6.2 Profile data . . . 299

APPENDIX H. MODEL DESCRIPTION OF DUT TURBINE 301
H.1 Basic Machine Parameters . . . 301
H.2 Rotor . . . 301
H.2.1 Geometry . . . 301
H.2.2 Aerodynamics . . . 301
H.2.3 Structural Properties . . . 310
H.3 Power train . . . 310
H.3.1 Layout . . . 310
H.3.2 Transmission . . . 310
H.3.3 Braking systems . . . 310
H.3.4 Electrical system . . . 310
H.3.5 Characteristics . . . 311
H.4 Tower . . . 311
H.4.1 Main Characteristics . . . 311
H.5 Control System . . . 312
H.5.1 Power Control . . . 312
H.5.2 Yaw Control . . . 312
H.5.3 Remaining Control Systems . . . 312
H.6 Blade structural distributions . . . 318

APPENDIX I. MODEL DESCRIPTION OF MIE TURBINE 319
I.1 Basic machine parameters . . . 319
I.2 Rotor . . . 319
I.2.1 Geometry . . . 319
I.2.2 Aerodynamics . . . 320
I.2.3 Structural properties . . . 320
I.3 Power train . . . 320
I.4 Tower . . . 321
I.5 Control Systems . . . 322
I.5.1 Power control . . . 322
I.5.2 Yaw control . . . 323
I.6 Measurements at turbine operation . . . 323
I.6.1 Power curve . . . 323
I.6.2 Profile data . . . 324

APPENDIX J. COMPARISON OF ANGLE OF ATTACK METHODS FOR NREL MEASUREMENTS 329
J.1 General . . . 329
J.2 Comparison of NREL power curve with b.e.m. calculations . . . 329
J.3 Results obtained with inverse b.e.m. method . . . 331
J.4 Results obtained with power method . . . 336
J.5 Results obtained with the stagnation (XFOIL) method . . . 343
J.6 Results obtained with the stagnation(windtunnel) method . . . 347
J.7 Recommendation on methods . . . 352

1. INTRODUCTION

This report describes the work which was performed in IEA Annex XIV 'Field Rotor Aerodynamics' and in IEA Annex XVIII 'Enhanced Field Rotor Aerodynamics'. In these Annexes the following institutes participated:

- Centre for Renewable Energy Sources, CRES, Greece;
- Delft University of Technology, DUT Netherlands;
- Imperial College, IC and Rutherford Appleton Laboratory, RAL, United Kingdom;
- Mie University, Mie, Japan;
- National Renewable Energy Laboratory, NREL, USA;
- Netherlands Energy Research Foundation, ECN, Netherlands (Operating Agent);
- RISØ National Laboratory, Denmark.

All these institutes have experimental facilities at which detailed aerodynamic measurements are performed on full scale horizontal axis wind turbines. These measurements aim at a better understanding of the aerodynamic behaviour of a wind turbine. A better understanding is required because the prediction of wind turbine aerodynamics is a very complex task. Several aerodynamic phenomena, like (steady and unsteady) stall, dynamic inflow, tower effects, yaw effects etc. contribute to unknown aerodynamic responses. These unknown responses complicate the design of cost-effective and reliable wind turbines considerably. Turbines behave unexpectedly, experiencing instabilities, power overshoots, or higher loads than expected.

In conventional experimental programmes the behaviour of a turbine is analysed by means of measurements of integrated, total (blade or rotor) loads. These loads consist of an aerodynamic and a mass induced component and are integrated over a certain spanwise length. This gives only indirect information about the aerodynamics at blade element level. At the end of the 80's the insight grew that direct measurements of aerodynamic properties relevant for dynamic load codes (i.e. lift, drag and moment coefficients, inflow angle, inflow velocity at several radial positions) were needed. As a result the participants of IEA Annex XIV initiated the construction of full scale aerodynamic test facilities at which these properties can be measured.

However, such aerodynamic field experiments are typically very time consuming, expensive and complicated through the large volumes of data and the extensive data reduction which are required. Furthermore, each turbine configuraton that is investigated experimentally may exhibit a very different aerodynamic response characteristic. Hence, the results which are obtained from the very time consuming, expensive and complicated experiments may have only a limited validity.

For this reason it was considered very advantageous to cooperate in these experiments. This cooperation is established in the IEA Annex XIV 'Field Rotor Aerodynamics' which commenced in 1992 and lasted until 1997. In IEA Annex XIV, the only participants were DUT, ECN, IC/RAL, NREL and RISØ.

The cooperation enabled the creation of an extensive database of aerodynamic measurements. This base provides unique aerodynamic data for a large number of wind turbine configurations, which can be used for model validation and model development. The resulting insights and models will have more general validity than those obtained from the experimental programs independantly.

Furthermore, the project served as a platform where very specific knowledge associated with aerodynamic measurements could be exchanged. This has been very instructive for all participants by which the experimental programs could be accelarated.

After the succesfull completion of IEA Annex XIV in 1997, the database has been made available for outside parties. The database has been supplied under the condition that feedback on the experiences with the measurements should be given to the participants of IEA Annex XIV. As such it was anticipated that new experiences of users could improve the quality of the database. Meanwhile Mie University from Japan and CRES from Greece initiated new measurement programs, where new measurements from DUT were still expected. As a consequence IEA Annex XVIII was initiated in which the maintenance of the database (partly on basis of recommendation from users) and the storage of new measurements were the main objectives. In IEA Annex XVIII IC/RAL was withdrawn but Mie University and CRES were added as participants.

In this final report, both IEA Annex XIV and IEA Annex XVIII are described. As a matter of fact the present report is based on the IEA Annex XIV report and as such many chapters remained unchanged from [1].

In the report, several items are adressed:

- The objectives of IEA Annex XIV and XVIII are described in chapter 2.
- The workprocedure is described in chapter 4.
- A description of all experimental facilities, including the measurement procedure is given in section 5. The description of the facilities is supplied by the participants. All contributions cover similar topics, but there are some differences in the degree of detail. A detailed aeroelastic description of all turbines involved in IEA Annex XIV is presented in Appendix D to Appendix I;
- When applying the results of the database, it should be realised that the mutual comparison of measurements from the base is complicated by the fact that the angle of attack and the dynamic pressures have been manipulated differently by the several participants. This issue is addressed in the chapters 6 and 7;
- A global description of the database is given in chapter 8. The harmonisation which had to take place in order to allow the user an easy access to the base is also described in this section. Among others, the file formats, the file types and the file names are explained. The prescribed conventions and notations are given in Appendix A. Note that, unless otherwise stated, these conventions and notations have been applied throughout the present report too;
- The experiences of the users are summarized in section 9;
- At the end of IEA Annex XVIII, individual institutes and consortia started preparations for, or even completed aerodynamic measurements, which are of a similar kind as the IEA Annex XIV/XVIII measurement, but which are taken in a wind tunnel environment. This is partly due to the fact that the IEA Annex XIV/XVIII measurements are performed in the open air, which makes the determination of the wind speed 'felt' by the turbine rather uncertain. This problematic will be discussed in section 10;
- The conclusions and recommendations which result from the project are presented in chapter 11.

2. OBJECTIVES OF IEA ANNEX XIV/IEA ANNEX XVIII

2.1 IEA Annex XIV

The objective of the IEA Annex XIV has been defined as the coordination of measuring programmes on the field rotor aerodynamic facilities of the participants in order to acquire the maximum of experimental data at minimum costs. As a result of the project, a base of experimental data was created which should serve as a basis for:

- the validation and development of design codes and
- the design of stall controlled turbines.

Although the main objective of IEA Annex XIV has been on the field of stall aerodynamics, the database of experimental data was also useful for many other purposes. Among others the aerodynamics of 'pre-stall' conditions, parked conditions, tower shadow and yaw misalignment is measured.

2.2 IEA Annex XVIII

The objectives of IEA Annex XVIII are basically similar to those of IEA Annex XIV. Emphasis was put on the maintenance of the database, on basis of the feedback which was given by the users of the database. Furthermore the storage of new measurements into the database was an important objective.

3. PARTICIPANTS

The following parties participated in IEA Annex XVIII:

- Centre for Renewable Energy Sources, CRES, Greece;
- Delft University of Technology, DUT Netherlands;
- Mie University, Mie, Japan;
- National Renewable Energy Laboratory, NREL, USA
- Netherlands Energy Research Foundation, ECN, Netherlands (Operating Agent)
- RISØ National Laboratory, Denmark.

DUT, NREL, ECN and RISØ participated in both IEA Annex XIV and Annex XVIII. In IEA Annex XIV, Imperial College together with Rutherford Appleton Laboratory, RAL was also a participant, but they were withdrawn from IEA Annex XVIII.

4. WORK PROCEDURE

The main objective of the IEA Annexes was to create an organized database of detailed aerodynamic measurements on several wind turbine configurations. In order to reach the objective, a number of different tasks were distinguished, which are listed below.

4.1 Definition of test matrix

In the initial phase of the IEA Annex XIV, the parties reached consensus about a joint program of measurements. The test matrix given below served as a guideline for the selection of the measurement campaigns (time series) to be supplied in the database, both in IEA Annex XIV as well as in IEA Annex XVIII.

	Re *) (-)	α_{mean} (^{o})	yaw angle (^{o})
ECN	1.8 10^6	-5 to + 40	$\pm$ 30 à 40
DUT	0.9 10^6	-5 to + 40	$\pm$ 30 à 40
NREL	0.7 10^6	-5 to + 40	$\pm$ 30 à 40
IC/RAL	1.0 10^6	-5 to + 40	
RISØ	1.0 10^6	-5 to + 40	$\pm$ 30 à 40
Mie	0.5 10^6	-5 to + 40	$\pm$ 30 à 40

*) Reynolds number at rotating conditions at 70% R;

It was agreed that rotating measurements should be supplied for:

- Mean yaw angle $\approx$ zero. This yields a more or less constant angle of attack.
- Mean yaw angle $\neq$ zero; In these campaigns the angle of attack variations are deliberately triggered.

Note that it was intended to supply measurements with pitch variations too. These measurements could be supplied by ECN and NREL. Within the course of the IEA Annexes the priority of these measurements was downgraded and in order to limit the amount of work these measurements were skipped.

At a later stage of IEA Annex XIV it was agreed that, apart from rotating measurements some parties would also supply measurements for non-rotating conditions.

Furthermore, the measurements of airfoil coefficients (2D values as well as rotating values) was added to the database in IEA Annex XVIII. Note that CRES has not been able to supply measurements within the project period.

4.2 Conventions and notations

To interpret the measurements it was considered extremely useful to have agreement on the conventions and notations. To this end a document was prepared which describes the conventions and notations. The document is annexed in Appendix A. It originates from the document which was prepared for the JOULE projects 'Dynamic Inflow', [2]. Special attention was paid to the rotational direction of the turbines. Most (but not all) of the turbines in the project rotated counter-clockwise (looking downwind to the rotor). This complicates the mutual comparison of results in particular under yawed conditions. For this reason some

coordinate systems were transformed such that a mutual comparison of results was possible. The conventions and notations from Annex XIV were also used as a basis for the conventions to be used in the JOULE project 'Dynamic Stall And Three Dimensional Effects', [3].

4.2.1 Format of the files, filetypes, filenames

In order to facilitate the selection of signals from a file, it was considered essential that all files were supplied in the same format. Also the file names and file types were harmonized. This item is further discussed in section 8.

It turned out that the large datafiles led to a 'psychological barrier' for potential users. This was mainly caused by the decision to exchange files which contain a huge amount of measured information, although in most cases only a selection of the data is required. However, it was considered impractical to prepare specific data files for different users. Therefore much effort was spent on the agreement of a common format and common conventions and the documentation of the database. This includes statistical overviews and time traces plots of every file. This made it possible for all users to extract the relevant information in a relatively convenient way. Within the course of IEA Annex XVIII some Fortran 77 programs were stored into the database by which it was possible to extract the most popular signals from the RISØ and NREL datafiles.

4.3 Selection of campaigns

In order to fill out the test matrix, campaigns were selected on basis of statistical data (mean values, minimum values, maximum values and standard deviations) of a selected number of signals.

4.4 Supply, storage and documentation of data files

The data is stored on an ECN internet site and on CD-ROM. In IEA Annex XIV the results could also be retrieved from an ftp site by anonymous ftp. Several data exchange rounds appeared to be necessary before a satisfactory result was achieved. The content of the database was documented by means of status reports. In these reports, the format of every file was documented together with the statistical overviews of the several campaigns, see Appendix C.

4.4.1 Machine data report

For the interpretation of the measured data it was considered useful to have the availability of the aerodynamic, geometric and elastic data of all the facilities which are involved in the project. Therefore a questionnaire was made which specifies the machine data of all the turbines which are involved in the project. The results are reported in Appendix D to Appendix I.

4.5 Angle of attack report

One of the main problems in aerodynamic field experiments is the definition of the angle of attack. In wind tunnel experiments, the angle of attack is easily known from the wind tunnel set angle. However in rotating conditions such an angle is not known. Often the angle of attack is measured with a flow sensor some

distance ahead of the blade element. This angle however cannot be translated straightforwardly to an equivalent wind tunnel angle of attack and corrections have to be applied. These corrections are different for every participant. Other participants derived the angle of attack from the pressure distribution. Consequently the comparison of the measurements from the different participants may be obscured by differences in the definition of the angle of attack.

Within the course of IEA Annex XIV, a discussion document about this subject has been prepared by ECN. This document served as food for discussion at several meetings. This issue is further adressed in section 6.

4.6 Meetings

In IEA Annex XIV, a total of 7 meetings (including a preparatory meeting) have been held. In IEA Annex XVIII 6 meetings were held. The meetings were attended by all the institutes who were involved in the Annex and they were always held at the institutes and a visit to the experimental facilities was one of the agenda points.

Detailed minutes of every meeting were prepared.

A short report on the various meetings can be found in Appendix B.

4.7 IEA Annex XVIII: Storage of the database and access to the database

After the completion of IEA Annex XIV, the database has been made available. Until October 1999, most users received the database on a CD-ROM. The CD-ROM was supplied with an accompanying letter in which feedback was requested from the user on the experiences obtained with the database. In October 1999 the database became available on the Internet site. Access to the Internet database itself was only given after a registration form has been filled out in which feedback on the experiences with the database was promised.

It should be emphasised that the arrangements are based on a 'Gentleman's (Ladies) agreement. As such they rely on the goodwill of the users.

5. DESCRIPTION OF EXPERIMENTAL FACILITES

5.1 ECN test turbine

5.1.1 Introduction

The aerodynamic experiments at ECN were performed in two different phases:

- The non-rotating phase (1993-1994): In this phase the blade was mounted vertically on a non-rotating facility in the free stream. This test aimed at acquiring data at free stream conditions without rotational effects. Furthermore the instrumentation could be tested relatively easy in order to prepare for the next phase:
- The rotating phase (1995-1997). In this phase the blade was mounted on the HAT-25 experimental wind turbine and data were acquired under rotation. Furthermore some non-rotating measurements have been repeated. In this report the measurements from the rotating phase are reported only.

More information on the facility can be found in [4] and [5].

5.1.2 Global characteristics of facility

- Blade: Aerpac 25 WPX blade mounted on the HAT-25 experimental wind turbine, see figure 5.1.
- Number of blades: 2
- Blade span (from flange to tip) = 12.1 m
- Rotor diameter = 27.44 m
- Blade profile: NACA44xx
- Blade with twist and taper: Twist $\approx$ 12 degrees, root chord = 1.5 m, tip chord = 0.412 m.
- Pressure tap measurements around profiles at 3 different radial stations, see figure 5.2.
- Inflow angle and inflow velocity measured at inboard station with 5 hole probe, see figure 5.2.

Location

The HAT-25 wind turbine is located at ECN near Petten in the Netherlands. Figure 5.3 gives a picture of the site. The prevailing wind direction is from South-West, at which most of the measurements are taken. In this direction, the terrain upstream of the turbine is obscured by dunes over around 600 m. As a result, the turbulence intensities at the site may depend strongly on the conditions. Generally, the values of the turbulence intensities are between 5% and 20%.

5.1.3 Instrumentation

Blade instrumentation:

- Pressure taps at 3 rotor blade sections, see [4].
  These taps are positioned at 36%, 64% and 82% of the rotor radius.
  All 3 sections are measured simultaneously:
  There are 47 taps per station, see figure 5.4.
  Extreme care was taken to manufacture taps with a surface roughness of the order of the one of the rotor blade (10 μm). The diameter of a pressure tap is

Figure 5.1 *ECN test facility*

1mm. A so called minitube connects a pressure tap to a pressure transducer. Each minitube is mounted perpendicular and flush to the local rotor blade surface. The length of all minitubes is 1.1 m and their internal diameter is 1 mm. For this kind of tubes it has been found experimentally that acoustic damping is small for frequencies up to 40 Hz, [6]. The pressures at the surface of the blade are measured with the Scannivalve Hyscan 2000 system, which has a scan rate up to 100 kHz. A total of 9 Scanivalve ZOC-14 pressure scanners are used to measure these blade pressures. 5 Scanivalve ZOC-14 pressure scanners have a full-scale range of about 2.5 kPa (30% station, and pressure sides of the 60% station and the 80% station), 2 Scanivalve ZOC-14's have a range of about 5 kPa (suction side of the 60% station), and 2 Scanivalve ZOC-14's have a range of about 12 kPa (suction side of the 80% station). The absolute error of the scanners is about 5.0 Pa, 7.5 Pa and 5.6 Pa, respectively. The ZOC-14 modules are mounted inside the rotor blade. Six modules (those of the 30% and the 60% station) are operating in a thermally

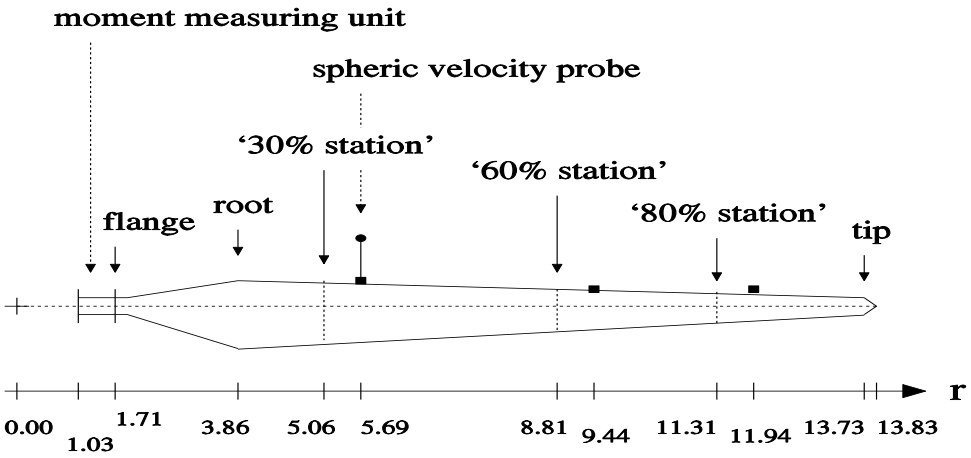

Figure 5.2 *Instrumentation of ECN blade*

controlled environment (Scanivalve TCU) and three modules (the ones at the 80% station) are mounted on a heating element in order to minimise temperature differences. For calibration, a pressure generator (Scanivalve Calmod 2000) in combination with a secondary standard (Mensor Model 11603) is used, see below.

For each station the 48th sensor is short-circuited, which means the measuring side of the sensor is connected to the reference side of the sensor. (The other 47 sensors are connected to the 47 taps.) As a result, the pressure reading of this sensor should be zero. If this reading is not zero, an error in the Hyscan system may have occurred. Inspection of the pressure readings from a short-circuited sensor thus allows for an assessment of the quality of the measured pressure data.

An automatic purge option was available.

The pressures are measured relative to an unknown reference pressure. The pressure inside the blade near the hub is used as reference.

- Spheric velocity probe: The magnitude and the direction of the flow towards a rotor blade section is measured with a spheric velocity probe. A spheric velocity probe consists of a sphere and a rod (figure 5.5). The sphere contains the pressure taps and the pressure sensors. The cylindrical rod connects the sphere to the leading edge of the rotor blade.

  At the surface of the sphere five pressure taps are located: one centre tap and two pairs of symmetrically opposite taps (figure 5.6). The centre tap is located on the x axis of the sphere. The two pairs of taps are in two perpendicular planes; the position of a tap in a plane is given by the base angle. (The base angle is the angle between the tap and the centre tap.) For a spheric probe to work well it is essential that the centre hole is on the x axis and the four base angles are equal. The specifications for a spheric probe are described separately [7].

  The pressure difference between the absolute pressure in a tap and a reference pressure is measured by a Scanivalve ZOC23 pressure sensor with a range of

Figure 5.3 *The site where the HAT-25 experimental wind turbine is located. Also indicated is the mast where wind speed and wind direction are measured*

about 2.5 kPa and an absolute error of about 5 Pa. This sensor is mounted inside the sphere and connected to the Hyscan 2000 system. The ZOC23 module is *not* operating in a thermally controlled environment. In order to mimimise temperature differences, foam (Neoprene) was put into the sphere. In addition, a platinum resistance thermometer element (Rössel RL-4330/1-B-1) was mounted on the ZOC23 module so that temperature changes can be monitored. The output of this thermometer element was connected to the Hyscan 2000 system via the Scanivalve EIM, see below. The relation between AD counts and engineering units was determined by calibration; the corresponding calibration coefficients were included in the 'initfile' of the data processing.

The layout of the eight sensors of the ZOC23 module is as follows: three sensors are connected to each of tap #1, #2 and #3; two sensors are connected to tap #4; two sensors are connected to tap #5; and one sensor is connected to the reference. This layout ensures two pressure readings are available from the taps which are most sensitive to changes in the angle of attack. (In the analyses of the current field measurements the computation of the probe inflow velocity and direction was however based on one reading only.) In addition, it ensures a short-circuited pressure sensor is available, which allows for an inspection of the quality of the data.

The sphere has a diameter of 58 mm and the base angle of the pressure taps is 14.8°. The rod has a length of 1.07 m and is mounted at a radial position

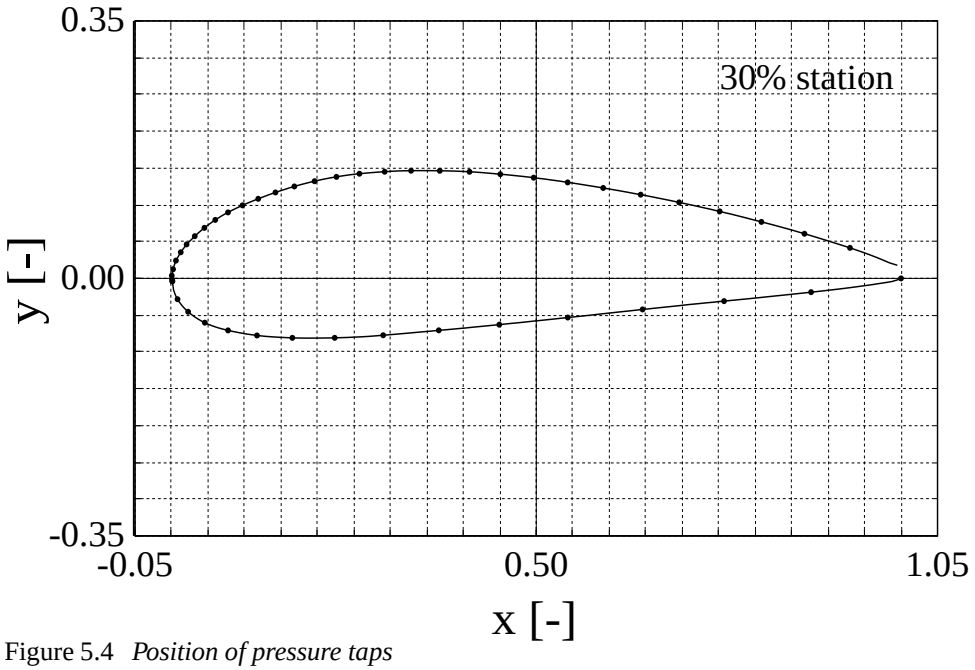

Figure 5.4 *Position of pressure taps*

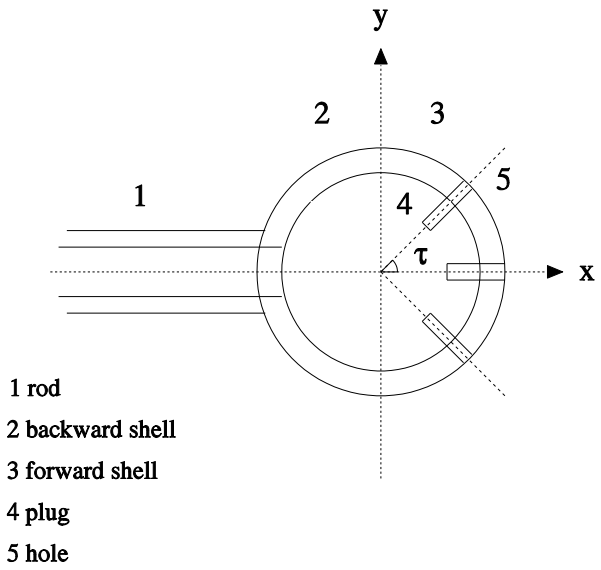

Figure 5.5 *A schematic of the spheric probe. Indicated is the base angle τ.*

r =5.69 m (42% of the rotor radius; 35% station). It is oriented at 13.5° to the chord and at 3.0° to the cross-section of this station; the probe axis crosses the local chord at $x/c = 0$. Figure 5.7 shows a schematic of the spheric velocity probe at the 35% station of the rotor blade. The construction, calibration and data handling of this probe are described separately, see [8].

Additional signals

- Wind turbine signals
  - Nacelle orientation
  - Rotor speed
  - Rotor azimuth

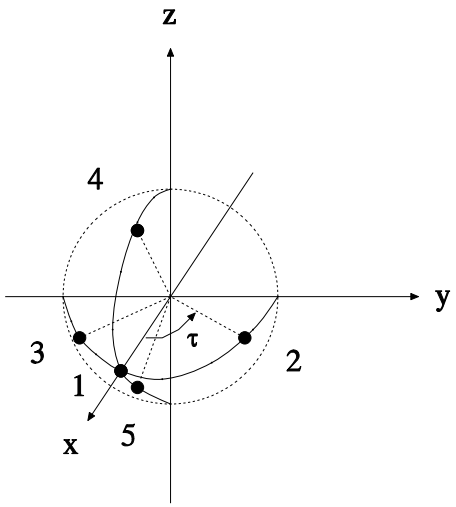

Figure 5.6 *The location of the pressure taps at the surface of the sphere of the spheric probe. Indicated is the base angle τ.*

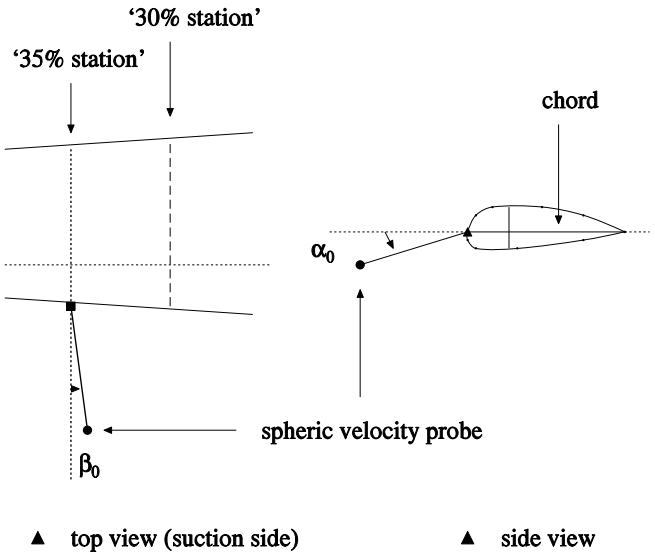

Figure 5.7 *The location of the spheric velocity probe at the 35% station. Indicated are the probe orientation angles $\alpha_0 = 13.5°$ and $\beta_0 = 3°$.*

  - Blade pitch angles
  - Rotor shaft torque
  - Axial force on the rotor
  - Root lead-lag bending moments
  - Root flap bending moments
- Ambient conditions
  - Wind speed at three heights:
    - V_{hub}; Ambient wind speed at hub height;
    - V_{up}; Ambient wind speed at h = hub height + 10 m;
    - V_{low}; Ambient wind speed at h = hub height - 10 m;

The wind speeds are measured with mast B which is indicated in figure 5.3
- Wind direction at h = hub height + 10 m
- Atmospheric pressure
- Air temperature

Measurement system components

A detailed description of the instrumentation is given in [4] and [5]. As stated above, the aerodynamic measurement system is based on the Scannivalve's Hyscan system.

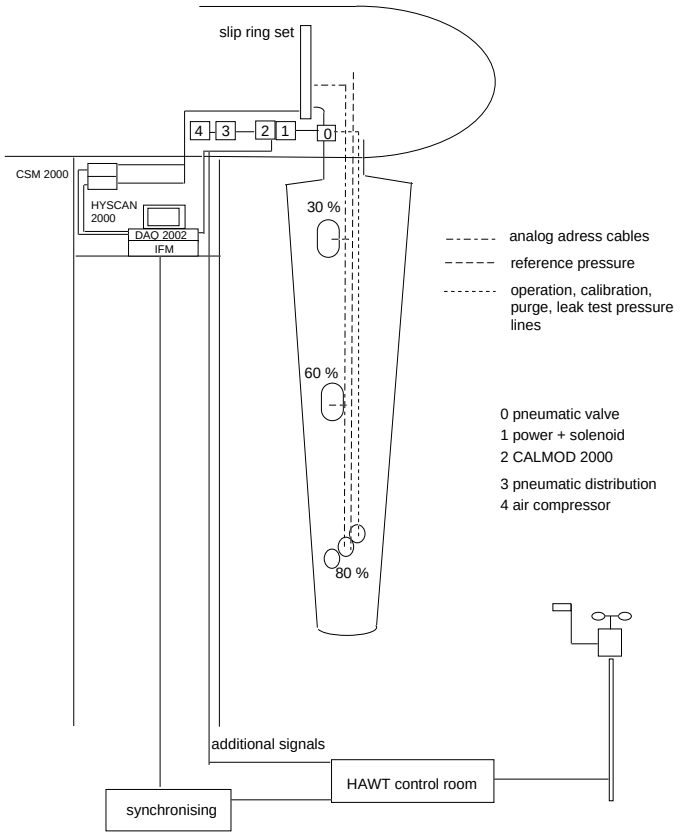

Figure 5.8 *ECN: Measurement system*

Apart from the pressure scanners this system consists of (see also figure 5.8):

- DAQ2002 data acquisition system.
  The DAQ2002 is a self contained, PC based, high speed data acquisition system. Measurements are conditionally stored on the hard disc of the PC and then transmitted to the host computer. The PC is located on a platform approximately 3 metres below the rotor axis.
- IFM 2000
  The IFM 2000 is required when using ZOC modules with the HYSCAN system. It is an interface module that contains: line drivers and addressing circuitry, the frame list memory, multiplexers and amplifiers, interval times and A/D clock logic.
- CALSYS 2000 Calibration system:

This system consists of the CALMOD 2000 Calibrator Modules and the PSC 2000 Power Solenoid Conrol Module.
The CALMOD 2000 is designed to generate known pressures for individual pressure sensor correction. The CALMOD 2000 can perform quick or full calibrations: Zero calibration, 4 point positive calibration, 4 point negative calibration, or a full 7 point calibration. This calibration system operateas in a closed loop routine with the DAQ 2002 yielding minimum calibration times, system leak detection, and data reliability.
The CALMOD 2000 is placed in the nacelle of the turbine. The ZOC modules in the blade are accessable via a pressure valve which is mounted close to the root of the blade. The test sessions include calibration sequenses when the turbine in stopped. With the aid of the pressure valve, the CALMOD 2000 is adapted to the ZOC modules.
The PSC 2000 Power Solenoid Control Unit provides 24 volt power for the calibrator modules and the solenoids for the ZOC calibration valves. The PSC 2000 also allows pneumatic control to ZOC modules.

- CSM 2000 Cable Service Unit:
  The CSM 2000 is used to service the ZOC modules. The CSM 2000 provides DC power and can support a maximum of 8 ZOC electronic pressure scanners. The CSM receives address information from the IFM 2000 and distributes it to the ZOC modules. It also returns the analog signals from the ZOC modules to the IFM 2000. A built in power supply provides +/- 15 VDC power to the modules.

The data acquisition system for the additional signals is located in the HAT control room, see figure 5.3. The aerodynamic measurements and the measurements of the additional signals are synchronised, so that they can be merged.

Transfer of all rotor signals is achieved through slip-rings.

5.1.4 Measurement speed

All data channels which originate from the Hyscan system are sampled with 128 Hz or 64 Hz effectively. The additional signals are sampled with 64 Hz or 8 Hz and oversampled to 128 Hz or 64 Hz, whichever needed.

5.1.5 Data reduction

Pre-processing of acquired data:

- Three-point median filter, and
- First-order Butterworth filter
  (bandwidth 10 Hz)

The effect of filtering is illustrated in figure 5.9 and 5.10.

For each station the measured pressure differences are reduced to

- Pressure distributions,
- Normal forces per unit length,
- Tangential forces per unit length,
- Inflow velocities, and
- Angles of attack.

For the velocity probe the measured pressure differences are reduced to

- Inflow velocities,
- Angles of attack, and

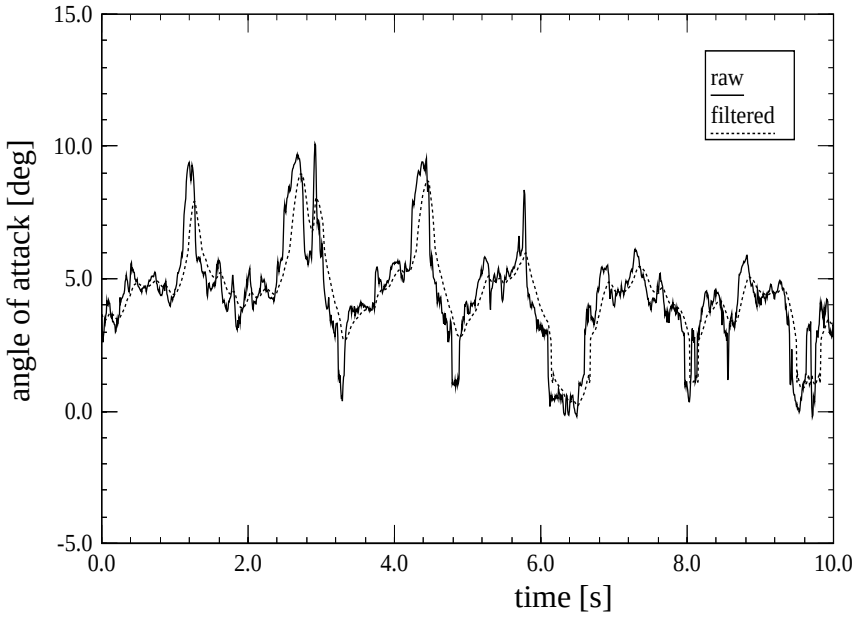

Figure 5.9 *ECN: The effect of applying the filter seen on a time trace of the measured angle of attack*

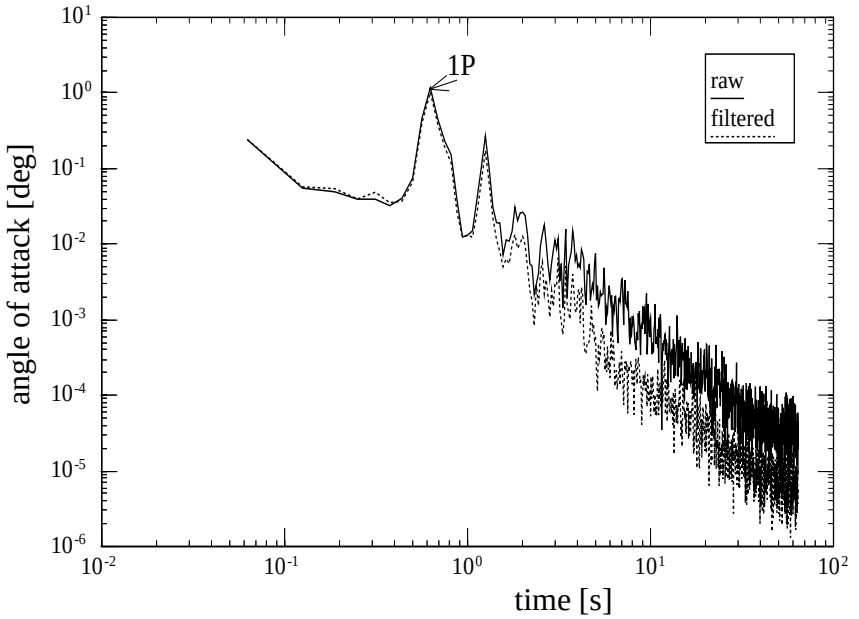

Figure 5.10 *ECN: The effect of applying the filter seen on a power spectrum of the measured angle of attack*

- Cross-flow angles.

Pressure distribution

$p'_j \equiv p_j - p_{ref}$ = pressure difference measured in the jth pressure tap.

$p'_{j,cor} \equiv p'_j + p_{cent}$ = compensated pressure difference, i.e. the pressure difference in the jth tap compensated for the pressure due to the centrifugal force

$$p_{cent} = p_a \left(\exp\left(\frac{\rho\Omega^2}{2p_a}(r_t^2 - r_m^2) \right) - \exp\left(\frac{\rho\Omega^2}{2p_a}(r_r^2 - r_m^2) \right) \right),$$

ρ = air density,
r_t = radial position of tap,

r_m = radial position of sensor membrane,
r_r = radial position of the entrance to reference tube.

Pressure coefficient

$$c_{p,j} \equiv \frac{p'_{j,cor}}{p'_{ST,cor}},$$

$p'_{ST,cor}$ = stagnation pressure
(i.e. the largest positive pressure difference in the compensated pressure distribution).

Normal force per unit length:

$$n = \sum_{j=PS} p'_{j,cor} x'_j c - \sum_{j=SS} p'_{j,cor} x'_j c,$$

x'_j = non-dimensional length corresponding to the jth pressure tap,
c = chord length.

Normal force coefficient:

$$c_n \equiv \frac{n}{p'_{ST,cor} c}.$$

Tangential force per unit length:

$$t = \sum_{j=LE} p'_{j,cor} y'_j c - \sum_{j=TE} p'_{j,cor} y'_j c,$$

y'_j = non-dimensional length corresponding to the jth pressure tap.

Tangential force coefficient:

$$c_t \equiv \frac{t}{p'_{ST,cor} c}.$$

Stagnation angle of attack:
Direction of the flow towards an airfoil section is obtained from the position (x_{ST}, y_{ST}) of the stagnation point on the airfoil surface

$$\alpha_{ST} = \arctan\left(\frac{-y_{ST}}{x_M - x_{ST}}\right) + c_0 + c_1 x_{ST},$$

calibrated against pressure distributions measured in a windtunnel.

Error analysis on stagnation angle of attack on basis of a windtunnel calibration

$$\Delta\alpha_{ST} \leq 1\ ^\circ \text{ for } \alpha_{ST} \leq 10\ ^\circ$$
$$\Delta\alpha_{ST} \leq 2\ ^\circ \text{ for } 10\ ^\circ < \alpha_{ST} \leq 30\ ^\circ.$$

Inflow velocity:
The inflow velocity is the characteristic value of the speed of the flow towards a rotor blade section, which is obtained from the stagnation pressure:

$$U_{ST} \equiv \sqrt{\frac{2p'_{ST,cor}}{\rho}}.$$

Probe inflow velocity and probe angle of attack:
The magnitude and direction of the flow towards the spheric velocity probe in terms of

- Probe inflow velocity U_p,
- Probe angle of attack α_p, and
- Probe cross-flow angle β_p;

which are obtained by iteratively solving an estimative relation based on inviscid flow theory (no upwash correction).

Error analysis on probe inflow velocity and angle of attack On basis of a wind tunnel calibration:

$\Delta U_p = 0.4$ m/s at $U_p = 10$ m/s and
$\Delta U_p = 1.0$ m/s at $U_p = 35$ m/s;

$\Delta\alpha_p \leq 2.5°$ for $0° \leq \alpha_p \leq 30°$ at $U_p = 10$ m/s and
$\Delta\alpha_p \leq 1.5°$ for $0° \leq \alpha_p \leq 30°$ at $U_p = 35$ m/s.

5.2 IC/RAL test turbine

5.2.1 Global characteristics of facility

- Blade: LM - 8.5 blade mounted on a Windharvester wind turbine.
- Number of blades: 3
- Blade span (from flange to tip) = 8.2 m
- Rotor diameter = 17 m
- Blade profile: NACA632xxx
- Blade with twist and taper: Twist = 15 degrees, root chord = 1.09 m, tip chord = 0.445 m.
- Pressure tap measurements around profiles at 6 different radial stations, see figure 5.11.
- Inflow angle and inflow velocity is measured on 3 locations with 5 hole pitot probes, see figure 5.11 and 5.12.

Figure 5.11 *Instrumentation of IC/RAL blade*

Location

The experimental facility is located at the Rutherford Appleton Laboratory's wind site, about 80 km West of London: The Laboratory is set on a plateau to the north of a range of hills called The Ridgeway. From the turbine position (the base has an altitude of 135.82m) the following features may influence the wind:

- N to NE: Mix height buildings, the nearest large building being 20m high, 200m away

- East: A smooth grassed mound summit 150m about 150m away
- SE to W: Gentle gradient open farmland, the Ridgeway running East to West has a maximum altitude of about 220m, 1.5km away
- W to NW: Small woodland (about 300m away) with a low cropped field close to the turbine.

The prevailing winds are from the Southwest with an annual mean of about 4.5m/s and typically 17for the roughness is 0.03m.

5.2.2 Instrumentation

Briefly the instrumentation system consists of two loggers: One is situated in the hub, collecting data from the rotor, another logger collects data from ground fixed transducers. There is a communication link to allow remote control and file transfer with the hub based logger. The data from the loggers is synchronised with a pulse stream so that the separate data files can be merged together.

Hub mounted PC-based logger

The decision to mount a logger in the hub was made to reduce the need for a large number of slip-rings - about 40 tracks would have been needed - instead only: power, a communication link and a synchronisation pulse is needed.

The logger is based on an IBM-PC compatible passive backplane and has five boards:

- CPU and RAM (386-33 MHz and 16 MByte). The reasonably large memory allows temporary storage of up to about 7 Million samples in a 'RAM-disk'.
- Floppy disk emulator (1.44 MB ROM, 1.44 MB SRAM). The floppy disk emulator means the system has no moving parts and is sufficient to store control programs and the operating system.
- Serial communications (RS422, 288 kbaud). The communication allow a remote terminal and file transfer including programs and data from another PC.
- Video adapter. This allows bench use during development.
- Data acquisition and Control (14-bit, 16 channel, 100 ksamples/sec, five 16 bit counters). This collects data and provides control signals to the system of transducers.

Blade instrumentation

A new blade was purchased from LM Glasfiber, the manufacturer, into which the instrumentation has been installed. The main data comes from about 180 tappings on the blade, these are distributed as follows, see figure 5.11

- Six stations along the blade each with 26 tappings: The stations are arranged approximately square to the leading edge at 20%, 30%, 40%, 50%, 65% and 80% radius. There is a greater concentration of holes near the leading edge where the larger pressure gradients are found.
- Three inflow speed and direction probes: These are five hole Pitot probes mounted to protrude from the upwind side of the blade so that the point is about two-thirds of a chord ahead of the blade. The probes are 25 mm diameter with a hemispherical head with five tappings (one central and four at a 45 degree incidence), and a set of manifolded 'Static' tapping on the cylindrical body. The design is based on one found in [9]. Calibration data for these were collected in a separate wind tunnel experiment and were found to be independant of speed over the range expected on the turbine. The angle of attack calibration is very linear over a range of +/- 15 degrees and still smooth up to +/- 30 degrees, a

function based on angle of attack and the pressure readings from all six ports is calculated to represent the calibration.
- The positions of the tappings and probes were chosen based on modelling with a blade element model providing the angle of attack input to a two dimensional panel code. The resulting positioning for the surface tappings is typical of aerofoil experiments, however the position of the probes is perhaps novel, not being straight out from the leading edge. The panel code was used to indicate a velocity field around the section, and iterated through the likely range of angle of attack, then for each point the variance of direction compared with the incident flow was calculated. A region emanating from roughly a third of a chord behind the leading edge and in a direction about 45 degrees from the chord line on the pressure side had a region of minima, so the probe head is placed in this region oriented to aim at the mean inflow direction.

Tubing, pressure transducers and measuring speed

The surface pressure tappings and probe ports are connected by tubes (diameter 1mm, up to 1.3 m long) to 64 port differential Scannivalve pressure transducer blocks, each block serving two stations and one probe. These have 32 sensors each, a valving system (pneumatically operated) switches the sensors to look at two sets, thus covering the 64 inputs. Ths scanning between sensors is achieved (electronically) by multiplexing the input to the block's amplifier. The transducer blocks can operate at 20,000 samples per second, thus a scan of all 32 sensors will take just under 2 milliseconds. The blocks are enclosed in thermally controlled and insulated boxes to keep their temperature above condensation temperature and to maintain accuracy of the sensors.

Other measurements from the rotor

- Azimuth position: An incremental shaft encoder which gives 2880 pulses per revolution provides positional information and is used for the triggering of data scans.
- Root bending moments: Two strain gauge bridges for flatwise and edgewise moments have been included which can help to confirm summed blade forces.
- Temperatures: The pressure sensors' main source of error is due to drift from temperature effects, so as well as the thermal control, the temperature of the blocks are measured by platinum resistance thermometers (PRT). A separate PRT is mounted on the inner surface of the blade skin to give local temperature.
- Reference Pressure: This is included for on-line calibration of the main pressure transducers. It has very good linearity (< 0.01 % FSD) and repeatability.

Interfacing, Control and Signal Conditioning

The transducers require significant control, both electronic and pneumatic, this is needed for multiplexing and routing of reference and calibration pressures. This system includes custom digital electronics controlled by the loggin PC. The signal conditioning for the PRT's and strain gauges is included in this unit.

Software

This software is written in 'Turbo Pascal' with some assembler code subroutines for speed. The 'Turbo Pascal' development environment is installed on the hub logging computer to aid debugging, it is useful because it is very compact.

The data collection regimes and supervisory actions are controlled by first editing a 'Recipe' file, sending it to the hub-logger and then running the data collection

program based on these settings.

Communication link

The hub logger communicates, through Fibre Optic link to another PC, in the test site control building about 150 m away. A Fibre Optic link was chosen to be sure of no problems with range and to provide immunity for the site's quite high electromagnetic interferences.

Ground fixed measurements

The ground PC is in the same building as an existing logging system (from wind diesel research). During these experiments a pulse is sent from the hub synchronised with scans of the pressure sensors to trigger this logger - it measures:

- Electrical machine power from fast response (40 ms) power transducers.
- Yaw position from an analogue shaft encoder.
- Incident wind speed and direction from two meteorological masts, two diameters away from the turbine, the instruments are at hub height (15.5 m).
- Ambient air pressures and temperatures

5.2.3 Data reduction

- The MATLAB environment has been used to handle most of the data processing, thus the first process is to load the raw data files from the two logging systems
- There have been some problems with data corruption - some of the error were correctable coding errors and have been fixed, others have been corrected using multipoint median filters.
- The data has been calibrated to engineering units and the synchronisation (between the two streams) has been checked. The result has then been stored in the MATLAB format (IEEE double precision floating point) as the working set. No filtering has been carried out on this data.
- From the pressure data, the blade geometry and wind tunnel probe calibrations the following have been derived:
  - Section lift forces per unit length
  - Inflow direction and dynamic pressures at the probes

  These do not include corrections for centrifugal effects, thus the pressures are effectively as if they were measured at the sensor radius, which is approximately the same as the probe radius.

Notes:

- Lift forces are calculated using the fractional chord length positions of the tapping holes thus are: per unit span, per unit chord; thus all that remains to determine the coefficients is to divide by an appropriate dynamic pressure.
- The inflow measurement include the outwash angle (compared with the tangent) thus direction and velocity CAN be corrected according to the geometry of the blade.
- Inflow and lift coefficients have been obtained as follows:
  - The air density is assumed constant over the site thus the site meteorological measurements are used to obtain an air density, thus the velocity at the probe can be determined. This is transferred to test section radius by adding (or subtracting) the difference in radial velocities. The dynamic pressure is then recalculated as two components. The angles are corrected assuming that the probe remains at the same proportional relative position compared with the chords at its radius and at the test radius. The Angle of Attack (at transferred

probe position) is then:

$$\alpha_{Pr} = \arctan(\frac{V_{ax}}{V_{tan}}) - \theta \tag{5.1}$$

with V_{ax} the axial speed and V_{tan} the tangential speed and the dynamic pressures are:

$$q_{Pr,a} = 1/2 \cdot \rho \cdot (V_{ax}^2 + V_{tan}^2) \tag{5.2}$$

$$q_{Pr,b} = 1/2 \cdot \rho \cdot (V_{outwash}^2) \tag{5.3}$$

with $V_{outwash}$ the outwash speed.

- Using the above angle and the angle of the section lift force:

$$\alpha_L = \arctan(\frac{t}{n}) \tag{5.4}$$

a quadratic relation is fitted for low angles and extrapolated to larger angles. This assumes that the pressure distribution represents the components of lift found in inviscid theory (which always has its lift force perpendicular to the flow).

- The dynamic pressure measured at the probe ($q_{Pr,a}$, above) has been used as the denominator for calculation of the coefficients. This is known not to be accurate as upwash also affects this - a similar process to the angle of attack correction is needed.
  A study with a reliable 2-D Navier-Stokes solver may be interesting to support or correct this method - the components of force caused by skin friction must be treated separately in the analysis - standard aerofoil packages automatically sum them before presentation to the user.

Figure 5.12 *Instrumentation of probes at IC/RAL blade*

5.3 NREL test turbine

The aerodynamic experiments at NREL were performed in four different phases, see below and [10]. Measurements from the phases II, III and IV are stored into the database.

5.3.1 Global characteristics of facility

- Blade: NREL in house, mounted on an experimental turbine.
- Number of blades: 3
- Blade span (from flange to tip) = 4.521 m
- Rotor diameter = 10 m
- Blade profile: NREL S809
- Two tests:
  - Phase II: Blade without twist and taper
  - Phase III and IV: Blade without taper but with twist: Twist = 45 degrees.
- Detailed pressure tap measurements around profiles at 4 (Phase II) or 5 (Phase III and IV) different radial stations. Pairs of taps at 6 (Phase II) or 10 (Phase III and IV) different radial stations.
- Inflow angle is measured at the 4 or 5 primary stations with wind vanes (Phase II and Phase III) or 5-hole probes (Phase IV). Inflow velocity is measured at the 4 or 5 primary stations with pitot probes (Phase II and Phase III) or 5-hole probes (Phase IV).

Location
All atmospheric testing was conducted at the National Renewable Energy Laboratory's (NREL) National Wind Technology Center (NWTC) located 10 miles north of Golden, Colorado, U.S.A. Winter winds are dominant at this site from a prevailing direction of 292 degrees from True North. Although the local terrain is flat, with grassy vegetation extending over 0.8 km upwind, the site is situated approximately 5 km from the base of the Rocky Mountains which are located directly upwind. The wind turbine was unobstructed by other wind turbines or structures.

Experiment overview
The Combined Experiment was begun in 1987 and continues today under the title of the Unsteady Aerodynamics Experiment. The program was divided into four phases. Phase I planning began in 1987 and resulted in valuable knowledge and experience with these types of measurements (Butterfield et al., [11]). Untwisted blades were used again in Phase II which began in the spring of 1989, and the pressure instrumentation was expanded to four span locations. Optimally twisted blades were designed for Phase III of the project which began in 1993. The fourth phase, initiated late 1995, also used the twisted blades but the flow angle measurements were improved. The significant differences between the Phase II, Phase III, and Phase IV configurations are described in table 5.1 below.

Test Turbine
The Unsteady Aerodynamics Experiment Test Turbine is a modified Grumman Wind Stream 33. It is a 10-m-diameter, three-bladed, downwind, free-yaw turbine equipped with full span pitch capability that can be manually controlled during the testing to provide fixed-pitch (stall-controlled) operation at any pitch angle desired. The turbine is supported on a guyed-pole tower, 0.4064 m in diameter,

Table 5.1 *Unsteady Aerodynamics Experiment Configuration Differences*

	Phase II	Phase III	Phase IV
Blades	Untwisted	Twisted	Twisted
Local Flow Angle (LFA) Measurement Device	Flag	Flag	5-Hole Probe
Span locations instrumented with LFA sensors	4	4	5
Span locations instrumented with pressure taps	4	5	5
Azimuth angle measurements and RPM calculations	Poor	Good	Good
Meteorological instrumentation	Vertical Plane Array	Horizontal and Vertical Shear	Horizontal and Vertical Shear
Selections of data during which yaw brake engaged	Yes	No	Yes
Campaign Duration	5 minutes	10 minutes	10 minutes
Boom extension and camera mounted on hub	Yes	No	Yes
Video	Yes	No	Yes

that is equipped with a hinged base and gin pole to allow it to be tilted down easily. An electric winch is used to lower and raise the system during installation. A manually operated yaw brake was added to allow fixed yaw operation at arbitrary yaw positions. This yaw retention system had a strain-gaged link to measure yaw moments in Phase II and Phase IV. A relatively constant yaw angle and non-zero yaw moment indicates the yaw brake was engaged during data acquisition. Also added was a mechanical caliper rotor brake system that could be operated manually from the control shed. A complete listing of turbine specifications may be found in Appendix F.

The drive train is unchanged from the original Grumman configuration. The rotor operates at a nominal 72 rpm. Low-speed shaft torque is transferred through a 25.1:1 gearbox ratio to the high-speed shaft which is connected to the generator. The inertia of the Phase IV rotor (twisted blades, instrumentation boxes, boom, hub, and camera) was determined by measuring low-speed shaft torque, power, and rpm during turbine start-up. An estimate of drive train (low-speed shaft, gearbox, and high-speed shaft) stiffness was also obtained from this test. The inertia of the entire rotating system (rotor and drive train) was measured with a pendulum test. Data collected during operation of the instrumented turbine provided measurements of the generator slip and total efficiency of the drive train. The machine description in Appendix F lists all of these results, and the layout of the nacelle is pictured in figure 5.13.

The most significant configuration change to the original Grumman turbine was the blade design. The NREL S809 airfoil replaced the original Grumman airfoil. The S809 airfoil was developed by Airfoils, Inc., under contract to NREL (Somers, Unpublished, [12]). The primary reason this airfoil was chosen was that a well-documented wind tunnel data base that included pressure distributions, separation boundary locations, drag data, and flow-visualization data was available. The S809 airfoil was used in both the untwisted and twisted configurations which are pictured in Figures 5.14 and 5.15, respectively.

Figure 5.13 *NREL: Nacelle layout*

The untwisted and twisted blades were similar in design and fabrication. Both had a constant 0.457 m chord, and a planform view of the blades is shown in Figure 5.16. The intent in the design of twisted blades was to maintain a constant angle of attack along the span of the blade at a wind speed of 8 m/s (Simms, Fingersh, and Butterfield, [13]). The twist distribution of the blades used in Phases III and IV is listed in Appendix F. The thickness and airfoil distribution of the twisted blades were nearly identical to that of the untwisted blades with the spar enlargement extending to 25% span instead of 30% span. Both sets of blades were fiberglass/epoxy composite, but the spar in the twisted blades was carbon fiber as opposed to the fiberglass/epoxy spar used in the untwisted blades. They were designed to be stiff to mitigate aeroelastic blade responses. The dynamic characteristics of the blades were tailored to avoid coalescence of rotor harmonics with flap-wise, edge-wise, and torsional natural frequencies. To minimize the possibility of aeroelastic instabilities, the mass and elastic axes were aligned with the aerodynamic axis. The instrumented blade was painted black to contrast with the white tufts that were used for flow visualization. The pitch shaft is less stiff than the inboard sections of the blade, and most of the flap deflection occurs in this region. For this reason, the pitch shaft must be included in a blade or hub model and is included with the estimated blade mass and stiffness distributions in Appendix F.

Meteorological (Met) Towers

During Phase II, the inflow conditions were measured at three locations in the predominantly upwind direction (292 degrees): the North met tower, the Local met tower, and the Vertical Plane Array (VPA). The North met tower was 50 m tall and located 500 m upwind of the turbine. Large-scale atmospheric inflow conditions were measured at this location in the form of wind speed and direction at four elevations (5 m, 10 m, 20 m, and 50 m), temperature at 5 m and at 50 m, and barometric pressure. Local inflow measurements were made 12 m upwind

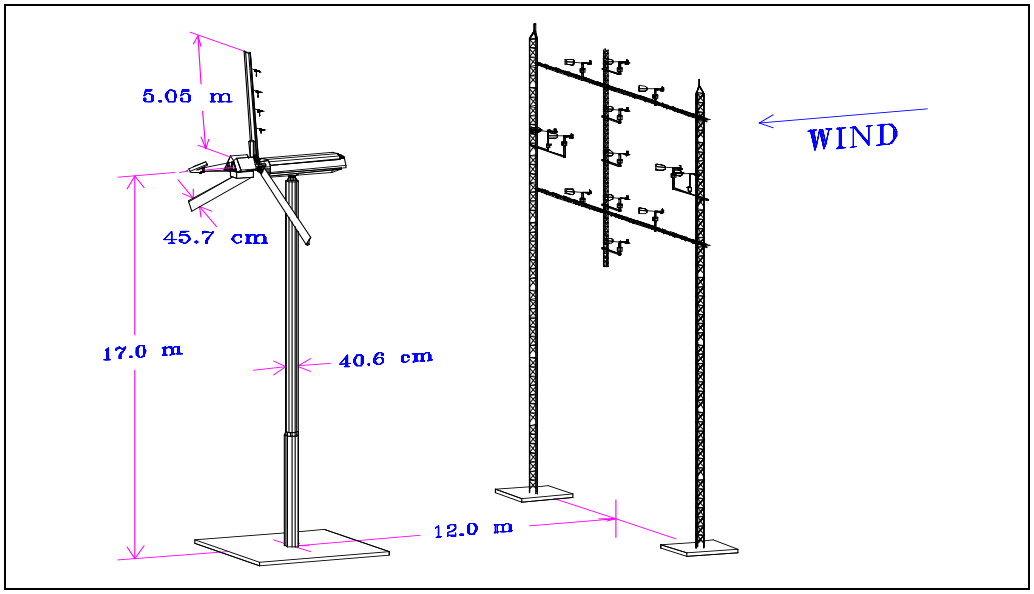

Figure 5.14 *NREL: Phase II (untwisted blade) test configuration*

of the turbine on the VPA which is depicted in figure 5.17. Two Rohn 45-G guyed met towers supported three cross-booms, where 11 prop-vane and 2 bi-vane anemometers measured inlet flow magnitude and direction. Eight of the prop-vane anemometers were arranged in a circle corresponding to 80% of the blade span at approximately hub height. The remaining prop-vane anemometers were spaced evenly inside the circle. The two bi-vane anemometers were mounted outside the circle on the horizontal axis. Also located 12 m upwind of the turbine and 20 m to the north was the 16.8 m Local met tower. Sonic anemometer measurements and hot-film temperature measurements originated from this tower, but this data was not available for selections placed in the data base. Detailed discussion of the anemometry used in the Phase II portion of the experiment appears in Butterfield et al., ([11]). Table 5.2 lists all of the channels related to measurements made on the Phase II met towers that were included in the data base.

In order to comply with the conventions established by the Annex, all of the wind direction measurements were converted to yaw error measurements by subtracting the turbine angle. These angles were measured in accordance with the counter-clockwise rotating turbine convention.

Inflow conditions were again measured directly upwind of the turbine during Phases III and IV, but the North met tower was not used. Instead, a taller Local met tower was used to measure shear and stability near the turbine. Three met towers placed 1.5D upwind of the turbine supported multiple cup anemometers, bi-vane anemometers and one sonic anemometer. The cup anemometers provided more accurate wind speed measurements than the prop-vane anemometers used during Phase II because the cup anemometers have a higher frequency response and are not susceptible to gyroscopic effects. Temperature and barometric pressure

Table 5.2 *Phase II (Untwisted Blade) Local Inflow Measurements*

Identification	Description	Units
V(w,1)	VPA Prop Vane Wind Speed (6:00)	m/s
V(w,2)	VPA Prop Vane Wind Speed (6:00 @ 40% Span)	m/s
V(w,3)	VPA Prop Vane Wind Speed (4:30)	m/s
V(w,4)	VPA Prop Vane Wind Speed (7:30)	m/s
V(w,5)	VPA Bi-Vane Wind Speed (3:00 @ 100% Span)	m/s
V(w,6)	VPA Prop Vane Wind Speed (3:00)	m/s
V(w,7)	VPA Prop Vane Wind Speed Hub Height	m/s
V(w,8)	VPA Prop Vane Wind Speed (9:00)	m/s
V(w,9)	VPA Bi-Vane Wind Speed (9:00 @ 100% Span)	m/s
V(w,10)	VPA Prop Vane Wind Speed (1:30)	m/s
V(w,11)	VPA Prop Vane Wind Speed (10:30)	m/s
V(w,12)	VPA Prop Vane Wind Speed (12:00 @ 40% Span)	m/s
V(w,13)	VPA Prop Vane Wind Speed (12:00)	m/s
V(w,14)	North met Wind Speed 5m	m/s
V(w,15)	North met Wind Speed 20m	m/s
V(w,16)	North met Wind Speed 50m	m/s
phi(y,1)	VPA Bi-Vane Wind Direction (3:00 @100% Span) - Yaw Angle	deg
phi(y,2)	VPA Bi-Vane Wind Direction Hub Height - Yaw Angle	deg
phi(y,3)	VPA Bi-Vane Wind Direction (9:00 @100% Span) - Yaw Angle	deg
phi(y,4)	North met Wind Direction 5m - Yaw Angle	deg ')
phi(y,5)	North met Wind Direction 10m - Yaw Angle	deg ')
phi(y,6)	North met Wind Direction 20m - Yaw Angle	deg
phi(y,7)	North met Wind Direction 50m - Yaw Angle	deg
alpha (w,1)	VPA Bi-Vane Wind Elevation Angle (3:00 @100% Span)	deg
alpha (w,2)	VPA Bi-Vane Wind Elevation Angle (9:00 @100% Span)	deg
5mairT	North met Temperature 5m	K
deltaT	North met Delta Temperature (50m-5m)	K
Baro Press	Barometric Pressure	Pa

') These channels do not appear in all data base selections.

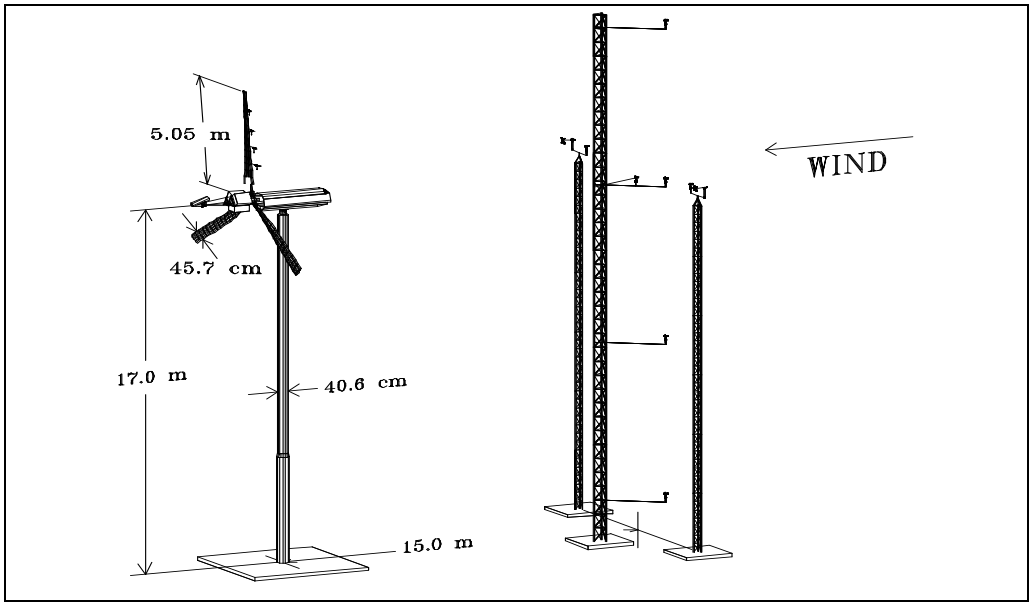

Figure 5.15 *NREL: Phase III and Phase IV (twisted blade) test configuration*

measurements were also made. Figure 5.18 shows the three instrumented met towers. Phase III and Phase IV meteorological channel descriptions are shown in table 5.3.

5.3.2 Instrumentation

Pressure taps

The most important yet most difficult measurements were the blade surface pressures. The quality of the aerodynamic performance coefficients depends on the accuracy of individual pressure tap measurements. Each coefficient for a particular radial station was the integrated value of the measured pressure distribution. The measurement approach was to install small pressure taps in the surface of the blade skin. Each opening was mounted flush to the airfoil surface and was 1.016 mm in diameter. The flush profile was necessary to prevent the taps themselves from disturbing the flow. Stainless steel tubes, 0.15 m in length, were installed inside the blade's skin during manufacturing to carry surface pressures to the pressure transducer. A short piece of plastic tubing joined the tubes to the transducers. The taps were aligned along the chord (instead of being staggered) so that spanwise variations in pressure distributions would not distort measured chord-wise distributions. As illustrated in Figure 5.19, the taps were concentrated toward the leading edge to achieve stronger resolution in the more active areas of the pressure distributions.

The Phase II experiment used 28 pressure taps at four primary radial locations: 30% span, 47% span, 63% span, and 80% span. During Phases III and IV, 22 taps were instrumented at five primary spanwise locations: 30% span, 47% span,

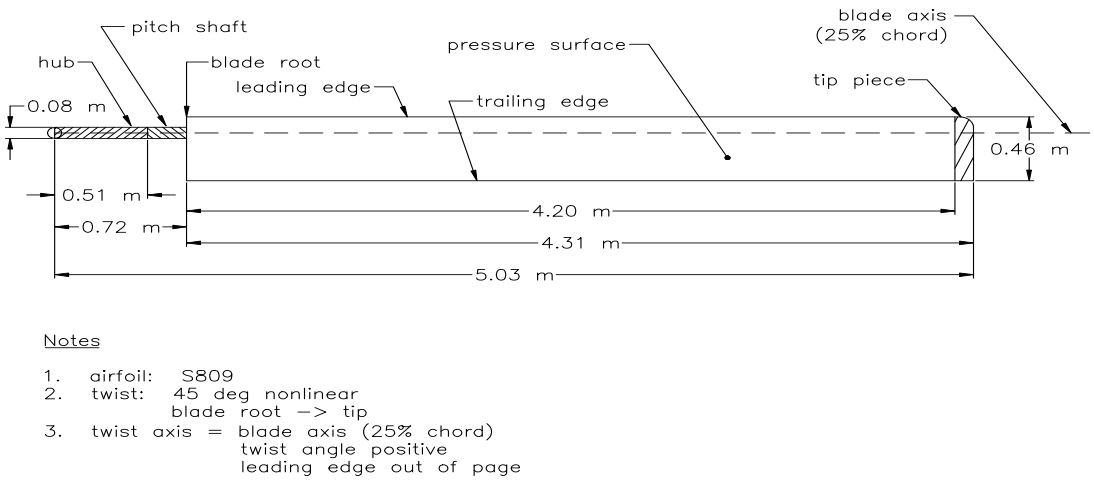

Figure 5.16 *NREL: Planform of the blades*

63% span, 80% span, and 95% span. Pairs of taps at 4% chord and 36% chord were installed at various other intermediate span locations (36%, 41%, 52%, 58%, 69%, 74%, 85%, 90%, 92%, and 98%). Figure 5.19 depicts the blade layout for Phase III. Recall that there were no pressure taps outboard of 80% span during Phase II.

Based on tests performed in the first phase of the experiment, dynamic corrections were deemed unnecessary (Butterfield et al., [11]). Gain amplifications and phase effects that occur as a function of tube frequency and tube length were measured. These effects were not significant up to a frequency of 80 Hz, and the measured pressure data showed no appreciable information above 40 Hz.

Pressure Transducer

Because the dynamic pressure varied significantly along the span due to rotational effects, transducers with different measurement ranges were used. The nominal transducer ranges used during different test phases are listed in table 5.4. The transducers, Pressure Systems model ESP-32, scanned port to port at 16,667 Hz completing a scan of all pressure taps at approximately 520 Hz. One transducer was used at each primary span location to measure up to 32 channels of differential pressures between the pressure taps (local static pressure) and the reference pressure located in an instrumentation box mounted on the hub. Each transducer was installed inside the blade as close to the pressure taps as possible. These electronic scanner-type transducers provided remote calibration capability through a pneumatically operated valve. The capacity to purge all of the pressure taps with dry nitrogen was used periodically to prevent moisture or small particles from affecting the pressure measurements.

Table 5.3 *Phase III and Phase IV (Twisted Blade) Local Inflow Measurements*

Identification	Description	Units
V(w,1)	Local met Wind Speed 2.4m	m/s
V(w,2)	Local met Wind Speed 10.06 m	m/s
V(w,3)	North local met Wind Speed 17.02m (hub height)	m/s
V(w,4)	Local met Wind Speed 17.02m (hub height)	m/s
V(w,5)	Sonic nr. 1 Wind Speed (horizontal) 17.02m (hub height)	m/s
V(w,6)	South local met Wind Speed 17.02m (hub height)	m/s
V(w,7)	Local met Wind Speed 24.38m	m/s
phi(y,1)	North local met Wind Direction 17.02m (hub height) - yaw angle	deg
phi(y,2)	Sonic nr. 1 Wind Direction 17.02m (hub height) - yaw angle	deg
phi(y,3)	South local met Wind Direction 17.02m (hub height) - yaw angle	deg
alpha(w,1)	North local met Wind Elevation Angle 17.02m (hub height)	deg
alpha(w,2)	South local met Wind Elevation Angle 17.02m (hub height)	deg
2mairT	Local met temperature 2.4m	K
24mairT	Local met temperature 24.48m	K ')
22mdT	Local met delta temperature (24m-2m)	K ')
2mdpT	Local met dewpoint temperature 2.4m	K
Baro Press	Barometric pressure	Pa

') These channels do not appear in all data base selections.

Table 5.4 *Nominal, Full-Scale, Pressure Transducer Measurement Ranges*

	Phase II	Phase III and Phase IV
30% Span	+/- 2970 Pa (0.4 psi)	+/- 2488 Pa (10" H2O)
47% Span	+/- 2970 Pa (0.4 psi)	+/- 2488 Pa (10" H2O)
63% Span	+/- 8274 Pa (1.2 psi)	+/- 4977 Pa (20" H2O)
80% Span	+/- 8274 Pa (1.2 psi)	+/- 10, 342 Pa (1.5 psi)
95% Span		+/- 10, 342 Pa (1.5 psi)

Figure 5.17 *NREL: Phase II (Untwisted blade) Meteorological instrumentation; Side view looking downwind toward 292 degrees. Meteorological instruments are 1.2D (12 m) upwind of the turbine tower.*

Pressure System Controller (PSC)

Remote control of ESP-32 pressure transducer calibration, scanner addressing, and demultiplexing of the analog multiplexed signals were performed by the PSC, a hub-mounted microprocessor control unit designed by NREL (Butterfield et al., [11]). The PSC was completely redesigned from Phase II to Phase III to improve the accuracy and the user interface. Currently up to 155 pressure channels may be processed simultaneously. All pressure ports were scanned at 520 Hz with a port-to-port settling time of 60 microsec. The objective was to provide 100 Hz bandwidth frequency response to enable study of dynamic stall behavior on the rotating wind turbine blade.

Once the PSC scanned the pressure port addresses, the samples were passed as digital signals to the pulse code modulation (PCM) encoder. The PCM system

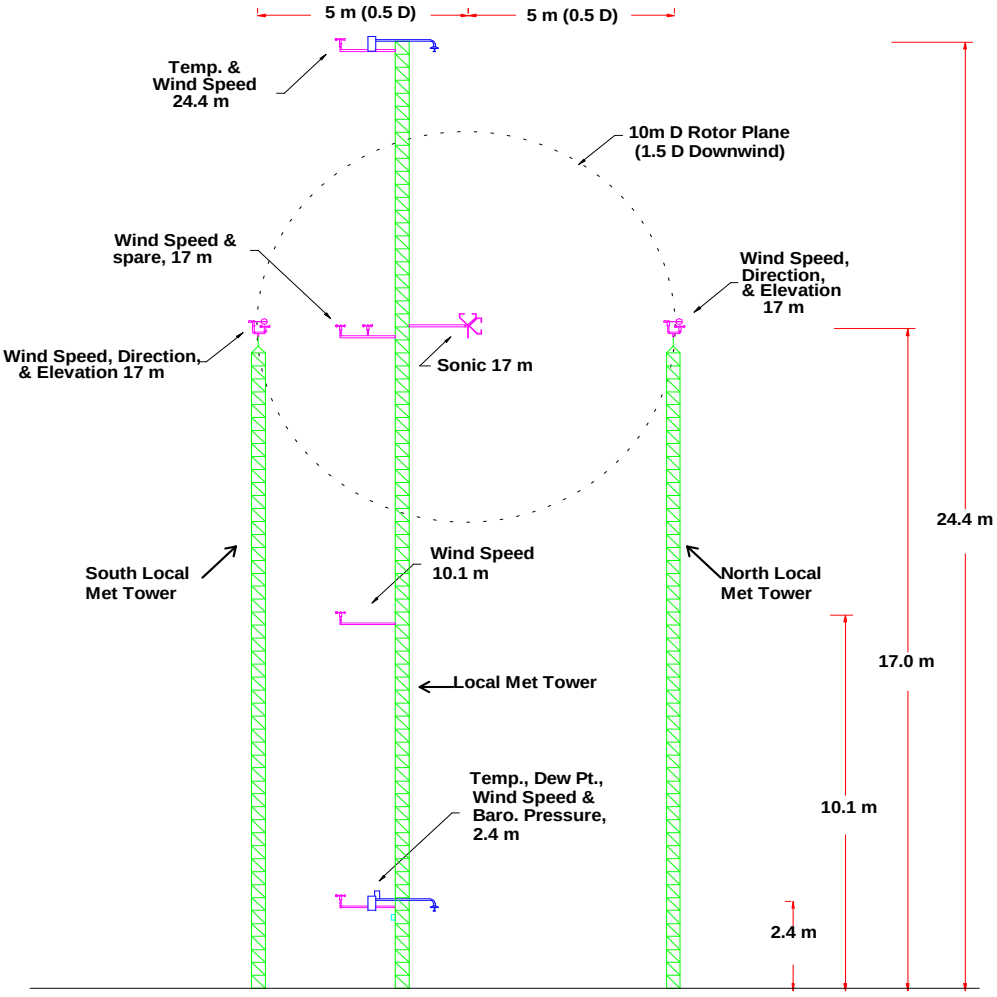

Figure 5.18 *NREL: Phase III and Phase IV (twisted blade) Meteorological instrumentation; Side view looking downwind toward 112 degrees. Meteorological instruments are 1.5D (15 m) upwind of the turbine tower.*

multiplexed the 62 channels of data into one data stream which was conducted through a single coaxial cable. The PCM streams were passed over slip rings to the control building and were recorded on optical disk for later processing.

The PSC pneumatic control valves and ramp calibration sequence is discussed in the Phase I report ([11]) and summarized in section 5.3.3. The only changes between Phase II and Phases III and IV were that a more accurate calibration reference pressure was used, and calibrations were automated by a computer-controlled processing system.

Local Flow Angle (LFA) Transducers

Geometric angle of attack (AOA) measurements are fairly easy to make in a wind tunnel where the air flow is precisely controlled, but in the field environment the

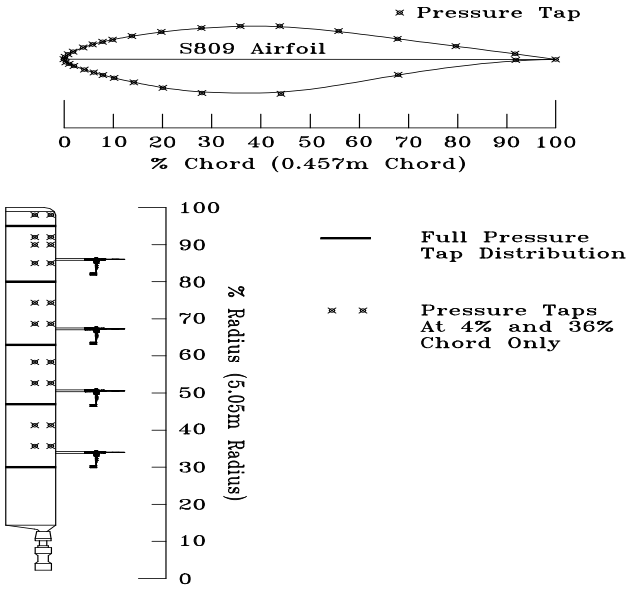

Figure 5.19 *NREL: Configuration of Phase III (twisted) instrumented blade. During Phase II, there were no taps outboard of 80% span. During Phase IV, the local flow angle flags were replaced with 5-hole probes at all 5 primary locations*

difficulty in obtaining angle of attack measurements increases. To accomplish this, it was necessary to make measurements of the local inflow in front of the blade. The flow angle sensor illustrated in Figure 5.20 was developed by NREL for this purpose (Butterfield et al., [11]) and was used in Phase II and Phase III tests. It consisted of a lightweight, rigid flag that aligned itself with the local flow. During Phase II tests, a commercial rotary position sensor mounted in a custom housing measured the flag angle within 1.0 degree accuracy over the range of -20 deg to 40 deg The analog signals generated were sent to the hub, multiplexed, and recorded with the other signals by the data acquisition system. This analog position encoder was replaced with a digital resolver during Phase III testing. The flag extended 36 cm (34 cm during Phase II) ahead of the leading edge and was aligned with the pressure taps. The sensor was attached to the blade 4% outboard of the four primary pressure stations (30%, 47%, 63%, and 80%) in order to minimize flow disturbances on the blade near the pressure taps. During Phase II the flag sensor was actually mounted at 86% span measuring a local flow angle at 82% span instead of 80% span. However, in the data base files corresponding to the Phase II test, this local flow angle is associated with the 80% span pressure tap location. Processing of the data revealed that during Phase II the flag at 47% span did not work properly for most of the duration of testing so it was removed from the processed data files. Table 5.5 describes the local flow angle measurements for Phase II and Phase III.

During Phase III, a five-hole probe was mounted 4% inboard of the 95% span

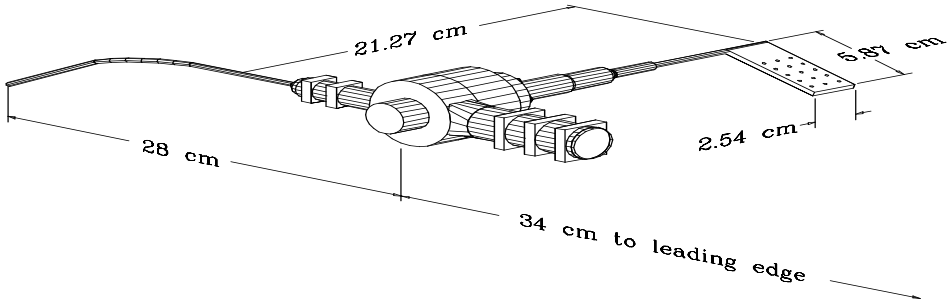

Figure 5.20 *NREL: Phase II Flag Local Flow Angle sensor. During Phase III, the sensor was located 36 cm from the leading edge*

Table 5.5 *Phase II and Phase III Local Flow Angle Measurements (Flag)*

Identification	Description	Units
alpha (m,1)	30% Local Flow Angle (LFA) (Flag)	deg
alpha(m,4)	47% Local Flow Angle (LFA) (Flag)	deg ')
alpha(m,7)	63% Local Flow Angle (LFA) (Flag)	deg
alpha(m,10)	80% Local Flow Angle (LFA) (Flag)	deg ")

') Phase III only

") actually measured at 82% span during Phase II

pressure station in order to test this new device for measuring local flow angle. This data was not included in any of the Phase III files supplied to the Annex XIV data base, but the test did prove that the five hole probe provided greater dynamic response than the flag which is necessary in studying dynamic stall (Fingersh and Robinson, [14]). Therefore all of the flag sensors were replaced with five hole probes during Phase IV testing. The probes, depicted in Figure 5.21, extended 37 cm ahead of the leading edge at an angle 20 degrees below the chordline and measured local flow angles over the range -15 to 55 degrees. Each probe was mounted 4% span outboard of the primary pressure stations except at the 95% pressure tap station where the probe was mounted 4% span inboard. Note that the local flow angle measurement from the probe is no longer aligned with the full-chord pressure measurements as was the local flow angle measured with the flag. These measurements were identified with the corresponding percent span location instead of the corresponding pressure station number as were the flag measurements. In addition to the local flow angle, the five hole probes used in Phase IV provided measurement of the dynamic pressure and spanwise flow angle. Neural network models were used to create a surface based on data obtained from wind tunnel probe calibrations (Fingersh and Robinson, [14]). Resulting surfaces were implemented as lookup tables in the post-processing software. The pressures

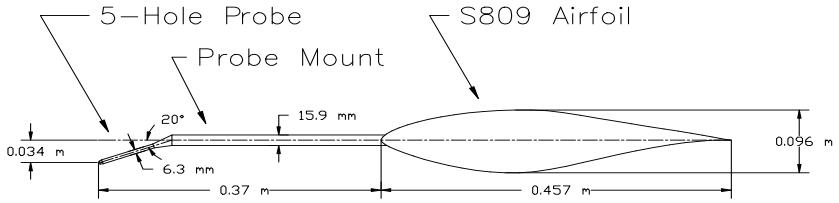

Figure 5.21 *NREL: Phase IV Five hole-probe local flow sensor.*

Table 5.6 *Phase IV Local Flow Angle Measurements (5-Hole Probe)*

Identification	Description	Units
alpha(m,34)	34% Local Flow Angle (LFA) (5-hole probe)	deg
alpha(m,51)	51% Local Flow Angle (LFA) (5-hole probe)	deg
alpha(m,67)	67% Local Flow Angle (LFA) (5-hole probe)	deg
alpha(m,84)	84% Local Flow Angle (LFA) (5-hole probe)	deg
alpha(m,91)	91% Local Flow Angle (LFA) (5-hole probe)	deg
alpha(x,34)	Crosswise flow angle at 34% span	deg
alpha(x,51)	Crosswise flow angle at 51% span	deg
alpha(x,67)	Crosswise flow angle at 67% span	deg
alpha(x,84)	Crosswise flow angle at 84% span	deg
alpha(x,91)	Crosswise flow angle at 91% span	deg

from each of the five holes in the probe were recorded, but only the resulting dynamic pressure, local flow angle, and crossflow angle were included in the data base. Table 5.6 describes the local flow angle measurements made during Phase IV.

Strain Gages and Accelerometers

Blade, tower, rotor, and yaw loads were measured with strain gages during Phase II testing. Five spanwise locations on the instrumented blade, root (8.6% span), 20% span, 40% span, 50% span, and 90% span, were instrumented with strain gages to measure blade flap-wise bending while two locations, root (8% span) and 50% span, were instrumented to measure edge bending. Blade pitching moment (blade torsion) was measured at the root (8% span), 50% span and 70% span. Root flap and edge bending moments were also measured on the other two blades. Bending of the low speed shaft in two orthogonal planes was measured as well as the low speed shaft torque. Loads in the non-rotating environment were also measured. Gages were mounted on two tower bending axes at the point just above

Table 5.7 *Phase II (Untwisted Blades) Load Measurements*

Identification	Description	Units
M(1)	Strain Blade 1A, root flap bending moment	Nm
M(2)	Strain Blade 1B, root flap bending moment	Nm
M(3)	Strain Blade 1, root edge bending moment	Nm
M(4)	Strain Blade 1, 20% flap bending moment	Nm
M(5)	Strain Blade 1, 40% flap bending moment	Nm
M(6)	Strain Blade 1, 50% flap bending moment	Nm
M(7)	Strain Blade 1, 50% edge bending moment	Nm
M(8)	Blade 1 torsion at 50% span	Nm
M(9)	Blade 1 torsion at 70% span	Nm ')
M(10)	Strain Blade 1, 90% flap bending moment	Nm
M(11)	Strain Blade 2, root flap bending moment	Nm
M(12)	Strain Blade 3, root flap bending moment	Nm
M(13)	Strain X-X Low speed shaft bending moment (horizontal axis)	Nm
M(14)	Strain Y-Y Low speed shaft bending moment (vertical axis)	Nm
M(15)	Strain Low speed shaft torque A	Nm
M(16)	Strain Low speed shaft torque B	Nm
M(17)	Blade 1 root torque (link)	Nm
M(18)	Tower bending moment about East-West Axis (X)	Nm
M(19)	Tower bending moment about North-South Axis (Y)	Nm
M(20)	Yaw Moment	Nm
M(21)	Estimated Aerodynamic Thrust	N
M(22)	Estimated Aerodynamic Torque	Nm

') These channels do not appear in all data base selections.

the guy wire attachment. These gages were oriented to measure bending parallel and perpendicular to the direction of the prevailing wind. Gages were mounted on the arm of the yaw brake to measure yaw moment when the yaw brake was engaged. All load measurements corresponding to Phase II tests are listed in table 5.7. Estimates of aerodynamic thrust and torque resulting from methods described in section 5.3.3 were also included in the data base.

Similar measurements were made during Phases III and IV testing periods. Flap and edge bending moments were recorded from strain gages mounted at the root (8% span), 25%, and 60% span on the instrumented blade. Flap and edge bending measurements were taken at the root of the other two blades, and low speed shaft bending in two planes as well as low speed shaft torque measurements were also obtained. There were no pitching moment measurements made in either of these phases of the experiment. Instead of measuring tower bending with strain gages, accelerometers were placed in the nacelle to determine yaw, pitch and fore-aft motion. Accelerometers in the tip of each blade measured movement in the flap and edge directions. During Phase IV, strain gages were used to measure yaw moment. These measurements are listed in table 5.8 below.

Strain gages measuring root flap and edge loads were applied to the steel pitch shaft adjacent to the blade attachment location. The pitch shaft was reduced to a uniform, cylindrical, 80 mm diameter at 8% span (Phase II) or 8.6% span (Phase III and IV), the location where the strain gages were applied. The uniform,

Table 5.8 *Phase III and Phase IV (Twisted Blade) Load Measurements*

Identification	Description	Units	comment
M(1)	Strain Blade 1 root flap bending moment	Nm	
M(2)	Strain Blade 1 root edge bending moment	Nm	
M(3)	Strain Blade 1 25% flap bending moment	Nm ')	
M(4)	Strain Blade 1 25% edge bending moment	Nm ')	
M(5)	Strain Blade 1 60% flap bending moment	Nm ')	
M(6)	Strain Blade 1 60% edge bending moment	Nm ')	
M(7)	Accelerometer Blade 1-Flap	m/s^2	
M(8)	Accelerometer Blade 1-Edge	m/s^2	
M(9)	Strain Blade 2 root flap bending moment	Nm	
M(10)	Strain Blade 2 root edge bending moment	Nm	
M(11)	Accelerometer Blade 2-Flap	m/s^2	
M(12)	Accelerometer Blade 2-Edge	m/s^2	
M(13)	Strain Blade 3 root flap bending moment	Nm	
M(14)	Strain Blade 3 root edge bending moment	Nm	
M(15)	Accelerometer Blade 3-Flap	m/s^2	
M(16)	Accelerometer Blade 3-Edge	m/s^2	
M(17)	Strain X-X Low speed shaft bending moment	Nm	
M(18)	Strain Y-Y Low speed shaft bending moment	Nm	
M(19)	Strain Low speed shaft torque	Nm	
M(20)	Nacelle Accelerometer Yaw	m/s^2	
M(21)	Nacelle Accelerometer Fore-Aft	m/s^2 ')	
M(22)	Nacelle Accelerometer Pitch	m/s^2	
M(23)	Estimated Aerodynamic Thrust	N	Phase III
M(24)	Estimated Aerodynamic Torque	Nm	Phase III
M(23)	Nacelle Yaw Moment	Nm	Phase IV
M(24)	Estimated Aerodynamic Thrust	N	Phase IV
M(25)	Estimated Aerodynamic Torque	Nm	Phase IV

') These channels do not appear in all data base selections.

cylindrical region eliminates geometry effects while measuring flap and edge bending moments. This cylindrical section of the blade root is illustrated in figure 5.19.

Strain gages on the instrumented blades consisted of four active gage elements mounted inside the fiberglass blade skin. The gages were installed inside the skin during the blade manufacturing process to preserve the exterior airfoil shape and surface smoothness. The strain gages were positioned carefully to minimize flap-wise and edge-wise cross-talk. A maximum of 4% cross-talk was measured during the blade pull and strain gage calibration tests (Butterfield et al., [11]). These cross-channel interference effects were not considered significant, and corrections were not applied to the data.

Calibration of the low-speed shaft torque channel introduced errors during phase II and phase III. Equations that correct for the calibration errors are included in Appendix Appendix F.

Miscellaneous Transducers

Various sensors were used to measure yaw position, pitch angle and rotor azimuth position. In Phase II, gear-driven potentiometers were used to measure yaw position and pitch angle of the instrumented blade. The rotor azimuth position was measured with an analog rotary position encoder connected to the low-speed shaft via a gear and chain. This device created discontinuities and non-linearities due to its physical limitations in the transition from 0 to 360 degrees. The data were therefore corrected during post-processing through insertion of an idealized saw-tooth between adjacent 180 degree transition points. This provided a clean transition from 0 to 360 degrees and smooth linear values throughout the rest of the cycle. However, the rotational frequency channel (RPM), calculated during post-processing, was affected by this smoothing of the data so it must be regarded with speculation.

During Phases III and IV, gear-driven, BEI model R-25 optical absolute position encoders replaced the gear-driven potentiometers measuring yaw position and rotor azimuth position. Each of the blades was instrumented with an encoder for pitch measurements. These digital measurements significantly reduced uncertainty in subsequent measurements.

Generator power was monitored using an Ohio Semitronics, Inc. (OSI) power watt transducer during all phases of testing. Absolute reference pressure was measured using a Setra 270 Absolute Pressure transducer located inside the instrumentation box containing the reference pressure during Phase II only. All of these miscellaneous channels are listed in table 5.9.

Flow Visualization

Flow visualization was achieved through the use of tufts attached to the surface of the blade during Phase II and Phase IV testing. The tufts were made of thin, white, polyester thread measuring approximately 0.25 mm in diameter and 45 mm in length. A small drop of fast drying glue held each of the tufts to the downwind side of the instrumented blade. Tufts were placed in rows spaced 76 mm apart in the blade spanwise direction.

Two high-shutter-speed cameras were mounted in the rotating frame during Phase II and Phase IV testing. A Panasonic camera with a Rainbow zoom lens and remote control iris and focus adjustments was mounted on the end of a lightweight, 3 m

Table 5.9 *Phase II, Phase III, and Phase IV Miscellaneous Transducers*

Identification	Description	Units
phi(r,b)	Blade azimuth angle	deg
phi(turb)	Yaw angle	deg
omega	RPM	rpm
theta1	Blade 1 Pitch Angle	
	(Digital Blade 1 pitch in Phases III and IV)	deg
theta2	Digital Blade 2 pitch	deg ')
theta3	Digital Blade 3 pitch	deg ')
Power	Generator Power	kW
Abs Ref Press	Absolute reference pressure	Pa ")

') Phase III and Phase IV only.
") Phase II only.

boom which was attached to the hub, as shown in figure 5.15. The boom was designed to be stiff with a system fundamental frequency exceeding 10 cycles per revolution (10P), and the axes of the boom and camera were mass balanced about the axis of rotation. The camera angle was remotely adjustable to display various span locations on the blade. During all three phases of testing an additional high-shutter-speed video camera was mounted at the root of the instrumented blade to provide a view of the blade span. This camera pitched with the blade to provide a full span picture of all the tufts at one time. The mass of this camera was included in the mass of the blades listed in Appendix E during Phases III and IV. However, during Phase II, the blades were balanced before the camera was mounted. Additional equipment, such as the data acquisition system, the PSC, and lighting for night testing, were also mounted on the hub. Variations in the mass of the hub due to various combinations of this equipment for each phase of the experiment are noted in Appendix F.

5.3.3 Measuring procedure

Data acquisition and measuring speed

A customized digital PCM-based hardware system for data acquisition was developed and tested throughout Phase I of the Combined Experiment (Simms and Butterfield, 1990, [15]). The same hardware was used during Phase II, but upgrades were made for Phases III and IV. The number of measured channels increased from 185 in Phase II to 201 in Phase IV. Throughout Phase II testing, the inflow measurements and the non-rotating turbine measurements were acquired at slower sample rates than that of the rotating measurements. The slower rate channels were interpolated during post-processing to a common 520.83 rate for all channels. During Phases III and IV, all of the channels were sampled at 520.83 Hz. Data were stored on 14-track magnetic tape during Phase II data acquisition, but recent technological advances in personal computing provided the capability for real time data collection and storage on optical disk during Phases III and IV. Copies of the optical disks and the processed engineering unit files were recorded on compact disks for storage.

Preparation of the data provided to the data base required filtration and decimation. The MATLAB program was used to first digitally filter and then decimate the data to a 52 Hz sample rate. Time series data (except azimuth angle and time channels) were passed through a 4-pole Butterworth 10 Hz filter in both forward

and backward time directions resulting in 8-pole, 0 phase, 10 Hz Butterworth filtering. All channels were then decimated by 10 to achieve the resulting 52 Hz sample rate. The effect of applying these filters is illustrated in the figures 5.22 and 5.23.

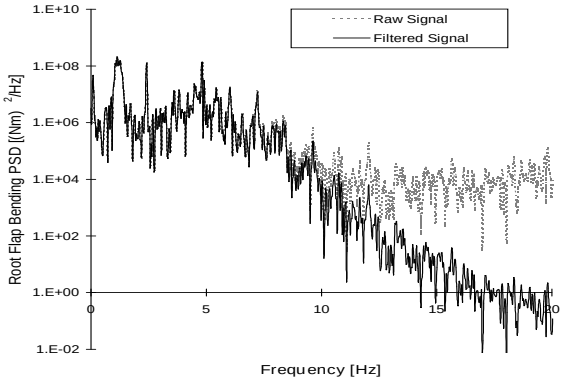

Figure 5.22 *NREL:The effect of applying the filter seen on a power spectrum*

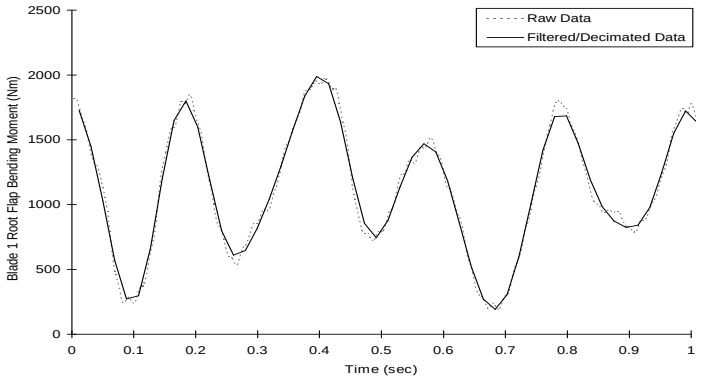

Figure 5.23 *NREL: The effect of applying the filter seen on a time trace*

Calibration Procedures

Calibrations of the pressure channels were performed in the manner described in Simms and Butterfield ([16]) by using a motorized syringe to apply positive and negative pressure to all scanning transducers simultaneously over their entire measurement range. This was done before and after each ten minute campaign by remote control while the turbine was in motion. Calibration coefficients were derived by performing a least-squares regression on each of the pressure channels referenced to the precision differential pressure transducer signal. In order to verify lack of drift in the pressure transducers, comparisons between pre- and post-calibrations were made.

Table 5.10 *Uncertainty Analysis Results for Selected Measured Channels*

Measurement	Units	Measurement Range	Total Estimated Uncertainty	% Full Scale Error
Pressures at 30% Span ')	Pa	+/- 2970	+/- 12	0.2
Pressures at 47% Span ')	Pa	+/- 2970	+/- 18	0.3
Pressures at 63% Span ')	Pa	+/- 8274	+/- 33	0.2
Pressures at 80% Span ')	Pa	+/- 8274	+/- 50	0.3
Angle of attack	deg	-22 to +40	+/- 1.0	1.6
Wind velocity	m/s	0 to 37	+/- 0.5	1.4
Blade pitch angle	deg	-10 to 71	+/- 1.0	1.2
Blade azimuth angle	deg	0 to 360	+/- 1.0	2.8

') All pressures are differentials between hub reference and blade surface pressures.

A variety of calibration procedures were used to ensure that the non-pressure channels maintained required accuracy levels. The preferred method of calibrating channels in the field was to use an "end-to-end" procedure where a known load was applied and the effect measured. This enabled the full system measurement path to be calibrated. An example is strain gage calibration where weights suspended from the blade caused a known strain gage bending moment. For other channels, it was impossible to perform full-path calibrations in situ. For example, the anemometers required a known wind velocity and were thus calibrated in a wind tunnel. In these cases, a two-part calibration was used. The first part relied on the factory-specified transducer calibration. The second part was an "electronics cal" where known reference voltages were inserted in place of the transducer signal, and the system electronics path was calibrated separately. The frequency of these calibrations depended on transducer and measurement system specifications and varied with use and application.

The calibration procedures were established to ensure that all recorded data values were within the stated error limits. Uncertainty analysis results for selected measured channels used during Phase II are presented in table 5.10, (from Miller et al., Unpublished, [17]). Total estimated uncertainty values listed in the table are expressed in engineering units, and represent random and bias error components. The uncertainty is also expressed in terms of percent full scale error. Detailed measurement uncertainty estimates for Phase II data channels can be found in Butterfield et al. ([11]). Error analysis and calibration procedures specific to wind turbine field testing are described in McNiff and Simms ([18]).

A data base of resulting calibration coefficients was maintained and applied to raw data values to produce engineering unit data files. Because all of the measured channels were linear, only slope and offset calibration coefficients were applied.

Surface pressures

Differential pressures between the blade surface pressure and the hub reference pressure were measured by the ESP-32 pressure transducers. For all blade surface pressure measurements, the common reference pressure source was the pressure inside one of the rotating instrumentation boxes on the hub. The reference tap of each transducer was connected to a single reference line that was terminated inside the instrumentation box. The hub mounted instrumentation box was damped to atmospheric pressure through an orifice which resulted in a time constant of

approximately 5-10 seconds. This damping provided a relatively stable pressure reference which closely tracked atmospheric pressure. The effects of centrifugal force on air in the tube were corrected per equations 5.5 and 5.6 as described in Miller et al, [17].

$$p_{cor} = p_{meas} + p_{cent} \tag{5.5}$$

$$p_{cent} = 0.5\rho(\Omega \cdot r)^2 \tag{5.6}$$

where
p_{cor} = differential pressure corrected for centrifugal force, Pa
p_{meas} = pressure differential measured at blade-mounted transducer, Pa
p_{cent} = centrifugal force correction, Pa
ρ = air density, kg/m^3
r = radial distance to surface pressure tap, m
Ω = rotor speed, rad/s

The associated pressure files in the data base contain p_{cor}–the measured difference in pressure between the surface tap pressure and the hub pressure corrected for effects of centrifugal force. If a pressure tube was damaged, the interpolated value between the two adjoining taps was calculated. These channels were noted as P(deriv) in the log files to indicate interpolation instead of actual measurement. A separate file for each of the full chord span locations (30%, 47%, 63%, 80%, and 95%) as well as each of the intermediate span locations (36%, 41%, 52%, 58%, 69%, 74%, 85%, 90%, 92%, and 98%) was placed in the data base.

Dynamic Pressure

A total pressure Pitot probe attached to the local flow angle flag pictured in figure 5.20 measured dynamic pressure during Phases II and III. To prevent flow disturbance, the probe extended 0.64 m (0.62 m during Phase II) ahead of the leading edge of the airfoil and was mounted 4% outboard of each primary pressure station (30%, 47%, 63%, and 80%). Again, the probe was mounted at 86% span instead of 84% span during Phase II. Each probe was connected to an ESP-32 transducer via 0.15 cm diameter stainless steel tubing. A short piece of plastic tubing was used to join the tubes to the transducer. The probes measured the difference between the stagnation and reference pressures with less than 10% error for inflow angles between -40 deg and 40 deg ([19]). To maximize the probe's effectiveness, they were bent so the measurement range would coincide with the nominal operating conditions. During Phase IV the five-hole probe provided a dynamic pressure measurement 0.36 m ahead of the leading edge at an angle of 20 deg below the chordline. The five-hole probes were mounted in the same locations as the total pressure probes with the addition of one at 91% span. The dynamic pressure was corrected for centrifugal effects in the same manner as the individual pressure taps using equations 5.5 and 5.6.

The dynamic pressure was also estimated from the stagnation point pressure at each of the full-chord pressure tap locations. The location on the blade at which the local velocity equals zero was considered to be the stagnation point, and the corresponding pressure at that location was used as the stagnation pressure. The resolution of the pressure taps on the lower surface was assumed sufficient to extract the maximum positive surface pressure, especially at lower angles of attack where the stagnation point was near the leading edge. According to Shipley

Table 5.11 *Dynamic Pressure Measurements*

Identification	Description	Units
q(stag,1)	Stagnation Pressure at 30% span	Pa
q(stag,4)	Stagnation Pressure at 47% span	Pa
q(stag,7)	Stagnation Pressure at 63% span	Pa
q(stag,10)	Stagnation Pressure at 80% span	Pa
q(stag,14)	Stagnation Pressure at 95% span	Pa
q(dyn,34)	Dynamic Pressure, 34% span	Pa
q(dyn,51)	Dynamic Pressure, 51% span	Pa
q(dyn,67)	Dynamic Pressure, 67% span	Pa
q(dyn,84)	Dynamic Pressure, 84% span	Pa ')
q(dyn,86)	Dynamic Pressure, 86% span	Pa ")
q(dyn,91)	Dynamic Pressure, 91% span	Pa ')

") Phase II only.
') Phase III and IV only.

et al. ([20]) the stagnation point normalization method is the preferred method of estimating dynamic pressure on the blade. Dynamic pressure measurements are listed in table 5.11.

Force coefficients
Each of the measured blade surface pressure values was normalized by the stagnation pressure at the corresponding span location as shown in equation 5.7.

$$C_p = \frac{p_{cor}}{q_{stag}} \tag{5.7}$$

where
C_p = normalized pressure coefficient, dimensionless
p_{cor} = differential pressure corrected for centrifugal force, Pa
q_{stag} = stagnation point dynamic pressure (corrected for centrifugal force), Pa.

The pressure distributions for rotating-blade data were integrated to compute normal force coefficients (c_n) and tangent force coefficients (c_t) per unit length. These are fundamental coefficients that are commonly used to describe airfoil performance from pressure measurements because their derivation is independent of the angle-of-attack measurement. They represent the forces acting perpendicular and parallel to the airfoil chord, respectively. The average pressure between two adjacent taps was first projected onto the chord line, integrated to determine the c_n values, and then projected onto an axis orthogonal to the chord and integrated to compute c_t values. This procedure is described in detail by [21]. Equations 5.8 and 5.9 give the integration procedure used to determine c_n and c_t. The x and y values begin at the trailing edge, cover the upper surface of the blade, and then the lower surface, ending at the starting point, the trailing edge.

$$c_n = \sum_{i=1}^{nr.taps} \frac{C_{p,i} + C_{p,i+1}}{2}(x_{i+1} - x_i) \tag{5.8}$$

$$c_t = -\sum_{i=1}^{nr.taps} \frac{C_{p,i} + C_{p,i+1}}{2}(y_{i+1} - y_i) \tag{5.9}$$

where,
C_p = normalized pressure coefficient
x_i = distance along chord line from leading edge to i^{th} pressure tap
y_i = distance from chord line along axis orthogonal to chord to i^{th} pressure tap

In a similar integral procedure, pitching moment coefficients (c_m) were determined. The pitching moment represents the total moment about the pitch axis (1/4 chord) due to the normal and tangential forces at a pressure tap with the vertical or horizontal distance from the pitch axis as the moment arm. This equation is given in 5.10:

$$c_m = -\sum_{i=1}^{nr.taps} \frac{C_{p,i} + C_{p,i+1}}{2}(x_{i+1} - x_i)(\frac{x_{i+1} - x_i}{2} + x_i - 0.25)$$

$$+ \sum_{i=1}^{nr.taps} \frac{C_{p,i} + C_{p,i+1}}{2}(y_{i+1} - y_i)(\frac{y_{i+1} - y_i}{2} + y_i) \quad (5.10)$$

All other airfoil performance coefficients, such as lift (c_l), pressure drag (c_{dp}), torque (c_{torque}), and thrust (c_{thrust}), were computed using the c_n and c_t values in conjunction with their reference angles. Torque and thrust coefficients were calculated as a function of blade pitch angle (ϕ) and local twist angle (β), both of which were easily measured. Lift and pressure drag coefficients, on the other hand, rely upon the angle of attack (α) which is not as easily acquired. For this reason, only torque and thrust coefficients were included in the data base, but the equations used to determine lift and pressure drag coefficients are shown in the equations 5.11 to 5.14.

$$c_{torque} = c_n \sin(\phi + \beta) + c_t \cos(\phi + \beta) \quad (5.11)$$

$$c_{thrust} = c_n \sin(\phi + \beta) - c_t \sin(\phi + \beta) \quad (5.12)$$

$$c_l = c_n \cos(\alpha) + c_t \sin(\alpha) \quad (5.13)$$

$$c_{dp} = c_n \sin(\alpha) - c_t \cos(\alpha) \quad (5.14)$$

Torque and thrust coefficients were integrated along the span of the blade and multiplied by the number of blades to provide a rough estimate of the total aerodynamic thrust and torque applied to the entire rotor. All of the aerodynamic force coefficients included in the data base are listed in table 5.12. The estimated aerodynamic thrust and torque appeared with the turbine load measurements in table 5.7 for Phase II and table 5.8 for Phases III and IV.

Angle of Attack

Wind tunnel tests were performed with the flag sensor mounted on a full-chord scale airfoil section in order to develop a correction for upwash and to determine the dynamic characteristics of the flag. The configuration and resulting data are explained in the Phase I report (Butterfield et al., [11]). The upwash correction derived from wind tunnel testing was applied to all of the local flow angle measurements, including those made with the five-hole probes, as 5.15, 5.16 and 5.17.

$$\alpha = 0.58090 \cdot \mathrm{alpha}_m - 0.46470 (\alpha_m < -10 \mathrm{degrees}) \quad (5.15)$$

Table 5.12 *Force coefficients*

Identification	Description	Units
cn1	Normal force at 30% span	Cn
cn4	Normal force at 47% span	Cn
cn7	Normal force at 63% span	Cn
cn10	Normal force at 80% span	Cn
cn14	Normal force at 95% span	Cn ')
ct1	Tangent force at 30% span	Ct
ct4	Tangent force at 47% span	Ct
ct7	Tangent force at 63% span	Ct
ct10	Tangent force at 80% span	Ct
ct14	Tangent force at 95% span	Ct ')
cth1	Thrust Coefficient at 30% span	Cth
cth4	Thrust Coefficient at 47% span	Cth
cth7	Thrust Coefficient at 63% span	Cth
cth10	Thrust Coefficient at 80% span	Cth
cth14	Thrust Coefficient at 95% span	Cth ')
ctq1	Torque Coefficient at 30% span	Ctq
ctq4	Torque Coefficient at 47% span	Ctq
ctq7	Torque Coefficient at 63% span	Ctq
ctq10	Torque Coefficient at 80% span	Ctq
ctq14	Torque Coefficient at 95% span	Ctq ')
cm1	Pitch Moment Coefficient at 30% span	Cm
cm4	Pitch Moment Coefficient at 47% span	Cm
cm7	Pitch Moment Coefficient at 63% span	Cm
cm10	Pitch Moment Coefficient at 80% span	Cm
cm14	Pitch Moment Coefficient at 95% span	Cm ')

') Phases III and IV only.

Table 5.13 *Phase II and Phase III Upwash Corrected LFA Measurements*

Identification	Description	Units
alpha(c,1)	AOA 30% span (upwash corrected)	deg
alpha(c,4)	AOA 47% span (upwash corrected)	deg ')
alpha(c,7)	AOA 63% span (upwash corrected)	deg
alpha(c,10)	AOA 80% span (upwash corrected)	deg

') Appears in Phase III only.

Table 5.14 *Phase IV Upwash Corrected LFA and Crossflow Angle Measurements*

Identification	Description	Units
alpha(c,34)	AOA 34% span (upwash corrected)	deg
alpha(c,51)	AOA 51% span (upwash corrected)	deg
alpha(c,67)	AOA 67% span (upwash corrected)	deg
alpha(c,84)	AOA 84% span (upwash corrected)	deg
alpha(c,91)	AOA 91% span (upwash corrected)	deg

$$\alpha = -5.427\mathrm{E}^{-5} \cdot \alpha_{\mathrm{m}}^3 + 6.713\mathrm{E}^{-3} \cdot \alpha_{\mathrm{m}}^2 + 0.617 \cdot \alpha_{\mathrm{m}} - 0.8293 \tag{5.16}$$

$$\alpha = 0.93421 \cdot \alpha_{\mathrm{m}} - 7.4174 (\alpha_{\mathrm{m}} > 60 \mathrm{degrees}) \tag{5.17}$$

where
α = upwash corrected angle of attack, deg
α_{m} = local flow angle measurement, deg

This upwash correction has proven satisfactory in displaying aerodynamic performance (Simms, Robinson, Hand, and Fingersh, [22]) for measurements made with the flag sensor, but confidence in this application of the upwash correction to the five-hole probe measurements has not yet been achieved. Both the local flow angle measurement and the upwash corrected result were included in the data base files. Channels associated with upwash corrected angle of attack for each phase of testing are listed in the tables 5.13 and 5.14.

Other Derived Channels

A sonic anemometer was used to measure wind velocity and direction in the u, v, and w orthogonal component directions. These vector components were transformed into magnitude and direction during post-processing. Only the resultant magnitude and direction were included in the data base files.

The Richardson number provides an indication of atmospheric stability based on temperature gradients and wind shear. This was calculated using the equations 5.18 to 5.20 and was included in the data base for all campaigns.

$$\mathrm{Ri} = \frac{\left(\frac{9.8}{\Theta_{\mathrm{m}}}\right)\left(\frac{\Delta\Theta}{\Delta Z}\right)}{\overline{V_{\mathrm{shear}}^2}} \tag{5.18}$$

$$\Theta = \mathrm{T}\frac{100,000}{\mathrm{P}}^{0.286} \tag{5.19}$$

$$\mathrm{V_{shear}} = \frac{\sum_{\mathrm{n=1}}^{\mathrm{N-1}} \frac{\mathrm{WS_{n+1}} - \mathrm{WS_n}}{\mathrm{Z_n} + 1 - \mathrm{Z_n}}}{\mathrm{N} - 1} \tag{5.20}$$

where

Ri = Richardson Number, dimensionless
Θ_m = Average Potential Temperature between top and bottom of tower, K
$\Delta\Theta$ = Potential Temperature difference between top and bottom of tower, K
ΔZ = Elevation difference between temperature measurements, m
V_{shear} = Average vertical wind shear over ΔZ, m/s/m
Θ = Potential temperature, K
T = Measured, dry-bulb temperature, K
P = Barometric pressure, Pa
N = Number of wind speed measurements
WS_n = Wind speed, m/s
Z_n = Elevation at n^{th} wind speed measurement, m

5.4 RISØ test turbine

The design and construction of the experimental facility was initiated back in 1987 funded by the Danish Ministry of energy and the DGXII research programme of The European Union. In 1989 the first measurement programme was carried out followed by new measurement campaigns in 1991, 1992 and 1993. Then in 1994 the facility was closed down.

5.4.1 Global characteristics of facility

The facility was developed to provide experimental results that could be used to identify the main mechanisms controlling the aerodynamic forces on a rotating HAWT blade in natural conditions. In particular, the measurements were carried out for use in quantifying the importance of 3D flow effects, unsteady effects and rotary wing effects on a stall regulated rotor. A detailed description of the facility and the experimental results can be found in the references [23], [24] and [25].

The key feature of the facility is a system that enables the measurement on the rotating blade of the local aerodynamic forces and the local inflow to the blade. On basis of such measured quantities the airfoil characteristics c_l and c_d as function of instantaneous angle of attack α can be derived for the rotating blade at different spanwise stations and compared with conventional 2D airfoil data.

The measurements have been carried out on the 100 kW Tellus machine at the wind turbine test site at Riso. It is a fixed pitch, stall controlled, three bladed turbine, see figure 5.25. The turbine has a double wound generator which gives the following two synchronous rotational rotor speeds:

- 47.5 rpm, 47.9 rpm at rated power
- 35.6 rpm, 36.3 rpm at rated power

The tower is of the lattice type with three main tower poles and its height is 29.3 m. The blade type is the LM 8.2 m blade which has both twist and taper, see figure 5.24.

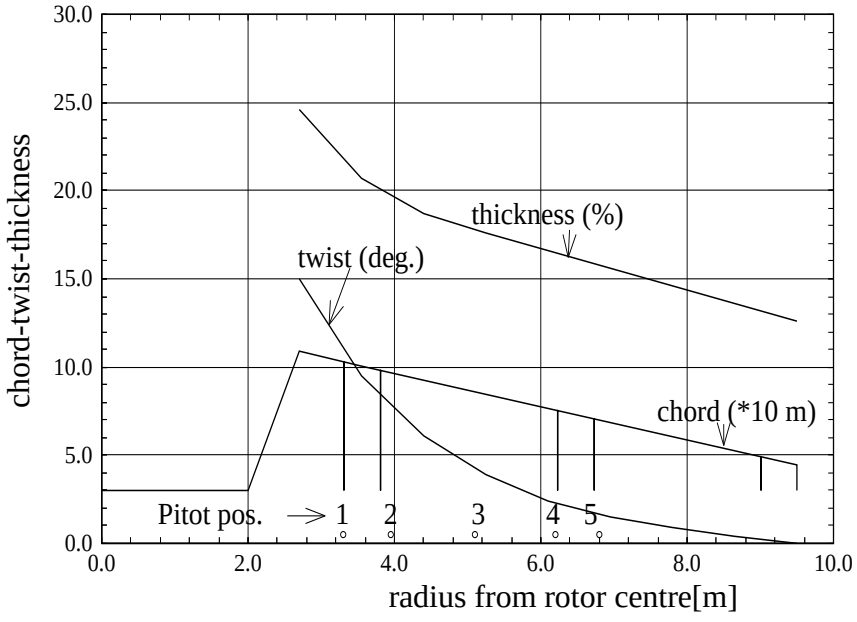

Figure 5.24 *RISØ, The planform data for the test blade including positions of the three blade segments and the positions for the attachment holes for the pitot tube*

Figure 5.25 *The 100 kW stall regulated wind turbine used for the RISØ experiments*

A few data on the turbine are listed below:

Rotor:
- Hub height: 29.3 m
- Number of blades: 3
- Rotor diameter: 19.0 m
- Swept area: 284 m^2
- Tilt: 5 deg
- Coning: 0 deg
- Blade tip angle (measured):
  - 1.8 deg
  - 1.8 deg
  - 1.5 deg
- Power control: stall
- Direction of rotor rotation (seen in front): anti-clockwise

Blades:
- Type: LM-Glasfiber 8.2 m, cantilevered GRP
- Spar material: GRP
- Shell material: GRP
- Blade length: 8.2 m
- Profiled blade length: 6.8 m
- Blade extensions: 1 m
- Root chord: 1.09 m
- Tip chord: 0.45 m
- Blade twist: 15 deg
- Blade profile: NACA 63n-2nn series
- Air brakes: Spoilers positioned on the suction side

Gearbox
- Gear ratio: 1:21.063

Location
The test site is situated at Riso on the east side of Roskilde Fjord running approximately south - north. The inflow conditions depend strongly on the wind direction with low turbulence intensities for west to north west directions whereas high turbulence intensities are found for most of the other directions.

5.4.2 Instrumentation

Blade instrumentation
One of the blades has been modified so that the aerodynamic forces on three segments of the blades can be measured, see figure 5.26. Each blade segment is 0.5 m in spanwise length and is suspended on a 3 component balance attached to the main spar of the blade, see figure 5.28.

The force components measured on each balance is the normal force N, the chordwise force T and the pitching moment M. The radial positions of the mid of the blade segments are the following, see figure 5.27

Segment 1:	Radius 3.56 m,	37 % radius
Segment 2:	Radius 6.48 m,	68 % radius
Segment 3:	Radius 9.26 m,	98 % radius

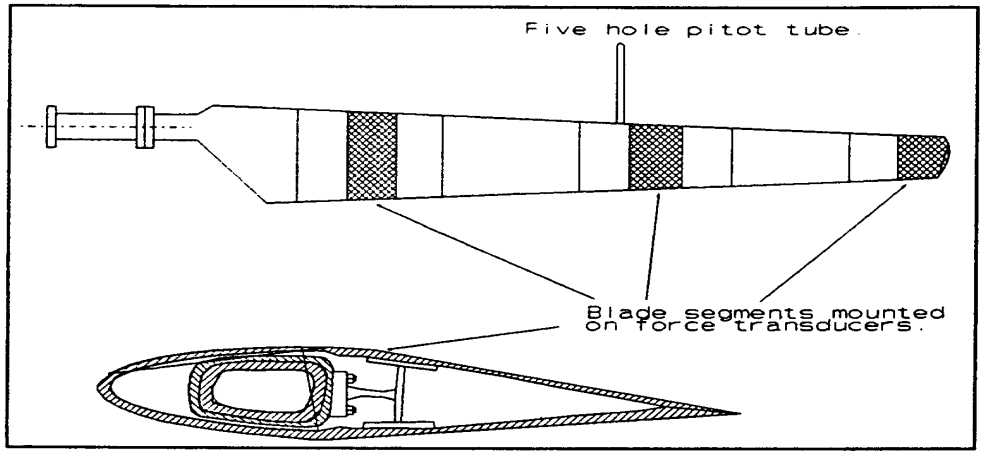

Figure 5.26 *RISØ, The principal layout of the test blade with the three blade segments and the pitot tube for measuring the inflow*

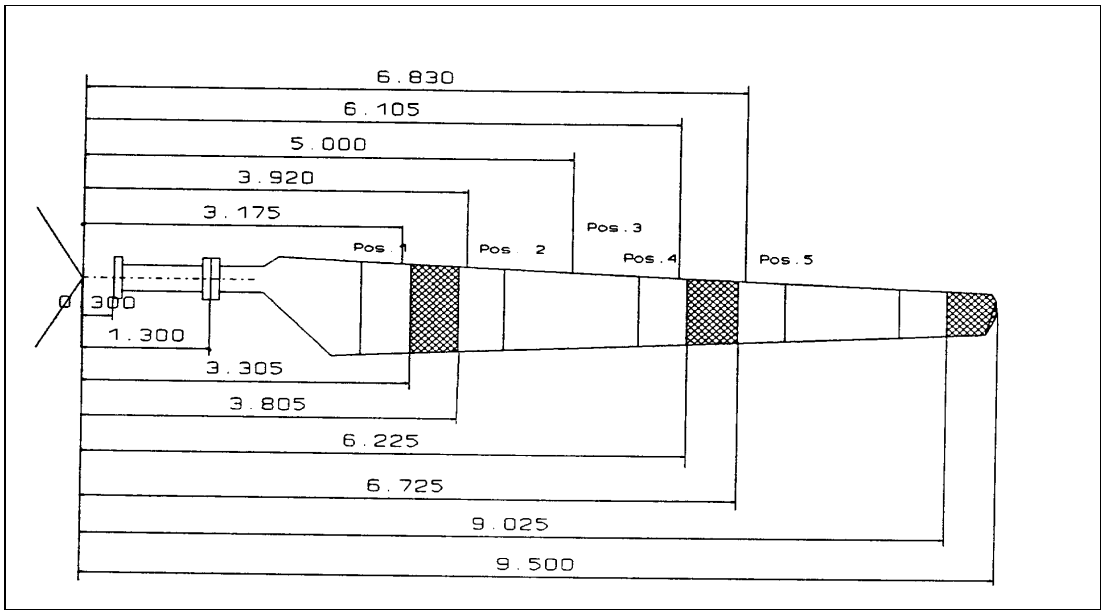

Figure 5.27 *The geometry data for the test blade. Positions for the pitot tube are shown on the upper part of the picture and blade segments on the lower part*

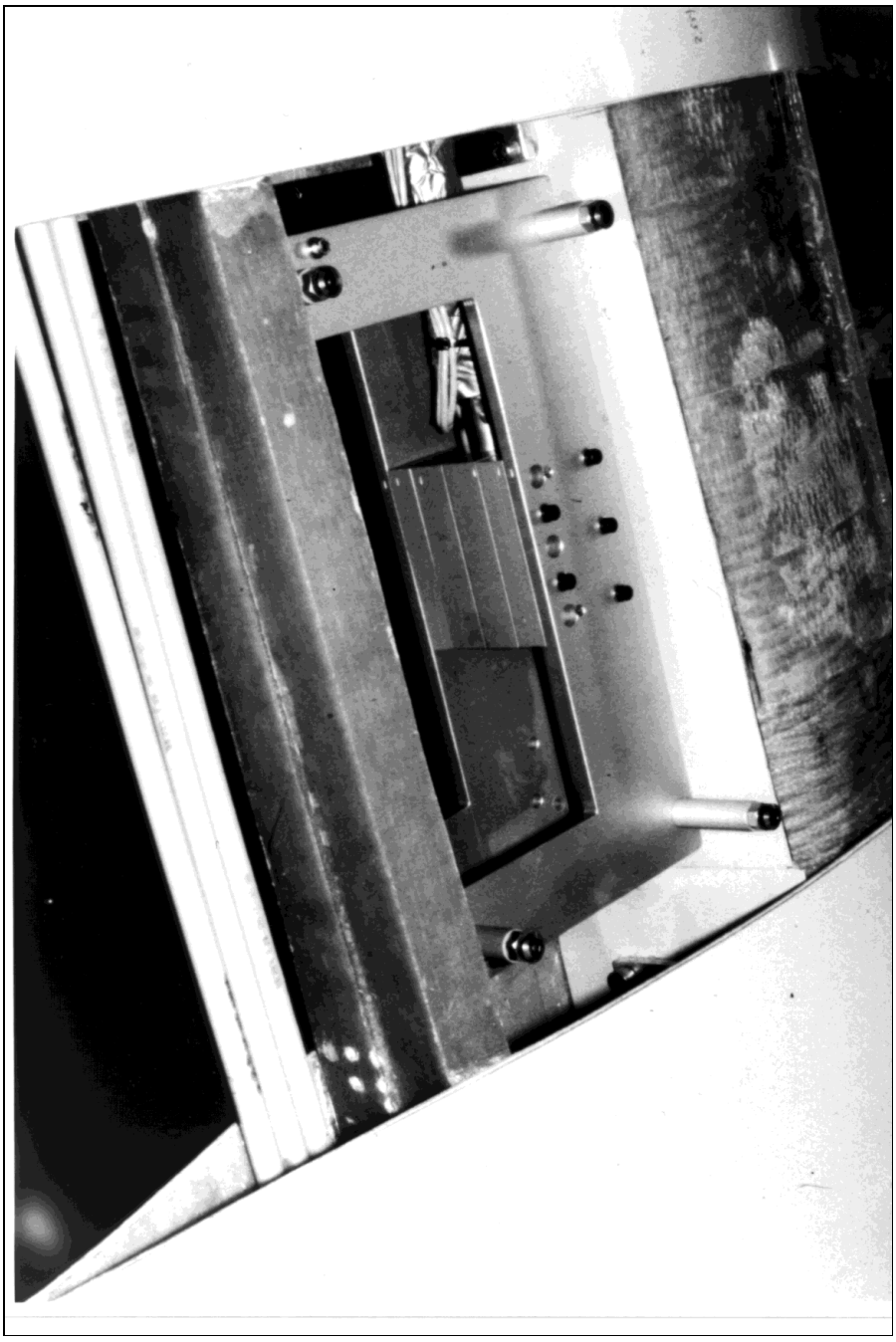

Figure 5.28 *RISØ, The balance and the supporting structure for one of the blade segments*

In order to derive the aerodynamic force component from the total measured force the inertial force component must be subtracted. This is done on basis of a measurement of the acceleration of each of the balance attachments to the main blade, see figure 5.29. The inflow to the blade has been measured with a five hole

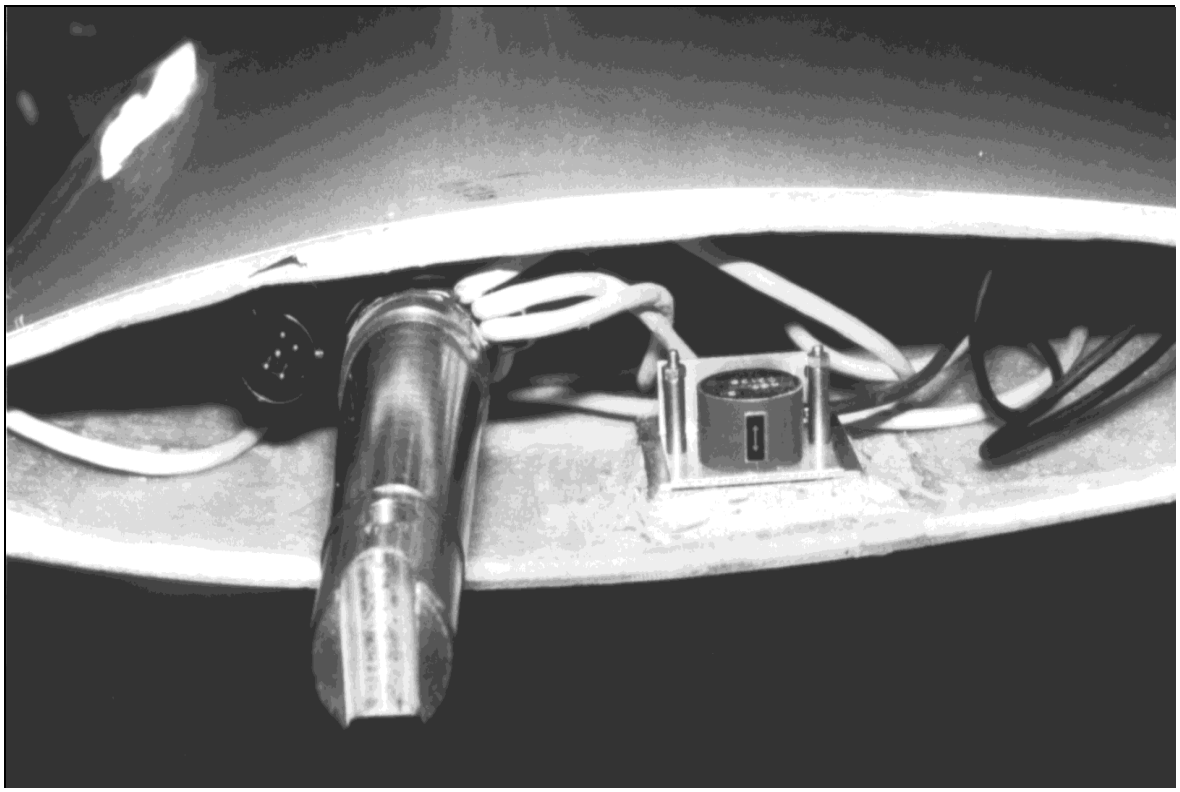

Figure 5.29 *RISØ, The balance for the blade tip segment and the accelerometer to measure flapwise acceleration in order to compensate for the structural force component in the total measured force*

pitot tube mounted on the blade about one chord length in front of the leading edge of the blade, see figure 5.30. The pitot tube can be positioned at different radial positions as marked on figure 5.27, but for all the measurements supplied to the IEA data base the pitot has been in position 5 which is just outboard the mid blade segment. The four pressure transducers for the pitot tube were build into the blade close to pitot tube so that the length of the flexible tubes was around 1.5 m.

Additional signals

The flapwise blade root moment was measured on all three blades. On the turbine the main shaft torque, rotational speed, electrical power, rotor position and yaw position was measured. In the meteorological tower placed about two turbine diameters to the west, wind speed and wind direction was measured at hub height. At the ground air temperature and air pressure was measured

5.4.3 Measuring speed

The complete data acquisition system was configured with the measurements from the meteorological mast and the wind turbine connected to a PC. The sensors were

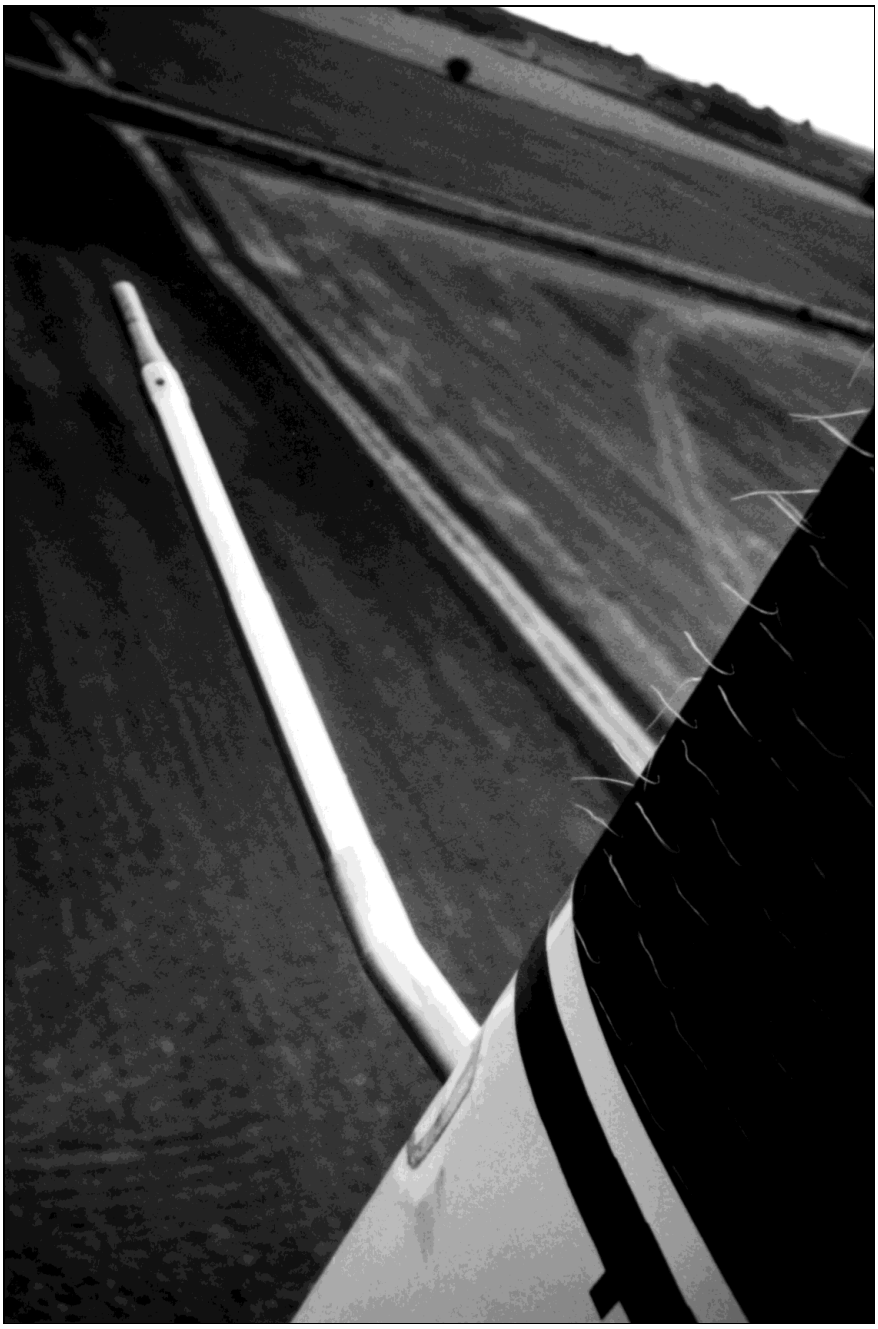

Figure 5.30 *RISØ, The five hole pitot tube measuring the inflow velocity vector to the blade*

supplied with 15 V and the signals are transferred with a voltage range from -5V to +5V. A 16 channel telemetry system was mounted on the rotor and the data were transmitted to the ground as PCM signals.

All the channels pass through a filter that protects the equipment from lightning. Before the digital sampling, the signals pass through an anti aliasing filter with a cut off frequency of 20 Hz. The sampling frequency for all channels was 25 Hz. Each measurement period is 10 min. and the data are kept as binary files in the form of time series.

5.4.4 Data reduction

All the data signals except rotor position are as a first step in the data processing filtered with a digital low pass filter with a cut off frequency between 2.5 and 3 Hz. The effect of this filtering is illustrated in figure 5.31 and 5.32

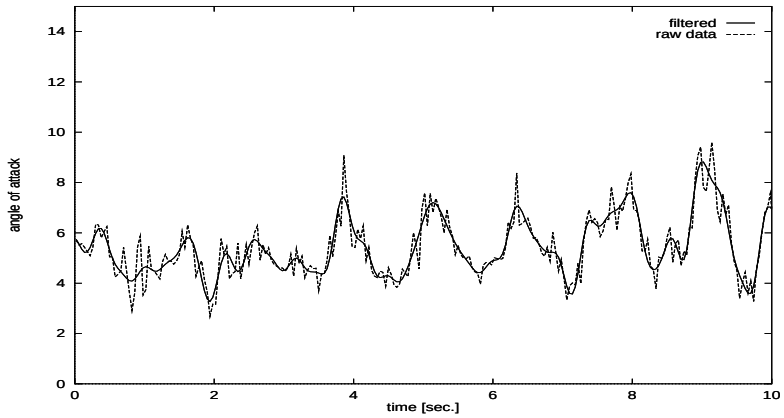

Figure 5.31 *RISØ:The effect of applying the filter seen on a time trace of the measured angle of attack*

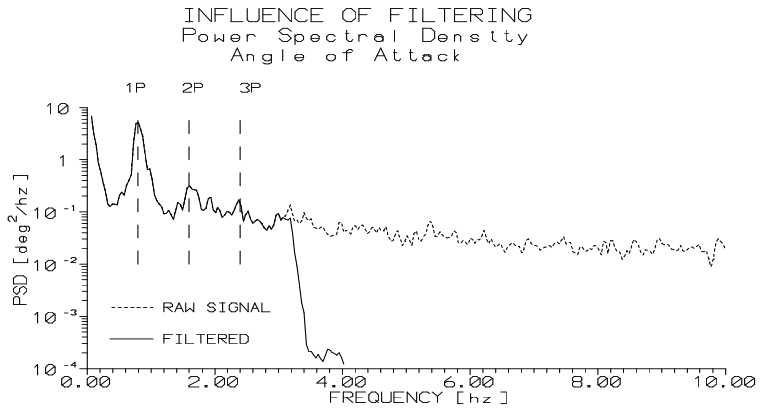

Figure 5.32 *RISØ: The effect of applying the filter seen on a power spectrum of the measured angle of attack*

The measured angle of attack and the relative velocity $\mathbf{W_{pitot}}$ are derived from the four measured pressure signals on the five hole pitot tube on the basis of calibrations in a wind tunnel. To derive the airfoil characteristics for the different blade segments $\mathbf{W_{pitot}}$ is scaled with the radius ratio between the pitot position and the radial position of the mid of the segment:

$$\mathbf{W_{segment}} = \mathbf{W_{pitot}} \cdot (\frac{\mathbf{r_{segment}}}{\mathbf{r_{pitot}}})$$

A thorough discussion of the correction of the measured angle of attack with the pitot tube $\alpha_{\mathbf{pitot}}$ is presented in [23]. Shortly, the objective with the correction is to achieve the same relation between angle of attack and rotor power as computed with the blade element momentum (BEM) theory below stall so that the measured airfoil characteristics can be used for rotor computations with this code.

The correction is simply a constant which is subtracted the measured angle of attack:

$$\alpha_{\text{segment}} = \alpha_{\text{pitot}} - 4.7[^{\circ}]$$

The airfoil coefficients $c_{n,i}$ and $c_{t,i}$ at segment i are now derived as:

$$c_{n,i} = \frac{N_i}{0.5\rho W_i^2 c_i l_i}$$

$$c_{t,i} = \frac{T_i}{0.5\rho W_i^2 c_i l_i}$$

where l_i is the spanwise length of the segment, N_i and T_i are the measured normal and tangential aerodynamic force on the segment, W_i the corrected inflow velocity as shown above and c_i is the chord on the mid of the segment.

5.5 DUT test turbine

For a very detailed description of the DUT facility reference is made to [26].

5.5.1 Global characteristics of facility

Figure 5.33 *DUT test facility*

- Blade: Prince Fiber Technics (Aerpac) mounted on an experimental turbine, see figure 5.33.
- Number of blades: 2
- Blade span (from flange to tip) = 4.4 m
- Rotor diameter = 10 m
- Blade profile: NLF(1)-0416
- Blade without twist and taper
- Pressure tap measurements around profiles at 4 different radial stations, see figure 5.34.
- The inflow velocity is measured with a pitot probe, see figure 5.34. The inflow angle is measured with a three hole probe mounted at 75% span. The length of this probe is 0.55c and the angle between the probe and the chord is 0 deg

(Annex XIV). In Annex XVIII, 6 hole

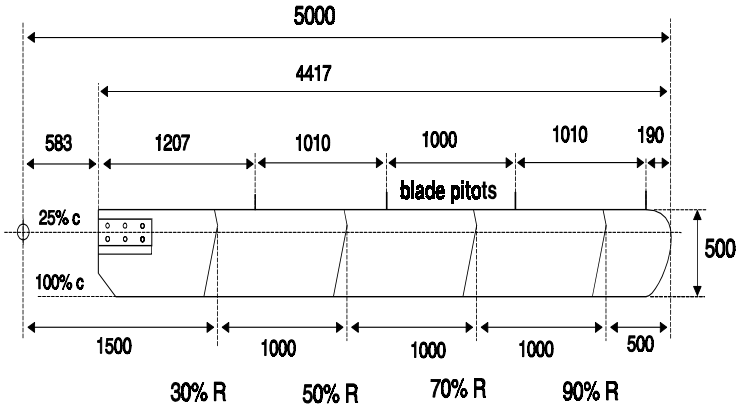

Figure 5.34 *DUT: Drawing of the instrumented blad with 4 spanwise locations of the pressure taps and the four blade pitots. The three hole flow direction probe was located at the 75% spanwise position (IEA Annex XIV)*

Location
The Open Air Rotor Research Facility is located at the Delft University of Technology near Delft in the Netherlands. Figure 5.35 gives a map of the site and environment. The prevailing wind direction is from South-West. A roughness hight of 0.25m was assumed. The turbulence level is not yet determined.

5.5.2 Instrumentation

- Pressure taps at 4 rotor blade sections, These taps are positioned at 30%, 50%, 70% and 90% of the rotor radius.
  Note that the sections are not measured simultaneously. In IEA Annex XIV measurements from the 30%, 50% and 70% station had been supplied only but in IEA Annex XVIII measurements from the 30%, 50% and 70% station have been supplied.
  There are 59 taps per station with 0.4 mm diameter, see the figures 5.36 to 5.39.
- In IEA Annex XIV, A 3 hole probe was mounted at the 75% span location. In IEA Annex XVIII 6 hole probes were available near 30%, 50% and 70% span;
- All signals from the rotor are transferred via sliprings. The voltage output from the transducers is transferred to current to reduce the variable resistance effects of the sliprings. The strain gauge signals from the hub are pulse coded before they are transmitted over the sliprings. Table 5.15 summarizes all the collected signals.
- Pressure System:
  The pressures were recorded with two high speed differential electronic transducers from Pressure System Incorporation, type Nr. ESP-32TL. One has a range of $\pm$ 1 Psi ($\pm$ 7000 Pa), the other has a range of $\pm$ 2.5 Psi (($\pm$ 17000 Pa)

Figure 5.35 *DUT: Map of the Open Air Rotor Research Facility and environment. The hight of the most important structures (trees) are given in meters on the drawing. The arrow denotes the North direction. The two circles indicate a distance of 100m and 250m respectively*

Each transducer has 32 ports and a built-in calibration facility. The reference port of the transducers was via a damper connected to a Kiel pitot tube on the hub. To obtain the static reference pressure this total pressure is numerically corrected with the dynamic pressure of the wind. The damper was placed close to the reference port of the transducers in the blade. A special designed three hole probe was used to measure the flow direction near the 70% radial section (IEA Annex XIV). Pulse tests were carried out to check the acoustic behaviour of the pressure tube systems. Maximum frequency response of a pressure port is several tens Hz.

- Damper:
  The reference port and the measurement ports of the transducers showed a different dynamic response. Therefore a damper was installed to make a numerical correction possible for the variation of the static pressure created by the vertical movement of the transducers (altitude effect). This pressure variation did not cancel out due the different dynamic response of the reference port and the measurement ports. The damper RC time was adjusted to 2.1 s. To

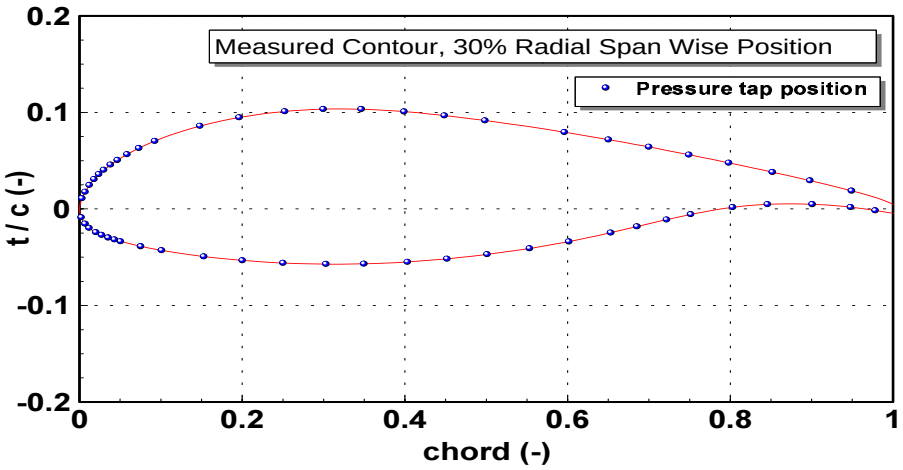

Figure 5.36 *DUT: Position of pressure taps on measured contour of the 30% radial spanwise section smoothed with XFOIL to reduce the effects of the inaccuracy of the contour measurement method*

avoid different behavior in dynamic response the pressure taps were connected to identical tubes of 70cm length and an inside diameter of 2mm for the brass tubes, and 1 mm for the flexible tubes.

- Wind Measurement:
  The wind speed and wind direction were measured with a Sonic wind meter on a mobile tower one rotor diameter upstream at hub axis height. In addition a cup anemometer was used at nearly the same position.
- Flow Patterns
  The flow pattern on the blade suction side surface was visualized with tufts. A rotating micro video camera, mounted near the hub, recorded the picture of these tufts. This picture was overlayed directly during the data acquisition with graphs of the pressure distribution ($C_p - x$) and other measurement data of interest. A special video overlay board was therefore installed in the PC-based data acquisition system.
- PC-based Data Acquisition System
  A 80486 PC runs the special custom written data acquisition software. The data acquisition software is written in Borland C++. The PC is equipped with an Advantech PCL818 100Khz 16 channel data 12 bits AD acquisition board. The Advantech board controls also the addressing lines of the multiplexed pressure transducers. A special hold switch in the transducer output lines speeds up the pressure measurements: the next pressure port is already addressed while the computer digitizes the previous pressure port. This reduces the settling time of the electronics. A Magni VGA Producer Pro board overlays the camera video signals with the screen output from the computer and sends the result to a standard S-VHS video recorder. The data acquisition software has the capacity to process and to display directly the data in a very flexible way. Only the original non corrected direct digitized values of each channel are stored with the calibration coefficient separate in the file header. A special replay function

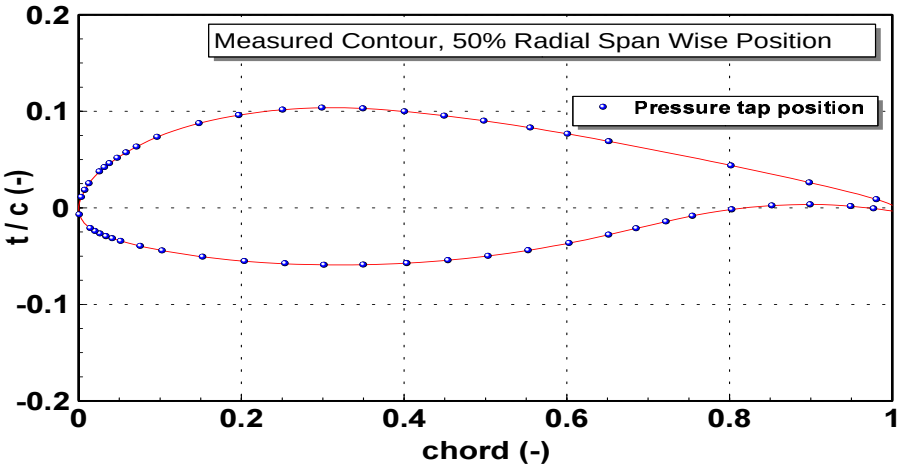

Figure 5.37 *DUT: Position of pressure taps on measured contour of the 50% radial spanwise section smoothed with XFOIL to reduce the effects of the inaccuracy of the contour measurement method*

Table 5.15 *Overview of collected and used instruments*

SIGNALS	INSTRUMENT
pressure taps on the blade, Kiel pitot tubes, three hole flow direction probe	PSI differential pressure transducers
wind speed	cup anemometer at a mobile tower
wind speed and wind direction	Gill Sonic wind meter at a mobile tower
temperature of transducers	PT 100 temperature sensor at transducer
blade flapping moments	strain gauges at the hub
tower bending moments	strain gauges at the tower
picture of tufts	rotating micro video camera at the hub
rotor torque	torque meter at the low speed shaft
rotor speed	tacho generator at generator, from six
azimuth position	degree azimuth pulse from one pulse per revolution

in the software allows to watch the collected data later in the same way as during the acquisition. During the process of collecting data and replay of the existing data files all the pressures and aerodynamic quantities are calculated from these rough data values.

5.5.3 Measurement Speed

All data channels were sampled at 333 Hz. These data readings were averaged directly on line in the memory of the data acquisition computer. The rotational speed of the rotor dictated how many readings were averaged: at every six degrees an averaged value of each data channel was recorded in the file. So the sampling rate of the stored data is 60 times the rotational speed. To reduce the electronic

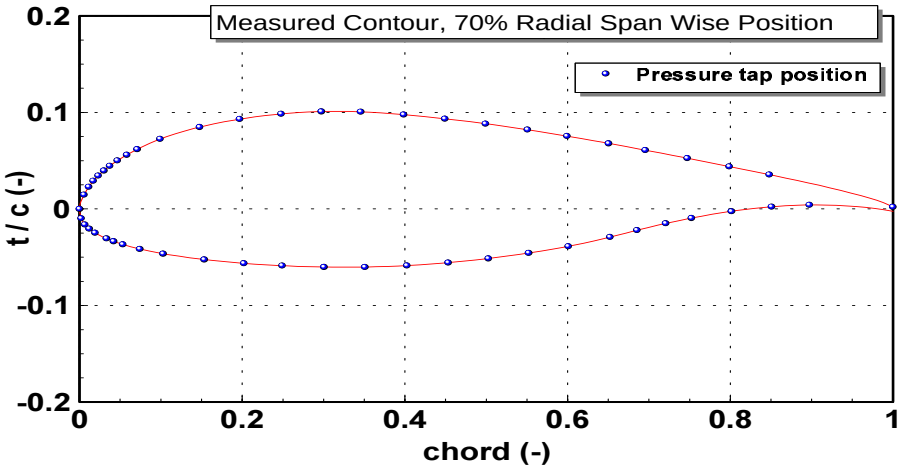

Figure 5.38 *DUT: Position of pressure taps on measured contour of the 70% radial spanwise section smoothed with XFOIL to reduce the effects of the inaccuracy of the contour measurement method*

scatter the data was averaged.

5.5.4 Calibration procedures

For every measurement series the pressure transducers were manually calibrated by applying six calibration pressures. The transducers have a built-in switch for switching between calibration mode and measurement mode. When the calibration was completed while the turbine was lowered on the ground, the turbine was erected in a few minutes. Each measurement port has its own calibration curve, which is a third degree polynom. The temperature of the transducers has an important influence on the calibration curves. In [27] the different influences on the calibration in relation to the accuracy of the pressure measurements are analyzed.

5.5.5 Data Reduction

For a more detailed description of the pressure correction formulae with the derivations, reference is made to appendix B of [26].

Pressure Data Correction

Three corrections on the pressure signals were employed:

1. a correction on the reference channel with the dynamic pressure $0.5\rho V^2$ of the wind speed (V), calculated from the wind meter signal. This correction is small but necessary, because the reference port is connected to a total Kiel pressure probe at the hub and not to an atmospheric static probe;
2. an individual centrifugal force correction on each pressure port. The radial position of the pressure tap r_{tap} determines the size of this centrifugal force correction;

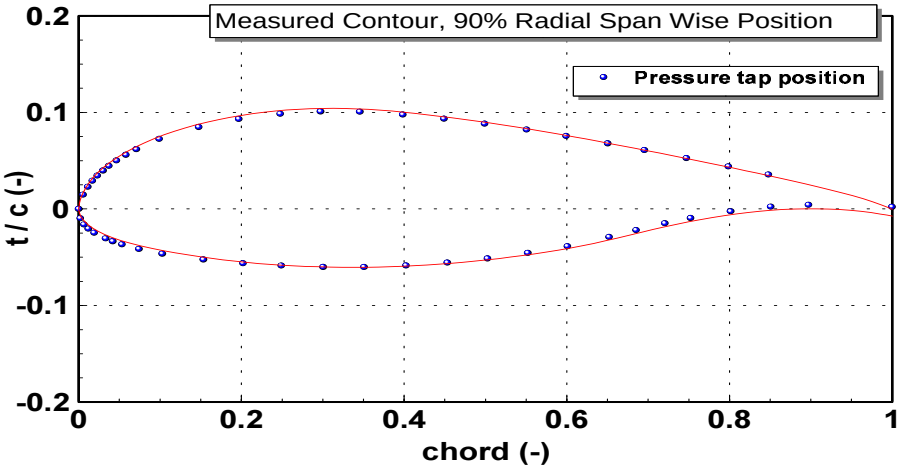

Figure 5.39 *DUT: Position of pressure taps on measured contour of the 90% radial spanwise section smoothed with XFOIL to reduce the effects of the inaccuracy of the contour measurement method*

3. a harmonic altitude correction. This correction is necessary because the reference port is stabilized as much as possible with a damper near the transducers in the reference tube. The amplitude of this effect is mainly determined by the radial location of the transducers. The correction (amplitude $\delta p_{harmonic}$ and phase ψ) was empirically fitted in such a way, that the value of the pressure coefficient C_p became nearly constant of the tap at the pressure side at 85% chord position. This location was chosen because wind tunnel measurements showed for this tap a nearly constant C_p value for a quite large range of angles of attack. The corrections are calculated on line during the data collection and again during the data replay, since only the non corrected data values were stored.

Calculation of C_p

The pressure coefficient C_p is defined as:

$$C_p = \frac{p_{tap} - p_{atm}}{q} = \frac{p_{tap} - p_{atm}}{p_{pt} - p_{atm}} \tag{5.21}$$

p_{tap} denotes the static pressure of a tap, p_{atm} is the atmospheric pressure, p_{pt} is the total pressure and q is the dynamic pressure. It was assumed that the static pressure did not differ from the p_{atm}. With the three corrections mentioned in the previous section 5.5.5 C_p was calculated finally with the formula:

$$C_p = \frac{\delta p_{tap} + 0.5\Omega^2 r_{tap}^2 + 0.5\rho V^2 - \delta p_{harmonic}\cos(\Omega t + \psi)}{\delta p_{pt} + 0.5\Omega^2 r_{tap}^2 + 0.5\rho V^2 - \delta p_{harmonic}\cos(\Omega t + \psi)} \tag{5.22}$$

δp_{tap} is the recorded value at the transducer port from a tap and δp_{pt} denotes the recorded value at the transducer port from the total pressure of the blade pitot. V is the undisturbed wind velocity, ρ is the air density and Ω is the rotational speed. The radial position of a pressure tap is r_{tap}.

Calculation of c_n, c_t and c_m

The normal force coefficient c_n, the tangential force coefficient c_t and moment coefficient of a section c_m are obtained directly by integrating the pressure distribution (C_p values) with the trapezium rule. For this calculation the location of the pressure tap nearest to the leading edge was shifted to the leading edge. c_m is calculated at the 25% chord point.

Data Filtering

Until this moment no data filtering with a low pass filter was done. Analysis made by other institutes (RISØ, FFA and ECN) showed that this is a useful technique to smooth the scatter in the experimental data.

Angle of Attack Determination

In section 6, more information is given about the DUT method to determine the angle of attack.

The angle of attack measurements which are performed for IEA Annex XIV are all recorded with a 3 hole probe. A theoretical correction for the 2D upwash and for the effect of finite span and power extraction process has been added.

Wind Tunnel Experiments

In January 1991 the 70% spanwise section was tested in the Low Speed Wind Tunnel of the Aerospace Faculty of the DUT. The tests are described and the results are given in the Appendix A of [28].

5.6 Mie test turbine

The pressure measurement setup has been prepared in cooperation with the Delft University of Technology since 1997.

5.6.1 Global characteristics of facility

- Blade: Mie in house, mounted on an experimental turbine, see figure 5.40.
- Number of blades: 3
- Blade span (from flange to tip) = 4.567 m
- Rotor diameter = 10 m
- Blade profile: DU91-W2-250 and DU93-W-210
- Blade with twist and taper
- Pressure tap measurements around profiles at 4 different radial stations, see Fig. 5.41.
- The inflow velocity and the inflow angle are measured with 2 five-hole spherical probes mounted at both sides of the measurement stations, see figure 5.41. The probe length is 1 chord and the angle between the probe and the chord is 0 deg.

Figure 5.40 *Mie test facility*

Location

The Open Air Rotor Research Facility is located at the Experimental Farm in the Mie University at Tsu City in Japan. Figure 5.42 shows a map of the site

Figure 5.41 *Mie: Drawing of the instrumented blade with 4 spanwise locations of the pressure taps and 2 five-hole spherical probes. The locations of five-hole probes were changed depending on the measurement stations*

and environment. The prevailing wind direction is from Northwest in winter. A roughness height of 0.15 m was assumed on the field. The forests with pine trees with a height of about 13 m lies on the right side when looking upwind to the turbine from a downwind position. The turbulence level has not yet been determined.

5.6.2 Instrumentation

- Pressure taps are positioned at 4 rotor blade sections at 32.5% , 50% , 70% and 90% of the rotor radius. There are 60 taps per station with 0.4 mm diameter, see Fig. 5.43. Note that the stations are not measured simultaneously.
- 2 five-hole spherical probes are mounted at both sides of the measurement stations. The five- hole spherical probes are mounted at:
  - 20.5% and 38.5% span locations for the 32.5% measurement station;
  - 38.5% and 56% span locations for the 50% measurement station;
  - 56% and 76% span locations for the 70% the measurement station;
  - 76% and 96% span locations for the 90% the measurement station.
- All signals from the rotor are transferred through white-gold slip-rings with 120 channels. The voltage output from the transducers is amplified to reduce the signal noise before they are transmitted over the slip-rings. The pitch angle is obtained from the signal of potentio- meter built in the pitch power-cylinder on low speed shaft. The azimuth position and rotor speed are detected by the pulse signals from the encoders. The yaw angle is measured with the use of the pulse signals from the encoders, which is mounted on the connection between nacelle and tower. Figures 5.44 and 5.45 show the schematic diagram of signal transfer. Table 5.16 summarizes all the collected signals.

- Pressure system:
  The pressures were recorded with eight high-speed differential electronic transducers from Scanivalve Corporation, ZOC23B series. One of them has a range of $\pm$ 2.5 Psi(17000Pa), the others have a range of $\pm$ 1Psi(7000Pa). Each transducer has 8 ports and a built-in calibration facility. The reference port of the

Figure 5.42 *Mie: Map of the Open Air Rotor Research Facility and environment. The location of the meteorological of anemometers and sonic wind speed meters are also indicated*

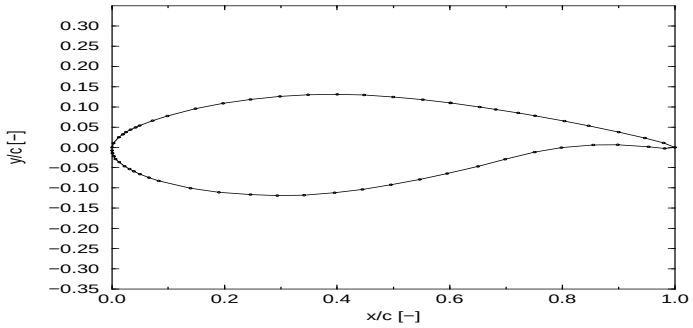

Figure 5.43 *Mie: Position of pressure taps*

transducers was connected to static pressure tap in the hub. 2 five-hole spherical probes were used to measure the dynamic pressure and flow direction near the measurement station. Pulse tests were carried out to check the response of the pressure systems. During one sampling interval no frequency response of a pressure port could be seen.

- Wind Measurement:
  The environmental wind speed and wind direction were measured with a sonic wind meter and six pairs of cup-anemometers and wind-vanes, which were installed at one rotor diameter upstream of rotor plane. The sonic wind meter was installed at hub axis height. Three pairs of cup-anemometers and wind-vanes were installed 9 meters to the left and the others were installed 9 meters to the right of the sonic speed meter. The anemometers at the top, middle and bottom levels have a height of 18.3, 13.3 and 8.3 meters, which correspond to

Figure 5.44 *Mie: Schematic diagram of signals and power train*

the height of the blade tip at top position, hub height, and the height of the blade tip at bottom position, respectively. The schematic layout of the sonic wind meter and anemometers are shown in Fig. 5.46.

- Flow Pattern:
  The flow pattern on the blade suction side surface was visualized with tufts. A rotating wireless CCD video camera SONY U-900 mounted near the hub took a picture of these tufts. The wireless signal from video camera was transmitted to an antenna on the ground. A video overlay board ATI Technologies ALL-IN-WONDER 128 was installed in the Pentium III 600MHz PC. This picture was overlayed with the data file name of pressure measurement.
- Data Acquisition System:
  A Pentium II PC runs the originally developed data acquisition software. The data acquisition software is written in Microsoft Visual Basic. The PC is equipped with two Interface AZI-3121 50kHz 64 channel data 12bits AD acquisition boards. A video signal from a Pentium III 600MHz PC was transmitted to the Pentium II PC through a network board. The results of video signals with the screen output and sampled data were sent to a digital video recorder SONY DHR-1000.

5.6.3 Measurement speed

All the data channels were simultaneously sampled with 95 Hz, which was the maximum sampling speed of the computer for simultaneous sampling. One data file was composed with 7400 data in 78 seconds.

Figure 5.45 *Mie: Schematic diagram of instrumentation of pressure measurement*

SIGNALS	INSTRUMENT
pressure taps on the blade, five-hole probes	Scanivalve ZOC23B differential pressure transducers
2 dimensional wind speed and wind direction	six pairs of cup-anemometer and wind vane
3 dimensional wind speed, wind direction and air temperature	KAIJO sonic wind meter
picture of tufts	rotating CCD video camera at hub
pitch angle	potentio-meter in power cylinder on low speed shaft
yaw angle	pulse encoder between nacelle and tower
rotor speed	pulse encoder on middle shaft
azimuth position	pulse encoder on low speed shaft
electrical current, voltage and power	power tester

Table 5.16 *Overview of collected data and used instruments*

5.6.4 Calibration procedure

For every measurement series, the pressure transducers were manually calibrated by applying eight calibration pressures of -4500, -4000, -3000, -2000, -1000, 0, +1000 and +2000 Pa. The transducers have a built-in switch for switching between calibration mode and measurement mode by high pressure. To keep the switch position of the mode, high pressure should be supplied to the transducers by pressure tank on the hub (see Fig. 5.45). During the calibration the turbine was at a lowered position of 3 meters high. After the calibration the turbine was erected in a few minutes. Each measurement port has its own calibration curve, which is a second-degree polynomial. The maximum time span of the measurements between each calibration was around 90 minutes.

Figure 5.46 *Mie: Mie: Meteorological instrumentation. Meteorological instruments are 1D upwind of the turbine rotor plane*

5.6.5 Data reduction

Pressure Data Correction
An individual centrifugal force was corrected on each pressure port. The radial position of the pressure tap determines the amount of this centrifugal force correction.

Calculation of Dynamic Pressure and Flow Direction
The dynamic pressure and the flow direction at the measurement sections were calculated by interpolation of the data at 2 five-hole probes.

Calculation of c_n, c_t and c_m
The normal force coefficient c_n, the tangential force coefficient c_t and moment coefficient of a section c_m are obtained directly by integrating the pressure distribution with the trapezium rule. cm is calculated at the 25% chord point.

Data Filtering
At this moment no data filtering with a low pass filter was done.

Angle of Attack Determination
The angle of attack correction was done with the results of wind tunnel test.

Wind Tunnel Experiments

All the spanwise sections were tested in the Goettingen type wind tunnel with open test section of the Mie University. The blade was set in the tunnel with end plates to improve two- dimensionality. The dynamic pressure and the flow direction were measured by five-hole spherical probes mounted on the blade. The geometrical angle of attack of the blade relative to the uniform flow was measured using the protractors attached on the blade. The wind speed during the testing was set at 15 m/s, so that, the Reynolds number was different at each station, due the different chord lengths.

5.7 Discussion of differences between facilities

- The diameter of the facilities in the project range between 10 m (NREL, TUD, Mie) and 27 m (ECN).
- The number of blade is two (DUT, ECN) or three (NREL, RISØ, IC/RAL, Mie University).
- The blades of four facilities (ECN, RISØ, IC/RAL, Mie) are twisted and tapered. The blades of two facilities (DUT, NREL) are untwisted and untapered. In addition, NREL supplied measurements on a blade which is twisted only.
- The following aerodynamic airfoils can be found on the various turbines:
  - NACA 44xx (ECN)
  - NACA 632xx (RISØ and IC/RAL)
  - NLF 0416 (DUT)
  - NREL S809 (NREL)
  - DU91-W2-250 and DU93-W-210 (Mie)
- Most participants measure the pressure distribution around the profiles from which the aerodynamic forces are derived. RISØ measures the aerodynamic forces directly by means of balances, which includes the measurement of the skin friction. This reduces the amount of data considerably, which is the main reason why RISØ supplied 10 minute time series and the other institutes much shorter time series;
- All participants have instrumented at least three radial stations, i.e. a root station (around 30% span), a mid station (around 60% span) and a tip station (around 80% span). DUT and Mie have instrumented 4 stations. NREL has instrumented 4 (Phase II) or 5 (Phase III) stations. IC/RAL has instrumented 6 stations.
- At most facilities the different radial stations were measured simultaneously. At the IC/RAL turbine two stations were measured simultaneously, at the DUT and Mie turbine every station was measured separately.
- The IEA Annex XIV/XVIII measurements of IC/RAL, NREL and RISØ were all made at the same rotor speed and the same pitch angle. The angle of attack was set by means of the wind speed.
- In the DUT IEA Annex XIV/XVIII experiments the angle of attack was usually set by means of the rotor speed (and the wind speed).
- In Mie's IEA Annex XIV/XVIII experiments, the angle of attack was usually set by means of the pitch angle (and the wind speed). There were slight differences in rotor speed. Note that Mie University schedules to perform variable speed measurements, after IEA Annex XVIII is finished.
- In the ECN IEA Annex XIV/XVIII experiments, the angle of attack is set in various ways; by means of the wind speed, the rotor speed or the pitch angle.
- The number of taps per stations is 25 for IC/RAL, 32 for NREL, 47 for ECN, 60 for Mie and 59 for DUT, although not all taps were working at the latter.
- The measurement of free stream conditions is done in the following way:
  - NREL applied a vertical plane array, heavily instrumented with many anemometers in Phase II, which was placed $\approx$ 1D upstream in the dominant wind direction. In the Phase III and IV the inflow was measured in a slightly less extensive way. Nevertheless three masts were still available, which were placed $\approx$ 1D upstream in the dominant wind direction, which yields information on the wind field in vertical as well as horizontal direction;
  - Mie University also measures the inflow through three masts, which were placed $\approx$ 1D upstream in the dominant wind direction and which yields

information on the wind field in vertical as well as horizontal direction;
- DUT measures the inflow conditions at hub height with a mobile mast which is placed 1D upstream;
- ECN measures the inflow conditions at three heights with a meteorological masts, which is located ≈ 2D West from the turbine.
- RISØ measures the wind speed at hub height with a mast which is placed ≈ 2D West from the turbine;
- IC/RAL measure the inflow conditions from two meteorological masts, which are placed at different locations, 2D from the turbine;

6. ANGLE OF ATTACK IN FIELD EXPERIMENTS

6.1 General

The angle of attack is a crucial quantity in most aerodynamic models for 3D rotating wind turbines. It should be realised however that its definition is based on the definition of the angle of attack in a 2D wind tunnel situation, and that such angle of attack becomes hypothetical in the 3D rotating environment. Hence the angle of attack, defined in this way is not a physical quantity and consequently it cannot be measured straightforwardly.

First consider the angle of attack of a non-rotating blade profile which is placed in a windtunnel. The angle of attack ($\alpha_{0,stat}$) is defined as the angle between the chord and the undisturbed wind vector (denoted by $\overline{\mathrm{V}}_{0,\mathrm{stat}}$) which is aligned with the wind tunnel walls. Now suppose that the local inflow angle ($\alpha_{\mathrm{local,stat}}$) is measured ahead of the blade profile with a measuring device (i.e. a 5 hole pitot probe, windvane etc), see figure 6.1.

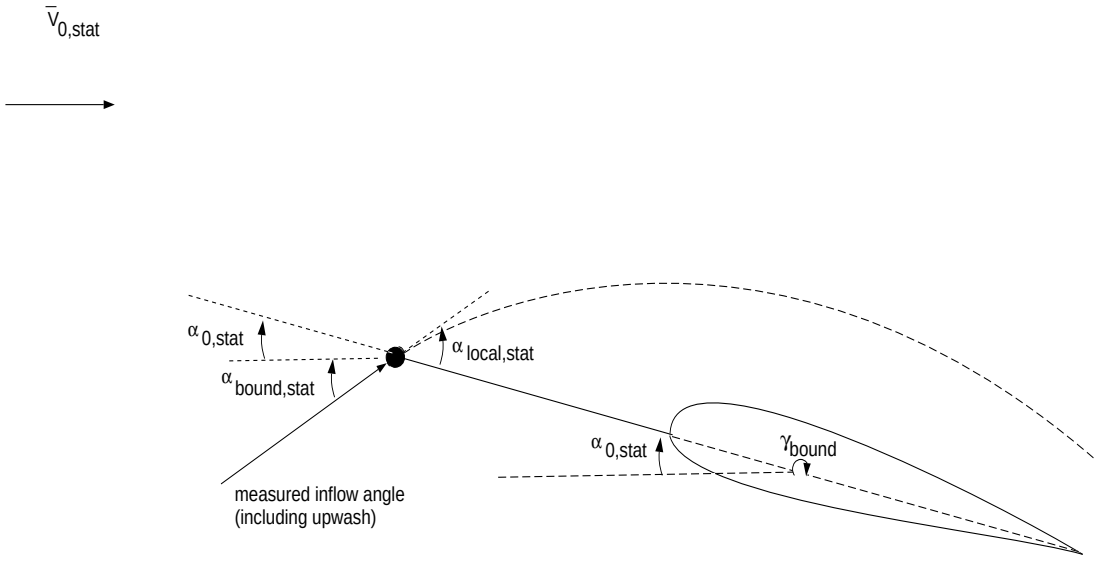

Figure 6.1 *Angle of attack in wind tunnel environment*

The figure shows that the angle of attack is related to this local inflow angle by:

$$\alpha_{0,\mathrm{stat}} = \alpha_{\mathrm{local,stat}} - \alpha_{\mathrm{bound,stat}} \tag{6.1}$$

with $\alpha_{bound,stat}$ the upwash angle induced by the bound vorticity. Note that in a windtunnel test under perfect 2D conditions there is no trailing vorticity and consequently, no wake induced velocity.

In a rotating wind turbine environment no such equivalent of $\overline{\mathrm{V}}_{0,\mathrm{stat}}$ is known. The undisturbed wind vector at infinity is not a good measure, since it does not

include the wake induced velocities. The wake induced velocities are present near the rotor plane and hence the angle of attack should be measured in the viscinity of the rotor. Therefore, in some IEA Annex XIV/XVIII experiments, the local inflow angle is measured ahead of the rotating blade profile ($\alpha_{\mathrm{local,rot}}$) with a five hole pitot probe or with a wind vane. Then, similar to the probe measurement of the inflow angle in the wind tunnel environment, this inflow angle too, differs from the angle of attack. In order to obtain the angle of attack, the upwash induced by the bound vorticity should be substracted in a way comparable to eqn. 6.1 :

$$\alpha_{0,\mathrm{rot}} = \alpha_{\mathrm{local,rot}} - \alpha_{\mathrm{bound,rot}} \tag{6.2}$$

This yields the angle of attack between the chord of the blade profile and the effective velocity (V_{eff}), where the effective velocity is composed of the free stream wind speed (V), the wake induced velocity (u_i) in axial direction and the rotational velocity ($\Omega \cdot r$), see figure 6.2. This hypothetical angle of attack is

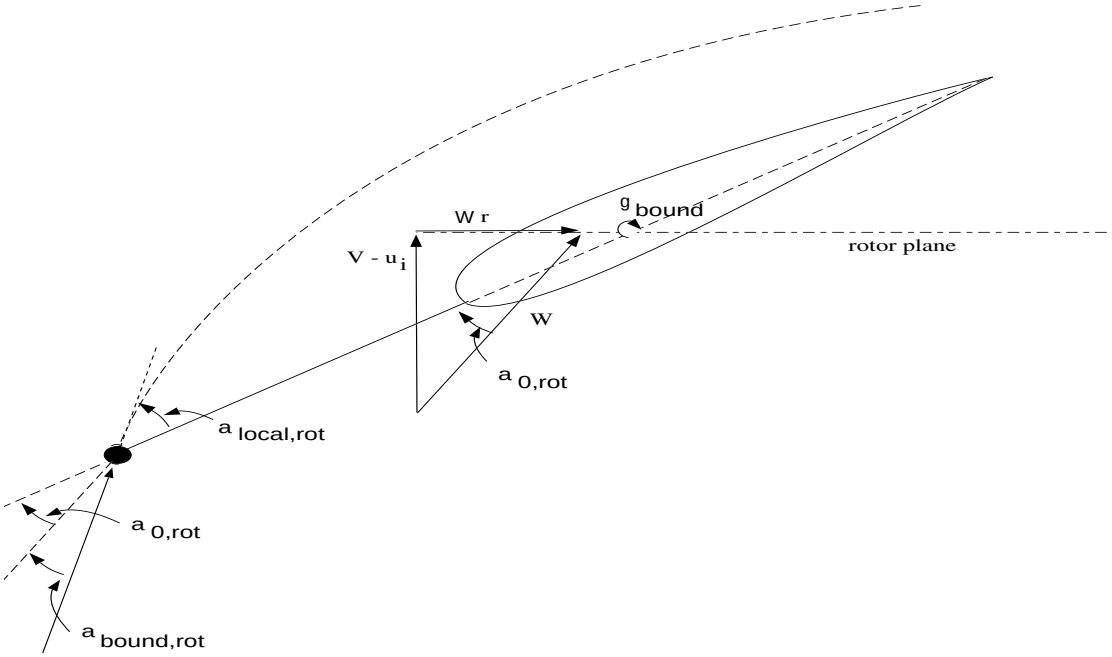

Figure 6.2 *Angle of attack for rotating wind turbine*

commonly used in aerodynamic models for wind turbines. Note that in fact also the wake induced velocity in tangential direction is present in $\alpha_{0,\mathrm{rot}}$. However this value is assumed to be small compared to $\Omega \cdot r$.

In equation 6.2 it is assumed that the wake induced velocity at the measurement point is equal to the value in the rotorplane. Calculations which are described in [29] show that at a position of 0.1 chord length upstream of the rotorplane the wake induced velocity differs $\approx$ 1% from the value in the rotorplane.

6.2 Methods available

Various methods for the determination of the angle of attack ($\alpha_{0,\mathrm{rot}}$) are known.

In this chapter several investigations are summarized, in which different methods for the angle of attack are introduced.

6.2.1 IEA Annex XIV investigation

Within IEA Annex XIV, ECN prepared a document about the angle of attack. This document served as a food for discussion at several project meetings. The methods discussed in the document are mainly based on the methods which are used in the present project. The method applied by IC/RAL is described in section 5.2. The description of this method arrived at the very end of the project and could not be included in the present analysis.

The following methods were discussed.

- Method based on measured $\mathbf{c_n}$ and $\mathbf{c_t}$ (Inverse b.e.m. method).
  This method is proposed in [30] and [28]. In the start of the project the method has been used by DUT, but in a later stage DUT determined the angle of attack differently, see section 6.2.2. In all Annex XIV experiments, the normal and tangential force on a blade section is measured. Assuming that these forces are uniform over an annular ring, the wake induced velocities can be derived according to the momentum theory (or if necessary from a turbulent wake state model). Since the free stream wind speed and the rotational velocity are known, this yields the effective velocity vector ($\overline{W}$), and consequently the angle of attack ($\alpha_{0,\mathrm{rot}}$).
- Method based on wind tunnel measurements (windtunnel method).
  This method is used by NREL, [31], see also section 5.3.3. A 2D scale model of the blade profile with a flow sensor 0.8 c ahead of the section is placed in a windtunnel. The angle of attack ($\alpha_{0,\mathrm{stat}}$) is known and the local inflow angle ($\alpha_{\mathrm{local,stat}}$) is measured with the flow sensor. Then the angle induced by the bound vorticity is calculated as the difference of both angles (see equation 6.1):

  $$\alpha_{\mathrm{bound,stat}} = \alpha_{\mathrm{local,stat}} - \alpha_{0,\mathrm{stat}} \tag{6.3}$$

  This correction is applied to the measured inflow angle with a similar device under rotating conditions:

  $$\alpha_{0,\mathrm{rot}} = \alpha_{\mathrm{local,rot}} - \alpha_{\mathrm{bound,stat}} \tag{6.4}$$

- Method based on position of stagnation point (stagnation method)
  The method is described in [32]. From the position of the stagnation point (which is obtained from the discrete measured pressure distribution) and the intersection point on the chord a stagnation angle is derived which is an estimate for the angle of attack. The position of the intersection point is determined with the 2D profile design code XFOIL, [33]. Then the position of the intersection point appears to be a weak function of the angle of attack and Reynolds number. Therefore it is assumed that the position of the intersection point depends on the profile geometry only.
  In the sequel two stagnation methods are introduced:
  1. The stagnation (XFOIL) method: The position of the intersection point is determined with a 2D profile code (XFOIL in the present situation).
  2. The stagnation (windtunnel) method: The position of the intersection point is determined from 2D wind tunnel measurements.

  Note that in the ideal situation both methods yield the same result, because they are based on the 'real' 2D stagnation point.
  The ECN method described in [32] can be considered as a combination of the two stagnation methods: The XFOIL stagnation point behaviour is corrected with empirical expressions. These empirical expressions have been obtained from wind tunnel measurements.

- Method based on measured power curve (power method)
  The method is used by Risø and described in [23], see also section 5.4.4. The method results in a correction which should be applied to the measured $\alpha_{local,rot}$. Thereto the power curve is calculated with the blade element momentum theory as function of the angle of attack at a certain spanwise position. The calculated power curve is compared with the measured power curve which is presented as function of the measured inflow angle ($\alpha_{local,rot}$) at the same position. There appears to be a good agreement between both curves if a constant correction to the measured inflow angle is applied.
- Method based on vortex wake calculations
  It is possible to calculate the flow field around the turbine with a 3D panel method, or a simplification of such a model (i.e. a lifting line method). The method yields the vorticity of the rotor blades and the wake. Then the angle induced by the bound vorticity along the blade ($\alpha_{\mathrm{bound,rot}}$) is determined. This angle is used to correct the local inflow angle ($\alpha_{\mathrm{local,rot}}$). In addition a panel method yields the normal force on every blade panel.
  A more simplified wake model is applied by DUT. The DUT method is described in section 6.2.2.

6.2.2 DUT investigation

In [26] the angle of attack for the DUT experiments has been determined with 4 methods:

- Inverse b.e.m. method.
- Angle of attack from the stagnation method.
- Angle of attack from a three hole probe.
  A theoretical upwash correction has been applied. The two dimensional upwash (assuming an infinite untwisted, untapered blade) is calculated using the Schlichting-Truckenbrodt correction, which is described in [34].
  A correction for finite span has been added. This correction is calculated by K. Brown [35].
  Note that the DUT blade is untwisted and untapered. Hence no corrections for twist and taper had to be introduced.
- Angle of attack from two pressure taps.
  The angle of attack was derived directly from two blade pressure taps. The two taps were considered as a built-in flow direction probe.

6.2.3 NREL investigations

In [20] a number of methods to determine the a.o.a. have been introduced.

- Analytic model.
  This method is basically similar to the inverse b.e.m. method, described above.
- Stagnation point normalization (Not to be confused with the stagnation methods described above). If the dynamic pressure is known (see section 7), the resultant inflow velocity can be determined. Then the angle of attack can iteratively be solved from the blade element geometrical relations.
- Pressure profile comparison.
  The static pressure profiles, obtained in a wind tunnel at different angles of attack are compared with the profiles measured on a rotating blade. The angle of attack corresponding to the wind tunnel profile which correlates most highly with the rotating profile was assigned to the rotating data. This method shows some similarity with the stagnation methods in which the stagnation pressures are compared. However, in the present method the complete pressure

distribution is compared.

In addition NREL has attempted to apply the stagnation wind tunnel method, see [36].

6.2.4 ECN and RISØ investigations

In addition to the studies described above, ECN and RISØ performed investigation which relate to the angle of attack. The ECN investigation was carried out in the the EU JOULE projects 'Dynamic Stall and 3D effects' and 'StallVib', [37] and [38]. ECN compared the angle of attack which result from the stagnation point method and from the velocity probe which is located near the 30% station. Note that the angle of attack from the velocity probe was not corrected for upwash effects. The results are discussed in section 6.3.4.

The RISØ investigations concern wind tunnel measurements on the same blade as used for the wind turbine measurements and a comparison between the measured angle of attack and the angle of attack from a full field three dimensional turbulence model. The results are presented in section 6.3.5.

6.3 Evaluation of methods

6.3.1 IEA Annex XIV investigation

The angles of attack from the inverse b.e.m. method, the power method and the stagnation methods were compared with the NREL angle of attack on basis of two NREL time series, one below rated wind speed, the other above rated wind speed. The aim of this study was to obtain insight in the effect of the different angle of attack methods applied in the IEA Annex XIV project. This will be helpful when measurements from different participants are compared mutually. The results are presented in Appendix J

The main conclusion are

- At low angles of attack, most methods agree very well in terms of mean values (disagreement < 1 degrees). For high angles of attack the differences in mean values are in the order of 4 degrees.
- The power method yields angles of attack which differ more from the NREL angle of attack.
- At high angles of attack, the stagnation methods could not be used for the NREL S809 profile due to the fact that in stall the stagnation point is no unique function of the angle of attack. This was also found in the NREL study presented in [36]. Under these conditions, the stagnation (windtunnel) method does not yield a solution at all. Furthermore the stagnation point under rotations remains rather close to the leading edge. This results in relatively small values of the angle even at high wind speeds near the root section.
- Although generally the differences in mean values were considered to be acceptabel the mutual differences in the standard deviation of the angles of attack was often in the order of 50%.

6.3.2 NREL investigation

In [20] the analytic model (i.e. the inverse b.e.m. method), the stagnation pressure profile normalisation technique and the pressure profile comparison technique are compared with the NREL measured angle of attack for a number of campaigns.

Note that in these investigations effects of yaw, tower and wind shear have been included. In a separate study NREL applied the stagnation wind tunnel method.

The conclusions from this NREL study were very similar to the conclusions from the IEA Annex XIV study.

- The best agreement with the NREL measured a.o.a.'s was found for the inverse b.e.m. angle of attack. However the frequency resolution of the inverse b.e.m. method is obviously poorer than for the other methods.
- The pressure profile comparison technique (to some extent comparable with the stagnation methods) gave, generally speaking, only a moderate agreement with the NREL a.o.a.
- The stagnation(windtunnel) method could not be applied for high angles of attack.
- The results from the stagnation pressure normalisation agreed reasonably with the NREL measured a.o.a's.
- Some confidence in the NREL measurements for angles of attack at low angles of attack is found from the fact that for these conditions, the NREL rotating measurements give $c_n - \alpha$ curves which agree well with the wind tunnel measurements. This turned out to be true for the twisted as well as the untwisted blade. The $c_n - \alpha$ curves are presented in Appendix F.

6.3.3 DUT investigation

In [26], the results from the methods presented in 6.2.2 are compared with 2D wind tunnel data.

DUT finds a rather large spread in the rotating $c_n - \alpha$ curve, obtained from an inverse bem method. Two explanations are offered:

- The lack of correlation between the measured wind speed upstream of the turbine and the wind speed at the rotor. This however is not consistant with the good results from the inverse b.e.m method described in the previous section.
- Only one sample per revolution is considered, and this sample is assumed to be representative for the complete revolution.

The probe method, the stagnation method and the 'two tap' method give a good agreement with wind tunnel data.

The DUT measurements supplied for the IEA Annex XIV database, were obtained from the three hole probe with a 2D upwash correction according to Schlichting-Truckenbrodt, see 6.2.2. Furthermore, the correction for finite span according to [35] has been applied, but this correction turned out to be very limited, although for the root station, this correction becomes more important. With the angle of attack, obtained in this way a rotating $c_n - \alpha$ curve is found which for low angles of attack agree well with the wind tunnel measurements.

The 2D upwash correction method has been assessed by reproducing the NREL upwash wind tunnel measurements. An excellent agreement was found (differences $<$ 2 degrees until α = 20 degrees, increasing to 4 degrees at α = 30 degrees).

Note that the final DUT measurements were done with a 6-hole probe, where the angle of attack is corrected with wind tunnel measurements.

6.3.4 ECN investigation

Within the EU JOULE projects 'Dynamic Stall and 3D effects' and 'StallVib', [37] and [38], ECN carried out two investigations.

The first comparison was based on averages and standard deviations of angles of attack α and inflow velocities W [37, section 3.3.5]. To this end the measurement 'ny_rot_e_003' was selected because both the stagnation point and the velocity probe method were applied in their calibration range here. By comparing measured angles of attack to 'geometric' angles of attack it was found that the stagnation angles correspond better to the geometric angles of attack than the probe angle of attack. This analysis of averages and standard deviations led to the conclusion a stagnation angle is the better estimate to the angle of attack.

With regard to the comparison on basis of averaged values it must be emphasized that the comparison is made with the 'geometric' angle of attack, not taking into account the effect of the wake induced velocity. Furthermore an upwash correction was not included in the probe angle of attack. Both these effects may influence the average value considerably.

The second comparison consisted of determining correlation and phase of the normal force coefficient c_n and the angle of attack α [38, section 2.6], where c_n and α were measured at the 30% station according to the stagnation point method and α was measured at the 35% station according to the velocity probe method. Also the 'stagnation angles' at the other stations at all stations were considered. As a test case the measurement 'ny_rot_e_001' was selected because for the 30% station the normal force coefficient is in the linear region. This analysis of correlation and phase led to the conclusion a stagnation angle is a better estimate to α than a probe angle of attack because it is better correlated to the normal force coefficient. The α signal from the 30% station however has too low an auto-correlation to be of use in time series analysis (in contrast to the α signals from the 60% and the 80% station).

6.3.5 RISØ investigation

In 1993 wind tunnel measurements were performed on the same blade as used for the wind turbine measurements [39]. The blade including the five hole pitot tube was placed in a 4x4 m jet in a wind tunnel facility in Jutland, Denmark. The jet was centred around the mid blade segment of the blade with the pitot tube in position 5 just outboard of the section and thus in the same position as used during the measurements on the turbine. Measurements were performed at a wind speed around 30 m/s and the angle of attack measurement from the pitot tube was compared with a measurement of the blade pitch which can be considered as the geometrical angle of attack. The comparison is presented in figure 6.3. As in the field rotor measurements no correction for upwash was introduced but it is seen that a good correlation is found in most of the considered interval with the biggest deviations at low angle of attack. The reason for a good correlation without a correction for upwash is that in this case as well as on the rotor the flow field is influenced by both upwash from the bound circulation around the blade and downwash from the shed vorticity due to the variation of the bound circulation along the blade span.

In another project [40] the statistical properties of the measured angle of attack have been compared with simulations of the inflow to the blade using a full field

Figure 6.3 *Comparison of the blade pitch angle and the angle of attack measured with the pitot tube during a wind tunnel experiment*

three-dimensional turbulence model. The power spectral density function of the angle of attack compared for the measurements and the simulations in figure 6.4. In general a good correlation is found in the frequency interval up to 3P which is around 2.5 Hz.

6.4 Angles of attack in final IEA Annex XVIII database

The angles of attack which are supplied to the final IEA Annex XVIII database are determined in the following ways:

- ECN: The angle of attack is determined using a stagnation point method, see section 5.1.5;
- NREL: The inflow angle was measured with a local flow sensor or from a five hole pitot probe. These probes were located near the pressure tap stations. The inflow angles were corrected for 2D upwash from wind tunnel measurements, see section 5.3.3;
- DUT: In IEA Annex XVIII, the inflow angle was measured with a 6 hole probe. These probes were located near the pressure tap stations. The inflow angles were corrected for 2D upwash from wind tunnel measurements; In addition the angle of attack is determined by matching the pressure distribution near the leading edge (i.e. C_p values of 4 pressure taps near the leading edge are matched);
- Mie University: The inflow angle is measured with 2 five-hole spherical probes mounted at both sides of the measurement stations. The inflow angle at the measurement station is determined by interpolation and corrected for 2D upwash which is measured in the wind tunnel, see section 5.6.5;
- RISØ: The angle of attack is determined from five hole pitot probe measurements at a location which can be different from the pressure tap locations. The

Figure 6.4 *Comparison of the power spectral density function of the angle of attack; measured with the pitot tube and simulated with an aeroelastic model including a three-dimensional turbulence model, respectively*

angles are corrected with the power method, i.e. such that the measured power curve coincides with the curve calculated with a BEM method, see section 5.4.4;
- IC/RAL: The angle of attack is determined from a five hole pitot probe near the pressure tap stations. A correction is applied which is based on inviscid theory, see section 5.2.3.

6.5 Conclusion on angle of attack methods

- The basic problem when considering the angle of attack in rotor aerodynamics is the fact that angle should be considered as a hypothetical quantity instead of a physical quantity. Hence it is not possible to measure this angle straightforwardly.
- From the investigations described in this section it is expected that, below stall the mutual differences in mean angles of attack will be in the order of 1 degree. Above stall, the agreement in mean values will be worse and in the order of 4 degrees.
- The mutual differences in the standard deviations of the angles of attack obtained with the different methods can be in the order of 50%.
- The frequency resolution of the inverse b.e.m. method is probably too poor for dynamic stall investigations.
- For the NREL S809 profile, the stagnation method cannot be used at high angles of attack.
- Most comparisons which have been made rely on time averaged data, Auto Power Spectral Densities and standard deviations. This implies that a possible phase lag is not considered. For example in the inverse b.e.m. method the wind speed is measured some distance from the turbine. This may introduce a phase lag. The same holds for the methods which rely on inflow angle measurements with a flow device. These devices are located a certain distance from the pressure taps in order to avoid flow distortion. The ECN investigation

described in section 6.3.4 indicates that this effect may be significant.

- Most turbines which have been used for the investigation had untwisted and untapered blades. If twist and taper are taken into account, the discrepancies may become larger. However it must be noted that under rotating conditions it is not necessarily true that an untwisted and untapered blade is 'more' 2-dimensional than a twisted and tapered blade: The twist of the blade will compensate the effect of rotation and hence the loading along the blade will be more or less constant for a twisted blade.
  There are two indications (no evidence!) that the twist effect and the finite span has a limited effect on the upwash:
  1. The $\mathrm{cl} - \alpha$ curve for the NREL twisted and untwisted blade are similar, using the same wind tunnel 2D upwash correction, see [36]! This implies that the disturbance of twist on the upwash correction is limited.
  2. The results presented in 6.3.3 indicate that also the finite span has limited effect on the the upwash.

  The RISØ investigation however indicates that there is an important effect from the variation of the bound vorticity along the blade. The shed vorticity which results from this variation yields an upwash which compensates the 2D upwash for the bound circulation.
- The good mutual agreement in mean angles of attack does not necessarily mean that the methods give accurate results. The main problem is the fact that the angle of attack which result from the different methods cannot be compared with the 'real' angle of attack, because the 'real' angle of attack according to the description from section 6.1 is a hypothetical quantity which is never known.

7. DYNAMIC PRESSURE AND NON-DIMENSIONALISATION IN FIELD EXPERIMENTS

7.1 General

The measured data which are considered in the IEA Annex XIV project are usually presented as coefficients which are non-dimensionalised with the dynamic pressure.

In a wind tunnel environment the value of the dynamic pressure can be obtained from the tunnel speed.

In a rotating environment, the dynamic pressure should be obtained from the local wind speed at the profile. This local wind speed cannot be derived straightforward from the free stream wind velocity and the rotational speed due to the presence of the wake induced velocities u_i and u_t. A comparison between three different methods for obtaining the dynamic pressure is reported in [20]. The results are discussed below.

Another problem is introduced by the fact the pressures are measured as differentials relative to an (unknown) reference pressure, see section 5. Hence the absolute pressures are unknown. This holds for the pressure tap measurements of DUT, ECN, NREL and IC/RAL and for the stagnation pressure measurements in all experiments (including the RISØ test).

As explained in section 5, most participants obtain the aerodynamic forces on a blade profile from integration of the pressure profile. The integration can generally be written as the difference of two integrations. For example the integration of the normal force is split into an integration over the suction side and over the pressure side. In general form the equations can be written as

$$f_{aero} = \int_{side1} (p_{side1} - p_{ref}) \cdot ds_{side1} - \int_{side2} (p_{side2} - p_{ref}) \cdot ds_{side2} \qquad (7.1)$$

Note that the pressure profiles and the reference pressure may be corrected for centrifugal forces or other phenomena. In the present discussion these corrections do not need to be adressed: The effect of the unknown reference pressure is analysed only qualitatively.

Now it may be assumed that all measurement systems in the present project are sufficiently fast, to assume that the reference pressure is approximately constant during the recording of the pressure profile around the section. Then the aerodynamic forces are obtained from:

$$f_{aero} = \int_{side1} p_{side1} \cdot ds_{side1} - \int_{side2} p_{side2} \cdot ds_{side2} \qquad (7.2)$$

Hence the reference pressure does not appear in the derivation of the aerodynamic forces and consequently the absolute value of the aerodynamic forces are not obscured by the unknown reference pressure (This is obviously also true for the RISØ experiments, where the aerodynamic forces are obtained from balance measurements).

The dynamic pressure is usually derived from probe measurements or from the maximum in the pressure distribution, see also section 7.2.

$$q = p_{pitot} - p_{ref} \tag{7.3}$$

or:

$$q = p_{max} - p_{ref} \tag{7.4}$$

Note that this gives rise to a systematic difference with respect to the wind tunnel coefficients, where the dynamic pressure is related to a static pressure. Such equivalent static pressure at a wind turbine does not exist.

An additional uncertainty from the reference pressure is introduced into the pressure coefficient. In the wind tunnel environment the pressure coefficient is defined as:

$$C_p = \frac{p_{tap} - p_\infty}{q} \tag{7.5}$$

With p_∞ the static pressure. In the field experiments, the pressure coefficient is obtained from:

$$C_p = \frac{p_{tap} - p_{ref}}{q} \tag{7.6}$$

As stated above, the denominator (q) is influenced by the reference pressure, but now the numerator is influenced too.

With regard to this subject, much discussion took place within the IEA Annex XIV group in particular on the harmonic ripple observed in the DUT experiments, see section 5.5.5. In the DUT measurements the reference pressure is stabilised by means of a damper, which causes the C_p to vary harmonically with the altitude. However until now, no such effect is observed in the measurements from the other institutes.

7.2 Methods available to determine the dynamic pressure

In [20] three different methods are introduced to obtain the dynamic pressure.

1. An analytic model.
   The local velocity components, and hence the dynamic pressure at each primary span location, were estimated from the geometry of the inflow relative to the turbine. The profile of the tower shadow velocity deficit was modeled using a cosine function. A b.e.m. code (PROP) was used to predict axial induction factors at each of the primary span locations over a range of wind speeds. The axial induction factors were adjusted for wake deformation under yawed conditions using a skewed wake correction. Only measured values of azimuth angle, yaw angle, and upwind wind speed were used. Then it is important to note that the dynamic pressure obtained from this method is <u>not</u> obscured by the uncertainty in reference pressure.
2. A stagnation pressure normalisation: The maximum positive value in the discrete pressure distribution is searched for. If necessary a curve fit is applied around the maximum, but this does not fundamentally change the method. Note that the maximum in the pressure distribution is measured relative to the reference pressure. The dynamic pressure is obtained from equation 7.4
3. A method in which the dynamic pressure is obtained from a pitot pressure probe.
   The pitot pressure is measured relative to the reference pressure. The dynamic pressure is obtained from equation 7.3.

7.3 Evaluation of methods

In [20], NREL compared the results of the methods presented in section 7.2 for several campaigns. It is found that the stagnation pressure normalisation methods yield dynamic pressures very closely to the probe dynamic pressures, despite the fact that the probes are placed some distance from the pressure taps. In contrast to this observation ECN concluded within the EU JOULE project 'StallVib' that the inflow velocity obtained with the stagnation method was a better estimate than a probe velocity, [38].

Although in [20], the dynamic pressures from the analytic model show a less good agreement with the measured dynamic pressures, the agreement is acceptable and the differences can probably be attributed to b.e.m. model deficiencies. This implies that the uncertainty in reference pressure has no severe consequences on the dynamic pressure.

In the RISØ investigation described in [40] the measured relative velocity was compared with simulations of the inflow to the blade using an advanced analytic model, i.e. a full field three-dimensional turbulence model. The power spectral density function of the angle of attack is compared for the measurements and the simulations in figure 7.1. In general a good correlation is found in the frequency

Figure 7.1 *Comparison of the power spectral density function of the angle of attack; measured with the pitot tube and simulated with an aeroelastic model including a three-dimensional turbulence model, respectively*

interval up to 3P which is around 2.5 Hz.

7.4 Conclusion on non-dimensionalisation of coefficients

A very encouraging result is that generally all methods which are used in the IEA Annex XIV project to determine the dynamic pressure, yield a good mutual agreement.

The reasonable agreement between the analytic models (which are not influenced by the unknown reference pressure) and the other methods indicates that the

uncertainty from the reference pressure on the aerodynamic coefficients may be limited.

It must be noted however that only a limited number of experimental facilities were considered in the studies and a more thorough investigation on the differences in dynamic pressure methods from the participants is required.

8. DESCRIPTION OF DATABASE

8.1 Conventions and notations

The prescribed definition of conventions and notations are given in Appendix A. The data are supplied in SI-units.

8.2 Format of the files, filetypes

The following type of measurements are stored in the database:

- Time series: The number of time series files is more than 400 with a length of 22000 s
- Profile coefficients measured under rotating conditions ($c_n - \alpha$, $c_t - \alpha$ etc)
- 2D profile and pressure coefficients
- Power curves

8.2.1 Time series

In order to facilate the selection of signals from a file, it was considered essential that the file formats were harmonised.

Three types of files had to be supplied:

1. Log files. These files contain general information about the measurement procedure. It should also contain:
   - Date and time of measurement
   - Air density, pressure and temperature
   - Information which is needed to read the other files (like the number of pressure taps, the number of anemometers, etc.)
2. Profile files.
   - These files contain the wind speeds, the wind directions, the rotor speed, the pitch angle, the mechanical loads, the angles of attack, the dynamic pressures, the profile coefficients (c_n, c_t and c_m) all as f(t,ϕ_r).
   - A guideline for the format is given in table 8.1.
   - The first records of the file are reserved for the statistics: mean value, standard deviation, min-max values; The remaining records contain the actual measurements as f(t,ϕ_r).
   - The first column is reserved for the time, the second column is reserved for the azimuth angle. The time steps are denoted by t_1 to t_n with n the number of time steps.
   - The columns 3,4 — etc are reserved for:
     - The wind speed(s) and the yaw misalignment. The yaw misalignment is the wind direction relative to the nacelle position. The wind speed and wind directions can be measured at more than one position. In table 8.1 the wind speeds are denoted by $V_{w,1}$ to $V_{w,NW}$ and $\phi_{y,1}$ to $\phi_{y,NW}$ with NW the number of sensors;
     - Rotor speed, denoted by Ω;
     - Pitch angle, denoted by θ;
     - Mechanical loads, denoted by M_1 to M_{NL}, with NL the number of loads which are measured;
     - Profile coefficients, i.e. lift coefficient, drag coefficient and moment coefficient. In table 8.1 the notation is summarized through: C_1 to

C_N, with N the number of radial positions where measurements are performed;

- Angles of attack, denoted by $\alpha_{1,i}$ to $\alpha_{N,i}$; The second index i is introduced to allow parties the supply of angles of attack which are obtained with different procedures (i.e. inverse bem and probe value).
- Dynamic pressures, denoted by $q_{1,i}$ to $q_{N,i}$. As for the angle of attack the second index i is introduced to allow parties the supply of different values of the dynamic pressure.
- Atmospheric pressure, ambient temperature, etc.

3. Pressure files.
   - These files contain the pressure recordings. One file is supplied per instrumented section. Hence, if N instrumented sections were active during a measurement campaign, this implies that N files should be supplied.
   - A guideline for the the format of the pressure files is given in table 8.2.
   - The first record of the file is reserved for the position of the pressure taps (in % chord). The number of pressure taps is denoted by NP. Preferably, the pressure tap order should be such that $x_{i,1}$ is the pressure tap at the leading edge of the suction side and $x_{i,NP}$ is the pressure tap at the leading edge of the pressure side (hence a clockwise ordering, when looking to the profile with the suction side above and the leading edge to the left).
   - The records 2 to 5 are reserved for the statistics: mean value, standard deviation, min-max values; the remaining records contain the actual measurements as f(t,ϕ_r). The first column is reserved for the time, the second column is reserved for the azimuth angle. The time steps are denoted by t_1 to t_n with n the number of time steps.
   - The columns 3,4 — etc are reserved for the pressures. The pressures are supplied in the same order as the pressure tap positions. Hence $p_{i,1}$ is the pressure at the leading edge of the suction side and $p_{i,NP}$ is the pressure at the leading edge of the pressure side.

Note that the above given format specifications only serve as a guideline. Each partner may have his own reasons to apply (slight) modifications. In such cases it is required that the log-file provides the user all necessary information about the precise format. Furthermore the addition of comment lines may clarify the content of the files.

8.2.2 Airfoil coefficients measured under rotating conditions

- The rotating sectional characteristics are supplied in the following form:
  - $c_n - \alpha$;
  - $c_t - \alpha$;
  - $c_m - \alpha$ (optional);
  - $c_n - c_t$ (optional);

  For each characteristic and for each instrumented section the results are stored in a separate file, i.e. if $c_n - \alpha$, $c_t - \alpha$ and $c_n - c_t$ are available for 5 sections, the number of files is 15.
  The first column in this type of file is the angle of attack (in case of the $c_n - c_t$ characteristic the first column is the c_t). The second column is the coefficient.
  In the first records the identification of the signals is given. Some participants supplied the rotating sectional characteristics for different pitch angles. In these

cases 2 columns have been added for every pitch angle, i.e. if the characteristics are measured for 2 pitch angles (θ_1 and θ_2) the coefficients for θ_1 are given in the first two columns and the coefficients for θ_2 are given in the third and fourth column. The pitch angles are given in the header of the file.

8.2.3 Profile and pressure coefficients measured under 2D conditions

- The 2D sectional characteristics are supplied as function of the angle of attack in a number of separate files: 1 file per coefficient, per section, i.e. if the $c_l - \alpha$ and $c_d - \alpha$ characteristics are measured for 5 sections, there are 10 different files. The first column is the angle of attack, the second column is the coefficient. In the first records the identification of the measurement campaigns and the signals is given.
- The 2D pressure coefficients are supplied as function of the angle of attack in 1 file. The first column is the angle of attack, the remaining columns give the pressure coefficient for the different pressure taps (Note that they all count from trailing edge to leading edge along the pressure side, followed by the taps from leading edge to trailing edge at the pressure side). In the first records the identification of the signals is given. The x-y position of the pressure taps is also given in the first records.

8.2.4 Power curves

The rotating power curves are supplied as function of wind speed. In these files, the first column gives the wind speed, the second column gives the electrical power. Some participants supplied a third column with mechanical power. In the first records the identification of the signals is given.

8.3 Filenames

8.3.1 Time series

The filenames are structured as follows:
'(n)y_ext1_ext2_ext3_n.rad'

- (n)y refers to (non)-yawed conditions;
- ext1 refers to the file type:
  - log = log file
  - prof = file with wind conditions and profile data;
  - p1—-pN = files with pressures
- ext2 refers to the type of experiment:
  - rot = rotating conditions
  - non = non-rotating conditions
- ext3 refers to the name of the participant:
  - d = DUT
  - e = ECN
  - i = IC/RAL
  - nu = NREL untwisted blade, phase II (section 5.3)
  - nt = NREL twisted blade, phase III (section 5.3)
  - ntp = NREL twisted blade, phase IV (section 5.3)
  - r = RISØ
  - m = Mie University

- n is the unique label of the experiment
- rad is the radial position (only for experiments from DUT and Mie University).

For example ny_p03_rot_nt_001 is the first NREL datafile of phase III which contains the pressure data of the 3rd blade section obtained for non yawed conditions.

Actually the filenames may be abbreviated in case the operating system allows only a limited number of characters for the filename.

8.3.2 Airfoil coefficients measured under rotating conditions

- Airfoil coefficients: The filenames of the $c_n - \alpha$, $c_t - \alpha$ and $c_m - \alpha$ characteristics are structured as follows: 'cxan_rot_ext1'. For the $c_n - c_t$ the file name structure is: 'cnct$n$_rot_ext1'
  - x identifies the load: n = normal force coefficient, t = tangential force coefficient, m = moment coefficient;
  - n identifies the section number or radial position (explained in the header of the file)
  - ext1 refers to the name of the participant, i.e. similar to 'ext3' in section 8.3.1.

8.3.3 Profile and pressure coefficients measured under 2D conditions

The filenames are structured as follows: 'cxan_2D_ext1'

- x identifies the load: l = lift coefficient, d = drag coefficient, m = moment coefficient, p = pressure coefficient.
- Only if applicable: n identifies the section number (explained in the header of the file);
- ext1 refers to the name of the participant, i.e. similar to 'ext3' in section 8.3.1. For NREL, the extention 'n' is used, instead of nu, nt or ntp.

Occasionally the Reynolds number or the presence of probes etc. can also be found in the filename.

8.3.4 Power curve

The name of the power curve is: PV_ext1

- ext1 is the name of the participant, i.e. 'ext3' in section 8.3.1.

Table 8.1 *Suggested format of prof files*

	ϕ_{r}	$\mathrm{V_{W,1}} - \mathrm{V_{W,NW}}$	$\phi_{\mathrm{y,1}} - \phi_{\mathrm{y,NW}}$	Ω	θ	$\mathrm{M_1} - \mathrm{M_{NL}}$	$\alpha_{1,raw} - \alpha_{N,raw}$	$\alpha_{1,\mathrm{cor}} - \mathrm{etc}$	$\mathrm{q_{1,raw}} - \mathrm{q_{N,raw}}$	$\mathrm{q_{1,cor}} - \mathrm{etc}$	$\mathrm{C_1} - \mathrm{C_N}$	etc
ave	-	-	-	-	-	-	-	-	-	-	-	-
σ	-	-	-	-	-	-	-	-	-	-	-	-
max	-	-	-	-	-	-	-	-	-	-	-	-
min	-	-	-	-	-	-	-	-	-	-	-	-
$\mathrm{t_1}$	-	-	-	-	-	-	-	-	-	-	-	-
-	-	-	-	-	-	-	-	-	-	-	-	-
-	-	-	-	-	-	-	-	-	-	-	-	-
$\mathrm{t_n}$	-	-	-	-	-	-	-	-	-	-	-	-

Table 8.2 *Suggested format of pressure files for instrumented section i*

	ϕ_r	$p_{i,1}$	$p_{i,2}$	$p_{i,3}$ − − − − − − $p_{i,NP}$
		$x_{i,1}$	$x_{i,2}$	$x_{i,3}$ − − − − − − $x_{i,NP}$
ave	-	-	-	-
σ	-	-	-	-
max	-	-	-	-
min	-	-	-	-
t_1	-	-	-	-
-	-	-	-	-
-	-	-	-	-
t_n	-	-	-	-

9. USE OF THE DATABASE, EXPERIENCES FROM USERS

9.1 Users

As explained in section 4.7, until 1999, the database was only available on CD-ROM. Thereafter the data became available on an Internet site. Until the end of 2001, 23 users got access to the database, either through the CD-ROM or through the Internet site. Furthermore the EU-JOULE project group VISCEL got access to the data.

Also several students from different universities around the world have visited the database.

9.2 Comments from users

During the IEA Annex XVIII project period, several comments were received from users. They range from recommendations on accessibility, preferances for data formats, usefullness of data, errors in the data etc.

9.3 Use of the database

Some interesting topics which have been studied using aerodynamic field measurements are:

- Instationary and 3D Effects in stall, see i.e. [3] [41] and [42];
- Validation of codes (free wake panel methods, NS codes, bem-like methods), see i.e. [43], [44] and [45] and http://www.ae.gatech.edu/ lsankar/NREL;
- The variation of the induced velocities at yawed conditions, see i.e. [46].
- Rotor tower interaction, see i.e. [47].
- The effect of different pitch angles on the airfoil characteristics. It was already expected from helicopter and propellor experiences that the airfoil coefficients at rotation would differ from the 2D airfoil coefficients, i.e. at rotation a much higher maximum lift coefficient was expected in particular at the root of the blade. The field measurements led to a definite confirmation of this expectation and also gave some indications that the differences between 2D data and rotating data may depend heavily on the pitch angle, see the sections C.4.4 and D.6.1.

10. FIELD MEASUREMENTS VS. WIND TUNNEL MEASUREMENTS

At the end of IEA Annex XVIII, much activities were initiated to perform aerodynamic wind turbine measurements, similar to those from IEA Annex XIV/XVIII, in a wind tunnel environment.

In this respect the NASA-Ames test, which has been carried out by NREL in 2000 should be mentioned. In this experiment the NREL test turbine with a diameter of 10 meter was placed in the huge NASA-Ames wind tunnel (dimensions of the test section: 24.4 by 36.6 meters). Furthermore, in the beginning of 2001, the EU 5th framework project 'Mexico' started. This project lasts until 2003. In the Mexico project, measurements on a model turbine (expected diameter in the order of 4.5 m) will be carried out in the German Dutch Wind Tunnel, DNW.

The advantage of performing aerodynamic measurements in a wind tunnel environment is given by the fact that the conditions can be controlled, and more important, that the conditions are exactly known, by which the interpretation of results is facilitated.

Thereto it should be realised that the IEA Annex XIV/XVIII test turbines are located in a turbulent environment, where the inlow is measured with a limited number of anemometers on a limited number of meteorological masts. These masts are placed some distance from the turbine, at (usually) a fixed location which is not by definition upstream of the turbine. In this way the inflow conditions at the turbine are only known on a statistical basis (i.e. on basis of 1 minute averages). Although this implies that an investigation of relatively slow aerodynamic phenomena would be possible, the instanteneous inflow 'felt' by the turbine is unknown. Hence the investigation of high frequency phenomena (i.e. dynamic stall) is considerably complicated. As a matter of fact this implies some 'unbalance' in the measurements: The aerodynamic response of a blade segment is measured and known in detail, but the excitation to this response is partly unknown.

Despite these disadvantages, the free stream measurements also have important advantages. Basically the advantages lie in the fact that the results of the IEA Annex XIV/XVIII measurements are expected to be more representative for commercial wind turbines:

- The sizes of the free stream wind turbines can be larger than those of the wind tunnel turbines: Even in the very large NASA-Ames tunnel, the maximum possible diameter of the turbine is much smaller than the size of nowadays turbines;
- The turbulent environment, though complicating, is also present at 'real' wind turbines and as such the aerodynamic response of the turbine will be more representative.

11. CONCLUSIONS, LIMITATIONS AND RECOMMENDATIONS

11.1 Conclusions from IEA Annex XIV/XVIII

The overall objective of IEA Annex XIV and IEA Annex XVIII can be seen as a collaboration in performing full scale aerodynamic test programs and the creation and maintenance of a data base of aerodynamic measurements. After 10 years of close cooperation between institutes performing such experiments the objective was met:

- A unique database has been developed in which detailed aerodynamic measurements are stored.
  - The measurements are obtained on 6 different wind turbines: The diameter of these turbines ranges from 10 to 27 m. Very different blades have been considered:
    - Blades without twist and taper;
    - A blade with twist but without taper;
    - Blades with twist and taper;
  - Measurements have been supplied for very different conditions, including yaw misalignment. The angles of attack range between negative values and deep stall. The angle of attack has been varied by means of a variation in wind speed but also by means of pitch angle and rotor speed. Time series as well as sectional characteristics are supplied.
  - All parties have provided :
    - An aeroelastic model description to aid in the interpretation of the measurements;
    - Measurements of ambient conditions
    - Measurements of operational conditions
    - Measurements of global blade and rotor data (i.e. blade loads)
    - Measurements of local aerodynamic forces and inflow conditions.
- The access to the database is made as easy as possible. Thereto the files are stored in a uniform format. In addition, the conventions which have been applied in the database are uniform and the file names are prescribed. Furthermore, the database is documented and statistical overviews are supplied for every file, which will assist the user to select relevant data.
- The data are accessable on an Internet site at ECN, http://www.ecn.nl/unit_de/wind/annexxiv/index.html.
- In interpreting the measurements and when comparing field data with wind tunnel experiments it should be kept in mind that the definition of angle of attack, dynamic pressure and aerodynamic coefficients is less straightforward than in the wind tunnel case. Several methods are applied by the IEA Annex XIV participants for the determination of these quantities. A number of investigations were performed on behalf of Annex XIV or by the participants independantly which addressed the problem of angle of attack, dynamic pressure and aerodynamic coefficients:
  - In general, no conclusion could be drawn about the accuracy of the methods because no values for the 'real' angles of attack and dynamic pressure were available to compare with;

– A mutual comparison of results and a comparison with non-rotating wind tunnel data (from DUT and NREL) has led to the following indications:
  * The mutual agreement between the mean angles of attack from the different methods was good (in the order of 1 to 4 degrees). However in terms of standard deviation, the differences were in the order of 50%.
  * The mutual agreement between the dynamic pressure from the different methods was good;
  * Although the unkown reference pressure can introduce uncertainties in the aerodynamic coefficients, the introduction of a method which did not suffer from this problem indicated that this uncertainty is limited.

  It must be noted that the above mentioned indications are still premature and mainly based on analysis and measurements of turbines with untwisted untapered blade. More investigation is required in order to draw more thorough conclusions.

11.2 Benefits from IEA Annex XIV and Annex XVIII

The main benefits from IEA Annex XIV/XVIII are (confirmed by most users of the database):

- A huge amount of local aerodynamic measurements has become available, which are stored into a well documented database. This database served as validation base for the development and validation of aerodynamic models. The supply of local aerodynamic data, is a major step forward in understanding the aerodynamic behaviour of a wind turbine: In conventional experimental programs only integrated blade (or rotor) quantities are measured from which the local aerodynamic properties can be derived only indirectly. Meanwhile data from the database have been used by many institutes. Generally speaking the users of the database were very positive;
- The IEA Annex XIV/XVIII served as a platform where very specific knowledge associated with aerodynamic measurements could be exchanged. All participants agree that this has been very instructive and enabled the acceleration of the experimental programs.
- The costs which are associated with the measurement programs of the different participants were in the order of 10000 kEuro.
  These costs can be justified when they are related to the advantages which result from the anticipated improvement in aerodynamic models. Even a small improvement in aerodynamic models will make it possible to design more reliable and cost effective wind turbines which has a large economic and environmental impact taking into account the rapid growth of wind energy capacity. It can be noted that the additional costs which were associated with IEA Annex XIV and IEA Annex XVIII were only a fraction of the total costs (in the order of 300 kEuro).

11.3 Limitations of measurements in IEA Annex XIV/XVIII database

In applying the results from the database one should realize the limitations of the experimental data. Several uncertainties need to be considered:

- Uncertainties introduced by the instrumentation, including calibrations. These uncertainties are believed to be limited. An exception may be the measurements at standstill which result in very low pressure levels and a poor accuracy.

- Uncertainties due to 'definition' problems of angle of attack, dynamic pressure and aerodynamic coefficients. The participants have manipulated these data in different ways.
- Uncertainties which originate from the (partly) unknown inflow conditions. These uncertainties are inevitible in view of the highly turbulent environment in which the wind turbine operates.
- The length of some time series may be too short for some investigations.

Apart from this there is an uncertainty from the aeroelastic model descriptions: In the interpretation of data the aeroelastic model description will be essential but it is known that some data from the model descriptions suffer from uncertainties whereas other data are not available.

11.4 Recommendations from IEA Annex XIV/XVIII

- Within IEA Annex XIV much effort had to spent on the exact definition of wind turbine conventions, notations and reference systems. This item was essential in the present project where data from different institutes had to be harmonized. This implied that the participants had to reprocess their datafiles and several data exchange rounds appeared to be necessary before all participants supplied the measurements according to the common specifications. It is recommended that the wind energy society should reach consensus about common conventions, definitions, notations and reference systems.
- The uncertainty which results from the definition problem of angle of attack, dynamic pressure and aerodynamic coefficients is still too large. More research on this field is required.
- The maximum rotor diameter in the present project was 27 m. Although at the start of the project, this was considered to be a medium sized turbine, the trend has been toward much larger machines and at the end of the project the turbine was regarded as a small turbine. It is recommended to proceed with experimental programs on larger scale wind turbines.
- The goal of IEA Annex XVI/XVIII was to create a database of aerodynamic measurements, not to analyse the measurements. Generally speaking only limited effort is spent on the use of the database and it is recommended to intensify these efforts.

REFERENCES

[1] J.G Schepers et al . "Final report of IEA Annex XIV' Field Rotor Aerodynamics"'. ECN-C-97-027, June 1997.

[2] H. Snel and J.G Schepers (ed.) . "JOULE1: Joint investigation of Dynamic Inflow Effects and Implementation of an Engineering Method". ECN-C-94-107, December 1994.

[3] A. Björck. "Dynamic Stall and Three Dimensional Effect ". FFA-TN –1995-31, FFA, 1995.

[4] A.J. Brand J.W.M. Dekker C.M. de Groot and M. Spath. "Overview of aerodynamic measurements on an Aerpac 25 WPX wind turbine blade at the HAT 25 experimental wind turbie ". ECN-DE-Memo--96-014, ECN, 1996.

[5] M. Späth. "Implementation of a pressure scanner system for a field rotor aerodynamics experiments ". ECN-R –93-017, ECN, 1993.

[6] M. Späth and N. Stefanatos. "Survey on frequency responses of pressure tubes installed in a 12.5 meter rotor blade ". ECN-I –92-028, ECN, September 1992.

[7] A.J. Brand. "Specifications for a spheric velocity probe ". ECN-CX –93-133, ECN, November 1993.

[8] A.J. Brand G.P. Corten and M. Späth. "Calibration and measuring procedure of a spheric velocity probe ". ECN-R –95-031, ECN, February 1996.

[9] D.W. Brye and R.C. Pankhurs. *"Pressure probe methods for determining wind speed and flow direction"*. HMSO, 1971.

[10] D.A. Simms M.M. Hand L.J. Fingersh and D.W. Jager. "Aerodynamics Experiment Phases II-IV Test Configurations and Available Data Campaigns", NREL/TP-500-25950, 1999.

[11] C.P. Butterfield et al. 'Combined Experiment PHASE I, final report". NREL TP- 257-4655, October 1992.

[12] D. Somers. "Design and Experimental Results for the S809 Airfoil", NREL/TP-442-6918, unpublished.

[13] D.A. Simms L.J. Fingersh and C.P. Butterfield. "NREL Unsteady Aerodynamics Experiment Phase III Test Objectives and Preliminary Results.". In *ASME/ETCE Conference, Houston, USA*, January 1995.

[14] L.J. Fingersh and M.C. Robinson. "Wind Tunnel Calibration of 5-hole Pressure Probes for Application to Wind Turbines". In *ASME Wind Energy Symposium, Reno USA*, January 1997.

[15] D.A. Simms and C.P. Butterfield. "PC-Based PCM Telemetry Data Reduction System Hardware.,"SERI/TP-257-3662, 1990.

[16] D.A. Simms and C.P. Butterfield. "A PC-Based Telemetry System for Acquiring and Reducing Data from Multiple PCM Streams. "SERI/TP-257-4123, 1991.

[17] M.S. Miller et al. "Determination of Data Reliability for Phase II of the Combined Experiment," NREL unpublished.

[18] B. McNiff and D.A. Simms. "Error Analysis in Wind Turbine Field Testing". In *Windpower '92 Proceedings, Seattle, USA*, October 22-23 1992.

[19] S.A. Huyer D.A. Simms and M.C. Robinson. "Unsteady Aerodynamics Associated with a Horizontal-Axis Wind Turbine". *American Institute of Aeronautics and Astronautics Journal, Volume 34, No. 10.*, July-Sept. 1996.

[20] D.E. Shipley et al. 'Techniques for the determination of local dynamic pressure and angle of attack on a horizontal axis wind turbine blade". NREL TP- 442-7393, May 1995.

[21] A. Pope and J.J. Harper. *"Low speed Wind Tunnel Testing"*. New York, John

Wiley and Sons, 1966.

[22] D.A. Simms M.C. Robinson M.M. Hand and L.J. Fingersh. “Characterization and Comparison of Baseline Aerodynamic Performance of Optimally-Twisted Versus Non-Twisted HAWT Blades”, Prepared for 15th ASME Wind Energy Symposium, NREL/TP-442-20281, January 1996.

[23] H.A. Madsen. ‘Aerodynamics of a Horizontal-Axis Wind Turbine in Natural Conditions”. Risø M-2903, Risø National Laboratory, September 1991.

[24] H.A. Madsen. ‘Aerodynamics of a Horizontal-Axis Wind Turbine in Natural Conditions- Raw data overview”. Risø M-2902, Risø National Laboratory, September 1991.

[25] H.A. Madsen. “Structural Dynamics of a 100 kW HAWT”. Risø M-2887, Risø National Laboratory, February 1991.

[26] A. Bruining . “Aerodynamics characteristics of a 10 m diameter rotating wind turbine blade, ” University of Delft, IW-084R, September 1996.

[27] G.P. Corten. “Accuracy Analysis of Field Pressure Measurements, perspective for future measurements ” Delft University of Technology, DUT-IvW-95085R, June 1995.

[28] A. Bruining G.J.W. van Bussel C.P. Corten and W.A. Timmer. “Pressure distributions from a wind turbine blade; field measurements compared to 2-dimensional wind tunnel data ”. DUT-IvW- 93065R, Delft University of Technology, August 1993.

[29] J.G. Schepers. “Calculation of induced velocities upstream of the WPS-30 turbine”, ECN, February 1992.

[30] H. Snel, R. Houwink and Bosschers J. “Sectional prediction of lift coefficients on rotating wind turbine blades in stall ”. ECN-C –93-052, ECN, May 1993.

[31] C.P. Butterfield. “Three-dimensional airfoil performance measurements on a rotating wing”. In *Proceedings of EWEC Conference, Glasgow, 10-13 July 1989*, July 1989.

[32] A.J. Brand. “To estimate the angle of attack of an airfoil from the pressure distribution ”. ECN-R –94-002, ECN, January 1994.

[33] M. Drela. “XFOIL: An analysis and design system for low Reynolds number airfoils”. *Low Reynolds number aerodynamics, Lecture notes in Engineering 54*, 1989.

[34] H. Schlichting and E. Truckenbrodt. “Aerodynamics of the Airplane ” McGraw-Hill, ISBN 0-07-055341-6,, 1979.

[35] K. Brown. “Results 3D free wake panel method, ” University of Bristol (UK), E-mail document to A. Bruining, May 1995.

[36] J.G. Schepers. “Minutes of the fifth meeting of the IEA Annex ’Field Rotor Aerodynamics’ held at Netherlands Energy Research Foundation (NL) on June 14th, 1996”. DE-Memo- 96-41, ECN, July 1996.

[37] A.J. Brand J.W.M. Dekker C.M. de Groot and M. Spath. “Aerodynamic field data from the HAT25 experimental wind turbine - Contribution to the EC/NOVEM project ‘Dynamic Stall and Three-dimensional effects ”. ECN-R--96-037, ECN, 1996.

[38] A.J. Brand. “ECN Progress Report Work Package #1 EU STALLVIB project; Actions M-1, M-2 and M-4 ”. DE-Memo-96-045, ECN-Renewable Energy, 1996.

[39] I. Antoniou, H.A. Madsen and F. Rasmussen. “Wind Tunnel Measurements on a LM 8.2 m Blade”. Risø I-800(EN), Risø National Laboratory, December 1995.

[40] A. Kretz, H.A. Madsen and J.T. Petersen. "Measured and Simulated Turbulence - Compared at a Section of a Rotating Wind Turbine Blade". Risø R-671(EN), Risø National Laboratory, March 1994.

[41] J.G. Petersen et al. "Prediction of Dynamic Loads and Induced Vibrations in Stall". R 1045 (EN), RISØ, May 1998.

[42] H.A. Madsen et al. "Field Rotor Measurements - Data sets Prepared for Analysis of Stall Hysteresis". RISØ-R 1046 (EN), RISØ National Laboratory, May 1998.

[43] P.K. Chaviaropoulos et al . "Viscous and Aeroelastic effects on Wind turbine blades. The Viscel project". In *European Wind Energy Conference, EWEC*, July 2001.

[44] P. Strzelczyk. On simple vortex theory of horizontal axis wind turbines. Technical Report , Rzeszow University of Technology, Faculty of Mechanical Engineering and Aviations, June 1998.

[45] L. Bermudez, A. Velasquez and A. Matesanz. "Numerical Simulation of Unsteady Aerodynamic Effects in Horizontal Axis Wind Turbines". *Solar Energy*, 68, 2000.

[46] H.A. Madsen . "Yaw simulation using a 3D actuator disc model". In *IEA aerodynamics Symposium, Stockholm*, November 1999.

[47] J.M.R. Graham and C.J. Brown. Rotow-investigation of the aerodynamic interaction between wind turbine rotor blades and the tower and its impact on wind turbine design, final publishable report. Technical Report , Department of Aeronautics, Imperial College of Science and Medicine, London, UK, September 2000.

[48] J.G. Schepers and H. Snel (ed.) . "JOULE2: Dynamic Inflow: Yawed Conditions and Partial Span Pitch". ECN-C-95-056, June 1995.

[49] J.G. Schepers. "Minutes of the preparatory meeting of the IEA Annex 'Field Rotor Aerodynamics' held at the University of Delft on December 2nd, 1992". DE-Memo- 92-79, ECN, December 1992.

[50] J.G. Schepers. "Minutes of the first meeting of the IEA Annex 'Field Rotor Aerodynamics' held at Risø National Lab. (DK) on September 16th and 17th, 1993". DE-Memo- 93-72, ECN, September 1993.

[51] J.G. Schepers. "Minutes of the second meeting of the IEA Annex 'Field Rotor Aerodynamics' held at the Technical University of Delft (NL) on March 17th and 18th, 1994". DE-Memo- 94-28, ECN, March 1994.

[52] J.G. Schepers. "Minutes of the third meeting of the IEA Annex 'Field Rotor Aerodynamics' held at Rutherford Appleton Laboratory (UK) on April 5th , 1995". DE-Memo- 95-23, ECN, March 1995.

[53] J.G. Schepers. "Minutes of the fourth meeting of the IEA Annex 'Field Rotor Aerodynamics' held at National Renewable Energy Laboratory (USA) on February 5th and 6th , 1996". DE-Memo- 96-13, ECN, February 1996.

[54] J.G. Schepers. "Minutes of the preparatory meeting of IEA Annex XVIII". DE-Memo- 97-062, ECN, December 1997.

[55] J.G. Schepers. "Minutes of the first meeting of IEA Annex XVIII". DE-Memo- 98-059, ECN, July 1998.

[56] J.G. Schepers. "Minutes of the second meeting of IEA Annex XVIII". ZW-Memo- 99-018, ECN, March 1999.

[57] J.G. Schepers. "Minutes of the third meeting of IEA Annex XVIII". Technical report, ECN, December 1999.

[58] J.G. Schepers. "Minutes of the fourth meeting of IEA Annex XVIII". Wind-Memo-, ECN, April 2001.

[59] L.W.M.M Rademakers and P.A. van der Werff. “Verification of wind turbine design codes with the ’Dutch Handbook wind data for wind turbine design’, ECN-I–92-048 ”, December 1992.
[60] H.J.T. Kooijman. “Smart rotor, feasibility study for a passive pitch regulation of a wind turbine rotor blade,” ECN-I-96-011, March 1996.
[61] A.J. Brand. “Aerodynamic Field Data of a Non-Rotating Blade”. ECN-C--95-063, ECN, August 1995.
[62] Lekkerkerk, F.L. "Regelstrategieen van de 25 m HAWT (In Dutch)", ECN-83-120, Juni 1983.
[63] I.H. Abbott and A.E. Doenhoff. *Theory of Wing Sections*. Dover Publications, Inc, 1958.
[64] J.G. Schepers. “PVOPT, Theory and test cases, ” ECN-C–96-057, January 1996.
[65] J.G. Schepers. “GAPHAT – III, Model description and verification (Dutch) ”. ECN -I–91-054, ECN, Juli 1991.

APPENDIX A. CONVENTIONS, REFERENCE SYSTEMS AND NOTATIONS

A.1 Introduction

This appendix describes the sign conventions, reference systems and notations to be used within the IEA Annex XIV 'Field Rotor Aerodynamics'.

Experiences in several aerodynamic research projects, where a large number of participants work together, has learnt that there is an urgent need to reach a general consensus about sign conventions between the aerodynamicists in wind turbine society. Confusion about this matter has often caused unnecessary severe misunderstandings in interpretation of results.

The conventions which are suggested in this document draw heavily on those which are used in the EU Joule projects Dynamic Inflow, see [48]. The main exception is in the sign of the blade azimuth angle. In the Dynamic Inflow project, this angle was defined zero when the blade was pointing down. Due to the fact that all measurements in the present project were taken with blade azimuth angle zero when the blade is pointing up, this definition was adopted. Furthermore, there is a difference in the rotating axis system, which is defined in section A.3. For the present project the x-axis is defined positive from leading edge to trailing edge, in accordance with the common definition used for local aerodynamic pressure measurements. In the Dynamic Inflow project the x-axis was defined positive in rotational direction, in accordance with the common definition used for load measurements

It is very important to note that the notations refer to a clockwise rotating wind turbine, looking downwind to the rotor. In most cases, the conventions for a counter clockwise rotating wind turbine can be obtained by mirroring. This is demonstrated in some of the figures shown below. Note that mirroring invalidates the right hand rule for vectors.

A.2 Definitions

A.2.1 (Blade) azimuth angle ($\phi_{r,b}$ and ϕ_r)

See figure A.1.

- Blade azimuth angle: $\phi_{r,b}$ = angle of blade number 1; Blade numbering, see section A.2.2.
- Azimuth angle: ϕ_r = angle in the rotorplane, not necessarily the position of the blade.

The zero azimuth is in vertical upward direction.

A.2.2 Blade numbering (1, 2 and 3)

See figure A.1. The order in which the blades pass the tower is for a three bladed turbine: 1,2,3

A.2.3 Turbine angle (ϕ_{turb})

The turbine angle gives the angle of the nacelle w.r.t. the true (not magnetic) North. For a clockwise rotating wind turbine, the turbine angle = 90^o when the

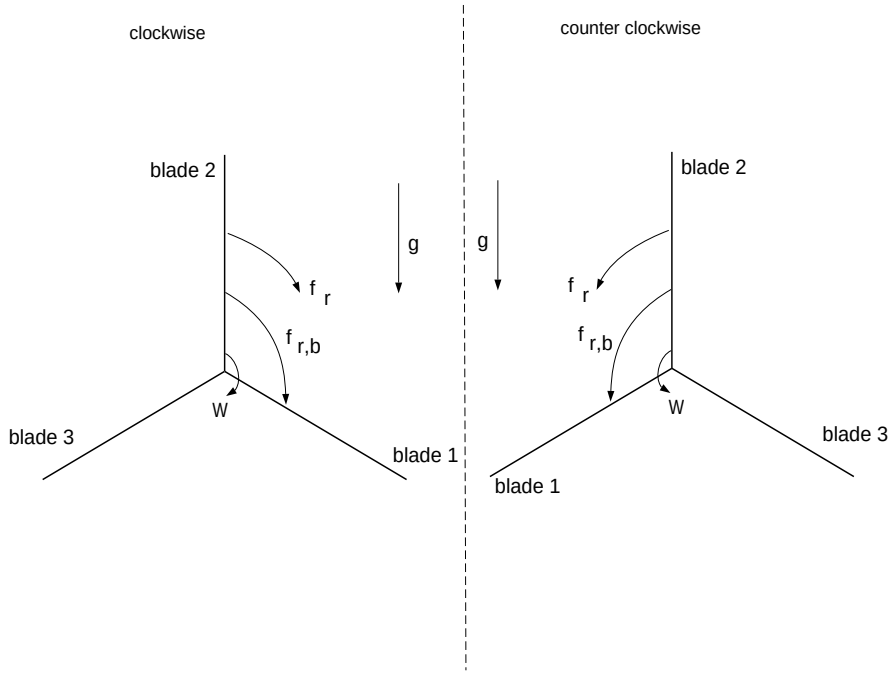

Figure A.1 *(Blade) azimuth angle and blade numbering*

turbine is oriented to the East (this means that the upstream direction is to the East). See figure A.2.

A.2.4 Ambient wind conditions

The ambient wind conditions are described by means of the wind speeds, wind shears and wind directions.

- V_∞; Ambient wind speed;
- V_{hub}; Ambient wind speed at hub height;
- V_{up}; Ambient wind speed at h = hub height + R;
- V_{low}; Ambient wind speed at h = hub height - R;
- δV_{up}; Relative vertical wind shear in upper rotor plane $= \frac{V_{up}-V_{hub}}{V_{hub}}$;
- δV_{low}; Relative vertical wind shear in upper rotor plane $= \frac{V_{hub}-V_{low}}{V_{hub}}$;
- $\phi_{w,hub}$; Wind direction at hub height;
- $\phi_{w,up}$; Wind direction at h = hub height + R;
- $\phi_{w,low}$; Wind direction at h = hub height -R.

The wind direction is given w.r.t. true North. For a clockwise rotating wind turbine, the wind direction = 90°, when the wind comes from the East, see figure A.2

A.2.5 Yaw angle (ϕ_y)

The yaw angle is given as the difference of the wind direction and the position of the nacelle, see figure A.2

$\phi_y = \phi_w - \phi_{turb}$

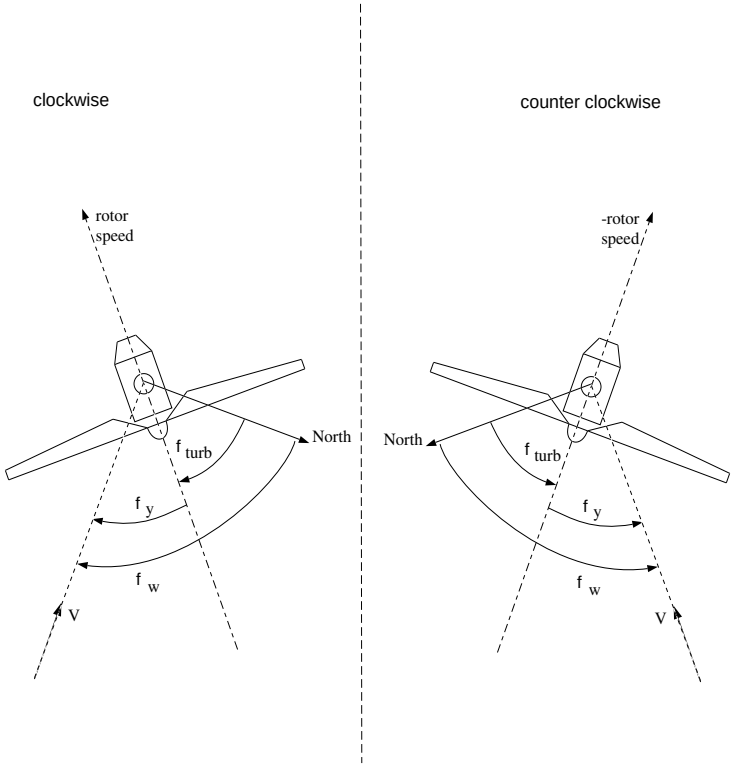

Figure A.2 *yaw angle and wind direction*

A.2.6 Pitch angle (θ) and twist (ϵ)

See figure A.3, in which:

- β = local blade angle, angle between the chordline of the blade element and the rotorplane, positive when it points in the opposite wind direction.
  - full span pitch: $\beta = \theta + \epsilon$
  - partial span pitch:
    - inner part of the blade: $\beta = \epsilon$
    - tip: $\beta = \theta_t + \epsilon$

- θ = pitch angle; θ_t = tip angle.
  By definition: $\theta_{(t)} = 0^o$, if chordline of tip-station stands in the rotor plane, see figure A.4; Positive when it points in the opposite wind direction, and decreases the angle of attack.
- ϵ = twist angle of the blade relative to tip station

A.2.7 Angle of attack and inflow conditions

For a rotating wind turbine environment the angle of attack is a hypothetical quantity which cannot be measured straightforward.

For this reason a distinction is made between the theoretical inflow conditions according to the blade element-momentum theory (quantities with subscripts 'b.e.m.') and the inflow conditions which are derived from measured quantities (quantities with subscripts 'm').

The latter might be inflow conditions which are determined with a measurement device like a five hole pitot probe or a wind vane. However, the inflow conditions may also be determined from measured forces on a blade section.

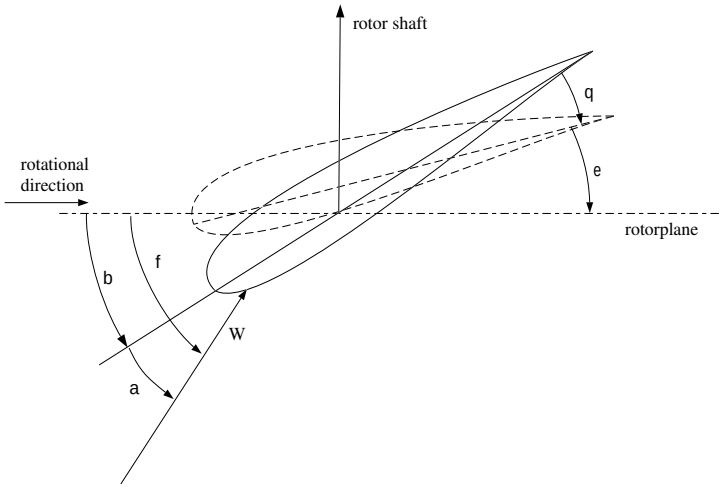

Figure A.3 *Twist, pitch angle and angle of attack*

Blade element conventions

The inflow angle ($\phi_{b.e.m.}$) gives the angle between the effective (resultant) wind velocity at the blade element and the rotorplane. From velocity diagram, see figure A.5:

$$\mathrm{tg}\phi_{\mathrm{b.e.m.}} = \frac{\mathrm{V}_\infty - \mathrm{u}_{\mathrm{i,b.e.m.}}}{\omega_{\mathrm{b.e.m.}} \cdot \mathrm{r} + \mathrm{V}_\mathrm{r}} = \frac{(1 - \mathrm{a}_{\mathrm{b.e.m.}}) \cdot \mathrm{V}_\infty}{(1 + \mathrm{a}'_{\mathrm{b.e.m.}})\mathrm{V}_\mathrm{r}} \qquad \text{(A.1)}$$

(Assuming that there is no yaw misalignment).

in which:

- $\mathrm{V}_\mathrm{r} = \Omega \cdot \mathrm{r}$
- Ω = rotational speed = $\mathrm{d}\phi_{\mathrm{r,b}}/\mathrm{dt}$;
- r = radial position;
- $\mathrm{u}_{\mathrm{i,b.e.m.}}$ = induced velocity, axial to the rotor plane (positive when it is in the opposite direction of the undisturbed wind speed)
- $\omega_{\mathrm{b.e.m.}}$ = rotational induced velocity (positive when it is in the opposite direction of the rotational speed)
- $\mathrm{a}_{\mathrm{b.e.m.}}$= axial induction factor = $\frac{u_{i,b.e.m.}}{V}$
- $\mathrm{a}'_{\mathrm{b.e.m.}}$ = tangential induction factor = $\frac{\omega_{b.e.m.}}{\Omega}$

Then the effective incoming wind speed ($\mathrm{W}_{\mathrm{b.e.m.}}$) and dynamic pressure ($\mathrm{q}_{\mathrm{b.e.m.}}$) are defined as:

$$\mathrm{W}_{\mathrm{b.e.m.}} = \sqrt{(1 - \mathrm{a}_{\mathrm{b.e.m.}})^2 \cdot \mathrm{V}_\infty^2 + (1 + \mathrm{a}'_{\mathrm{b.e.m.}})^2 \mathrm{V}_\mathrm{r}^2}$$

$$\mathrm{q}_{\mathrm{b.e.m.}} = 0.5 \cdot \rho \mathrm{W}_{\mathrm{b.e.m.}}^2$$

In addition, a dynamic pressure related to the rotational velocity (V_r) and the

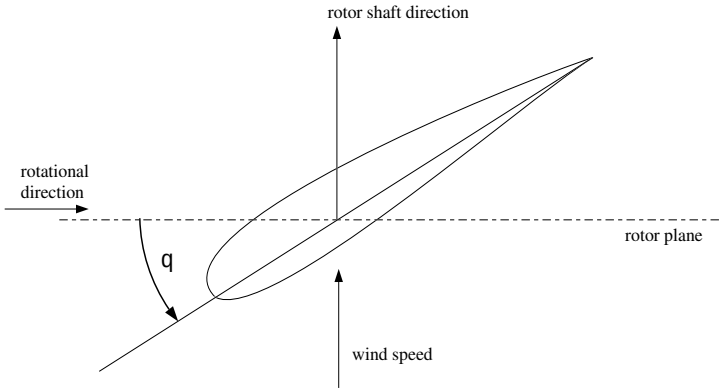

Figure A.4 *Pitch angle at tip station*

helical velocity (V_h) are introduced:

$$q_r = 0.5 \cdot \rho V_r^2$$
$$q_h = 0.5 \cdot \rho V_h^2$$
$$V_h = \sqrt{V_\infty^2 + V_r^2}$$

The angle of attack ($\alpha_{b.e.m.}$) is the angle between the effective wind speed and the chordline:

$$\alpha_{b.e.m.} = \phi_{b.e.m.} - \beta \tag{A.2}$$

Measured inflow conditions
The inflow angle, the angle of attack and the inflow velocity derived from measured quantities are denoted by ϕ_m, α_m and W_m resp.

The definition will be dependant on the measurement methods and corrections which are applied.

A distinction is made in the dynamic pressure which is found from the highest positive pressure which is measured along the profile ($q_{m,pres}$) and a dynamic pressure which is derived from the wind speed from a measurement device ($q_{m,dev}$).

A.2.8 Aerodynamic forces, moments and coefficients

Aerodynamic forces and moments
The aerodynamic forces can be either actual forces or forces per unit length. Lowercase symbols (n, t, l, d and m) are used to indicate forces and moments per unit length whereas the corresponding uppercase symbols (N ,T, L, D and M) represent actual forces/moments expressed in [N]/[Nm], see also figure A.5.

- The aerodynamic normal force per unit length n_i [N/m] is perpendicular to the chord of the ith aerofoil section,
- The aerodynamic tangential force per unit length t_i [N/m] is along the chord of the ith aerofoil section,
- The aerodynamic lift force per unit length l_i [N/m] is perpendicular to the effective wind speed W_i of the ith aerofoil section; $l_i = n_i \cos\alpha_i - t_i \sin\alpha_i$,
- The aerodynamic drag force per unit length d_i [N/m] is along the effective wind speed vector W_i of the ith aerofoil section; $d_i = n_i \sin\alpha_i + t_i \cos\alpha_i$,
- The aerodynamic moment per unit length of the ith aerofoil section is m_i [N]. The moment axis is located at the quart chord line. Positive is nose-up.

Aerodynamic coefficients

In this chapter, the aerodynamic forces of section number i are made dimensionless with the dynamic pressure q_i and the chord length c_i. As made clear in the previous sections the dynamic pressure can be determined in several ways. Obviously it is very important to specify how q is determined. If nothing else is stated the coefficients are made non-dimensional with $q_i = 0.5 \cdot \rho \cdot W^2$. If the coefficients have the subscript r or h they are made non-dimensional with q_r resp. q_h. With the exception of the pressure coefficient, all section coefficients use the lowercase symbol c.

- $C_{p,i,j}$ = the pressure coefficient = $(p_{i,j} - p_\infty)/q_i$
- $c_{n,i}$ = the section normal force coefficient = n_i/q_i;
- $c_{t,i}$ = the section tangential force coefficient = t_i/q_i;
- $c_{l,i}$ = the section lift coefficient = l_i/q_i;
- $c_{d,i}$ = the section drag coefficient = d_i/q_i

A.2.9 Unsteady conditions

Reduced frequencies and non-dimensional times can be defined. In the literature it is found that both the chord and the half chord is used for non-dimensionalisation. Within the present project it is recommended to use the half chord:

- The reduced frequency (k) is given by: $k = \omega \cdot c/(2 \cdot W)$
  with:
  ω = circular frequency of oscillation and W explained in section A.2.7.
- The non-dimensional effective pitch rate (θ^+) is given by: $\theta^+ = \dot{\theta} \cdot c/(2 \cdot W)$
  with:
  $\dot{\theta}$ = the pitch rate = $d\theta/dt$.
- The non-dimensional angle of attack rate is given by: $\alpha^+ = \dot{\alpha} \cdot c/(2 \cdot W)$
  with:
  $\dot{\alpha}$ = the angle of attack rate = $d\alpha/dt$.
- The non-dimensional time delay is given by: $\tau = \Delta t \cdot W/(2 \cdot c)$
  The non-dimensional time is having the same symbol:
  $\tau = t \cdot W/(2 \cdot c)$
- If some other quantity is introduced it is again recommended to use the half chord for the non-dimensionalisation. A dimensionless length would thus be: $2 \cdot t \cdot W/c$

A.3 Reference systems

Three reference systems are introduced, see the figures A.5 to A.8. **Note that these figures refer to a clockwise rotating wind turbine. For a counter clockwise turbine, the x_{rot} direction is opposite.**

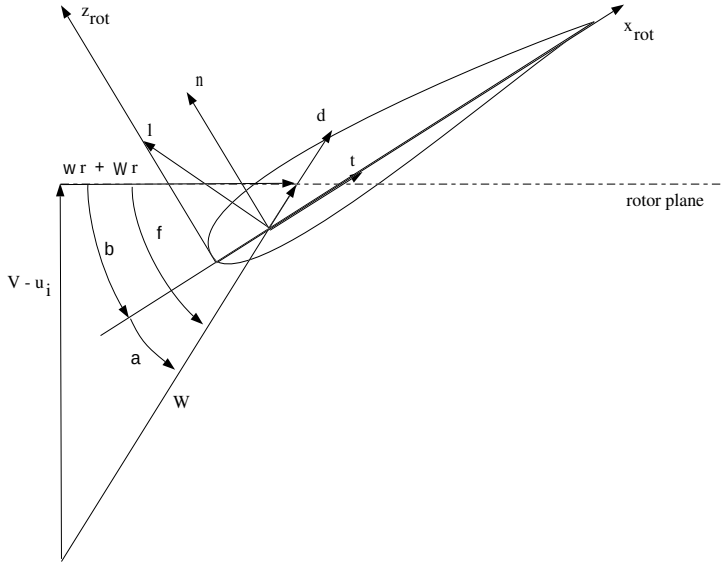

Figure A.5 *Velocity diagram, local aerodynamic forces and rotating coordinate system*

- A fixed, non-rotating axis system $(\mathrm{xyz})_{\mathrm{N}}$, related to the nacelle and with origin at the top tower centre;
- A fixed, non-rotating axis system $(\mathrm{xyz})_{\mathrm{H}}$ with origin at the rotor hub centre;
- A rotating axis system $(\mathrm{xyz})_{\mathrm{rot}}$ with origin at the leading edge of blade section i.

The tilt angle (α_{t}) is defined as the angle between the rotorshaft and the horizontal. The cone angle (α_{c}) is defined as the angle between the blades and the rotor plane.

A.3.1 Fixed $(\mathrm{xyz})_{\mathrm{N}}$ coordinate system

- $\mathrm{x_N}, \mathrm{y_N}, \mathrm{z_N}$: right handed coordinate system, origin in top tower centre;
- $\mathrm{y_N}$-axis: along the tower centre line, positive in vertical upward direction.
- $\mathrm{x_N}$-axis: along the rotor shaft (assuming zero tilt angle);
- $\mathrm{z_N}$-axis: to the right, looking downstream to the rotor.

Nacelle loads:

- $\mathrm{x_N}$: $\mathrm{F_{ax,N}}$ = axial force on nacelle, positive in downstream direction
- $\mathrm{y_N}$: $\mathrm{F_{vert}}$ = vertical force on nacelle, positive in upward direction
- $\mathrm{z_N}$: $\mathrm{F_{lat}}$ = lateral force on nacelle, positive when the force acts to the right, standing in front of the rotor.
- $\mathrm{x_N}$: $\mathrm{M_{torq,N}}$ = Moment around $\mathrm{x_N}$-axis (clockwise) or -$\mathrm{x_N}$-axis (counter clockwise). For normal operation, the rotor shaft torque is positive.
- $\mathrm{y_N}$: $\mathrm{M_{yaw}}$ = yaw moment. For a clockwise rotating wind turbine it is positive when it is a destabilizing yaw moment i.e. the yaw misalignment is increased by a positive yaw moment.
- -$\mathrm{z_N}$: $\mathrm{M_{tilt}}$ = tilt moment, positive when it increases the tilt angle

A.3.2 Fixed $(xyz)_H$ coordinate system

- x_H, y_H, z_H: right handed coordinate system, origin in rotor centre;
- x_H-axis: along the rotor shaft, positive in dowstream direction;
- y_H-axis: along the vertical upward direction (assuming zero tilt angle);
- z_H-axis: to the right, looking downstream to the rotor.

Hub loads:

- x_H: F_{ax} = axial force along rotorshaft, positive in downstream direction
- y_H: $F_{vert,H}$ = 'vertical' (assuming zero tilt angle) force on hub, positive in upward direction
- z_H: $F_{lat,H}$ = lateral force on hub, positive when the force acts to the right, standing in front of the rotor;
- x_H: $M_{torq,H}$ = Rotorshaft torque; Moment around x_H-axis (clockwise) or -x_H-axis (counter clockwise). For normal operation, the rotor shaft torque will be positive.
- y_H: $M_{yaw,H}$ = 'yaw' moment (assuming zero tilt angle);
- -z_H: $M_{tilt,H}$ = 'tilt' moment (assuming zero tilt angle), positive when it increases the tilt angle.

A.3.3 Rotating $(xyz)_{rot}$ coordinate system

- $x_{rot}, y_{rot}, z_{rot}$: right handed (only for clockwise rotation) coordinate system, origin at the leading edge of blade section i.
- x_{rot}-axis: along chord line, positive from leading edge (x=0) to trailing edge (x=c);
- z_{rot}-axis: perpendicular to chord line; positive in upwind direction;
- y_{rot}-axis: along rotor blade axis positive from root to tip;

Blade loads:

- z_{rot}: F_{flat} = flat shear force, positive in downwind direction
- x_{rot}: F_{edge} = edge shear force, positive in rotational direction
- z_{rot} (clockwise) or -z_{rot} : M_{edge} = edge moment, positive in rotational direction
- x_{rot}: M_{flat} = flat moment, positive in downwind direction.

A transformation from the $(xyz)_N$-coordinate system to the $(xyz)_{rot}$-axis system can be made in the following way:

- From $(xyz)_N$ to $(xyz)_H$:
  - rotate α_t around z_N axis;
  - translate $-d_n$ along the x_H to have the origin in the rotor centre (d_n is the rotoroverhang).
- From $(xyz)_H$ to $(xyz)_{rot}$:
  - A translation x_t, y_t, z_t to the origin of the local coordinate system $(xyz)_{rot}$. (x_t, y_t, z_t is the origin of the local coordinate system $(xyz)_{rot}$ in the $(xyz)_H$ system when $\phi_{r,b} = 0$ assuming that we are dealing with blade number 1).
  - Rearrange: $x_{rot,temp} = -z_H$ and $z_{rot,temp} = x_H$;
  - Rotate α_c around $x_{rot,temp}$-axis;
  - Rotate β around y_{rot}-axis.

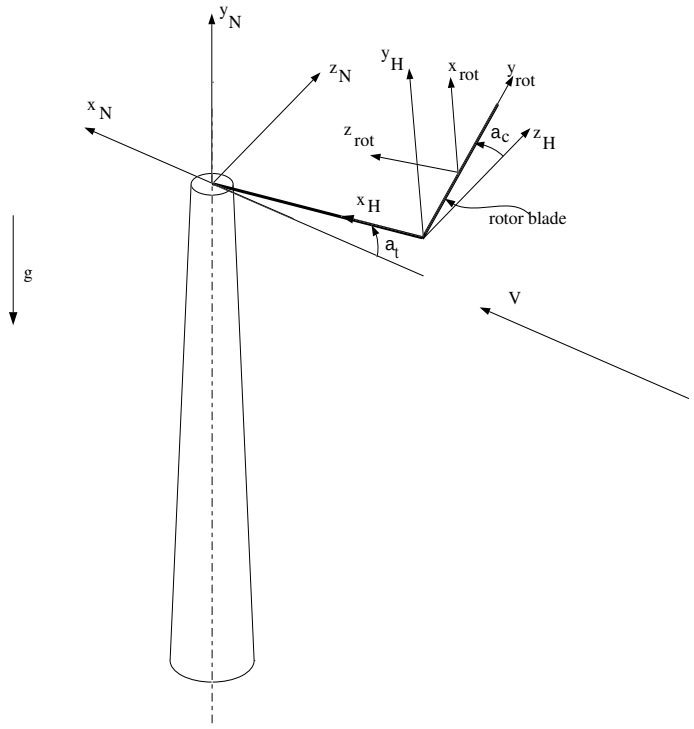

Figure A.6 *Coordinate systems ($\phi_{r,b} = 90^o$)*

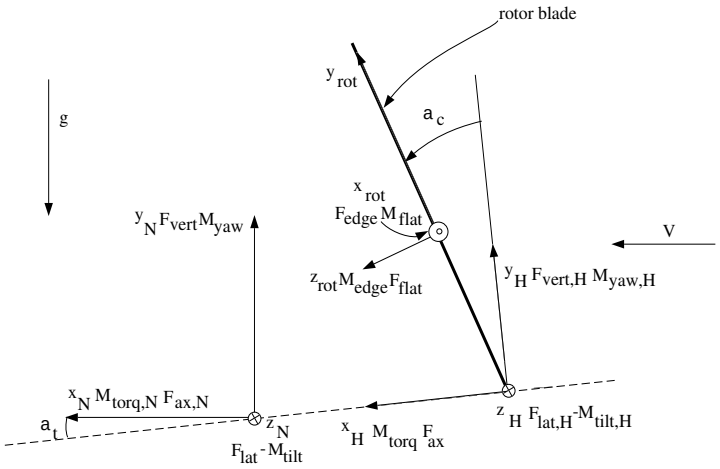

Figure A.7 *Coordinate systems in side view ($\phi_{r,b} = 0^o$)*

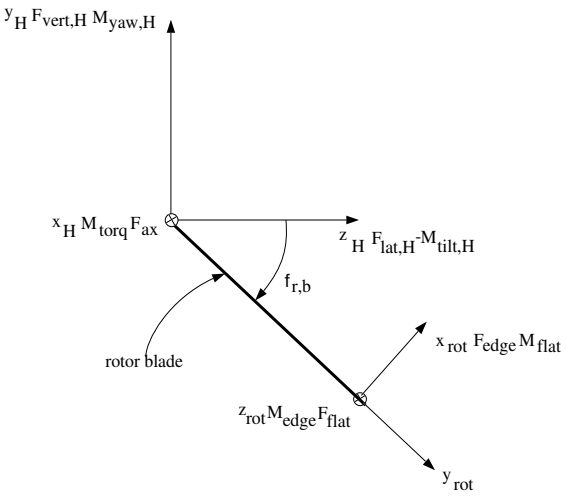

Figure A.8 *Coordinate systems in front view*

A.4 Abbreviations, symbols and units

Abbreviations

HAWT	Horizontal Axis Wind Turbine
2D	Two-dimensional
3D	Three-dimensional
a.o.a.	Angle of attack
b.e.m.	Blade element momentum

Symbols and units

A	$[m^2]$	blade cross sectional area
AR	[-]	aspect ratio; for a HAWT blade taken as $S_b/(\overline{c}^2)$
a	[-]	axial induction factor, see section A.2.7
a'	[-]	tangential induction factor, see section A.2.7
B	[-]	number of blades
$C_{D.ax}$	[-]	axial force coefficient: $C_{D.ax} = \frac{F_{ax}}{0.5\rho V^2 \pi R^2}$
$C_{L,max}$	[-]	maximum lift coefficient
C_p	[-]	pressure coefficient, see section A.2.8
C_P	[-]	power coefficient
c	[m]	chord length
$\overline{c}$	[m]	mean aerofoil chord of the blade
c_d	[-]	section drag coefficient, see section A.2.8
$c_{d,ax}$	[-]	local axial force coefficient, $c_{d.ax} = \frac{f_{ax}}{0.5\rho V^2 2\pi r}$
c_t	[-]	section lead coefficient of profile, see section A.2.8
c_l	[-]	section lift coefficient, see section A.2.8
$c_{l,max}$	[-]	section maximum lift coefficient
$c_{l,\alpha}$	$[rad^{-1}]$	$\frac{dc_l}{d\alpha}$
c_m	[-]	aerodynamic section moment coefficient, with reference to 25% chord, positive when nose up, see section A.2.8
c_n	[-]	section normal force coefficient, see section A.2.8
D	[m] or [N]	rotor diameter or drag
d	[N/m]	section drag, see section A.2.8
d_n	[m]	rotor overhang
E	$[N/m^2]$	Young's modulus
F_{flat}	[kN]	flat shear force, see section A.3.3
F_{edge}	[kN]	edge shear force, see section A.3.3
F_{ax}	[kN]	axial force, see section A.3.1
F_{lat}	[kN]	lateral force , see section A.3.1
f_{ax}	[N/m]	local axial force
g	$[m/s^2]$	gravitational acceleration
h	[m]	height
I	[-] or $[m^4]$	turbulence intensity or moment of inertia
k	[-]	reduced frequency, see section A.2.9
L	[N]	lift
l	[N/m]	section lift force perpendicular to the effective wind speed, see section A.2.8
M	[-] or [Nm]	Mach number or moment with reference to 25% chord, positive nose up, see section A.2.8

M_{edge}	[kNm]	edgewise moment, see section A.3.3
M_{flat}	[kNm]	flapping moment, see section A.3.3
M_{tilt}	[kNm]	tilting moment, see section A.3.1
M_{torq}	[kNm]	rotorshaft torque, see section A.3.2
M_{yaw}	[kNm]	yawing moment, see section A.3.1
m	[N]	section moment with reference to 25% chord, positive nose up, see section A.2.8
N	[N]	normal force perpendicular to the chord, see section A.2.8
n	[N/m]	section aerodynamic normal force perpendicular to the chord, see section A.2.8
nc	[-]	number of pressure tap locations around the chord
nm	[-]	number of mechanical load locations
ns	[-]	number of instrumented span locations
nw	[-]	number of instrumented wind measurement locations
P	[Hz] or [W]	rotational frequency (= $\Omega/2\pi$) or power
p	[Pa]	static pressure
p_{pitot}	[Pa]	pitot pressure
q	[Pa]	dynamic pressure, see section A.2.7
R	[m]	rotor radius
Re	[-]	Reynolds number (= $W \cdot c/\nu$)
s	[m]	aerofoil arc length coordinate
S	[m^2]	turbine swept area ($S = \pi \cdot R^2$)
S_b	[m^2]	blade projected area ($S_b = \int_{r_{hub}}^{R} c \cdot dr$)
r	[m]	radial position, r = 0 at rotor shaft
T	[N]	thrust (= axial force) or tangential force, see section A.2.8
t	[s] or [m] or [N/m]	time or blade section thickness or tangential force along chord, see section A.2.8
W	[m/s]	effective wind speed seen by blade, see section A.2.7
V	[m/s]	horizontal incoming (undisturbed) wind speed
V_r	[m/s]	rotational velocity ($\Omega \cdot r$)
V_h	[m/s]	helical velocity ($\Omega \cdot r$)
u_i	[m/s]	axial induced velocity, see section A.2.7
x,y,z		coordinate systems, see section A.3
x_m	[m]	position of intersection point along the chord
α	[^{o}]	angle of attack, see section A.2.6
α_c	[^{o}]	cone angle, see section A.3
α_t	[^{o}]	tilt angle, see section A.3
α_0	[^{o}]	angle of attack at zero lift
$\dot{\alpha}$	[rad/s or $^\circ$/s]	angle of attack rate; if not explicitly stated in rad/s, see section A.2.9
α^+	[-]	non-dimensional angle of attack rate, see section A.2.9
β	[^{o}]	local blade angle, see section A.2.7
Γ	[m^2/s]	vortex strength
γ	[m/s]	vorticity density
ϵ	[^{o}]	twist angle relative to tip station, see section A.2.7
δV	[-]	vertical wind shear, see section A.2.4
τ	[-]	non-dimensional time (delay), see section A.2.9
θ	[^{o}]	pitch angle, see section A.2.6
θ_t, θ_{tip}	[^{o}]	tip angle, see section A.2.6
$\dot{\theta}$	[rad/s or or $^\circ$/s]	pitch rate, if not explicitly stated in rad/s
θ^+	[-]	effective non-dimensional pitch rate, see section A.2.9

λ	[-]	tip speed ratio = $\frac{\Omega.R}{V}$
λ_r	[-]	local tip speed ratio = $\frac{\Omega.r}{V}$
ρ	[kg/m^3]	air density or mass density
σ	[-]	local solidity (= Bc/2πr) or standard deviation
ϕ	[^{o}]	inflow angle, see section A.2.7
$\phi_{r,b}$	[^{o}]	blade azimuth angle, see section A.2.1
ϕ_r	[^{o}]	azimuth angle, see section A.2.1
ϕ_y, ϕ_{yaw}	[^{o}]	yaw misalignment angle, see section A.2.3
ϕ_{turb}	[^{o}]	yaw angle, see section A.2.3
ϕ_w	[^{o}]	wind direction, see section A.2.4
Ω	[rad/s;rpm]	rotational speed of rotor shaft; positive in clockwise direction, looking downstream to the rotor
ω	[rad/s]	circular frequency of oscillation, also used for rotational induced velocity, see section A.2.7

subscripts

a	amplitude
aer	aerodynamic
b.e.m.	according to blade-element-momentum notations
cent	centrifugal
dev	from measurement device
el	electrical
gen	generator
hub	hub height
h	helical
i	at spanwise location i
in	cut-in
j	at chordwise position j
low	lower part of rotor plane
m	derived from measurements, or mean
min	minimum
max	maximum
out	cut-out
pres	derived from pressure distribution
r	rotational
rat	rated
ref	reference
s	shedding or stalling point
stag	stagnation point
tap	at pressure tap
tip	at the tip
up	upper part of rotor plane
1P	1P averaged
∞	free stream

APPENDIX B. MEETINGS

B.1 IEA Annex XIV meetings

In IEA Annex XIV, a total of 7 meetings (including a preparatory meeting) have been held which were attended by all the institutes who were involved in the Annex. The meetings were always held at the institutes and a visit to the experimental facilities was one of the agenda points.

Detailed minutes of every meeting were prepared.

- A preparatory meeting was held at the Delft University of Technology on December 2nd 1992, see [49]. At this meeting agreement was reached on the workplan.
- The first meeting was held at RISØ National Laboratory on September 16th and 17th, 1993, see [50]. At this meeting a large number of technical aspects (a.o. the length of time series, scan frequency, definition of the angle of attack) and the problem of the selection of the most suitable datafiles was adressed.
- The second meeting was held at the University of Delft on March 17th and 18th 1994, see [51]. At this meeting a further discussion took place of the technical points which are mentioned at the second meeting. Furthermore a selection was made of the most suitable datafiles from NREL, RISØ and DUT.
- Subsequently, the IEA Annex XIV project became closely related to the EU JOULE project 'Dynamic Stall and 3D effects', [3]. All institutes which participate in the IEA Annex XIV were involved in the JOULE project as well and attended the project meetings of the JOULE project. For this reason no separate IEA Annex XIV meetings were held until April 5th 1995 at Rutherford Appleton Laboratory, see [52]. At this third meeting the main discussion point was the problem of the large datafiles which in the JOULE project has led to a 'psychological barrier' for potential users of the database. It was decided that even more emphasis should be put to the precise documentation of the format of the datafiles, by which the selection of the desired signals is relatively easy.
- A fourth meeting was held at NREL on February 5^{th} and 6^{th} 1996, see [53]. Between the third and the fourth meeting some of the measurement programs were accelerated considerably and much new data have been presented. Much attention was paid to the discussion document on the angle of attack.
- A fifth meeting was held at ECN on June 14^{th} 1996, see [36]. Again a considerable amount of new data was presented. In addition, the content of the final report was discussed in some detail.
- The sixth meeting was held at RISØ on February 20 and 21 1997. At that time a draft of the final report was available, which was discussed extensively. Also a proposal for an extension was discussed.

B.2 IEA Annex XVIII meetings

In IEA Annex XVIII, a total of 6 meetings (including a preparatory meeting) have been held.

Again, detailed minutes of every meeting were prepared.

- A preparatory meeting was held on November 26^{th}, 1997 at Imperial College [54]. At this meeting agreement was reached on the workplan.
- The first meeting was held at NREL on June 18 and 19, 1998 [55]. At this meeting the status of the facilities was discussed with emphasis on the 'new'

measurements to be performed by Mie University. Furthermore it was decided to invite CRES, which initiated a full scale aerodynamic test program, to IEA Annex XVIII;

- The second meeting was held at the Institute of Wind Energy of the Technical University of Delft on March 8 and 9, 1999, see [56]. At this meeting an inventory was made of the experiences of the users. On basis of this inventory it was decided to add profile data to the database as well as 2D pressure distributions. Furthermore it was decided to make some Fortran programs which the most 'popular' signals from some files can be extracted.
- The third meeting was held at the Mie University (Japan) on September 29 and September 30, 1999 [57]. At this meeting most of the recommendations given by the users had been implemented. Furthermore the set-up of the Internet site had been discussed.
- Between the third and the fourth meeting, NREL succesfully completed aerodynamic measurements on their 10 m turbine in the NASA-Ames wind tunnel. Within this period the EU-5th framework project 'Mexico' was also approved. In this project aerodynamic measurements will be performed in the German Dutch Wind Tunnel, DNW. As a consequence the perspective of full scale aerodynamic measurements was discussed at the fourth meeting, which was held at the National Renewable Energies Laboratory (USA) on December 7, 2000, [58], in conjuction with the IEA's 14th symposium on 'Aerodynamics of Wind Turbines' and the second NASA-Ames Science Panel Meeting. The 'move' of aerodynamic measurements to the wind tunnel environment was encouraged. Many uncertainties can be eliminated in this way which facilitates the interpretation considerably. Nevertheless it was believed that full scale aerodynamic measurements, which are taken in a turbulent environment, are much more representative for the commercial practice, also due to the larger sizes which are possible. As such they are complementary to the wind tunnel measurements. At the fourth meeting, the measurements which meanwhile had become available were also discussed at the fourth meeting;
- The fifth meeting was held at RISØ on June 27th 2001. At this meeting a draft of the final report was discussed as well as the measurements which had become available from Mie University.

APPENDIX C. CONTENT OF IEA ANNEX XIV DATABASE

C.1 Global description of the content of the database

For the definition of filenames, file types and formats, reference is made to section 8.

On the following pages the directory tree and the content of the database is listed. The datafiles are stored as zip file. Note that the filenames in the database may be slightly different from the prescribed ones. This was caused by the limitation on the maximum number of characters for the filename which were allowed by some operating systems. The difference lies mainly in the absence of 'rot' in the time series filenames, which indicates the rotating situation. In the case of a file name abbreviation, a 'keyfile' is added to the set of files which explains the filename. Practically speaking, the limitation on the number of characters only appeared for the campaings stored until approximately 1998. Thereafter all commonly used operating systems accepted longer filenames.

The directory tree in section C.2 shows that main directories are 'utils/' and 'data/'. 'Utils/' contains some auxiliary programs which extract signals from the RISØ and NREL files. In directory 'data/' the measurement campaigns are stored. This directory is further subdivided into subdirectories for every participant, which are further subdivided into subdirectories '2d' (i.e. 2D profile coefficients and pressure distributions), 'stilltim/' (i.e. time series at standstill) 'rottim/' (i.e. time series at rotating conditions) and 'rotcoef/' (i.e. coefficients at rotating conditions). Some of these subdirectories are further subdivided, i.e. into subdirectories for the different span locations (DUT and Mie), or for the different phases (NREL). The subdirectory 'pit_vari/' gives the rotating profile coefficients for different pitch angles.

For the time series, it is reminded that there are three different filetypes:
1. A log file;
2. A prof file;
3. Pressure files.

The zipfiles and the filenames of the time series which are listed in the following sections should be read as a set of files. For example, in table C.14, see section C.8.3, the set ny_rot_e_001 (ecn/2d/rottim/ny_e_1.zip) contains the following files:
- ny_log_rot_e_001: The log file;
- ny_prof_rot_e_001: The prof file;
- ny_pxx_rot_e_001 (xx is 01 to 03): 3 Pressure files.

These files are zipped to file /data/ecn/2d/rottim/ny_e_1.zip, see section C.2.

C.2 Directory tree

```
utils/
      riso_select.zip
      nrel_select.zip
data/
     riso/
          2d/
                    coef2d_r.zip
```

```
     rottim/
               ny_r_1.zip to ny_r_5.zip
               y_r_1.zip to y_r_3.zip
     rotcoef/
               coef_r.zip

nrel/
     2d/
               coef2d_n.zip
     stilltim/
                nt/
                    non_nt_1.zip
     rottim/
                nt/
                    ny_nt_1.zip to ny_nt_4.zip
                    y_nt_1.zip to y_nt_8.zip
                nu/
                    ny_nu_1.zip to ny_nu_5.zip
                    y_nu_1.zip to y_nu_8.zip
                ntp/
                    ny_ntp_1.zip to ny_ntp_8.zip
                    y_ntp_1.zip to y_ntp_9.zip
     rotcoef/
                nt/
                    coef_nt.zip
                nu/
                    coef_nu.zip
                ntp/
                    pit3/
                              coef_ntp.zip
                    pit_vari/
                              coef_ntp.zip
ecn/
    2d/
                coef2d_e.zip
    stilltim/
                non_e_17.zip to non_e_21.zip
    rottim/
                ny_e_1.zip to ny_e_25.zip
                y_e_1.zip to y_e_21.zip
    rotcoef/
                pit_vari
                         coef_e.zip

dut/
    2d/
                coef2d_d.zip

    stilltim/
                70percent/
                         non_d_001_70.zip to non_d_016_70.zip
    rottim/
                30percent/
                          ny_d_001_30.zip to ny_d_030_30.zip
                          y_d_001_30.zip to y_d_148_30.zip
                50percent/
                          ny_d_001_50.zip to ny_d_009_50.zip
                          y_d_001_50.zip to y_d_023_50.zip
```

```
                    70percent/
                              ny_d_001_70.zip to ny_d_014_70.zip
                              y_d_001_70.zip to y_d_036_70.zip
          icral/
            rottim/
                    ny_i_001.zip

      mie/
            2d/
                    coef2d_m.zip
            rottim/
                    50percent/
                              ny_m_001_50.zip
                              y_m_001_50.zip to y_m_002_50.zip
                    70percent/
                              ny_m_001_70.zip
                              y_m_001_70.zip to y_m_002_70.zip
                    90percent/
                              y_m_001_90.zip to y_m_003_90.zip
             rotcoef/
                    coef_m.zip
```

C.3 NREL time series

Note that there are mutual differences in 'prof' file format. There appear to be 9 different formats. In table C.1 these are identified with f(ormat)A to fI. The table shows the mutual similarities and differences between the prof file formats for the datasets which have been supplied. It is recalled that the institute description for the NREL campaign is 'nu', 'nt', or 'ntp' for the untwisted (phase II), twisted (phase III) and twisted with probes (phase IV) data respectively, see section 8. A further description of these datasets is given in the following sections.

C.3.1 NREL time series: Non-rotating campaigns, twisted configuration

NREL supplied one measurement for non-rotating conditions on the twisted blade configuration. The file is stored in directory '/data/nrel/stilltim/nt'. In table C.2 a global overview of this campaign is listed. Note that the most outboard intrumented section for this campaign is 47%. Figure C.1 shows time series of selected signals.

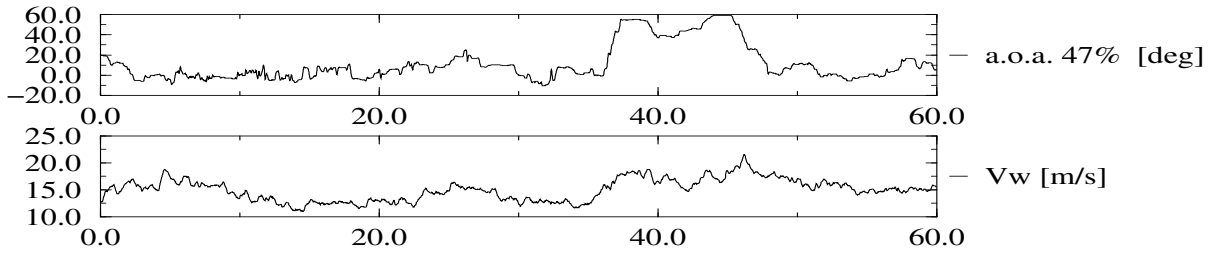

Figure C.1 *NREL: Time series of campaign non_nt_001*

Table C.1 *Format NREL measurement files*

filename	fA	fB	fC	fD	fE	fF	fG	fH	fI
ny-rot-nu-001				x					
ny-rot-nu-002					x				
ny-rot-nu-003						x			
ny-rot-nu-004									x
ny-rot-nu-005									x
ny-rot-nt-001	x								
ny-rot-nt-002		x							
ny-rot-nt-003		x							
ny-rot-nt-004		x							
ny-rot-ntp-xxx			x						
y-rot-nu-001				x					
y-rot-nu-002				x					
y-rot-nu-003					x				
y-rot-nu-004									x
y-rot-nu-005				x					
y-rot-nu-006					x				
y-rot-nu-007						x			
y-rot-nu-008					x				
y-rot-nt-001							x		
y-rot-nt-002								x	
y-rot-nt-003								x	
y-rot-nt-004							x		
y-rot-nt-005		x							
y-rot-nt-006		x							
y-rot-nt-007		x							
y-rot-nt-008		x							
y-rot-ntp-xxx			x						

Table C.2 *Global overview of NREL measurement files, non-rotating conditions (twisted)*

file	NREL filename	$\overline{\alpha(47\%)}$ deg	$\overline{V}$ m/s	$\overline{\text{Power}}$ kW	$\overline{\theta_{tip}}$ deg	duration s
non-nt-001	parked1	11.47	14.97	0.07442	62.43	60.0

C.3.2 NREL time series: Non-yawed campaigns, untwisted configuration, phase II data

The files are stored in directory '/data/nrel/rottim/nu' and numbered in order of increasing angle of attack (= wind speed), see table C.3. Due to errors introduced by the azimuth angle potentiometer, the rotor speed calculation was not reliable in all Phase II data. For this reason, the rpm channel is not included in the time series figures. The constant speed generator ran at approximately 72 rpm.

Table C.3 *Global overview of NREL measurement files, non-yawed conditions (untwisted, phase II)*

file	NREL filename	$\overline{\alpha_{80\%}}$ deg	$\overline{V}$ m/s	$\overline{\text{Power}}$ kW	$\overline{\theta_{tip}}$ deg	$\overline{\Omega}$ rpm	duration s
ny-rot-nu-001	d7042	0.6	7.2	0.8	12.0	72	60.0
ny-rot-nu-002	d6731	5.1	10.5	6.7	11.9	72	60.0
ny-rot-nu-003	d7112	8.8	12.9	9.8	12.0	72	60.0
ny-rot-nu-004	d7141	13.3	16.3	13.5	12.3	72	60.0
ny-rot-nu-005	d7212	18.1	19.2	14.5	11.8	72	60.0

C.3.3 NREL time series: Non-yawed campaigns, twisted configuration

NREL time series: Non-yawed campaigns, twisted configuration, phase III data)

The files are stored in directory '/data/nrel/rottim/nt' and numbered in order of increasing angle of attack (= wind speed), see table C.4.

Table C.4 *Global overview of NREL measurement files, non-yawed conditions (twisted, phase III)*

file	NREL filename	$\overline{\alpha_{80\%}}$ deg	$\overline{V}$ m/s	$\overline{\text{Power}}$ kW	$\overline{\theta_{tip}}$ deg	$\overline{\Omega}$ rpm	duration s
ny-rot-nt-001	data1	4.1	7.0	2.9	2.4	71.8	60.0
ny-rot-nt-002	data3	10.7	10.6	9.9	3.4	72.2	60.0
ny-rot-nt-003	data6	14.3	12.8	11.1	2.8	72.3	60.0
ny-rot-nt-004	data5	18.4	15.8	10.4	3.5	72.22	60.0

NREL time series: Non-yawed campaigns, twisted configuration, phase IV data

The files are stored in directory '/data/nrel/rottim/ntp'. The files 1 to 5 are numbered in order of increasing angle of attack (= wind speed), see table C.5. The files 6,7, and 8 are measured at different unusual pitch angles in order to get some insight into the 3D aerodynamic behaviour for different loadings.

Table C.5 *Global overview of NREL measurement files, non-yawed conditions (twisted, phase IV)*

file	NREL filename	$\overline{\alpha_{95\%}}$ deg	$\overline{V}$ m/s	$\overline{\text{Power}}$ kW	$\overline{\theta_{tip}}$ deg	$\overline{\Omega}$ rpm	duration s
ny-rot-ntp-001	data48	4.3	7.1	3.3	3.0	71.8	60.0
ny-rot-ntp-002	data46	9.4	10.4	9.7	3.0	72.2	60.0
ny-rot-ntp-003	data92	12.1	12.9	11.1	2.6	72.3	60.0
ny-rot-ntp-004	data82	15.2	15.9	9.4	2.7	72.2	60.0
ny-rot-ntp-005	data81	18.4	19.3	10.1	2.9	72.2	60.0
ny-rot-ntp-006	d408012	12.5	17.1	17.9	8.3	72.8	60.0
ny-rot-ntp-007	d4m3004	13.1	10.2	5.8	-2.5	72.0	60.0
ny-rot-ntp-008	d4m9001	13.4	7.9	0.2	-8.9	72.3	60.0

C.3.4 NREL non-yawed campaigns, plots of time series

Time series, NREL non-yawed campaigns, untwisted blade, plots

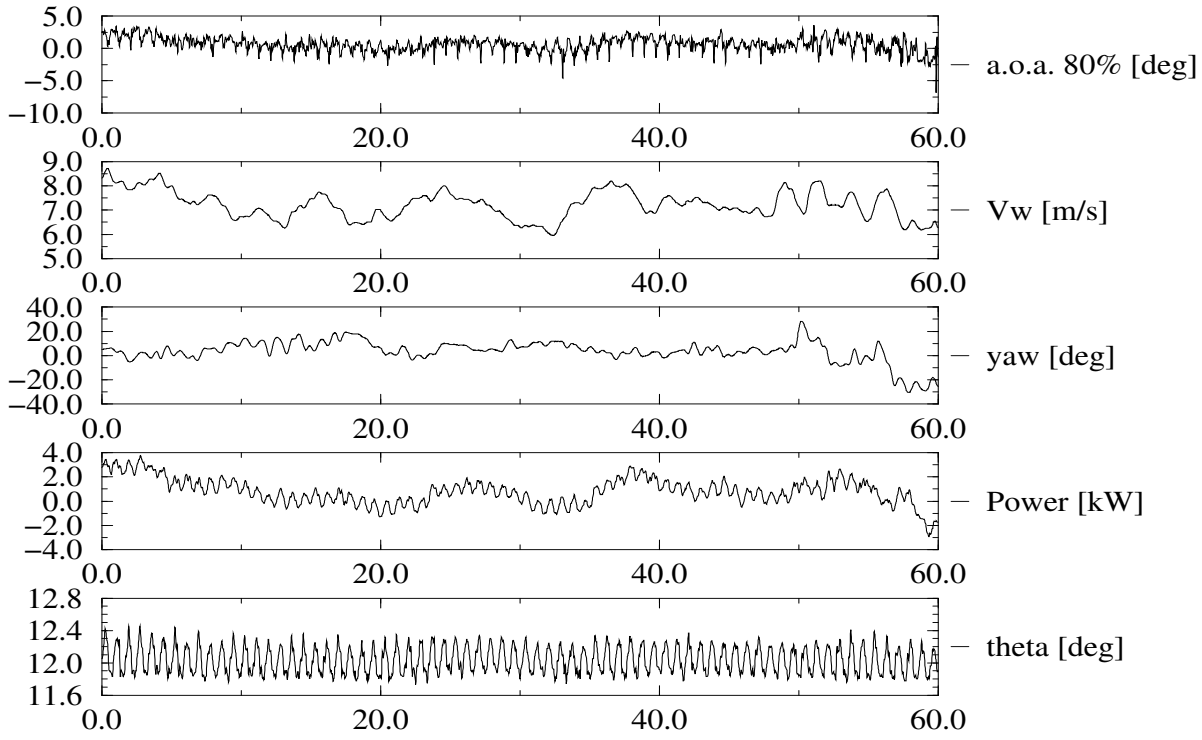

Figure C.2 *NREL: Time series of campaign ny_rot_nu_001*

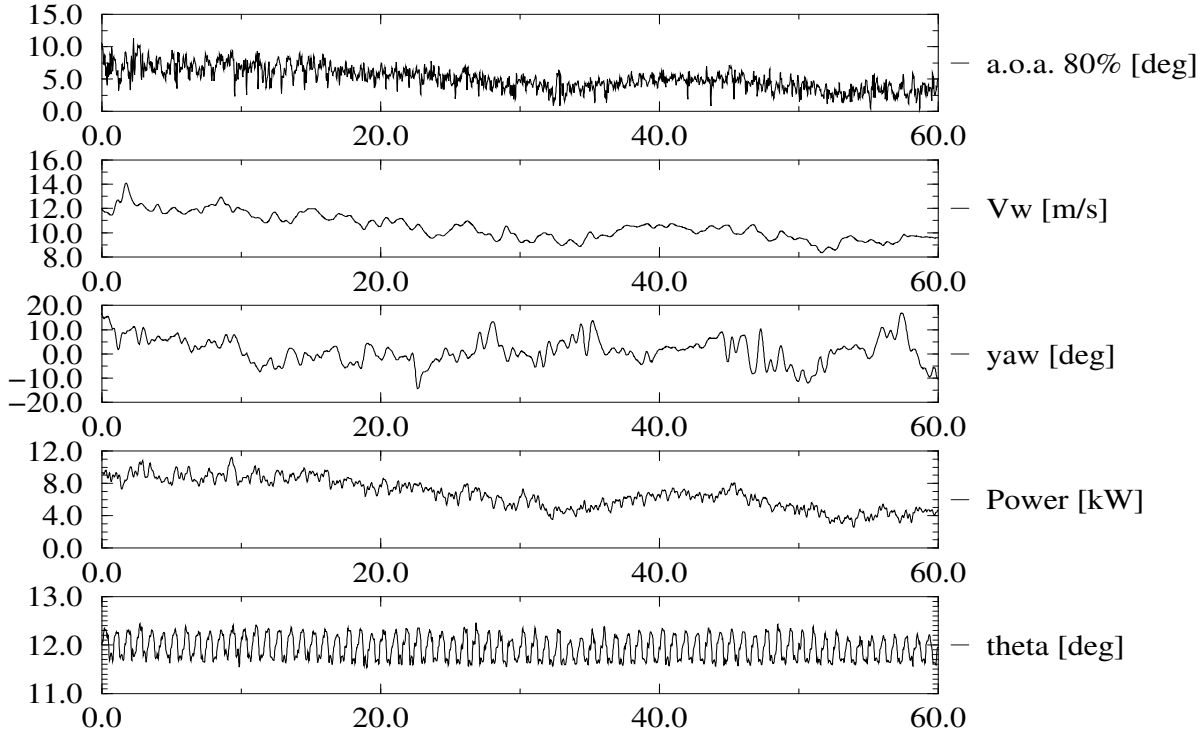

Figure C.3 *NREL: Time series of campaign ny_rot_nu_002*

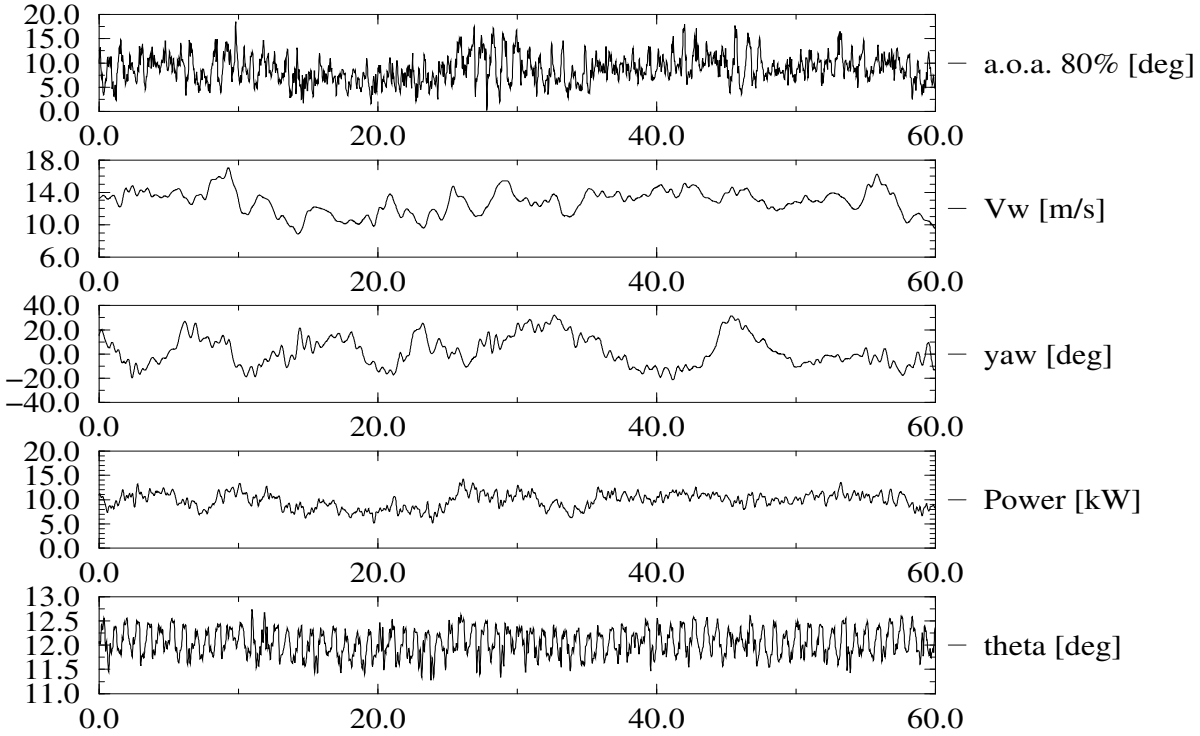

Figure C.4 *NREL: Time series of campaign ny_rot_nu_003*

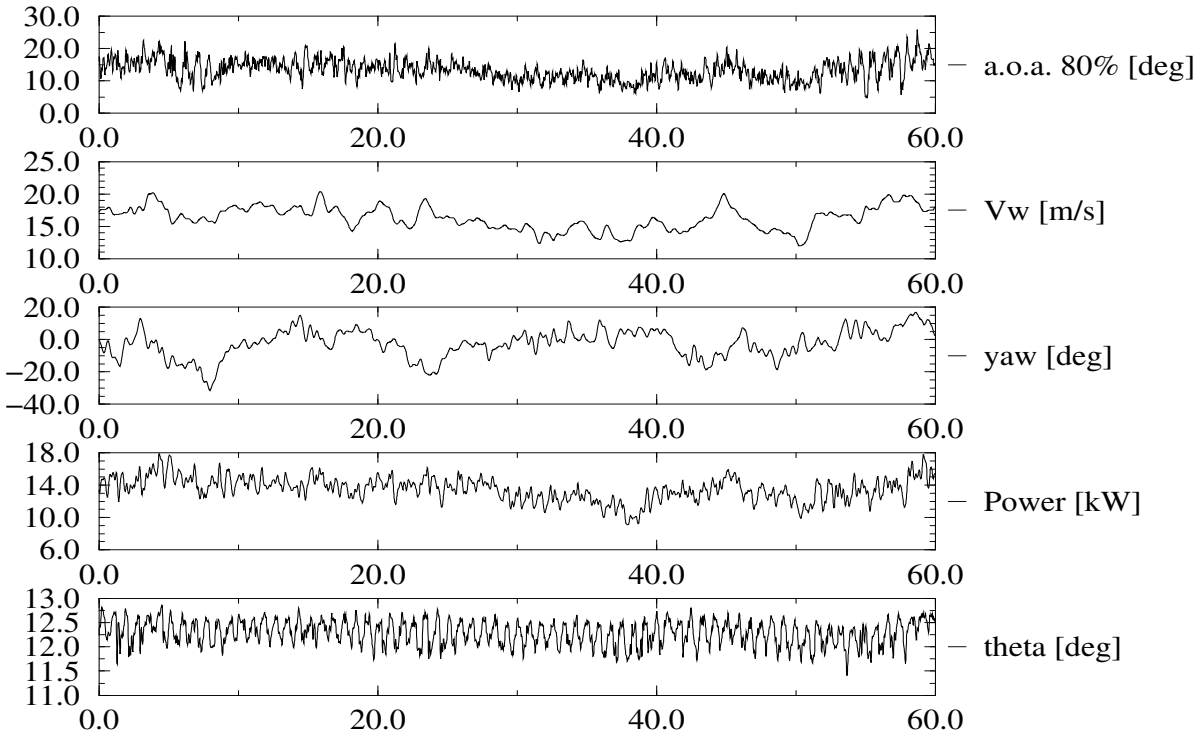

Figure C.5 *NREL: Time series of campaign ny_rot_nu_004*

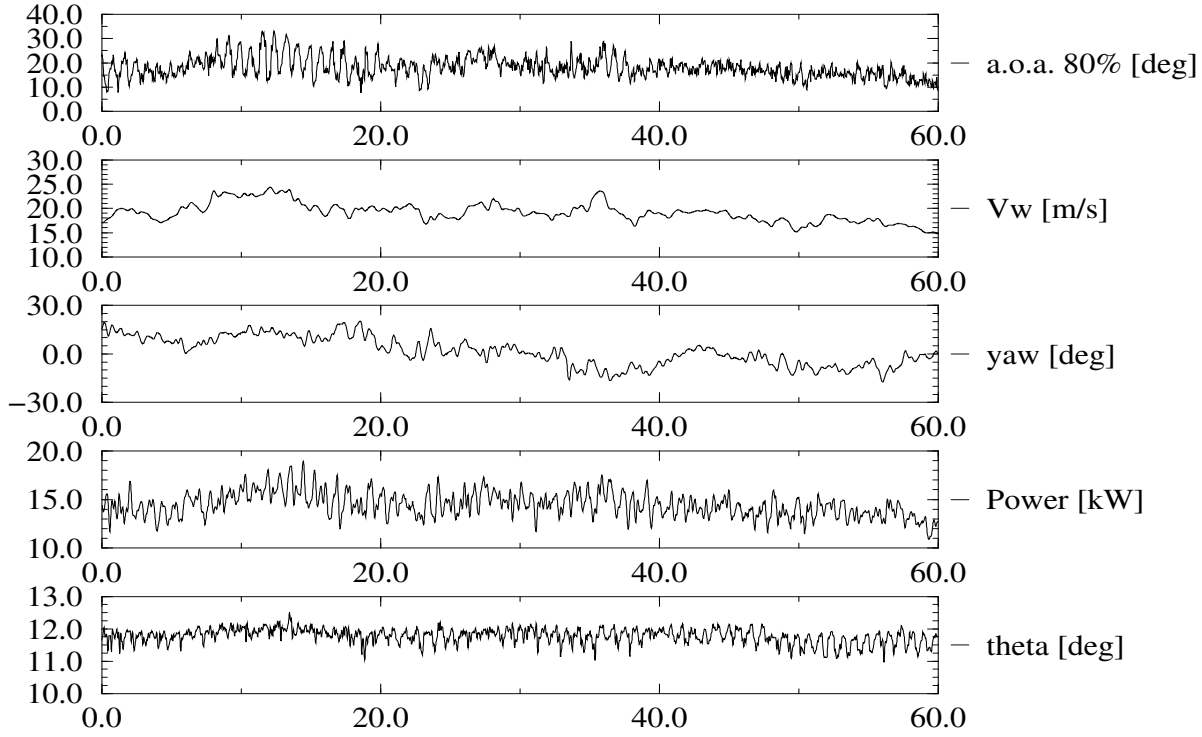

Figure C.6 *NREL: Time series of campaign ny_rot_nu_005*

Time series, NREL non-yawed campaigns, twisted blade (Phase III), plots

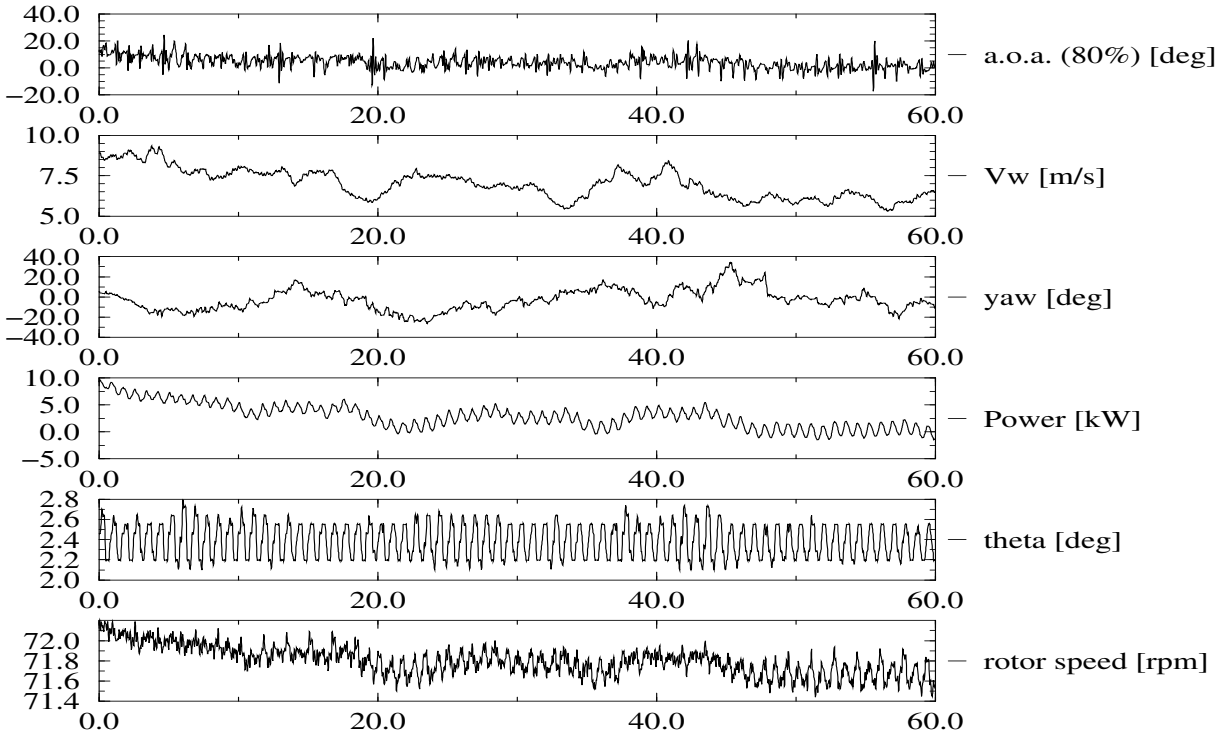

Figure C.7 *NREL: Time series of campaign ny_rot_nt_001*

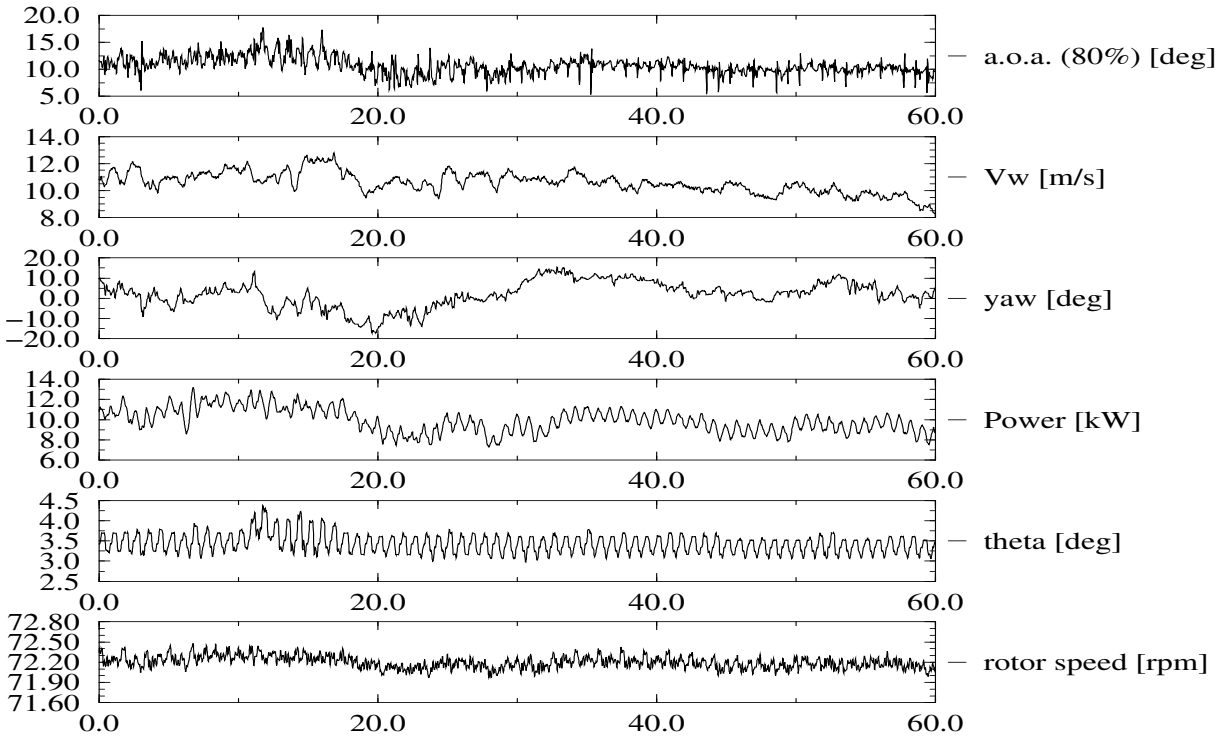

Figure C.8 *NREL: Time series of campaign ny_rot_nt_002*

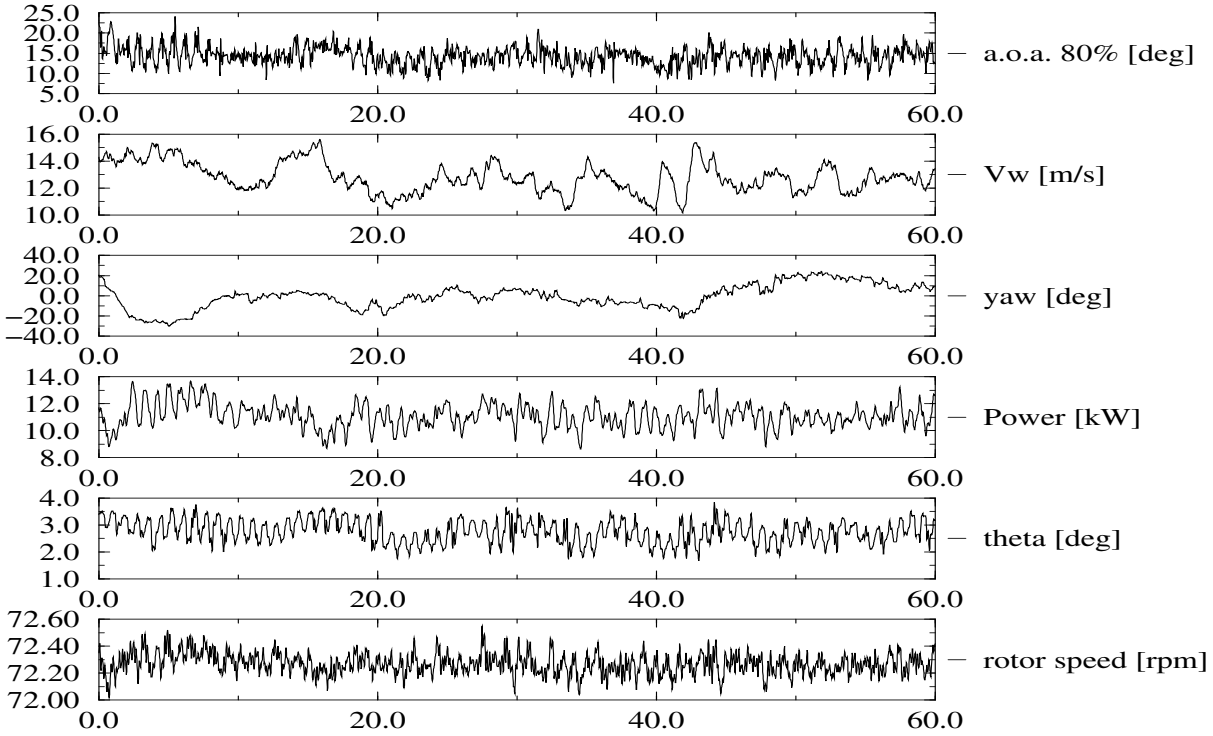

Figure C.9 *NREL: Time series of campaign ny_rot_nt_003*

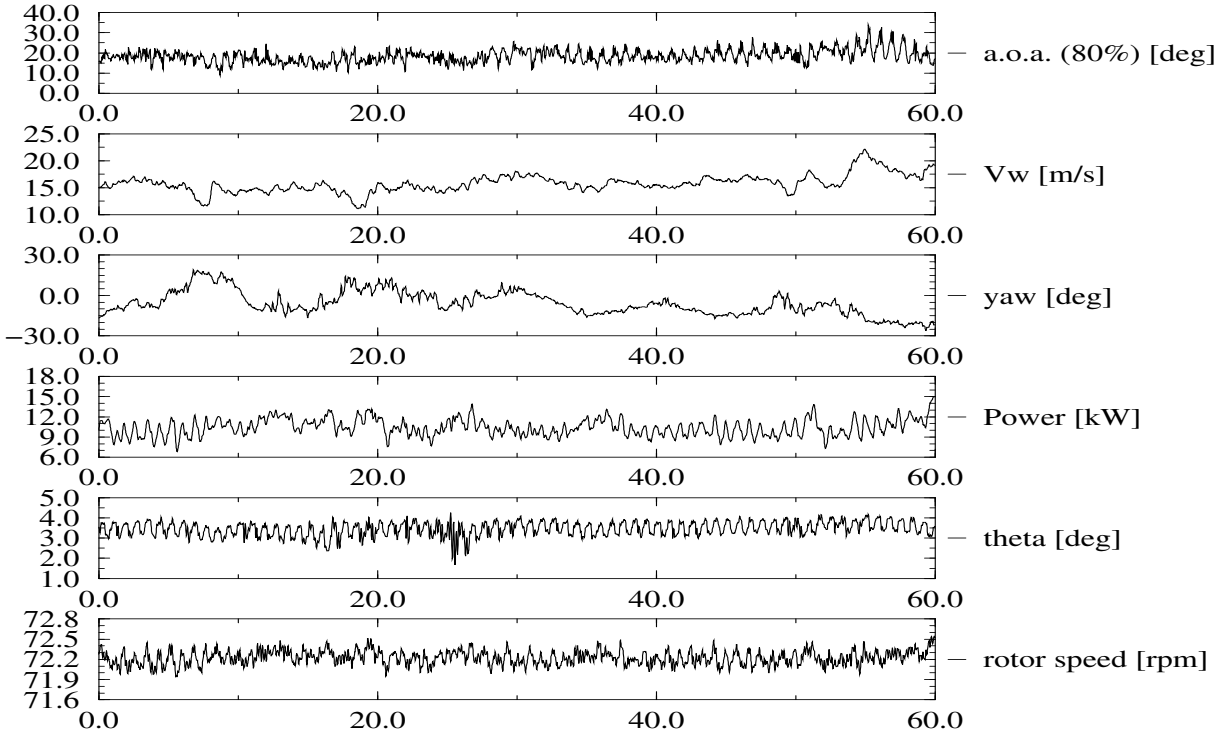

Figure C.10 *NREL: Time series of campaign ny_rot_nt_004*

Time series, NREL non-yawed campaigns, twisted blade (Phase IV), plots

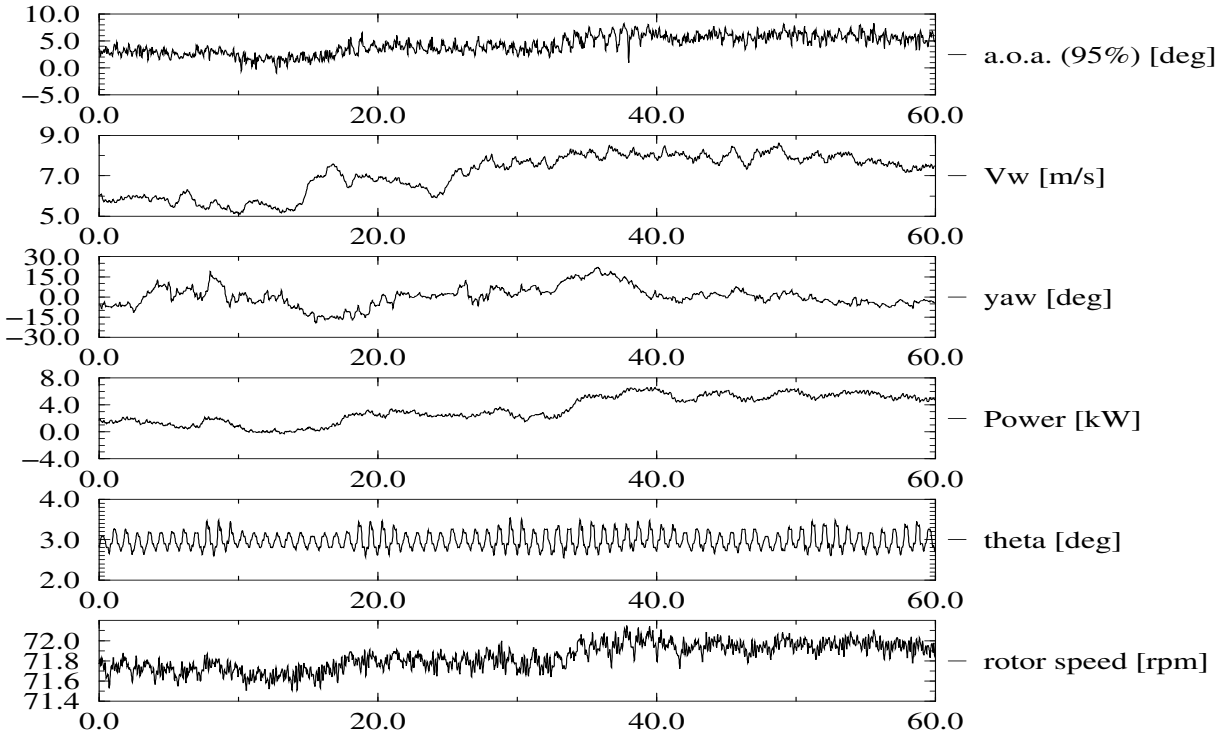

Figure C.11 *NREL: Time series of campaign ny_rot_ntp_001*

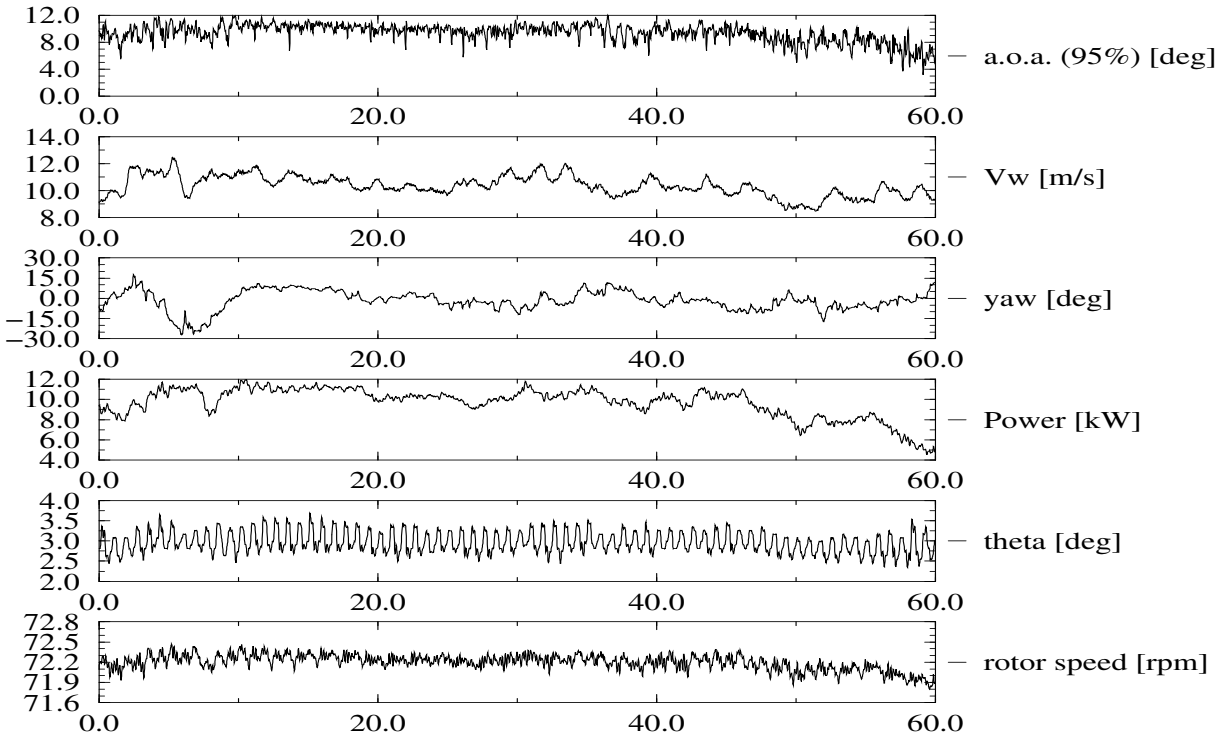

Figure C.12 *NREL: Time series of campaign ny_rot_ntp_002*

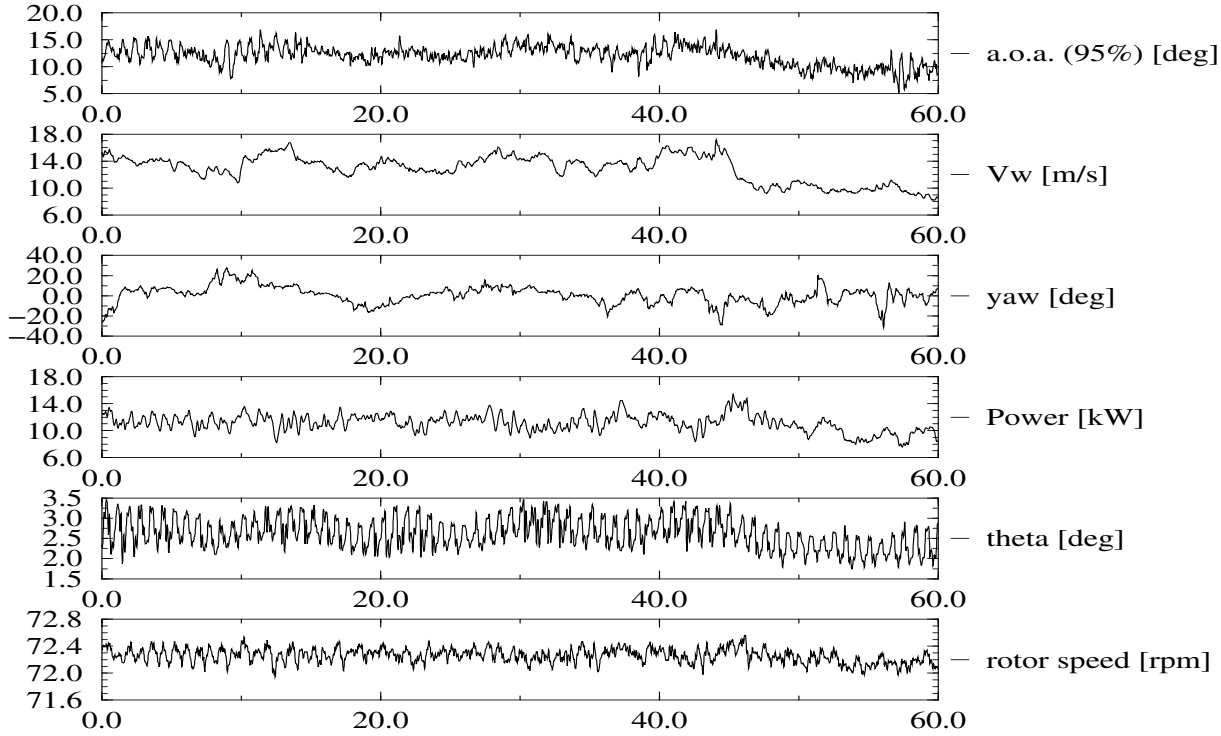

Figure C.13 *NREL: Time series of campaign ny_rot_ntp_003*

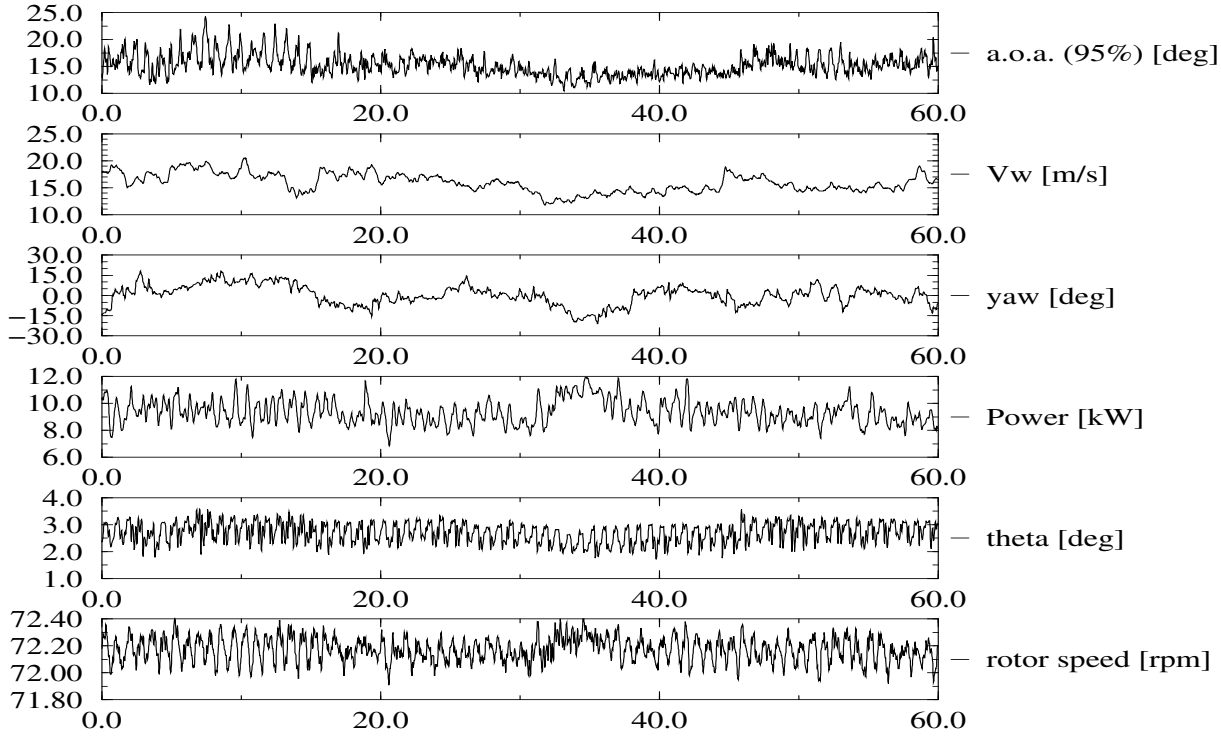

Figure C.14 *NREL: Time series of campaign ny_rot_ntp_004*

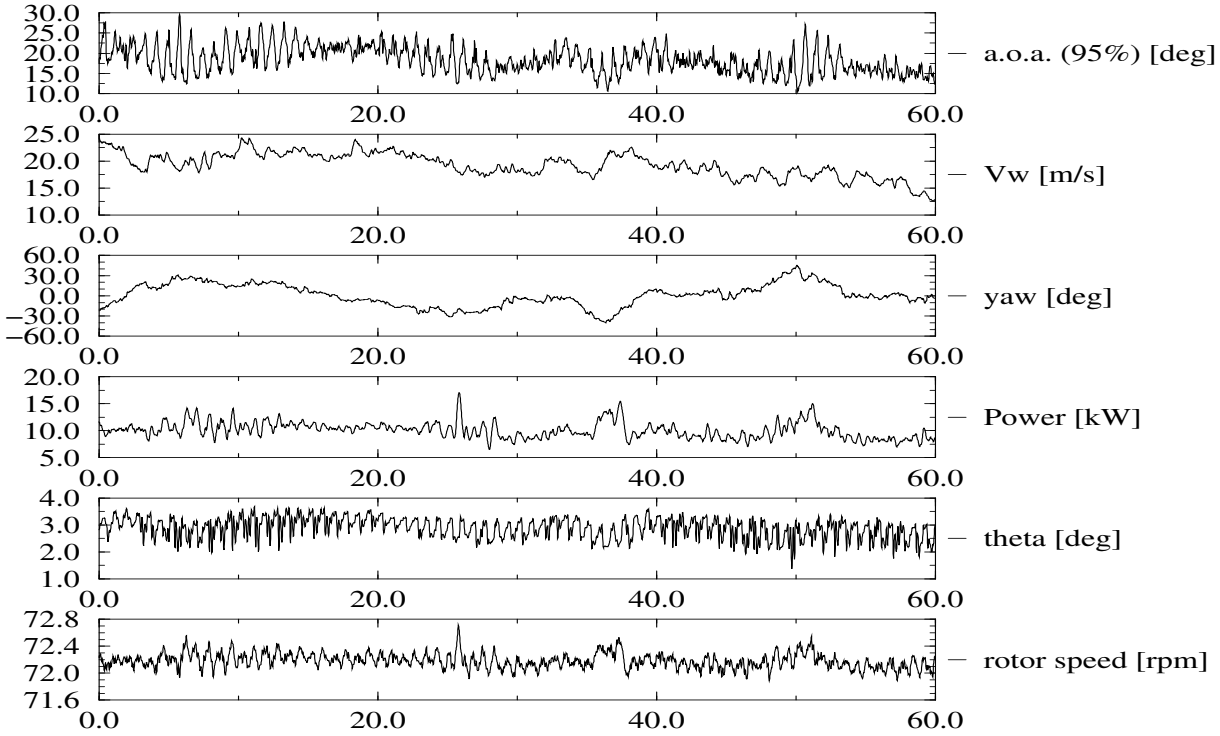

Figure C.15 *NREL: Time series of campaign ny_rot_ntp_005*

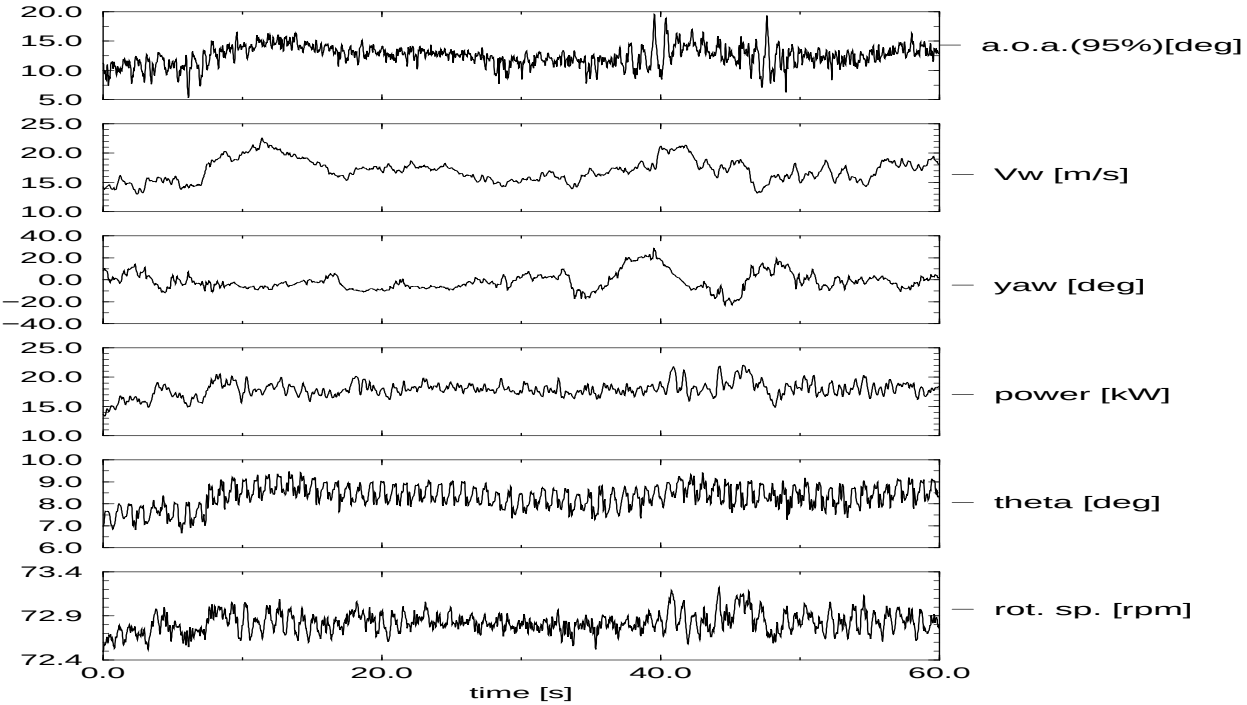

Figure C.16 *NREL: Time series of campaign ny_rot_ntp_006*

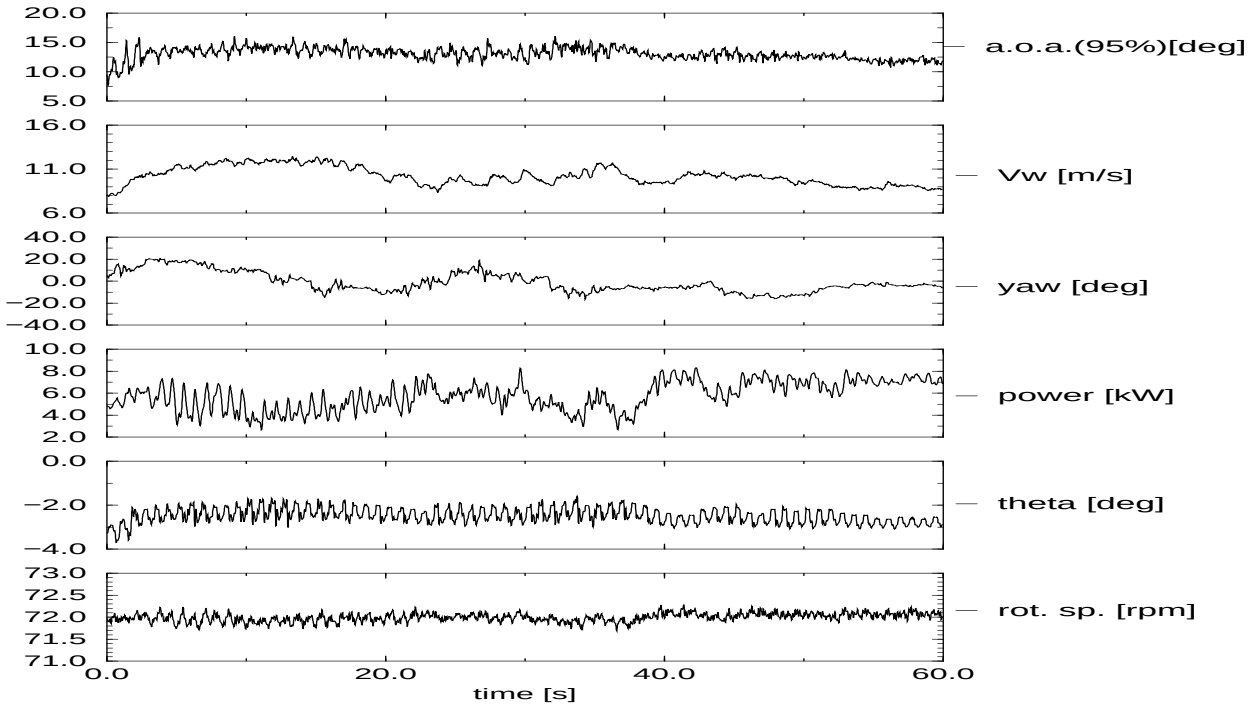

Figure C.17 *NREL: Time series of campaign ny_rot_ntp_007*

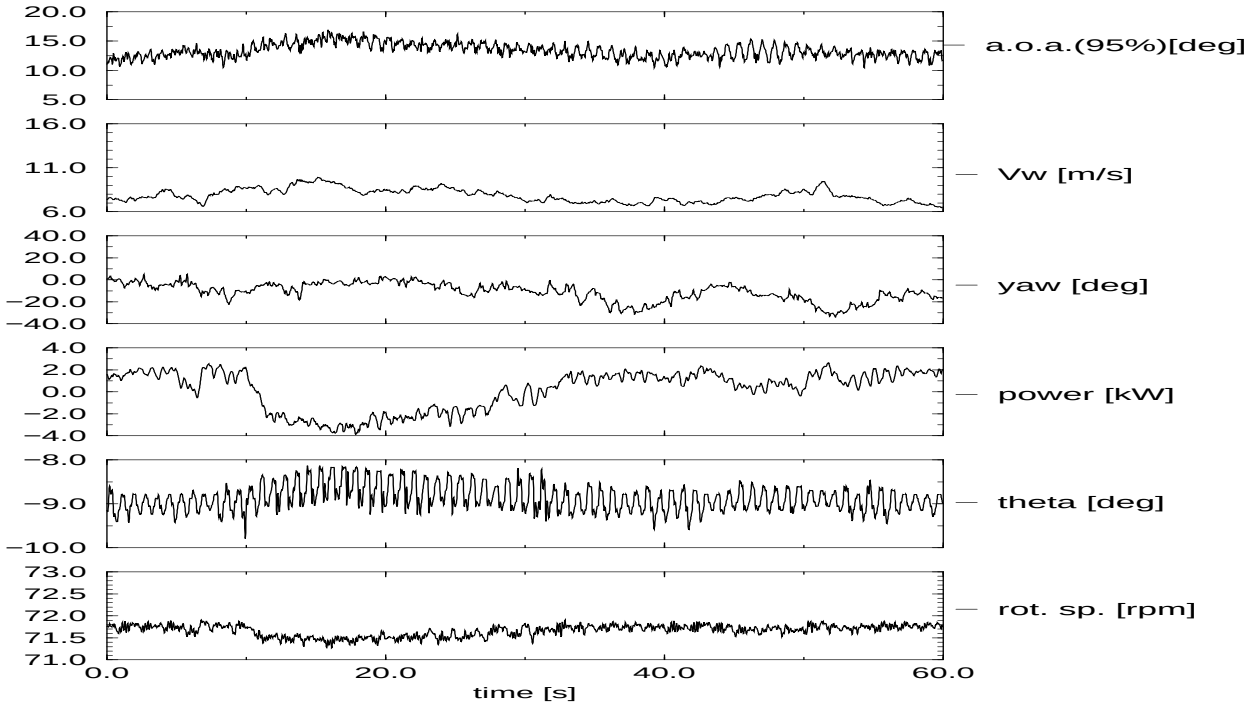

Figure C.18 *NREL: Time series of campaign ny_rot_ntp_008*

C.3.5 NREL time series: Yawed campaigns, untwisted configuration, phase II data

The files are stored in directory '/data/nrel/rottim/nu'. The files are sorted in yaw angle bins of approximately 5 degrees and numbered in order of increasing yaw angle. Within every yaw angle bin, the files are numbered in order of increasing angle of attack (= wind speed), see table C.6. Due to errors introduced by the azimuth angle potentiometer, the rotor speed calculation was not reliable in all Phase II data. For this reason, the rpm channel is not included in the time series figures. The constant speed generator ran at approximately 72 rpm.

Table C.6 *Global overview of NREL measurement files, yawed conditions (untwisted, phase II)*

file	NREL filename	$\overline{\alpha_{80\%}}$ deg	$\overline{V}$ m/s	$\overline{\phi_y}$ deg	$\overline{\text{Power}}$ kW	$\overline{\theta_{tip}}$ deg	$\overline{\Omega}$ rpm	duration s
y-rot-nu-001	d6931	-2.5	6.1	-35.4	-3.2	12.2	72	15.0
y-rot-nu-002	d7021	-0.1	7.0	-18.5	-0.3	12.0	72	15.0
y-rot-nu-003	d6711	3.9	10.2	-14.4	5.2	12.0	72	15.0
y-rot-nu-004	d7231	8.3	13.3	-19.0	9.9	11.4	72	15.0
y-rot-nu-005	d7012	0.6	7.8	21.4	0.5	12.0	72	15.0
y-rot-nu-006	d6731	3.0	8.8	24.2	3.4	11.9	72	15.0
y-rot-nu-007	d7221	8.5	13.1	22.8	9.2	11.4	72	15.0
y-rot-nu-008	d6731	0.3	8.2	39.4	-0.2	11.8	72	15.0

C.3.6 NREL time series: Yawed campaigns, twisted configuration

NREL time series: yawed campaigns, twisted configuration, phase III data
The files are stored in directory '/data/nrel/rottim/nt'. The files are sorted in yaw angle bins of approximately 5 degrees and numbered in order of increasing yaw angle. Within every yaw angle bin, the files are numbered in order of increasing angle of attack (= wind speed), see subsection C.7.

Table C.7 *Global overview of NREL measurement files, yawed conditions, twisted (Phase III)*

file	NREL filename	$\overline{\alpha_{80\%}}$ deg	$\overline{V}$ m/s	$\overline{\phi_{yaw}}$ deg	$\overline{\text{Power}}$ kW	$\overline{\theta_{tip}}$ deg	$\overline{\Omega}$ rpm	duration s
y-rot-nt-001	data9	0.6	7.2	-42.4	-1.8	5.8	71.6	15.0
y-rot-nt-002	data16	-0.1	6.4	-21.8	4.7	5.5	71.7	15.0
y-rot-nt-003	data16	14.3	11.7	-22.3	-4.1	5.7	71.9	15.0
y-rot-nt-004	data12	16.3	14.3	-23.8	11.0	6.0	72.3	15.0
y-rot-nt-005	data1	5.6	7.5	15.6	3.2	2.3	71.8	15.0
y-rot-nt-006	data6	11.6	11.7	18.5	8.7	1.8	72.2	15.0
y-rot-nt-007	data3	11.8	12.8	20.7	9.6	3.7	72.2	15.0
y-rot-nt-008	data1	6.2	8.8	34.9	3.5	2.4	71.8	15.0

NREL time series: Yawed campaigns, twisted configuration, phase IV data
The files are stored in directory '/data/nrel/rottim/ntp'. The files are sorted in yaw angle bins of approximately 5 degrees and numbered in order of increasing yaw

angle. Within every yaw angle bin, the files are numbered in order of increasing angle of attack (= wind speed), see table C.8.

Table C.8 *Global overview of NREL measurement files, yawed conditions, twisted (Phase IV)*

file	NREL filename	$\overline{\alpha_{95\%}}$ deg	$\overline{V}$ m/s	$\overline{\phi_{yaw}}$ deg	$\overline{Power}$ kW	$\overline{\theta_{tip}}$ deg	$\overline{\Omega}$ rpm	duration s
y-rot-ntp-001	data94	3.0	6.7	-38.2	1.1	2.2	71.7	15.0
y-rot-ntp-002	data72	2.1	6.8	-18.7	0.6	3.4	71.7	15.0
y-rot-ntp-003	data74	8.8	10.2	-17.6	8.8	3.0	72.2	15.0
y-rot-ntp-004	data30	11.4	12.5	-21.2	11.1	2.9	72.3	15.0
y-rot-ntp-005	data89	3.6	7.1	22.7	2.0	2.7	71.8	15.0
y-rot-ntp-006	data79	8.4	9.9	21.9	7.9	2.9	72.1	15.0
y-rot-ntp-007	data97	10.6	12.6	21.9	8.2	2.3	72.1	15.0
y-rot-ntp-008	data80	1.7	7.0	40.1	-0.1	2.8	71.6	15.0
y-rot-ntp-009	data79	7.9	10.3	41.4	6.6	2.93	72.0	15.0

C.3.7 NREL yawed campaigns, plots of time series

Time series, NREL yawed campaigns, untwisted blade, plots

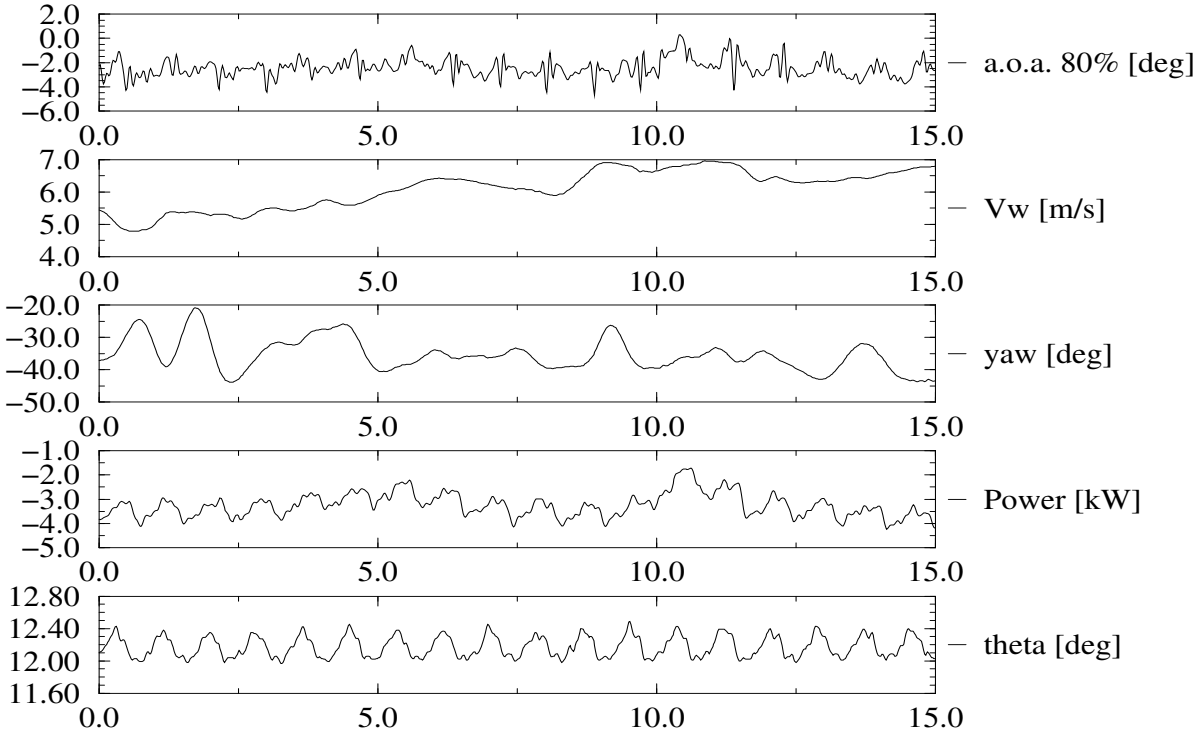

Figure C.19 *NREL: Time series of campaign y_rot_nu_001*

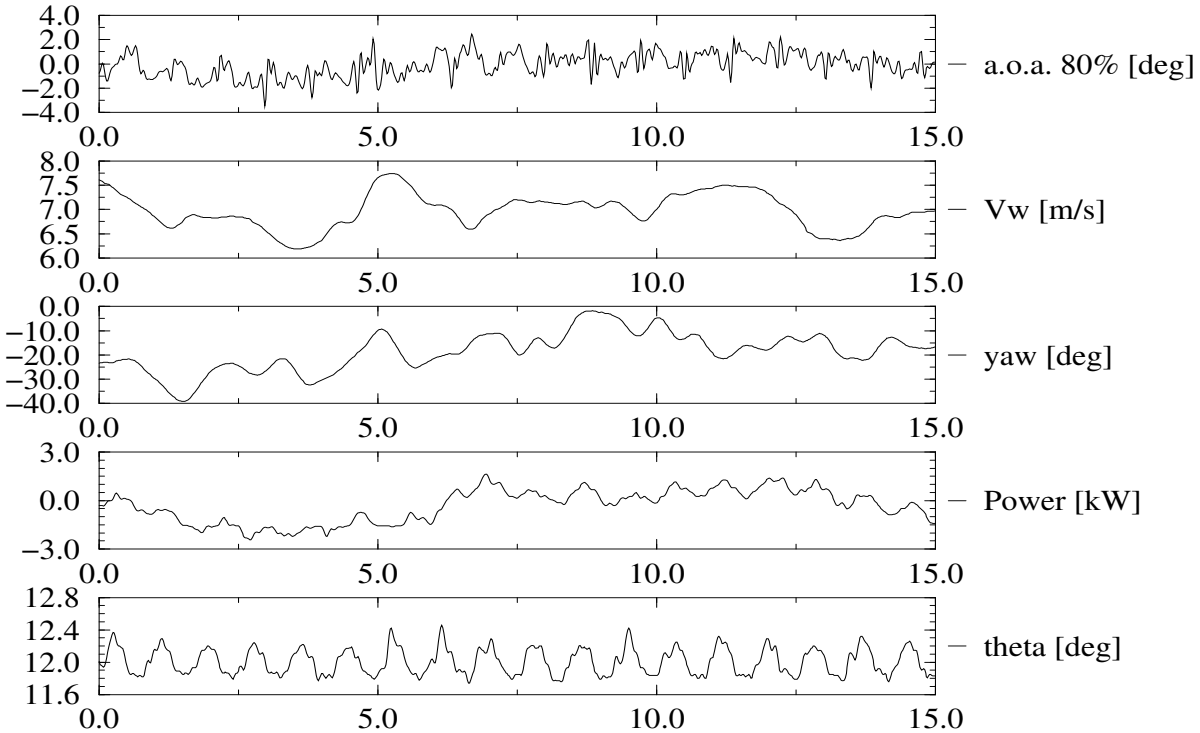

Figure C.20 *NREL: Time series of campaign y_rot_nu_002*

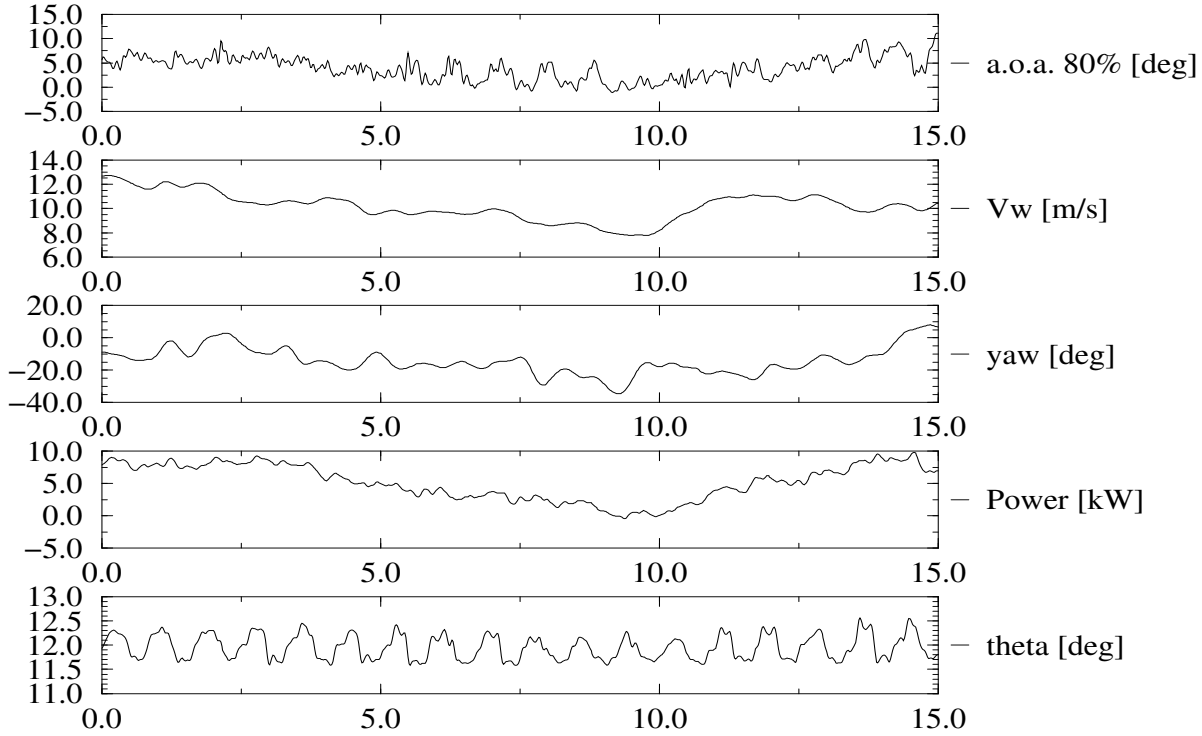

Figure C.21 *NREL: Time series of campaign y_rot_nu_003*

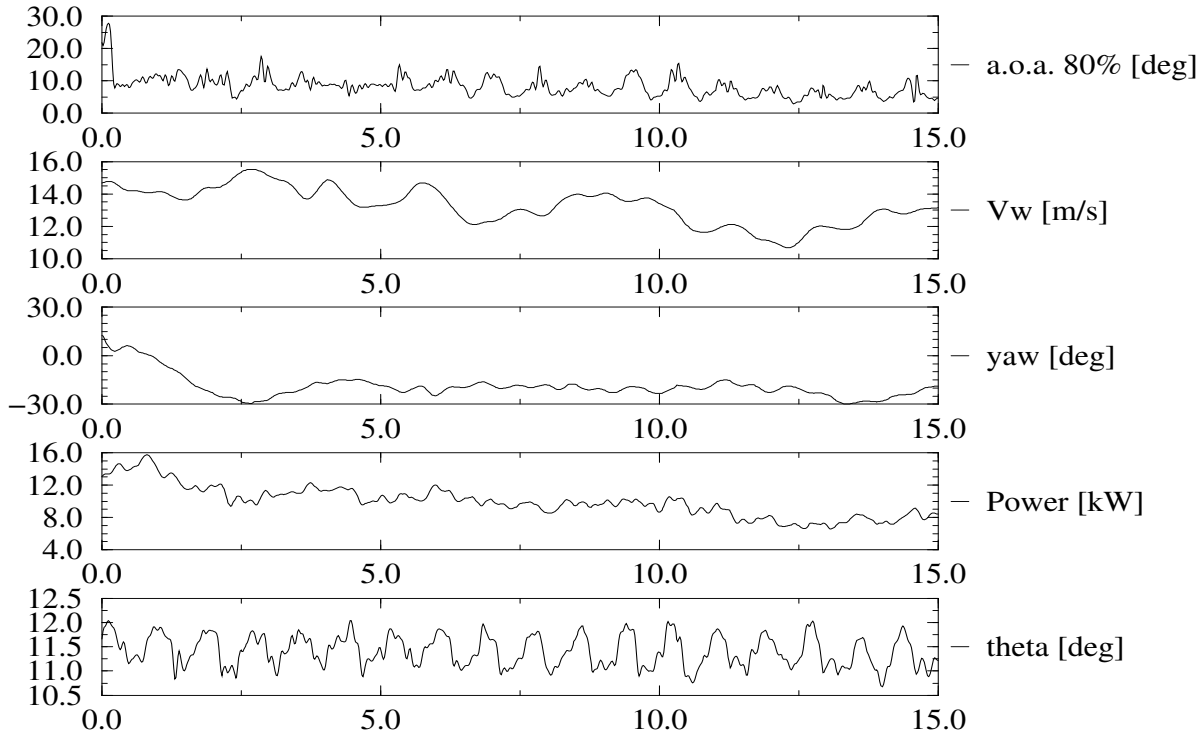

Figure C.22 *NREL: Time series of campaign y_rot_nu_004*

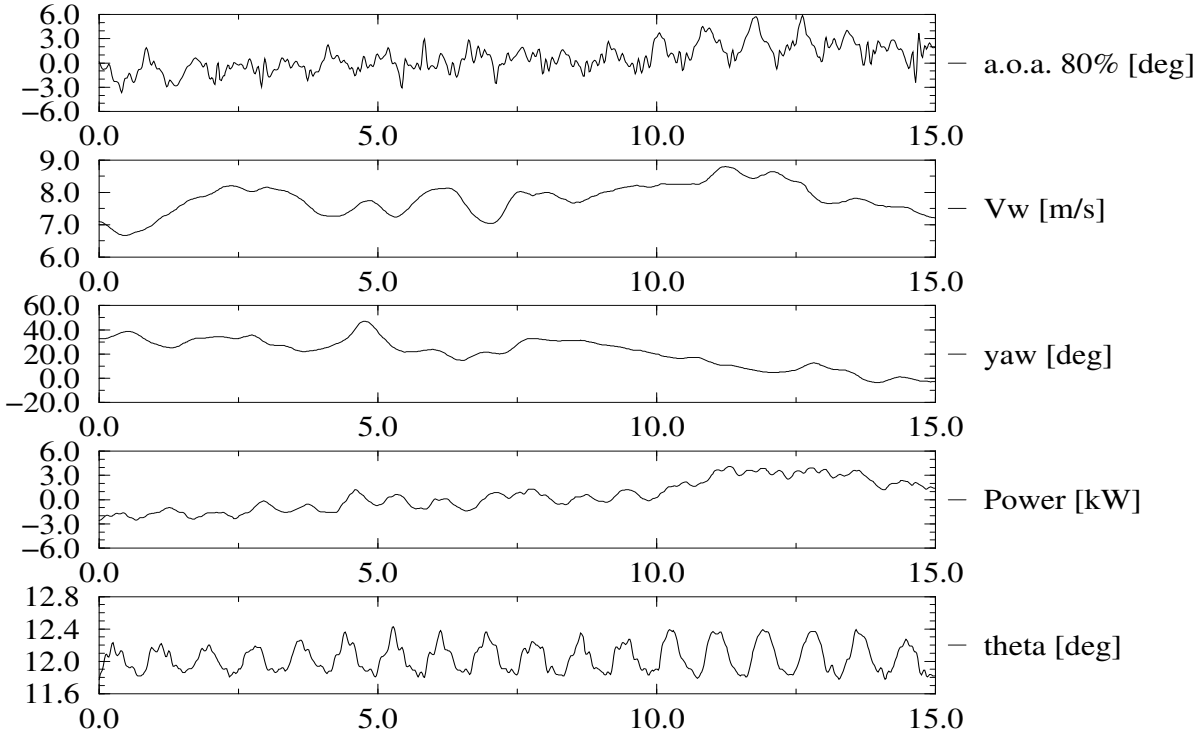

Figure C.23 *NREL: Time series of campaign y_rot_nu_005*

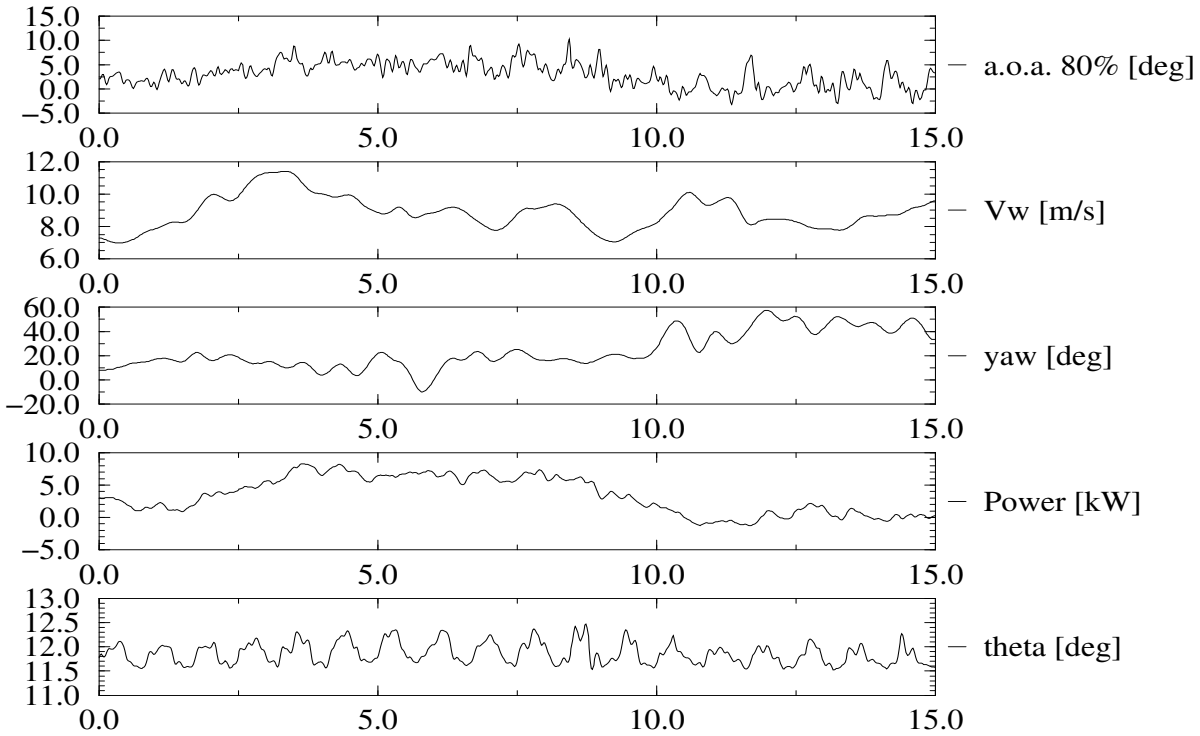

Figure C.24 *NREL: Time series of campaign y_rot_nu_006*

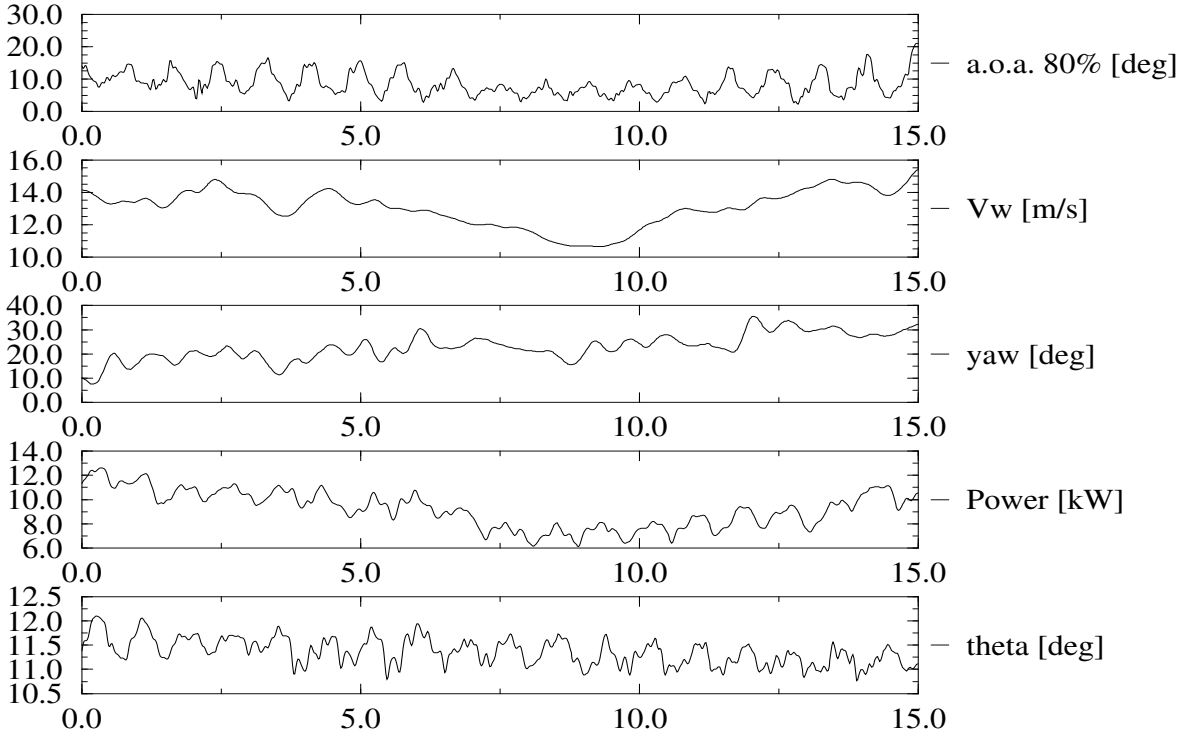

Figure C.25 *NREL: Time series of campaign y_rot_nu_007*

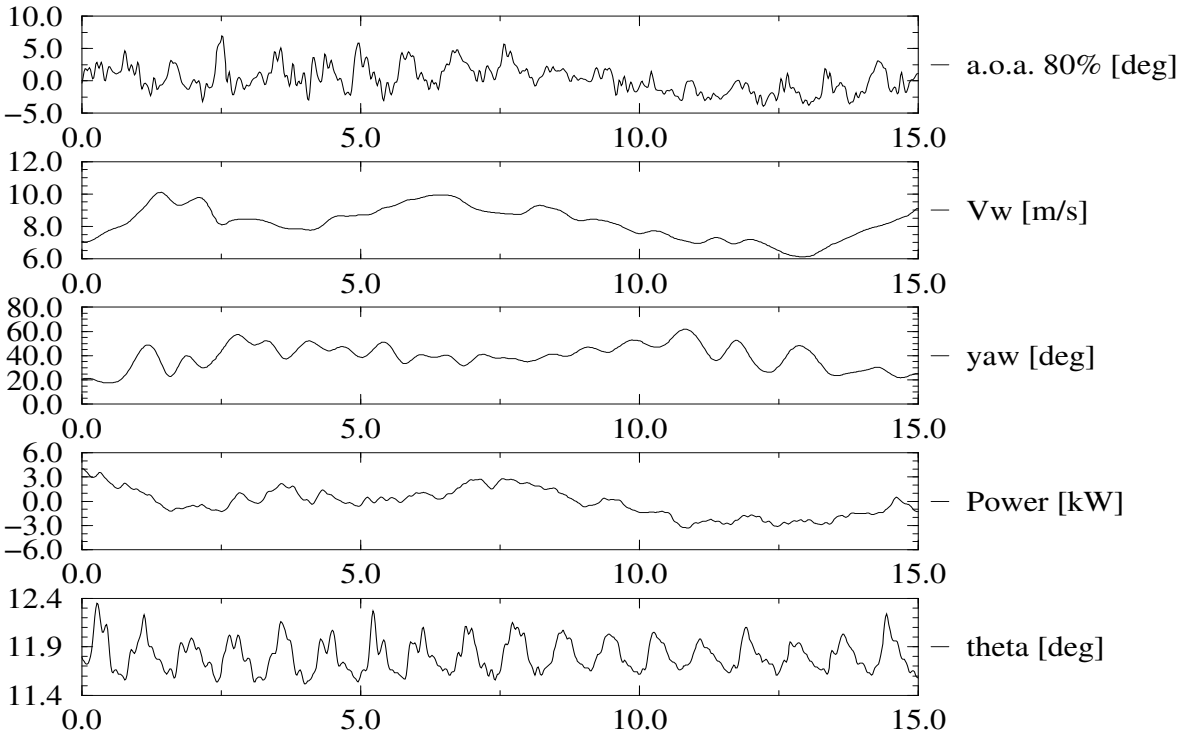

Figure C.26 *NREL: Time series of campaign y_rot_nu_008*

Time series, NREL yawed campaigns, twisted blade (Phase III), plots

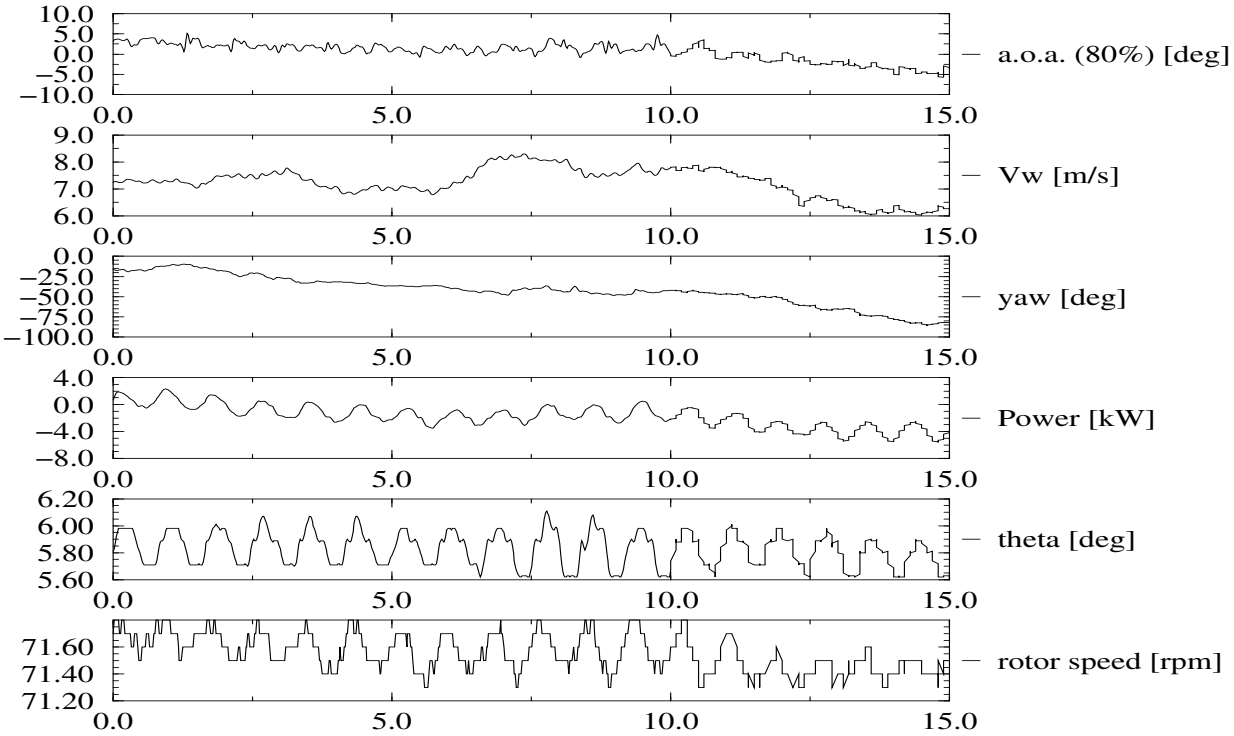

Figure C.27 *NREL: Time series of campaign y_rot_nt_001*

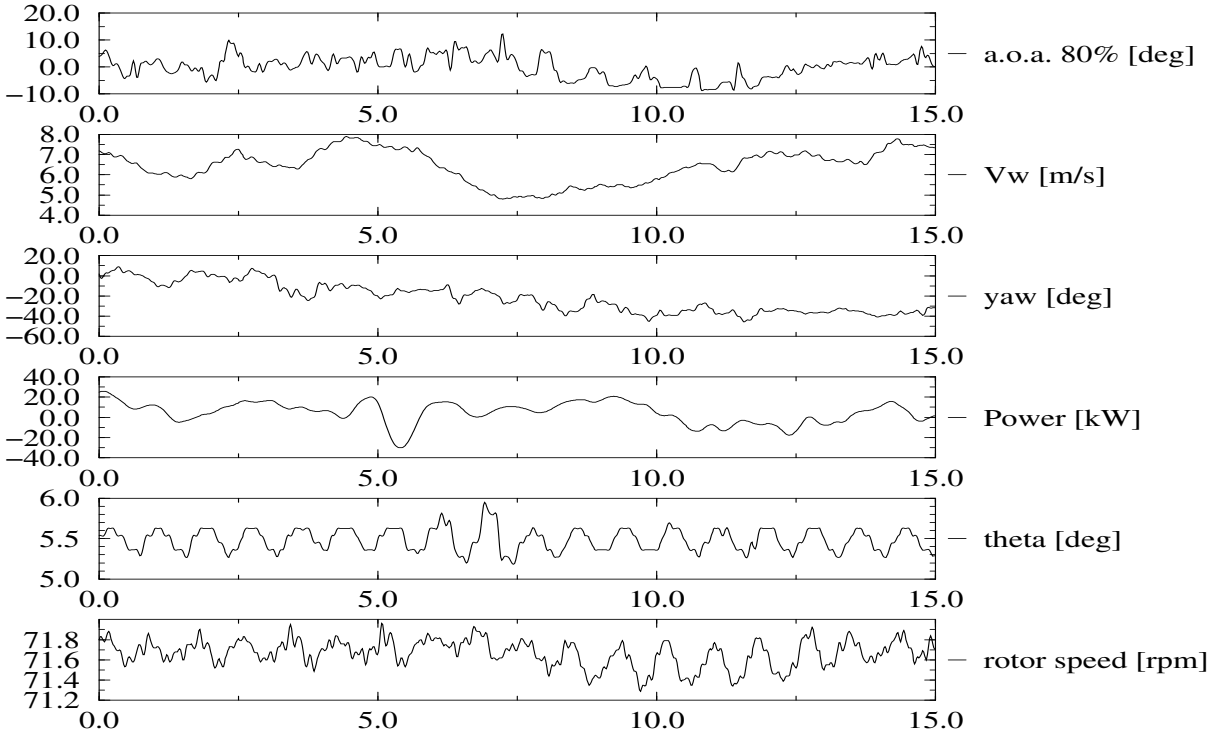

Figure C.28 *NREL: Time series of campaign y_rot_nt_002*

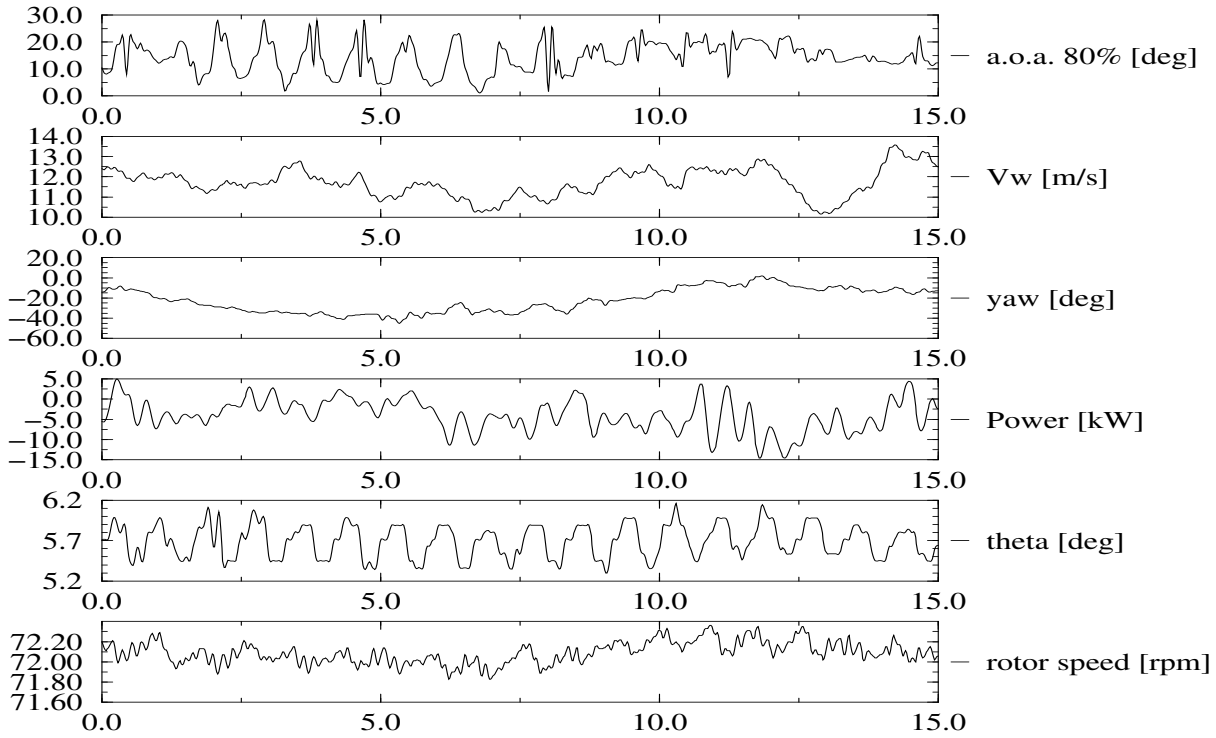

Figure C.29 *NREL: Time series of campaign y_rot_nt_003*

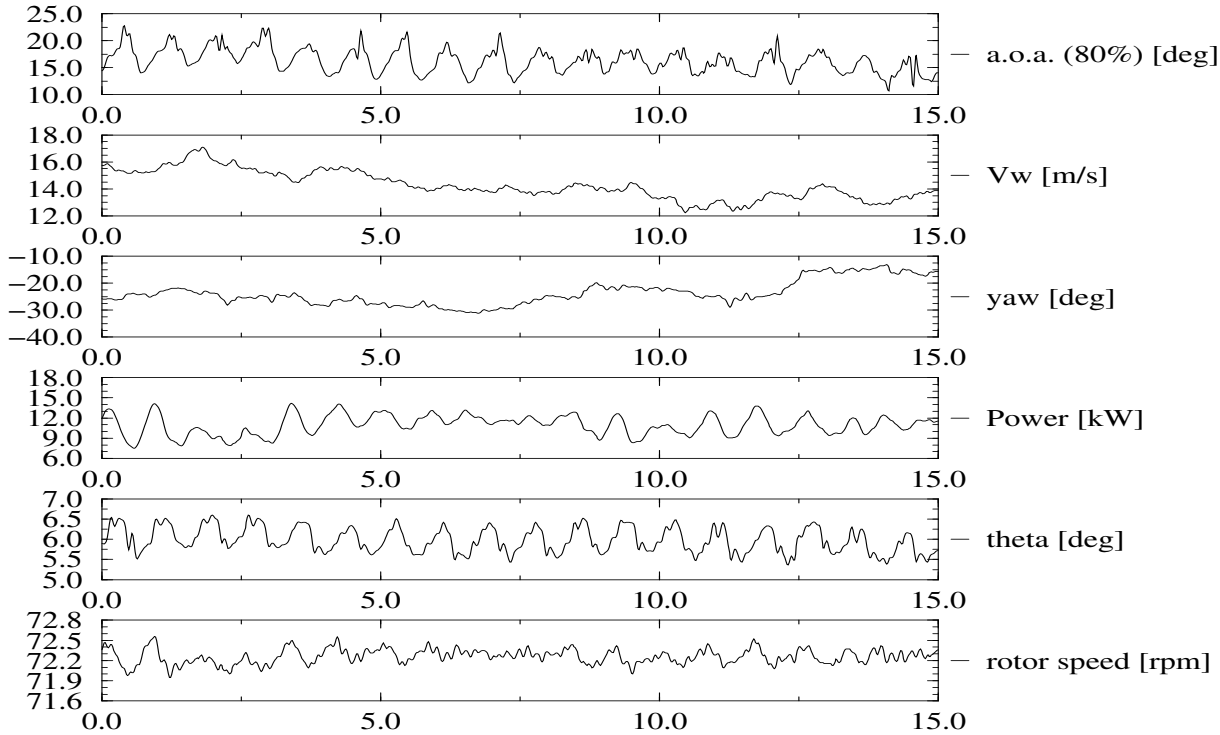

Figure C.30 *NREL: Time series of campaign y_rot_nt_004*

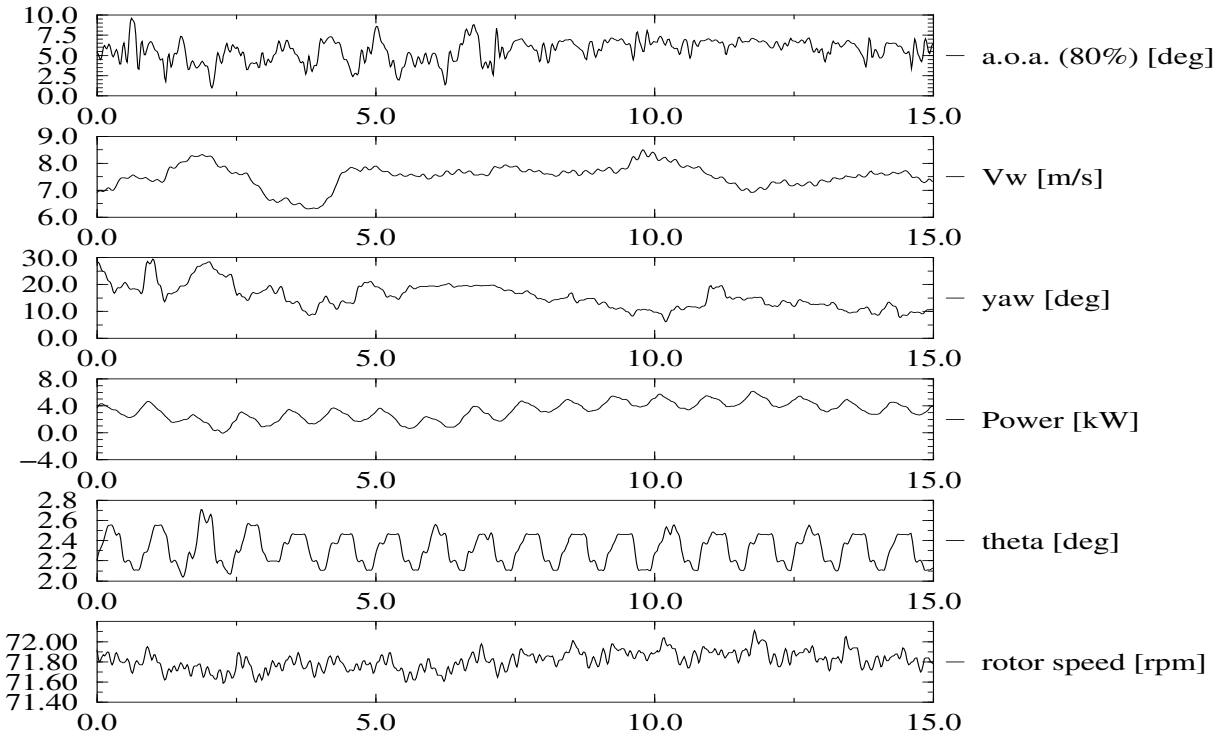

Figure C.31 *NREL: Time series of campaign y_rot_nt_005*

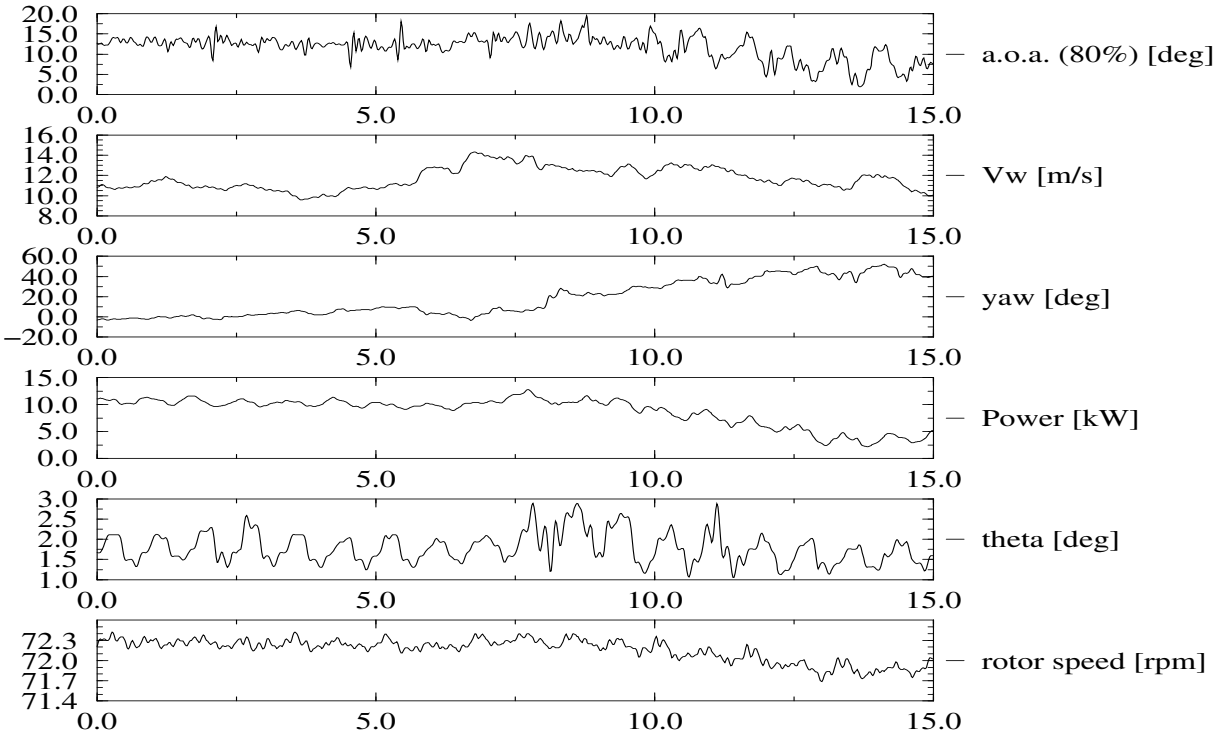

Figure C.32 *NREL: Time series of campaign y_rot_nt_006*

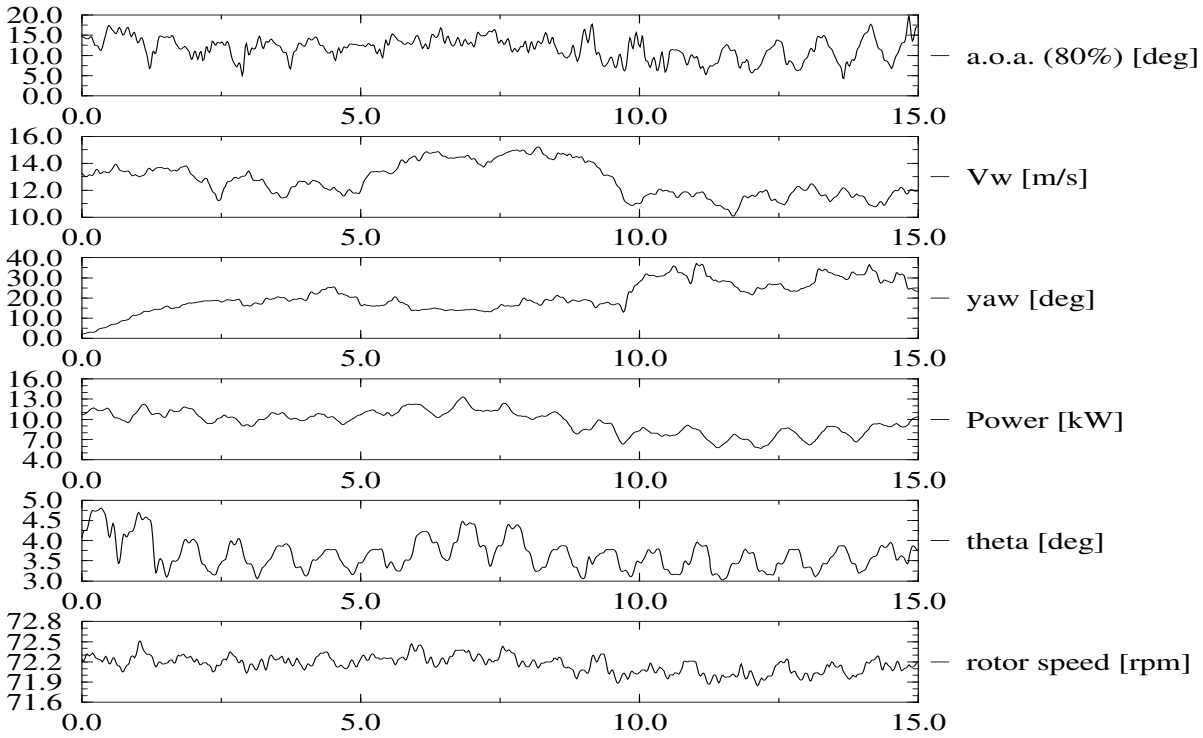

Figure C.33 *NREL: Time series of campaign y_rot_nt_007*

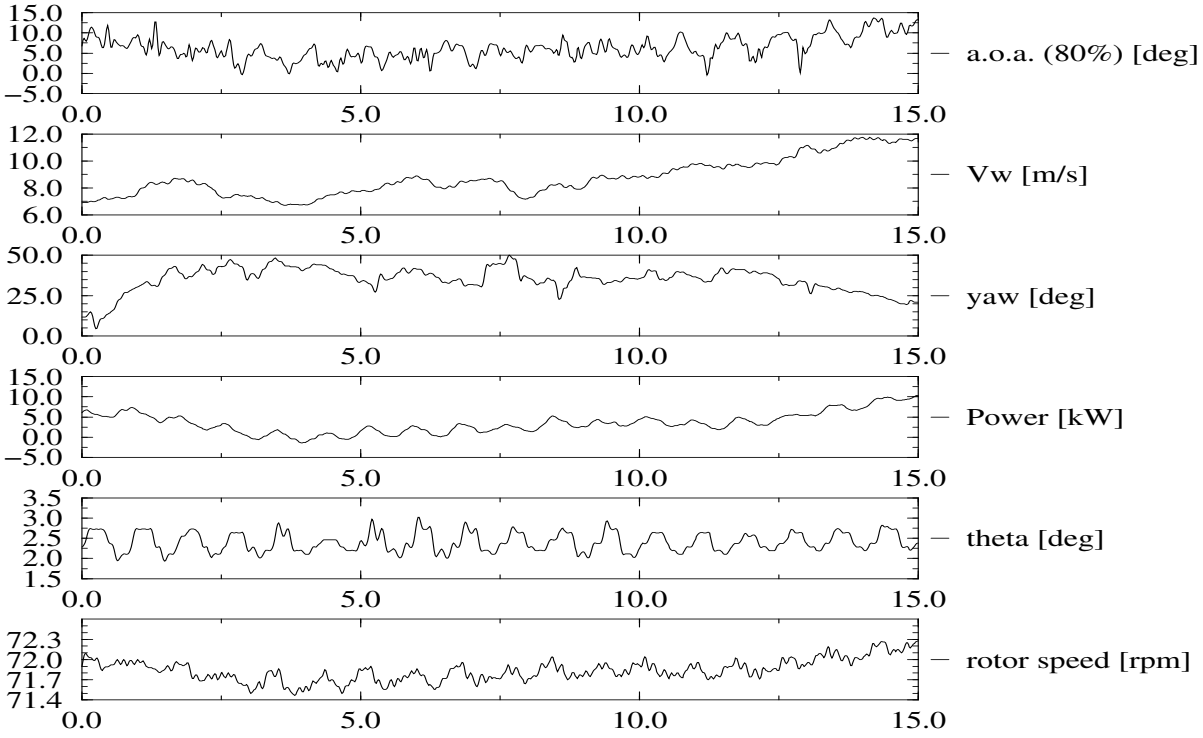

Figure C.34 *NREL: Time series of campaign y_rot_nt_008*

Time series, NREL yawed campaigns, twisted blade (Phase IV), plots

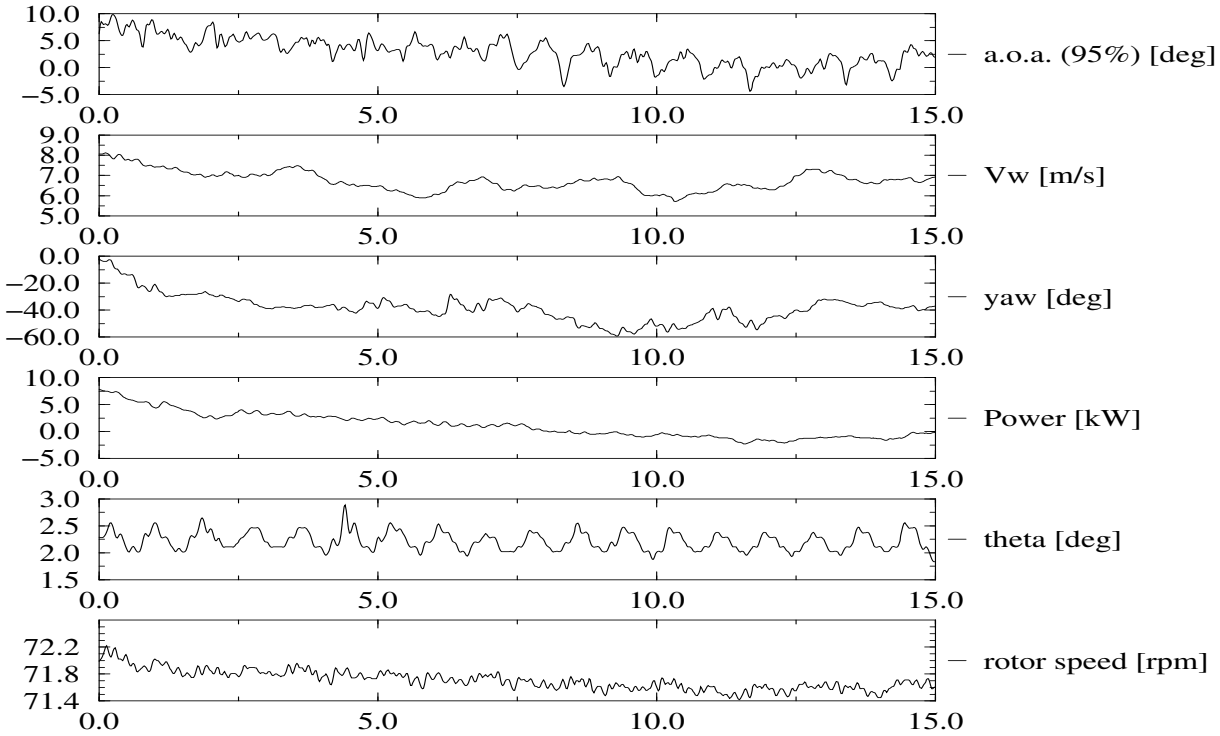

Figure C.35 *NREL: Time series of campaign y_rot_ntp_001*

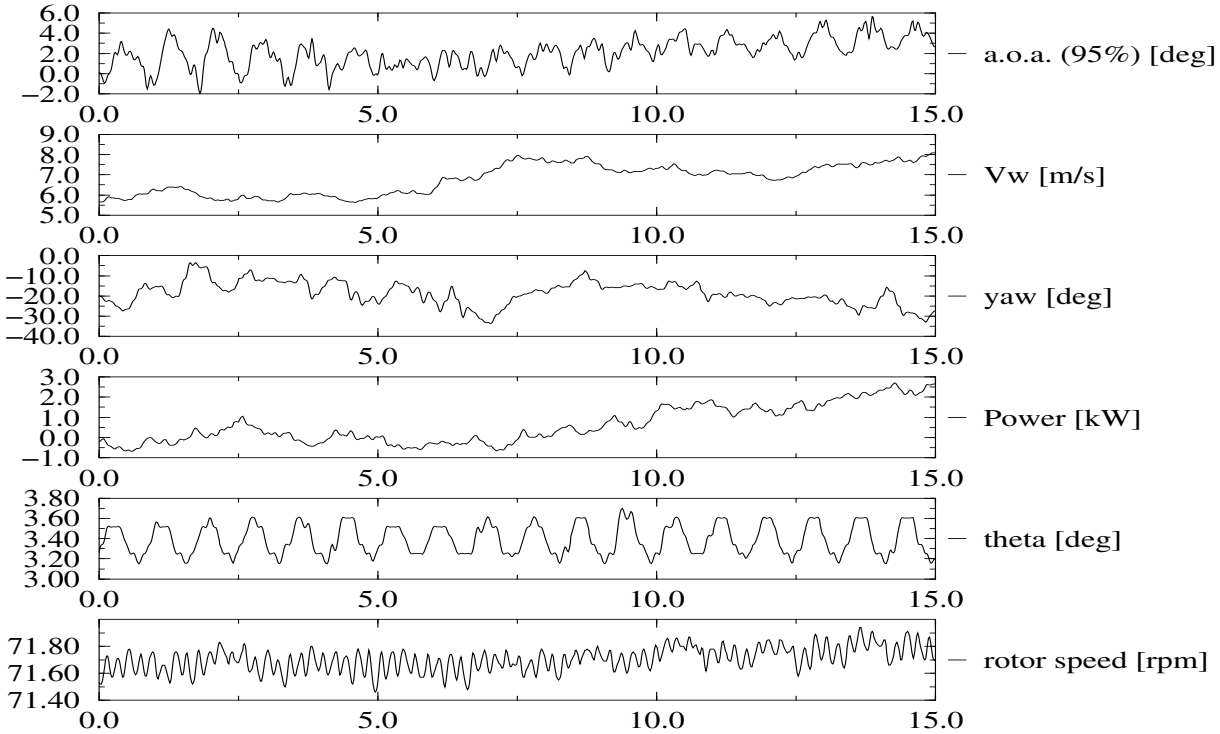

Figure C.36 *NREL: Time series of campaign y_rot_ntp_002*

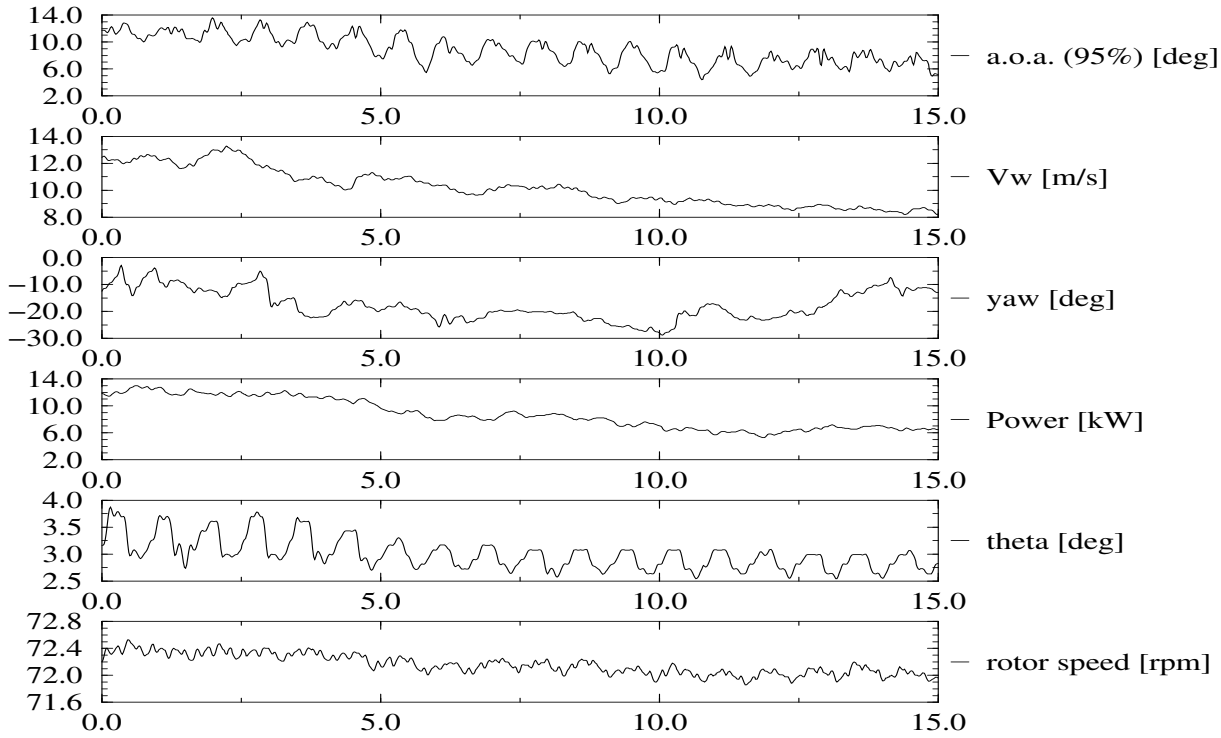

Figure C.37 *NREL: Time series of campaign y_rot_ntp_003*

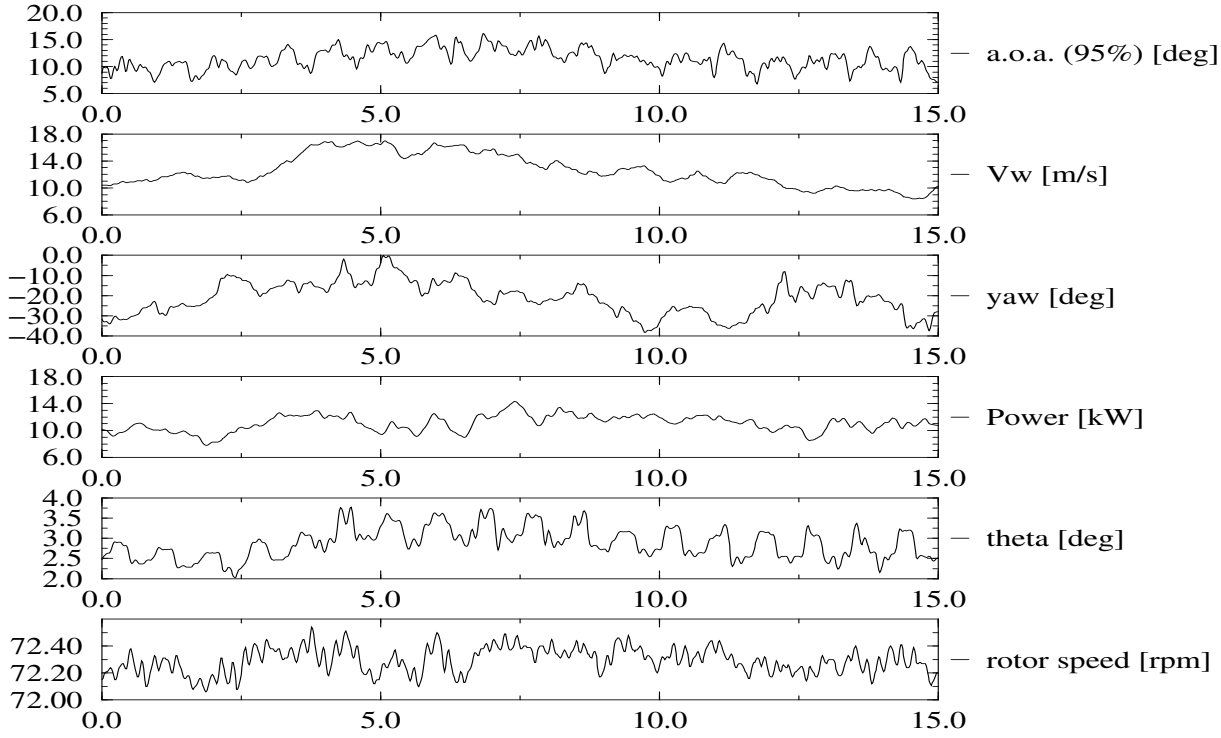

Figure C.38 *NREL: Time series of campaign y_rot_ntp_004*

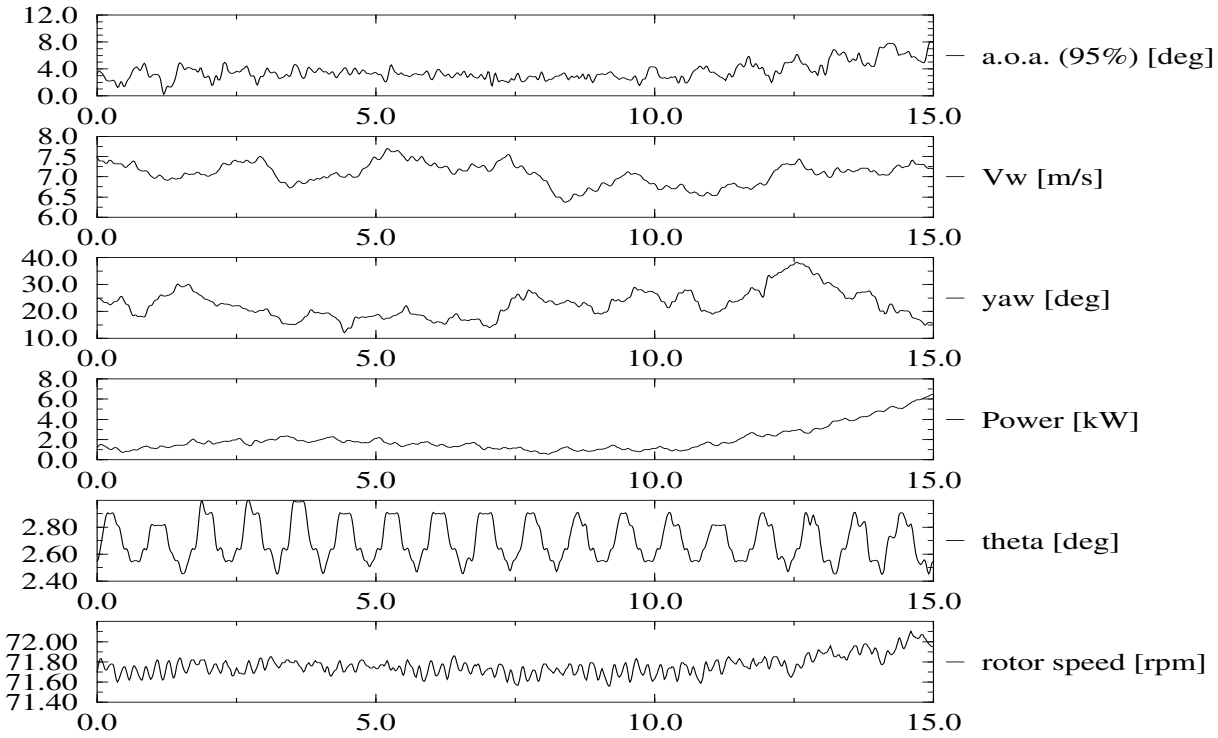

Figure C.39 *NREL: Time series of campaign y_rot_ntp_005*

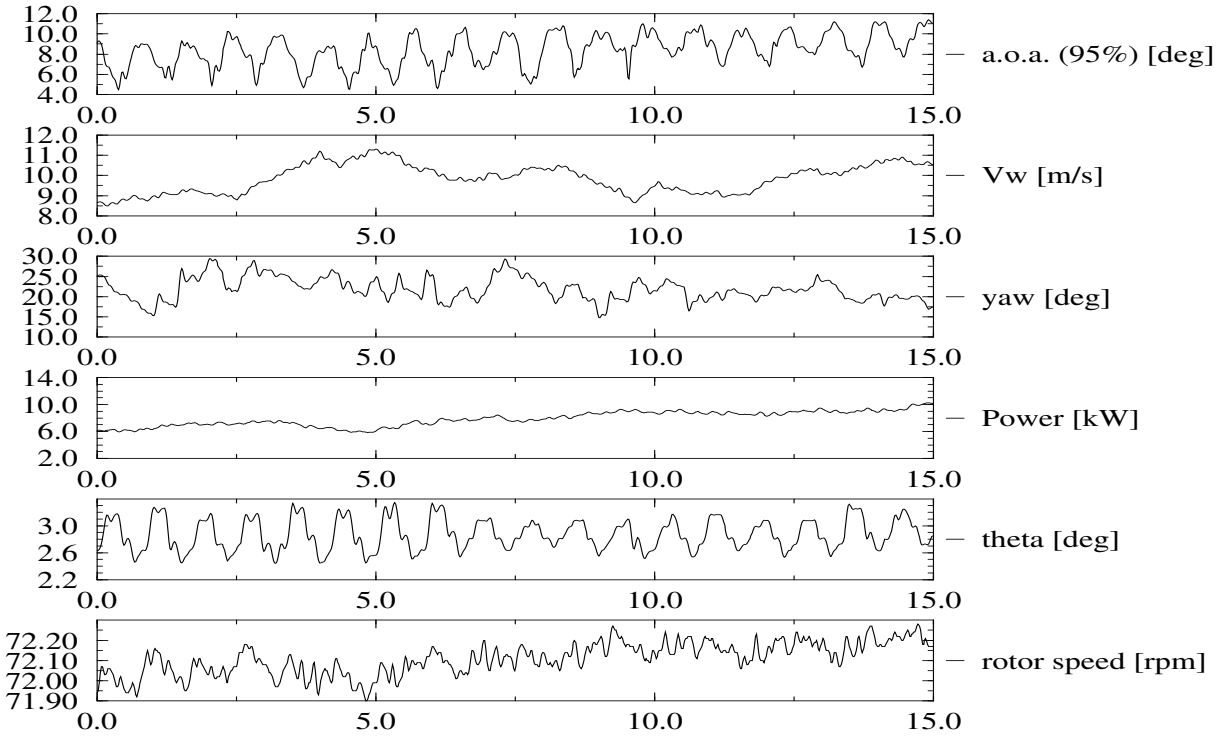

Figure C.40 *NREL: Time series of campaign y_rot_ntp_006*

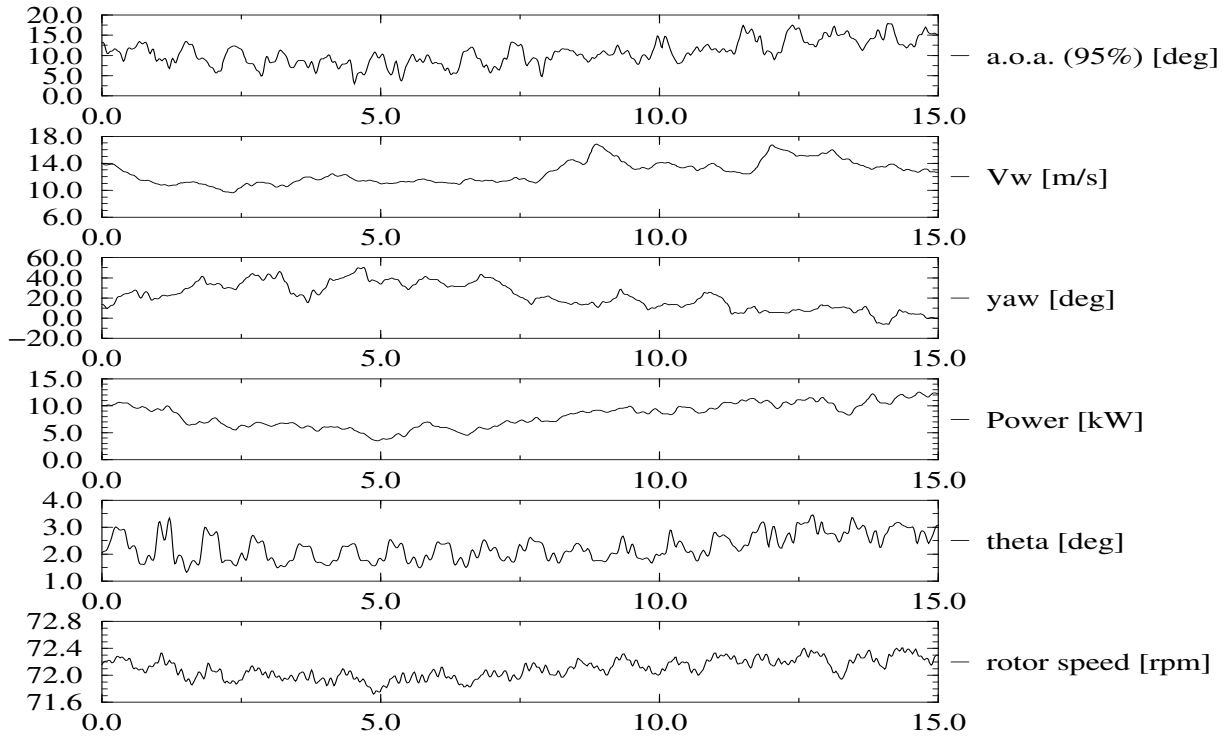

Figure C.41 *NREL: Time series of campaign y_rot_ntp_007*

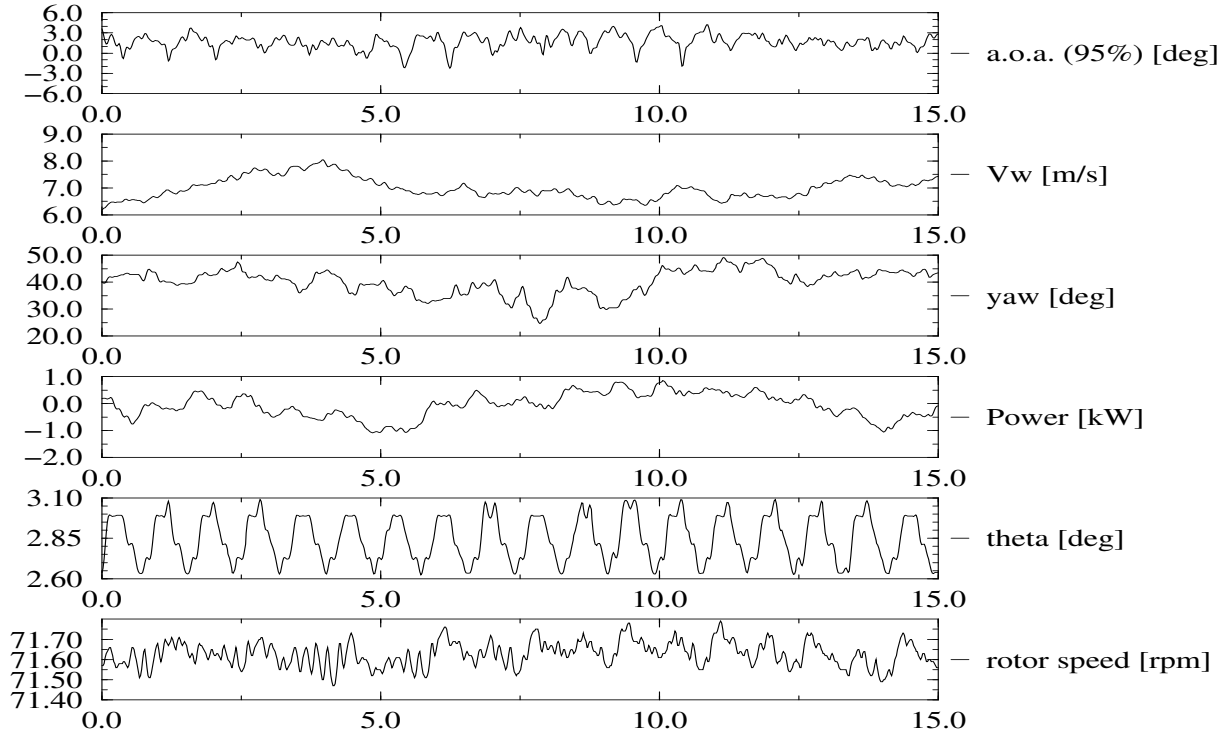

Figure C.42 *NREL: Time series of campaign y_rot_ntp_008*

C.4 NREL turbine and sectional coefficients

It is recalled that the institute description for the NREL campaign is 'nu', 'nt', or 'ntp' for the untwisted (phase II), twisted (phase III) and twisted with probes (phase IV) data respectively, see section 8.

C.4.1 NREL, 2D profile coefficients and pressure distributions

: The 2D profile coefficients for the S809 profile are zipped into '/data/nrel/2D/coef2d_n.zip, which contain the following 3 files:

- cla_2D_n. This file contains the $c_l - \alpha$ data, see table F.3 and F.4;
- cda_2D_n, This file contains the $c_d - \alpha$ data, see table F.3 and F.4;
- cpa_2D_n. This file contains the $c_p - x/c, \alpha$ data.

C.4.2 NREL rotating profile coefficients, untwisted configuration, phase II data

The 3D profile coefficients from phase II are zipped into '/data/nrel/rotcoef/nu/coef_nu.zip, which contain the following 10 files:

- cna1_rot_nu: This file contains the $c_n - \alpha$ data for the 30% section.
- cna7_rot_nu: This file contains the $c_n - \alpha$ data for the 63% section.
- cna10_rot_nu: This file contains the $c_n - \alpha$ data for the 80% section.
- cta1_rot_nu: This file contains the $c_t - \alpha$ data for the 30% section.
- cta7_rot_nu: This file contains the $c_t - \alpha$ data for the 63% section.
- cta10_rot_nu: This file contains the $c_t - \alpha$ data for the 80% section.
- cnct1_rot_nu: This file contains the $c_t - c_n$ data for the 30% section.
- cnct7_rot_nu: This file contains the $c_t - c_n$ data for the 63% section.
- cnct10_rot_nu: This file contains the $c_t - c_n$ data for the 80% section.
- PV_nu: This file contains the power curve of phase II.

The data are shown graphically in the figures F.1, F.2 and F.3.

C.4.3 NREL rotating profile coefficients, twisted configuration, phase III data)

The3D profile coefficients from phase III are zipped into '/data/nrel/rotcoef/nt/coef_nt.zip, which contain the following 10 files:

- cna1_rot_nt: This file contains the $c_n - \alpha$ data for the 30% section.
- cna7_rot_nt: This file contains the $c_n - \alpha$ data for the 63% section.
- cna10_rot_nt: This file contains the $c_n - \alpha$ data for the 80% section.
- cta1_rot_nt: This file contains the $c_t - \alpha$ data for the 30% section.
- cta7_rot_nt: This file contains the $c_t - \alpha$ data for the 63% section.
- cta10_rot_nt: This file contains the $c_t - \alpha$ data for the 80% section.
- cnct1_rot_nt: This file contains the $c_t - c_n$ data for the 30% section.
- cnct7_rot_nt: This file contains the $c_t - c_n$ data for the 63% section.
- cnct10_rot_nt: This file contains the $c_t - c_n$ data for the 80% section.
- PV_nt: This file contains the power curve of phase III.

The data are shown graphically in the figures F.4, F.5 and F.6.

C.4.4 NREL rotating profile coefficients, twisted configuration, phase IV data

The 3D profile coefficients from phase IV are zipped into '/data/nrel/rotcoef/ntp/pit3/coef_ntp.zip, which contain the following 12 files:

- cna1_rot_ntp: This file contains the $c_n - \alpha$ data for the 30% section.
- cna7_rot_ntp: This file contains the $c_n - \alpha$ data for the 63% section.
- cna10_rot_ntp: This file contains the $c_n - \alpha$ data for the 80% section.
- cna14_rot_ntp: This file contains the $c_n - \alpha$ data for the 95% section.
- cta1_rot_ntp: This file contains the $c_t - \alpha$ data for the 30% section.
- cta7_rot_ntp: This file contains the $c_t - \alpha$ data for the 63% section.
- cta10_rot_ntp: This file contains the $c_t - \alpha$ data for the 80% section.
- cta14_rot_ntp: This file contains the $c_t - \alpha$ data for the 95% section.
- cnct1_rot_ntp: This file contains the $c_t - c_n$ data for the 30% section.
- cnct7_rot_ntp: This file contains the $c_t - c_n$ data for the 63% section.
- cnct10_rot_ntp: This file contains the $c_t - c_n$ data for the 80% section.
- cnct14_rot_ntp: This file contains the $c_t - c_n$ data for the 95% section.

The data are shown graphically in the figures F.7, F.8 and F.9. These profile coefficients have been measured at a (default) pitch angle of approximately 3 degrees.

In addition NREL supplied files which contain phase IV profile coefficients at pitch angles, which differ from this default value. These files are zipped into '/data/nrel/rotcoef/ntp/pit_vari/coef_ntp.zip', which again contains 12 files, with names similar as the file names given above for a pitch angle of 3 degrees.

The data for the 47% section (binned on angle of attack) for the different pitch angles are shown graphically in figure C.43. It is interesting to note that the $cn - \alpha$ curve is strongly dependant on the pitch angle. A similar trend is found in ECN's data, see section D.6.1.

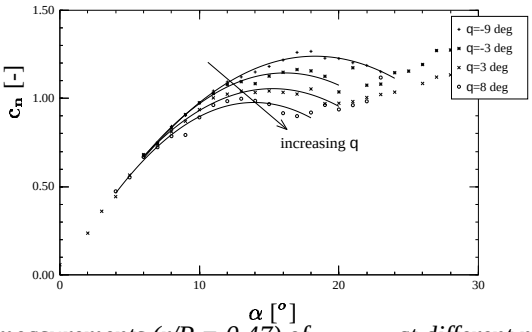

Figure C.43 *NREL measurements (r/R = 0.47) of* $c_n - \alpha$ *at different pitch angles*

C.5 IC/RAL time series

One IC/RAL campaign has been supplied where aerodynamic measurements are made at the 5th station at r/R = 0.65. The files of the campaign are stored into the directory '/data/icral/rottim/'.

C.5.1 IC/RAL time series: Non-yawed campaign

In table C.9 the global overview of the IC/RAL campaign is given. The data and the way in which IC/RAL organised their files differs slightly from the procedure which was applied by the remaining institutes. For this reason it is recommended to read the log file carefully. An important difference is the supply of a revolution count instead of the rotational speed. However the rotational speed is approximately constant and from the revolution counts an averaged rotor speed of 38.6 rpm is found. Furthermore no statistical data are added in the begin of the data file (Some statistical data are supplied in the log file). The angles of attack are in radians instead of degrees. Unfortunately, there is an error in the pressure file. The number of signals per record is one more than it should be. Hence every record contains a part of the next record also. The tip angle is fixed at 2.5 degrees.

Table C.9 *Global overview of IC/RAL measurement files, non-yawed conditions*

file	IC/RAL file name	$\overline{\alpha_{65\%}}$ deg	$\overline{V}$ m/s	$\overline{\text{Power}}$ kW	$\overline{\theta_{tip}}$ deg	$\overline{\Omega}$ rpm	$\overline{\phi_{yaw}}$ deg	duration s
ny-rot-i-001	set601	4.68	5.68	4.46	2.5	36.8	10.65	44.32

C.5.2 IC/RAL non-yawed campaigns, plots of time series

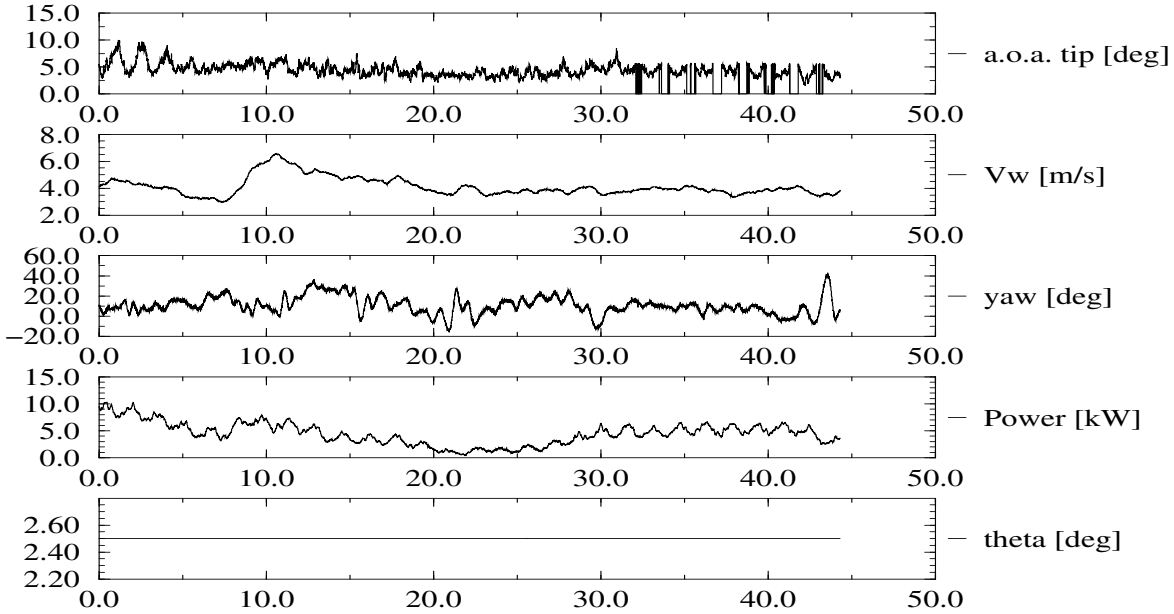

Figure C.44 *IC/RAL: Time series of campaign ny_rot_i_001*

C.6 RISØ time series

The format of all RISØ files is the same.

C.6.1 RISØ time series: Non-yawed campaigns

The files are stored into the directory '/data/riso/rottim/' and numbered in order of increasing angle of attack (= wind speed), see table C.10.

Table C.10 *Global overview of RISØ measurement files, non-yawed conditions*

file	RISØ file name	$\overline{\alpha_{71\%}}$ deg	$\overline{V}$ m/s	$\overline{\text{Power}}$ kW	$\overline{\theta_{tip}}$ deg	$\overline{\Omega}$ rpm	duration s
ny-rot-r-001	tl200101	6.9	7.2	29.3	0.0	47.6	596.3
ny-rot-r-002	tl260106	8.4	8.4	41.1	0.0	47.6	596.3
ny-rot-r-003	tl260104	11.1	10.1	63.4	0.0	47.6	596.3
ny-rot-r-004	tl210113	13.9	11.9	85.8	0.0	47.6	596.3
ny-rot-r-005	tl210101	16.9	14.1	91.5	0.0	47.6	596.3

C.6.2 RISØ non-yawed campaigns, plots of time series

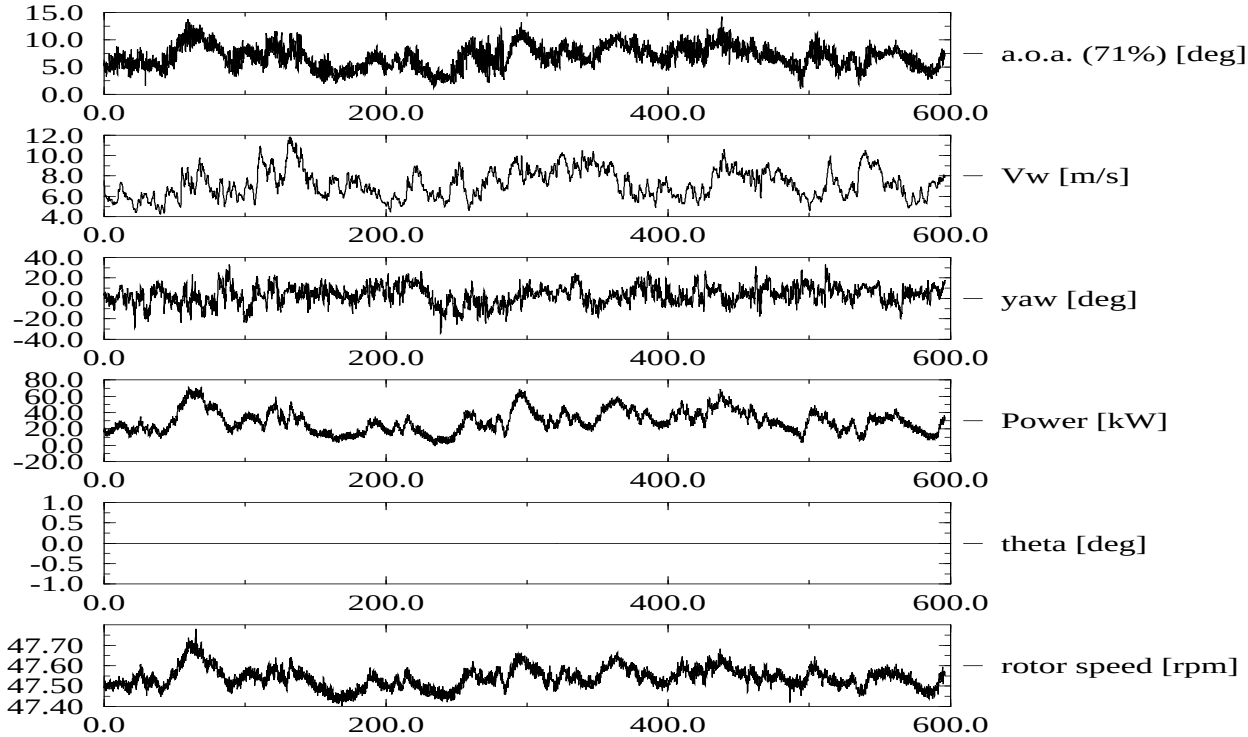

Figure C.45 *RISØ: Time series of campaign ny_rot_r_001*

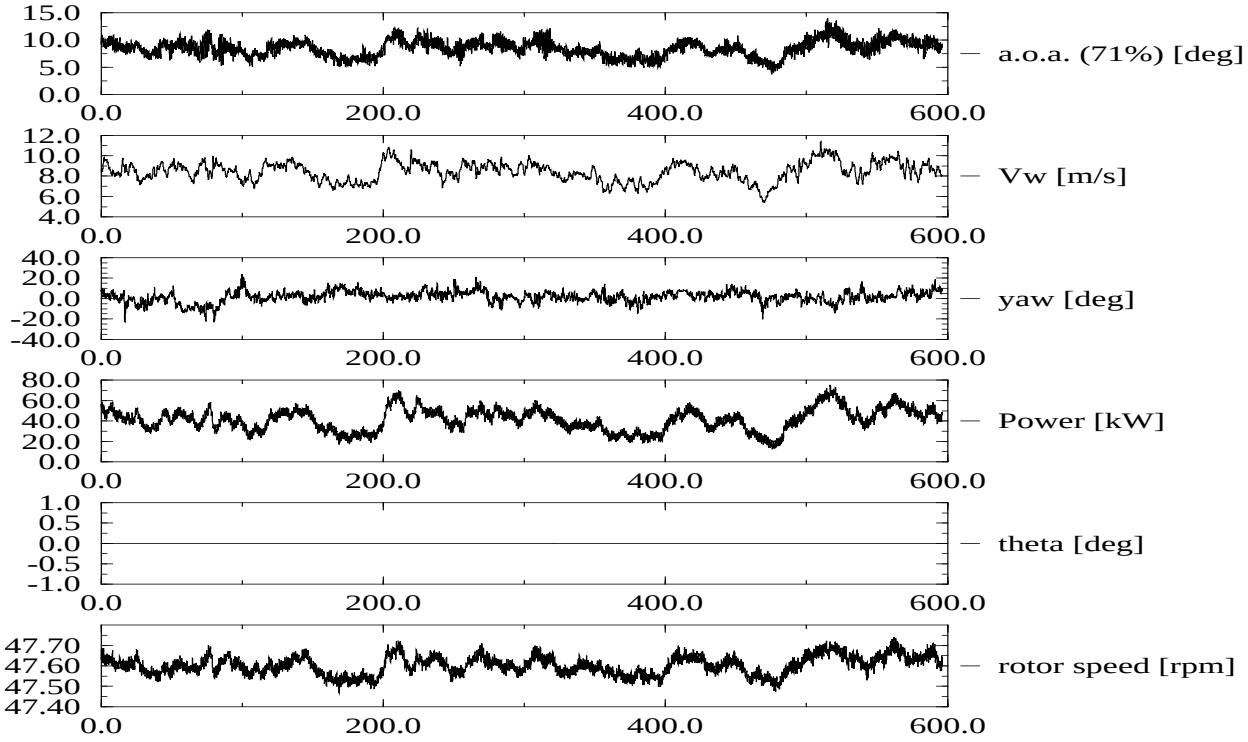

Figure C.46 *RISØ: Time series of campaign ny_rot_r_002*

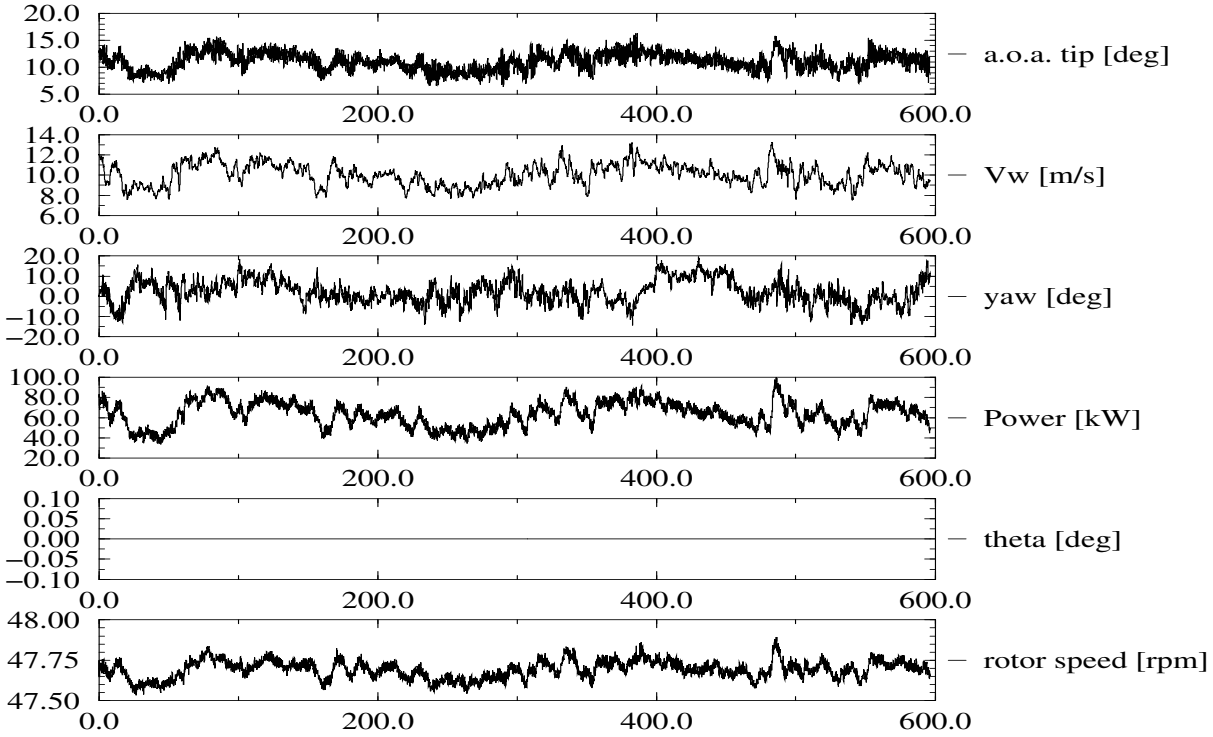

Figure C.47 *RISØ: Time series of campaign ny_rot_r_003*

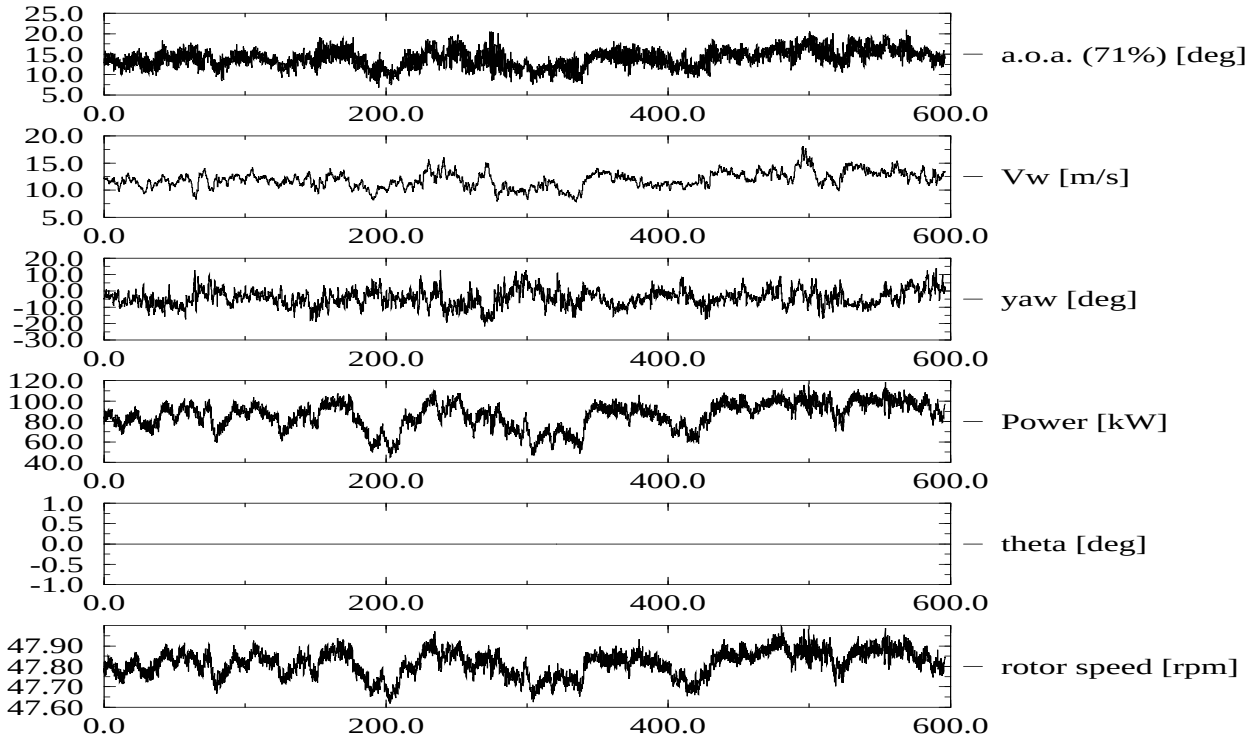

Figure C.48 *RISØ: Time series of campaign ny_rot_r_004*

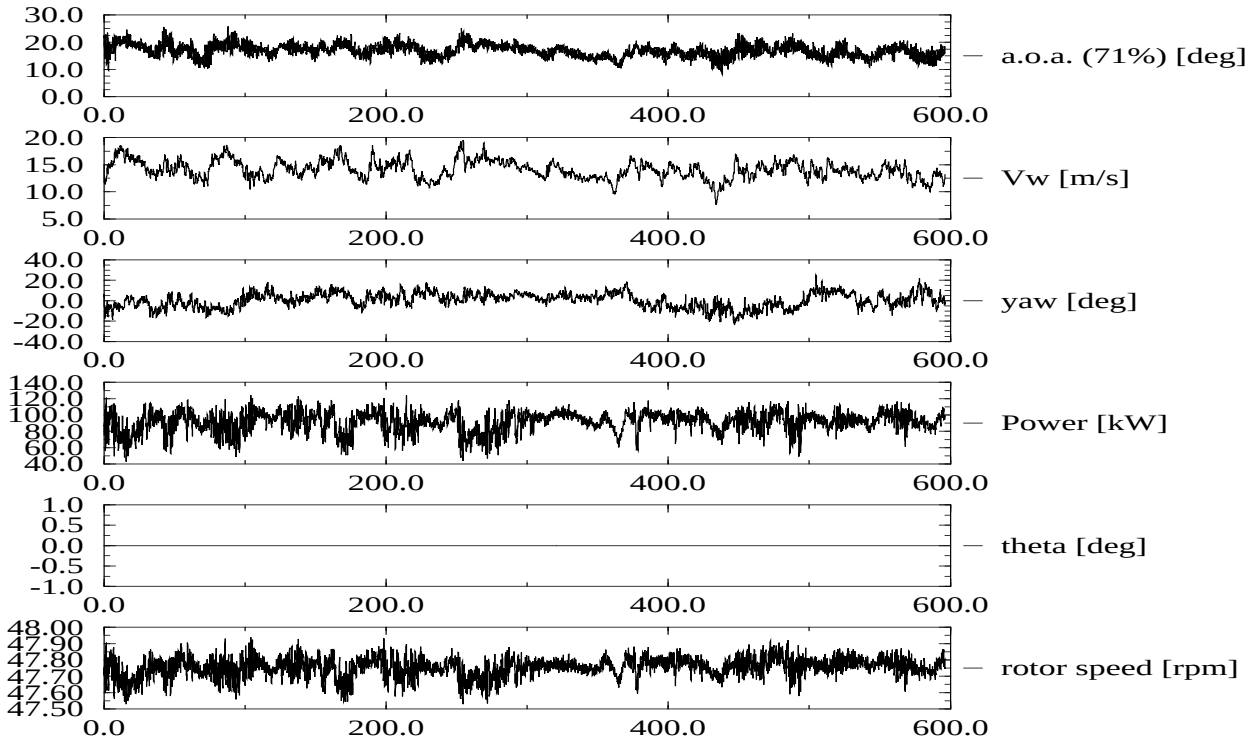

Figure C.49 *RISØ: Time series of campaign ny_rot_r_005*

C.6.3 RISØ time series: Yawed campaigns

The files are stored into the directory '/data/riso/rottim/' and sorted in order of decreasing yaw angle, see table C.11. Note that for these files, no log files have been supplied.

Table C.11 *Global overview of RISØ measurement files, yawed conditions*

file	RISØ file name	$\overline{\alpha_{71\%}}$ deg	$\overline{\mathrm{V}}$ m/s	$\overline{\phi_{\mathrm{yaw}}}$ ^{o}	$\overline{\mathrm{Power}}$ kW	$\overline{\theta_{\mathrm{tip}}}$ deg	$\overline{\Omega}$ rpm	duration s
y-rot-r-001	tl210116	11.3	10.7	15.45	66.11	0.0	47.7	596.3
y-rot-r-002	tl210114	13.4	11.8	9.3	82.66	0.0	47.8	596.3
y-rot-r-003	tl210112	14.3	12.3	-12.0	86.2	0.0	47.8	596.3

C.6.4 RISØ yawed campaigns, plots of time series

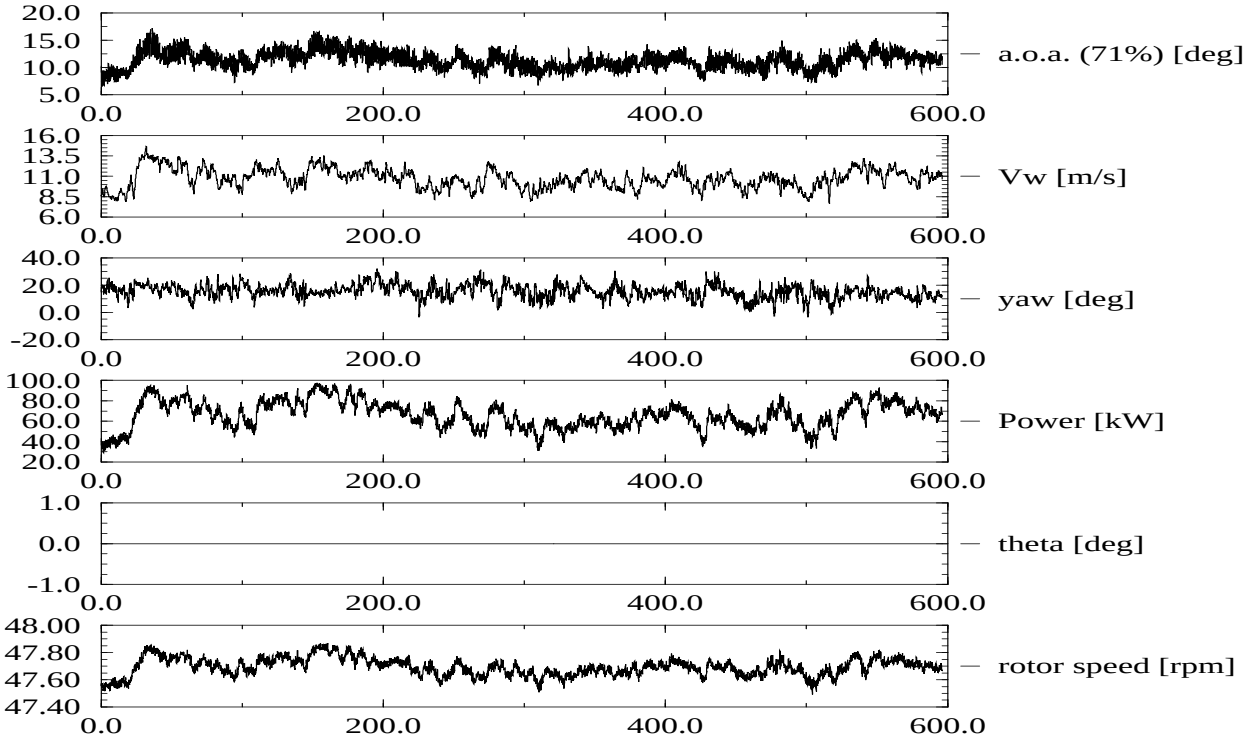

Figure C.50 *RISØ: Time series of campaign y_rot_r_001*

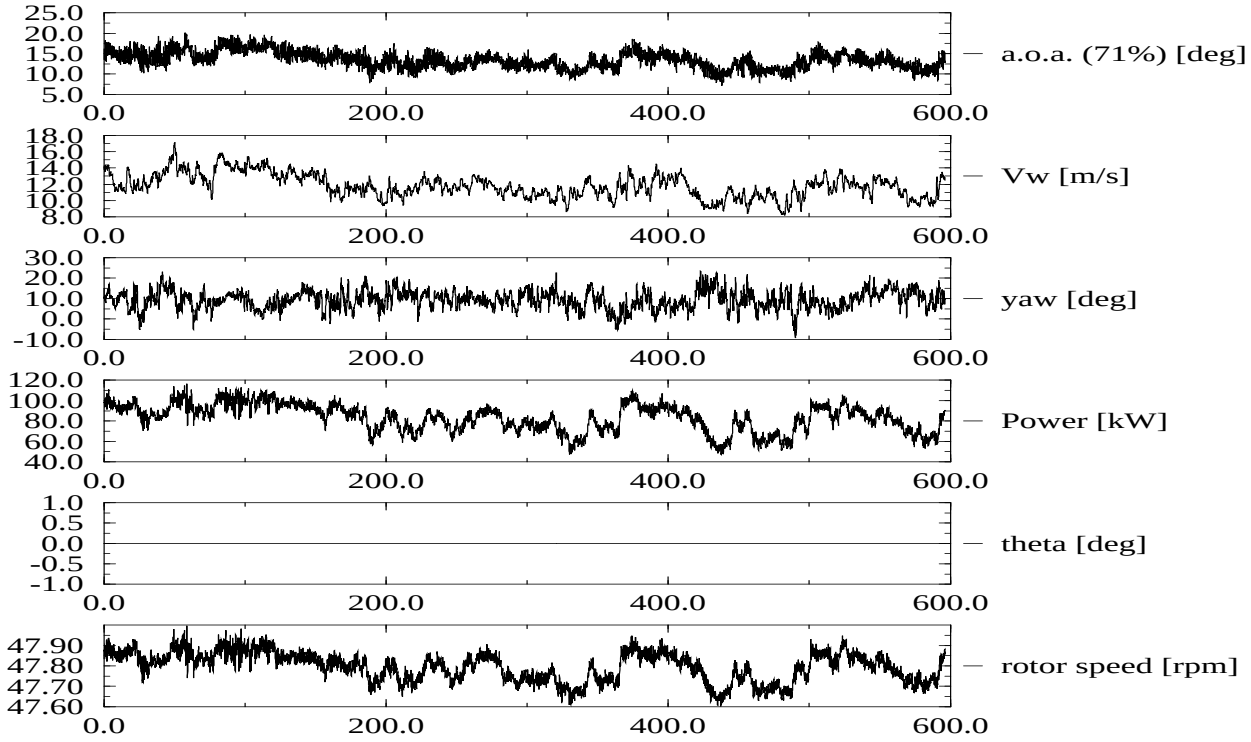

Figure C.51 *RISØ: Time series of campaign y_rot_r_002*

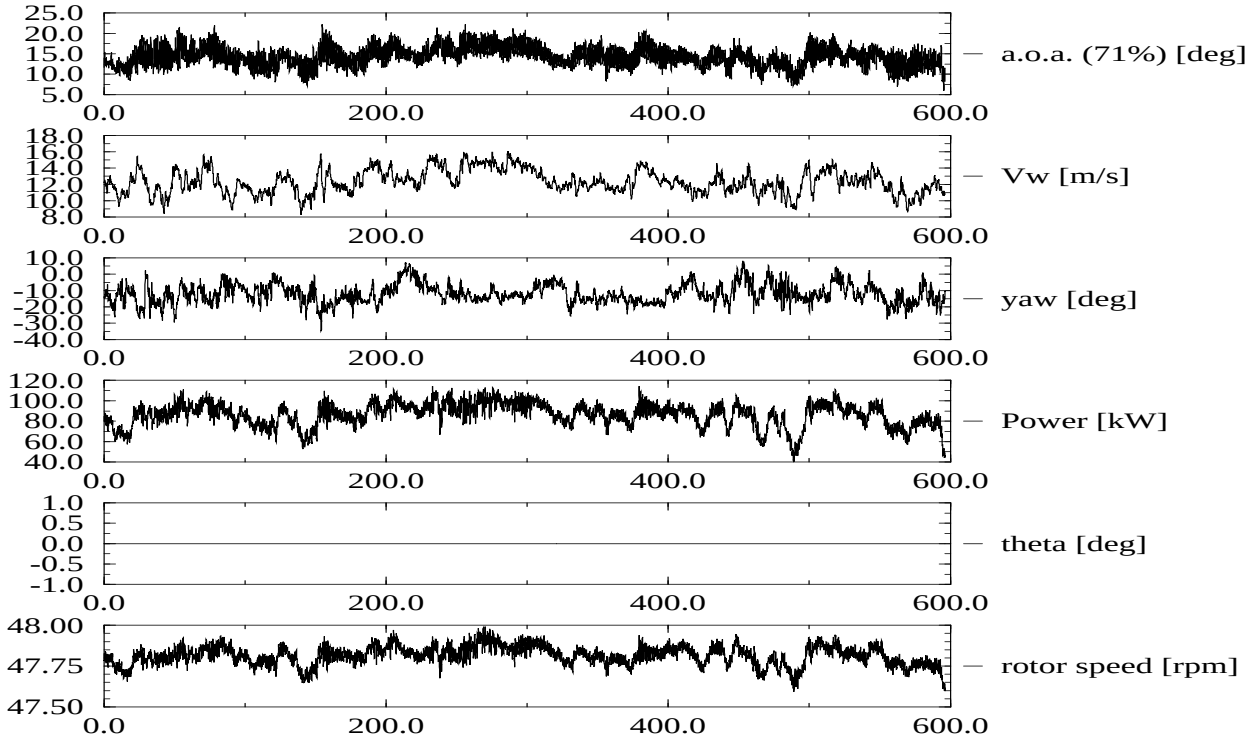

Figure C.52 *RISØ: Time series of campaign y_rot_r_003*

C.7 RISØ turbine and sectional coefficients

C.7.1 RISØ, 2D profile coefficients

The 2D profile coefficients for the blade of the RISØ test turbine are zipped into '/data/riso/2d/coef2d_r.zip, which contain the following 10 files:

- cla1_2Dṙ. This file contains the $c_l - \alpha$ data for the NACA63212 profile;
- cla2_2Dṙ. This file contains the $c_l - \alpha$ data for the NACA63215 profile;
- cla3_2Dṙ. This file contains the $c_l - \alpha$ data for the NACA63218 profile;
- cla4_2Dṙ. This file contains the $c_l - \alpha$ data for the NACA63221 profile;
- cla5_2Dṙ. This file contains the $c_l - \alpha$ data for the NACA63225 profile;
- cda1_2Dṙ. This file contains the $c_d - \alpha$ data for the NACA63212 profile;
- cda2_2Dṙ. This file contains the $c_d - \alpha$ data for the NACA63215 profile;
- cda3_2Dṙ. This file contains the $c_d - \alpha$ data for the NACA63218 profile;
- cda4_2Dṙ. This file contains the $c_d - \alpha$ data for the NACA63221 profile;
- cda5_2Dṙ. This file contains the $c_d - \alpha$ data for the NACA63225 profile;

The data are shown in table G.3 and G.4;

C.7.2 RISØ, rotating profile coefficients

The RISØ 3D , rotating profile coefficients are zipped into '/data/risoe/rotcoef/coef_r.zip, which contain the following 6 files:

- cna1_rot_r: This file contains the $c_n - \alpha$ data for the 37% section.
- cna2_rot_r: This file contains the $c_n - \alpha$ data for the 68% section.
- cna3_rot_r: This file contains the $c_n - \alpha$ data for the 98% section.
- cta2_rot_r: This file contains the $c_t - \alpha$ data for the 68% section.
- cta3_rot_r: This file contains the $c_t - \alpha$ data for the 98% section.
- PV_r: This file contains the power curve for the RISØ test turbine.

The data are shown graphically in the figures G.6 and G.7

C.8 ECN time series

Note that there are mutual differences in 'prof' file format. There appear to be 4 different formats. In table C.12 these are identified with f(ormat)A and fB. The table shows the mutual similarities and differences between the prof file formats for the datasets which have been supplied. A further description of these datasets is given in the following sections.

Table C.12 *Format of ECN measurement files*

file	fA	fB
non-e-018 to non-e-021	x	
ny-rot-001 to ny-rot-004	x	
ny-rot-005 to ny-rot-008		x
ny-rot-009 to ny-rot-025	x	
y-rot-001 to y-rot-021		x

C.8.1 ECN time series: Non-rotating campaigns

The files are stored into the directory '/data/ecn/stilltim/' and numbered in order of increasing angle of attack, see table C.13.

Table C.13 *Global overview of ECN measurement files, non-rotating conditions*

file	ECN file name	$\overline{\alpha_{80\%}}$ deg	$\overline{V}$ m/s	duration s
non-e-017	114.339	-3.75	12.35	68.85
non-e-018	114.340	11.76	12.26	68.85
non-e-019	111.301	14.8	9.65	68.85
non-e-020	111.302	30.8	11.43	68.85
non-e-021	111.303	37.1	9.54	68.85

C.8.2 ECN non-rotating campaigns, plots of time series

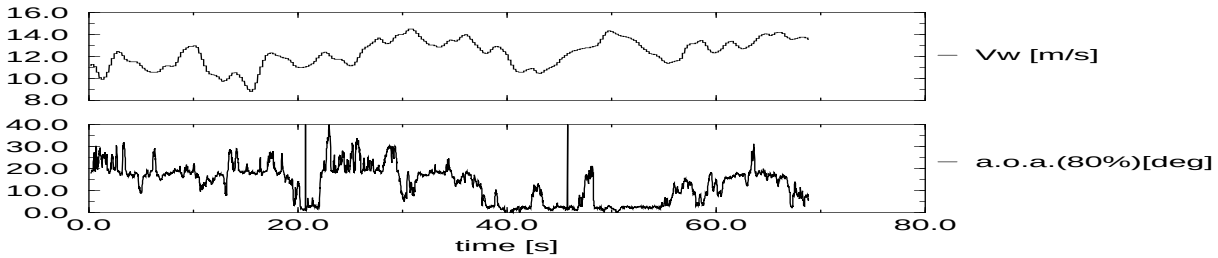

Figure C.53 *ECN: Time series of campaign non_e_018*

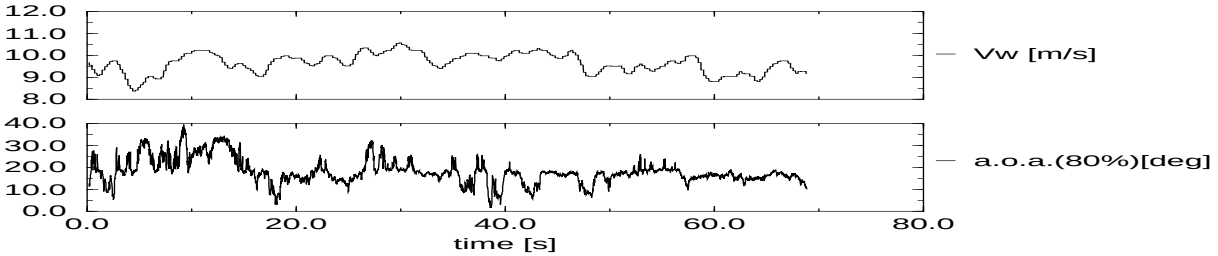

Figure C.54 *ECN: Time series of campaign non_e_019*

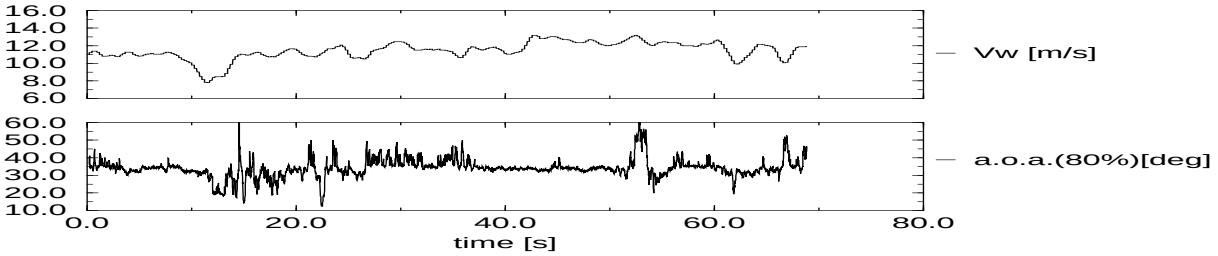

Figure C.55 *ECN: Time series of campaign non_e_020*

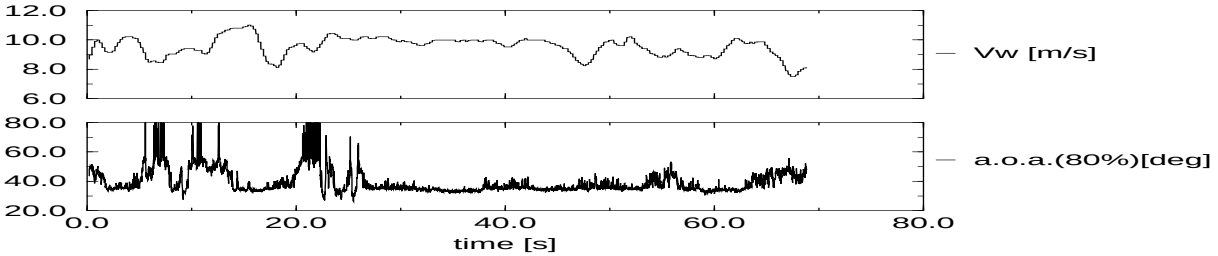

Figure C.56 *ECN: Time series of campaign non_e_021*

C.8.3 ECN time series: Non-yawed campaigns

The files are stored into the directory '/data/ecn/rottim/'. The non-yawed campaigns can be subdivided in three different sets:

- Measurements at approximately constant wind speed and rotor speed: Angle of attack variation through pitch angle, table C.14; The files are numbered in order of increasing angle of attack (= decreasing pitch angle).
- Measurements at approximately constant rotor speed: Angle of attack variation through wind speed and pitch angle, table C.15; The files are numbered in order of decreasing pitch angle. A pitch angle bin of approximately 1.5 degrees is applied. Within every pitch angle bin, the files are numbered in order of increasing angle of attack (= wind speed).
- Measurements at approximately constant wind speed: Angle of attack variation through rotor speed and pitch angle, table C.16; The files are numbered in order of increasing rotor speed. At the same time the pitch angle decreases. As a result the angle of attack remains approximately constant.

Table C.14 *Global overview of ECN measurement files, non-yawed conditions, a.o.a. set by pitch angle*

file	ECN filename	$\overline{\alpha_{80\%}}$ deg	$\overline{\mathrm{V}}$ m/s	$\overline{\mathrm{Power}}$ kW	$\overline{\theta_{\mathrm{tip}}}$ deg	$\overline{\Omega}$ rpm	duration s
ny-rot-e-001	215.398	0.08	9.15	29.17	9.7	36.7	70.31
ny-rot-e-002	215.397	2.58	9.70	64.56	6.5	37.3	70.31
ny-rot-e-003	215.396	5.01	10.36	65.89	2.5	37.3	70.31
ny-rot-e-004	215.395	10.39	10.39	76.06	-0.7	37.5	70.31
ny-rot-e-005	215.394	19.44	10.97	94.35	-4.6	37.8	70.31
ny-rot-e-006	215.393	19.84	8.52	49.77	-7.0	37.0	70.31
ny-rot-e-007	215.392	25.35	9.71	30.20	-10.3	36.7	70.31
ny-rot-e-008	215.391	31.57	9.96	10.94	-12.6	36.3	70.31

Table C.15 *Global overview of ECN measurement files, non-yawed conditions, a.o.a. set by wind speed and pitch angle*

file	ECN filename	$\overline{\alpha_{80\%}}$ deg	$\overline{V}$ m/s	$\overline{\text{Power}}$ kW	$\overline{\theta_{tip}}$ deg	$\overline{\Omega}$ rpm	duration s
ny-rot-e-009	712.398	2.38	6.55	40.45	4.6	33.1	62.50
ny-rot-e-010	714.398	6.18	11.60	76.30	4.7	32.9	62.50
ny-rot-e-012	714.397	15.95	10.97	127.20	1.6	33.8	62.50
ny-rot-e-013	712.397	6.35	6.78	44.96	0.0	33.2	62.50
ny-rot-e-014	711.396	2.74	4.62	1.95	-1.5	32.2	62.50
ny-rot-e-015	712.396	5.72	7.05	28.02	-1.5	32.9	62.50
ny-rot-e-016	714.396	19.86	11.74	118.30	-1.5	33.6	62.50
ny-rot-e-017	711.395	0.08	4.35	7.25	-3.6	32.4	62.50
ny-rot-e-018	712.395	10.18	6.93	31.43	-3.6	32.9	62.50
ny-rot-e-019	714.395	22.49	11.69	102.20	-3.5	33.3	62.50

Table C.16 *Global overview of ECN measurement files, non-yawed conditions, a.o.a. set rotor speed and pitch angle*

file	ECN filename	$\overline{\alpha_{80\%}}$ deg	$\overline{V}$ m/s	$\overline{\text{Power}}$ kW	$\overline{\theta_{tip}}$ deg	$\overline{\Omega}$ rpm	duration s
ny-rot-e-020	812.439	8.95	6.94	19.44	4.5	20.1	62.50
ny-rot-e-021	813.439	12.13	7.10	33.88	0.5	25.3	62.50
ny-rot-e-022	814.439	12.29	6.50	26.49	-3.1	28.0	62.50
ny-rot-e-023	815.439	9.79	7.04	19.14	-5.1	32.7	62.50
ny-rot-e-024	816.439	7.26	5.46	6.01	-6.6	37.2	62.50
ny-rot-e-025	817.439	14.15	6.93	35.33	-8.2	42.7	62.50

C.8.4 ECN non-yawed campaigns, plots of time series

Time series, ECN non-yawed campaigns, a.o.a. set by pitch angle, plots

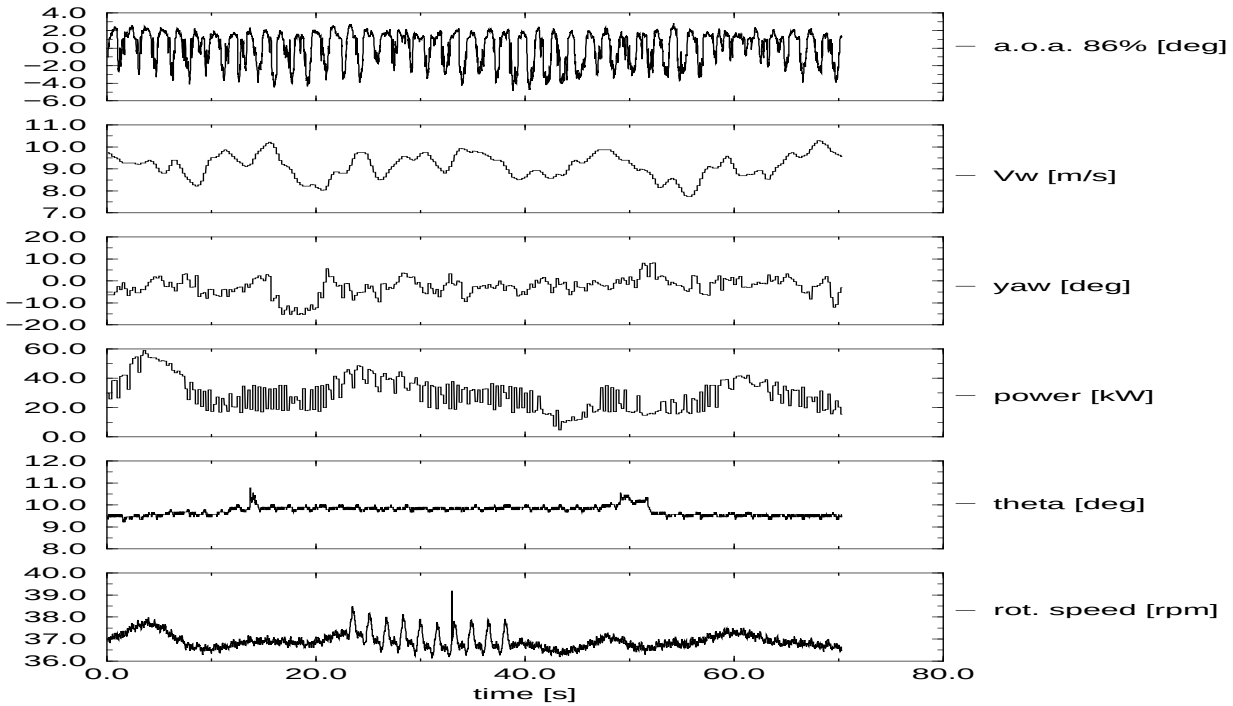

Figure C.57 *ECN: Time series of campaign ny_rot_e_001*

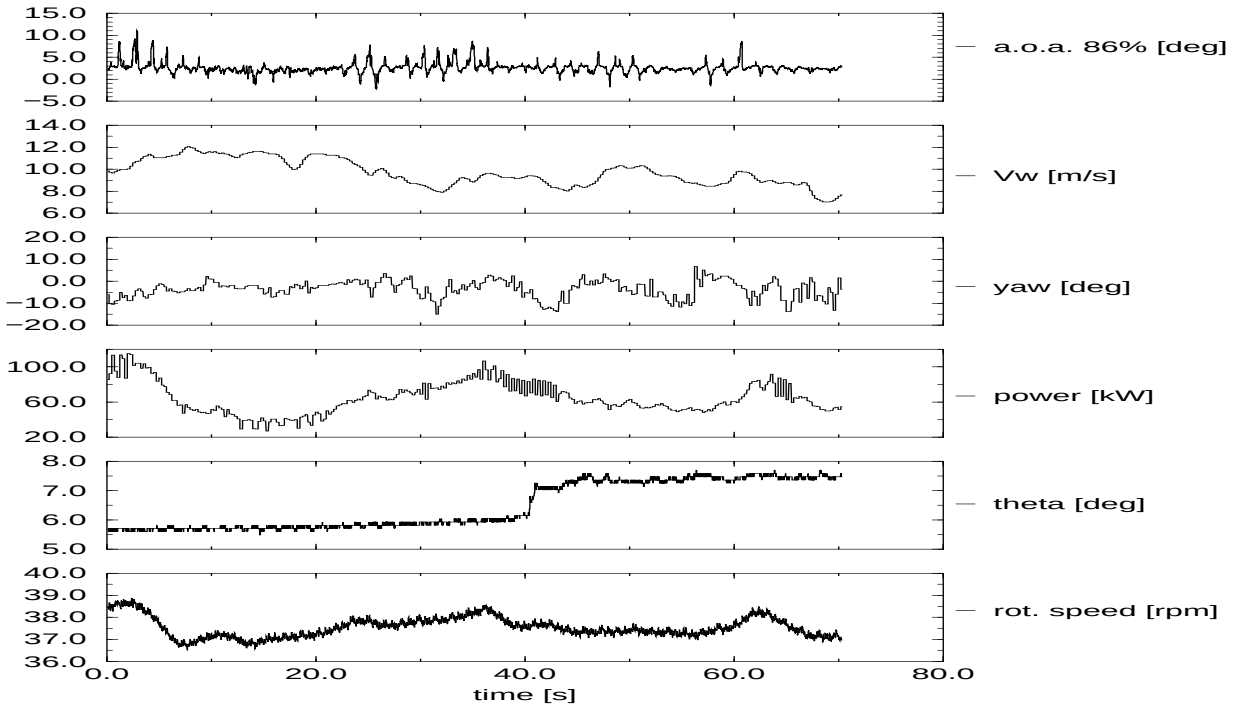

Figure C.58 *ECN: Time series of campaign ny_rot_e_002*

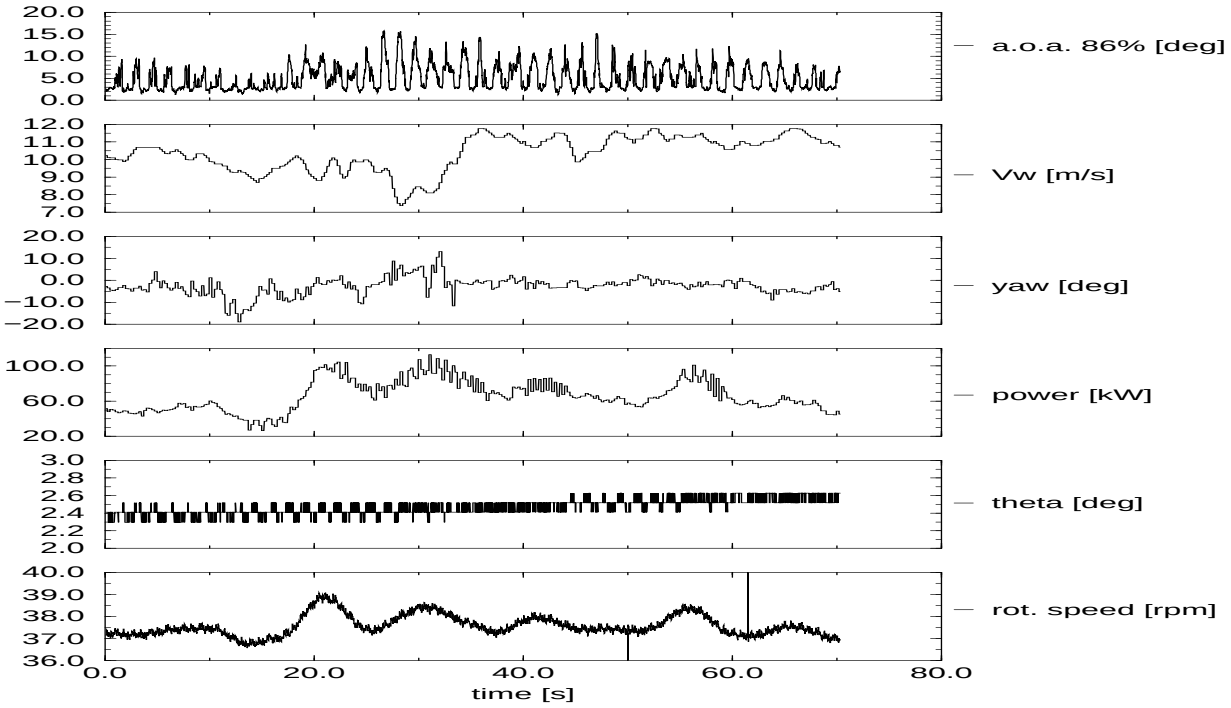

Figure C.59 *ECN: Time series of campaign ny_rot_e_003*

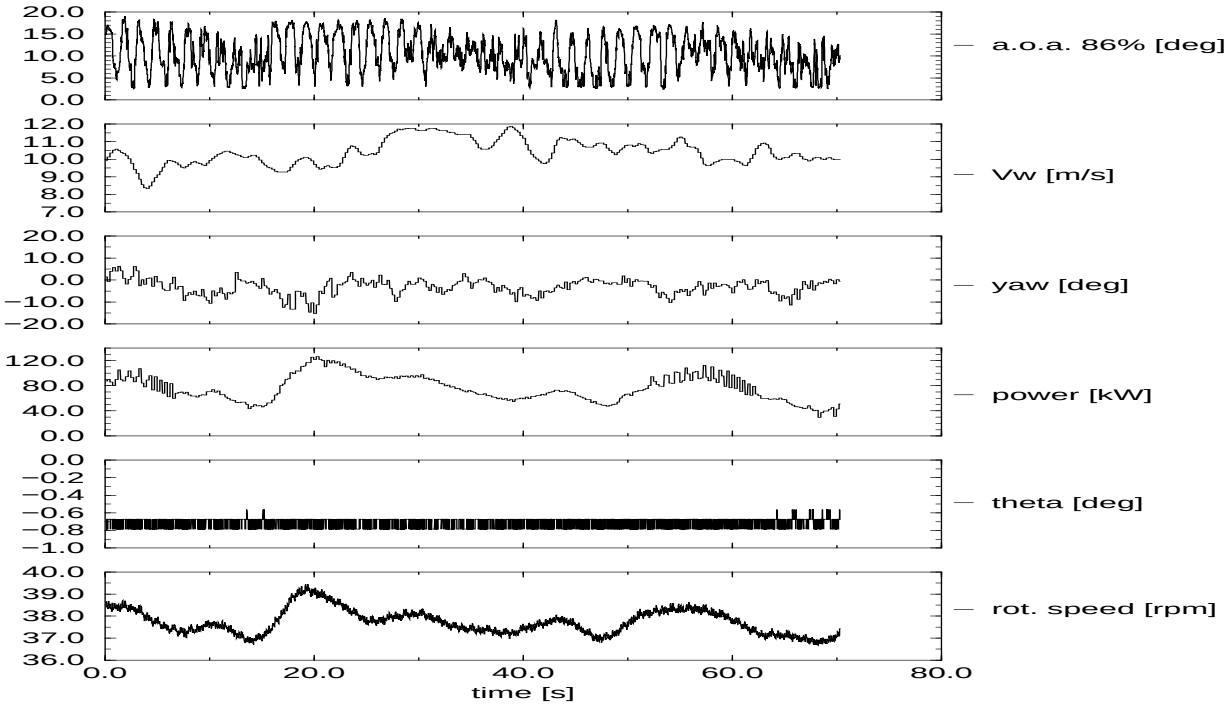

Figure C.60 *ECN: Time series of campaign ny_rot_e_004*

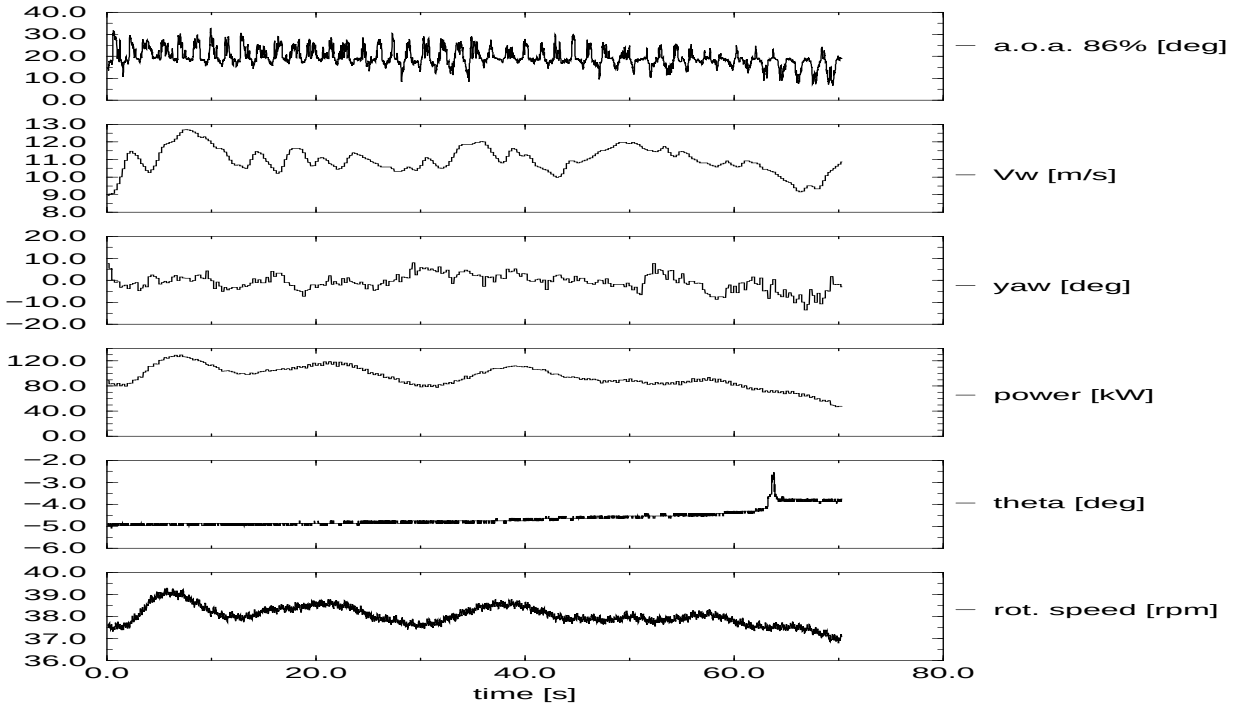

Figure C.61 *ECN: Time series of campaign ny_rot_e_005*

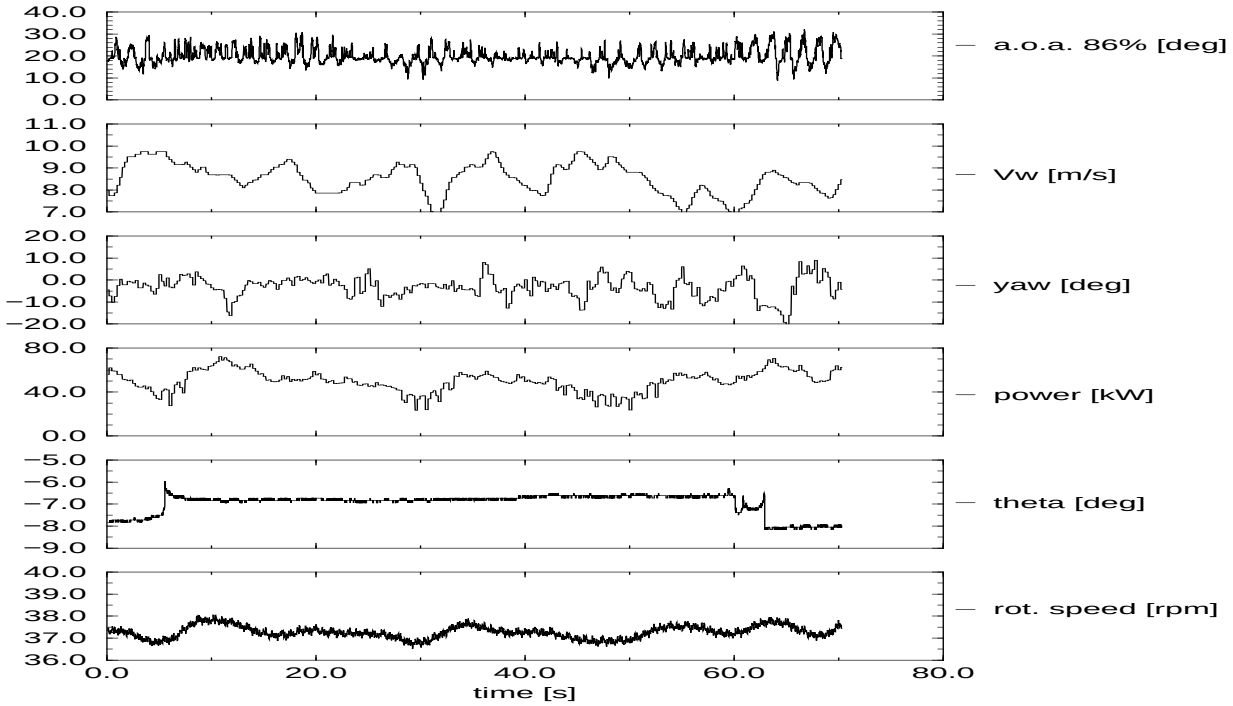

Figure C.62 *ECN: Time series of campaign ny_rot_e_006*

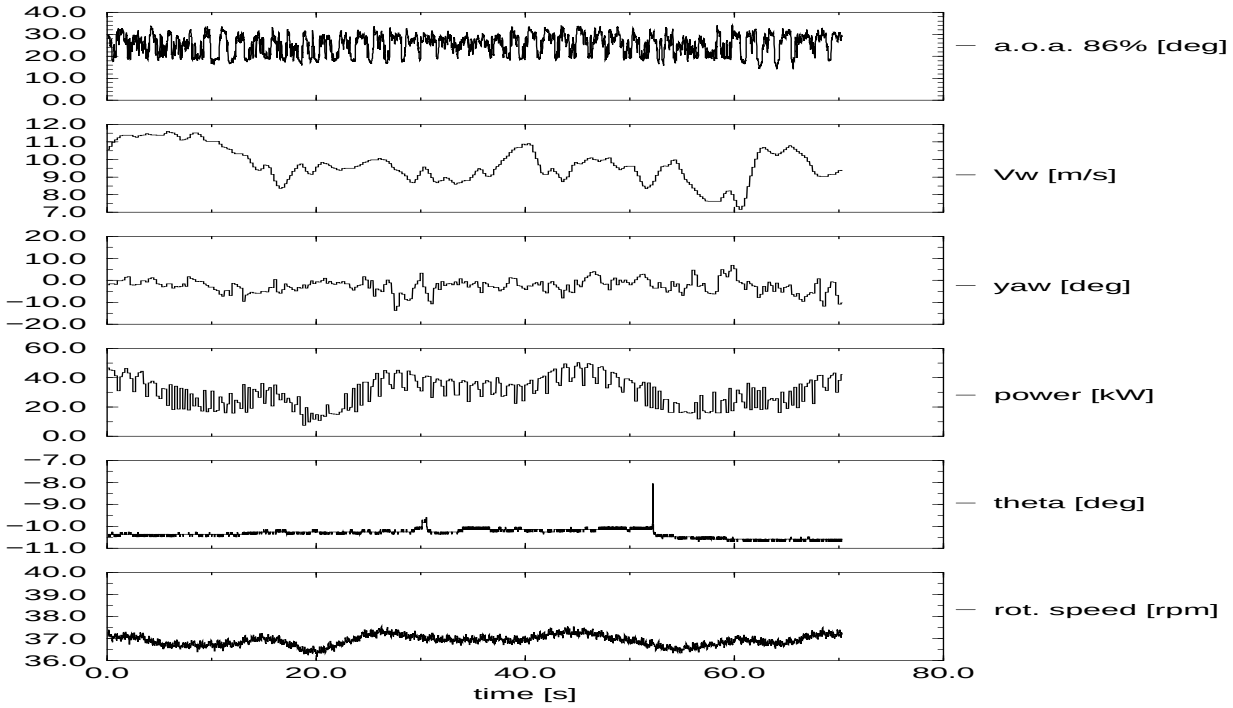

Figure C.63 *ECN: Time series of campaign ny_rot_e_007*

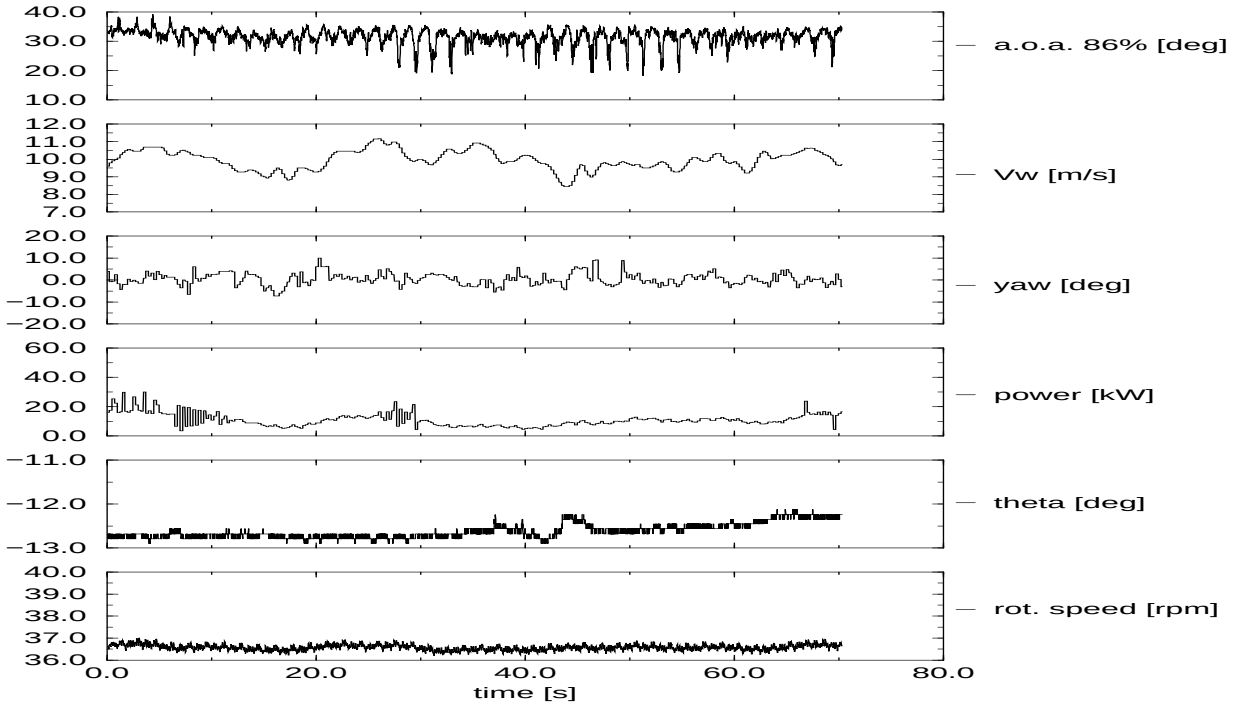

Figure C.64 *ECN: Time series of campaign ny_rot_e_008*

Time series, ECN non-yawed campaigns, a.o.a. set by wind speed and pitch angle, plots

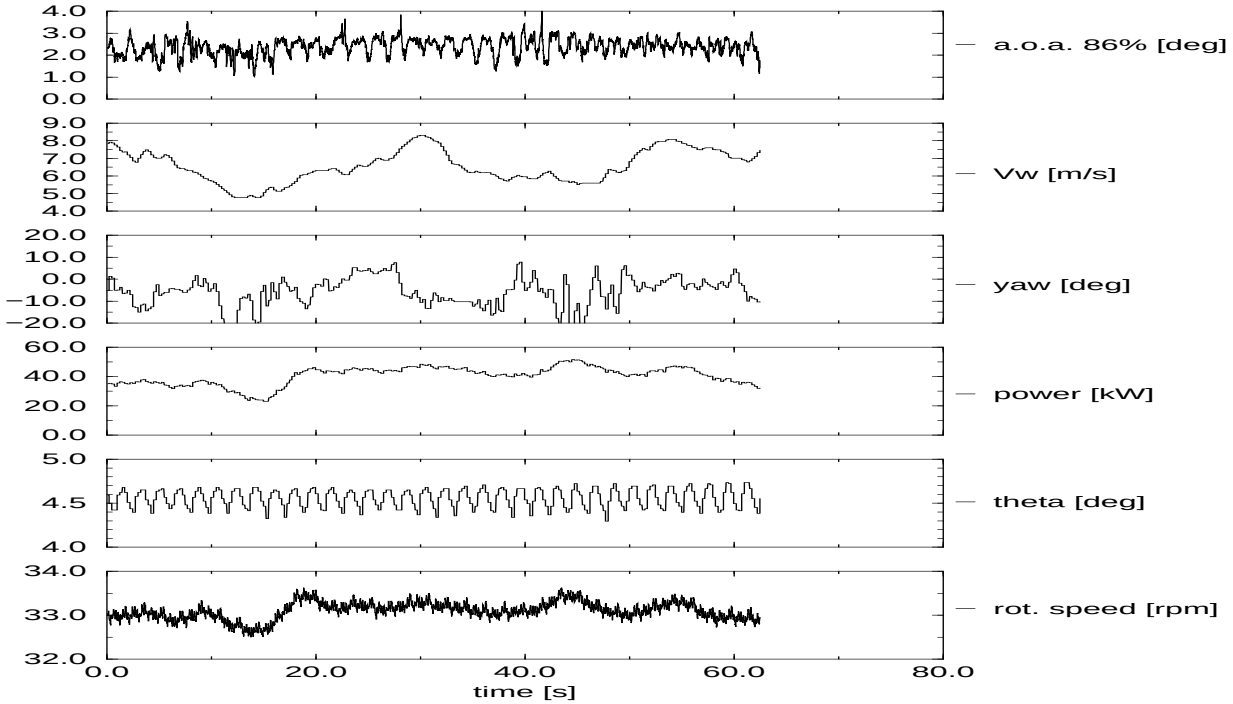

Figure C.65 *ECN: Time series of campaign ny_rot_e_009*

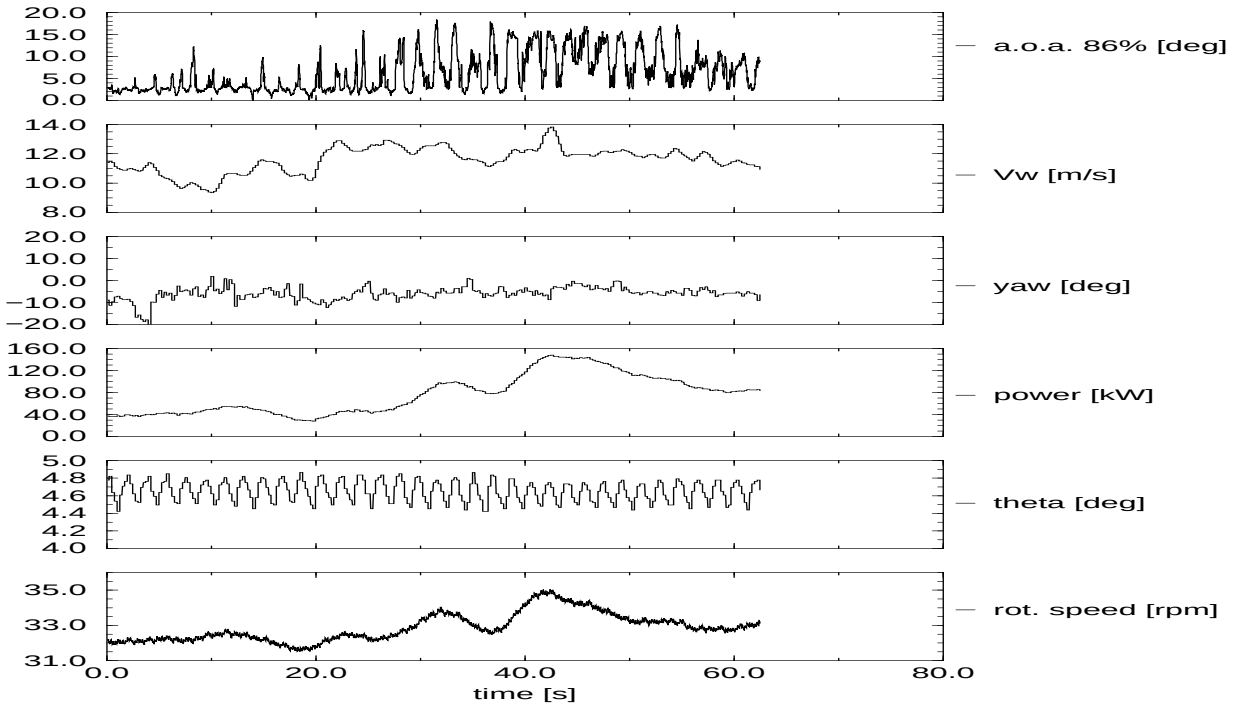

Figure C.66 *ECN: Time series of campaign ny_rot_e_010*

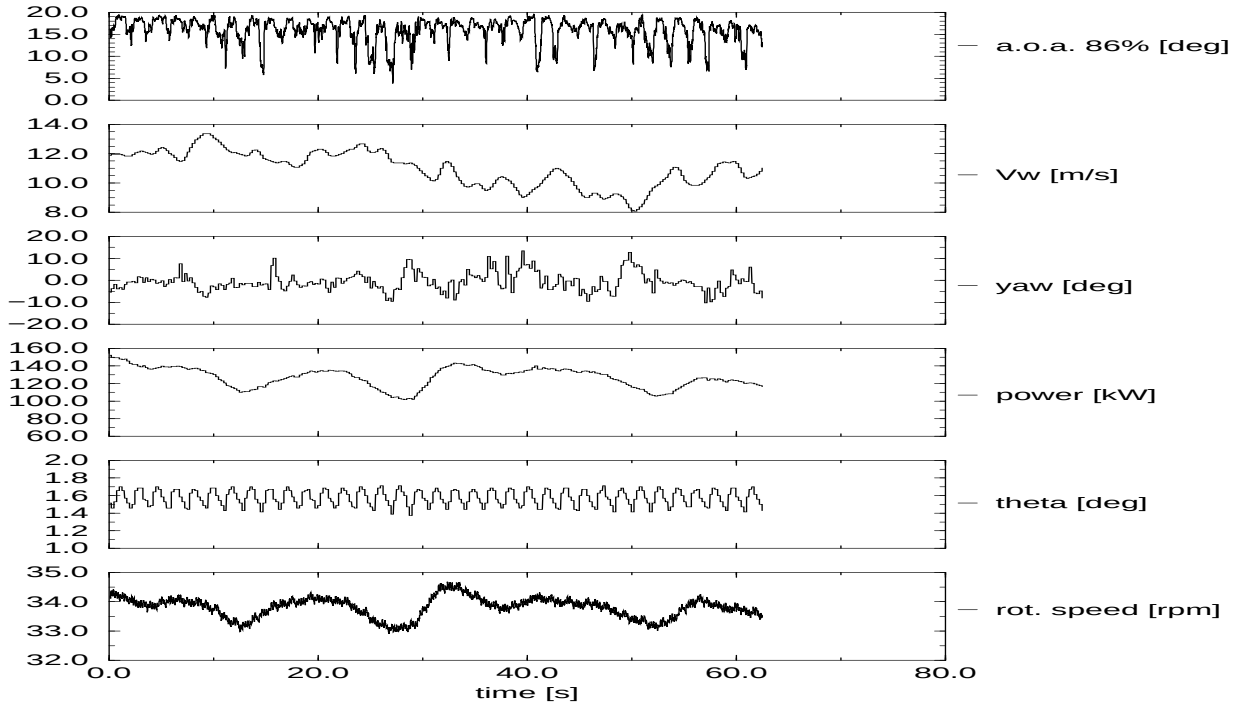

Figure C.67 *ECN: Time series of campaign ny_rot_e_012*

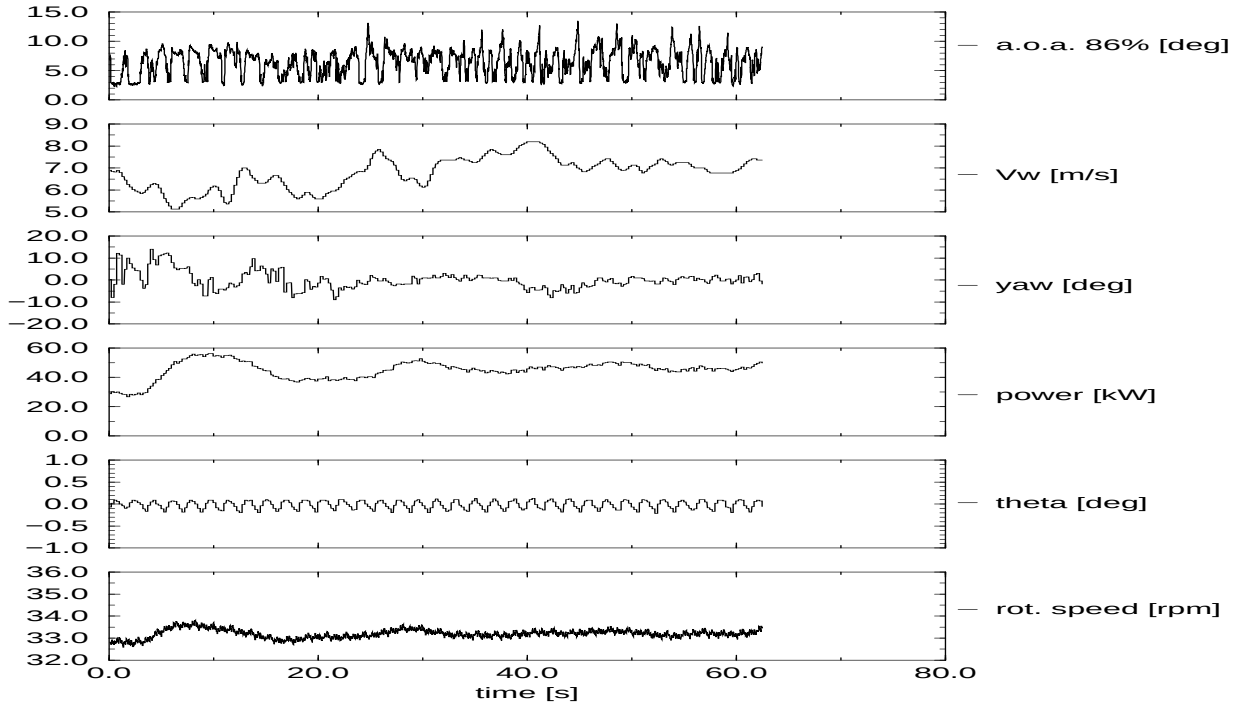

Figure C.68 *ECN: Time series of campaign ny_rot_e_013*

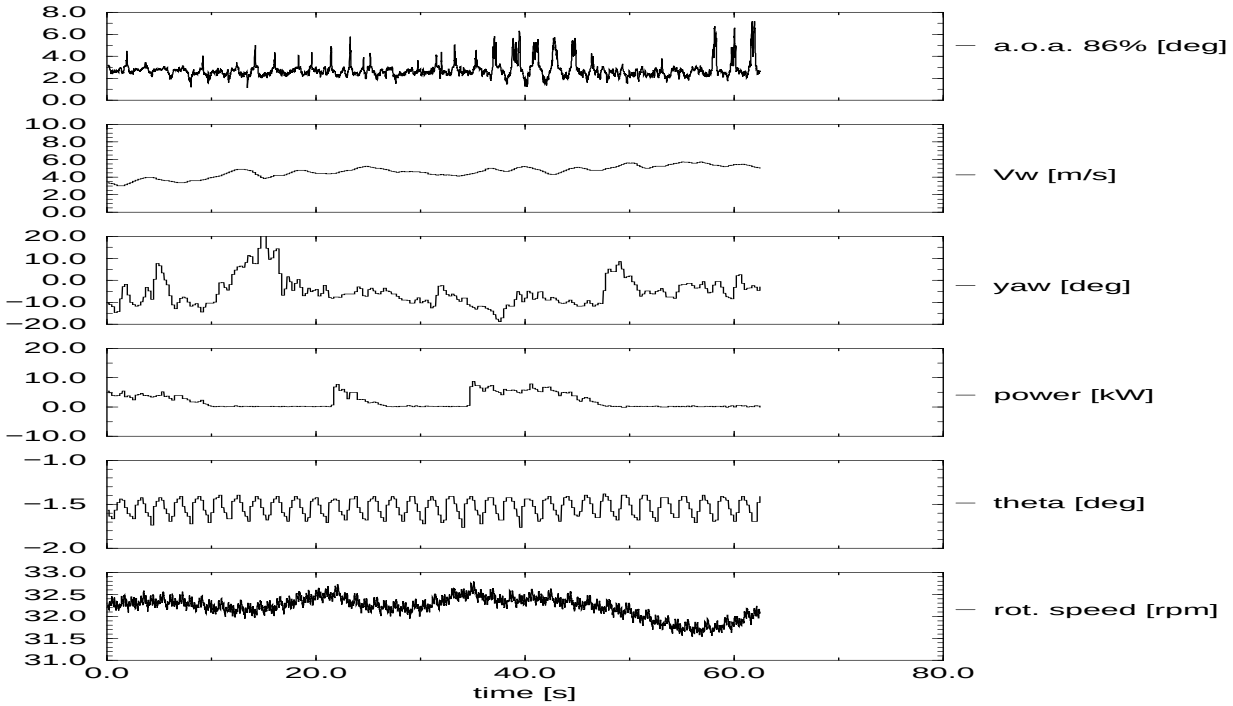

Figure C.69 *ECN: Time series of campaign ny_rot_e_014*

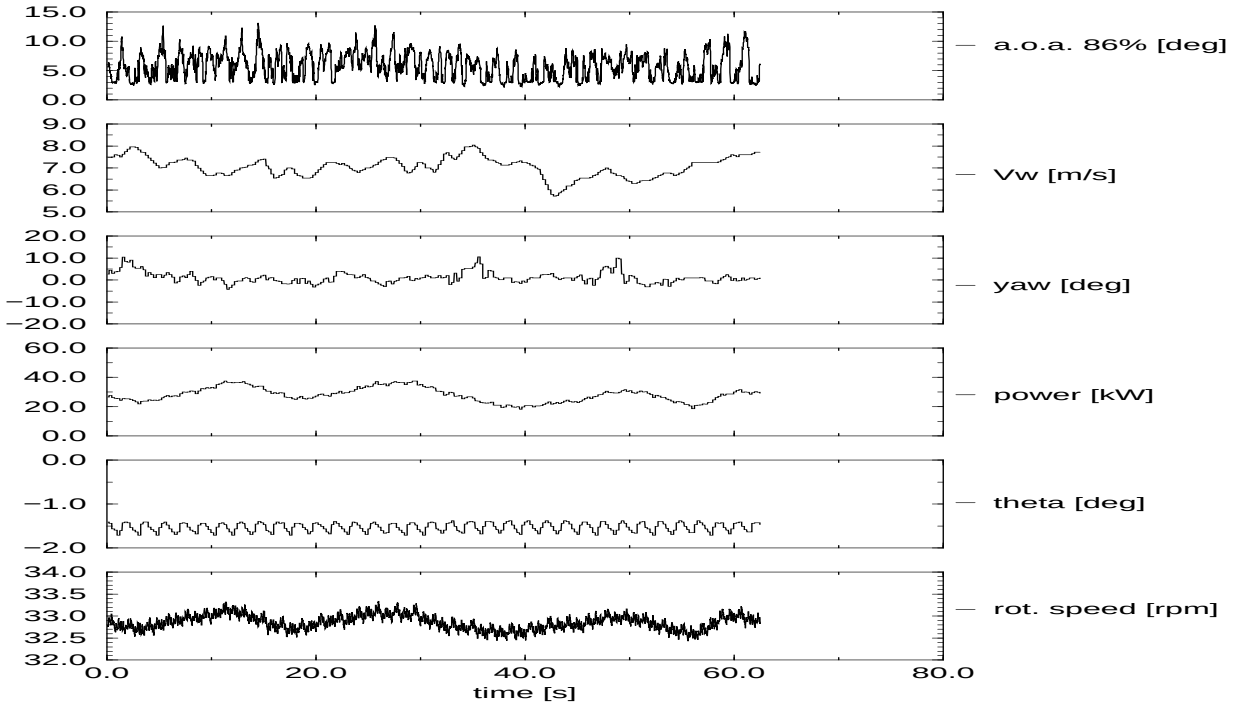

Figure C.70 *ECN: Time series of campaign ny_rot_e_015*

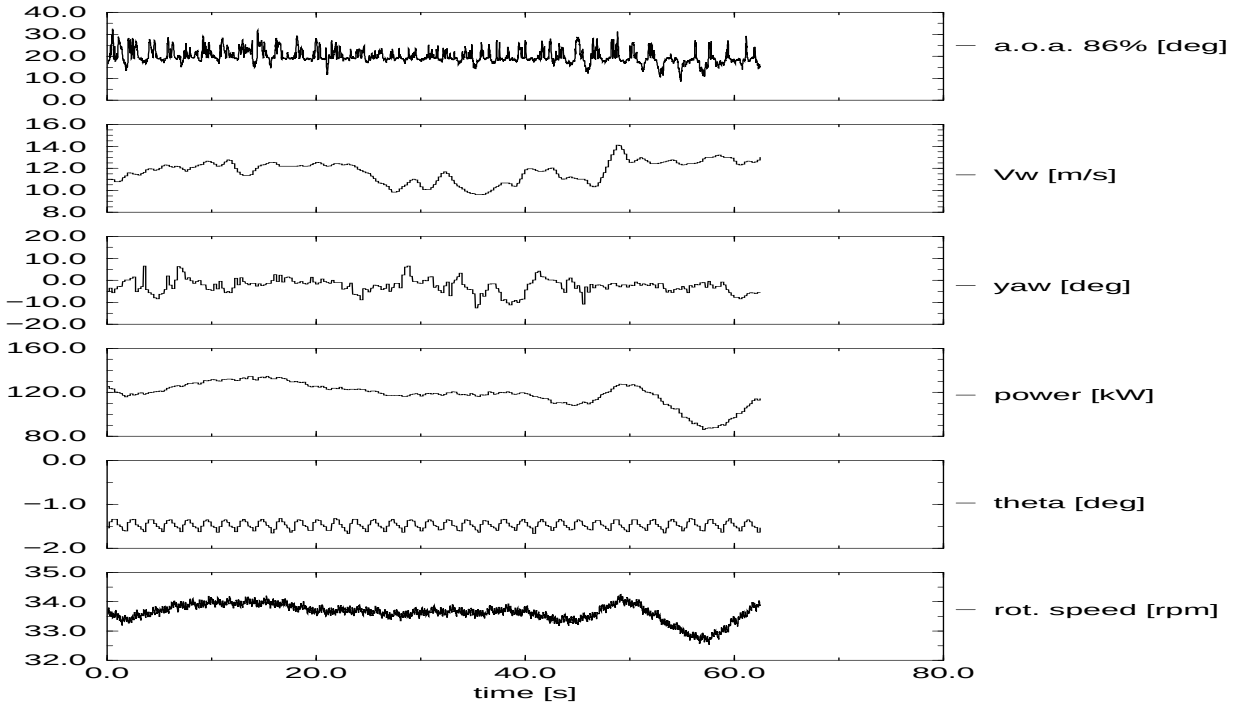

Figure C.71 *ECN: Time series of campaign ny_rot_e_016*

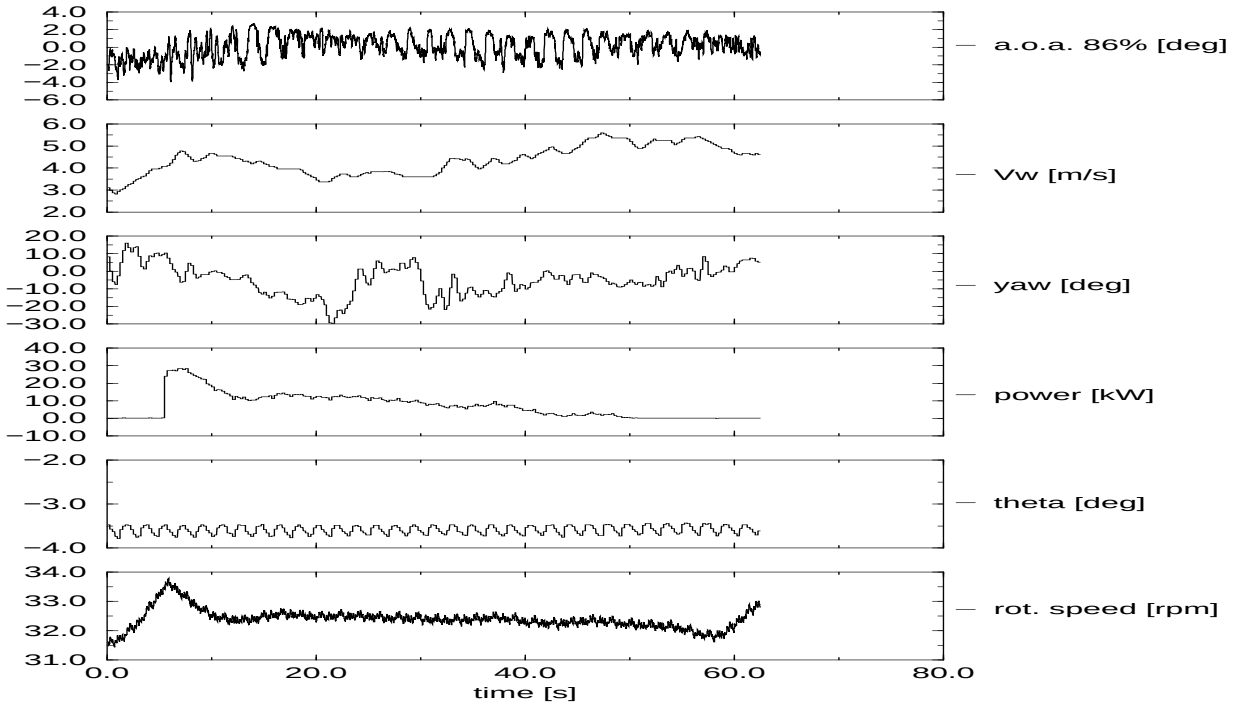

Figure C.72 *ECN: Time series of campaign ny_rot_e_017*

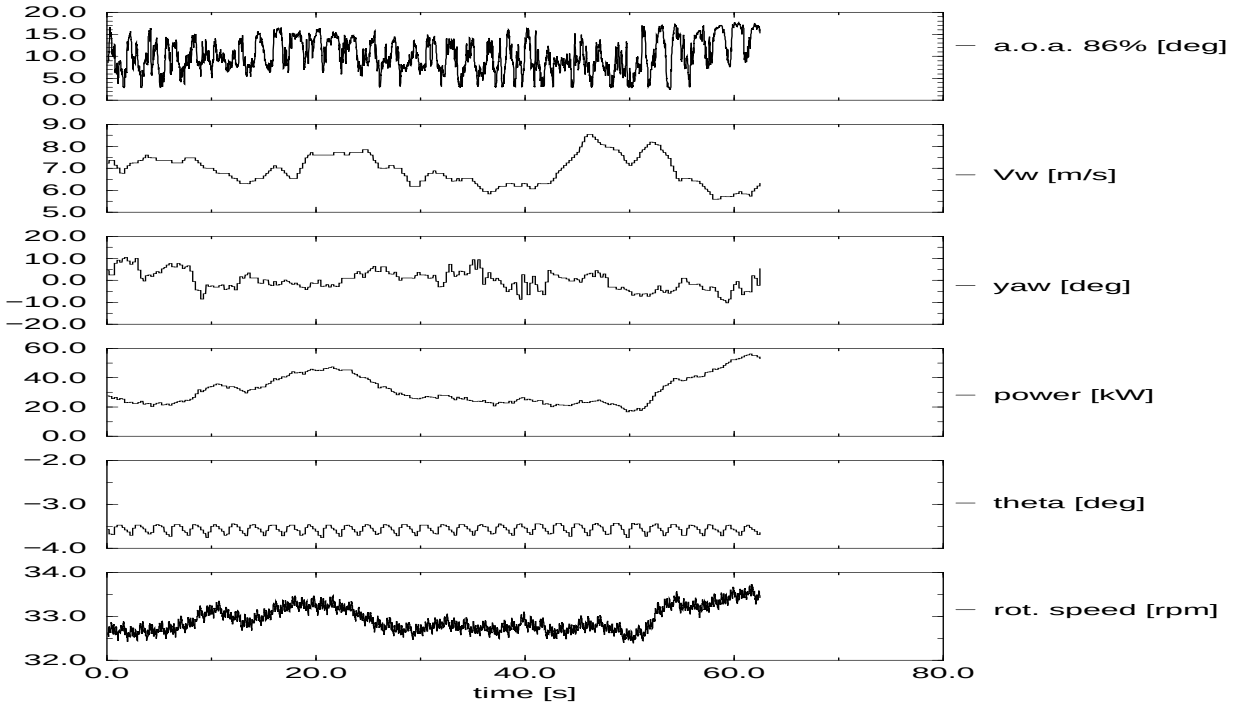

Figure C.73 *ECN: Time series of campaign ny_rot_e_018*

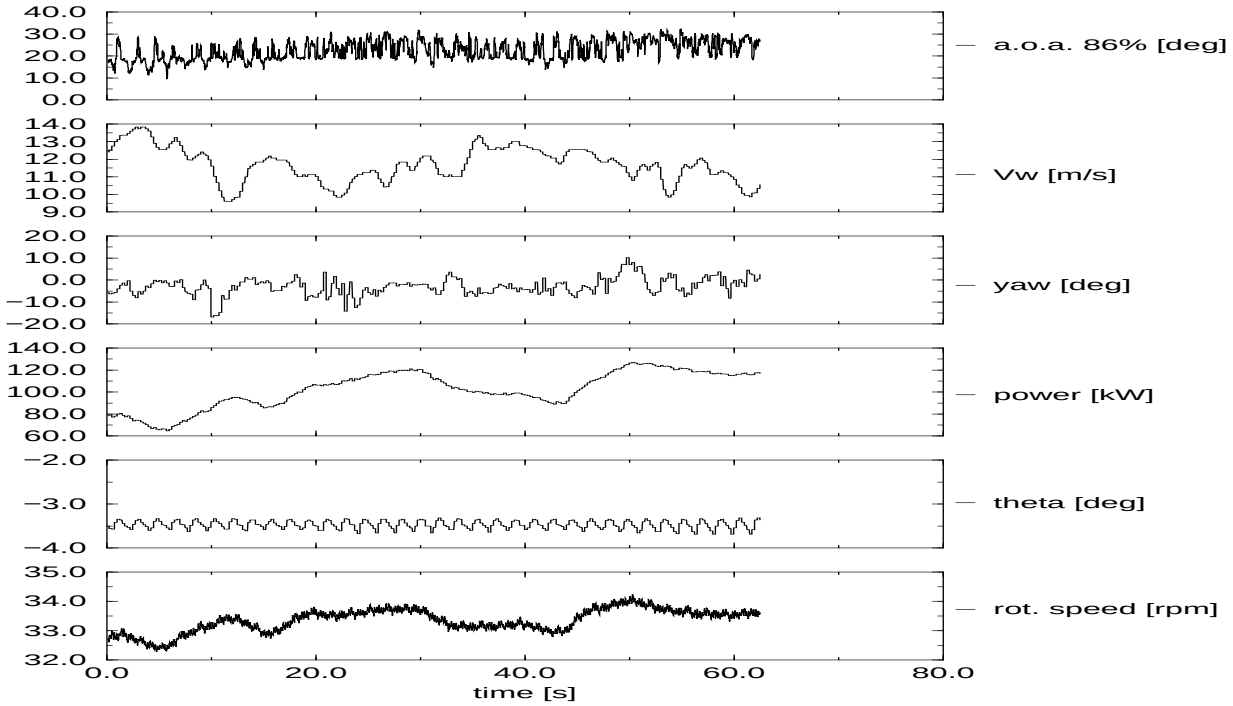

Figure C.74 *ECN: Time series of campaign ny_rot_e_019*

Time series, ECN non-yawed campaigns, a.o.a. set by rotor speed and pitch angle, plots

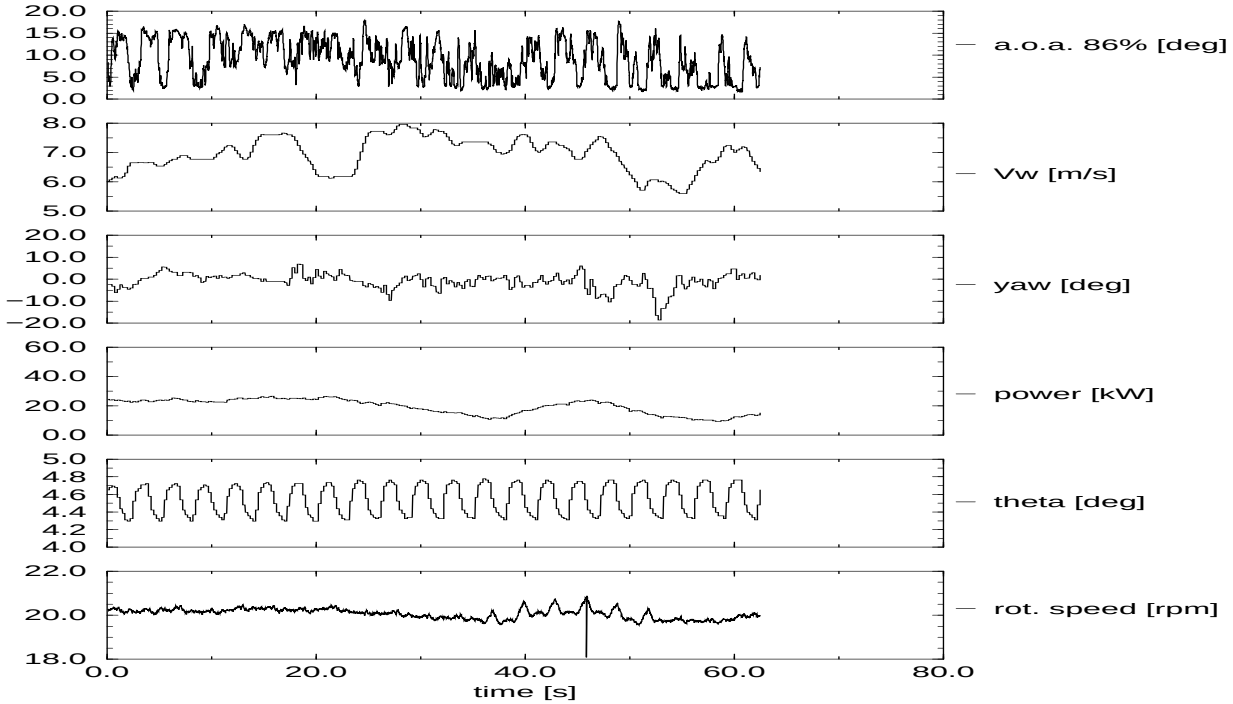

Figure C.75 *ECN: Time series of campaign ny_rot_e_020*

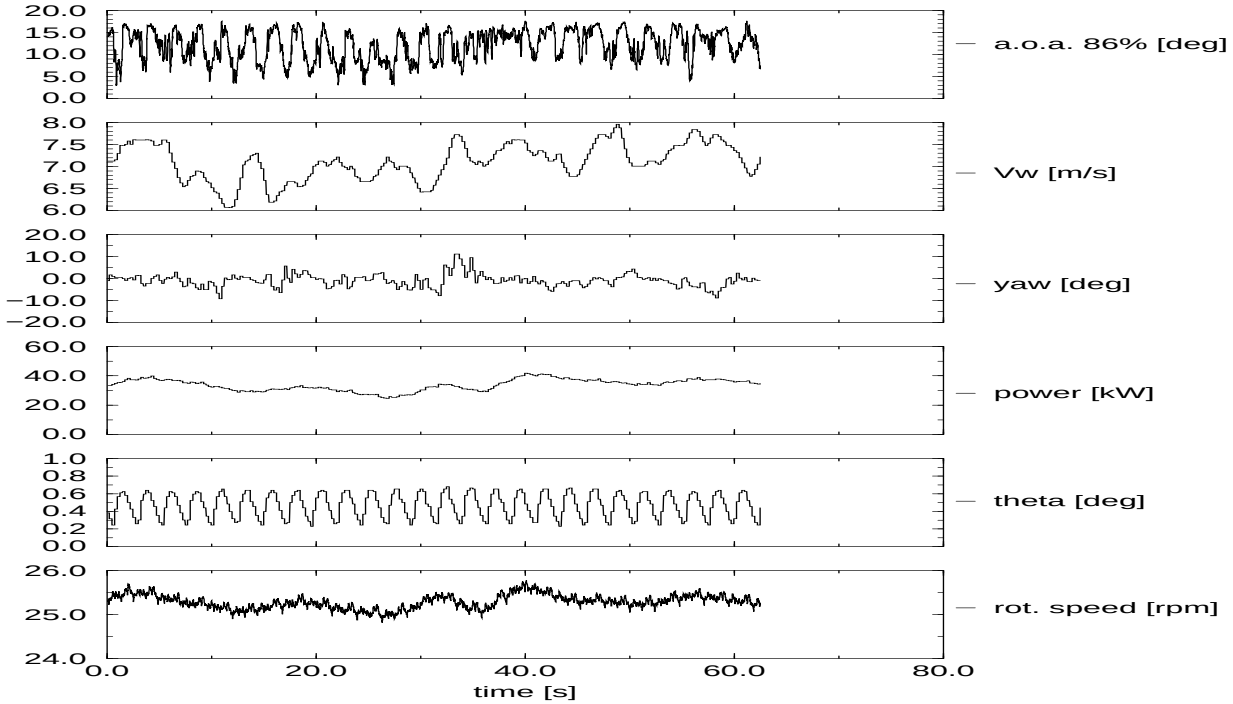

Figure C.76 *ECN: Time series of campaign ny_rot_e_021*

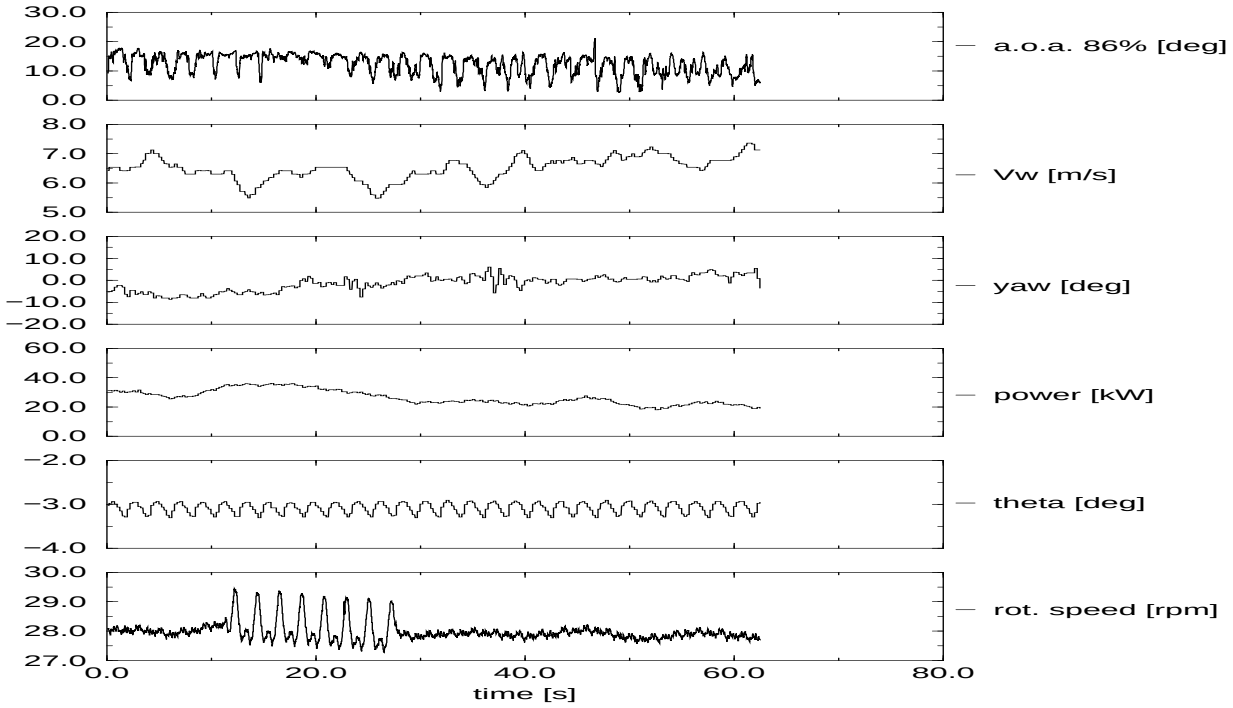

Figure C.77 *ECN: Time series of campaign ny_rot_e_022*

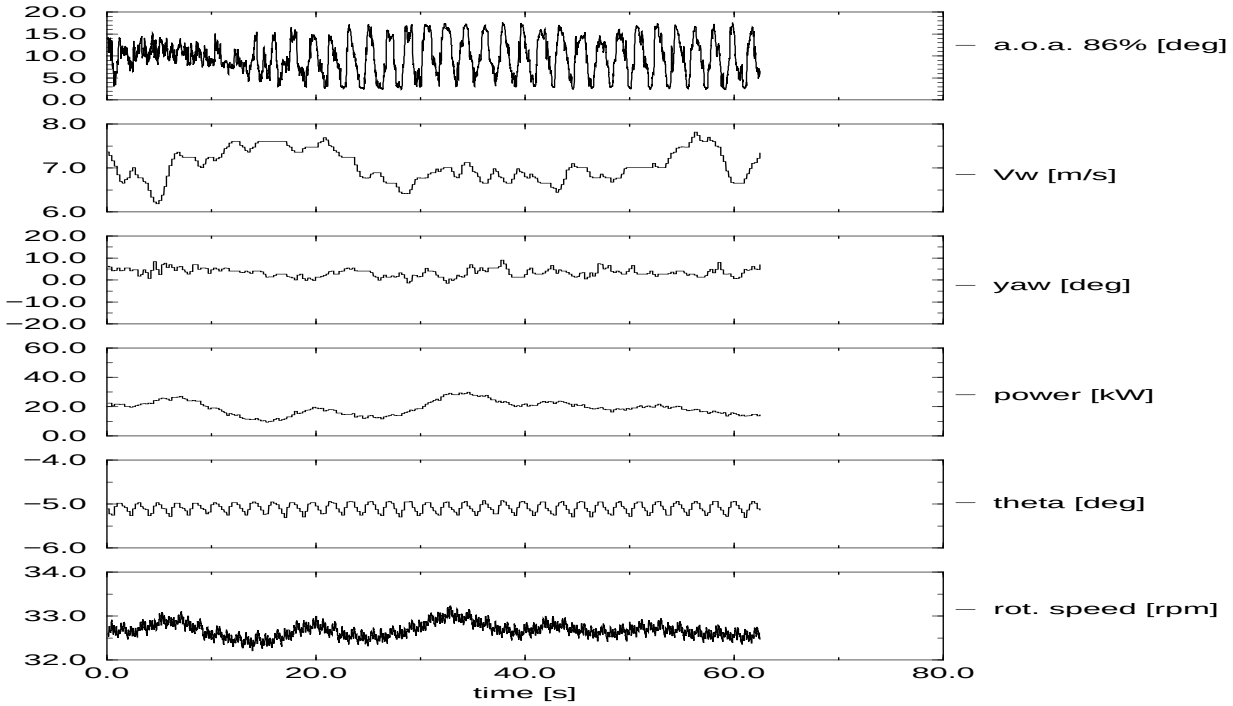

Figure C.78 *ECN: Time series of campaign ny_rot_e_023*

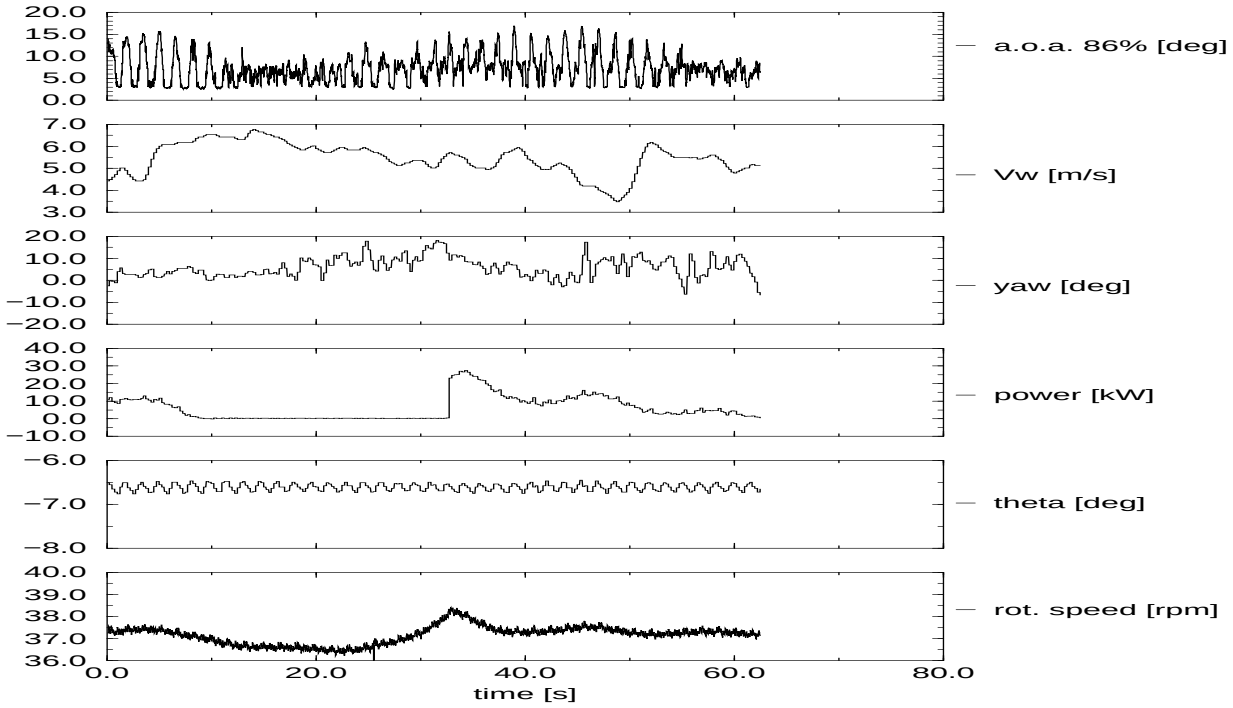

Figure C.79 *ECN: Time series of campaign ny_rot_e_024*

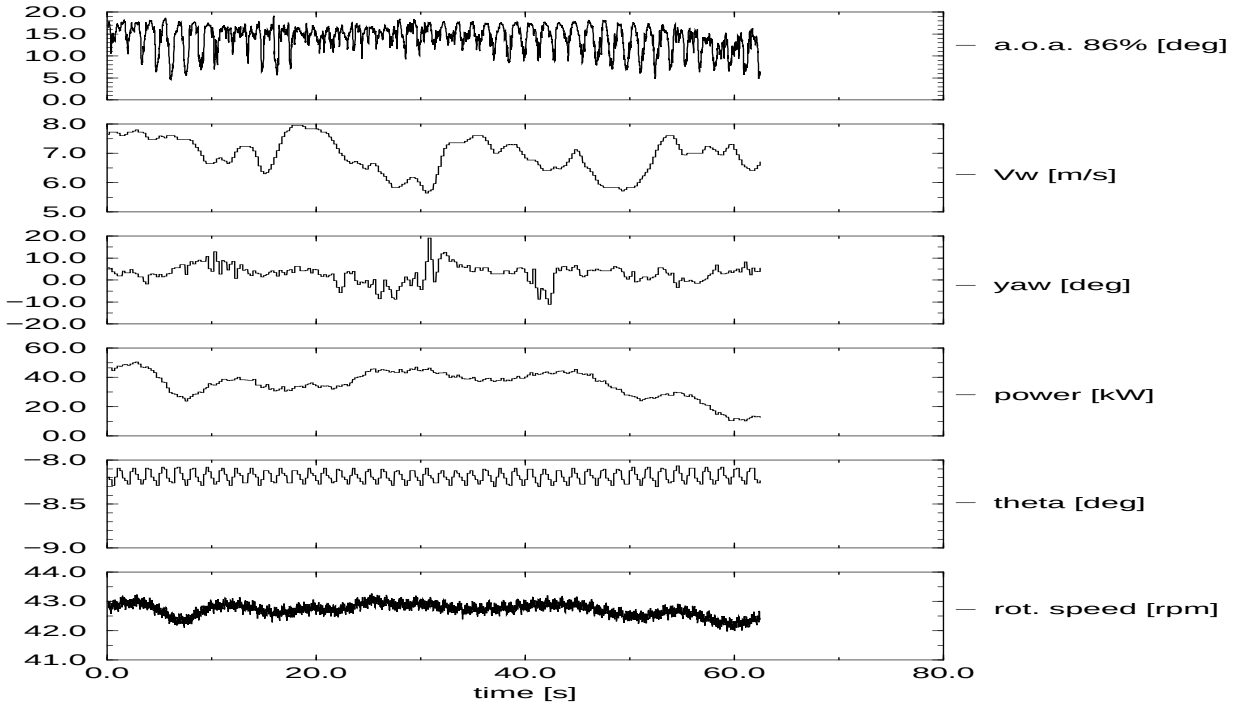

Figure C.80 *ECN: Time series of campaign ny_rot_e_025*

C.8.5 ECN time series: Yawed campaigns

The files are stored into the directory '/data/ecn/rottim/'. They are sorted in yaw angle bins of approximately 5 degrees and numbered in order of decreasing yaw angle. Within every yaw angle bin, the files are numbered in order of increasing angle of attack, see table C.17.

Table C.17 *Global overview of ECN measurement files for yawed conditions*

file	ECN filename	$\overline{\alpha_{80\%}}$ deg	$\overline{V}$ m/s	$\overline{\phi_y}$ deg	$\overline{\text{Power}}$ kW	$\overline{\theta_{tip}}$ deg	$\overline{\Omega}$ rpm	duration s
y-rot-e-001	471.459	11.84	9.46	42.9	32.90	-5.82	37.10	70.31
y-rot-e-002	471.458	17.95	8.40	39.8	33.22	-8.83	37.10	70.31
y-rot-e-003	471.457	21.98	8.50	42.5	13.72	-11.83	36.67	70.31
y-rot-e-004	461.455	13.98	8.93	27.6	50.60	-5.83	37.44	70.31
y-rot-e-005	461.454	16.10	7.92	27.1	26.21	-8.82	36.99	70.31
y-rot-e-006	461.453	22.25	8.15	28.5	16.39	-11.82	36.78	70.31
y-rot-e-007	451.452	14.76	9.76	16.4	58.16	-5.82	37.60	70.31
y-rot-e-008	451.450	22.89	8.18	14.2	20.45	-11.83	36.87	70.31
y-rot-e-009	451.451	21.01	7.80	13.1	56.49	-8.82	37.50	70.31
y-rot-e-010	441.449	15.00	7.77	-7.3	59.69	-5.83	37.59	70.31
y-rot-e-011	441.448	22.16	9.24	-6.4	66.54	-8.84	37.69	70.31
y-rot-e-012	441.447	27.21	9.67	-9.0	40.19	-11.83	37.22	70.31
y-rot-e-013	431.446	18.41	7.31	-22.0	95.55	-5.85	38.26	70.31
y-rot-e-014	421.442	20.76	7.62	-24.2	56.73	-8.86	37.49	70.31
y-rot-e-015	431.445	20.98	6.88	-18.6	60.84	-8.85	37.59	70.31
y-rot-e-016	431.444	26.48	8.33	-19.5	38.47	-11.85	37.18	70.31
y-rot-e-017	421.443	17.80	8.19	-30.0	85.10	-5.86	38.01	70.31
y-rot-e-018	421.441	27.54	9.04	-34.0	42.46	-11.86	37.24	70.31
y-rot-e-019	411.440	16.20	9.70	-50.7	63.91	-5.86	37.62	70.31
y-rot-e-020	411.439	20.03	9.57	-49.2	48.36	-8.85	37.32	70.31
y-rot-e-021	411.438	26.50	10.12	-49.2	37.68	-11.86	37.11	70.31

C.8.6 ECN yawed campaigns, plots of time series

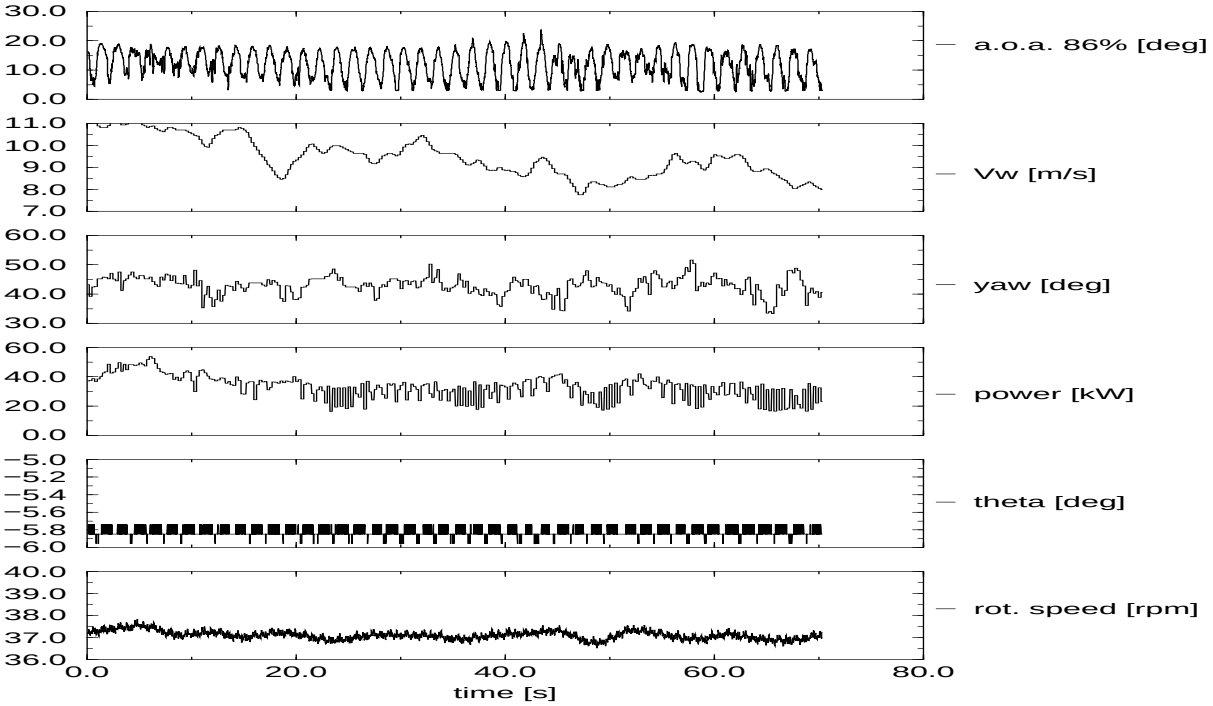

Figure C.81 *ECN: Time series of campaign y_rot_e_001*

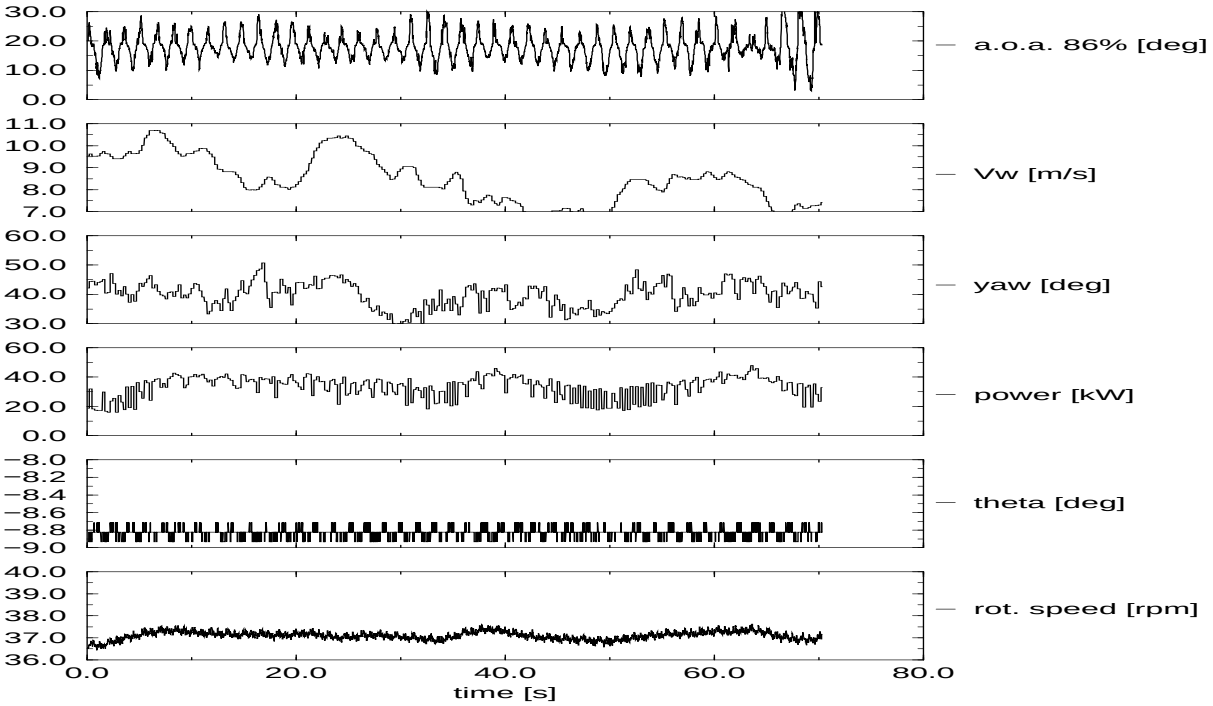

Figure C.82 *ECN: Time series of campaign y_rot_e_002*

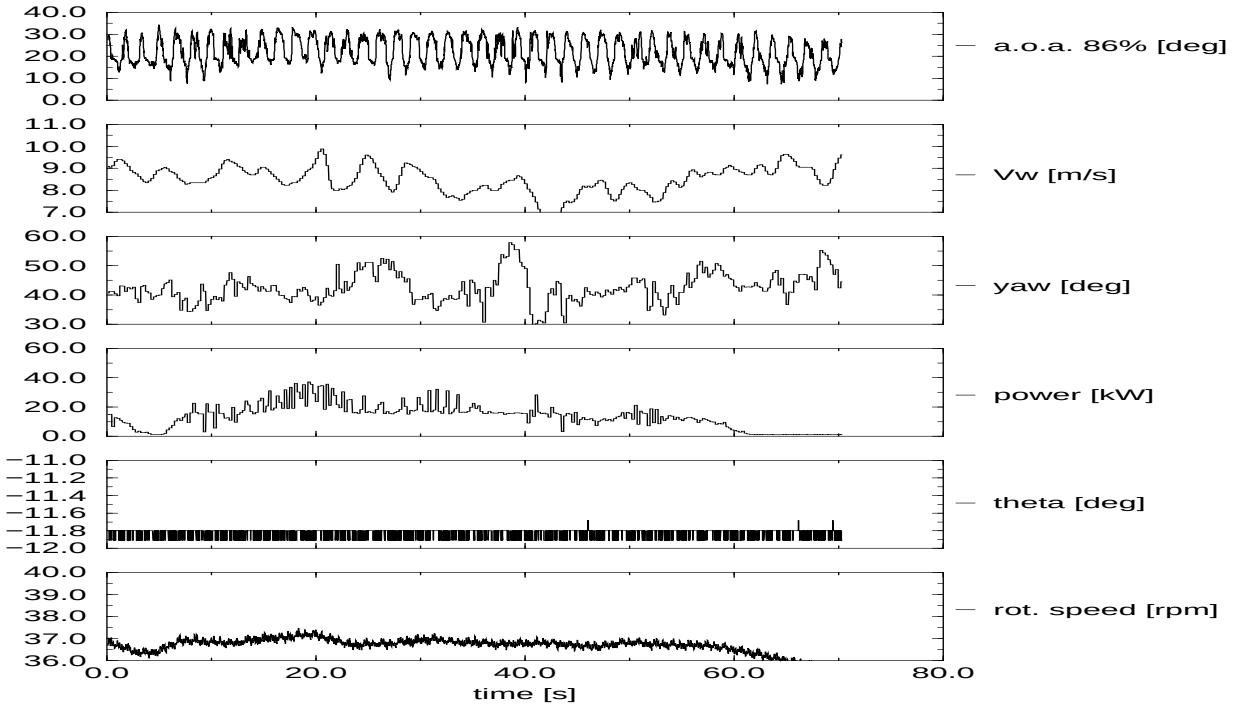

Figure C.83 *ECN: Time series of campaign y_rot_e_003*

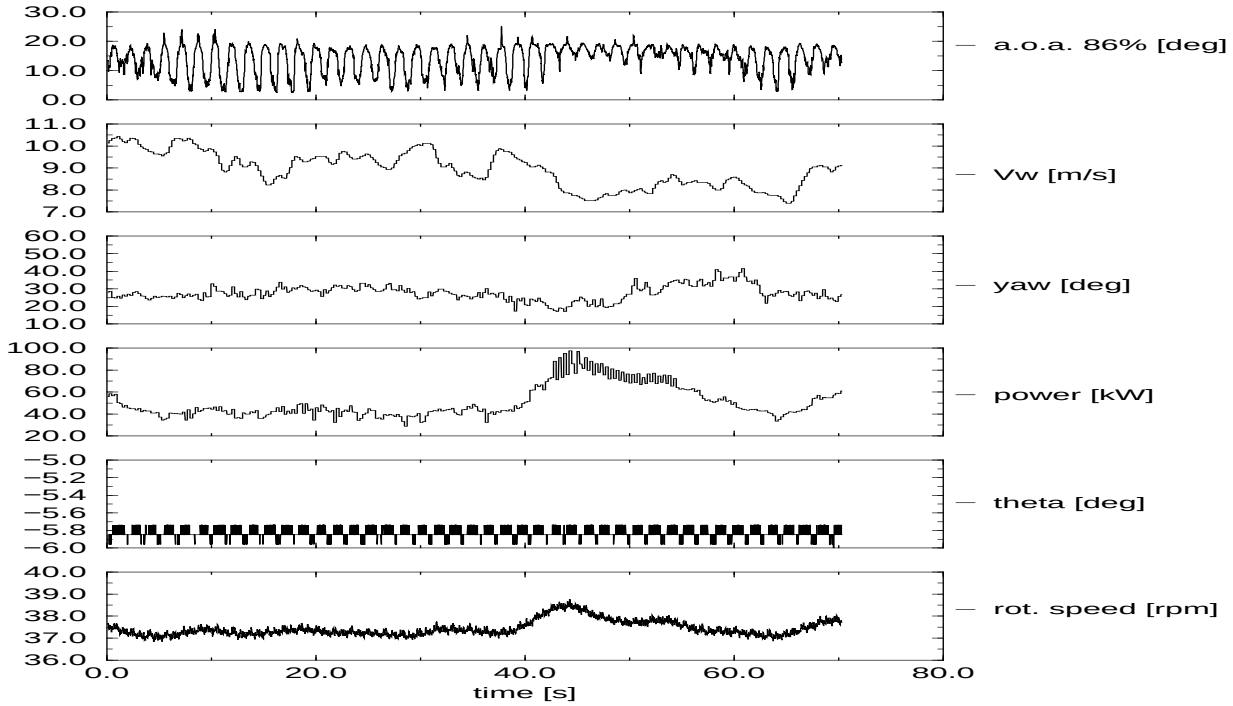

Figure C.84 *ECN: Time series of campaign y_rot_e_004*

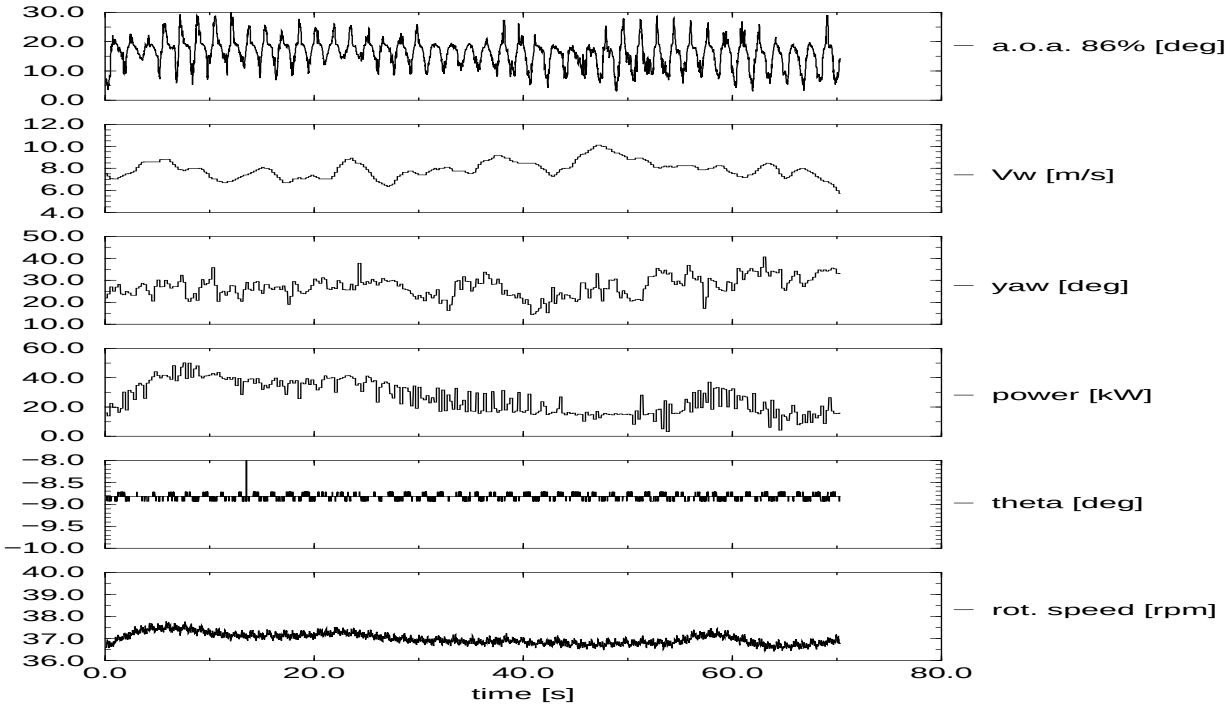

Figure C.85 *ECN: Time series of campaign y_rot_e_005*

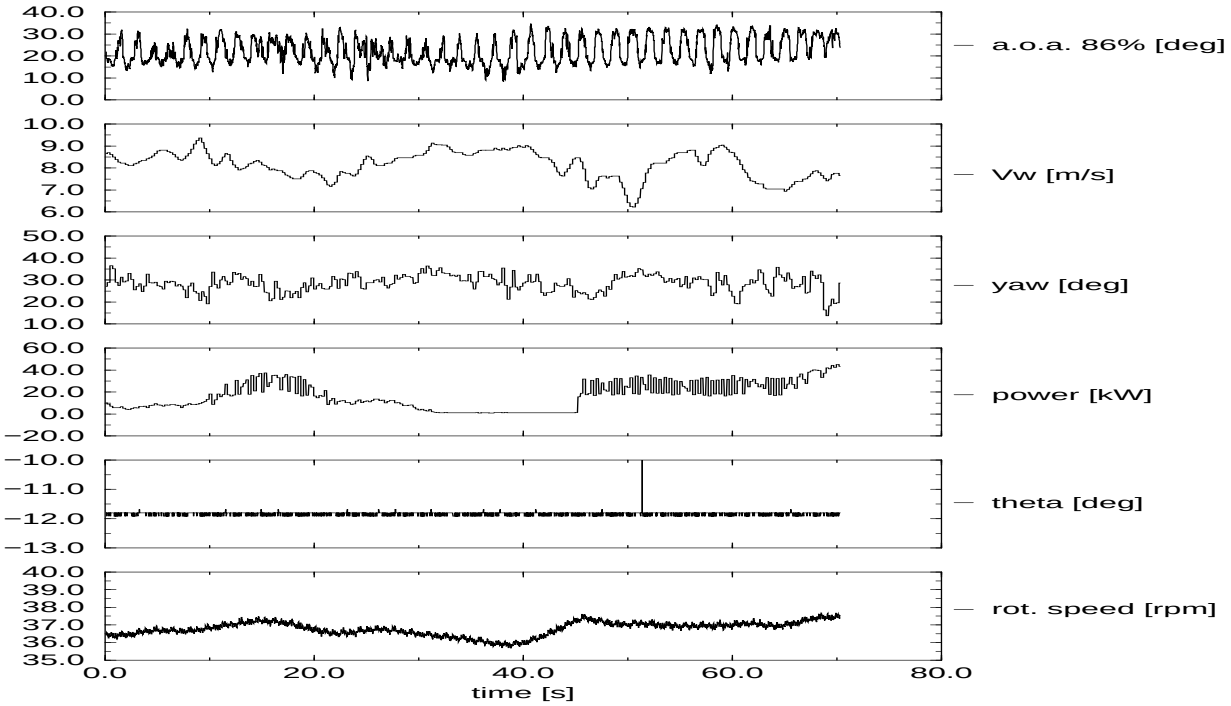

Figure C.86 *ECN: Time series of campaign y_rot_e_006*

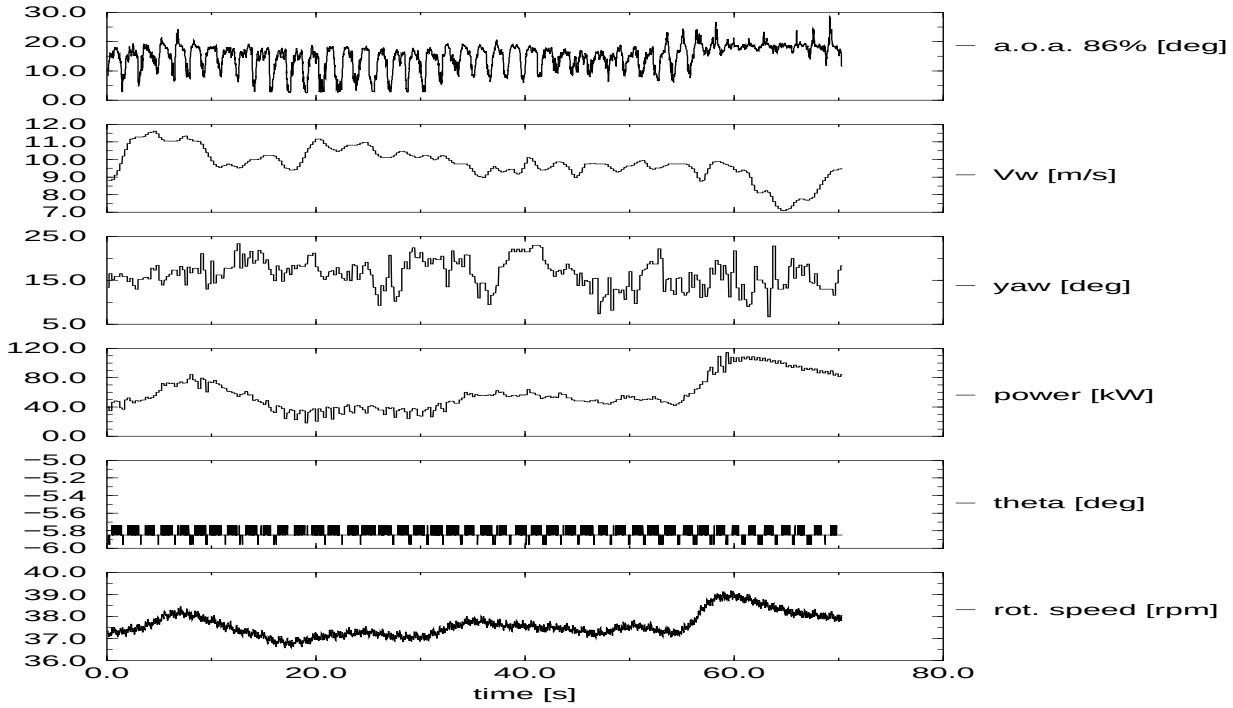

Figure C.87 *ECN: Time series of campaign y_rot_e_007*

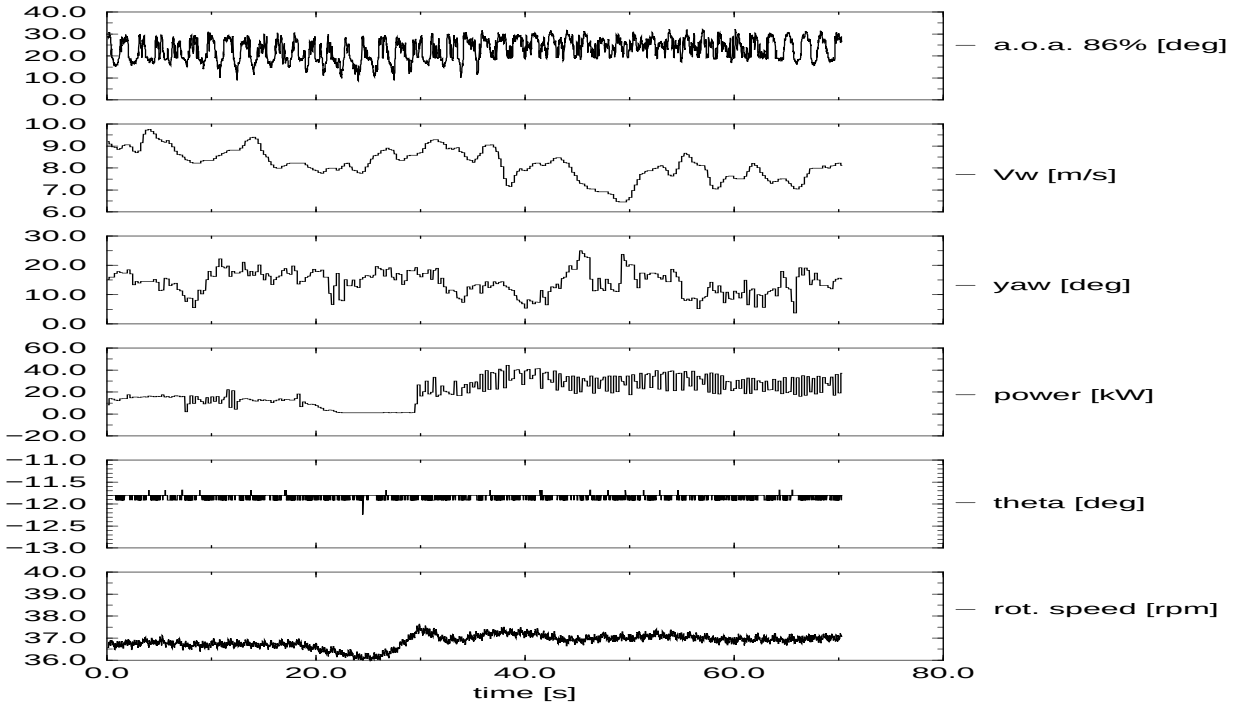

Figure C.88 *ECN: Time series of campaign y_rot_e_008*

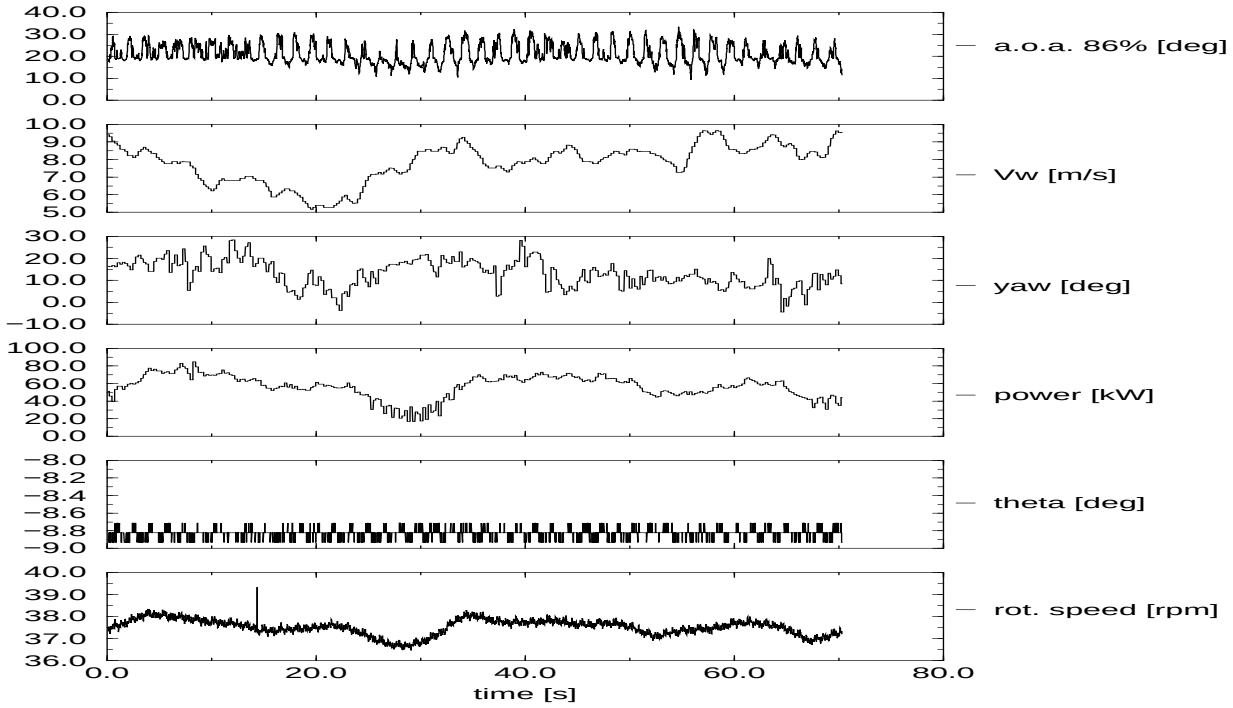

Figure C.89 *ECN: Time series of campaign y_rot_e_009*

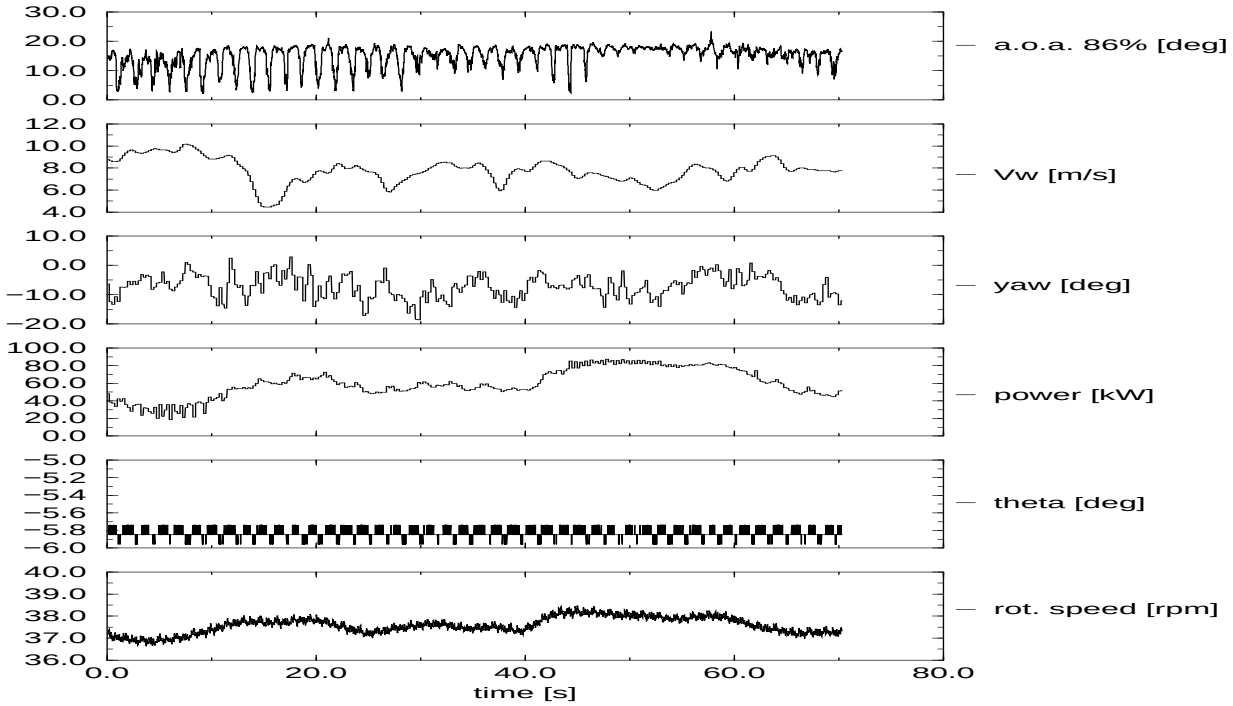

Figure C.90 *ECN: Time series of campaign y_rot_e_010*

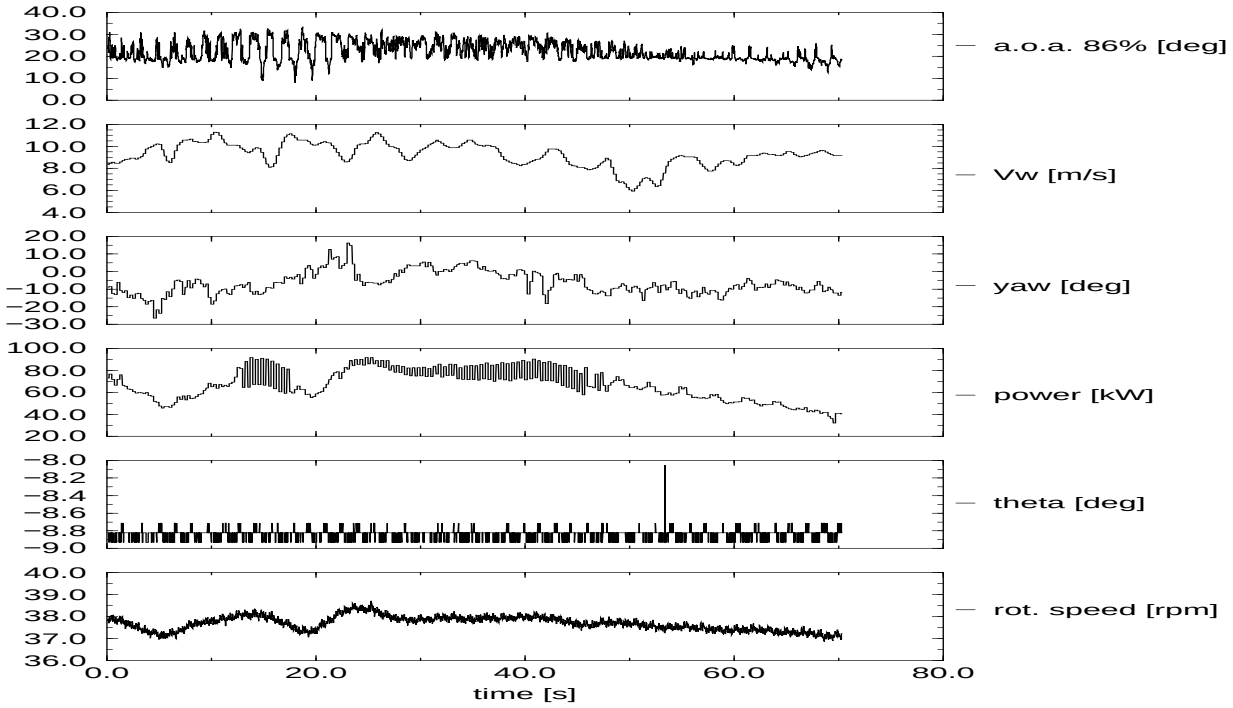

Figure C.91 *ECN: Time series of campaign y_rot_e_011*

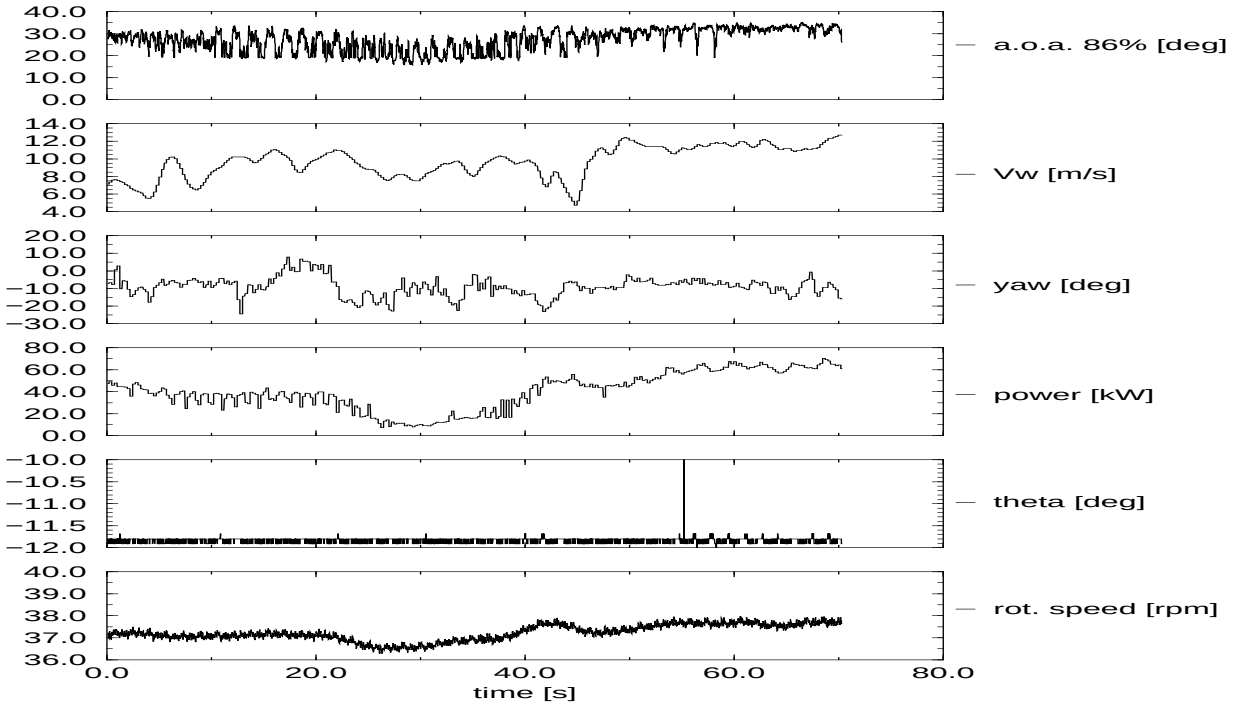

Figure C.92 *ECN: Time series of campaign y_rot_e_012*

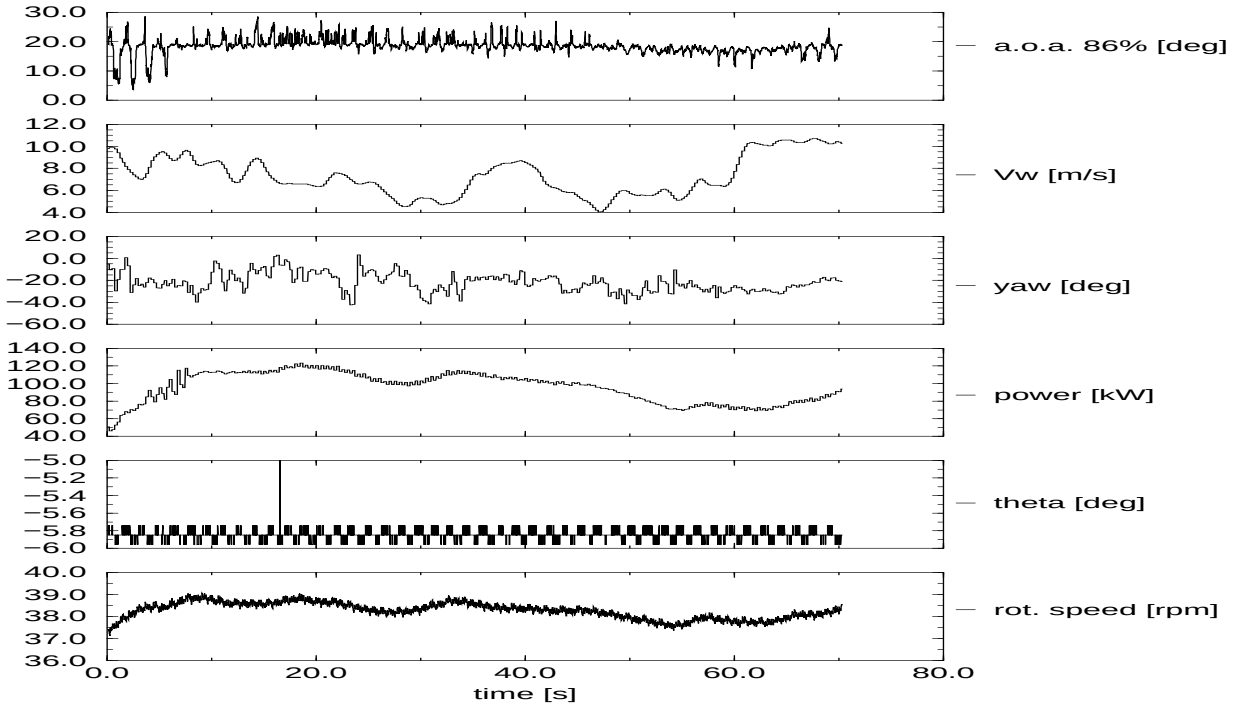

Figure C.93 *ECN: Time series of campaign y_rot_e_013*

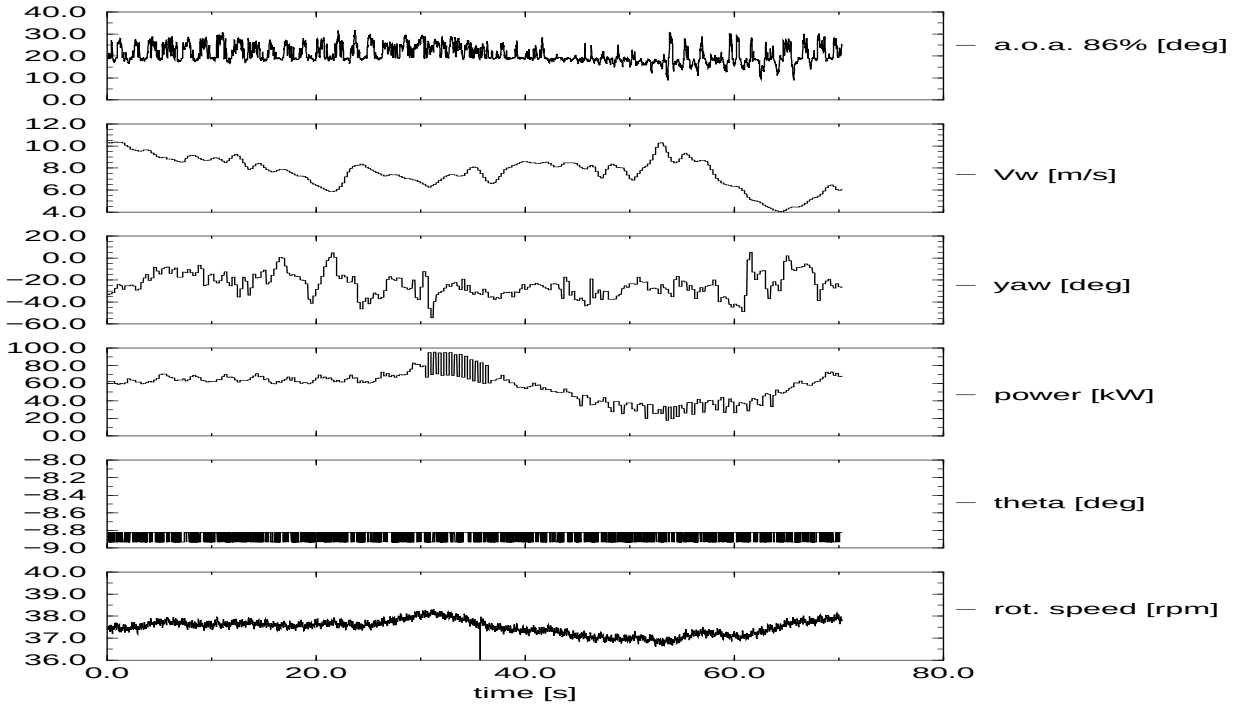

Figure C.94 *ECN: Time series of campaign y_rot_e_014*

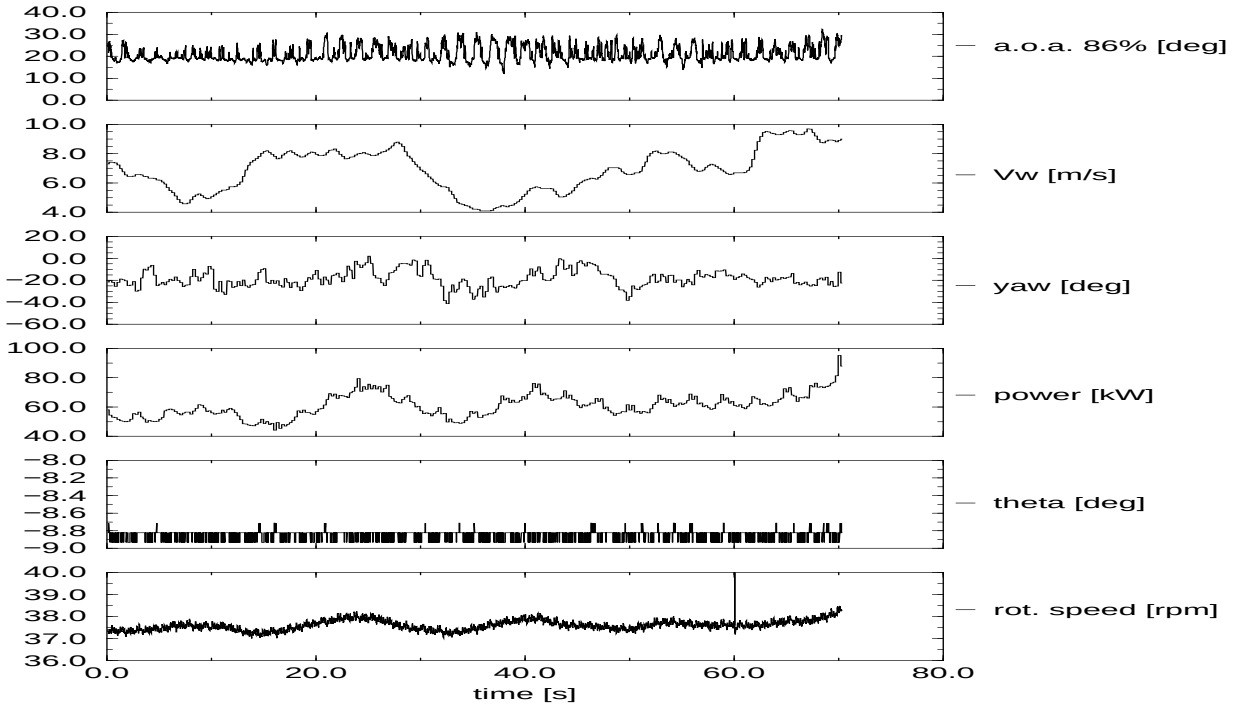

Figure C.95 *ECN: Time series of campaign y_rot_e_015*

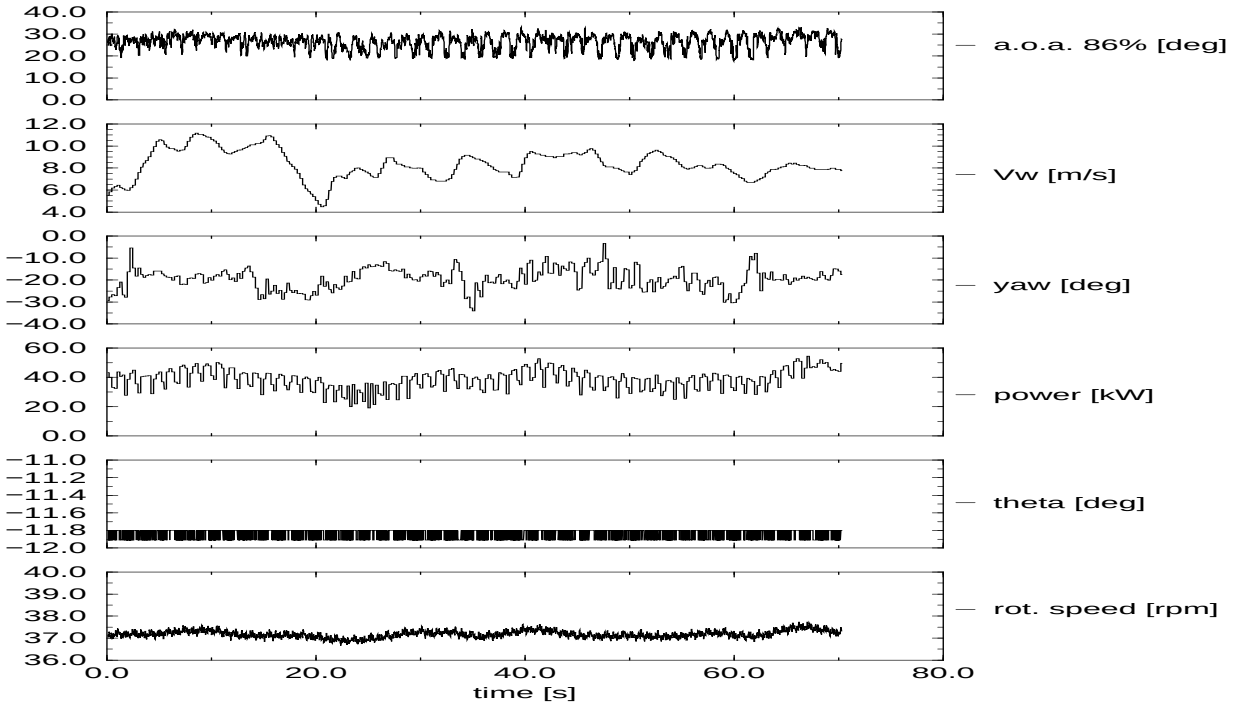

Figure C.96 *ECN: Time series of campaign y_rot_e_016*

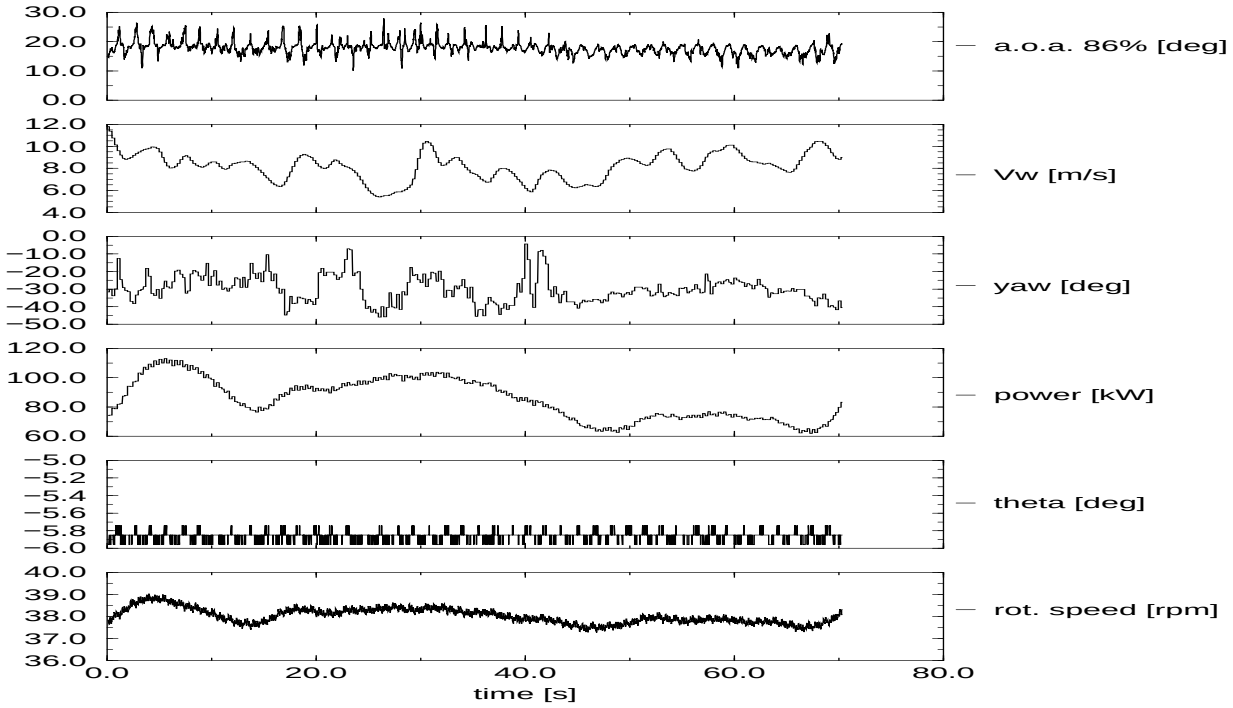

Figure C.97 *ECN: Time series of campaign y_rot_e_017*

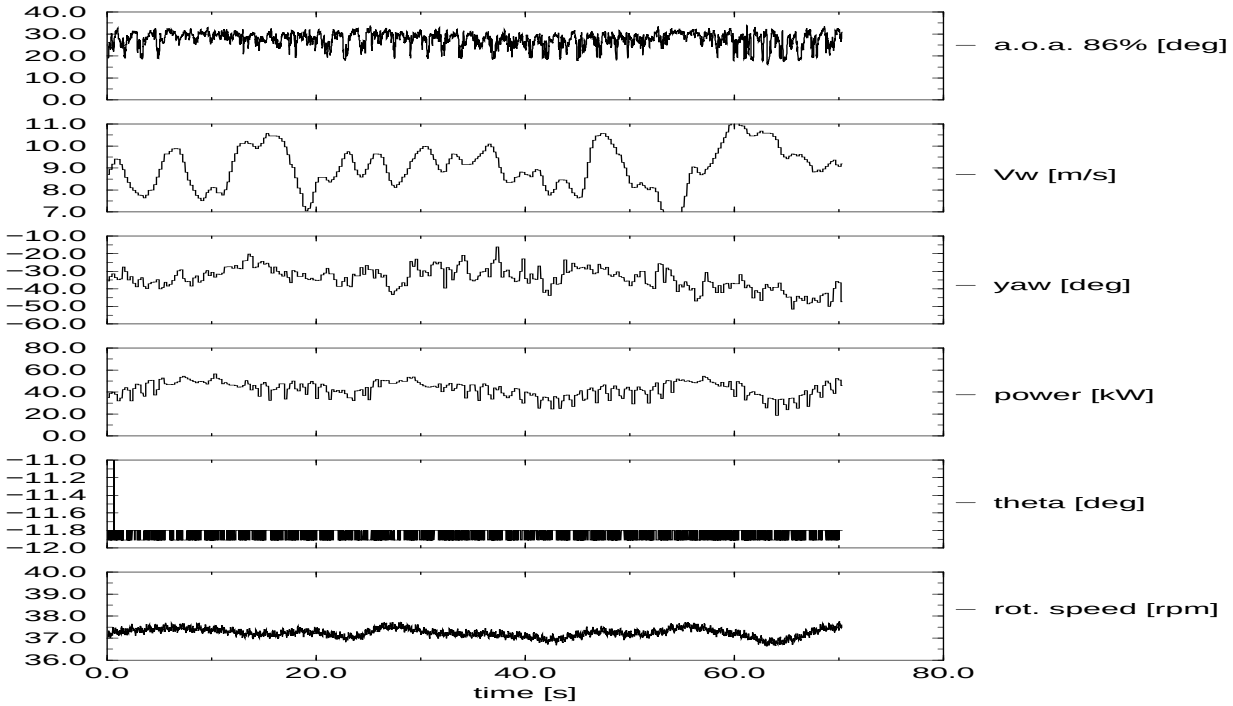

Figure C.98 *ECN: Time series of campaign y_rot_e_018*

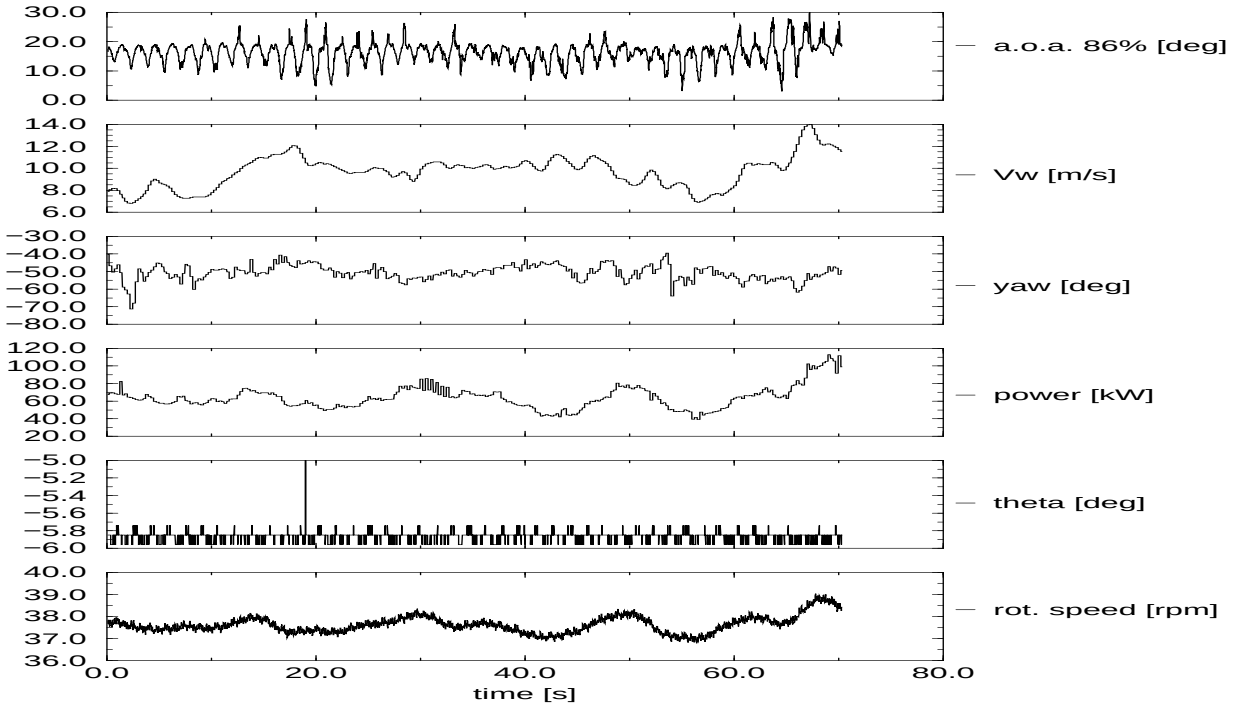

Figure C.99 *ECN: Time series of campaign y_rot_e_019*

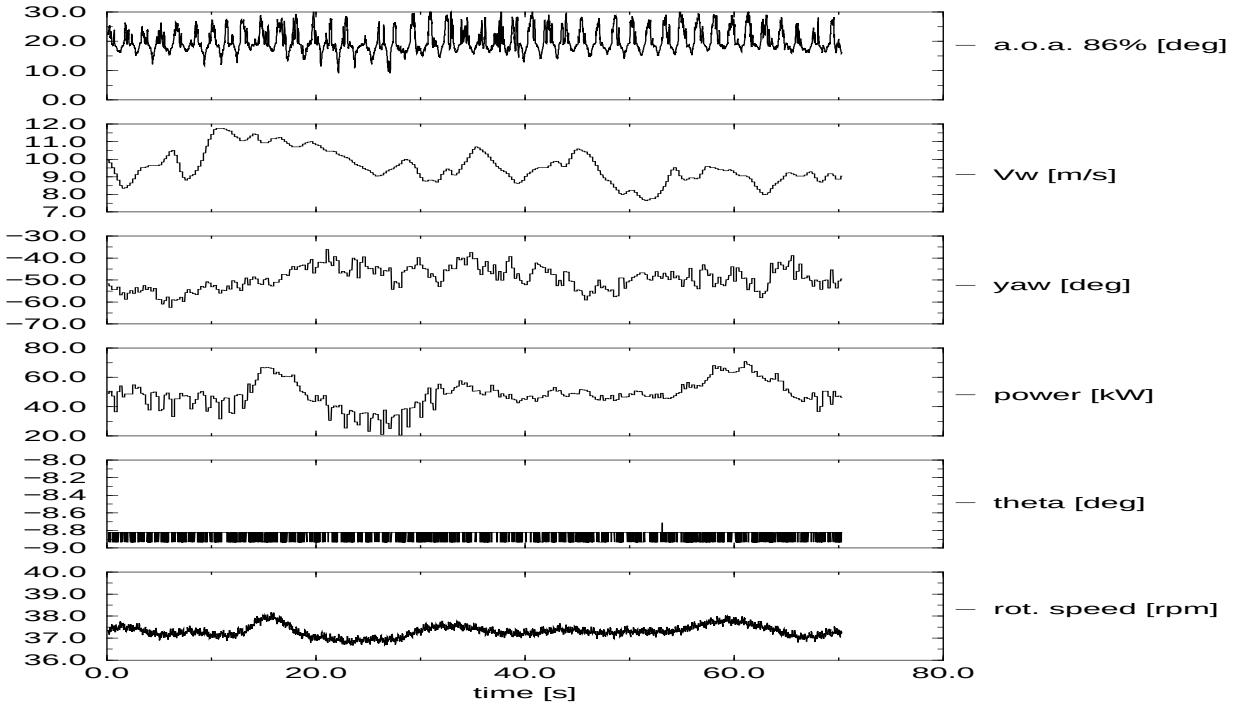

Figure C.100 *ECN: Time series of campaign y_rot_e_020*

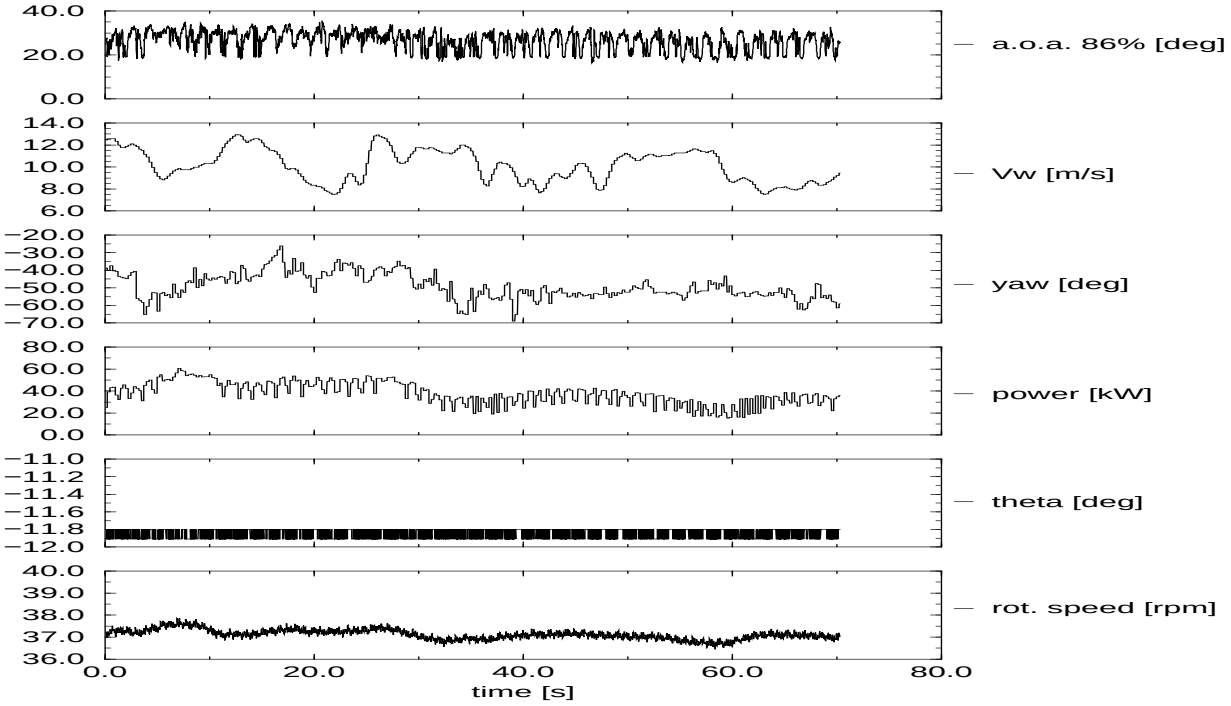

Figure C.101 *ECN: Time series of campaign y_rot_e_021*

C.9 ECN turbine and sectional coefficients

C.9.1 ECN, 2D profile coefficients

The 2D profile coefficients for the ECN test turbine are zipped into '/data/ecn/2D/coef2d_e.zip, which contain the following 10 files:

- cla1_2D_e; This file contains the $c_l - \alpha$ data for the NACA4423 profile at 30% span;
- cla2_2D_e; This file contains the $c_l - \alpha$ data for the NACA4420 profile at 60% span;
- cla3_2D_e; This file contains the $c_l - \alpha$ data for the NACA4418 at 80% span;
- cda1_2D_e This file contains the $c_d - \alpha$ data for the NACA4423 profile at 30% span;
- cda2_2D_e This file contains the $c_d - \alpha$ data for the NACA4420 profile at 60% span;
- cda3_2D_e This file contains the $c_d - \alpha$ data for the NACA4418 profile at 80% span;

The data are shown in figure D.8 and D.9;

C.9.2 ECN, rotating profile coefficients

The ECN 3D, rotating profile coefficients are measured for different angles of attack. The data are zipped into '/data/ecn/rotcoef/pit_vari/coef_e.zip, which contains the following 9 files:

- cna1_rot_e: This file contains the $c_n - \alpha$ data for the 30% section.
- cna2_rot_e: This file contains the $c_n - \alpha$ data for the 60% section.
- cna3_rot_e: This file contains the $c_n - \alpha$ data for the 80% section.
- cta1_rot_e: This file contains the $c_t - \alpha$ data for the 30% section.
- cta2_rot_e: This file contains the $c_t - \alpha$ data for the 60% section.
- cta3_rot_e: This file contains the $c_t - \alpha$ data for the 80% section.
- cnct1_rot_e: This file contains the $c_n - c_t$ data for the 30% section.
- cnct2_rot_e: This file contains the $c_n - c_t$ data for the 60% section.
- cnct3_rot_e: This file contains the $c_n - c_t$ data for the 80% section.

Some of the data are shown graphically in the figures C.102 to C.107.

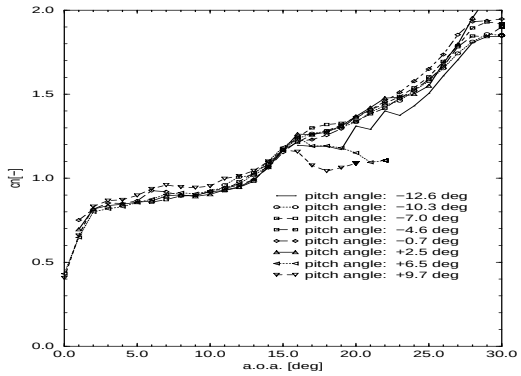

Figure C.102 *ECN measurements (r/R = 0.3) of* $c_n - \alpha$ *at different pitch angles*

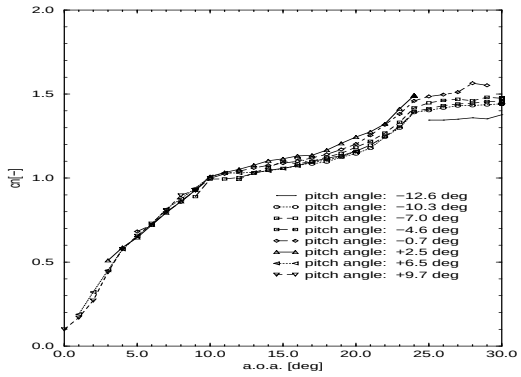

Figure C.103 *ECN measurements (r/R = 0.6) of* $c_n - \alpha$ *at different pitch angles*

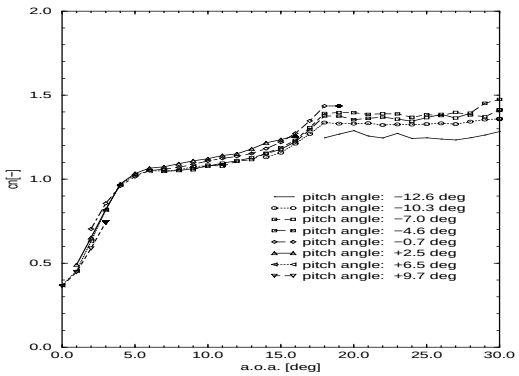

Figure C.104 *ECN measurements (r/R = 0.8) of* $c_n - \alpha$ *at different pitch angles*

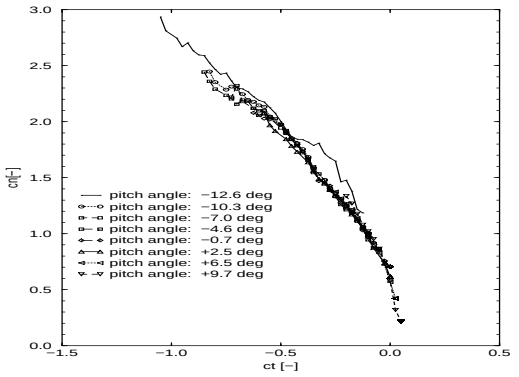

Figure C.105 *ECN measurements (r/R = 0.3) of* $c_n - c_t$ *at different pitch angles*

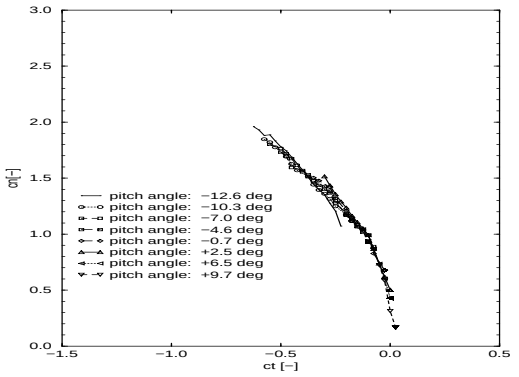

Figure C.106 *ECN measurements (r/R = 0.6) of* $c_n - c_t$ *at different pitch angles*

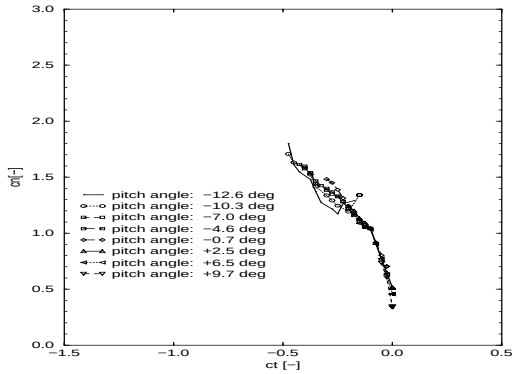

Figure C.107 *ECN measurements (r/R = 0.8) of* $c_n - c_t$ *at different pitch angles*

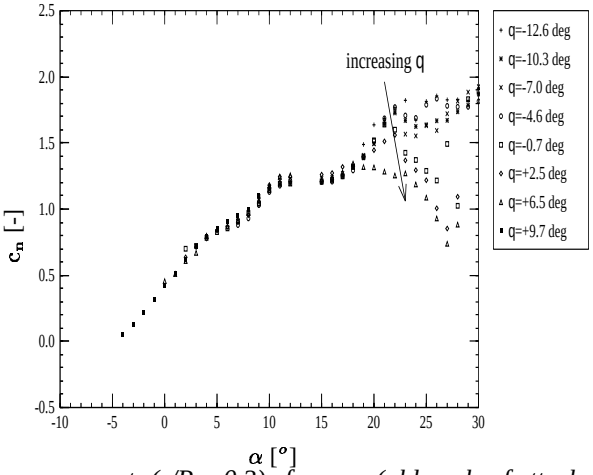

Figure C.108 *ECN measurements (r/R = 0.3) of* $c_n - \alpha$ *(old angle of attack definition) at different pitch angles*

C.10 DUT time series

C.10.1 DUT time series: Non-rotating campaigns

The files are stored into directory 'data/dut/stilltim/70percent/'. They are sorted in order of increasing angle of attack. Non-rotating campaings are only available for the 70% section.

Table C.18 *Global overview of DUT measurement file for non-rotating conditions*

file	DUT filename	$\overline{V}$ m/s	$\overline{\phi_y}$ deg	$\overline{\Omega}$ rpm	$\overline{\text{Power}}$ kW	$\overline{\alpha_{70\%}}$ deg	$\overline{\theta_{tip}}$ deg	duration s
non-d_001.70	PC330708	0.339	4.577	0.383	0.197	-2.907	4.0	69.267
non-d_002.70	PC340708	0.542	9.795	0.383	0.349	-2.375	4.0	62.622
non-d_003.70	PC320708	0.503	5.626	0.448	0.199	-2.251	4.0	76.785
non-d_004.70	PC060712	0.768	10.118	0.627	0.498	-1.862	4.0	64.218
non-d_005.70	PC310708	0.550	10.258	0.446	0.231	-1.781	4.0	88.635
non-d_006.70	PC420708	0.351	9.296	0.443	0.627	0.715	0.0	42.012
non-d_007.70	PC410708	0.475	10.724	0.214	0.265	0.856	0.0	36.756
non-d_008.70	PC440708	0.357	6.486	0.354	0.240	0.989	0.0	57.645
non-d_009.70	PC370708	0.423	7.056	0.204	0.254	1.007	0.0	48.720
non-d_010.70	PC360708	0.425	6.156	0.290	0.207	1.088	0.0	52.821
non-d_011.70	PC430708	0.503	8.798	0.440	0.452	1.160	0.0	48.633
non-d_012.70	PC400708	0.661	5.713	0.396	0.481	1.182	0.0	36.774
non-d_013.70	PC380708	0.686	11.971	0.434	0.817	1.476	0.0	44.403
non-d_014.70	PC450708	0.447	14.003	0.260	0.190	1.541	0.0	70.221
non-d_015.70	PC390708	0.801	10.437	0.576	0.620	1.629	0.0	41.790
non-d_016.70	PC350708	0.981	7.809	0.442	0.441	2.708	0.0	58.329

C.10.2 DUT non-rotating campaign, plots of time series

In this chapter only a limited number of time series for the non-rotating DUT campaigns are presented. Plots (pdf-files) for all campaigns can be found in the database: They are included in the zip files which contain the set of datafiles for every campaign.

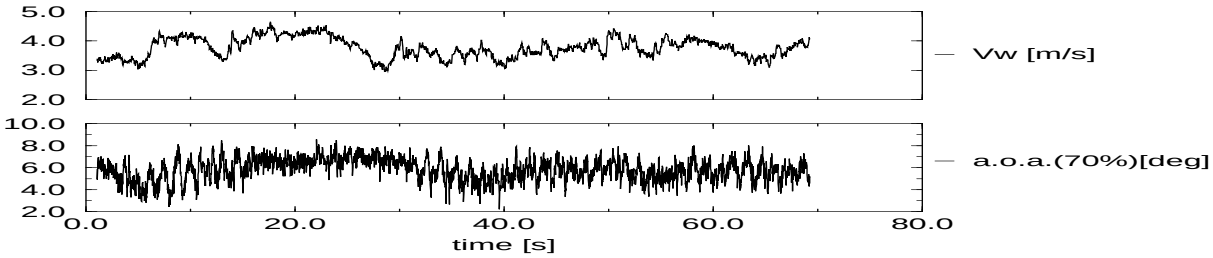

Figure C.109 *DUT: Time series of campaign non_d_001.70*

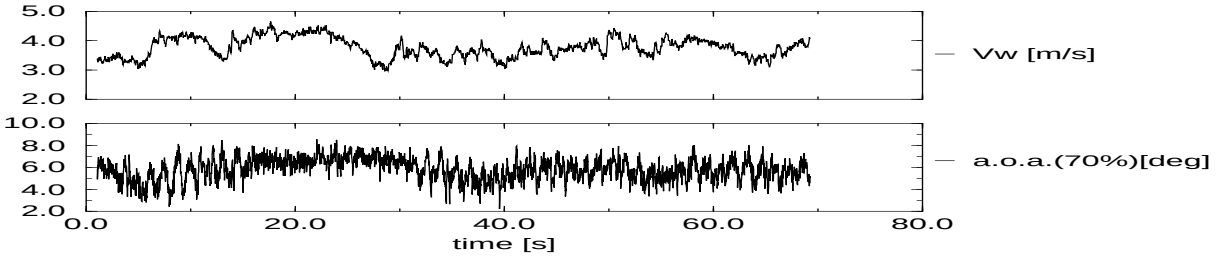

Figure C.110 *DUT: Time series of campaign non_d_006.70*

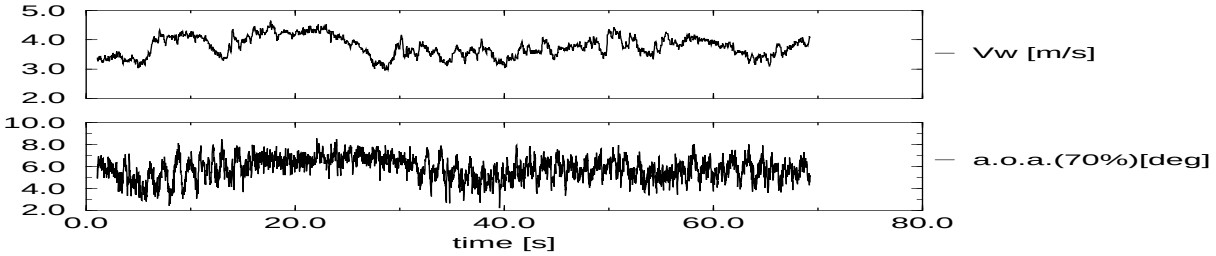

Figure C.111 *DUT: Time series of campaign non_d_011.70*

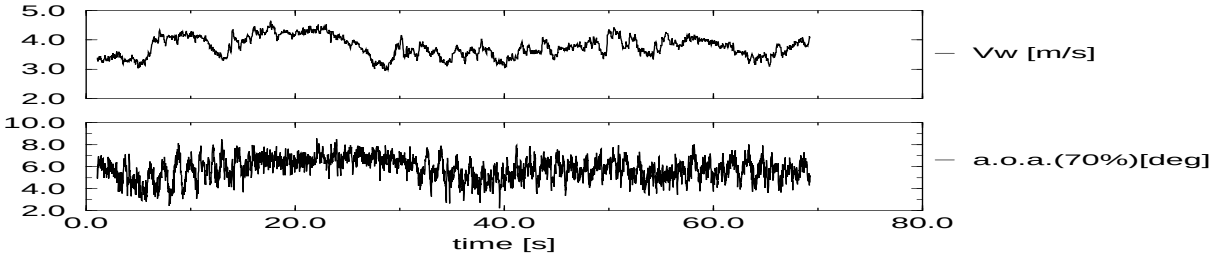

Figure C.112 *DUT: Time series of campaign non_d_016.70*

C.10.3 DUT time series: Non-yawed campaigns

It is noted that the angles of attack given in this section are derived from the geometrical angle of attack (atan (Ω. r/U)) and the pitch angle. The angles of attack from the 6-hole probes or from the match on the pressure distribution near the nose, see section 6.4 contain NaN's, which cannot be plotted.

DUT time series: Non-yawed campaigns at 30% span

The files are stored in directory '/data/dut/rottim/30percent' and numbered in order of increasing angle of attack, where the angle of attack is determined by the rotor speed, the wind speed and the pitch angle. see table C.19.

Table C.19 *Global overview of DUT non-yawed measurement files at 30% span*

file	DUT filename	$\overline{V}$ m/s	$\overline{\phi_y}$ deg	$\overline{\Omega}$ rpm	$\overline{\text{Power}}$ kW	$\overline{\alpha_{30\%}}$ deg	$\overline{\theta_{tip}}$ deg	duration s
ny_rot_d_001.30	PA110923	2.462	-3.105	101.60	-3.192	10.76	-2.0	41.835
ny_rot_d_002.30	PA120923	2.621	1.294	101.70	-3.242	11.31	-2.0	42.009
ny_rot_d_003.30	PA160923	2.192	-4.400	75.64	-1.226	12.40	-2.0	55.920
ny_rot_d_004.30	PA050923	2.722	4.216	86.30	-1.869	13.33	-2.0	49.176
ny_rot_d_005.30	PA090923	3.624	-2.144	96.36	-2.135	15.44	-2.0	44.136
ny_rot_d_006.30	PA321002	3.729	-2.735	91.27	-3.317	16.54	-2.0	46.194
ny_rot_d_007.30	PA191002	4.311	-2.573	95.77	-2.782	17.93	-2.0	44.061
ny_rot_d_008.30	PA221002	4.859	-0.677	106.20	-5.130	18.20	-2.0	39.873
ny_rot_d_009.30	PA300923	3.154	2.930	91.24	-3.156	18.37	-6.0	46.206
ny_rot_d_010.30	PA211002	5.595	1.937	106.50	-2.546	20.41	-2.0	40.119
ny_rot_d_011.30	PA440923	3.227	3.758	71.88	-1.105	21.76	-6.0	58.641
ny_rot_d_012.30	PA241002	5.329	3.700	91.63	0.338	22.17	-2.0	46.365
ny_rot_d_013.30	PA231002	5.648	-0.391	96.07	1.056	22.36	-2.0	44.238
ny_rot_d_014.30	PA330923	4.036	4.056	86.31	-1.736	22.42	-6.0	48.960
ny_rot_d_015.30	PA181002	5.684	3.008	96.09	-1.857	22.57	-2.0	44.283
ny_rot_d_016.30	PA400923	3.453	-1.293	71.82	-0.849	22.83	-6.0	58.650
ny_rot_d_017.30	PA030923	4.611	-4.104	76.22	0.262	23.02	-2.0	55.548
ny_rot_d_018.30	PA171002	5.859	-2.832	95.98	-1.772	23.15	-2.0	44.082
ny_rot_d_019.30	PA411002	5.403	1.994	86.42	-0.086	23.50	-2.0	48.825
ny_rot_d_020.30	PA900922	4.443	4.741	86.90	-0.055	23.99	-6.0	48.771
ny_rot_d_021.30	PA730922	3.760	4.100	71.74	0.306	24.28	-6.0	58.698
ny_rot_d_022.30	PA850922	5.601	-2.102	107.40	-0.208	24.31	-6.0	39.375
ny_rot_d_023.30	PA890922	4.794	3.644	91.66	0.679	24.36	-6.0	46.041
ny_rot_d_024.30	PA161002	6.258	-3.472	95.57	0.223	24.46	-2.0	44.481
ny_rot_d_025.30	PA111002	6.110	4.209	91.04	1.849	25.01	-2.0	46.692
ny_rot_d_026.30	PA261002	6.354	-3.005	91.61	0.752	25.70	-2.0	46.347
ny_rot_d_027.30	PA800922	5.180	-2.212	90.85	1.609	25.86	-6.0	46.425
ny_rot_d_028.30	PA251002	6.405	-2.079	91.49	2.111	25.94	-2.0	46.452
ny_rot_d_029.30	PA820922	6.424	0.562	96.31	3.631	28.84	-6.0	43.770
ny_rot_d_030.30	PA421002	6.996	3.351	86.46	4.285	29.17	-2.0	49.128

DUT time series: Non-yawed campaigns at 50% span

The files are stored in directory '/data/dut/rottim/50percent' and numbered in order of increasing angle of attack, where the angle of attack is determined by the rotor speed, the wind speed and the pitch angle. see table C.20.

Table C.20 *Global overview of DUT non-yawed measurement files at 50% span*

file	DUT filename	$\overline{V}$ m/s	$\overline{\phi_y}$ deg	$\overline{\Omega}$ rpm	$\overline{\text{Power}}$ kW	$\overline{\alpha_{50\%}}$ deg	$\overline{\theta_{tip}}$ deg	duration s
ny_rot_d_001.50	PB081124	4.297	2.134	85.65	1.618	10.83	0.0	34.764
ny_rot_d_002.50	PB101124	4.341	-0.488	69.80	2.369	13.30	0.0	43.236
ny_rot_d_003.50	PB091123	4.657	-4.878	69.79	2.222	14.28	0.0	42.921
ny_rot_d_004.50	PB091124	5.983	1.818	85.38	5.094	14.98	0.0	35.352
ny_rot_d_005.50	PB081123	4.255	-2.506	59.74	1.715	15.14	0.0	50.142
ny_rot_d_006.50	PB071124	5.618	3.579	69.08	4.223	17.22	0.0	43.527
ny_rot_d_007.50	PB051124	4.634	-2.759	49.66	2.056	19.55	0.0	60.294
ny_rot_d_008.50	PB061124	6.081	1.285	59.40	3.810	21.12	0.0	50.967
ny_rot_d_009.50	PB161123	4.887	-4.920	38.70	1.363	25.63	0.0	77.232

DUT time series: Non-yawed campaigns at 70% span
The files are stored in directory '/data/dut/rottim/70percent' and numbered in order of increasing angle of attack, where the angle of attack is determined by the rotor speed, the wind speed and the pitch angle. see table C.21.

Table C.21 *Global overview of DUT non-yawed measurement files at 70% span*

file	DUT filename	$\overline{V}$ m/s	$\overline{\phi_y}$ deg	$\overline{\Omega}$ rpm	$\overline{\text{Power}}$ kW	$\overline{\alpha_{70\%}}$ deg	$\overline{\theta_{tip}}$ deg	duration s
ny_rot_d_001.70	PC080803	3.265	-0.514	69.590	0.572	3.29	4.0	43.467
ny_rot_d_002.70	PC060803	2.985	-0.021	49.820	0.767	5.27	4.0	58.764
ny_rot_d_003.70	PC160712	3.020	-0.343	45.121	0.607	6.34	4.0	69.228
ny_rot_d_004.70	PC190712	4.564	0.941	59.974	1.695	7.71	4.0	51.963
ny_rot_d_005.70	PC300722	4.258	-0.124	54.610	1.949	7.99	4.0	58.122
ny_rot_d_006.70	PC180712	4.547	-0.327	54.163	1.662	8.89	4.0	57.669
ny_rot_d_007.70	PC210712	6.015	-4.420	69.708	4.729	9.22	4.0	45.396
ny_rot_d_008.70	PC170712	4.498	-2.711	50.139	1.647	9.74	4.0	62.316
ny_rot_d_009.70	PC310722	4.568	3.916	50.080	1.894	9.93	4.0	62.094
ny_rot_d_010.70	PC150712	3.740	0.244	39.383	0.959	10.51	4.0	79.992
ny_rot_d_011.70	PC070712	5.092	3.799	55.322	2.481	10.07	4.0	56.229
ny_rot_d_012.70	PC320722	5.314	-3.061	45.240	2.202	13.72	4.0	68.826
ny_rot_d_013.70	PC330722	4.637	-4.172	39.230	1.302	13.82	4.0	80.196
ny_rot_d_014.70	PC140712	4.908	1.376	34.683	1.222	17.05	4.0	90.312

C.10.4 DUT non-yawed campaigns, plots of time series

In this chapter, only a limited number of time series is shown for the non-yawed DUT campaings at the three different sections Plots (pdf-files) for all campaigns can be found in the database: They are included in the zip files which contain the set of datafiles for every campaign. It is reminded that the angle of attack is derived from the geometrical angle of attack and the pitch angle.

DUT time series: Non-yawed campaigns at 30% span, plots

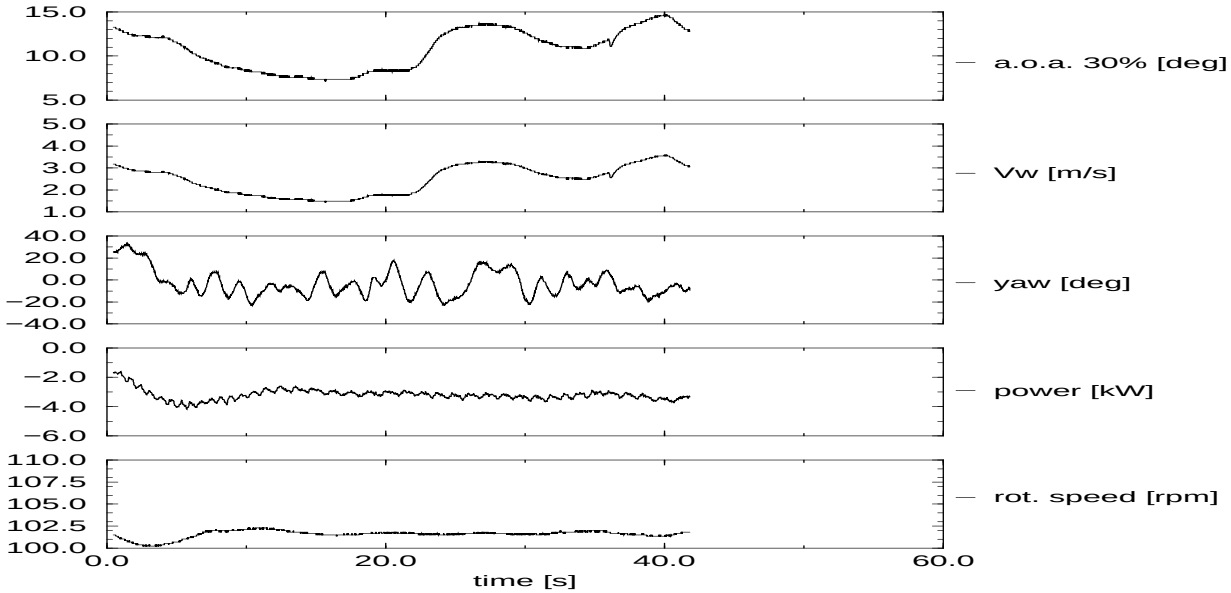

Figure C.113 *DUT: Time series of campaign ny_rot_d_001.30*

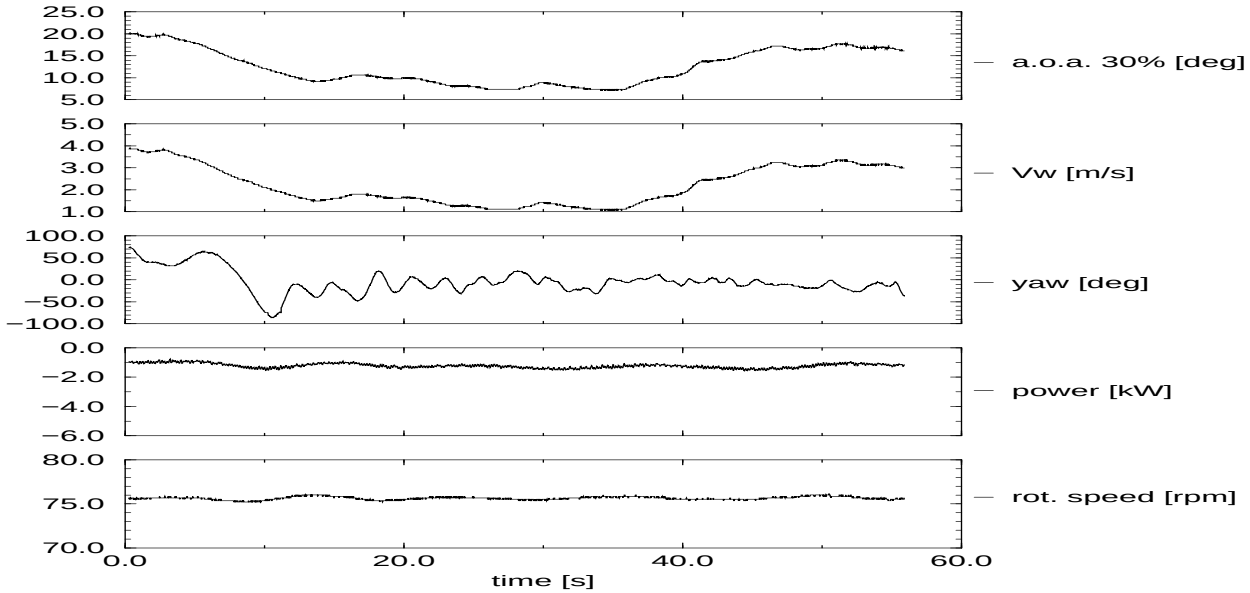

Figure C.114 *DUT: Time series of campaign ny_rot_d_003.30*

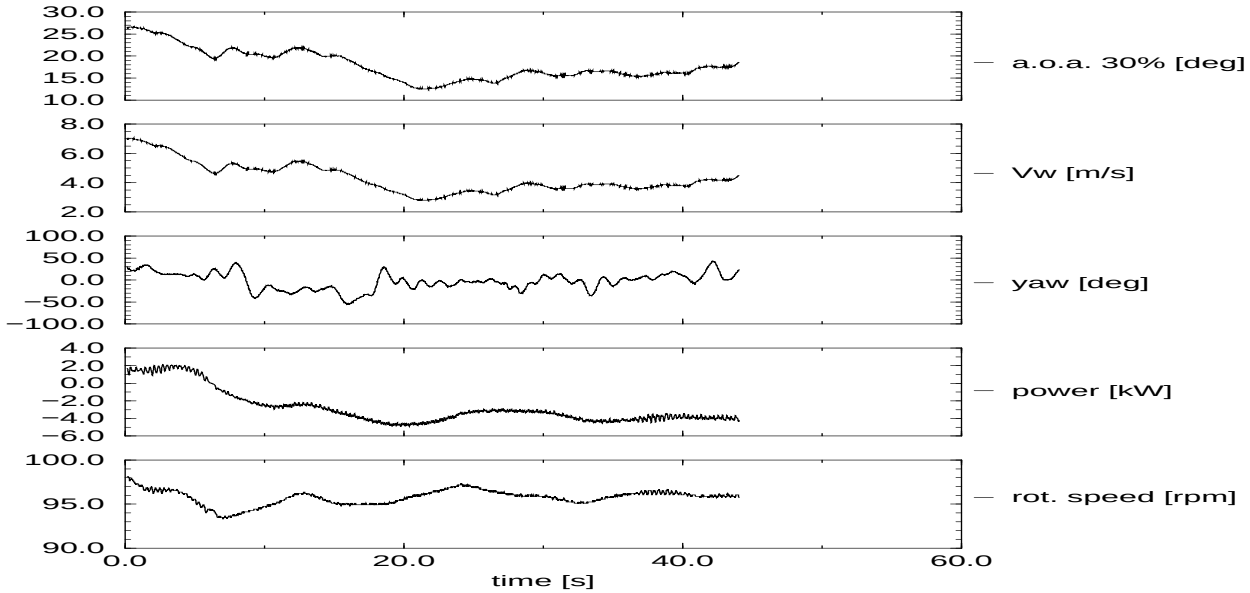

Figure C.115 *DUT: Time series of campaign ny_rot_d_007.30*

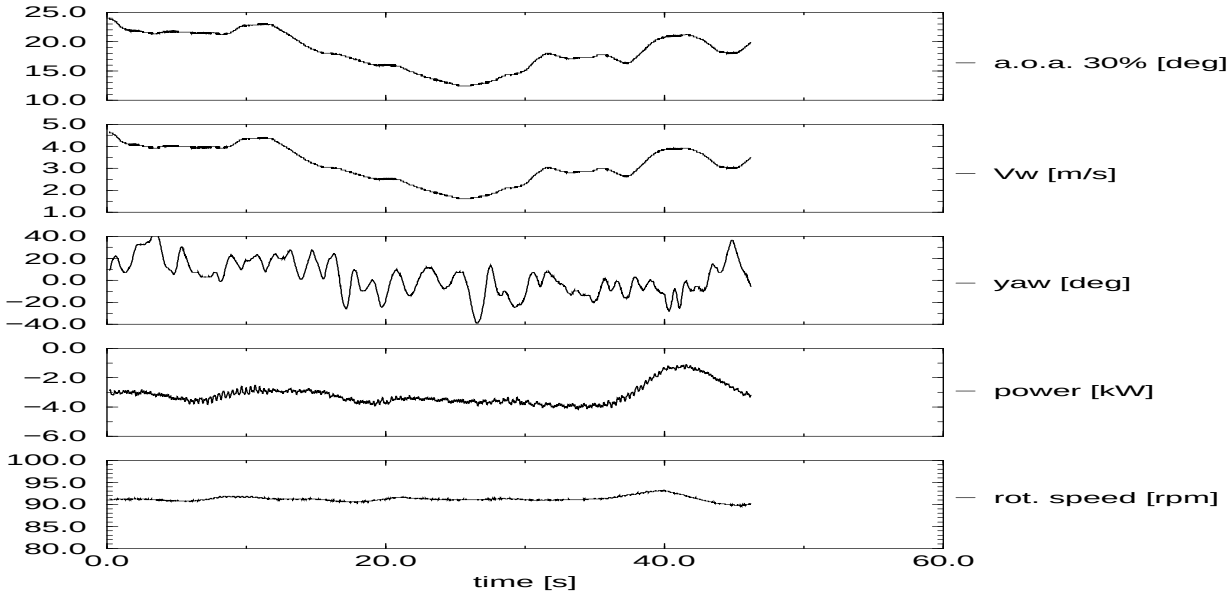

Figure C.116 *DUT: Time series of campaign ny_rot_d_009.30*

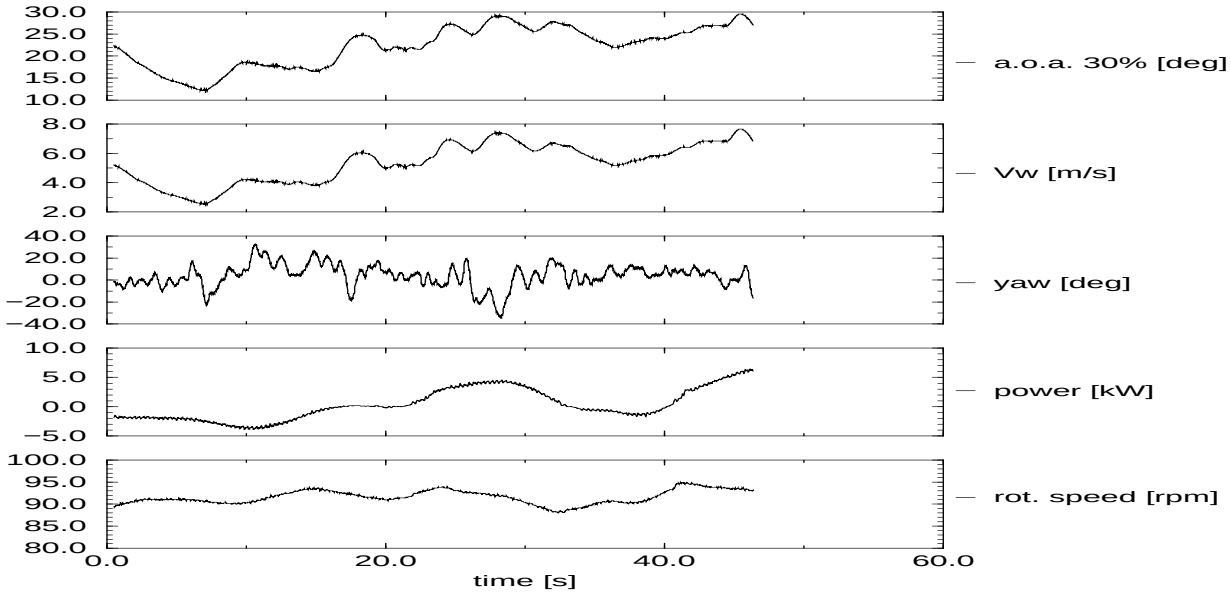

Figure C.117 *DUT: Time series of campaign ny_rot_d_012.30*

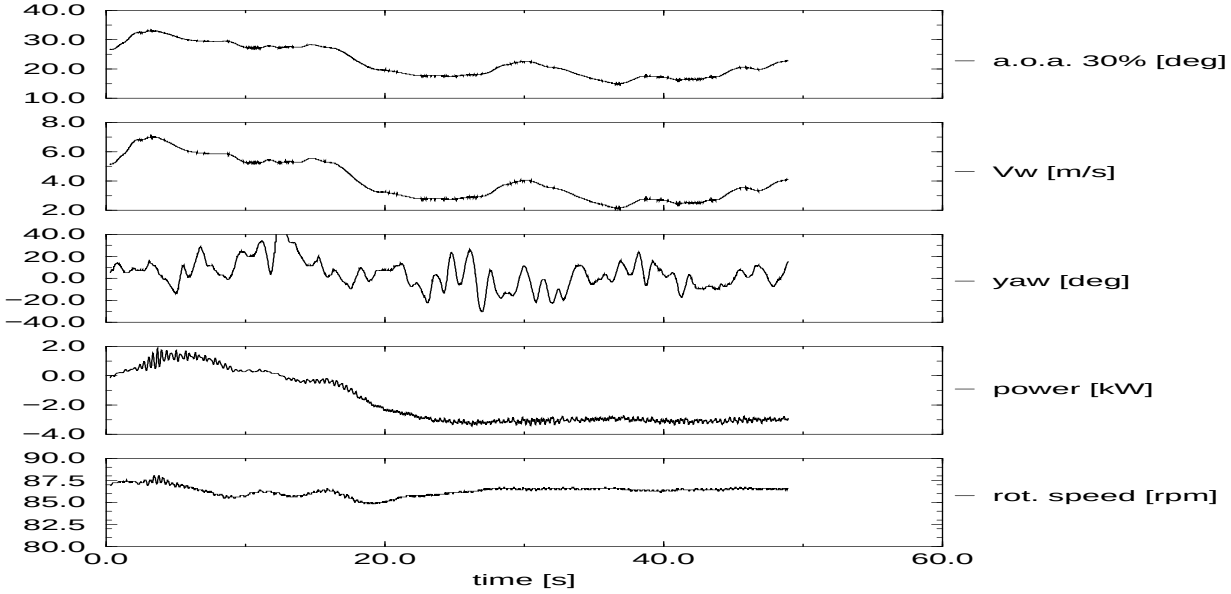

Figure C.118 *DUT: Time series of campaign ny_rot_d_014.30*

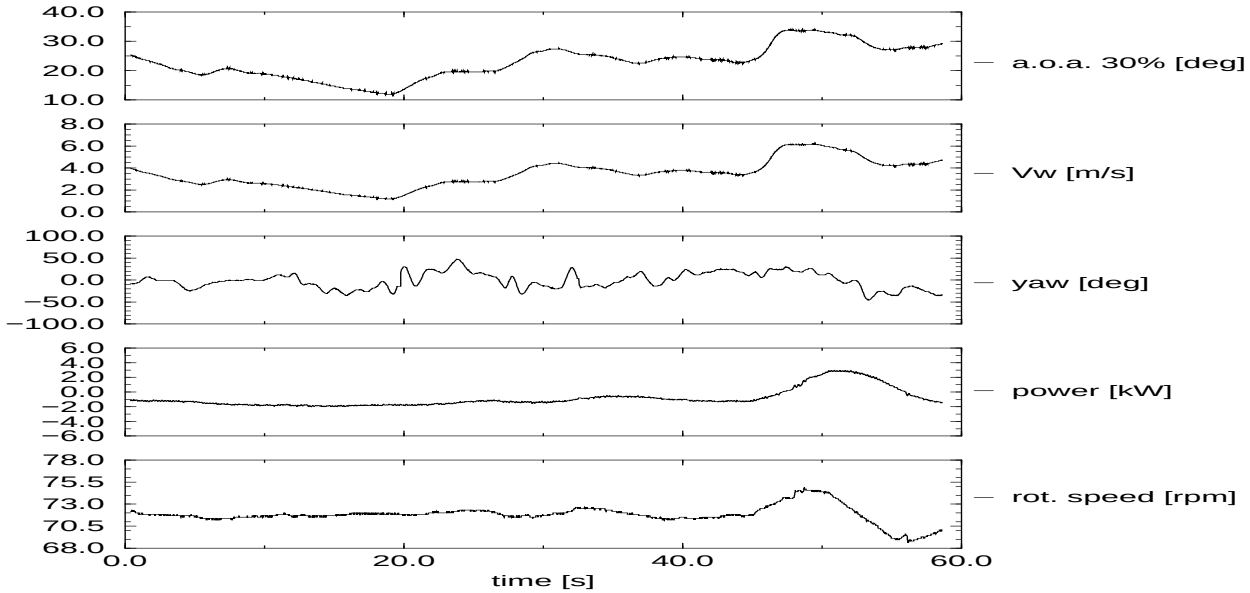

Figure C.119 *DUT: Time series of campaign ny_rot_d_016.30*

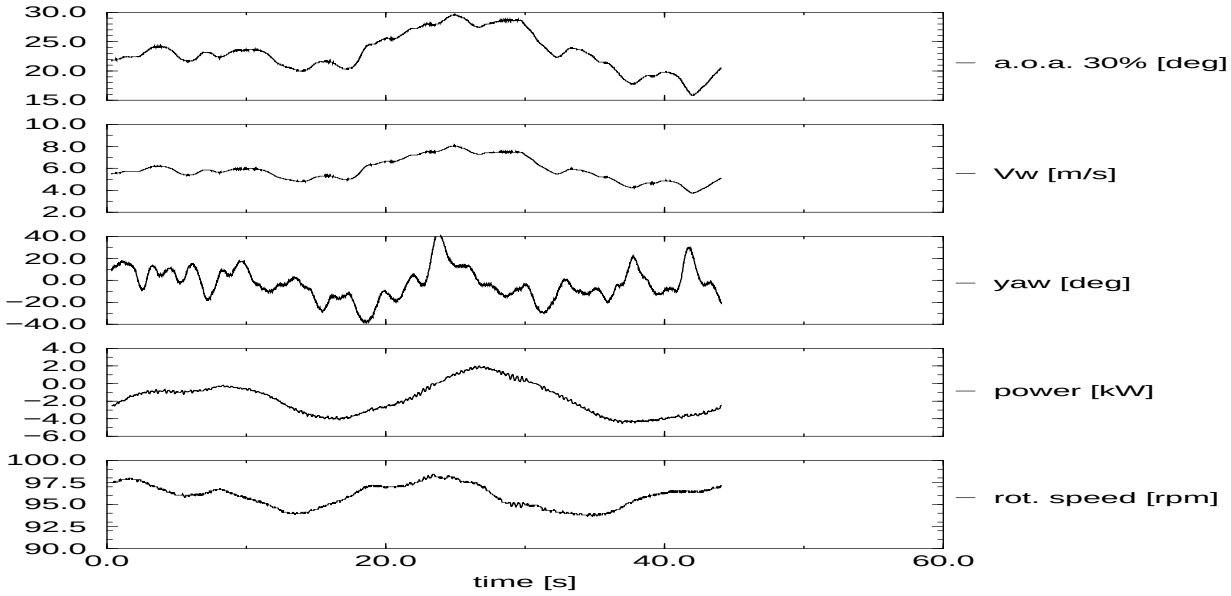

Figure C.120 *DUT: Time series of campaign ny_rot_d_018.30*

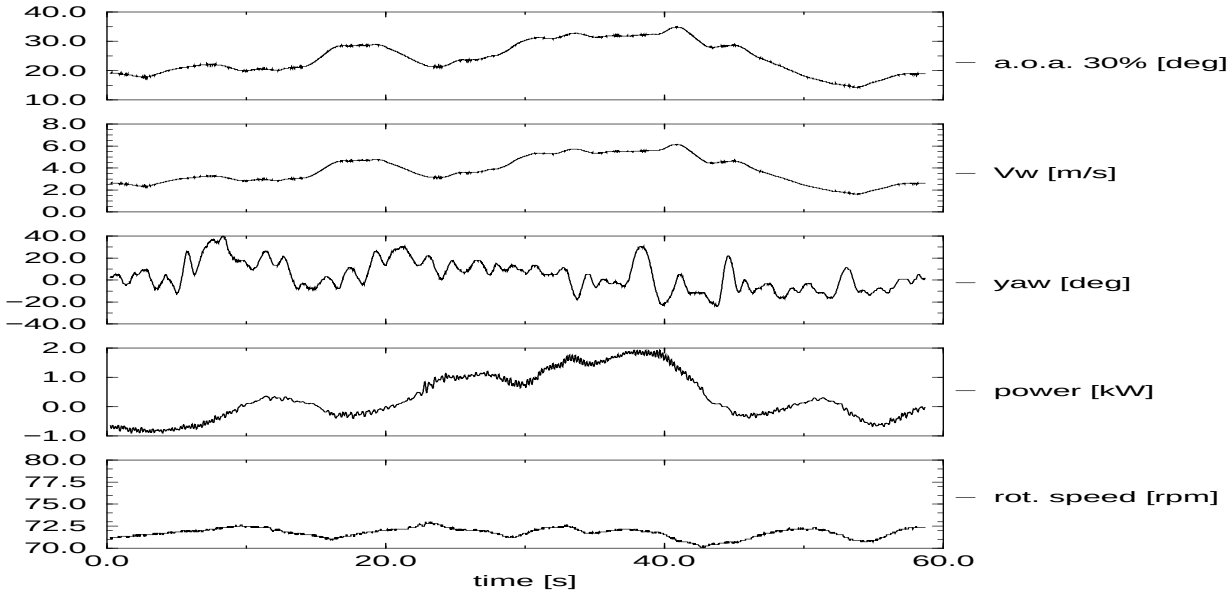

Figure C.121 *DUT: Time series of campaign ny_rot_d_021.30*

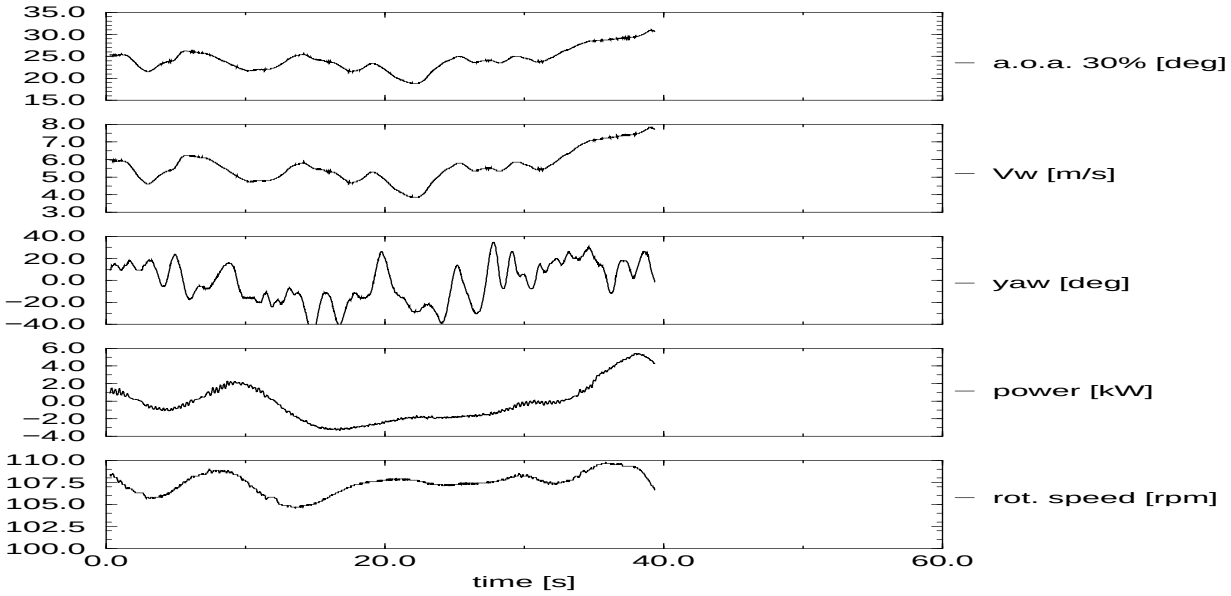

Figure C.122 *DUT: Time series of campaign ny_rot_d_022.30*

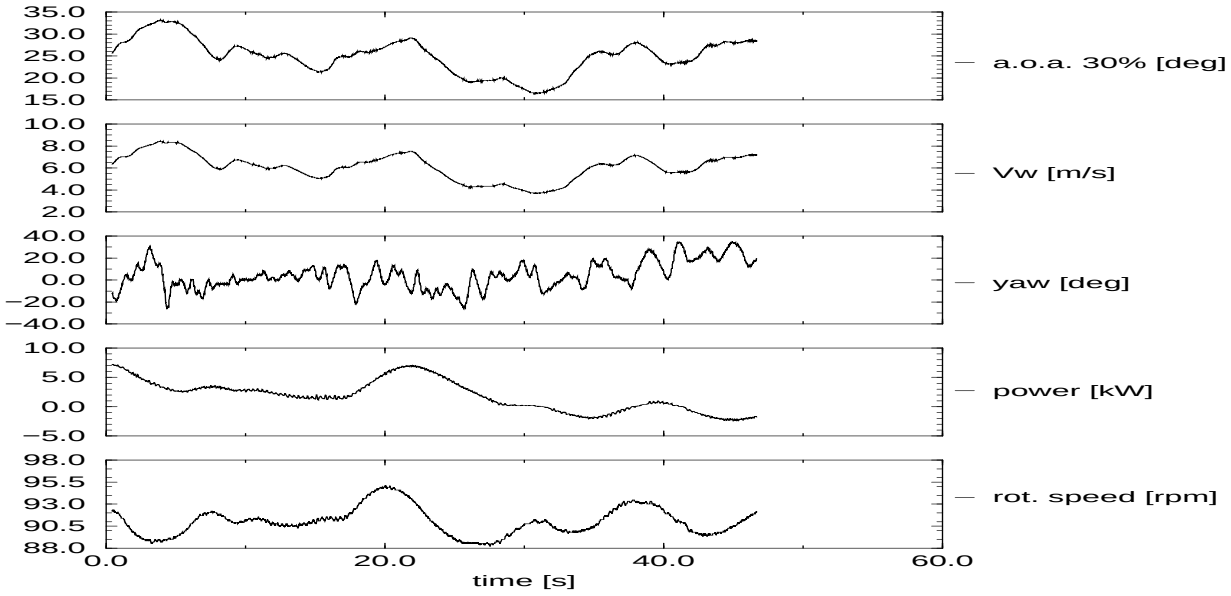

Figure C.123 *DUT: Time series of campaign ny_rot_d_025.30*

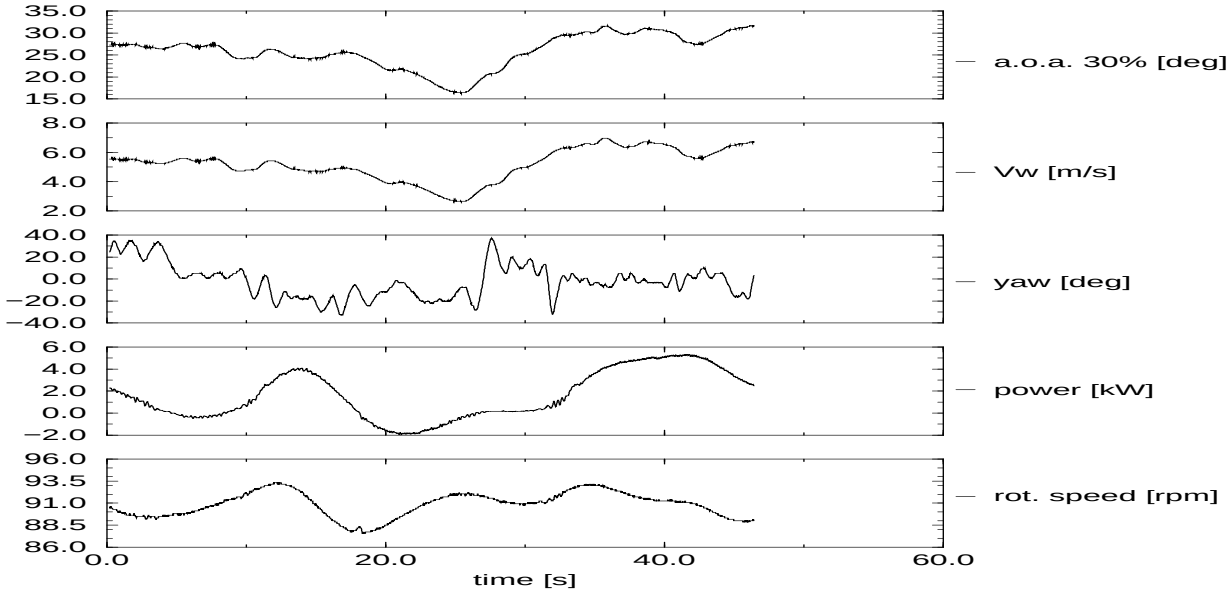

Figure C.124 *DUT: Time series of campaign ny_rot_d_027.30*

DUT time series: Non-yawed campaigns at 50% span, plots

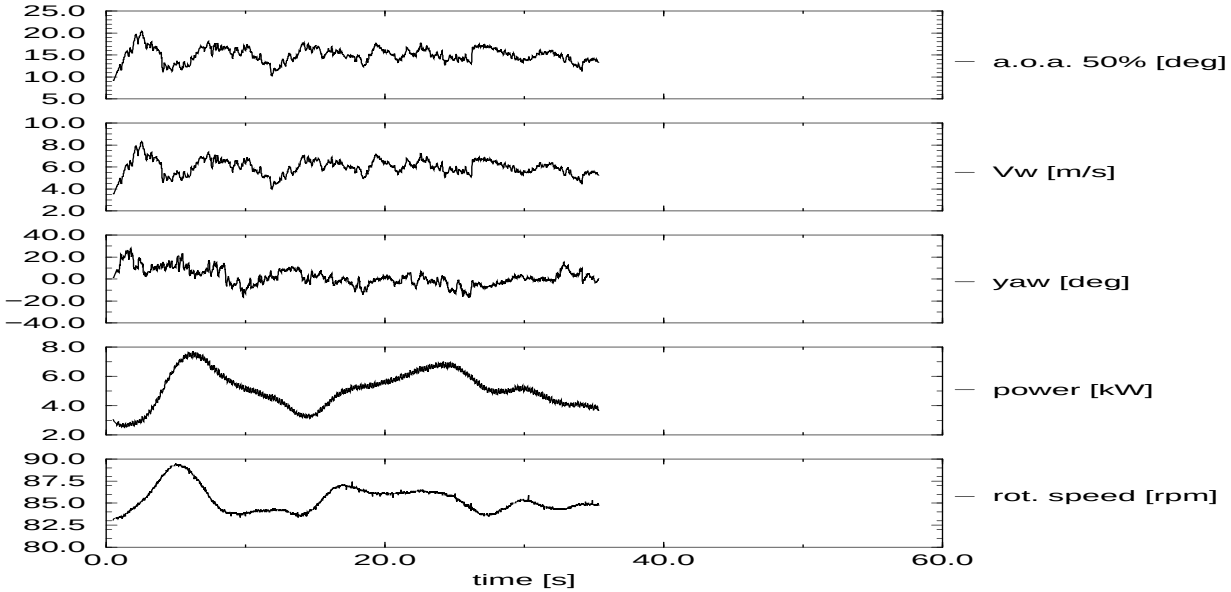

Figure C.125 *DUT: Time series of campaign ny_rot_d_004.50*

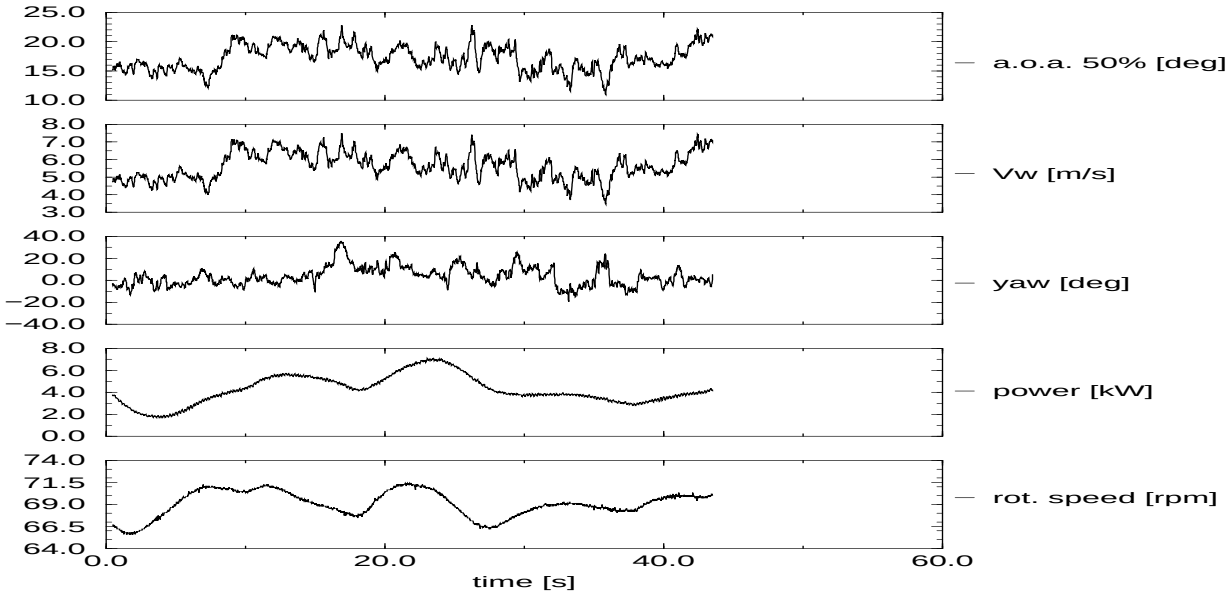

Figure C.126 *DUT: Time series of campaign ny_rot_d_006.50*

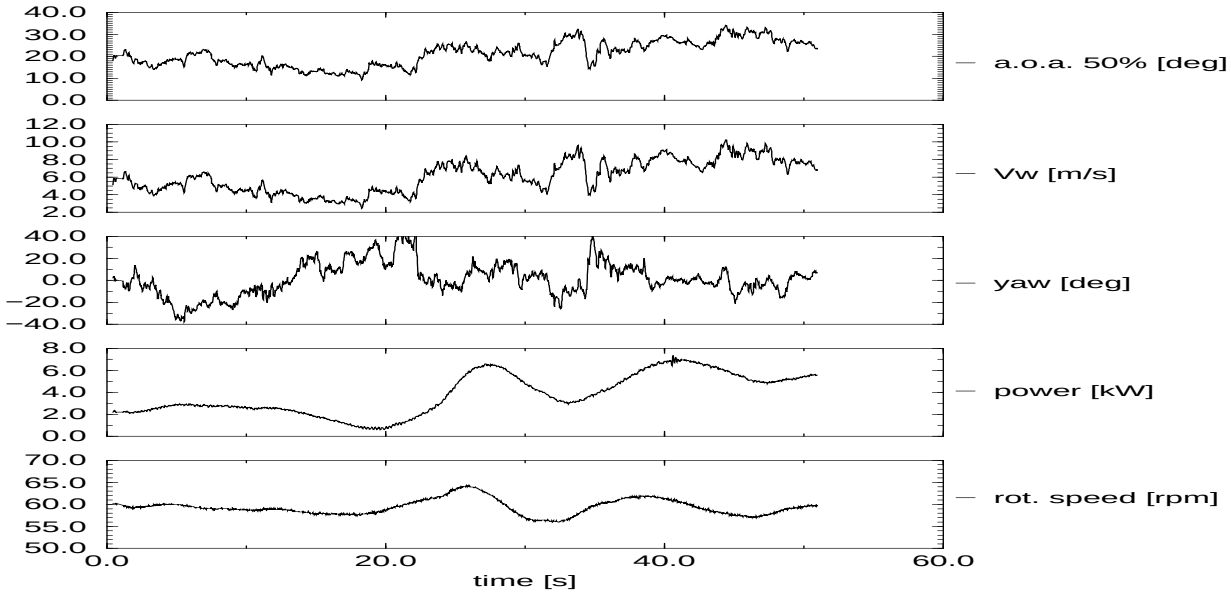

Figure C.127 *DUT: Time series of campaign ny_rot_d_008.50*

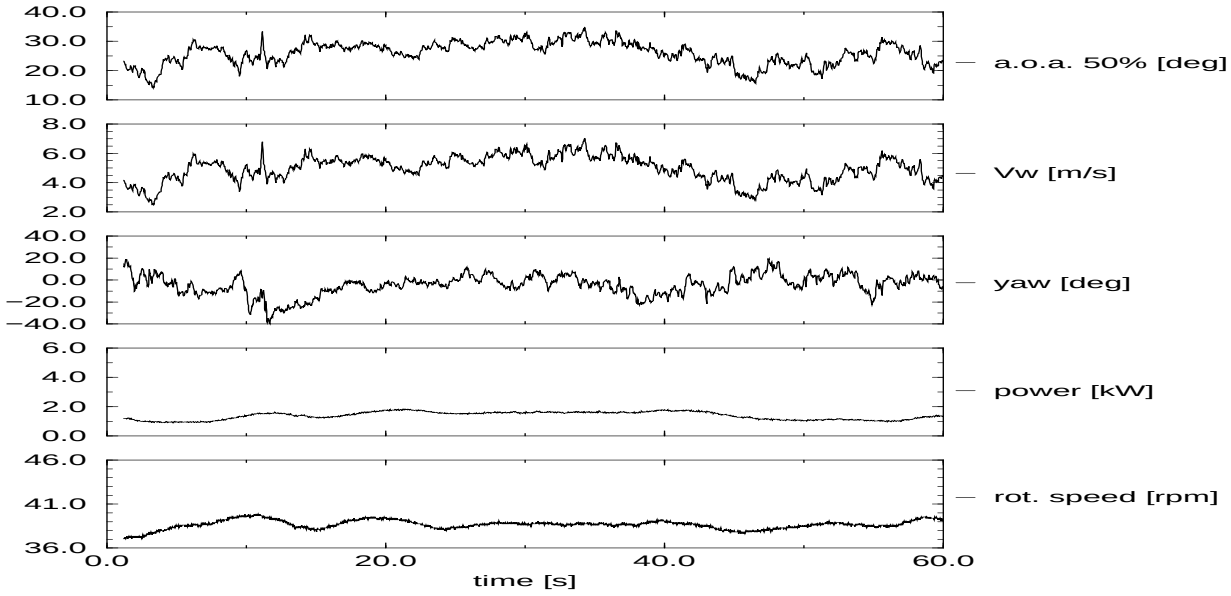

Figure C.128 *DUT: Time series of campaign ny_rot_d_009.50*

DUT time series: Non-yawed campaigns at 70% span, plots

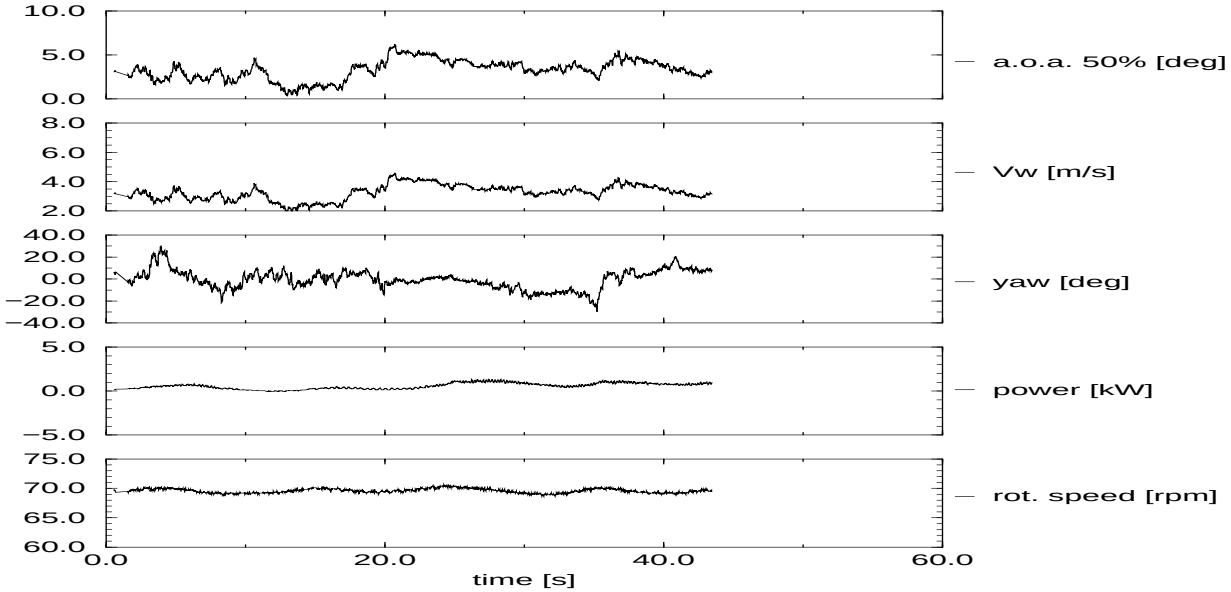

Figure C.129 *DUT: Time series of campaign ny_rot_d_001.70*

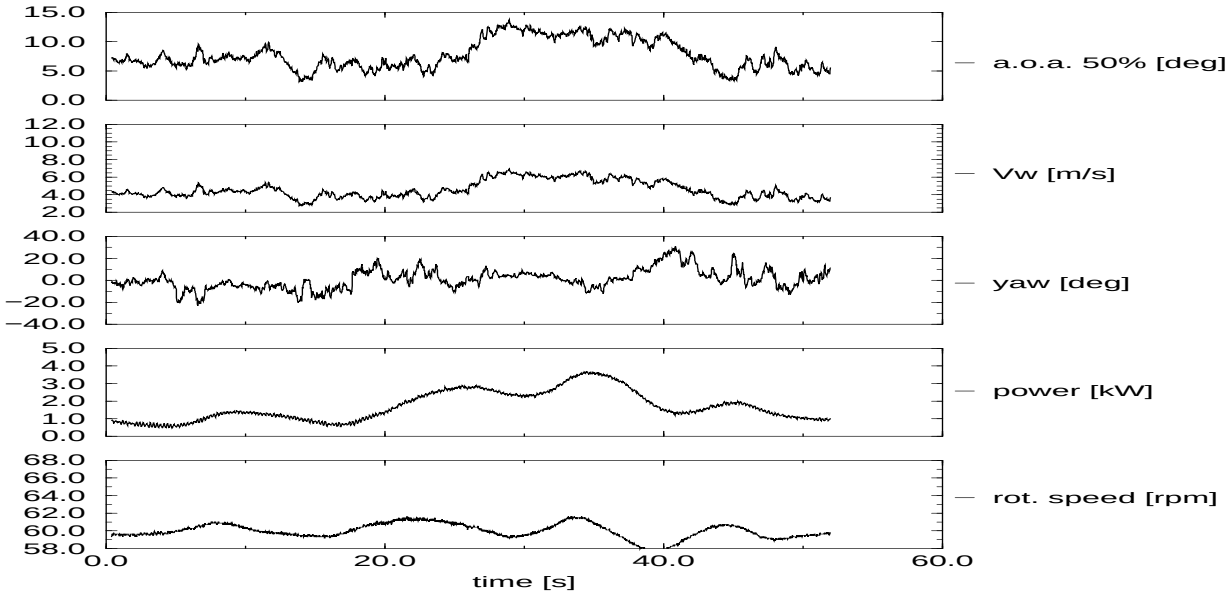

Figure C.130 *DUT: Time series of campaign ny_rot_d_004.70*

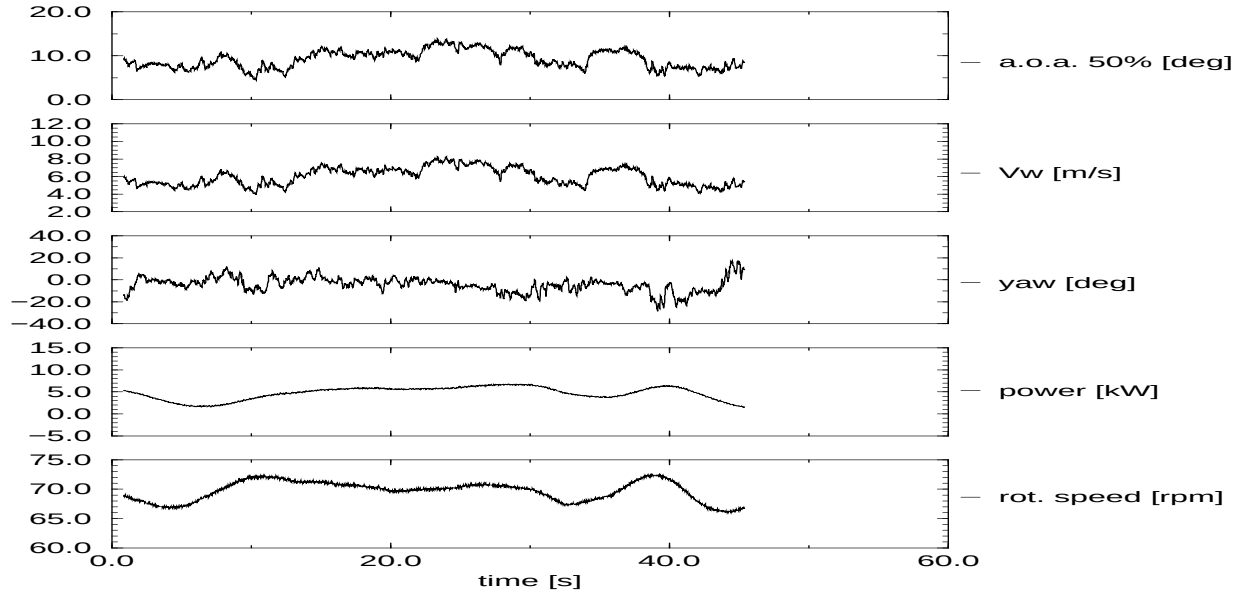

Figure C.131 *DUT: Time series of campaign ny_rot_d_007.70*

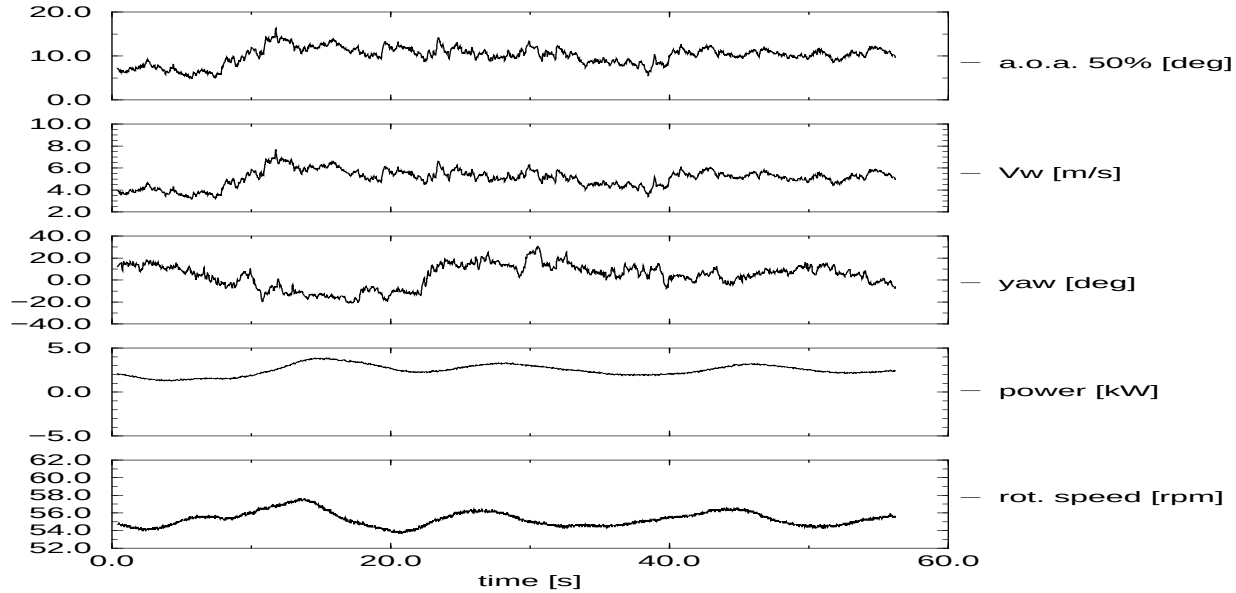

Figure C.132 *DUT: Time series of campaign ny_rot_d_011.70*

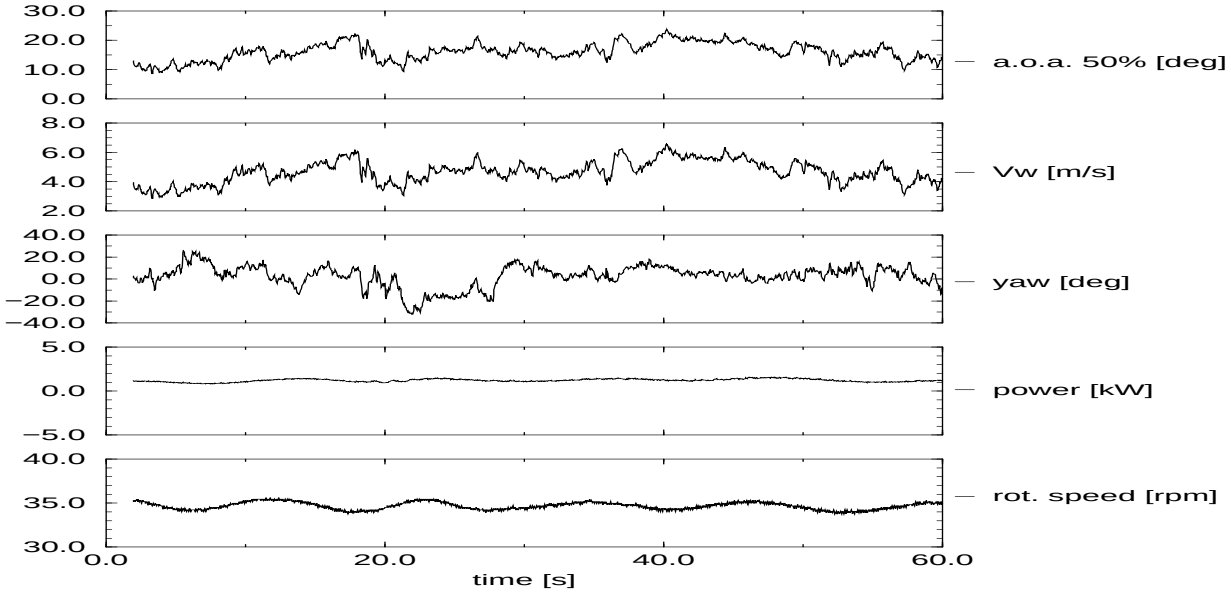

Figure C.133 *DUT: Time series of campaign ny_rot_d_014.70*

C.10.5 DUT time series: Yawed campaigns

It is noted that the angles of attack given in this section are derived from the geometrical angle of attack (atan (Ω.r/U)) and the pitch angle. The angles of attack from the 6-hole probes or from the match on the pressure distribution near the nose, see section 6.4 contain NaN's, which cannot be plotted.

DUT time series: Yawed campaigns, 30% section

The files are stored in directory '/data/dut/rottim/30percent'. The files are sorted in yaw angle bins of approximately 5 degrees and numbered in order of decreasing yaw angle. Within every yaw angle bin, the files are numbered in order of increasing angle of attack where the angle of attack is determined by the rotor speed, the wind speed and the pitch angle. see tables C.22 to C.25.

Table C.22 *Global overview of DUT yawed measurement files at 30% span*

file	DUT filename	$\overline{V}$ m/s	$\overline{\phi_y}$ deg	$\overline{\Omega}$ rpm	$\overline{\text{Power}}$ kW	$\overline{\alpha_{30\%}}$ deg	$\overline{\theta_{tip}}$ deg	duration s
y_rot_d_001.30	PA651002	5.470	50.83	86.30	-0.477	27.89	-6.0	49.062
y_rot_d_002.30	PA681002	6.417	46.72	91.51	0.064	30.04	-6.0	46.011
y_rot_d_003.30	PA641002	6.249	46.07	86.23	-0.254	30.66	-6.0	48.909
y_rot_d_004.30	PA751002	6.988	48.15	91.40	1.049	31.85	-6.0	46.272
y_rot_d_005.30	PA661002	6.690	46.02	86.25	0.552	32.16	-6.0	49.320
y_rot_d_006.30	PA220923	4.944	45.08	51.02	0.846	33.56	-2.0	82.557
y_rot_d_007.30	PA741002	5.583	41.78	91.74	-1.558	26.87	-6.0	46.278
y_rot_d_008.30	PA671002	6.809	41.92	86.32	0.594	32.60	-6.0	49.008
y_rot_d_009.30	PA430923	2.584	37.81	71.85	-1.558	18.85	-6.0	58.911
y_rot_d_010.30	PA581002	4.976	37.75	96.39	-2.391	24.16	-6.0	43.923
y_rot_d_011.30	PA210923	3.600	39.50	55.13	0.318	24.35	-2.0	76.185
y_rot_d_012.30	PA460923	4.469	39.68	71.89	-0.196	27.48	-6.0	58.503
y_rot_d_013.30	PA691002	5.731	39.45	91.71	-1.487	27.60	-6.0	45.972
y_rot_d_014.30	PA721002	6.066	35.21	91.69	-0.453	28.74	-6.0	46.170
y_rot_d_015.30	PA731002	6.236	37.63	91.37	0.862	29.43	-6.0	46.356
y_rot_d_016.30	PA631002	6.145	39.82	76.07	-0.094	33.12	-6.0	55.467
y_rot_d_017.30	PA390923	3.737	32.08	71.66	-0.592	24.23	-6.0	58.983
y_rot_d_018.30	PA180923	3.927	32.50	60.57	0.379	24.25	-2.0	69.666
y_rot_d_019.30	PA591002	5.132	31.70	96.09	-1.856	24.76	-6.0	44.340
y_rot_d_020.30	PA200923	3.776	32.57	55.15	0.491	25.34	-2.0	76.434
y_rot_d_021.30	PA711002	5.444	30.54	91.32	-1.958	26.73	-6.0	46.254
y_rot_d_022.30	PA711002	5.444	30.54	91.32	-1.958	26.73	-6.0	46.254
y_rot_d_023.30	PA501002	6.302	30.34	81.16	1.890	32.13	-6.0	52.254
y_rot_d_024.30	PA471002	6.576	30.05	75.06	2.578	35.07	-6.0	56.700
y_rot_d_025.30	PA080923	2.317	26.61	90.78	-2.359	11.22	-2.0	46.578
y_rot_d_026.30	PA240923	2.480	28.46	75.57	-1.157	13.76	-2.0	55.716
y_rot_d_027.30	PA060923	3.665	28.68	86.26	-1.368	17.12	-2.0	49.371
y_rot_d_028.30	PA270923	3.698	29.20	102.10	-4.417	18.97	-6.0	41.370

Table C.23 *Global overview of DUT yawed measurement files at 30% span, ctd*

file	DUT	$\overline{V}$	$\overline{\phi_y}$	$\overline{\Omega}$	$\overline{\text{Power}}$	$\overline{\alpha_{30\%}}$	$\overline{\theta_{tip}}$	duration
	filename	m/s	deg	rpm	kW	deg	deg	s
y_rot_d_029.30	PA290923	3.914	27.03	96.23	-3.459	20.46	-6.0	44.163
y_rot_d_030.30	PA750922	3.898	26.12	76.03	0.143	23.93	-6.0	55.746
y_rot_d_031.30	PA601002	5.610	27.78	101.90	-0.242	25.27	-6.0	41.937
y_rot_d_032.30	PA481002	5.101	26.04	75.02	0.885	29.31	-6.0	56.625
y_rot_d_033.30	PA561002	6.389	28.87	91.45	1.728	29.93	-6.0	46.299
y_rot_d_034.30	PA461002	5.319	26.47	75.28	1.629	30.16	-6.0	56.196
y_rot_d_035.30	PA511002	6.124	28.10	81.13	1.010	31.38	-6.0	51.936
y_rot_d_036.30	PA130923	3.772	22.16	107.30	-3.009	14.59	-2.0	39.642
y_rot_d_037.30	PA140923	4.287	24.91	96.03	-1.697	17.79	-2.0	44.472
y_rot_d_038.30	PA040923	4.185	22.92	76.10	-0.336	21.26	-2.0	55.695
y_rot_d_039.30	PA621002	4.546	20.97	101.80	-3.743	21.80	-6.0	41.460
y_rot_d_040.30	PA310923	4.375	20.70	91.39	-2.162	22.85	-6.0	46.434
y_rot_d_041.30	PA760922	3.688	23.40	75.66	0.312	23.13	-6.0	55.704
y_rot_d_042.30	PA540923	3.475	20.59	65.61	-0.533	24.59	-6.0	64.308
y_rot_d_043.30	PA551002	4.862	23.07	91.53	-2.588	24.64	-6.0	46.353
y_rot_d_044.30	PA571002	6.320	24.90	91.46	0.263	29.70	-6.0	46.143
y_rot_d_045.30	PA531002	6.284	20.37	86.28	1.890	30.61	-6.0	49.293
y_rot_d_046.30	PA451002	5.638	22.47	75.18	1.545	31.44	-6.0	56.115
y_rot_d_047.30	PA521002	6.880	24.52	86.25	1.604	32.72	-6.0	48.948
y_rot_d_048.30	PA491002	6.308	22.96	75.41	1.961	33.78	-6.0	56.103
y_rot_d_049.30	PA830922	3.060	17.56	102.30	-2.088	16.78	-6.0	41.472
y_rot_d_050.30	PA770922	3.480	16.52	86.14	-0.968	20.41	-6.0	49.014
y_rot_d_051.30	PA920922	4.546	15.49	71.40	0.578	28.02	-6.0	58.827
y_rot_d_052.30	PA541002	6.484	15.38	91.61	1.104	30.14	-6.0	46.020
y_rot_d_053.30	PA070923	2.748	13.05	90.73	-2.282	12.88	-2.0	46.638
y_rot_d_054.30	PA280923	2.658	11.15	96.16	-4.226	15.94	-6.0	43.908
y_rot_d_055.30	PA840922	3.774	10.75	102.20	-1.691	19.18	-6.0	41.217
y_rot_d_056.30	PA150923	4.256	14.70	86.29	-0.928	19.41	-2.0	49.137
y_rot_d_057.30	PA790922	3.508	12.23	90.82	-1.120	19.77	-6.0	46.893
y_rot_d_058.30	PA350923	3.025	10.72	75.91	-1.459	20.16	-6.0	55.719
y_rot_d_059.30	PA450923	3.268	10.21	71.93	-1.312	22.11	-6.0	58.932
y_rot_d_060.30	PA170923	3.839	14.67	65.85	0.044	22.29	-2.0	64.215
y_rot_d_061.30	PA420923	3.315	10.14	71.75	-0.944	22.34	-6.0	58.767
y_rot_d_062.30	PA810922	4.678	14.27	96.73	0.578	22.89	-6.0	43.659
y_rot_d_063.30	PA611002	5.148	13.73	101.60	-3.054	23.86	-6.0	41.967
y_rot_d_064.30	PA370923	3.926	12.78	75.88	-0.867	24.15	-6.0	55.566
y_rot_d_065.30	PA490923	3.980	10.33	71.05	-0.744	25.60	-6.0	59.127
y_rot_d_066.30	PA381002	6.310	10.46	86.19	2.471	26.89	-2.0	49.488
y_rot_d_067.30	PA371002	6.880	10.79	86.71	2.953	28.68	-2.0	48.573
y_rot_d_070.30	PA230923	2.425	6.97	75.54	-1.199	13.52	-2.0	55.899
y_rot_d_071.30	PA100923	4.074	5.49	96.45	-2.119	17.00	-2.0	43.863
y_rot_d_072.30	PA260923	3.184	7.93	102.10	-4.554	17.19	-6.0	41.520
y_rot_d_073.30	PA190923	2.813	9.24	60.55	-0.279	18.37	-2.0	69.789
y_rot_d_074.30	PA360923	2.986	6.94	75.90	-1.590	19.97	-6.0	55.560
y_rot_d_075.30	PA740922	2.872	8.02	71.65	-0.456	20.28	-6.0	58.707
y_rot_d_076.30	PA331002	4.943	5.65	91.72	-1.322	20.69	-2.0	46.146
y_rot_d_077.30	PA340923	3.254	6.12	75.80	-1.511	21.26	-6.0	55.503

Table C.24 *Global overview of DUT yawed measurement files at 30% span, ctd*

file	DUT filename	$\overline{V}$ m/s	$\overline{\phi_y}$ deg	$\overline{\Omega}$ rpm	$\overline{\text{Power}}$ kW	$\overline{\alpha_{30\%}}$ deg	$\overline{\theta_{tip}}$ deg	duration s
y_rot_d_078.30	PA380923	3.858	5.87	75.69	-1.001	23.84	-6.0	56.238
y_rot_d_079.30	PA351002	5.823	6.19	91.04	1.878	24.05	-2.0	46.344
y_rot_d_080.30	PA320923	4.869	5.46	86.67	-1.029	25.55	-6.0	48.738
y_rot_d_081.30	PA410923	4.359	5.58	72.15	0.188	26.81	-6.0	58.359
y_rot_d_082.30	PA860922	6.699	7.39	107.30	4.051	27.59	-6.0	39.426
y_rot_d_083.30	PA391002	6.559	5.97	86.69	2.590	27.60	-2.0	48.726
y_rot_d_084.30	PA291002	6.901	6.59	91.08	2.798	27.64	-2.0	46.506
y_rot_d_085.30	PA910922	4.794	9.79	76.13	1.376	27.73	-6.0	55.407
y_rot_d_086.30	PA431002	6.616	7.80	86.52	2.460	27.82	-2.0	48.738
y_rot_d_087.30	PA780922	5.660	6.42	86.10	2.960	28.65	-6.0	49.410
y_rot_d_088.30	PA341002	7.371	8.42	91.50	3.564	29.10	-2.0	46.452
y_rot_d_089.30	PA401002	7.634	5.33	86.17	4.583	31.30	-2.0	49.188
y_rot_d_090.30	PA301002	3.674	-7.82	91.29	-2.129	16.25	-2.0	46.455
y_rot_d_091.30	PA141002	4.517	-5.01	96.09	-2.403	18.58	-2.0	44.403
y_rot_d_092.30	PA281002	4.961	-9.95	91.50	-0.337	20.96	-2.0	46.143
y_rot_d_093.30	PA311002	4.909	-6.15	91.15	-2.433	20.87	-2.0	46.230
y_rot_d_094.30	PA131002	5.736	-5.02	95.80	0.430	22.76	-2.0	44.520
y_rot_d_095.30	PA271002	6.184	-6.28	91.18	1.687	25.29	-2.0	46.485
y_rot_d_096.30	PA101002	5.990	-5.77	85.97	1.867	25.61	-2.0	49.311
y_rot_d_097.30	PA151002	6.838	-6.74	96.56	0.286	26.06	-2.0	43.920
y_rot_d_098.30	PA880922	5.810	-5.51	96.55	0.457	26.91	-6.0	43.488
y_rot_d_099.30	PA091002	7.315	-5.53	75.41	4.206	33.56	-2.0	56.373
y_rot_d_100.30	PA021002	7.429	-6.78	71.85	3.899	35.19	-2.0	58.995
y_rot_d_101.30	PA580922	2.526	-13.97	88.06	-1.343	16.31	-6.0	47.763
y_rot_d_102.30	PA550923	2.118	-13.99	65.58	-1.127	17.54	-6.0	64.419
y_rot_d_103.30	PA020923	4.259	-11.83	71.64	0.068	22.70	-2.0	59.316
y_rot_d_104.30	PA530923	3.459	-11.18	70.95	-1.121	23.21	-6.0	59.694
y_rot_d_105.30	PA680922	4.664	-12.42	86.24	0.614	24.92	-6.0	48.954
y_rot_d_106.30	PA051002	6.028	-11.68	86.01	0.413	25.83	-2.0	49.344
y_rot_d_107.30	PA540922	4.237	-13.11	71.72	0.989	26.53	-6.0	58.671
y_rot_d_108.30	PA061002	6.220	-15.00	85.41	2.132	26.71	-2.0	49.524
y_rot_d_109.30	PA081002	7.834	-11.74	91.18	5.663	30.58	-2.0	46.275
y_rot_d_110.30	PA011002	6.519	-12.97	71.90	2.329	31.89	-2.0	59.208
y_rot_d_111.30	PA710922	4.772	-10.55	60.38	1.731	32.64	-6.0	69.399
y_rot_d_112.30	PA041002	7.508	-13.55	75.59	4.212	34.05	-2.0	55.986
y_rot_d_113.30	PA590922	3.027	-16.26	92.33	-1.321	17.73	-6.0	45.783
y_rot_d_114.30	PA480923	2.657	-15.84	71.05	-1.389	19.36	-6.0	59.088
y_rot_d_115.30	PA640922	4.154	-19.46	105.20	-1.501	20.05	-6.0	40.416
y_rot_d_116.30	PA650922	4.473	-15.90	105.30	-1.610	21.12	-6.0	40.038
y_rot_d_117.30	PA690922	4.982	-18.53	75.59	1.765	28.66	-6.0	55.794
y_rot_d_118.30	PA700922	4.762	-19.75	71.61	1.684	28.84	-6.0	59.166
y_rot_d_119.30	PA600922	3.311	-20.92	92.29	-1.192	18.84	-6.0	46.353
y_rot_d_120.30	PA660922	4.114	-23.26	99.44	-1.361	20.72	-6.0	42.372
y_rot_d_121.30	PA550922	3.840	-20.75	77.18	0.204	23.47	-6.0	54.840
y_rot_d_122.30	PA530922	3.572	-20.86	71.66	0.136	23.51	-6.0	58.752
y_rot_d_123.30	PA811002	4.631	-22.43	86.46	-0.561	24.78	-6.0	49.443
y_rot_d_124.30	PA630922	5.443	-21.82	99.88	1.810	25.01	-6.0	42.345

Table C.25 *Global overview of DUT yawed measurement files at 30% span, ctd*

file	DUT filename	$\overline{V}$ m/s	$\overline{\phi_y}$ deg	$\overline{\Omega}$ rpm	$\overline{\text{Power}}$ kW	$\overline{\alpha_{30\%}}$ deg	$\overline{\theta_{tip}}$ deg	duration s
y_rot_d_125.30	PA620922	5.845	-24.60	99.58	2.142	26.42	-6.0	42.390
y_rot_d_126.30	PA670922	3.660	-29.75	91.98	-0.832	20.17	-6.0	45.963
y_rot_d_127.30	PA510923	3.253	-27.14	71.02	-0.968	22.17	-6.0	59.136
y_rot_d_128.30	PA570922	4.346	-28.86	87.89	0.448	23.38	-6.0	48.282
y_rot_d_129.30	PA801002	5.453	-28.64	86.55	0.224	27.77	-6.0	48.564
y_rot_d_130.30	PA470923	1.769	-30.29	71.00	-1.734	14.99	-6.0	59.187
y_rot_d_131.30	PA821002	4.643	-31.42	91.48	-1.963	23.80	-6.0	46.605
y_rot_d_132.30	PA771002	4.039	-38.40	75.73	-0.957	24.66	-6.0	55.731
y_rot_d_133.30	PA560922	4.511	-31.39	77.24	0.714	26.35	-6.0	54.918
y_rot_d_134.30	PA941002	4.942	-34.74	81.09	0.298	26.94	-6.0	51.951
y_rot_d_135.30	PA841002	5.784	-32.20	91.52	0.076	27.87	-6.0	46.236
y_rot_d_136.30	PA791002	5.776	-32.44	86.24	0.344	28.97	-6.0	48.954
y_rot_d_137.30	PA931002	5.598	-38.75	80.62	0.830	29.72	-6.0	52.593
y_rot_d_138.30	PA921002	6.343	-35.51	86.29	1.744	30.98	-6.0	48.999
y_rot_d_139.30	PA951002	6.382	-34.50	80.66	2.745	32.65	-6.0	52.551
y_rot_d_140.30	PA881002	7.315	-31.24	91.76	4.413	32.79	-6.0	46.416
y_rot_d_141.30	PA911002	4.361	-43.34	86.43	-0.659	23.66	-6.0	48.936
y_rot_d_142.30	PA831002	4.902	-41.58	91.39	-2.076	24.78	-6.0	46.347
y_rot_d_143.30	PA761002	4.669	-42.57	75.83	0.379	27.20	-6.0	55.968
y_rot_d_144.30	PA871002	5.680	-43.73	91.06	-0.223	27.52	-6.0	46.602
y_rot_d_145.30	PA891002	7.090	-43.03	85.97	2.377	33.54	-6.0	49.233
y_rot_d_146.30	PA901002	7.614	-40.52	86.22	3.374	35.16	-6.0	48.879
y_rot_d_147.30	PA851002	4.618	-47.36	96.41	-2.141	22.80	-6.0	43.866
y_rot_d_148.30	PA861002	5.213	-53.04	90.91	-0.359	25.88	-6.0	46.494

DUT time series: Yawed campaigns, 50% section

The files are stored in directory '/data/dut/rottim/50percent'. The files are sorted in yaw angle bins of approximately 5 degrees and numbered in order of decreasing yaw angle. Within every yaw angle bin, the files are numbered in order of increasing angle of attack where the angle of attack is determined by the rotor speed and the wind speed see table C.26.

Table C.26 *Global overview of DUT yawed measurement files at 50% span*

file	DUT filename	$\overline{V}$ m/s	$\overline{\phi_y}$ deg	$\overline{\Omega}$ rpm	$\overline{\text{Power}}$ kW	$\overline{\alpha_{50\%}}$ deg	$\overline{\theta_{tip}}$ deg	duration s
y_rot_d_001.50	PB231124	6.057	37.00	69.01	3.616	18.40	0.0	43.737
y_rot_d_002.50	PB241124	4.877	32.68	85.63	1.729	12.26	0.0	34.968
y_rot_d_003.50	PB251124	5.200	30.69	85.39	2.304	13.09	0.0	34.719
y_rot_d_004.50	PB261124	6.850	32.64	70.14	4.453	20.41	0.0	42.543
y_rot_d_005.50	PB281124	5.053	34.21	49.46	1.782	21.17	0.0	60.639
y_rot_d_006.50	PB271124	6.992	33.50	58.83	3.768	24.34	0.0	60.639
y_rot_d_007.50	PB211124	7.927	25.79	50.37	3.449	30.87	0.0	60.669
y_rot_d_008.50	PB221124	7.311	20.73	58.77	4.421	25.09	0.0	51.636
y_rot_d_009.50	PB041124	5.689	6.69	49.37	2.739	23.41	0.0	21.966
y_rot_d_010.50	PB111124	6.746	6.82	58.74	4.483	23.57	0.0	50.814
y_rot_d_011.50	PB111123	5.586	-6.65	89.64	3.654	13.38	0.0	33.270
y_rot_d_012.50	PB131123	4.777	-8.63	70.08	2.411	14.58	0.0	42.504
y_rot_d_013.50	PB101123	5.620	-5.50	79.22	3.895	15.12	0.0	38.244
y_rot_d_014.50	PB151123	4.849	-8.34	49.49	1.957	20.46	0.0	60.429
y_rot_d_015.50	PB071123	5.189	-5.66	49.65	2.475	21.68	0.0	60.162
y_rot_d_016.50	PB121123	6.117	-10.58	85.62	4.615	15.23	0.0	35.325
y_rot_d_017.50	PB141123	4.328	-10.69	59.87	1.815	15.39	0.0	49.737
y_rot_d_018.50	PB391124	3.837	-38.57	59.58	0.889	13.79	0.0	50.316
y_rot_d_019.50	PB441124	4.831	-39.18	69.65	1.795	14.78	0.0	42.933
y_rot_d_020.50	PB411124	6.898	-38.57	85.69	4.932	17.05	0.0	35.067
y_rot_d_021.50	PB431124	5.779	-49.15	85.49	1.754	14.43	0.0	35.076
y_rot_d_022.50	PB451124	5.003	-46.25	59.14	1.404	17.87	0.0	50.577
y_rot_d_023.50	PB401124	5.936	-45.77	69.37	2.411	18.02	0.0	43.779

DUT time series: Yawed campaigns, 70% section

The files are stored in directory '/data/dut/rottim/70percent'. The files are sorted in yaw angle bins of approximately 5 degrees and numbered in order of decreasing yaw angle. Within every yaw angle bin, the files are numbered in order of increasing angle of attack where the angle of attack is determined by the rotor speed and the wind speed see table C.27.

Table C.27 *Global overview of DUT yawed measurement files at 70% span*

file	DUT	$\overline{V}$	$\overline{\phi_y}$	$\overline{\Omega}$	$\overline{\text{Power}}$	$\overline{\alpha_{70\%}}$	$\overline{\theta_{tip}}$	duration
	filename	m/s	deg	rpm	kW	deg	deg	s
y_rot_d_001.70	PC170721	2.525	107.60	85.90	-0.60	0.585	4.0	36.867
y_rot_d_002.70	PC150721	1.712	97.01	69.69	-0.31	-0.167	4.0	44.952
y_rot_d_003.70	PC160721	3.173	77.22	75.52	-0.37	2.538	4.0	41.604
y_rot_d_004.70	PC140721	1.317	59.60	65.12	-0.22	-0.843	4.0	48.426
y_rot_d_005.70	PC130721	1.445	59.47	59.79	-0.11	-0.232	4.0	52.950
y_rot_d_006.70	PC130712	4.282	26.42	34.67	0.76	14.567	4.0	90.282
y_rot_d_007.70	PC220712	3.897	18.06	75.35	1.19	4.024	4.0	41.640
y_rot_d_008.70	PC070824	4.283	17.45	49.89	1.53	9.120	4.0	59.910
y_rot_d_009.70	PC090803	2.746	10.22	78.76	0.34	1.426	4.0	37.482
y_rot_d_010.70	PC050721	1.606	10.35	44.85	0.01	1.573	4.0	69.720
y_rot_d_011.70	PC070803	2.782	14.57	59.70	0.28	3.245	4.0	49.449
y_rot_d_012.70	PC260722	4.136	12.52	75.07	1.99	4.541	4.0	42.084
y_rot_d_013.70	PC100824	5.317	11.83	84.73	3.04	5.707	4.0	36.777
y_rot_d_014.70	PC140824	4.075	14.40	63.96	1.79	5.846	4.0	46.614
y_rot_d_015.70	PC080824	4.230	14.97	58.63	1.76	7.120	4.0	50.583
y_rot_d_016.70	PC090824	4.957	13.57	68.75	2.59	7.120	4.0	43.377
y_rot_d_017.70	PC110824	3.282	5.26	89.44	-0.42	1.717	4.0	35.442
y_rot_d_018.70	PC250722	3.319	6.32	84.53	0.34	2.109	4.0	37.248
y_rot_d_019.70	PC120824	3.450	5.03	75.19	0.60	3.128	4.0	40.353
y_rot_d_020.70	PC130824	4.368	8.69	64.02	2.12	6.540	4.0	46.653
y_rot_d_021.70	PC050803	2.841	6.14	38.95	0.65	7.230	4.0	75.279
y_rot_d_022.70	PC030824	4.231	8.57	29.62	0.59	17.190	4.0	98.274
y_rot_d_023.70	PC230712	3.536	-7.49	85.12	0.50	2.462	4.0	36.891
y_rot_d_024.70	PC270722	4.358	-8.51	70.43	1.66	5.573	4.0	44.286
y_rot_d_025.70	PC200712	4.224	-7.47	65.12	1.73	6.021	4.0	48.528
y_rot_d_026.70	PC060824	4.231	-6.47	44.44	1.36	10.540	4.0	67.179
y_rot_d_027.70	PC040721	2.361	-15.11	40.34	0.14	5.060	4.0	77.415
y_rot_d_028.70	PC280722	4.655	-10.63	65.37	1.72	6.940	4.0	48.147
y_rot_d_029.70	PC080712	4.329	-14.01	60.14	1.57	7.087	4.0	52.626
y_rot_d_030.70	PC340722	3.735	-10.18	34.20	0.78	12.540	4.0	91.527
y_rot_d_031.70	PC050824	4.272	-10.67	38.73	1.09	12.730	4.0	76.179
y_rot_d_032.70	PC100712	5.252	-17.85	70.63	2.97	7.415	4.0	44.418
y_rot_d_033.70	PC290722	5.780	-16.31	59.90	3.34	10.730	4.0	52.461
y_rot_d_034.70	PC090712	4.151	-25.73	64.92	0.90	5.890	4.0	48.021
y_rot_d_035.70	PC040803	3.993	-64.08	39.38	0.46	11.450	4.0	74.334
y_rot_d_036.70	PC030721	1.005	-97.15	34.77	-0.02	0.502	4.0	90.579

C.10.6 DUT yawed campaigns, plots of time series

In this chapter, only a limited number of time series is shown for the yawed DUT campaings at the three different sections. Plots (pdf-files) for all campaigns can be found in the database: They are included in the zip files which contain the set of datafiles for every campaign. It is reminded that the angle of attack is determined from the geometrical angle of attack and the pitch angle.

DUT time series: yawed campaigns at 30% span, plots

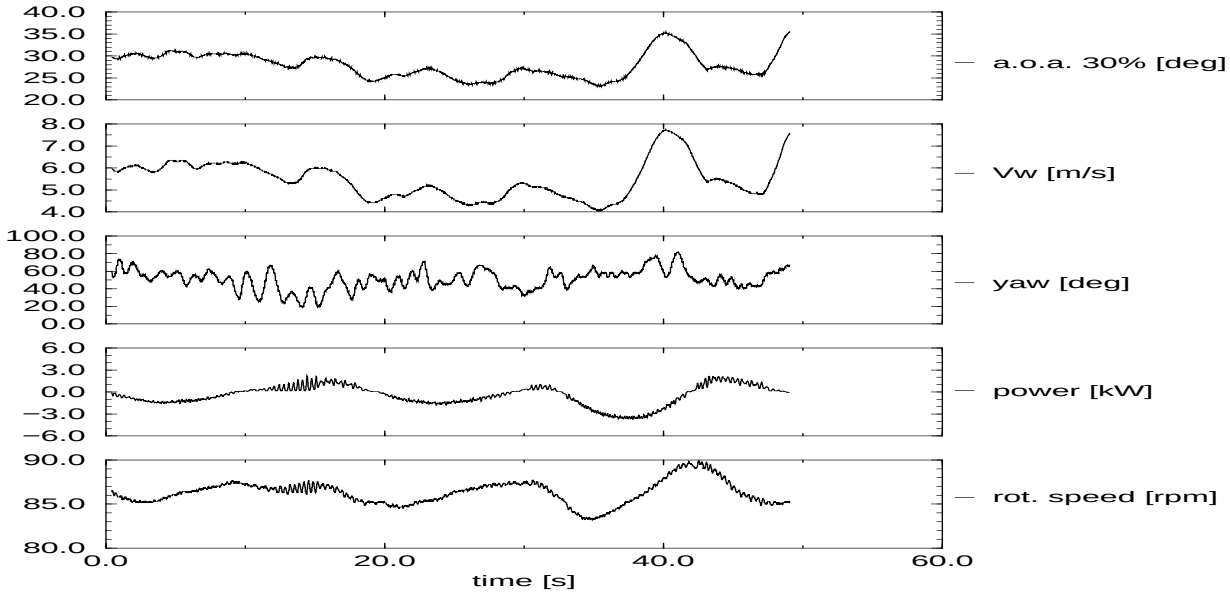

Figure C.134 *DUT: Time series of campaign y_rot_d_001.30*

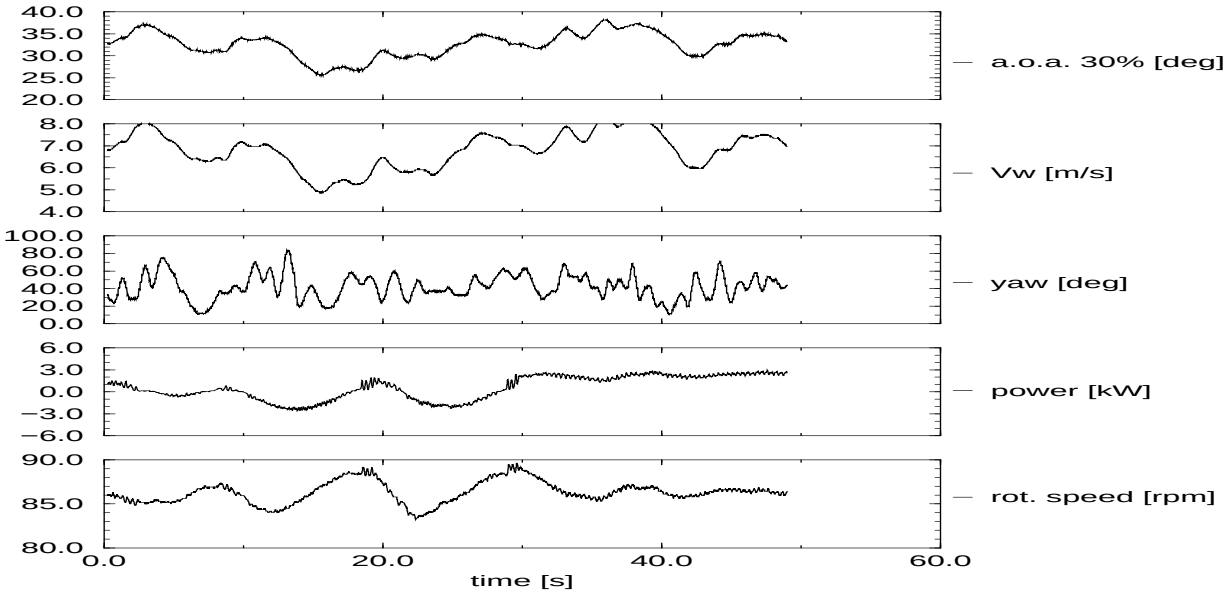

Figure C.135 *DUT: Time series of campaign y_rot_d_008.30*

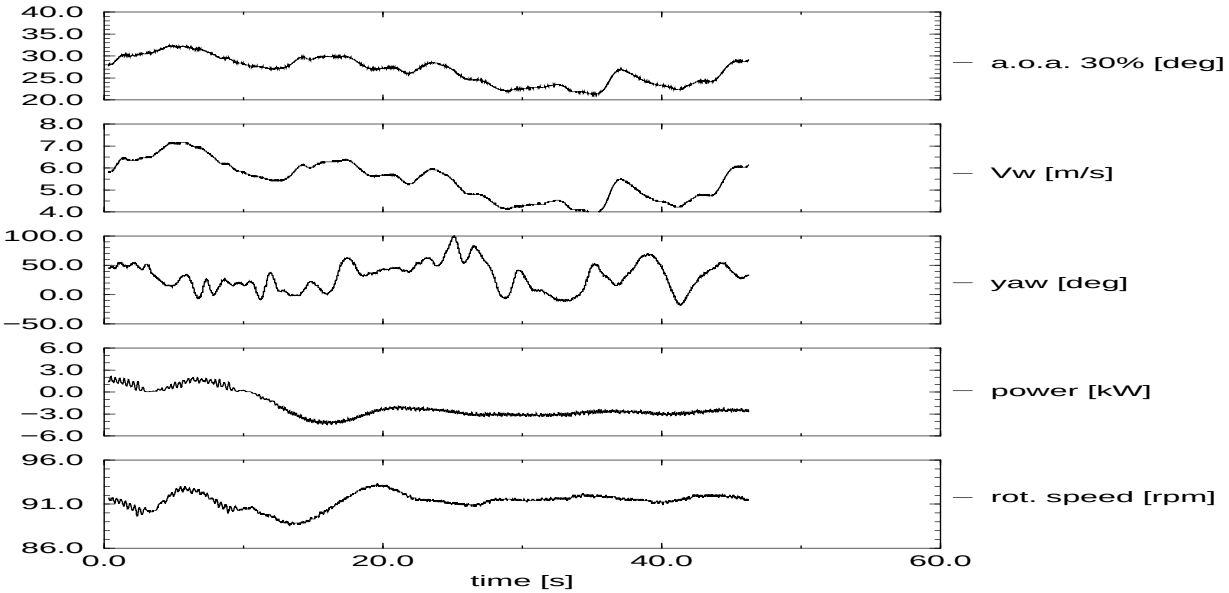

Figure C.136 *DUT: Time series of campaign y_rot_d_021.30*

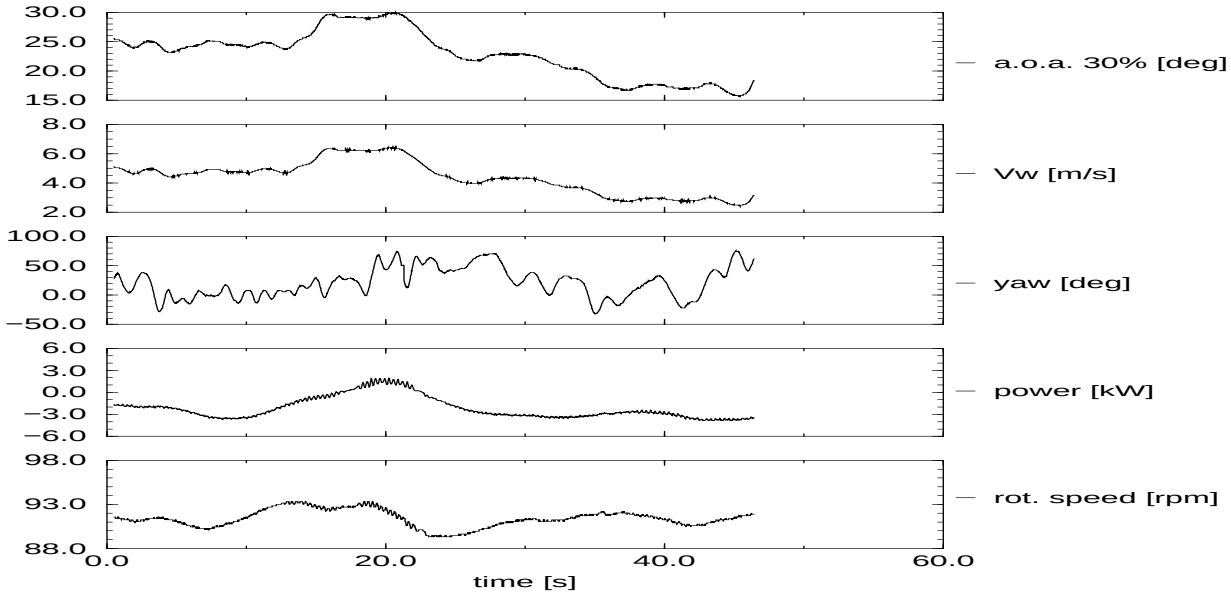

Figure C.137 *DUT: Time series of campaign y_rot_d_040.30*

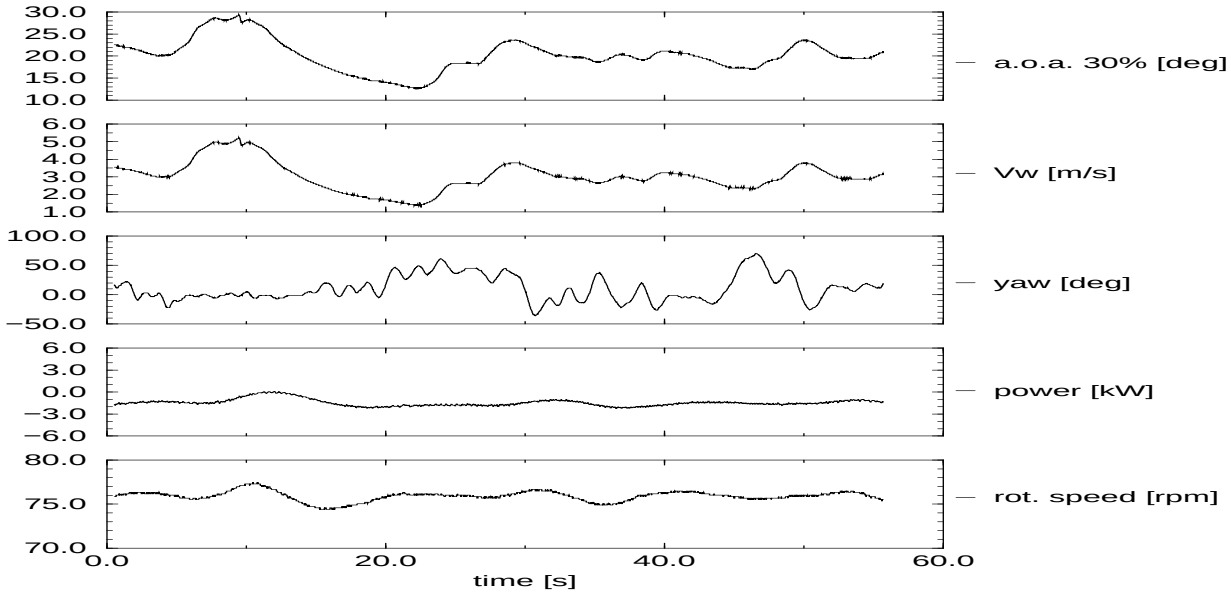

Figure C.138 *DUT: Time series of campaign y_rot_d_058.30*

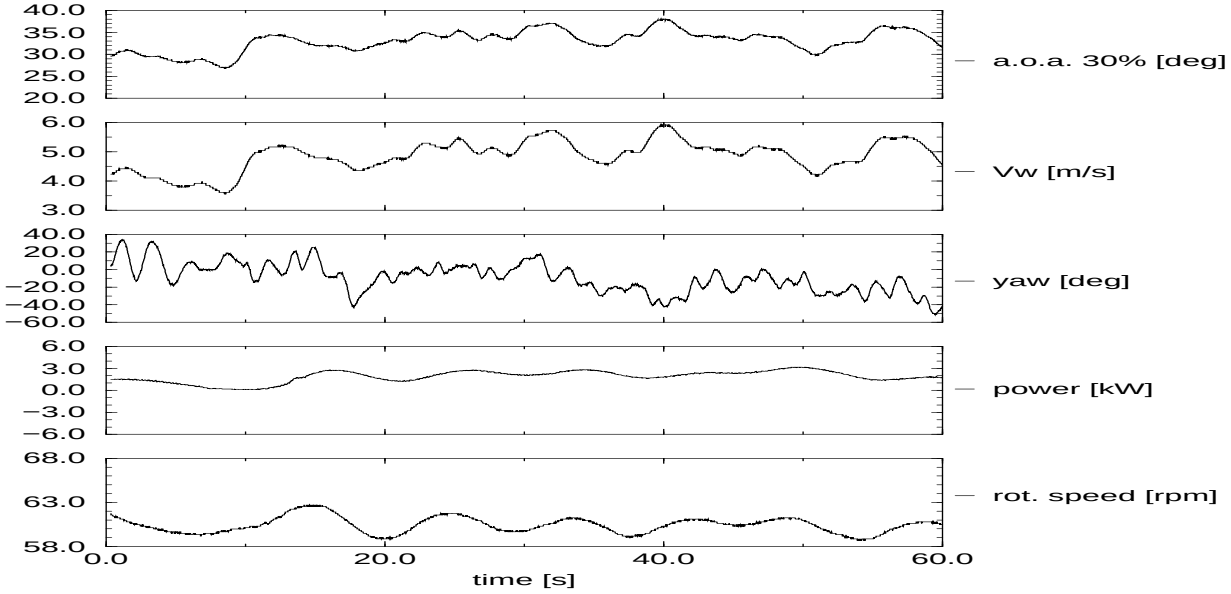

Figure C.139 *DUT: Time series of campaign y_rot_d_111.30*

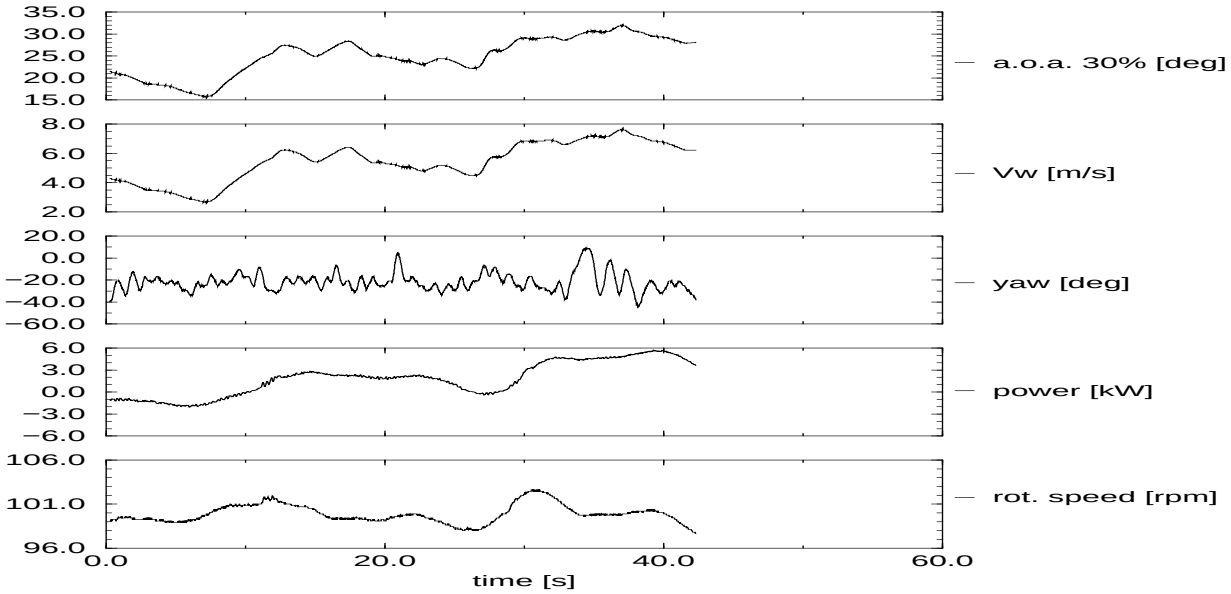

Figure C.140 *DUT: Time series of campaign y_rot_d_124.30*

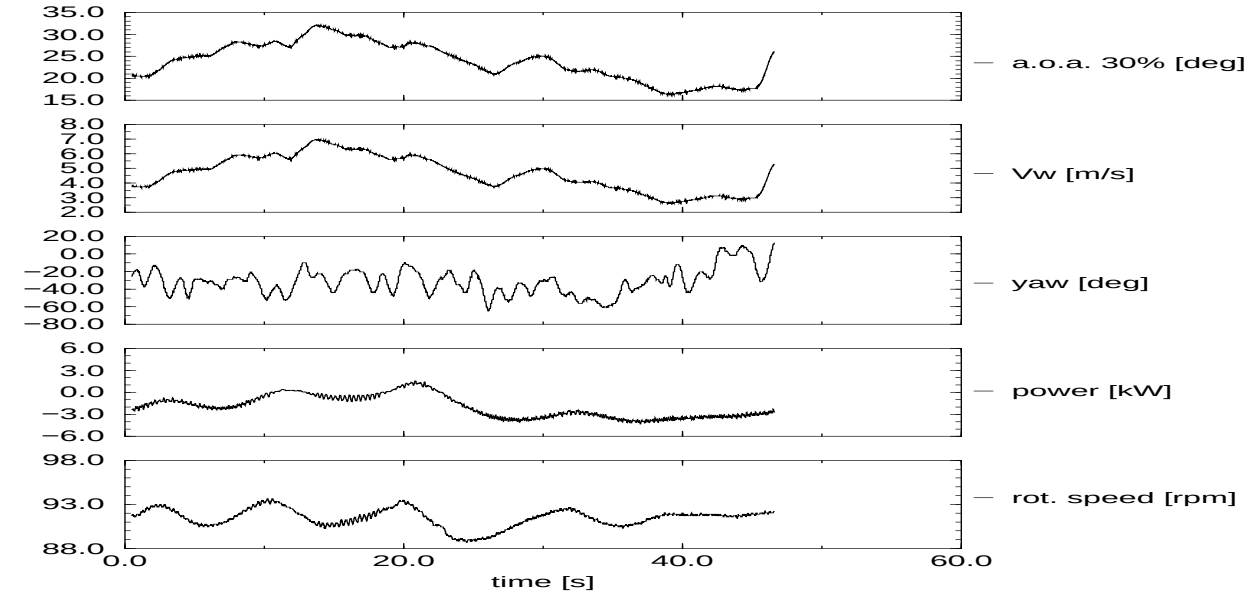

Figure C.141 *DUT: Time series of campaign y_rot_d_131.30*

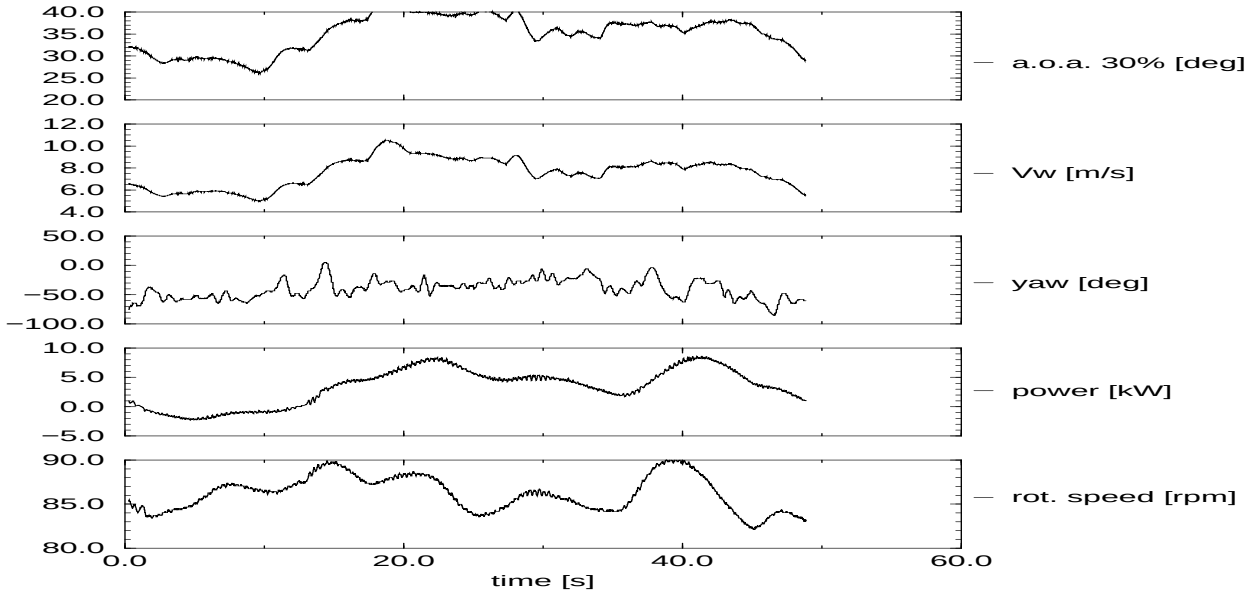

Figure C.142 *DUT: Time series of campaign y_rot_d_146.30*

DUT time series: Yawed campaigns at 50% span, plots

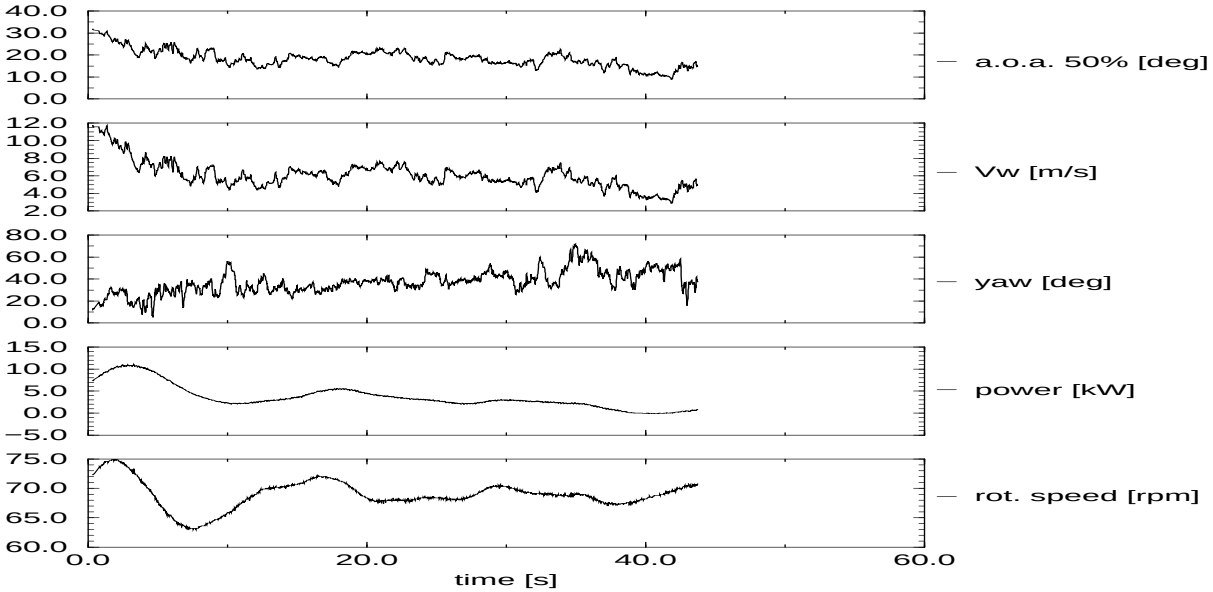

Figure C.143 *DUT: Time series of campaign y_rot_d_001.50*

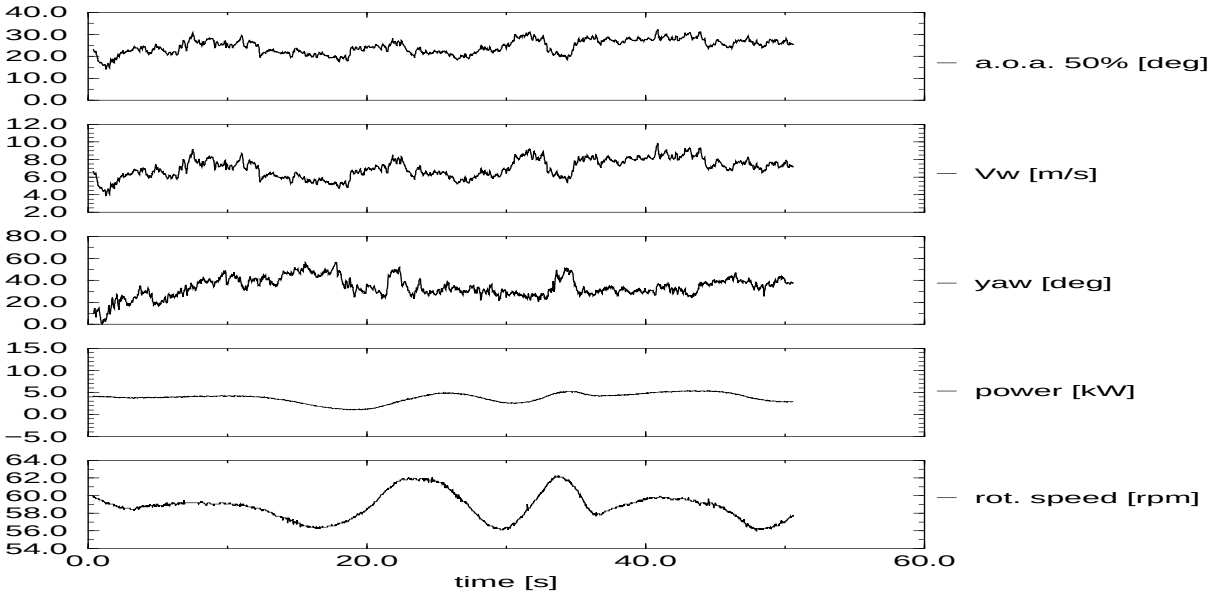

Figure C.144 *DUT: Time series of campaign y_rot_d_006.50*

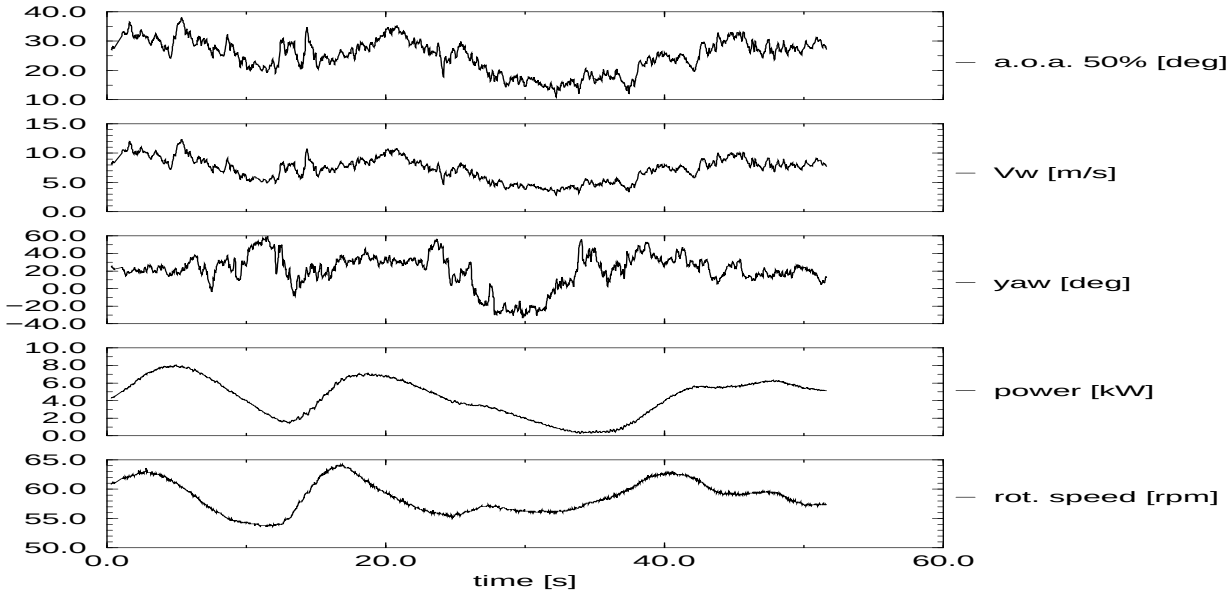

Figure C.145 *DUT: Time series of campaign y_rot_d_008.50*

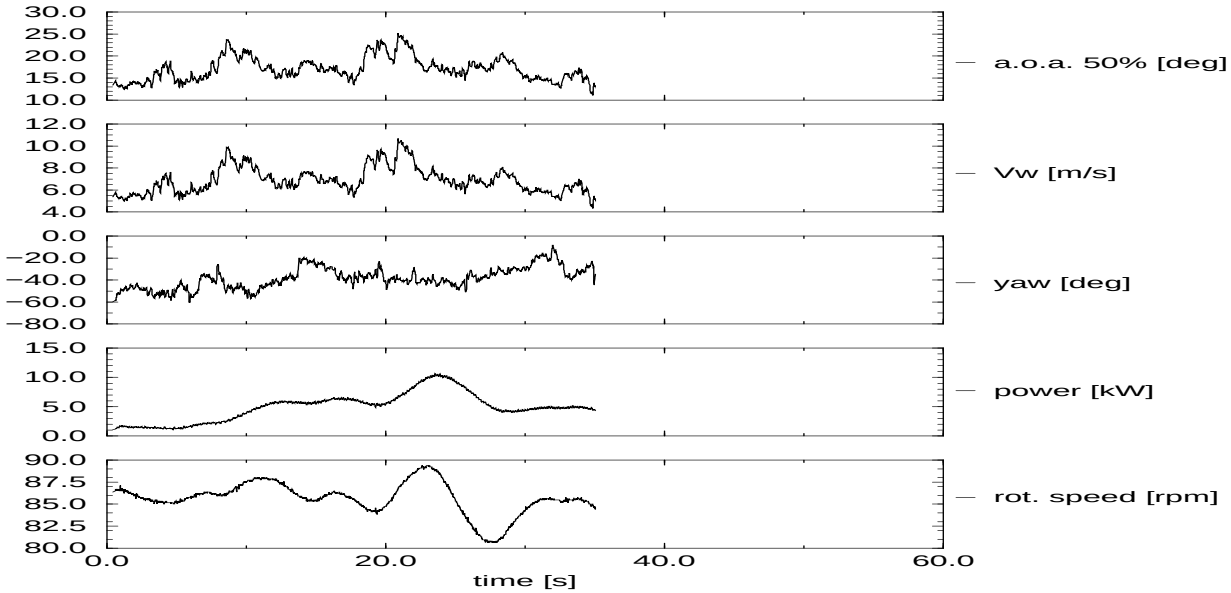

Figure C.146 *DUT: Time series of campaign y_rot_d_020.50*

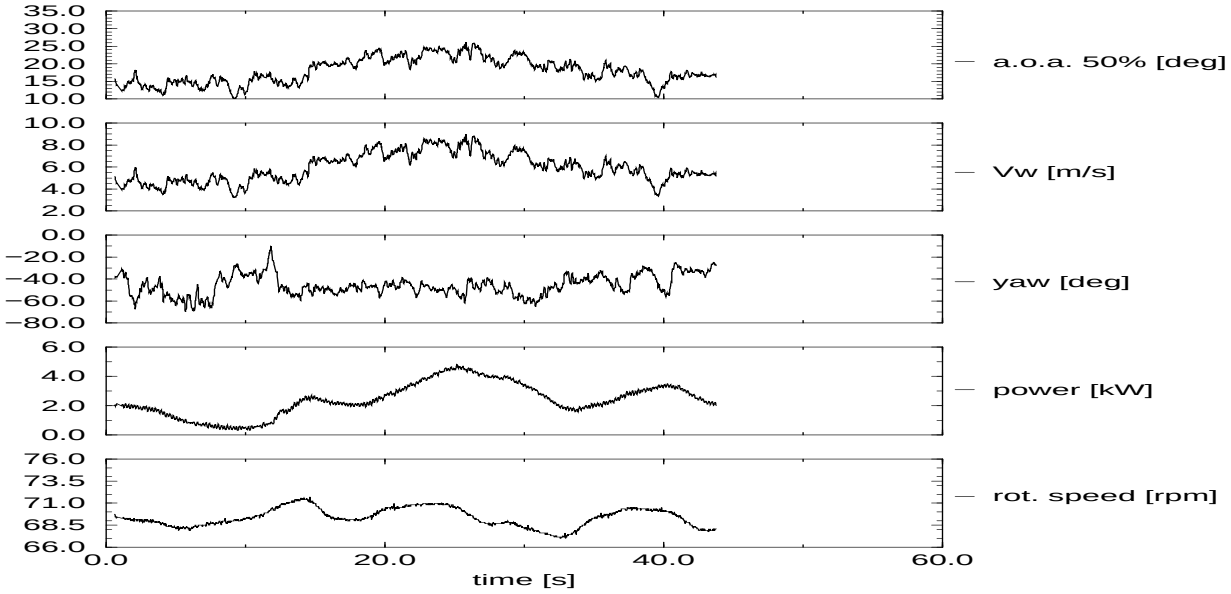

Figure C.147 *DUT: Time series of campaign y_rot_d_023.50*

DUT time series: Yawed campaigns at 70% span, plots

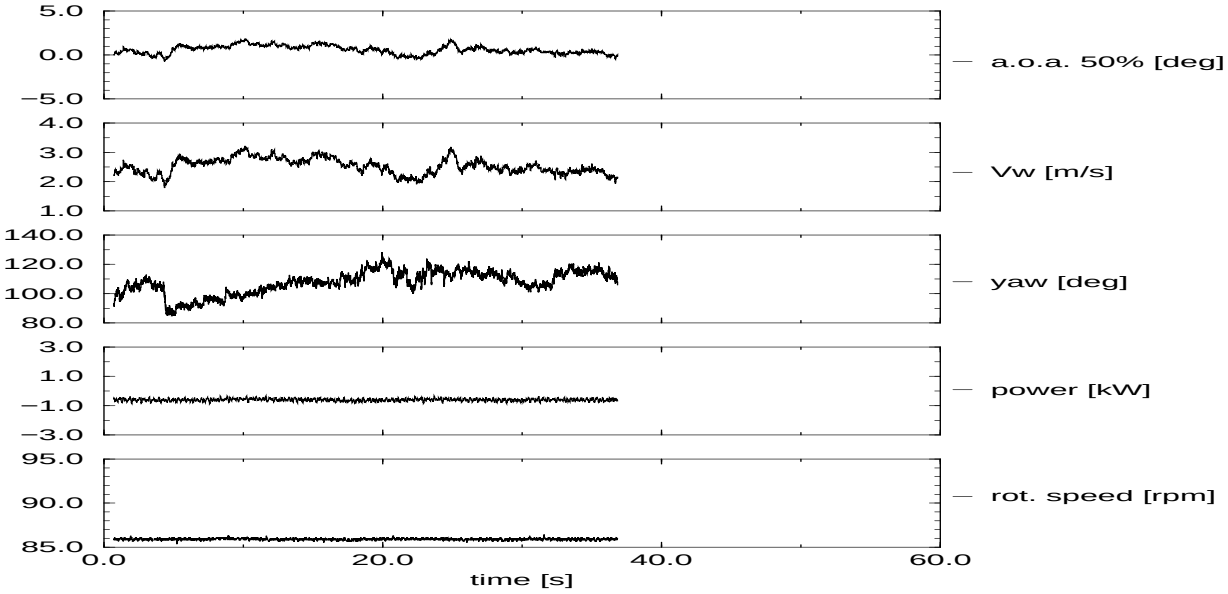

Figure C.148 *DUT: Time series of campaign y_rot_d_001.70*

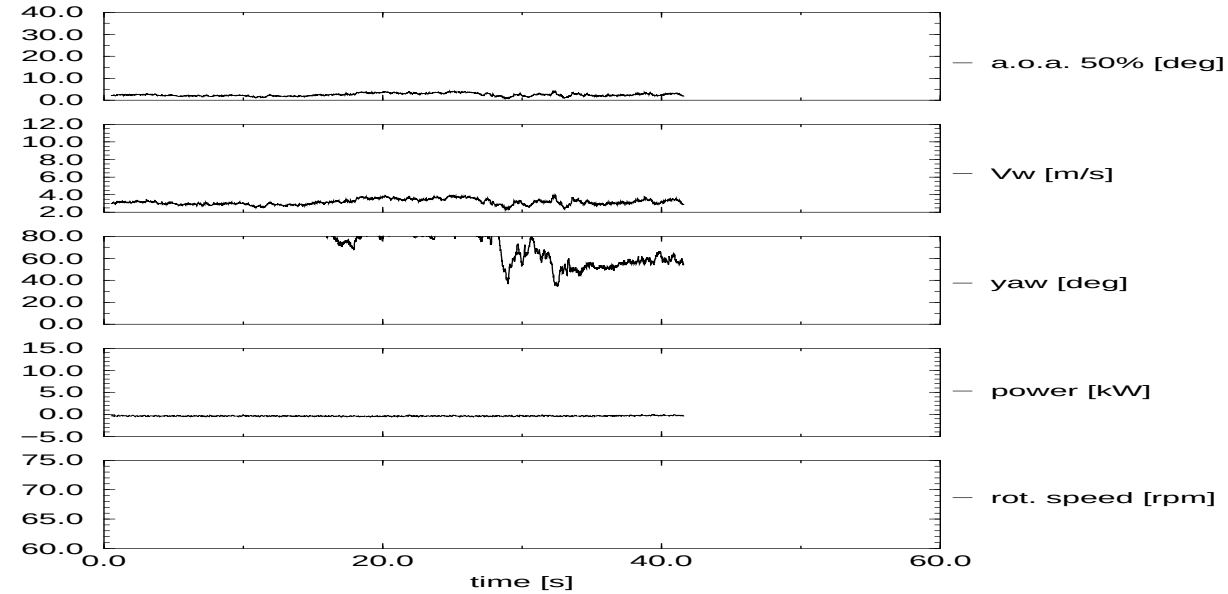

Figure C.149 *DUT: Time series of campaign y_rot_d_003.70*

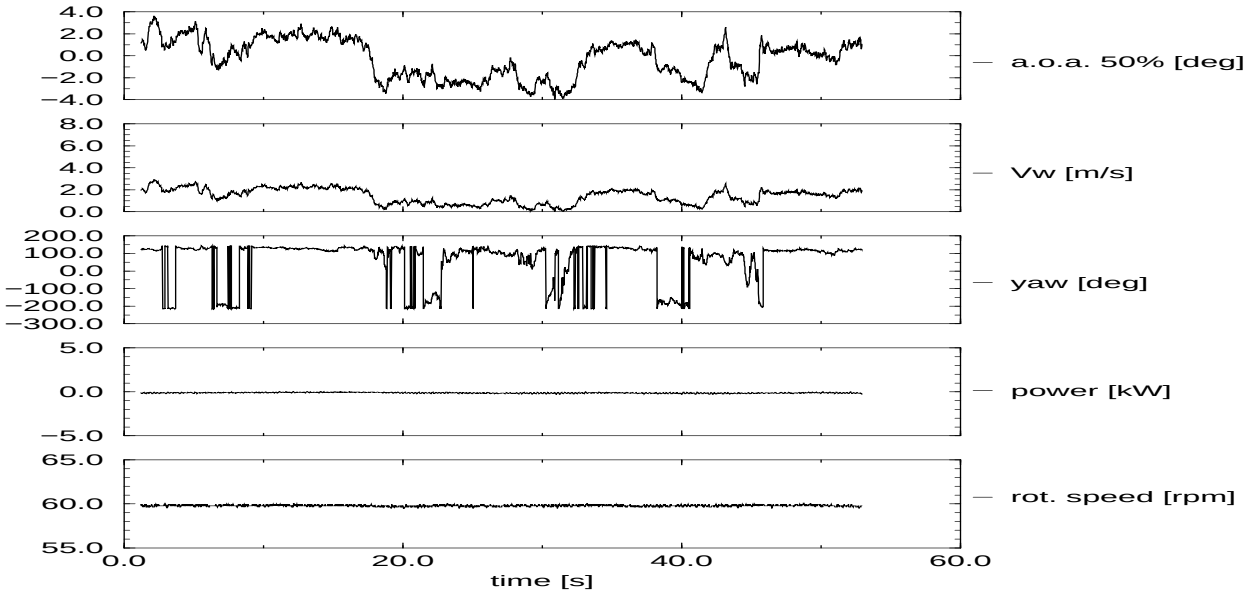

Figure C.150 *DUT: Time series of campaign y_rot_d_005.70*

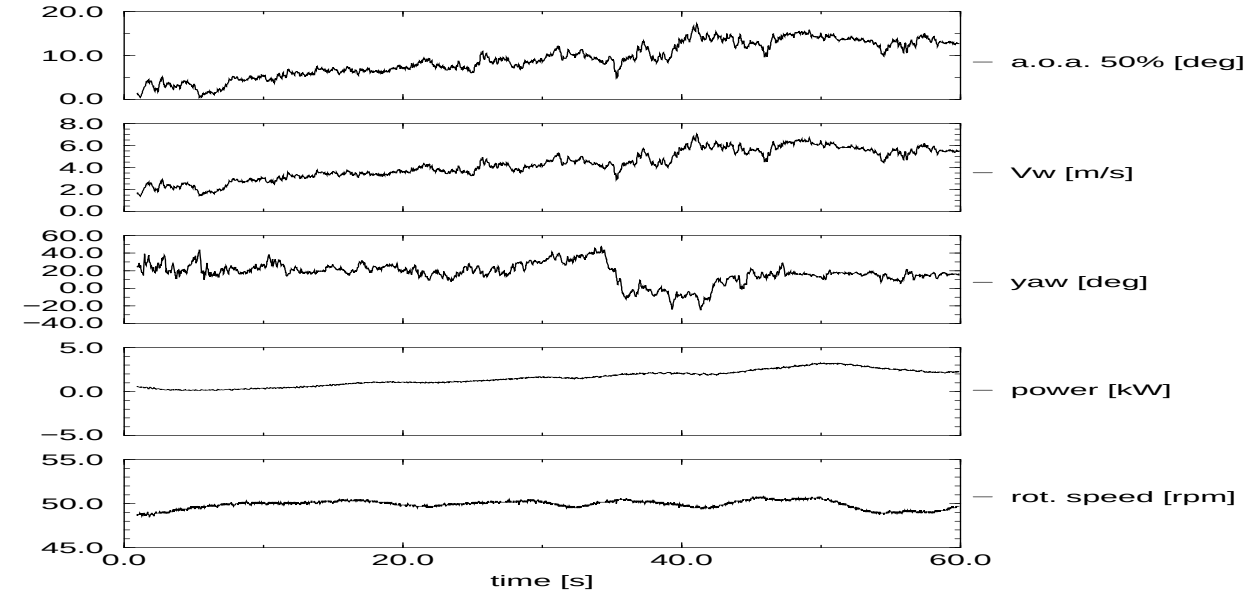

Figure C.151 *DUT: Time series of campaign y_rot_d_008.70*

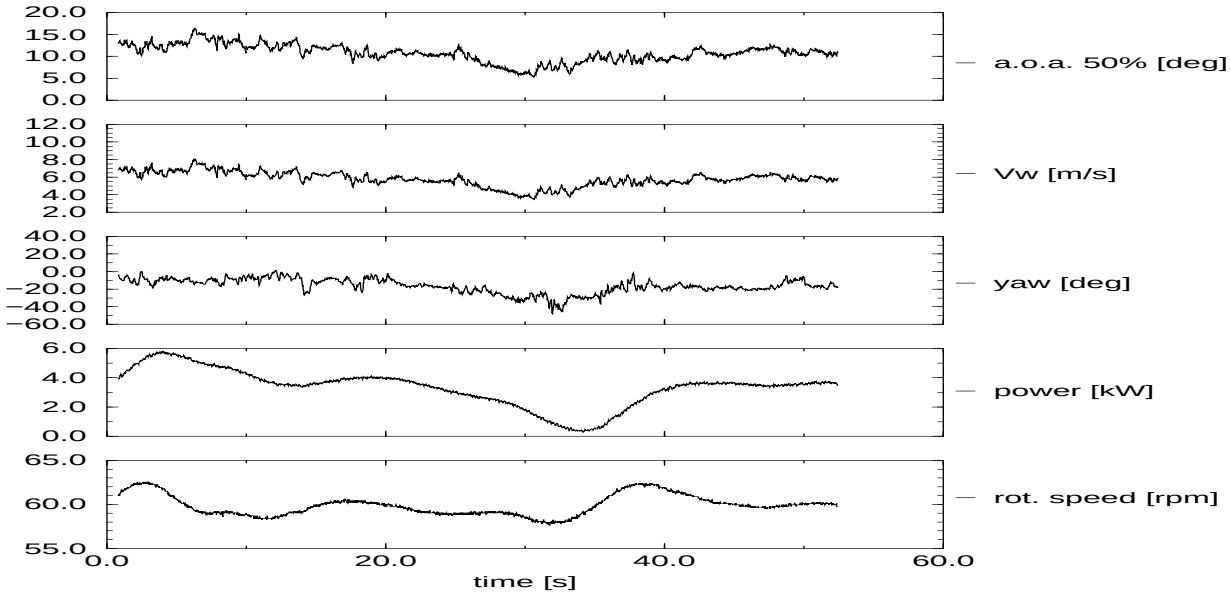

Figure C.152 *DUT: Time series of campaign y_rot_d_033.70*

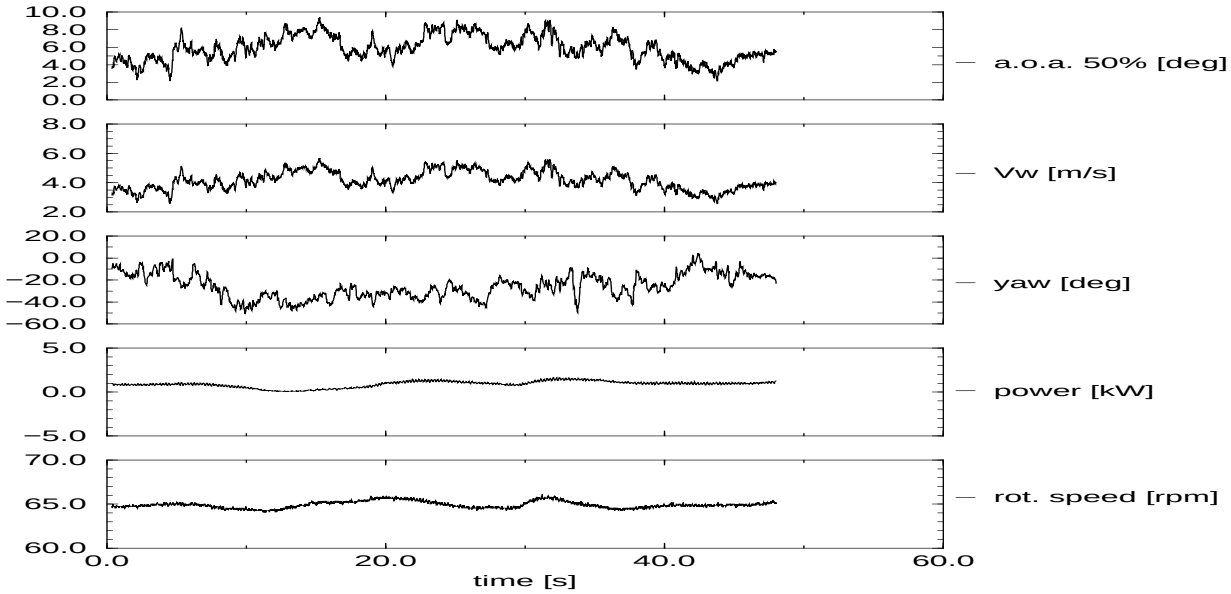

Figure C.153 *DUT: Time series of campaign y_rot_d_034.70*

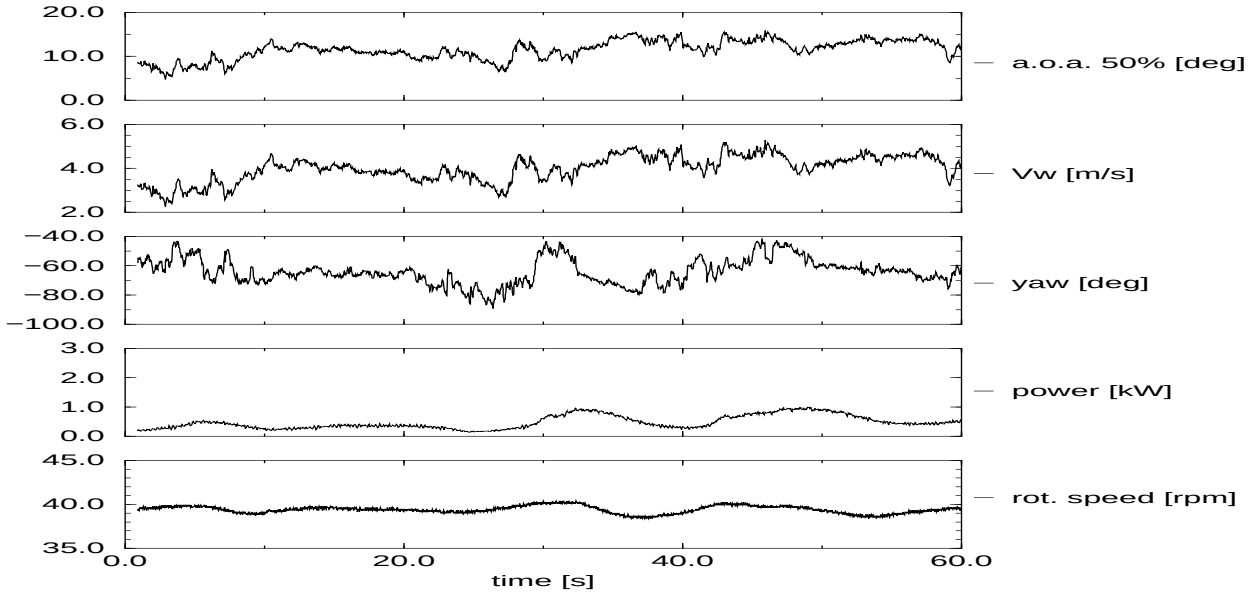

Figure C.154 *DUT: Time series of campaign y_rot_d_035.70*

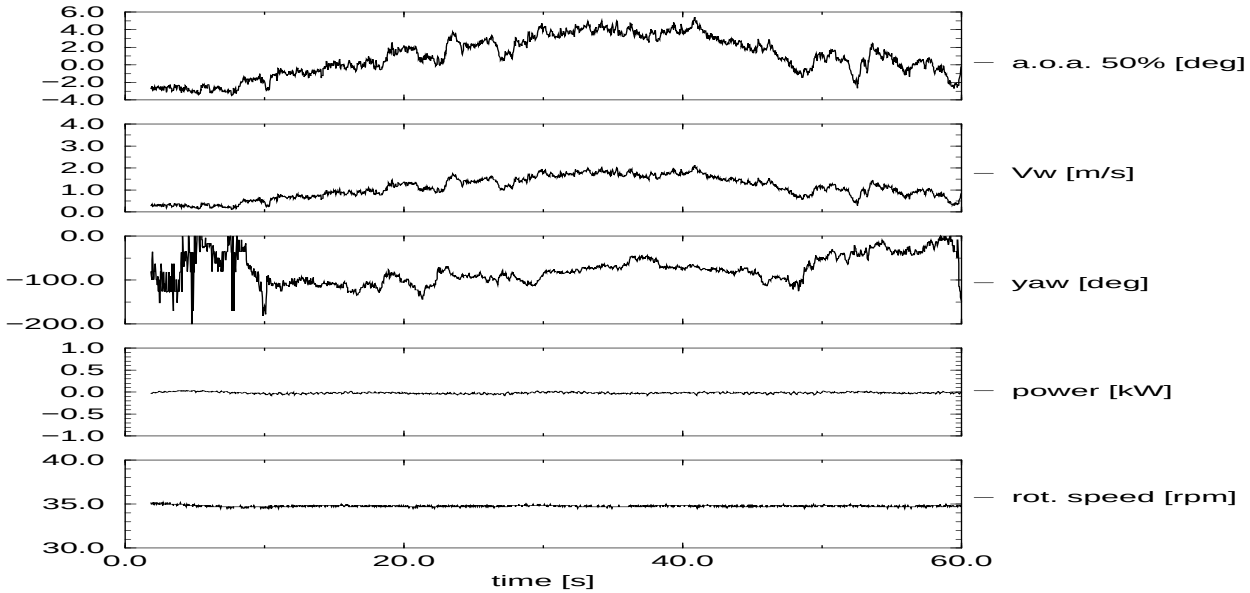

Figure C.155 *DUT: Time series of campaign y_rot_d_036.70*

C.11 DUT turbine and sectional coefficients

C.11.1 DUT, 2D profile coefficients

The 2D airfoil coefficients for the DUT test turbine are zipped into '/data/dut/2d/coef2d_d.zip, which contains the following files (Note that the drag coefficients have been derived from the pressure measurements):

- cla_2D_d_RE05, cda_2D_d_RE05, cda_2D_d_RE05, cma_2D_d_RE05, cta_2D_d_RE05, cna_2D_d_RE05: Airfoil coefficients (i.e. lift coefficient, pressure drag coefficient, moment coefficient, tangential force coefficient, normal force coefficient), at a Reynolds number of 0.5 10^6, clean configuration;
- cla_2D_d_RE10, cda_2D_d_RE10, cma_2D_d_RE10, cta_2D_d_RE10, cna_2D_d_RE10: Airfoil coefficients (i.e. lift coefficient, pressure drag coefficient, moment coefficient, tangential force coefficient, normal force coefficient) at a Reynolds number of 1.0 10^6, clean configuration;
- cla_2D_d_RE05_6probe_vg20, cda_2D_d_RE05_6probe_vg20, cda_2D_d_RE05_6probe_vg20, cma_2D_d_RE05_6probe_vg20, cta_2D_d_RE05_6probe_vg20, cna_2D_d_RE05_6probe_vg20: Airfoil coefficients (i.e. lift coefficient, pressure drag coefficient, moment coefficient, tangential force coefficient, normal force coefficient), at a Reynolds number of 0.5 10^6, from airfoil with vortex generators at 20% chord position and with 6-hole probe;
- cla_2D_d_RE10_6probe_vg20, cda_2D_d_RE10_6probe_vg20, cma_2D_d_RE10_6probe_vg20, cta_2D_d_RE10_6probe_vg20, cna_2D_d_RE10_6probe_vg20: Airfoil coefficients (i.e. lift coefficient, pressure drag coefficient, moment coefficient, tangential force coefficient, normal force coefficient) at a Reynolds number of 1.0 10^6, from airfoil with with vortex generators at 20% chord position and with 6-hole probe;
- cla_2D_d_RE10_3probe_vg20, cda_2D_d_RE10_3probe_vg20, cma_2D_d_RE10_3probe_vg20, cta_2D_d_RE10_3probe_vg20, cna_2D_d_RE10_3probe_vg20: Airfoil coefficients (i.e. lift coefficient, pressure drag coefficient, moment coefficient, tangential force coefficient, normal force coefficient) at a Reynolds number of 1.0 10^6, from airfoil with with vortex generators at 20% chord position and with 3-hole probe.

In addition the following file with 2D pressure coefficients have been stored:

- cpa_2D_RE10_noprobe_clean: Pressure coefficients from clean airfoil.
- cpa_2D_RE10_3probe_vg20: Pressure coefficients from airfoil with vortex generators at 20% chord position and with 3-hole probe.

C.12 Mie University time series

Mie University supplied 9 time series, i.e., 3 time series for the 50%, the 70% and the 90% section. Note that no time series were available for the 32.5% section. Most of the time series are supplied at a yaw angle larger than $\pm$ 5 degrees, and as such they are considered as yawed campaigns.

C.12.1 Mie time series: Non-yawed campaigns

Mie time series: Non-yawed campaigns at 50% span
The files are stored in directory '/data/mie/rottim/50percent'

Table C.28 *Global overview of Mie non-yawed measurement file at 50% span*

file	Mie filename	$\overline{\alpha_{50\%}}$ deg	$\overline{V}$ m/s	ϕ_y deg	$\overline{\text{Power}}$ kW	$\overline{\theta_{tip}}$ deg	$\overline{\Omega}$ rpm	duration s
ny_rot_m_001.50	AB9C2302_1	10.6	5.7	-0.3	1.4	1.3	91.7	84.039

Mie time series: Non-yawed campaigns at 70% span
The files are stored in directory '/data/mie/rottim/70percent'

Table C.29 *Global overview of Mie non-yawed measurement file at 70% span*

file	Mie filename	$\overline{\alpha_{70\%}}$ deg	$\overline{V}$ m/s	ϕ_y deg	$\overline{\text{Power}}$ kW	$\overline{\theta_{tip}}$ deg	$\overline{\Omega}$ rpm	duration s
ny_rot_m_001.70	AC010755_2	16.6	4.4	2.1	0.0	-1.7	80.0	87.352

C.12.2 Mie non-yawed campaigns, plots of time series

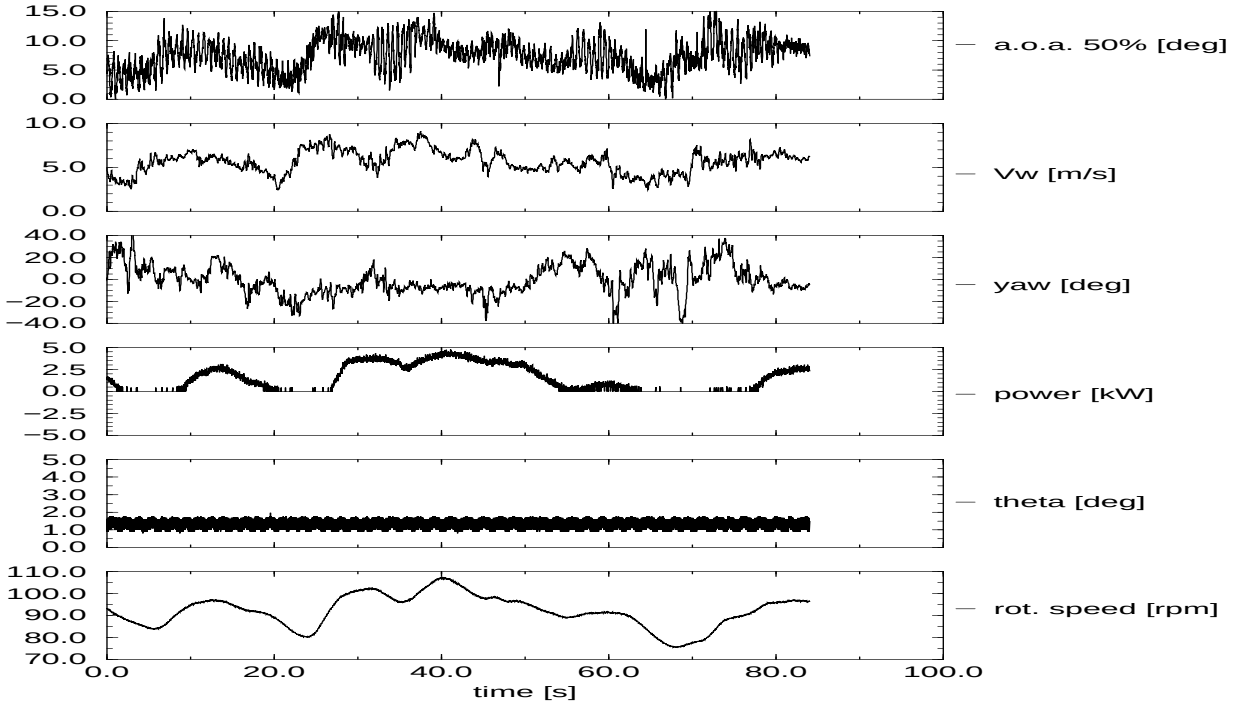

Figure C.156 *MIE: Time series of campaign ny_rot_m_001.50*

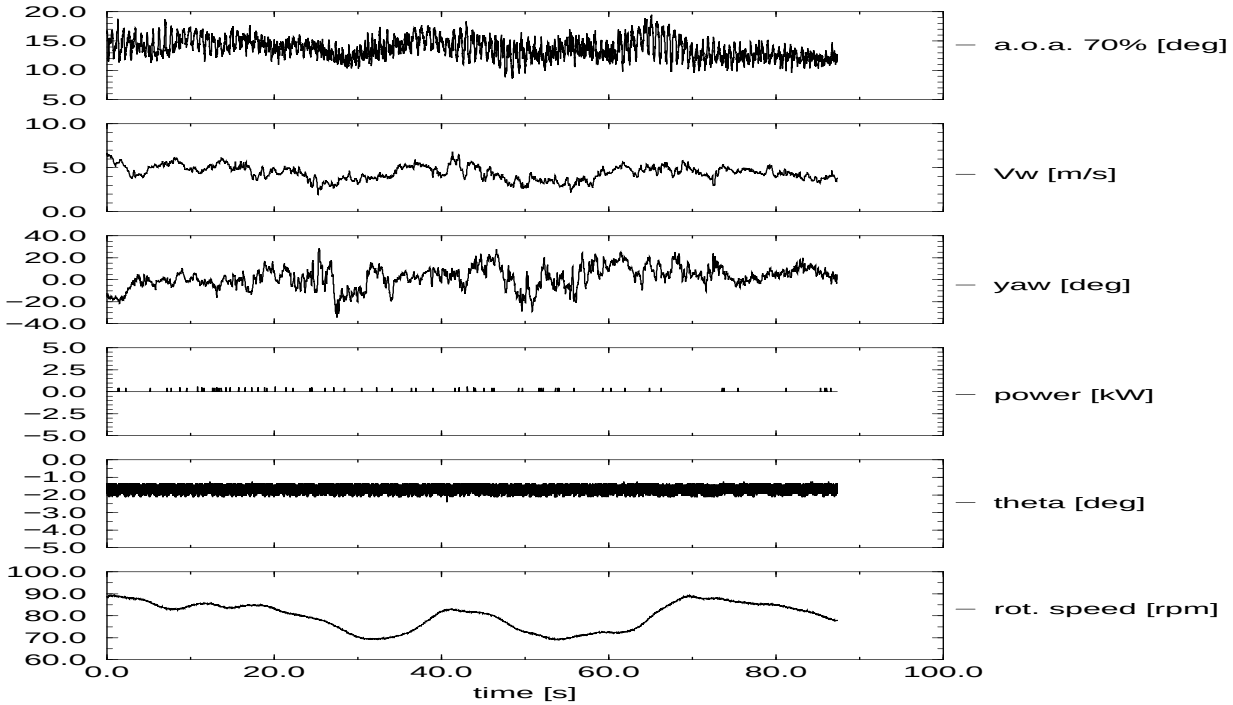

Figure C.157 *MIE: Time series of campaign ny_rot_m_001.70*

C.12.3 Mie time series: Yawed campaigns

Mie time series: Yawed campaigns, 50% section
The files are stored in directory '/data/mie/rottim/50percent'.

Table C.30 *Global overview of Mie yawed measurement files at 50% span*

file	Mie filename	$\overline{\alpha_{50\%}}$ deg	$\overline{V}$ m/s	ϕ_y deg	$\overline{\text{Power}}$ kW	$\overline{\theta_{tip}}$ deg	$\overline{\Omega}$ rpm	duration s
y_rot_m_001.50	AB9C2152_3	5.6	7.9	42.7	1.7	1.7	93.5	84.031
y_rot_m_002.50	AB9C2041_3	11.0	6.1	-42.5	1.0	1.3	89.5	84.047

Mie time series: Yawed campaigns, 70% section
The files are stored in directory '/data/mie/rottim/70percent'.

Table C.31 *Global overview of Mie yawed measurement files at 70% span*

file	Mie filename	$\overline{\alpha_{70\%}}$ deg	$\overline{V}$ m/s	ϕ_y deg	$\overline{\text{Power}}$ kW	$\overline{\theta_{tip}}$ deg	$\overline{\Omega}$ rpm	duration s
y_rot_m_001.70	AC010855_2	15.9	6.1	39.0	0.7	-3.7	85.2	83.941
y_rot_m_002.70	AC010815_3	17.5	6.8	-40.2	1.1	-0.5	91.7	84.129

Mie time series: Yawed campaigns, 90% section
The files are stored in directory '/data/mie/rottim/90percent'.

Table C.32 *Global overview of Mie yawed measurement files at 90% span*

file	Mie filename	$\overline{\alpha_{90\%}}$ deg	$\overline{V}$ m/s	ϕ_y deg	$\overline{\text{Power}}$ kW	$\overline{\theta_{tip}}$ deg	$\overline{\Omega}$ rpm	duration s
y_rot_m_001.90	AD013153_2	11.9	4.4	40.3	0.0	-2.2	77.4	84.266
y_rot_m_002.90	AD011731_3	20.8	6.3	11.6	0.1	-2.0	88.4	84.000
y_rot_m_003.90	AD012529_3	19.2	5.1	-41.5	0.0	-1.3	78.1	85.870

C.12.4 Mie yawed campaigns, plots of time series

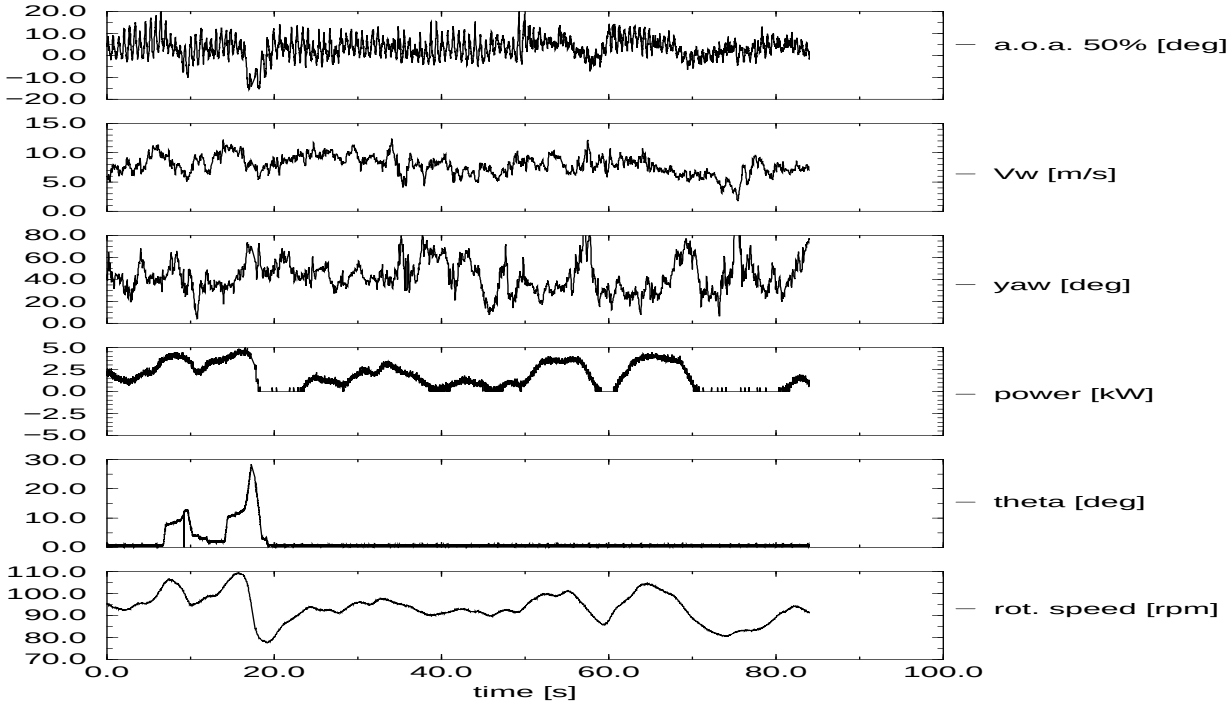

Figure C.158 *MIE: Time series of campaign y_rot_m_001.50*

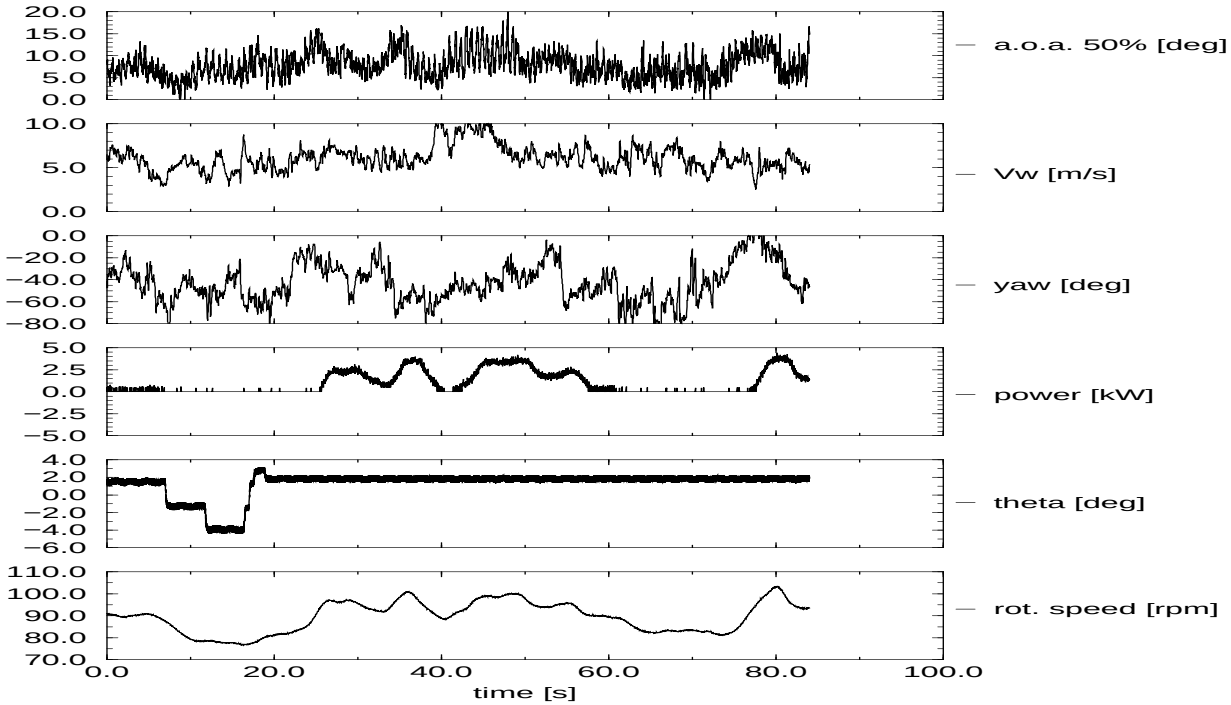

Figure C.159 *MIE: Time series of campaign y_rot_m_002.50*

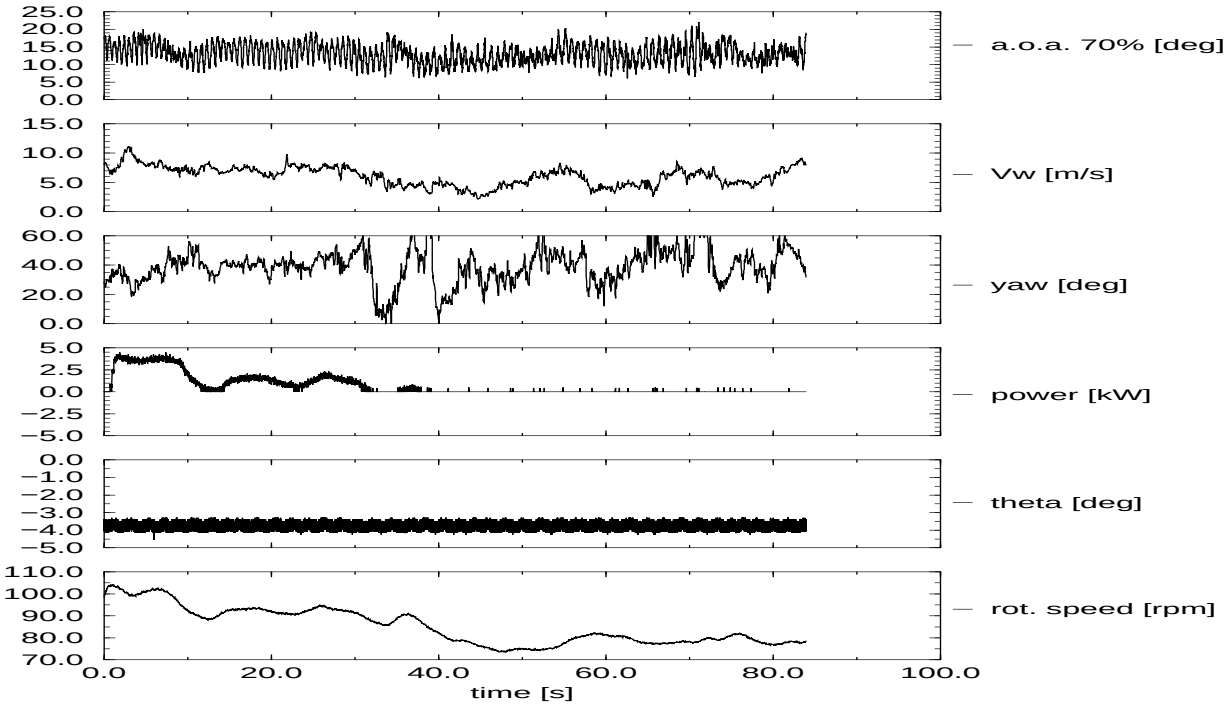

Figure C.160 *MIE: Time series of campaign y_rot_m_001.70*

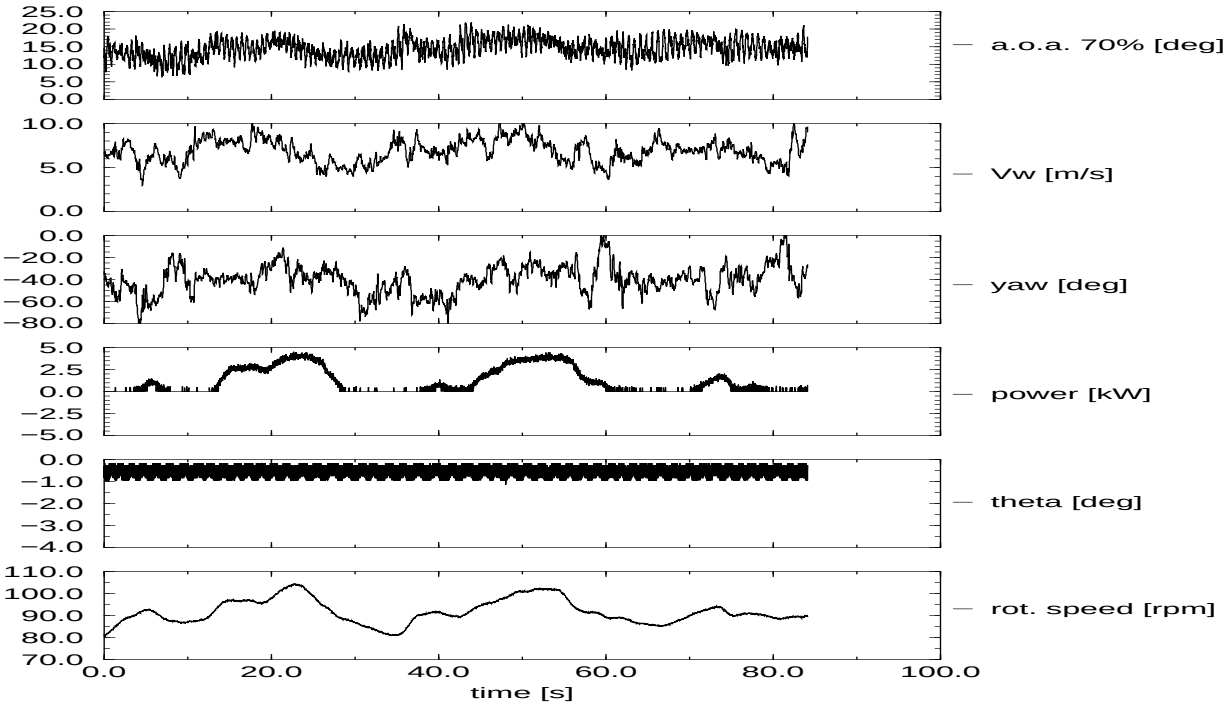

Figure C.161 *MIE: Time series of campaign y_rot_m_002.70*

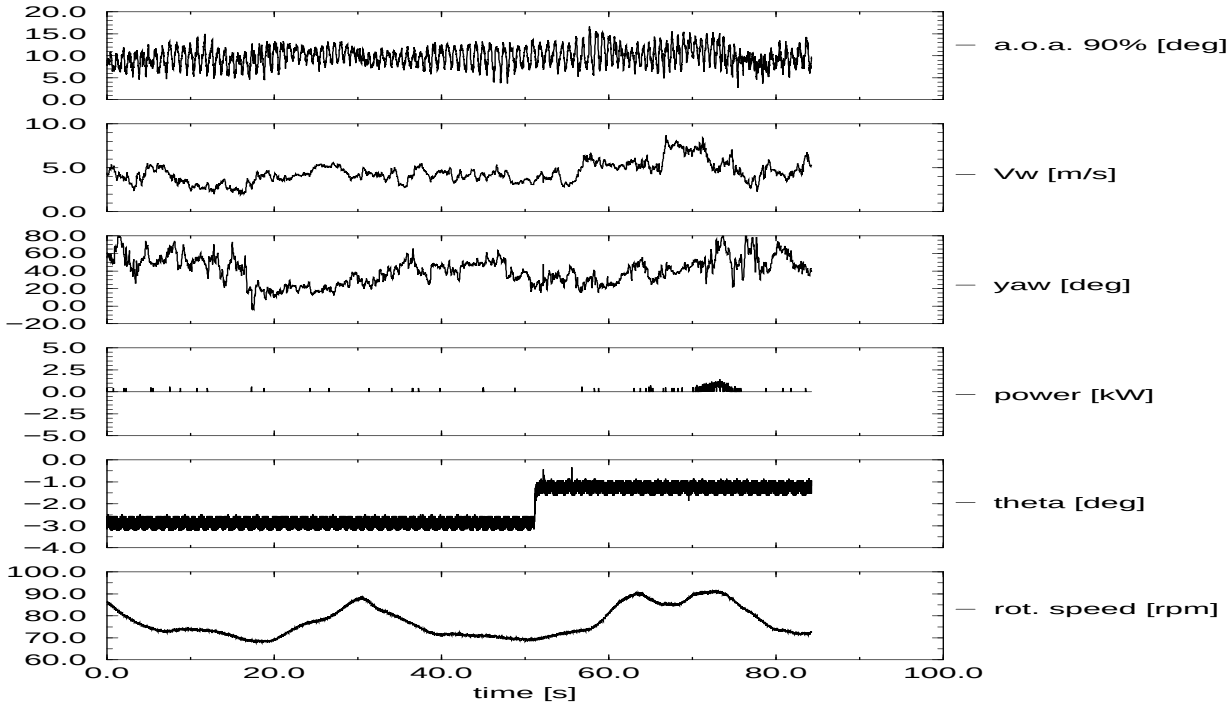

Figure C.162 *MIE: Time series of campaign y_rot_m_001.90*

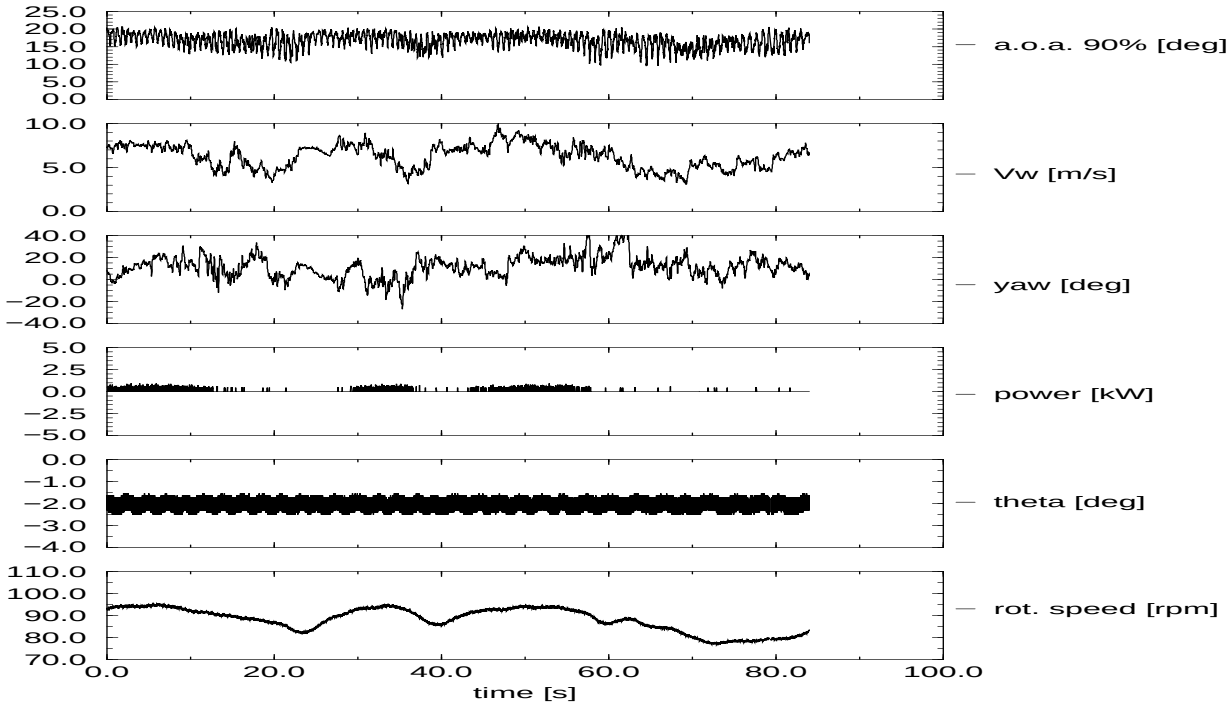

Figure C.163 *MIE: Time series of campaign y_rot_m_002.90*

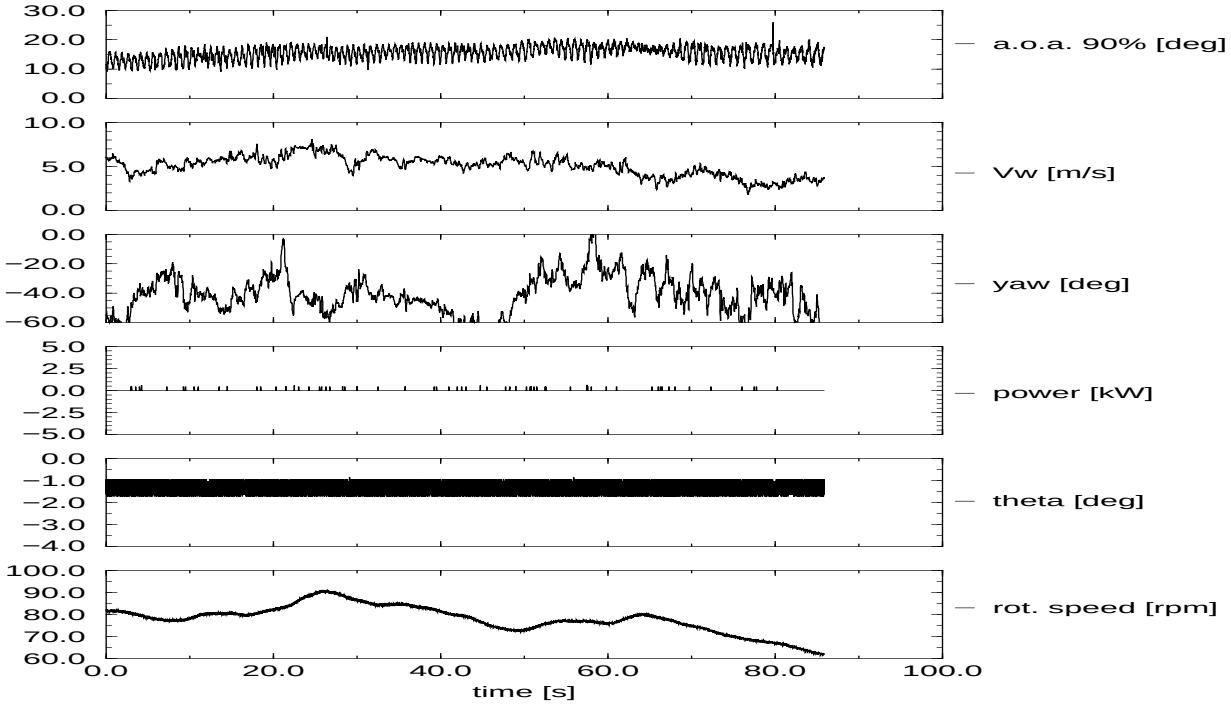

Figure C.164 *MIE: Time series of campaign y_rot_m_003.90*

C.13 Mie University turbine and sectional coefficients

C.13.1 Mie University, rotating coefficients

The rotating airfoil coefficients and the power curve for the Mie test turbine are stored into '/data/mie/rot_coef/coef_m.zip, which contains the following files:

- PV_m: Power curve (see figure I.6);
- cna33_ro.m: rotating $c_n - \alpha$ curve at 33% span;
- cna50_ro.m: rotating $c_n - \alpha$ curve at 50% span;
- cna70_ro.m: rotating $c_n - \alpha$ curve at 70% span;
- cna90_ro.m: rotating $c_n - \alpha$ curve at 90% span;
- cta33_ro.m: rotating $c_t - \alpha$ curve at 33% span;
- cta50_ro.m: rotating $c_t - \alpha$ curve at 50% span;
- cta70_ro.m: rotating $c_t - \alpha$ curve at 70% span;
- cta90_ro.m: rotating $c_t - \alpha$ curve at 90% span;

The rotating airfoil coefficients are presented in the figures C.165 and C.166.

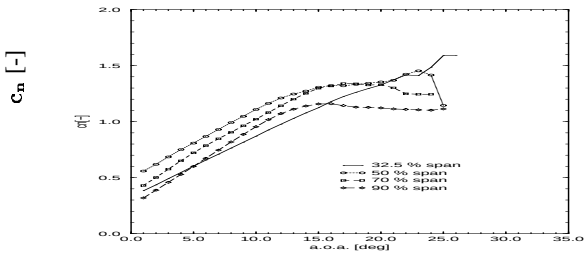

Figure C.165 *Mie measurements of* $c_n - \alpha$ *at different radial positions*

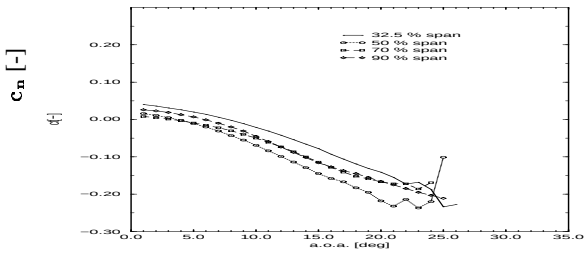

Figure C.166 *Mie measurements of* $c_t - \alpha$ *at different radial positions*

C.13.2 Mie University, 2D coefficients

The 2D airfoil coefficients for the Mie University test turbine are zipped into '/data/mie/2d/coef2d_m.zip, which contains the following 12 files:

- cna33_2D.m; This file contains the $c_n - \alpha$ data for the 32.5% span;
- cna50_2D.m; This file contains the $c_n - \alpha$ data for the 50% span;
- cna70_2D.m; This file contains the $c_n - \alpha$ data for the 70% span;
- cna90_2D.m; This file contains the $c_n - \alpha$ data for the 90% span;
- cta33_2D.m; This file contains the $c_t - \alpha$ data for the 32.5% span;
- cta50_2D.m; This file contains the $c_t - \alpha$ data for the 50% span;
- cta70_2D.m; This file contains the $c_t - \alpha$ data for the 70% span;
- cta90_2D.m; This file contains the $c_t - \alpha$ data for the 90% span;
- cpa33_2D.m; This file contains the $c_p(x/c) - \alpha$ data for the 32.5% span;
- cpa50_2D.m; This file contains the $c_p(x/c) - \alpha$ data for the 50% span;
- cpa70_2D.m; This file contains the $c_p(x/c) - \alpha$ data for the 70% span;

- cpa90_2D.m; This file contains the $\mathbf{c_p(x/c) - \alpha}$ data for the 90% span

The data are shown in the figures I.4 and I.5.

APPENDIX D. MODEL DESCRIPTION OF ECN TURBINE

For most of the data which are listed in the sequel, reference is made to [59] and [60].

D.1 Basic machine parameters

- Number of blades: 2
- Rotor diameter: 27.44 m
- Hub height: 22.4 m
- Type of rotor: Fixed
- Rotational speed: Fixed as well as variable speed operation, see section D.5.1
- Cut-in wind speed: $\approx$ 6 m/s
- Cut-out wind speed: $\approx$ 17 m/s
- Rated power: $\approx$ 300 kW (electrical)
- Tilt: 5 deg
- Cone: 5 deg
- Location of rotor: upwind
- Rotational direction: clockwise (looking downwind to the rotor)
- Rotor overhang: 4.6 m
- Power regulation: Experiment dependant

D.2 Rotor

D.2.1 Geometry

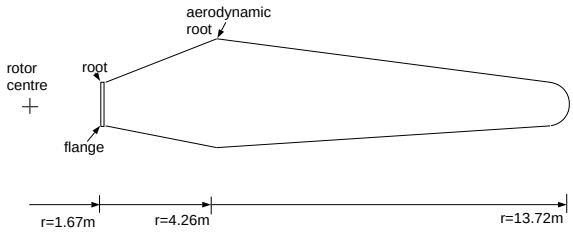

Figure D.1 *The layout of the Aerpac 25WPX blade*

- Blade type: Aerpac 25 WPX, see figure D.1.
- Root extension: 1.67 m
- Blade set angle: Experiment dependant
- Blade pitch: Fixed as well as variable pitch, see section D.5.1
- Blade profile: NACA 4418-24

Table D.1 provides the sectional chord, twist, thickness and aerofoil distributions as specified by the blade manufacturer.

There is some uncertainty in these values, in particular with regard to the outboard twist values of the instrumented sections: In the workshop the chord length, the twist and the thickness have been measured at the instrumented sections. The instrumented sections are located at distances r = 5.00 m, 8.80 m, 11.30 m from the rotor centre, which corresponds approximately to 30% blade span, 60% blade

Table D.1 *Blade geometric distributions*

Dist. from rotor centre[m]	chord [m]	twist [deg]	thick (%)	A'foil
1.67	0.550	12.0	100	-
1.9	0.550	12.0	100	-
3.08	1.208	12.0	37.4	NACA44
4.26	1.500	10.7	24	NACA44
5.45	1.364	8.2	22.6	NACA44
6.63	1.228	6.0	21.4	NACA44
7.81	1.091	4.2	20.4	NACA44
8.99	0.956	2.7	19.6	NACA44
10.17	0.820	1.5	19.0	NACA44
11.36	0.684	0.7	18.0	NACA44
12.54	0.548	0.2	18.0	NACA44
13.72	0.412	0.0	18.0	NACA44

Table D.2 *Blade geometric data for blade A measured in workshop*

Dist. from rotor centre[m]	chord [m]	twist [deg]	thick (%)
5.0	1.42	8.3	22.8
8.8	0.986	4.1	19.9
11.3	0.697	4.8	18.6

span and 80% blade span. The results of the measurements are presented in table D.2.

A graphical presentation is given in the figures D.2 to D.4. It is known that the chord lengths, the thickness and the twist for blade B (the non-instrumented blade) agree well with the 'manufacturer values'. Hence the values from table D.1 can be used for the chord length, the thickness and the twist of blade B.

The same holds for the twist of blade A at the inboard stations ($r <\approx 8.5\mathrm{m}$). However at $\approx$ 11 m there is a 'jump' in the twist distribution. Unfortunately this jump is only measured at one radial position. It is obvious that twist measurements at more radial positions are required in order to perform a reliable simulation. Until then the user will have to work according his own insight.

In table D.3 to D.5 the (measured) coordinates of the instrumented profiles are given.

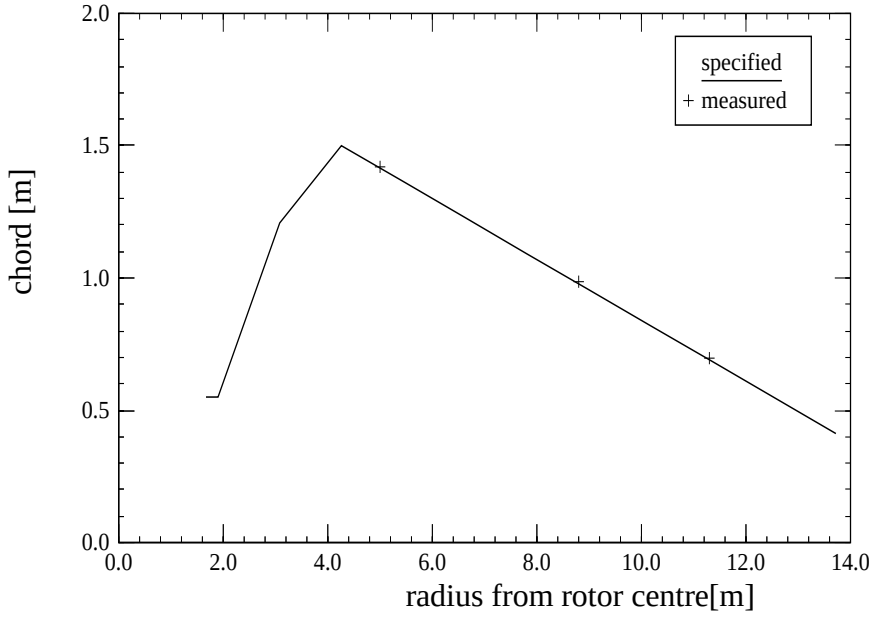

Figure D.2 *Measured and specified chord length*

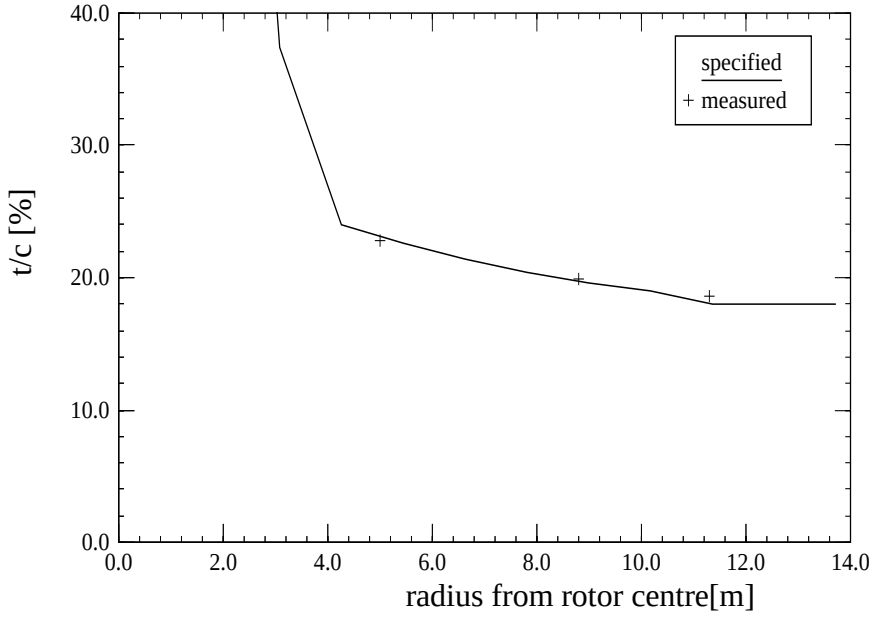

Figure D.3 *Measured and specified thickness*

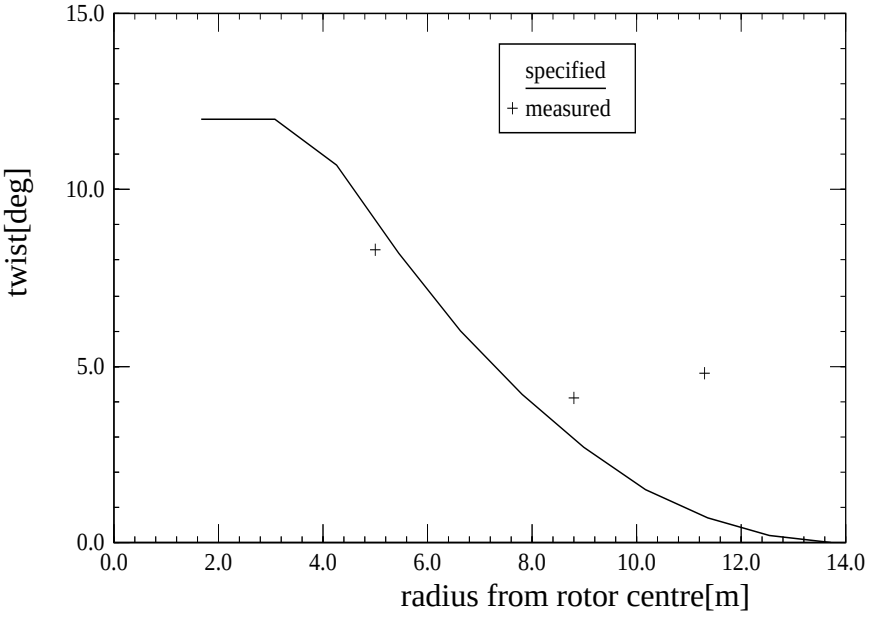

Figure D.4 *Measured and specified twist*

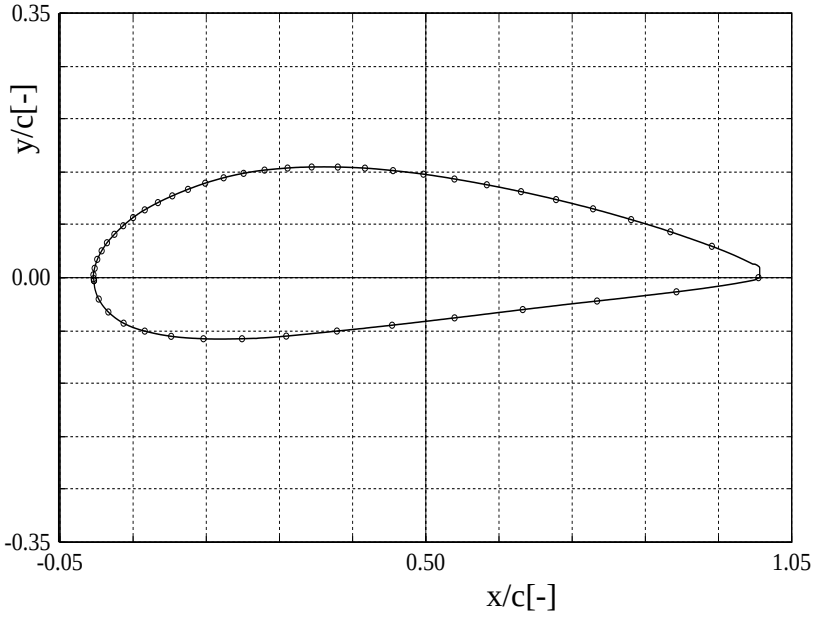

Figure D.5 *Geometry and tap position of 30% profile*

Table D.3 *Geometry of blade profile at 30% span*

See figure D.5

x/c [-]	y_{upper}/c[-]	y_{lower}/c [-]
0.00000	0.00000	-0.00010
0.00150	0.01030	-0.00760
0.00300	0.01560	-0.01610
0.00450	0.01980	-0.02050
0.00600	0.02350	-0.02410
0.00900	0.02930	-0.02950
0.01700	0.04130	-0.03980
0.02500	0.05060	-0.04730
0.03300	0.05840	-0.05310
0.04500	0.06860	-0.05990
0.05000	0.07240	-0.06220
0.06000	0.07950	-0.06590
0.07200	0.08690	-0.06940
0.08200	0.09200	-0.07170
0.09400	0.09780	-0.07410
0.10700	0.10350	-0.07620
0.11700	0.10750	-0.07760
0.12800	0.11170	-0.07870
0.13900	0.11570	-0.07960
0.15000	0.11930	-0.08020
0.16700	0.12460	-0.08090
0.18700	0.13000	-0.08120
0.21100	0.13530	-0.08100
0.23000	0.13870	-0.08060
0.25000	0.14150	-0.07990
0.29400	0.14520	-0.07700
0.33900	0.14650	-0.07310
0.38300	0.14600	-0.06920
0.42800	0.14360	-0.06490
0.47200	0.13960	-0.06060
0.52200	0.13360	-0.05540
0.56700	0.12690	-0.05070
0.61700	0.11850	-0.04530
0.66700	0.10920	-0.04000
0.71700	0.09890	-0.03490
0.76100	0.08870	-0.03060
0.80600	0.07750	-0.02610
0.85000	0.06580	-0.02160
0.88300	0.05610	-0.01810
0.91700	0.04560	-0.01420
0.94500	0.03640	-0.01070
0.96800	0.02790	-0.00740
0.98500	0.02080	-0.00470
0.99600	0.01730	-0.00230
1.00000	0.01520	-0.00060

Table D.4 *Geometry of blade profile at 60% span*

See figure D.6

x/c [-]	y_{upper}/c[-]	y_{lower}/c [-]
0.00000	0.00180	-0.02830
0.00150	0.00600	-0.03130
0.00300	0.00980	-0.03390
0.00450	0.01320	-0.03630
0.00600	0.01610	-0.03840
0.00900	0.02130	-0.04200
0.01700	0.03150	-0.04960
0.02500	0.03850	-0.05530
0.03300	0.04460	-0.05960
0.04500	0.05290	-0.06440
0.05000	0.05600	-0.06600
0.06000	0.06180	-0.06860
0.07200	0.06810	-0.07080
0.08200	0.07290	-0.07210
0.09400	0.07820	-0.07340
0.10700	0.08340	-0.07440
0.11700	0.08710	-0.07490
0.12800	0.09090	-0.07530
0.13900	0.09450	-0.07550
0.15000	0.09780	-0.07560
0.16700	0.10250	-0.07540
0.18700	0.10720	-0.07500
0.21100	0.11210	-0.07420
0.23000	0.11520	-0.07310
0.25000	0.11780	-0.07170
0.29400	0.12140	-0.06830
0.33900	0.12300	-0.06450
0.38300	0.12250	-0.06050
0.42800	0.12050	-0.05650
0.47200	0.11740	-0.05250
0.52200	0.11250	-0.04790
0.56700	0.10690	-0.04370
0.61700	0.09970	-0.03910
0.66700	0.09170	-0.03480
0.71700	0.08270	-0.03060
0.76100	0.07380	-0.02710
0.80600	0.06390	-0.02340
0.85000	0.05350	-0.01980
0.88300	0.04510	-0.01710
0.91700	0.03590	-0.01410
0.94500	0.02780	-0.01130
0.96800	0.02060	-0.00870
0.98500	0.01470	-0.00640
0.99600	0.00620	-0.00220
1.00000	0.00600	-0.00090

Table D.5 *Geometry of blade profile at 80% span*

See figure D.7

x/c [-]	y_{upper}/c[-]	y_{lower}/c [-]
0.00000	0.00020	-0.00010
0.00150	0.00510	-0.00160
0.00300	0.01230	-0.01900
0.00450	0.01700	-0.02130
0.00600	0.02110	-0.02380
0.00900	0.02720	-0.02760
0.01700	0.03890	-0.03420
0.02500	0.04700	-0.03920
0.03300	0.05370	-0.04310
0.04500	0.06230	-0.04750
0.05000	0.06540	-0.04890
0.06000	0.07120	-0.05100
0.07200	0.07740	-0.05300
0.08200	0.08190	-0.05440
0.09400	0.08680	-0.05560
0.10700	0.09150	-0.05670
0.11700	0.09480	-0.05740
0.12800	0.09830	-0.05790
0.13900	0.10150	-0.05820
0.15000	0.10440	-0.05840
0.16700	0.10860	-0.05840
0.18700	0.11300	-0.05810
0.21100	0.11750	-0.05750
0.23000	0.12030	-0.05690
0.25000	0.12270	-0.05590
0.29400	0.12600	-0.05330
0.33900	0.12720	-0.05070
0.38300	0.12650	-0.04790
0.42800	0.12410	-0.04480
0.47200	0.12030	-0.04160
0.52200	0.11460	-0.03790
0.56700	0.10840	-0.03490
0.61700	0.10050	-0.03160
0.66700	0.09170	-0.02840
0.71700	0.08220	-0.02550
0.76100	0.07320	-0.02290
0.80600	0.06290	-0.02040
0.85000	0.05170	-0.01800
0.88300	0.04290	-0.01630
0.91700	0.03370	-0.01450
0.94500	0.02600	-0.01270
0.96800	0.01940	-0.01100
0.98500	0.01440	-0.00930
0.99600	0.00940	-0.00570
0.99640	0.00900	-0.00530

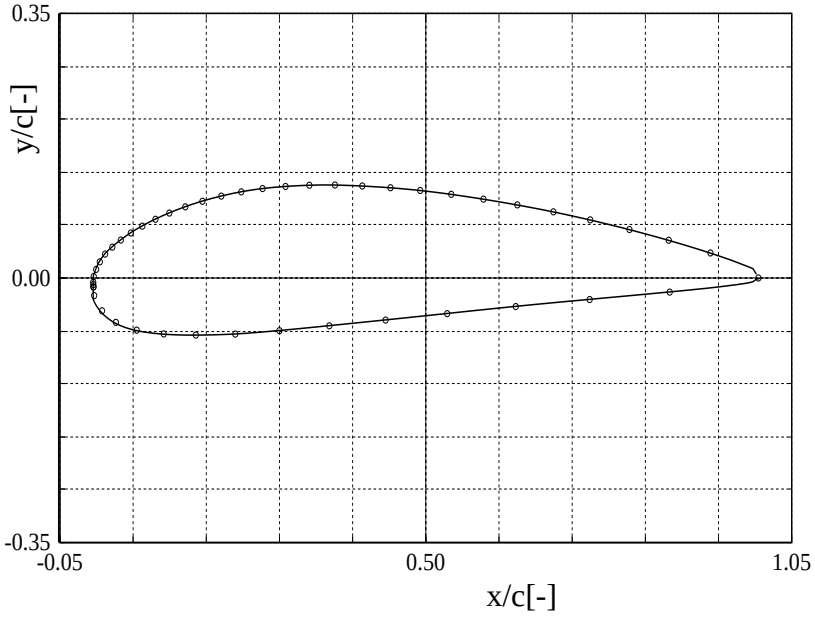

Figure D.6 *Geometry and tap position of 60% profile*

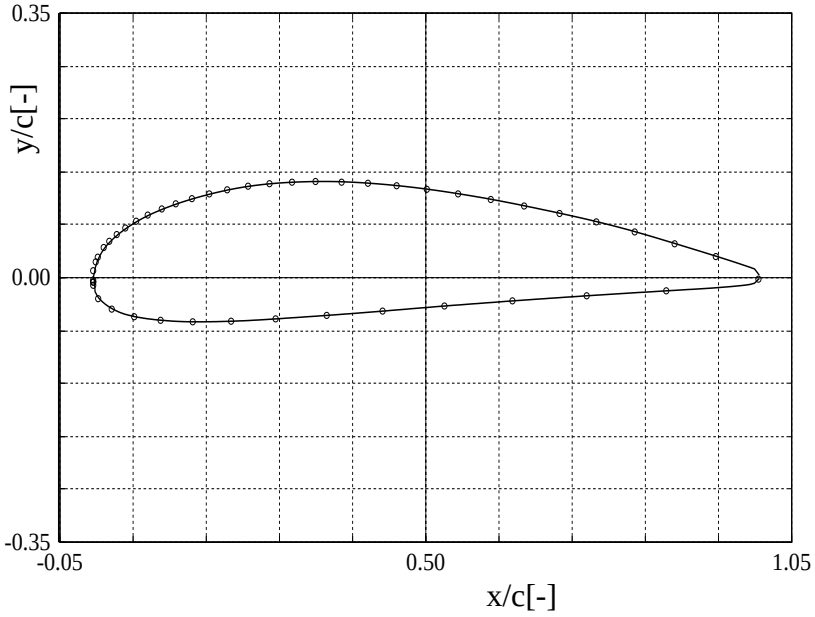

Figure D.7 *Geometry and tap position of 80% profile*

D.2.2 Aerodynamics

Figure D.8 and D.9 show the approximated lift and drag data respectively for the root, mid span and tip positions from [61].

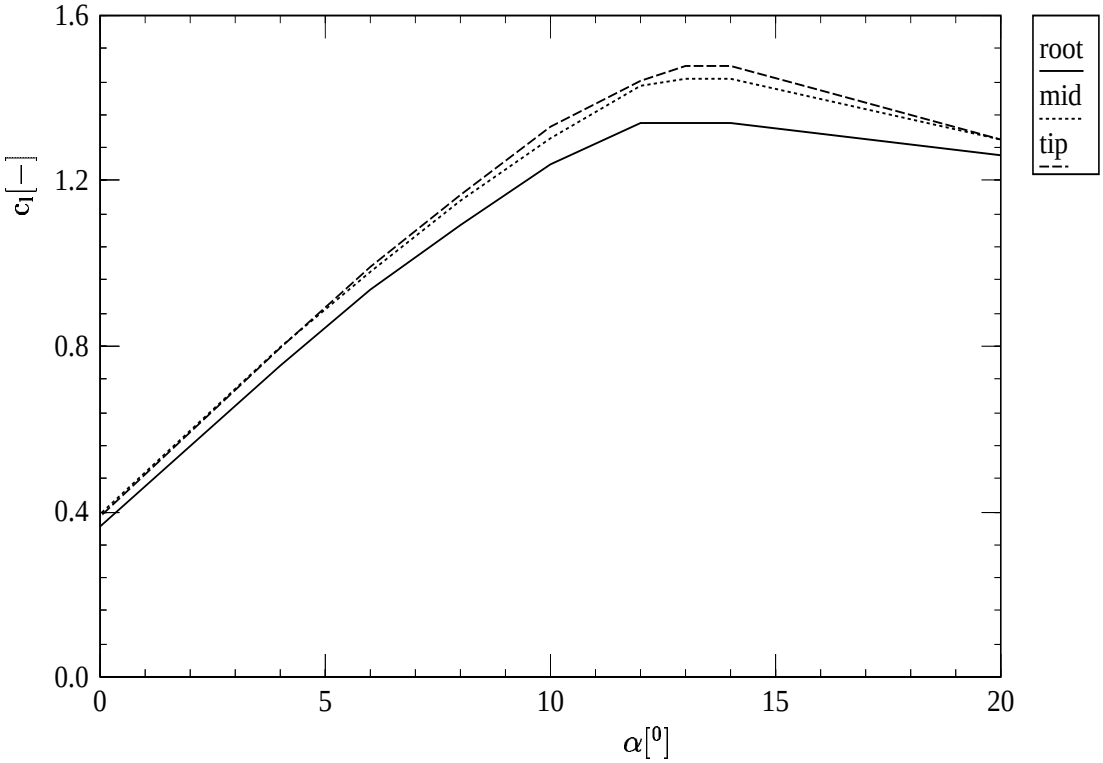

Figure D.8 *Lift versus angle of attack for 30% (NACA4423) , 60%(NACA4420) and 80% (NACA4418) (Estimated, 2D)*

D.2.3 Structural properties

- Rotor mass (including root): 2904 kg
- Hub mass (exluding the rotor): 629.2 kg
- Blade material: GRP

The blade masses, centre of gravity and eigenfrequencies (non-rotating) for both blades are listed below.

- mass of the instrumented blade outside root: 1168 kg
- mass of the non-instrumented blade outside root: 1107 kg
- centre of gravity of instrumented blade from root: 3.37 + 1.33= 4.70 m
- centre of gravity of non-instrumented blade from root: 3.61 + 1.33= 4.94 m
- first edgewise eigenfrequency of instrumented blade (standstill): 4.17 Hz
- first edgewise eigenfrequency of non-instrumented blade (standstill): 3.366 Hz
- first flatwise eigenfrequency of instrumented blade (standstill): 2.57 Hz
- first flatwise eigenfrequency of non-instrumented blade (standstill): 1.602 Hz

Note that the centre of gravity is derived from the measured static moment of inertia at r=1.33 m from the rotor centre, see [60].

The eigenfrequencies for the instrumented blade are measured. The eigenfrequencies for the non-instrumented blade are calculated from the stiffness data supplied by the manufacturer.

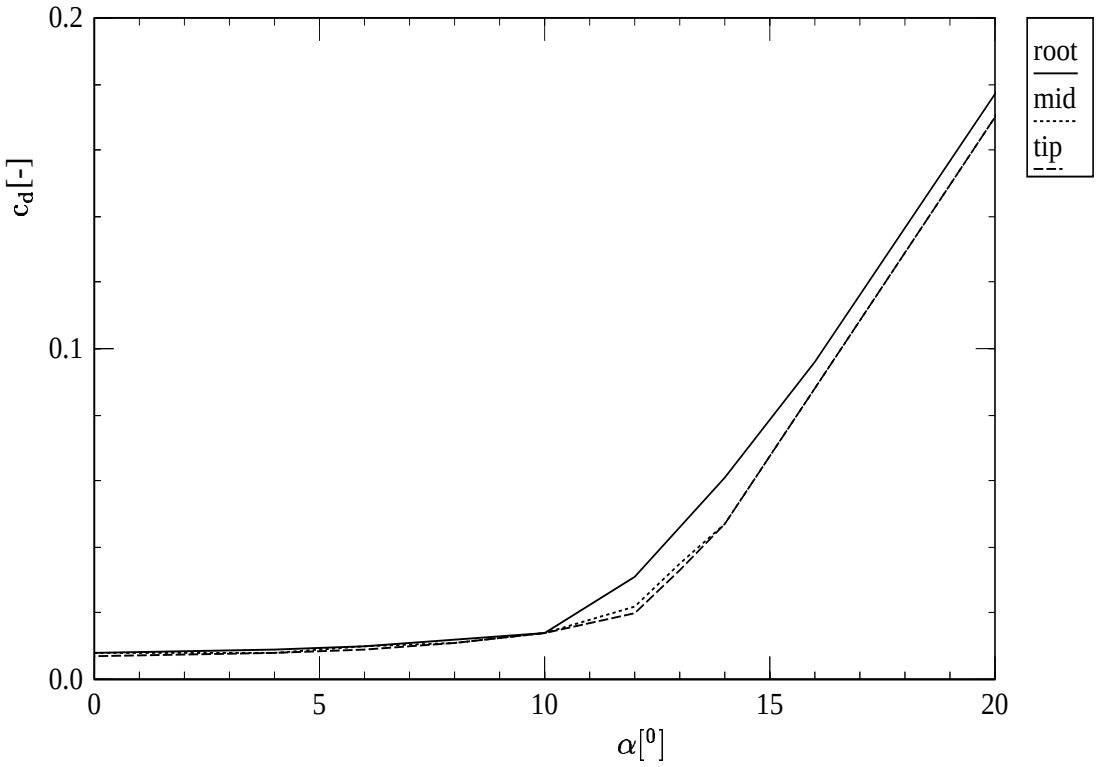

Figure D.9 *Drag versus angle of attack for 30%, 60% and 80% (Estimated, 2D)*

Table D.6 and D.7 provide the mass and stiffness distributions. It is emphasized that the mass distributions are tuned in order to achieve the correct blade masses and centres of gravity. The stiffness distribution (for r>1.67 m) is supplied by the manufacturer. The mass and stiffness distribution yield standstill eigenfrequencies for the instrumented blade of 2.51 and 4.262 Hz in flap resp. edgewise direction. This compares very well with the measured frequencies listed above.

Table D.6 *Mass distribution of blades*

Dist.from rotor centre [m]	mass [kg/m] instrumented	mass [kg/m] non-instrumented
1.00	314.81	314.81
1.665	314.81	314.81
1.67	916.13	826.09
1.9	916.13	826.09
1.91	113.22	105.93
2.49	105.40	98.31
3.67	89.77	83.05
4.85	97.20	74.79
6.04	77.32	66.10
7.22	61.81	55.93
8.40	63.76	45.76
9.58	49.39	35.59
10.76	31.51	24.37
11.95	35.99	16.10
13.15	16.50	50.
13.46	8.0	225.
13.77	0.	0

Table D.7 *Stiffness distribution of blades*

Dist.from rotor centre [m]	Edgewise stiffness [10^6 Nm^2]	Flatwise Stiffness [10^6Nm^2]
1.00	2931	2931
1.025	2931	2931
1.026	205.4	205.4
1.225	205.4	205.4
1.275	51.59	51.59
1.375	51.59	51.59
1.425	205.4	205.4
1.625	205.4	205.4
1.626	3609	3609
1.665	3609	3609
1.67	40300	42050
1.9	27.44	37.68
3.08	55.12	28.07
4.26	86.89	17.40
5.45	66.59	11.38
6.63	48.34	6.912
7.81	33.57	3.876
8.99	21.67	2.022
10.17	11.79	0.8896
11.36	5.464	0.3202

D.3 Power train

D.3.1 Layout

The power train consists of the rotor mounted on a low speed shaft coupled to a high speed shaft via a gearbox. The high speed shaft couples to a direct current generator.

D.3.2 Characteristics

- Rotor inertia [1]) : 59920 kg m²
- Inertia of rotating system [1]),[2]): 15060 kg m²
- Gearbox ratio : 20
- Gearbox inertia [1]) : 2900 kg m²
- Low speed shaft inertia [1]) : 800 kg m²
- High speed shaft inertia [1]) : 60 kg m²
- Generator inertia [1]) : 7700 kg m²
- Frequency of drive train : N/A
- Loss of torque in gearbox
  - constant part: 2150 Nm
  - part proportional to rotor speed: 142 Nm/(rad/s)

[1]) All inertias are refferring to low speed shaft
[2])hub,low speed shaft, gear box, brake, high speed shaft and generator.

D.4 Tower

D.4.1 Main characteristics

- Basic description: Cylindrical tower with conical base
  - Description of conical base
    - material: concrete
    - height: 8 m
    - base diameter: 8 m
    - diameter at h=8 m: 2.6 m
    - wall thickness: 0.3 m
  - Description of cylindrical part
    - material: steel
    - height: 12.6 m
    - diameter: 2.216 m
- Tower head mass (without hub and rotor): 28593 kg
- Position of tower head centre of gravity(without hub and rotor): 0.22 m down-wind of tower centre
- Inertia of nacelle around tower axis (without hub and rotor): 120071 kg m²

The tower eigenfrequencies are listed below:

first tower bending eigenfrequency:	2.9 hz
first tower torsion eigenfrequency:	11.0 hz

D.5 Control systems

D.5.1 Power control

The HAT-25 turbine, on which the instrumented blade is mounted is an experimental wind turbine, which can be operated under several power control modes, see [62]. The machine operates at (different) constant speeds or variable speed and power regulation is acheived by pitch or stall control. In the present project, the operational conditions followed from the measurement program.

D.6 Measurements at turbine operation

D.6.1 Profile data

See figure D.10 and D.11. An example of 'raw' data (i.e. data which are not binned) is given in figure D.12. Note that the pitch angle dependancy on the $\mathbf{c_n} - \alpha$ curves shows a similar behaviour as $\mathbf{c_n} - \alpha$ curves is the behaviour of the NREL curves, see C.4.4.

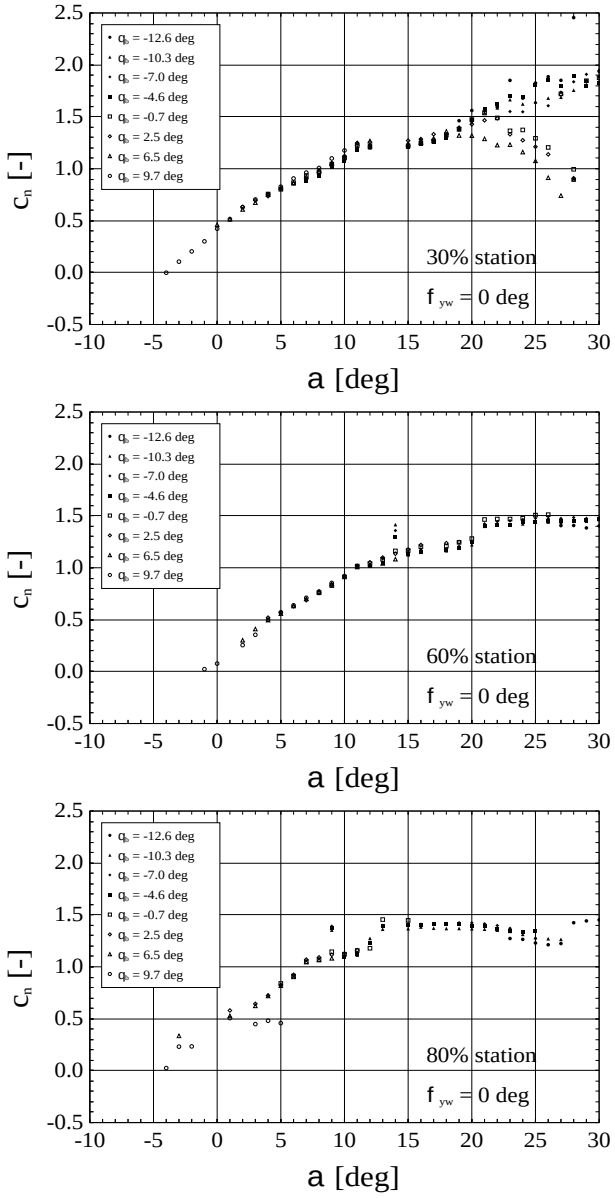

Figure D.10 *ECN;* $c_n - \alpha$*; 30% span (top), 60% span, 80% span (bottom)*

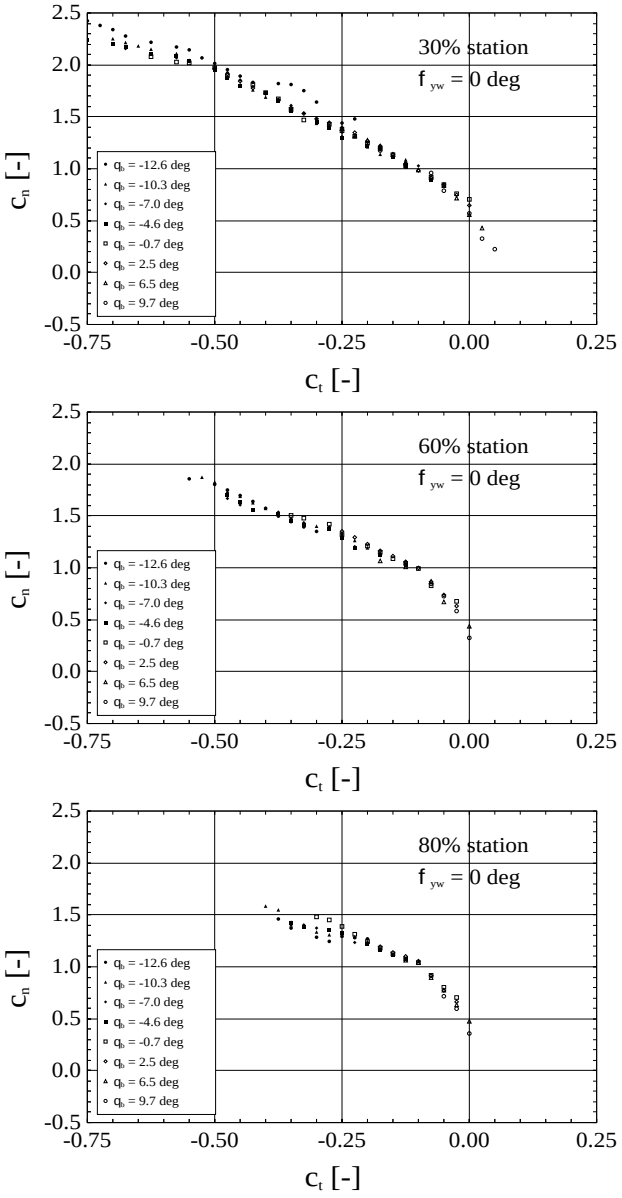

Figure D.11 *ECN;* $c_n - c_t$*; 30% span (top), 60% span, 80% span (bottom)*

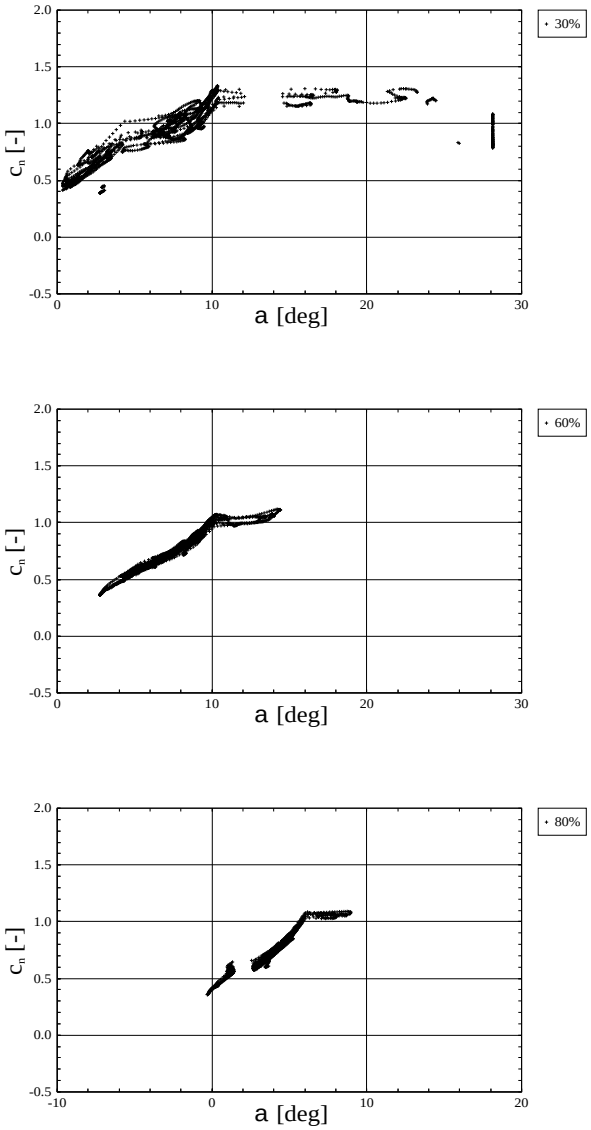

Figure D.12 *ECN; Example of 'raw'* $c_n - \alpha$*; 30% span (top), 60% span, 80% span (bottom)*

APPENDIX E. MODEL DESCRIPTION OF IC/RAL TURBINE

E.1 Basic machine parameters

- Number of blades: 3
- Rotor diameter: 16.90 m
- Hub height: 15.66 m
- Type of rotor: Fixed
- Rotational speed: Fixed at approx. 38.2 rpm
- Cut-in wind speed: 4 m/s (with motor assisted starting)
- Cut-out wind speed: 25 m/s (this has never occurred at Rutherford)
- Rated power: 45 kW of generator
- Tilt: 6 ^{o}
- Cone: 0 ^{o}
- Location of rotor: upwind
- Rotational direction: anticlockwise (looking downwind to the rotor)
- Rotor overhang: 1.205 m
- Power regulation: Stall

E.2 Rotor

The blades of the rotor are from different series of production. The instrumented blade is actually of the older series (as used by Risø, see Appendix G.

E.2.1 Geometry

- Blade type: LM 8.5 m VX, 8.2 m root to tip
- Blade root: 1.09 m (1.65m from axis)
- Hub radius: 0.25 m
- Blade set angle: 2.5 deg at tip
- Blade pitch: Fixed
- Blade profile: NACA 63-224 at root (1.65 m from axis) tapering to NACA 63-212 at tip.

Table E.1 provides more information on the sectional chord, twist and thickness distibution (as Risø). The tables E.2 to E.4 lists the the instrumented profile geometries.

Table E.1 *Planform data for the 17 m rotor with LM 8.2 m blades*

Dist. (m) from root	chord (m)	twist (deg.)	thickness (%)
1.400	1.090	15.000	24.600
2.250	1.000	9.500	20.700
3.100	.925	6.100	18.700
3.950	.845	3.900	17.600
4.800	.770	2.400	16.600
5.650	.685	1.500	15.600
6.500	.605	.900	14.600
7.350	.525	.400	13.600
8.200	.445	.000	12.600

Note: Root is at 0.25m from hub axis

Table E.2 *Profile geometry and position of pressure taps at 20% and 30% span*

	20%		30%	
tap	C [mm]	T[mm]	C[mm]	T[mm]
1	1090.0	0.0	1000.0	0.0
2	1035.5	-1.4	950.0	-0.7
3	817.5	-42.3	750.0	-32.1
4	681.3	-67.8	630.0	-54.4
5	545.0	-104.9	500.0	-79.8
6	348.8	-122.5	350.0	-93.0
7	190.8	-104.0	175.0	-79.8
8	109.0	-83.3	100.0	-64.1
9	54.5	-59.9	50.0	-46.3
10	27.3	-41.2	25.0	-32.6
11	0.0	0.0	0.0	0.0
12	6.8	25.9	6.2	20.2
13	13.6	33.4	12.5	26.7
14	27.3	48.0	25.0	37.5
15	54.5	68.3	50.0	53.3
16	81.8	84.5	75.0	65.6
17	109.0	96.1	100.0	75.0
18	163.5	116.1	150.0	90.3
19	337.9	142.8	345.0	113.8
20	436.0	142.9	400.0	112.1
21	545.0	128.9	500.0	101.8
22	654.0	105.6	600.0	84.1
23	763.0	77.0	700.0	62.0
24	872.0	46.7	800.0	38.1
25	1035.5	8.3	950.0	7.1

"C" denotes Chordwise from leading edge, "T" denotes Thickwise from chord,
Order: T.E. - Pressure Side - L.E. - Suction Side - T.E.

Table E.3 *Profile geometry and position of pressure taps at 40% and 50% span*

	40%		50%	
tap	C [mm]	T[mm]	C[mm]	T[mm]
1	925.0	0.0	845.0	0.0
2	878.7	-0.4	802.7	-0.2
3	693.7	-26.6	633.7	-22.7
4	573.5	-47.4	545.0	-37.2
5	462.5	-66.0	422.5	-56.4
6	370.0	-76.4	338.0	-65.5
7	161.9	-66.4	147.9	-56.9
8	92.5	-53.4	84.5	-45.7
9	46.2	-38.8	42.2	-33.3
10	23.1	-27.7	21.1	-23.9
11	0.0	0.0	0.0	0.0
12	5.8	17.1	5.3	14.7
13	11.6	22.9	10.6	19.8
14	23.1	31.6	21.1	27.3
15	46.2	44.8	42.2	38.8
16	69.4	55.0	63.4	47.5
17	92.5	63.1	84.5	54.6
18	138.7	75.8	126.7	65.4
19	277.5	94.8	253.5	82.0
20	370.0	94.7	338.0	82.0
21	462.5	86.4	422.5	75.0
22	555.0	71.8	507.0	62.5
23	647.5	53.2	591.5	46.5
24	740.0	33.1	676.0	29.1
25	878.7	6.3	802.7	5.6

"C" denotes Chordwise from leading edge, "T" denotes Thickwise from chord, Order: T.E. - Pressure Side - L.E. - Suction Side - T.E.

Table E.4 *Profile geometry and position of pressure taps at 65% and 80% span*

	65%		80%	
tap	C [mm]	T[mm]	C[mm]	T[mm]
1	727.5	0.0	605.0	0.0
2	691.1	0.0	574.7	0.1
3	545.6	-17.6	453.7	-13.0
4	363.7	-43.9	302.5	-32.6
5	291.0	-49.8	242.0	-37.0
6	218.2	-50.9	181.5	-37.8
7	127.3	-44.3	105.9	-32.9
8	72.7	-35.7	60.5	-26.6
9	36.4	-26.0	30.2	-19.4
10	18.2	-18.8	15.1	-14.1
11	0.0	0.0	0.0	0.0
12	4.6	11.7	3.8	8.9
13	9.1	15.6	7.6	11.7
14	18.2	21.7	15.1	16.5
15	36.4	30.8	30.2	23.5
16	54.6	37.8	45.4	28.8
17	72.7	43.3	60.5	32.9
18	109.1	51.9	90.7	39.5
19	160.1	60.0	133.1	45.8
20	211.0	64.8	175.4	49.4
21	269.2	66.0	217.8	50.4
22	436.5	50.2	363.0	38.6
23	509.2	37.5	423.5	29.1
24	582.0	23.6	484.0	18.5
25	691.1	4.6	574.7	3.7

"C" denotes Chordwise from leading edge, "T" denotes Thickwise from chord,
Order: T.E. - Pressure Side - L.E. - Suction Side - T.E.

E.2.2 Aerodynamics

Figure E.1 and E.2 show the approximated lift and drag data respectively for the root, mid span and tip positions. These are from Risø.

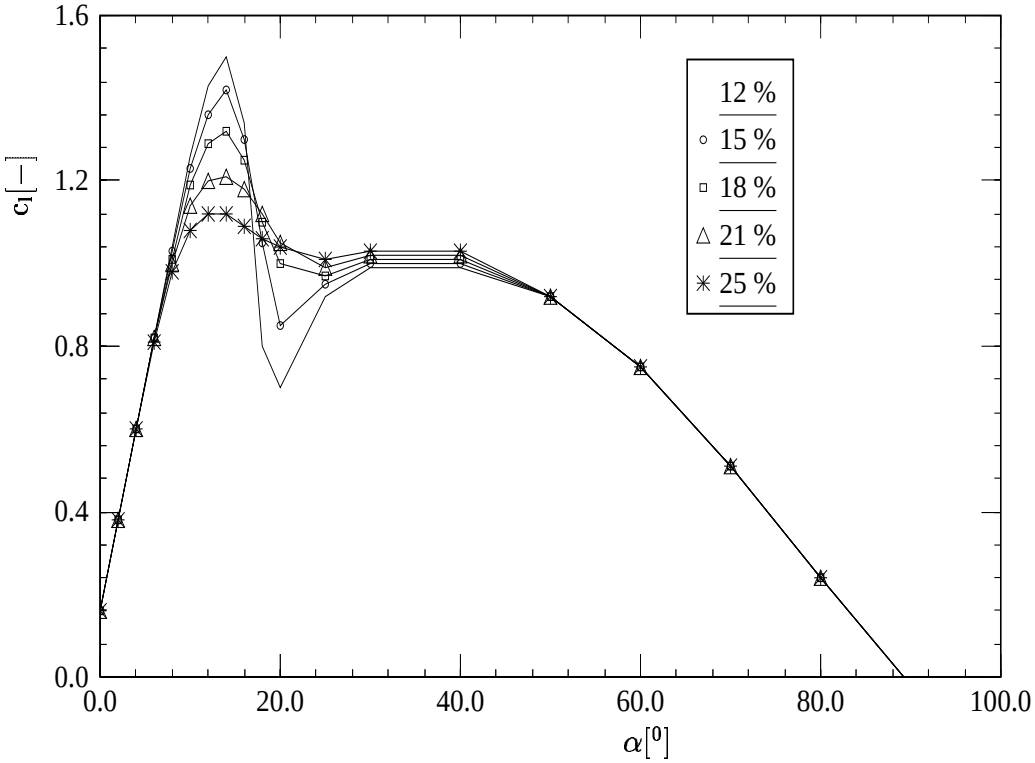

Figure E.1 *2D lift coefficient for the IC/RAL test blade*

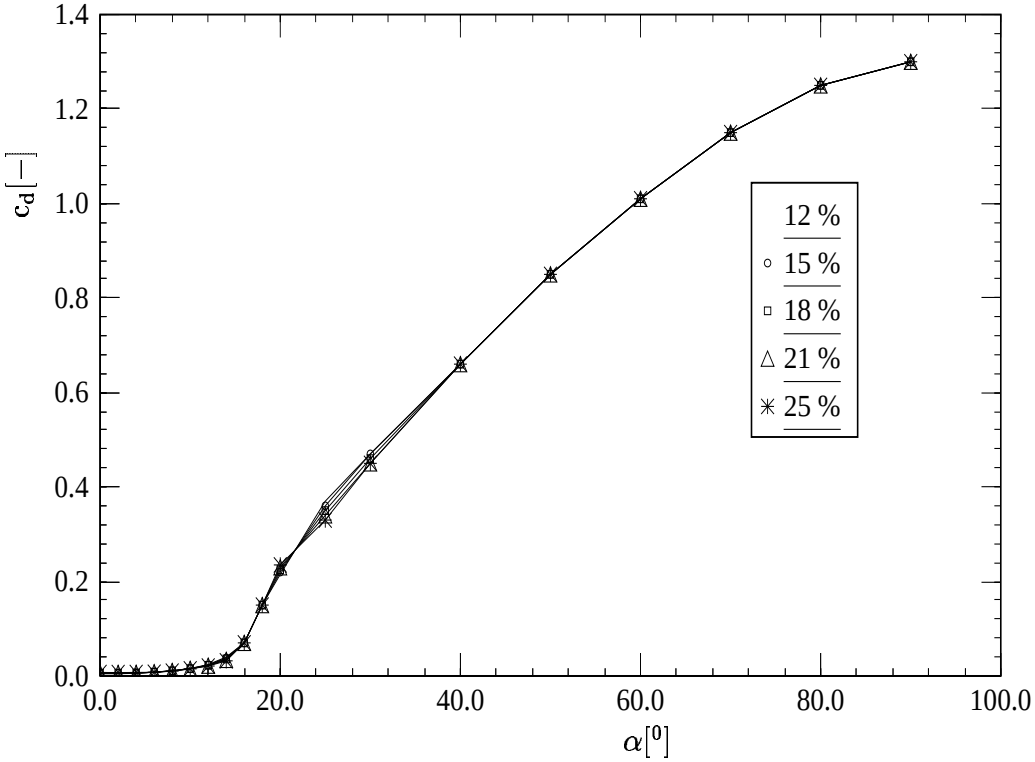

Figure E.2 *2D drag coefficient for the IC/RAL test blade*

E.2.3 Structural properties

- Rotor mass (total): 1429 kg
- Hub mass (exluding the rotor): 330 kg
- Blade material: Steel rootstock, GRP spar and skins

The blade masses, centre of gravity and eigenfrequencies (non-rotating) are listed below.

- mass of the instrumented blade outside root: 354.9 kg
- mass of the non-instrumented blades outside root: 372.2 kg
- centre of gravity of instrumented blade from root: 2.745 m
- centre of gravity of non-instrumented blade from root: 2.610 m
- first edgewise eigenfrequency of instrumented blade : 6.5 Hz
- first flatwise eigenfrequency of instrumented blade (standstill): 3.2 Hz

The mass and stiffness distributions are not known. The experiment to try and determine them has not given good results

E.3 Power trains

E.3.1 Layout

The power train consists of the rotor mounted on a low speed shaft coupled to a middle speed shaft via a gearbox, with a ratio of 19.58:1. The middle speed shaft is coupled to the high speed shaft by belts and pulleys with a ratio of 2:1. The high speed shaft couples directly to an induction generator. The mechanical brake has a spring applied, air released mechanism, its disk is attached to the low speed shaft.

E.3.2 Characteristics

	re.Own shaft	re. LS shaft	re. HS shaft	units
Inertia of rotating system (Total)		16364.8	10.650	kg m^2
Blade inertia (per blade)	4715	4715	3.068	kg m^2
Hub Inertia (Estimate from drawing)	22.8	22.8	0.015	kg m^2
Rotor inertia (Blades+Hub)	4715x3+22.8	14167.8	9.220	kg m^2
Wind Shaft Inertia (inc.BrakeDisk)	1.8	1.8	0.0012	kg m^2
Wind Shaft Stiffness (Hub to Gearbox)	3.26 10^6	3.2610^6	8.3210^5	Nm/rad
Gearbox inertia		34.2	0.0223	kg m^2
Mid speed shaft inertia (630mm pulley)	2.62	1004	0.655	kg m^2
High speed shaft inertia (315m pulley)	0.376	577	0.376	kg m^2
Generator inertia	0.378	580	0.378	kg m^2
Generator Efficiency (Motoring)	100%	92.7%		

Table E.5 *Generator slip (Motor data)*

Power:	100%	75%	50%
Slip:	2.6%	1.73%	1.13%
RPM:	1461	1474	1483

Table E.6 *Generator slip (Predicted)*

Power:	100%	75%	50%
Slip:	2.6%	1.73%	1.13%
RPM:	1461	1474	1483

- Gearbox stiffness assumed hard
- Gearbox suspension stiffness assumed hard
- Gearbox ratio 1:19.58
- Belt & Pulley Ratio 1:2.00

E.4 Tower

E.4.1 Main characteristics

- Basic description: Lattice, square plan
- Material: Round steel bar, 60mm, 40 mm diameters
- Height: 15 m
- Base plan dimensions: 3x3 m
- Top plan dimensions 0.5x0.5 m
- Tower mass 3500 kg
- Tower head mass (Nacelle without blades): 3800 kg
- 1st tower bending eigenfrequency: (With full tower top mass) 2.06 Hz

Experiment is requested to determine other characteristics such as damping and stiffnesses.

E.5 Control systems

The turbine has fairly simple control systems. The main elements of the control are oriented to safety and grid protection; These can initiate shutdown based on a variety of fault conditions.

E.5.1 Power control

Power control is provided by means of stall control. The generator is connected to the grid via a softstart interface.

E.5.2 Yaw control

The yaw control is provided by a fantail system. This has two fantails mounted at the rear of the nacelle, each with six flat blades. The subsequent gearing from this shaft to the yaw has a high reduction ratio with some backlash (about 1.5 revolutions of the fantails).

- Fantail rotors:
  - Diameter: 2 m
  - Pitch: 45 deg
  - Tip chord: 300 mm
  - Root chord: 100 mm at r=0.5 m
- Construction: Plywood trapezia on square section tubing.
- Gearing: $\approx$ 3600:1 reduction, chain worm gearbox, pinion and crown wheel

APPENDIX F. MODEL DESCRIPTION OF NREL TURBINE

F.1 Site data

Because of the altitude of the site, an air density of 0.9793 kg/m^3 is recommended.

F.2 Basic machine parameters

- Number of blades: 3
- Rotor diameter: 10.06 m
- Hub height: 17.03 m
- Type rotor: fixed
- Rotational speed: 71.63 rpm synchronous speed
- Cut-in wind speed: 6 m/s (tests were run at lower speeds)
- Cut-out wind speed not applicable (stall control)
- Rated power: 19.8 kW
- Tilt: 0 degrees
- Cone: 3 degrees 25'
- Location of rotor: downwind
- Rotational direction: Clockwise (viewed from downwind)
- Rotor overhang: 1.32 m
- Power regulation: Stall

F.3 Rotor

Geometry

- Blade type:
  - Phase II: NREL in house (Constant chord, no taper or twist)
  - Phase III and IV: NREL in house (Constant chord, no taper, highly twisted)
- Root extension: 0.723 m
- Blade set angle:
  - Phase II: approximately 12 degrees (see each data file)
  - Phase III and IV: approximately 3 degrees (see each data file)
- Blade pitch: fixed along the blade
- Blade profile: NREL S809
- Blade chord: 0.4572 m at all span stations.
- Blade twist:
  - Phase II: None
  - Phase III and IV: see table F.1
- Blade thickness:
  - Phase II:
    - at 14.4% span: t=43.0% chord (span refers to rotor centre)
    - between 14.4% and 30.0% span the thickness decreases linearly
    - at 30.0% span: t=20.95% chord
    - outboard of 30.0% span: t=20.95% chord
  - Phase III and IV:
    - at 14.4% span: t=43.0% chord (span refers to rotor centre)

    - between 14.4% and 25.0% span the thickness decreases linearly
    - at 25.0% span: t=20.95% chord
    - outboard of 25.0% span: t=20.95% chord

- Aerofoil distribution: Except for the root, the blade uses the S809 at all span locations, see table F.2. In the root sections the airfoil shape is altered by the enlarged spar. This enlargement is a (virtually) perfect circle (in cross section) at the root which is centered at the quarter chord. The thickness of the spar area enlargement varies from this maximum at the root to a thickness that fits inside the airfoil profile at the 30% span (and outboard). In between the root and the 30% span the spar area enlargement is squashed into consecutively thinner and thinner eliptic shapes, but each ellipse has a perimeter equal to the circumference of the base circle. The twisted blade used in Phases III and IV is similar, except that the spar enlargement fits within the airfoil at 25% span.

Table F.1 *Blade twist*

Radius from rotor centre [m]	Twist [^{o}]
0.724	44.67
0.880	39.39
1.132	32.29
1.383	26.56
1.634	21.95
1.886	18.19
2.137	15.10
2.389	12.52
2.640	10.35
2.892	8.50
3.143	6.91
3.395	5.52
3.646	4.32
3.897	3.25
4.149	2.30
4.400	1.45
4.652	0.69
4.903	0.00

F.3.1 Aerodynamics

See table F.3 and F.4.

F.3.2 Structural properties:

- Rotor mass:
  - Phase II: 147.7 kg + 13 kg root mounted camera
  - Phase III: 215.1 kg
  - Phase IV: 204 kg
- Hub mass:
  - Phase II: 269.1 kg (includes 3 instrumentation boxes, boom, camera)
  - Phase III: 263.5 kg (includes 3 instrumentation boxes)

Table F.2 *Profile coordinates, from "Combined Experiment Phase I Final Report", by C.P. Butterfield, W.P. Musial and D.A. Simms, NREL/TP-257-4655, October 1992*

x/c	y/c	x/c	y/c
0.00037	0.00275	0.00140	-0.00498
0.00575	0.01166	0.00933	-0.01272
0.01626	0.02133	0.02321	-0.02162
0.03158	0.03136	0.04223	-0.03144
0.05147	0.04143	0.06579	-0.04199
0.07568	0.05132	0.09325	-0.05301
0.10390	0.06082	0.12397	-0.06408
0.13580	0.06972	0.15752	-0.07467
0.17103	0.07786	0.19362	-0.08447
0.20920	0.08505	0.23175	-0.09326
0.24987	0.09113	0.27129	-0.10060
0.29259	0.09594	0.31188	-0.10589
0.33689	0.09933	0.35328	-0.10866
0.38223	0.10109	0.39541	-0.10842
0.42809	0.10101	0.43832	-0.10484
0.47384	0.09843	0.48234	-0.09756
0.52005	0.09237	0.52837	-0.08697
0.56801	0.08356	0.57663	-0.07442
0.61747	0.07379	0.62649	-0.06112
0.66718	0.06403	0.67710	-0.04792
0.71606	0.05462	0.72752	-0.03558
0.76314	0.04578	0.77668	-0.02466
0.80756	0.03761	0.82348	-0.01559
0.84854	0.03017	0.86677	-0.00859
0.88537	0.02335	0.90545	-0.00370
0.91763	0.01694	0.93852	-0.00075
0.94523	0.01101	0.96509	0.00054
0.96799	0.00600	0.98446	0.00065
0.98528	0.00245	0.99612	0.00024
0.99623	0.00054	1.00000	0.00000
1.00000	0.00000	0.00000	0.00000

  - Phase IV: 315.2 kg (includes 3 instrumentation boxes, boom, camera)

- Blade material: Fiberglass/epoxy composite
- Blade mass (outside root):
  - Phase II:
    - blade 1: 48.9 kg (Not including root mounted camera)
    - blade 2: 49.5 kg
    - blade 3: 49.3 kg
  - Phase III: 72.0 kg (Each blade, including root mounted camera)
  - Phase IV: 68.0 kg (Each blade, including root mounted camera)
- Blade c.g.:
  - Phase II:
    - blade 1:1.61 m from the root

Table F.3 *Profile coefficients, measured in Ohio State Windtunnel (RE = 1.06 10^6)*

α	c_l	c_d
3.5	0.545	0.0078
−8.1	−0.574	0.0742
−6.1	−0.547	
−4.2	−0.416	0.0117
−2.6	−0.198	0.0114
−0.5	0.056	0.0109
1.5	0.286	0.0102
3.6	0.535	0.0091
5.1	0.737	0.0069
7.1	0.914	0.0088
9.2	0.946	0.0525
11.2	0.967	
12.7	1.000	
14.9	1.029	
16.8	0.723	
18.6	0.726	

    - blade 2:1.68 m from the root
    - blade 3:1.63 m from the root
  - Phase III: 1.58 m from the root (all blades)
  - Phase IV: 1.53 m from the root (all blades)
- first edgewise eigenfrequency:
  - Phase II: 8.75 Hz
  - Phase III and IV:
    - noninstrumented blade: 8.16 Hz, 0.84% damping
    - instrumented blade: 7.97 Hz, 0.69% damping
- first flatwise eigenfrequency:
  - Phase II: 4.70 Hz
  - Phase III and IV:
    - noninstrumented blade: 4.94 Hz, 0.9% damping
    - instrumented blade: 4.79 Hz, 0.95% damping

F.4 Power train

F.4.1 Layout

The power train consists of the rotor mounted on a low speed shaft coupled to a high speed shaft via a gearbox. The high speed shaft couples directly to an induction generator. The mechanical brake is positioned on the high speed shaft.

F.4.2 Characteristics

- Rotor inertia: 1356 kg m^2 (w.r.t. low speed shaft, includes boom and instrumentation boxes)
- Inertia of rotating system: 1535 kg m^2 (w.r.t. low speed shaft, includes boom and instrumentation boxes)

Table F.4 *Profile coefficients, measured in Delft Wind Tunnel (RE = 1 10^6)*

α	c_l	c_d
−1.010.019	0.0095	
−0.01	0.139	0.0096
1.02	0.258	0.0096
2.05	0.378	0.0099
3.08	0.497	0.0100
4.10	0.617	0.0100
5.13	0.736	0.0097
6.16	0.851	0.0095
7.17	0.913	0.0127
8.20	0.952	0.0169
9.22	0.973	0.0247
10.21	0.952	0.0375
11.21	0.947	0.0725
12.22	1.007	0.0636
13.24	1.031	0.0703
14.24	1.055	0.0828
15.24	1.062	0.1081
16.24	1.043	0.1425
17.23	0.969	0.1853
18.20	0.938	0.1853
19.17	0.929	0.1853
20.15	0.923	0.1853

- Gearbox ratio: 25.13:1
- Gearbox inertia: Not available
- Gearbox stiffness: Not available
- Gearbox suspension stiffness: Not available
- Gearbox suspension damping: Not available
- High speed shaft inertia: Not available
- High speed shaft damping: 0.5 to 1.0 percent
- High speed shaft stiffness: Not available
- Generator inertia: 143 kg m^2 (w.r.t. low speed shaft)
- Generator slip: 1.59% at 20 kW
- Generator time constant: <0.025 sec (electro-mechanical time constant, for generator only)
- Frequency of drive train: 5.77 Hz
- Power train eff.(gearbox): 97%
- Power train eff.(misc.): 98% (windage, couplings, main shaft bearings)
- Power train eff.(generator): The efficiency curve (in %) of the combined system (gearbox+generator) vs. generator power (kW) is a sixth order polynomial as follows:

$$\mathrm{Eff} = 100 \cdot \mathrm{P_{gen}}/(4.53322310^{-3} \cdot \mathrm{P_{gen}^2} + 111.5023\mathrm{P_{gen}} + 150.0035)$$

This means that the efficiency is fairly constant at approximately 78%.
The low speed shaft torque measurement requires a correction due to calibration errors in the Phase II and Phase III data as follows:

Table F.5 *Structural properties for phase II. Pressure instrumentation and counterweights were included in mass distribution. The root mounted camera (13 kg) was not included in the mass distribution.*

Distance from rotor centre [m]	mass [kg/m]	Edgewise stiffness [Nm^2]	Flatwise stiffness [Nm^2]
5.030	5.59	37939	417556
4.527	5.59	37939	417556
4.024	6.57	49992	480118
3.521	7.29	61815	537514
3.019	8.02	73180	592614
2.516	8.75	84200	644844
2.013	9.72	95019	697074
1.510	12.14	115567	798091
1.007	17.00	406938	1169444
0.750	17.98	743278	998403
0.509	17.98	1369469	1439779
0.402		473517	473517

Table F.6 *Structural properties for phase III and IV. Structural properties for phase III and IV. Pressure instrumentation, counterweights and the root mounted camera were included in the mass distribution.*

Distance from rotor centre [m]	mass [kg/m]	Edgewise stiffness [Nm^2]	Flatwise stiffness [Nm^2]
5.029	9.32	46953	365070
4.526	9.25	46953	387600
4.023	10.22	65974	436440
3.520	11.19	84468	512420
3.018	12.06	105560	583420
2.515	12.95	123480	650900
2.012	13.49	149420	737010
1.509	16.92	232180	997640
1.006	46.09	710230	1332800
0.749	45.18	1302400	1556800
0.508	30.14	2320700	2322100
0.402		473517	473517

  - Phase II: $T_{corr} = 1.08 \cdot T_{measured} + 15.16$
  - Phase III: $T_{corr} = 0.97 \cdot T_{measured} - 196.43$

- Max. brake torque: 115.24 Nm
- Min. brake torque: 0.0 Nm
- The inertia of the low speed shaft + gearbox + high speed shaft may be found by substracting the rotor inertia from that of the rotating system
- The stiffness of the low speed shaft, gearbox and high speed shaft as a lumped parameter is 1.70 10^5 Nm/rad.

F.5 Tower

F.5.1 Main characteristics

- Basic description: 2 different diameter cylinders connected by a short conical section. The conical section base is 5.385 m above the ground. The conical section top is 6.300 m above the ground. The tower is further supported by 4 guy wires, attached 11.91 m above the ground. The guy wires descend to the ground at an angle 44.3 degrees below horizontal. The ground anchors for the four wires are at the following compass directions from the tower axis: 90, 180, 270 and 360 degrees.
- Tower material: 9.525 mm Corten Steel
- Tower height: 15.9 m
- Tower diameter(base): 0.4572 m
- Tower diameter(top): 0.4064 m
- Tower mass: 1481 kg
- Tower head mass: 1279 kg (hub, nacelle)
- Position of tower head c.g.: Not available
- Bending spring constant,tower: 48118 N/m
- Torsional stiffness: Not available
- Torsional damping: Not available
- Nacelle inertia: 1211 kg m^2
- First tower bending eigenfrequency(x): 5.49 Hz, 1.22% damping
- First tower bending eigenfrequency(y): 5.71 Hz, 1.49% damping
- First tower torsion eigenfrequency: Not available - this was never measured
- First tower/nacelle eigenfrequency (x): 1.95 Hz, 1.87% damping
- First tower/nacelle eigenfrequency (y): 1.94 Hz, 2.10% damping

F.6 Control systems

F.6.1 Power control

Power control is provided by means of stall control

F.6.2 Yaw control

Yaw control is provided by the free yaw of the downwind turbine

F.6.3 Remaining control systems

None

F.7 Modal Analysis

See table F.7.

F.8 Measurements at turbine operation

F.8.1 Power curve

See table F.8 and F.9.
Power curve based on binned baseline cycles. Baseline cycles consist of a single revolution of the blade where the average wind speed for the baseline cycle, the preceeding cycle, and the proceeding cycle had a standard deviation less than 5%

Table F.7 *Full system modal analysis (Phase II, untwisted blades)*

Mode Shape Description	Freq Hz	Damping %
1st tower bending fore-aft nacelle and rotor translating	1.7427	3.213
1st flap-1st asymm., coupled with nacelle yaw and tower torsion	2.495	2.962
1st flap-2nd asymm., coupled with nacelle pitch and tower fore-aft	3.424	1.773
1st flap-symmetric bending nacelle translating	4.029	1.591
2nd flap-1st asymm., coupled with 1st edge-asym. bending and nacelle pitch	5.555	1.531
1st edge-2nd asymm.,coupled with blade #1 flap bending	7.381	1.086
1st edge-asymm., coupled with boom side-to-side bending and nacelle yaw	8.935	1.269
2nd edge asym., coupled with blade #1 2nd flap, boom up and down, and nacelle pitch	11.17	0.894
3rd flap-asymm., coupled with boom side-to-side bending and nacelle yaw	12.341	1.137
3rd flap-asymm., coupled with boom up and down bending and nacelle pitch	14.172	0.973
4th flap-asymm., coupled with angle-of-attack probes local modes	17.394	0.847

of the mean. The average yaw error for the three cycles was between +/- 3 degrees with a standard deviation less than +/- 2.5 degrees.

F.8.2 Profile data

See figure F.1 to F.9. Profile data are based on binned baseline cycles, see section F.8.1.

Table F.8 *Power curve of turbine with untwisted blades at 12 degrees tip angle*

Wind Speed [m/s]	Generator Power [kW]
2	-4.65
4	-3.79
5	-2.31
6	-1.14
7	0.31
8	2.07
9	3.78
10	5.75
11	7.53
12	9.68
13	9.93
14	11.51
15	12.53
16	12.96
17	13.31
18	14.21
19	14.72
21	15.59
22	16.20

Table F.9 *Power curve of turbine with twisted blades at 3 degrees tip angle*

Wind Speed [m/s]	Generator Power [kW]
5	0.19
6	1.58
7	3.43
8	5.43
9	7.73
10	9.48
11	10.60
12	11.17
13	11.67
17	9.25
18	9.14

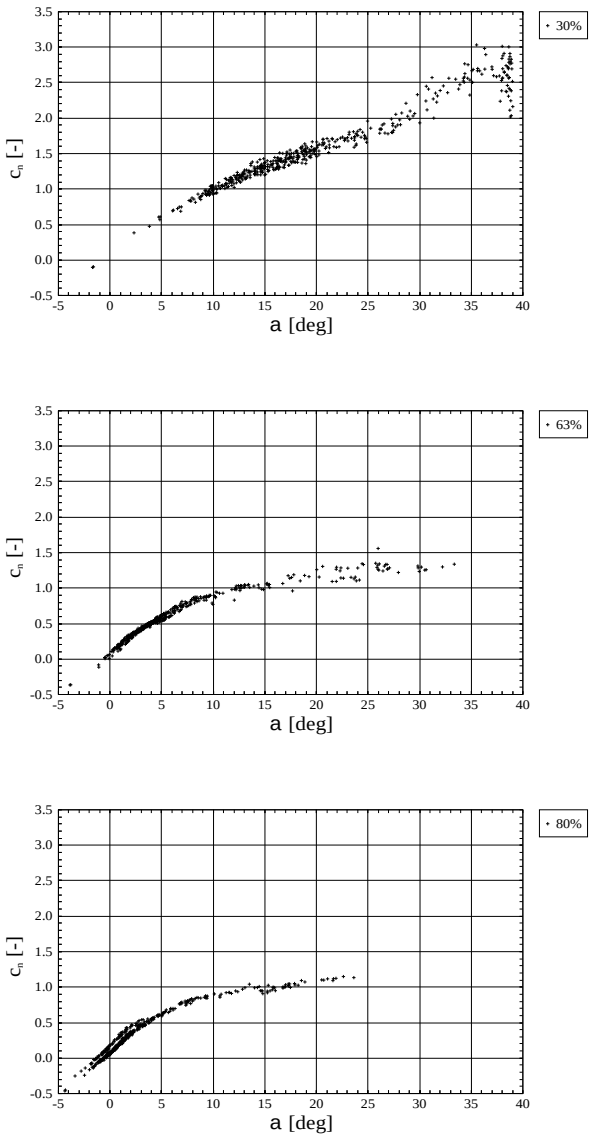

Figure F.1 *NREL; Phase II:* $c_n - \alpha$*; 30% span (top), 63% span, 80% span (bottom)*

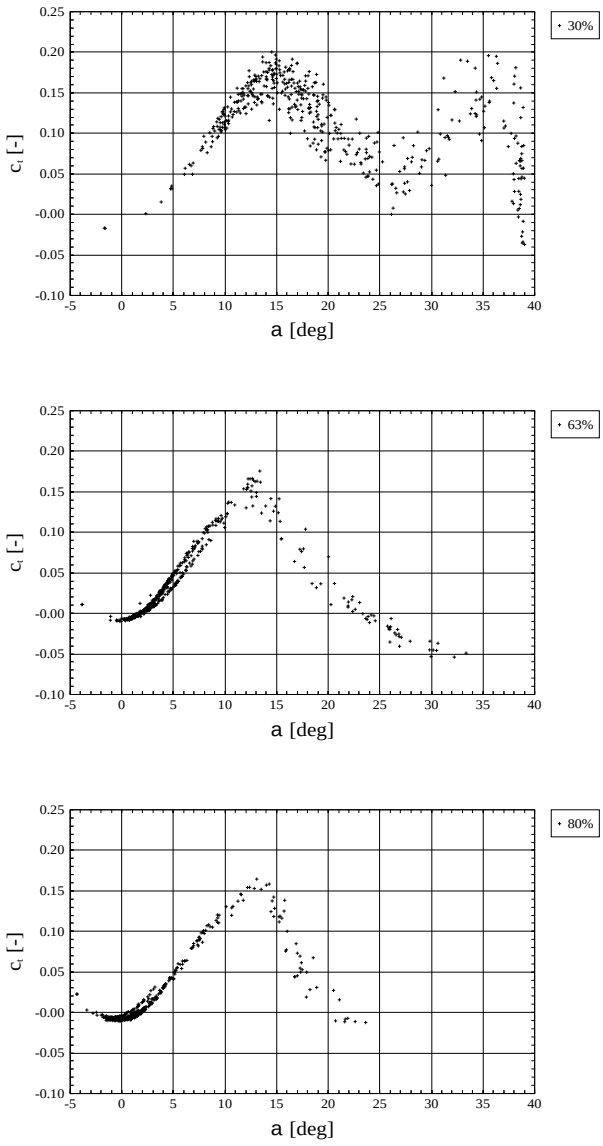

Figure F.2 *NREL; Phase II:* $c_t - \alpha$*; 30% span (top), 63% span, 80% span (bottom)*

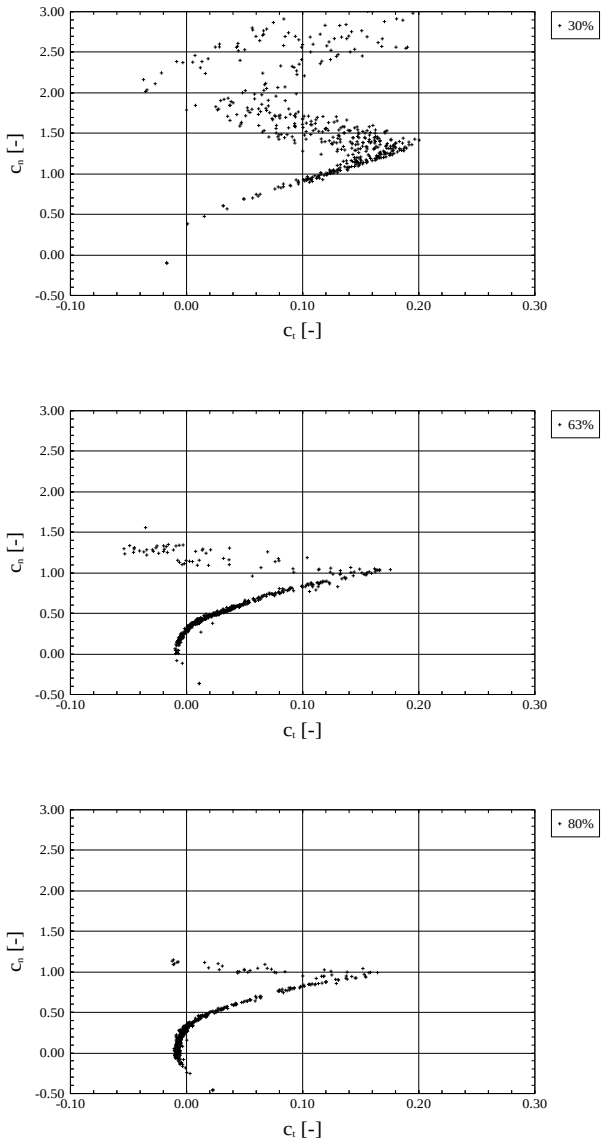

Figure F.3 *NREL; Phase II:* $c_n - c_t$*; 30% span (top), 63% span, 80% span (bottom)*

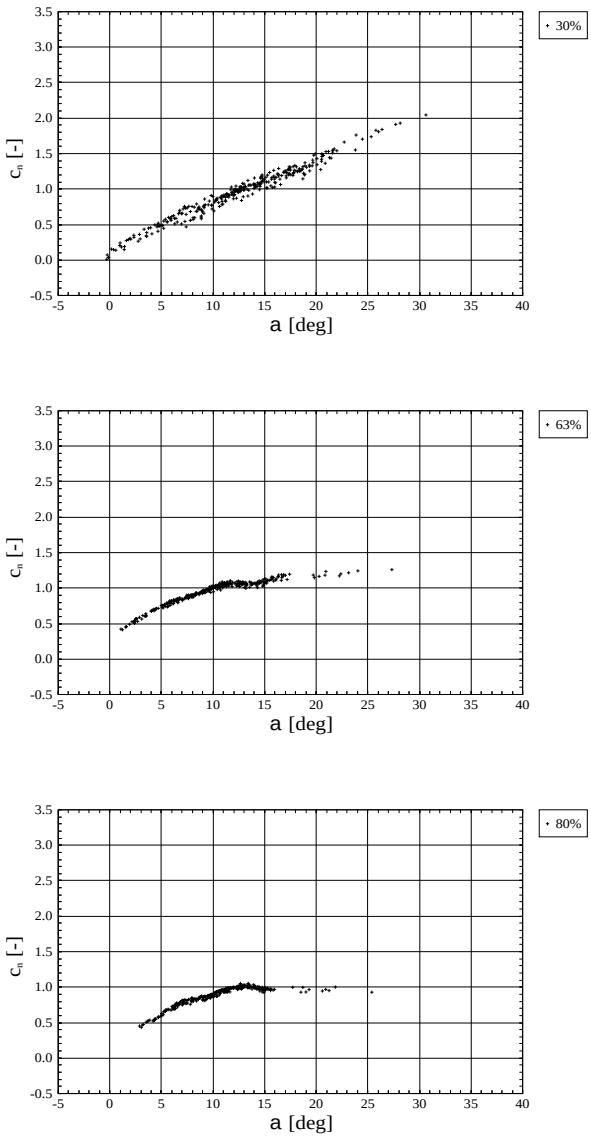

Figure F.4 *NREL; Phase III:* $c_n - \alpha$*; 30% span (top), 63% span, 80% span (bottom)*

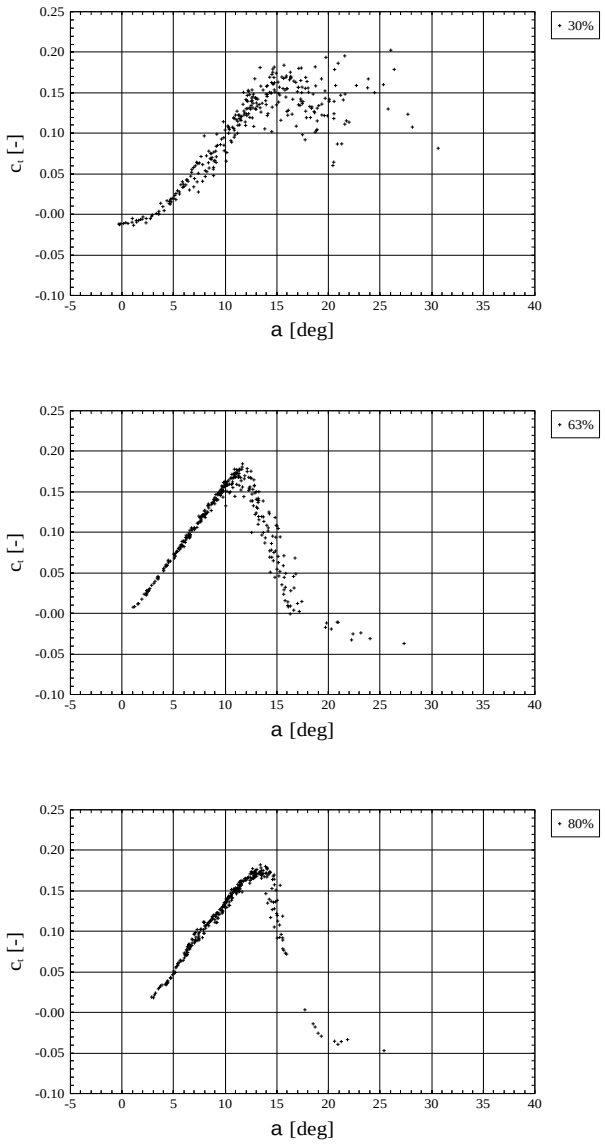

Figure F.5 *NREL; Phase III:* $c_t - \alpha$*; 30% span (top), 63% span, 80% span (bottom)*

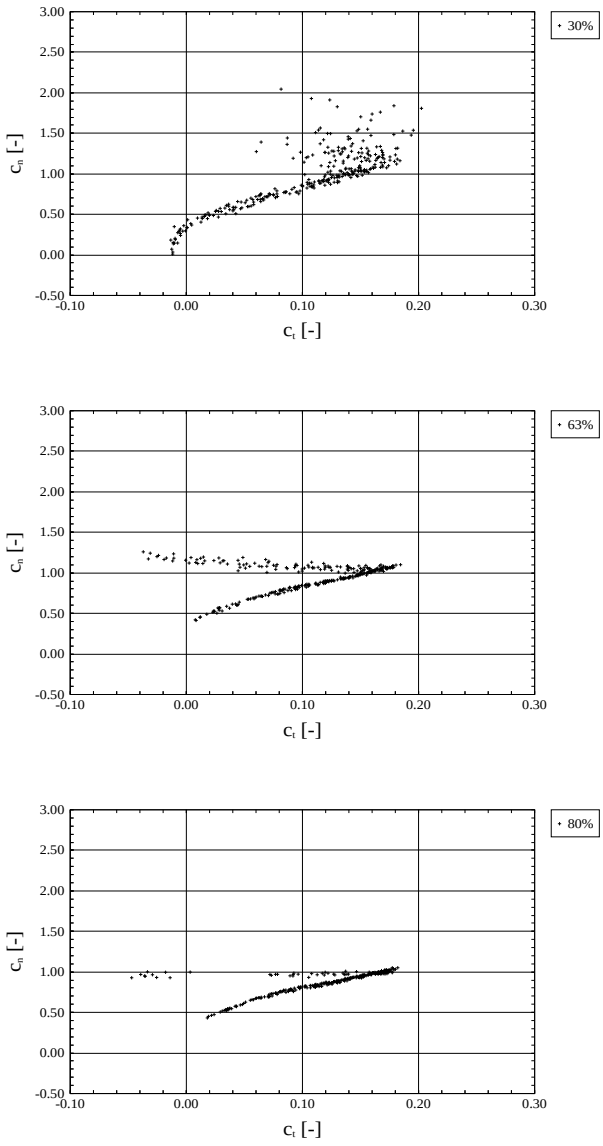

Figure F.6 *NREL; Phase III:* $c_n - c_t$*; 30% span (top), 63% span, 80% span (bottom)*

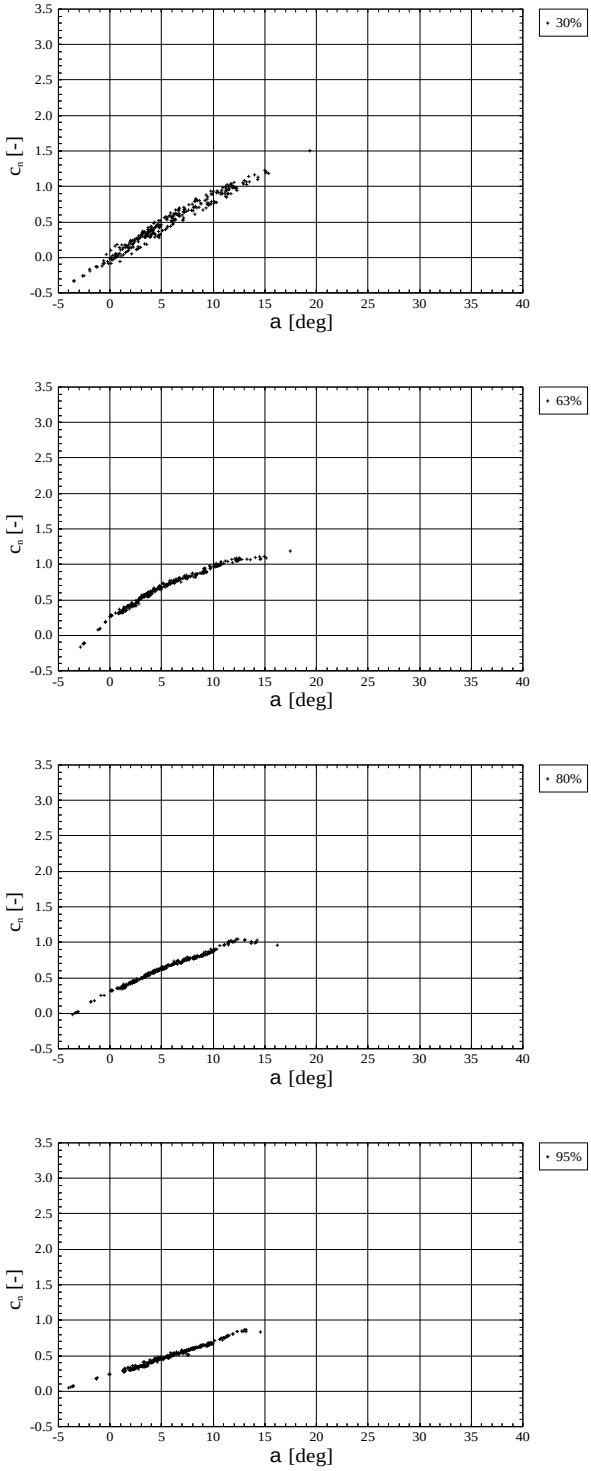

Figure F.7 *NREL; Phase IV:* $c_n - \alpha$*; 30% span (top), 67% span, 80% span and 95% span (bottom)*

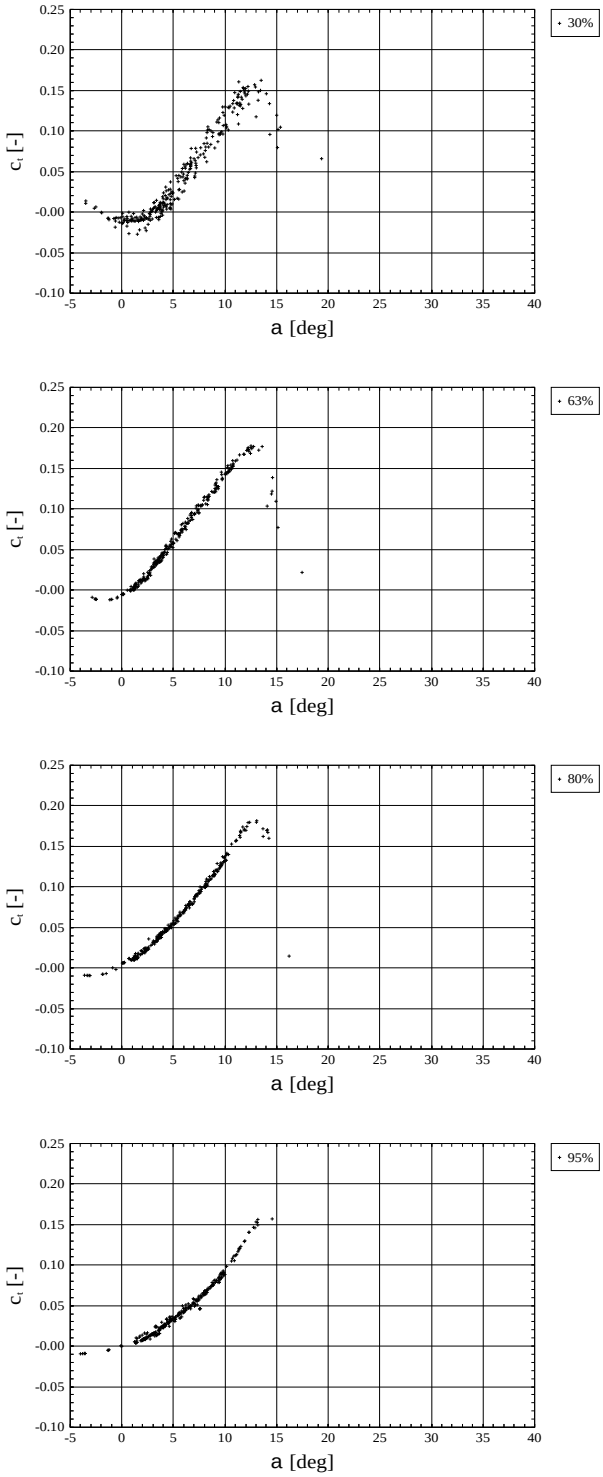

Figure F.8 *NREL; Phase IV:* $c_t - \alpha$*; 30% span (top), 67% span, 80% span and 95% span (bottom)*

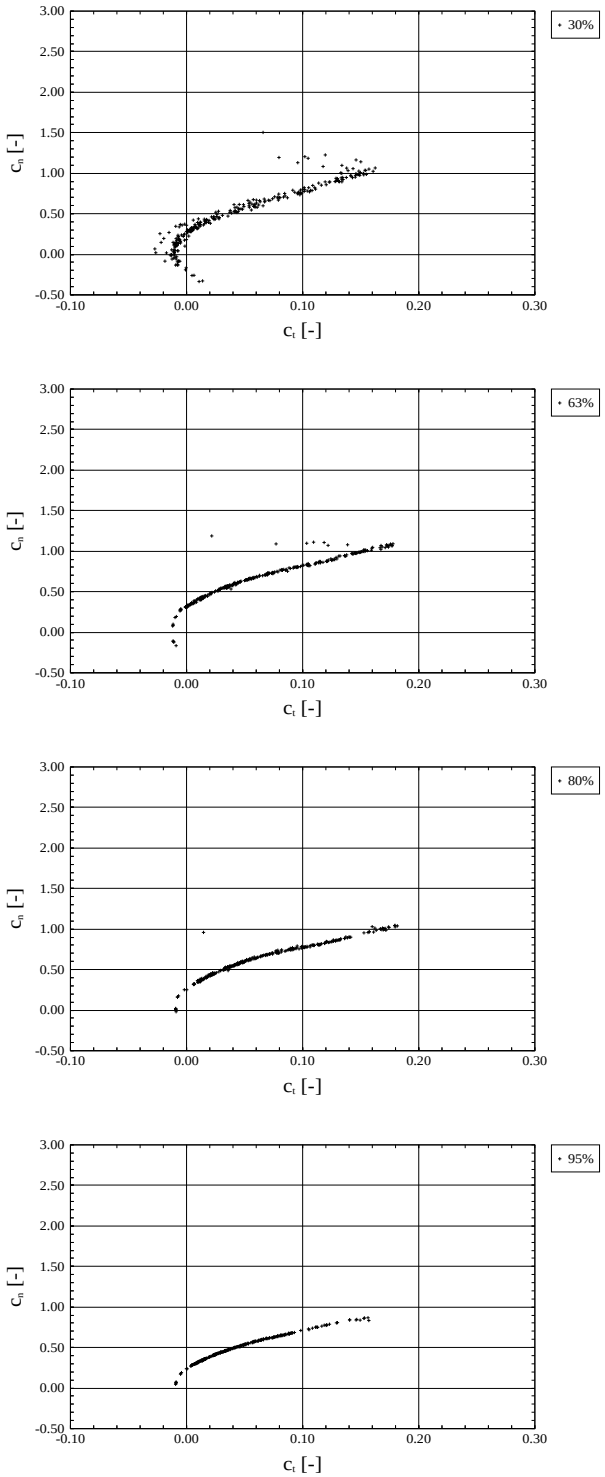

Figure F.9 *NREL; Phase IV:* $c_n - c_t$*; 30% span (top), 67% span, 80% span and 95% span (bottom)*

APPENDIX G. MODEL DESCRIPTION OF RISØ TURBINE

The Riso facility will be described below but more details of the experimentel setup can be found in [23], [24] and [25].

G.1 Basic machine parameters

- Number of blades: 3
- Rotor diameter: 19.0 m
- Swept area: 284 m²
- Hub height: 29.3 m
- Type of rotor: fixed
- Rotational speed: 35.6 and 47.5 rpm
- Cut-in wind speed: 4 m/s
- Cut-out wind speed:
- Rated Power: 100 kW
- Tilt: 5 deg.
- Cone: 0 deg.
- Location of rotor: upwind
- Rotational direction: anti clockwise
- Rotor overhang:
- Power regulation: stall
- Blade tip angle (measured):
  - 1.8 deg
  - 1.8 deg.
  - 1.5 deg.
- Power control: stall
- Direction of rotor rotation (seen in front): anti-clockwise

G.2 Rotor

LM 8.2 m blades with 1 m long blade root extensions are used on the three bladed rotor. Originally, the blades were designed for a 17 m diameter rotor configuration but with the root extensions the diameter is 19 m which is the configuration used in the present experimental setup.

G.2.1 Geometry

The following main data can be listed for the LM 8.2 m blade, see table G.1. The planform data for the 19 m rotor are shown in table G.2 and a graphical representation is presented in figure G.1

G.2.2 Aerodynamics

The 2D airfoil characteristics for the test blade are listed below in Table G.3 and G.4 and shown graphically in Figure G.2 and Figure G.3. The data are basically 2D data from "Abott and Doenhoff", [63] but with corrections for the actual Reynolds number for the test blade which differ from the test Reynolds number in "Abott and Doenhoff".

Table G.1 *Main data for the LM 8.2 m blades*

Type	LM-Glasfiber 8.2 m cantilevered GRP
Spar material	GRP
Shell material	GRP
Blade length	8.2 m
Profiled blade length	6.8 m
Blade extensions	1 m
Root chord	1.09 m
Tip chord	0.45 m
Blade twist	15 deg.
Blade profile	NACA 63n-2nn series
Air brakes	Spoilers positioned on the suction side

Table G.2 *Planform data for the 19 m rotor with LM 8.2.m blades*

radius (m)	chord (m)	twist (deg.)	thickness (%)
2.700	1.090	15.000	24.600
3.550	1.005	9.500	20.700
4.400	.925	6.100	18.700
5.250	.845	3.900	17.600
6.100	.765	2.400	16.600
6.950	.685	1.500	15.600
7.800	.605	.900	14.600
8.650	.525	.400	13.600
9.500	.445	.000	12.600

Table G.3 *2D lift coefficient for the RISØ test blade*

t/c:	12. %	15. %	18. %	21. %	25.%
α	c_l	c_l	c_l	c_l	c_l
0	.1 6	.16	.16	.16	.16
2.0	. 38	.38	.38	.38	.38
4.0	.60	.60	.60	.60	.60
6.0	.82	.82	.82	.82	.81
8.0	1.04	1.03	1.01	1.00	.98
10.0	1.26	1.23	1.19	1.14	1.08
12.0	1.43	1.36	1.29	1.20	1.12
14.0	1.50	1.42	1.32	1.21	1.12
16.0	1.34	1.30	1.25	1.18	1.09
18.0	.80	1.05	1.10	1.12	1.06
20.0	.70	.85	1.00	1.05	1.04
25.0	.92	.95	.97	.99	1.01
30.0	.99	1.00	1.01	1.02	1.03
40.0	.99	1.00	1.01	1.02	1.03
50.0	.92	.92	. 92	.92	.92
60.0	.75	.75	.75	.75	.75
70.0	.51	.51	.51	.51	.51
80.0	.24	.24	.24	.24	.24
90.0	-.02	-.02	-.02	-.02	-.02

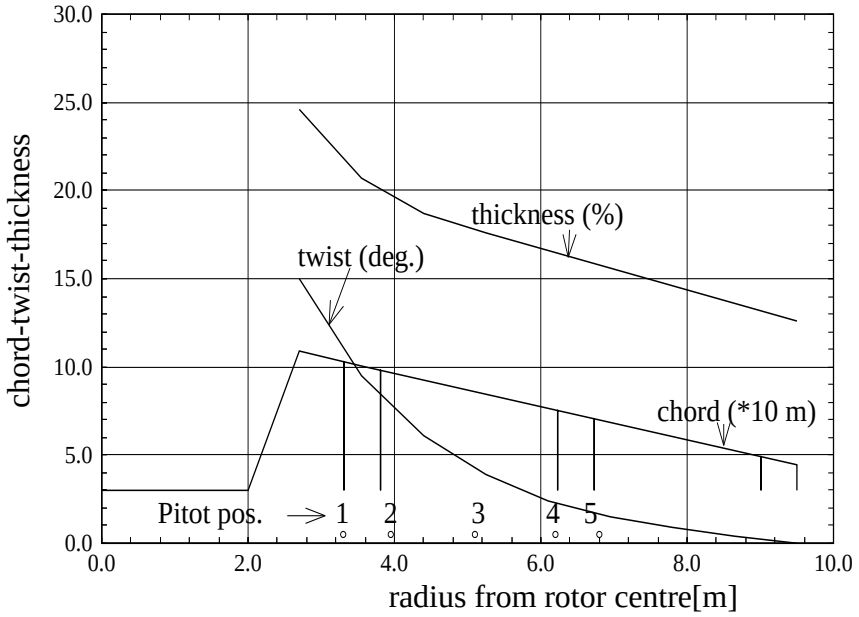

Figure G.1 *The planform data for the test blade including positions of the three blade segments and the positions for the attachment holes for the pitot tube*

Table G.4 *2D drag coefficient for the RISØ test blade*

t/c:	12. %	15. %	18. %	21. %	25.%
α	c_d	c_d	c_d	c_d	c_d
.0	.0048	.0052	.0058	.0064	.0073
2.0	.0048	.0052	.0058	.0063	.0072
4.0	.0056	.0058	.0061	.0065	.0073
6.0	.0080	.0080	.0080	.0079	.0078
8.0	.0110	.0110	.0108	.0105	.0102
10.0	.0158	.0156	.0154	.0152	.0150
12.0	.0240	.0230	.0225	.0218	.0210
14.0	.0400	.0380	.0360	.0340	.0320
16.0	.0700	.0700	.0700	.0700	.0700
18.0	.1500	.1500	.1500	.1500	.1500
20.0	.2150	.2200	.2250	.2300	.2350
25.0	.3700	.3600	.3500	.3400	.3300
30.0	.4700	.4700	.4600	.4500	.4500
40.0	.6600	.6600	.6600	.6600	.6600
50.0	.8500	.8500	.8500	.8500	.8500
60.0	1.0100	1.0100	1.0100	1.0100	1.0100
70.0	1.1500	1.1500	1.1500	1.1500	1.1500
80.0	1.2500	1.2500	1.2500	1.2500	1.2500
90.0	1.3000	1.3000	1.3000	1.3000	1.3000

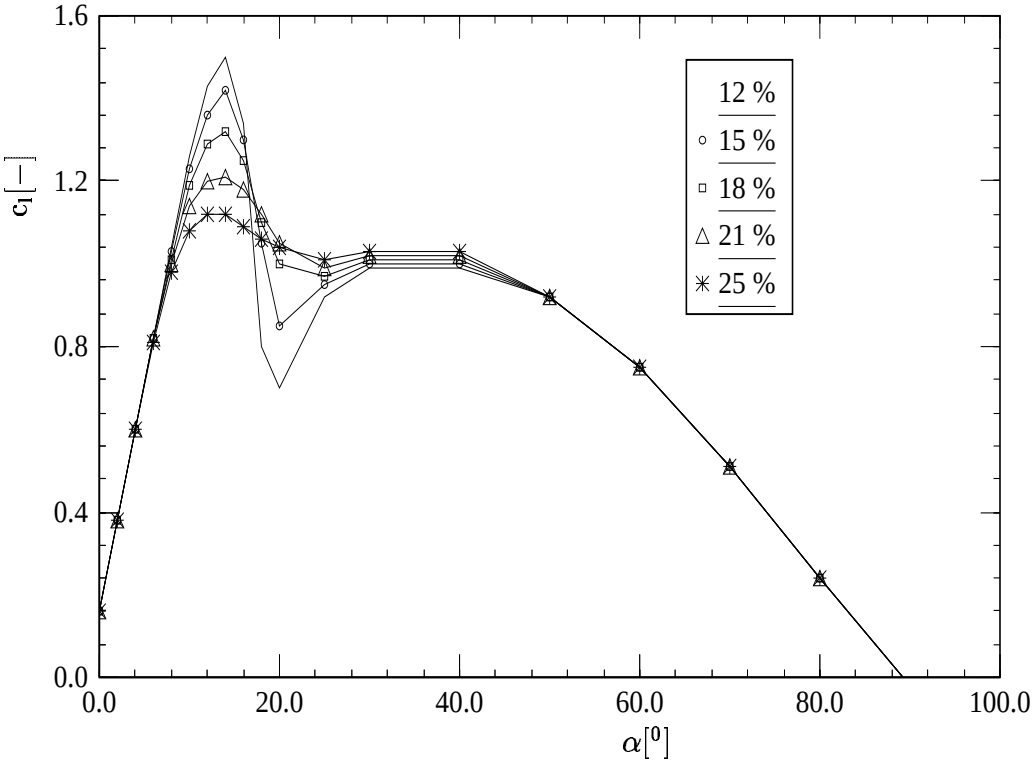

Figure G.2 *2D lift coefficient for the RISØ test blade*

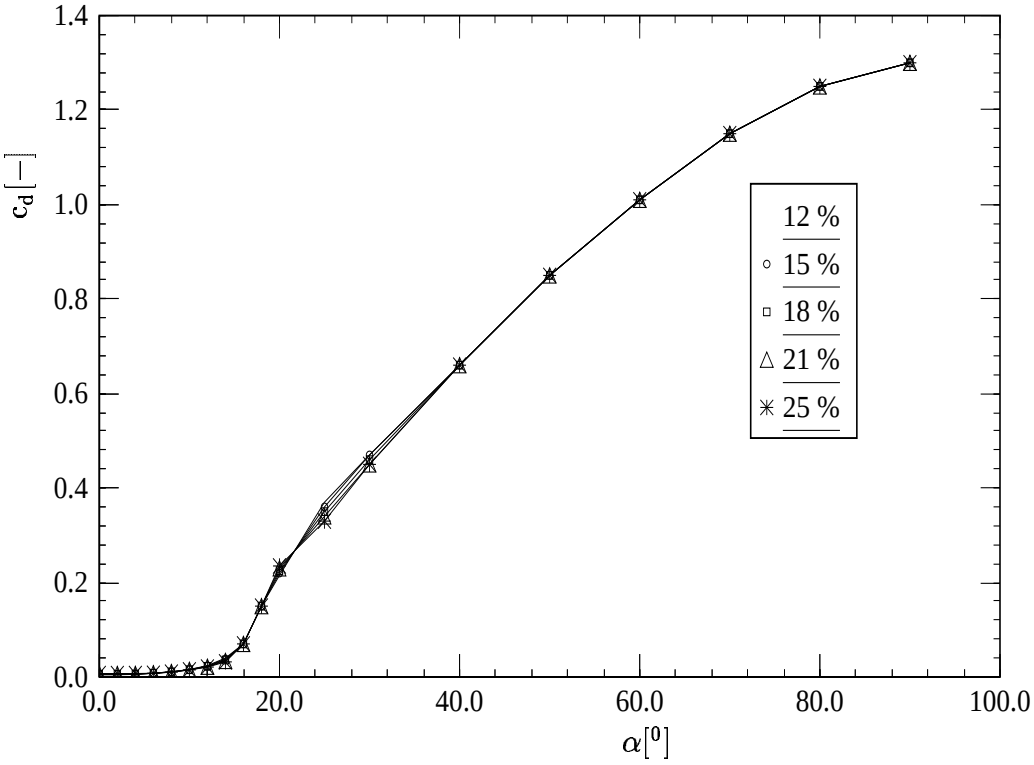

Figure G.3 *2D drag coefficient for the RISØ test blade*

G.2.3 Structural properties

- Rotor mass (blade + hub): 1940 kg
- Blade: 320 kg
- Blade material: GRP

Eigen frequencies measured with the blade mounted on a test rig:
- 1st flapwise bending: 2.50 Hz
- 2nd flapwise bending: 7.76 Hz
- 1st edgewise bending: 4.44 Hz

Eigen frequencies measured on stopped rotor in high wind:
- Symmetric, flapwise rotor mode: 2.59 Hz
- Symmetric edgewise rotor mode: 4.60 Hz

- Assymmetric rotor mode coupling with tower torsion: 1.71 Hz
- Assymmetric rotor mode coupling with 2nd. tower bending: 2.16 Hz

The mass and stiffness distribution of the blades are not known.

G.3 Power train

The principal layout of the power train is shown in figure G.4. The low speed shaft is supported by to main bearings and directly connected to the gearbox. The high speed shaft from the gearbox is coupled to the asynchronous generator with a flexible coupling.

Figure G.4 *2.8:Principal layout of the nacelle including the drive train*

G.4 Tower

G.4.1 Main characteristics

The tower is shown on a picture in figure 5.25 from section 5.4. It is made of three main steel poles and with a lattice of minor poles bolted together. The total weight of the tower is 7400 kg.

Eigen frequencies:

- The first tower bending mode: 1.56 Hz
- The first tower torsion mode coupling with the asymmetrical rotor mode 1.71 Hz

G.5 Control Systems

G.5.1 Power control

Power control is provided by means of stall control. The blade pitch is fixed and the turbine can be run at two different rotational speeds, 35.6 and 47.5 rpm which corresponds to maximum power of 32 and 95 kW.

G.5.2 Yaw control

The upwind rotor has a forced electrical yaw control.

G.6 Measurements at turbine operation

G.6.1 Power curve

See figure G.5.

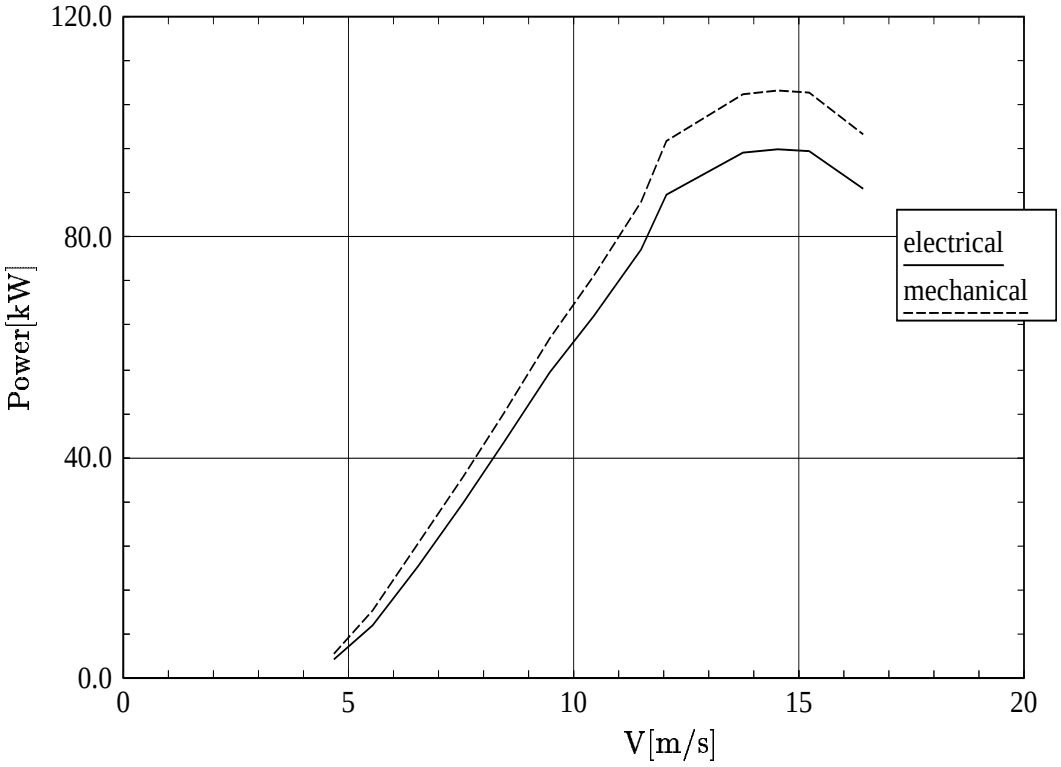

Figure G.5 *RISØ: Power curve*

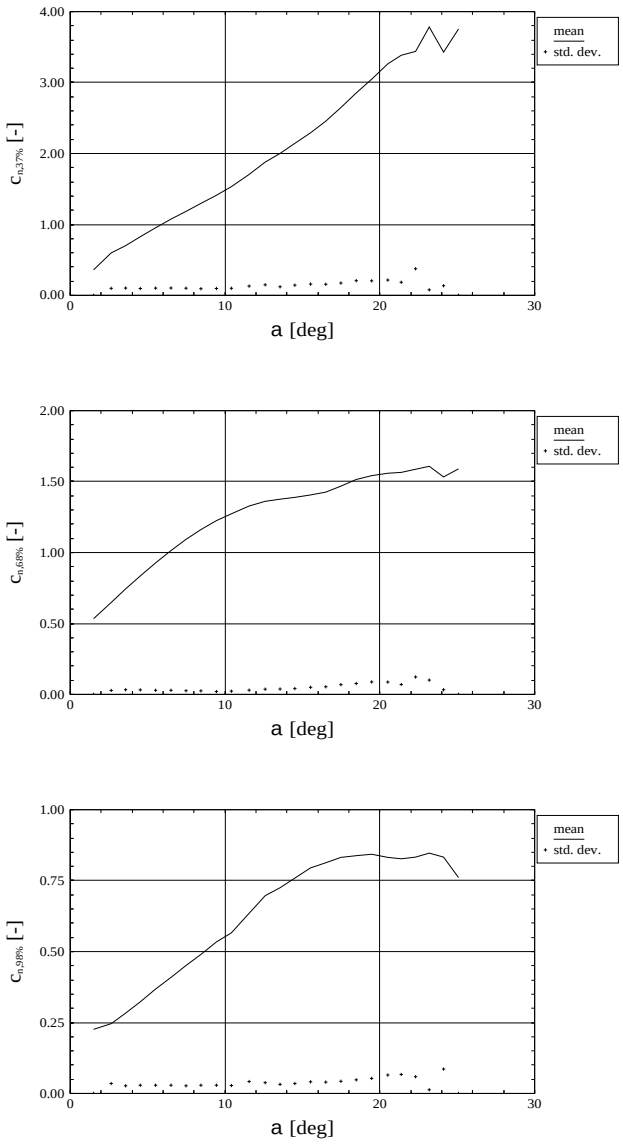

Figure G.6 *RISØ:* $c_n - \alpha$*; 37% span (top), 68% span, 98% span (bottom)*

G.6.2 Profile data

See figure G.6 and G.7. Mean values and standard deviations are given. It must be noted that in particular for the very low and high angles of attack the number of bins is limited. For the intermediate angles of attack the number of bins is in the order of 100 to 200. The profile data are all measured with the pitot tube in position 5 just outboard of segment 2. The angle of attack is thus referring two the inflow at segment two and no correctiopns has been introduced e.g. to compensate for the twist of the blade.

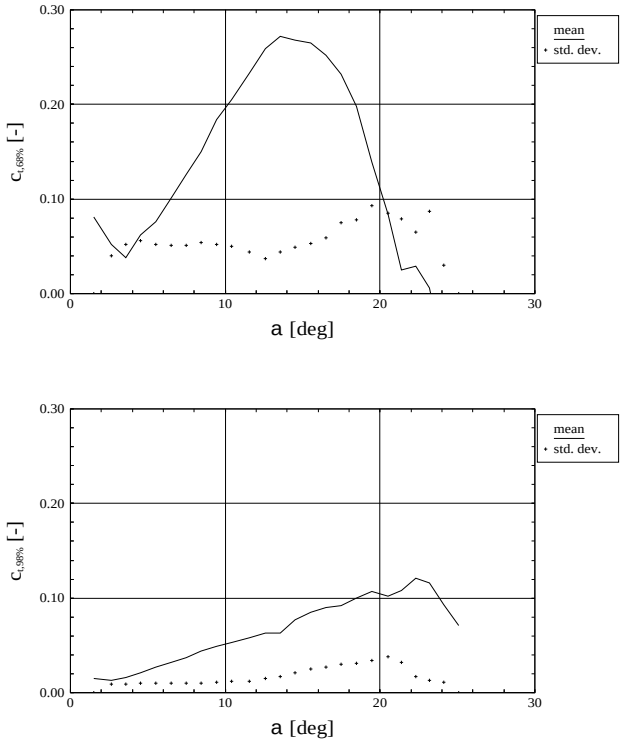

Figure G.7 *RISØ:* $c_t - \alpha$*; 68% span (top) and 98% span (bottom)*

APPENDIX H. MODEL DESCRIPTION OF DUT TURBINE

H.1 Basic Machine Parameters

- Easy tiltable tower
- Number of blades: 2
- Rotor diameter: 10 m
- Hub height: 15.3 m
- Type of rotor: fixed
- Rotational speed : adjusted to desired speed, kept constant within some rpm.
- Cut-in wind speed : 0 m/s automatic switching between motor and generator operation
- Cut-out wind speed : 10-12 m/s (load limits dictated by instrumented blade)
- Rated power: 32 kWatts (electrical)
- Tilt: 0 deg
- Cone: 0 deg
- Location of rotor : upwind
- Rotational direction: anti clockwise (looking down wind to rotor)
- Rotor overhang: 3 m
- Power regulation : rotor speed kept constant, fixed pitch (pitch is adjustable on the ground when turbine is lowered)

H.2 Rotor

H.2.1 Geometry

- Blade type: Prince Fiber Technics (Aerpac)
- Root extension: 0.6 m
- Blade length: 4.4 m
- Blade pitch set angle: adjustable between - 10 and + 10 deg. in 1 deg intervals when turbine is lowered
- Pitching axis line position: 25% chord
- Blade profile: NLF(1)-0416 airfoil (see tables H.2 to H.5 and the figures H.1 to H.12 for actual measured contours)
- Blade taper: none
- Blade root chord: 0.5 m
- Blade tip chord: 0.5 m
- Blade buildin twist: 0 deg

H.2.2 Aerodynamics

See the figures H.13 to H.15.

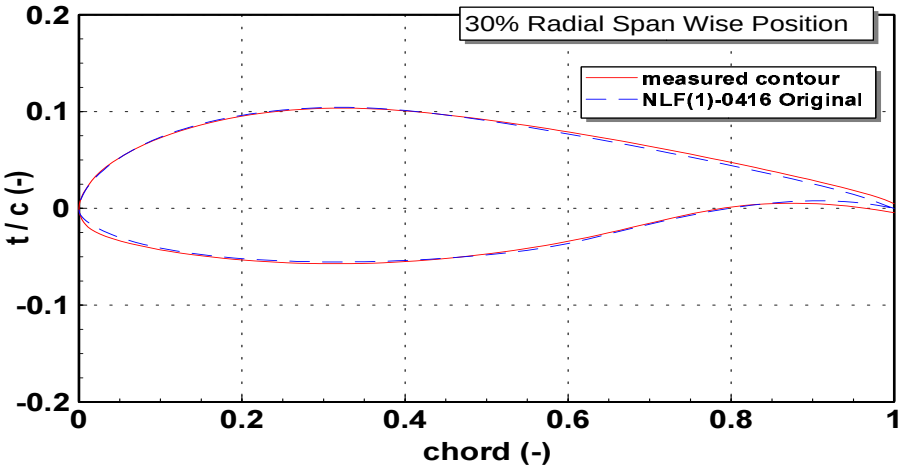

Figure H.1 *DUT: Comparison of the measured contour of the 30% radial spanwise section with the original contour*

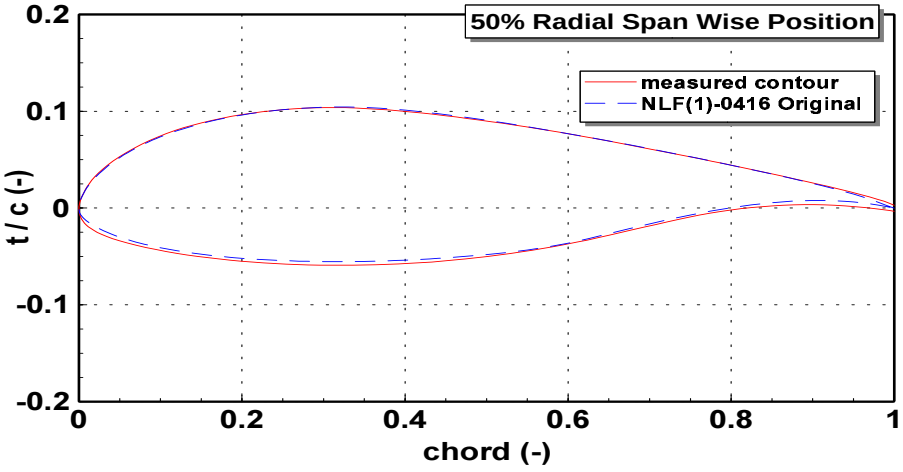

Figure H.2 *DUT: Comparison of the measured contour of the 50% radial spanwise section with the original contour*

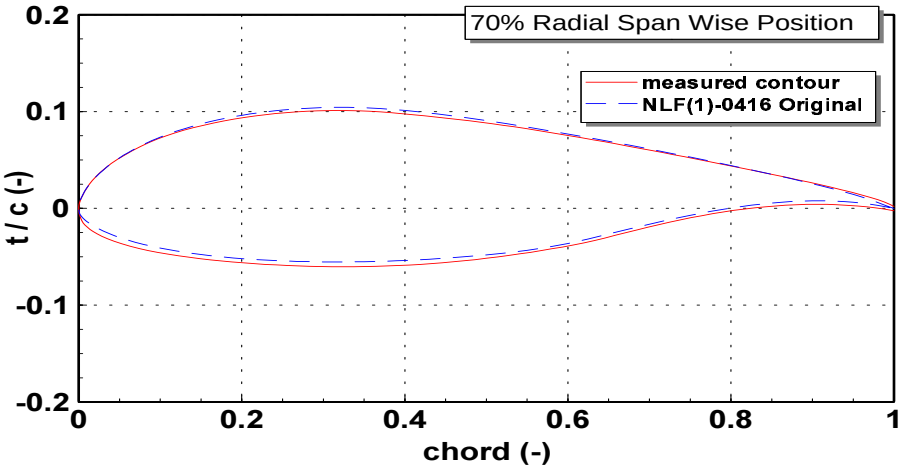

Figure H.3 *DUT: Comparison of the measured contour of the 70% radial spanwise section with the original contour*

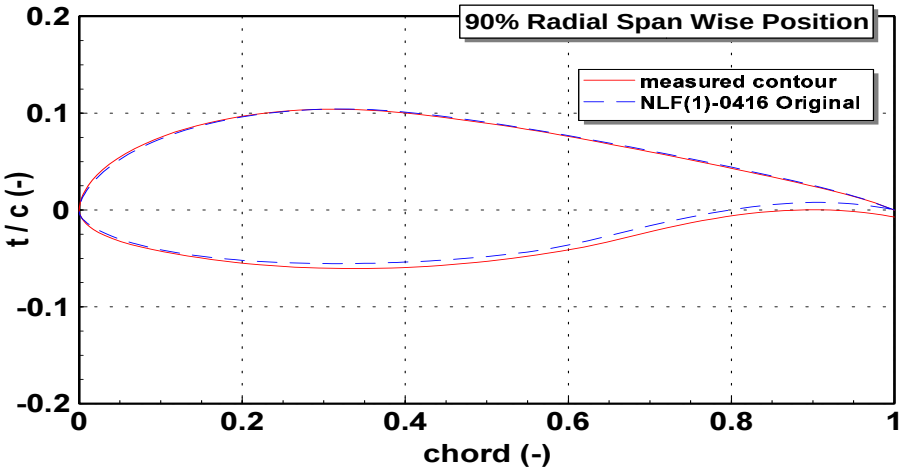

Figure H.4 *DUT: Comparison of the measured contour of the 90% radial spanwise section with the original contour*

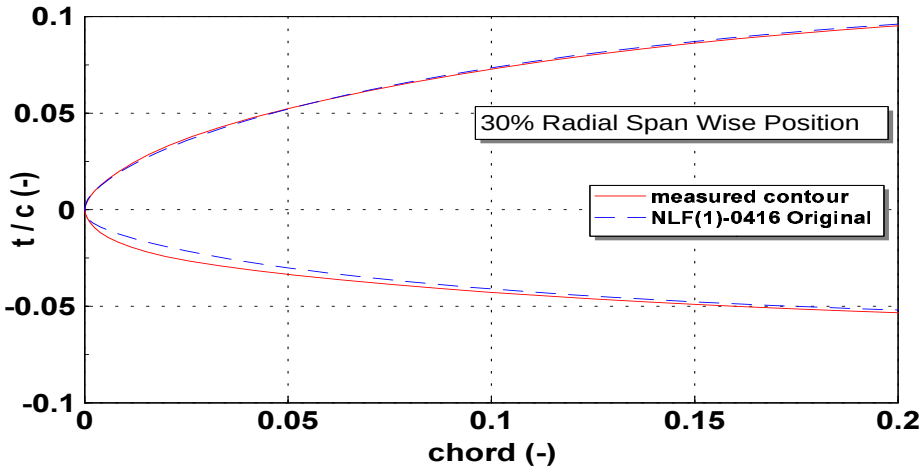

Figure H.5 *DUT: Comparison of the measured contour of the 30% radial spanwise section with the original contour, leading edge part*

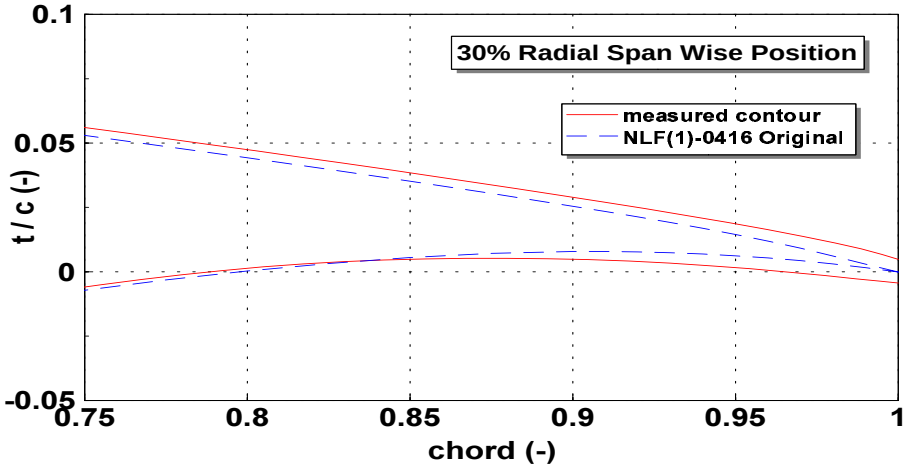

Figure H.6 *DUT: Comparison of the measured contour of the 30% radial spanwise section with the original contour, trailing edge part*

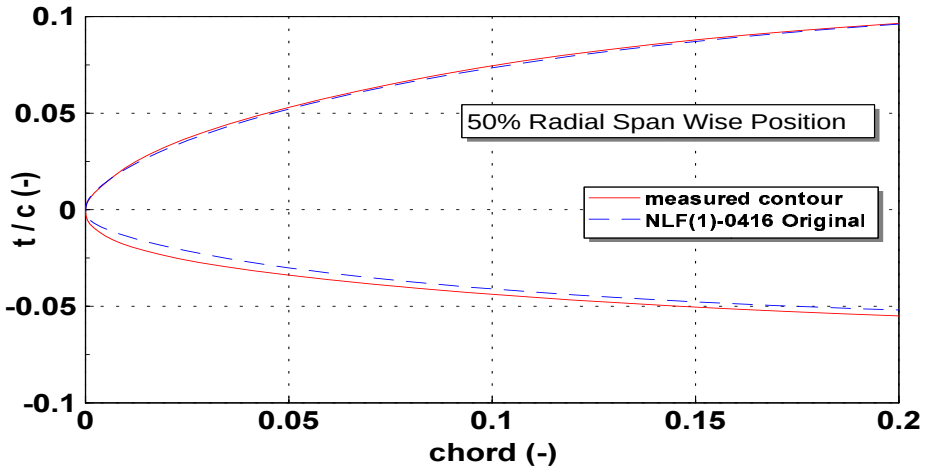

Figure H.7 *DUT: Comparison of the measured contour of the 50% radial spanwise section with the original contour, leading edge part*

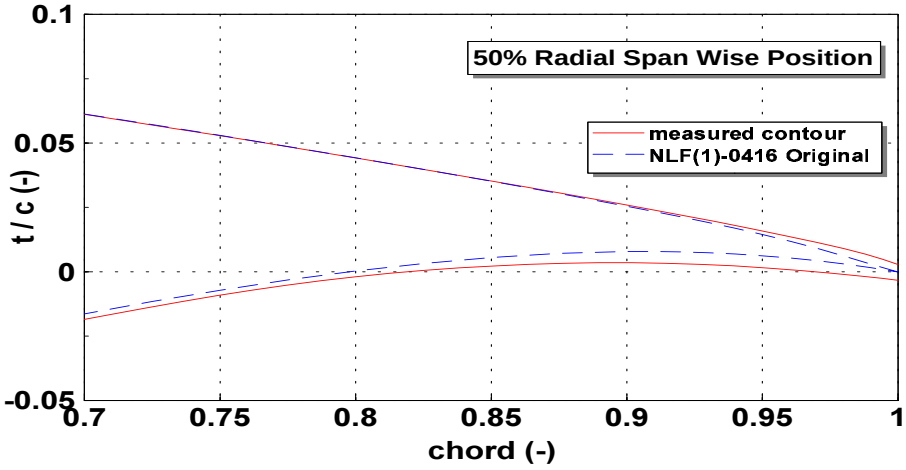

Figure H.8 *DUT: Comparison of the measured contour of the 50% radial spanwise section with the original contour, trailing edge part*

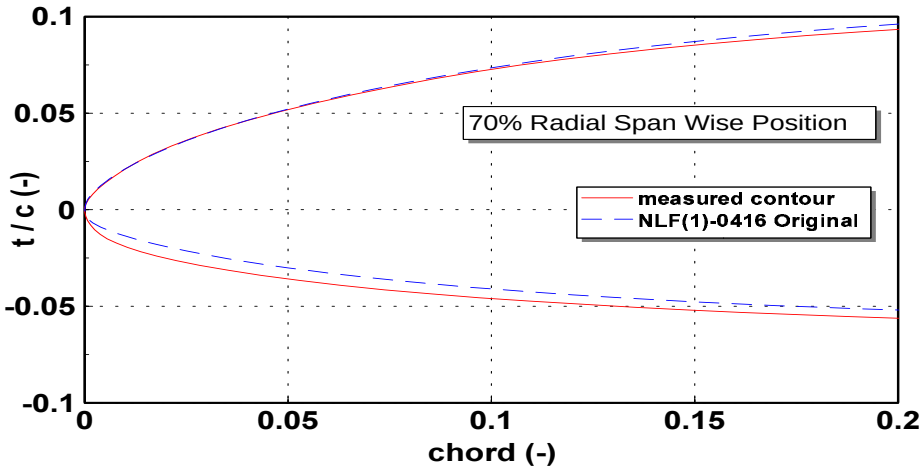

Figure H.9 *DUT: Comparison of the measured contour of the 70% radial spanwise section with the original contour, leading edge part*

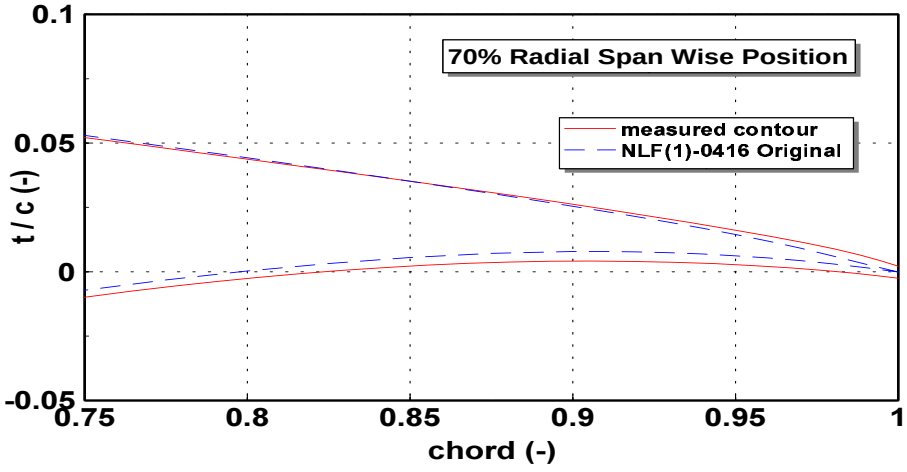

Figure H.10 *DUT: Comparison of the measured contour of the 70% radial spanwise section with the original contour, trailing edge part*

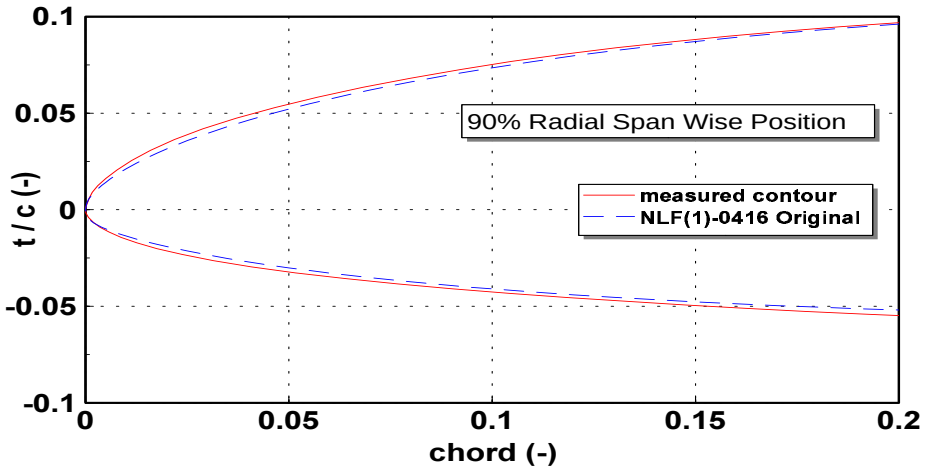

Figure H.11 *DUT: Comparison of the measured contour of the 90% radial spanwise section with the original contour, leading edge part*

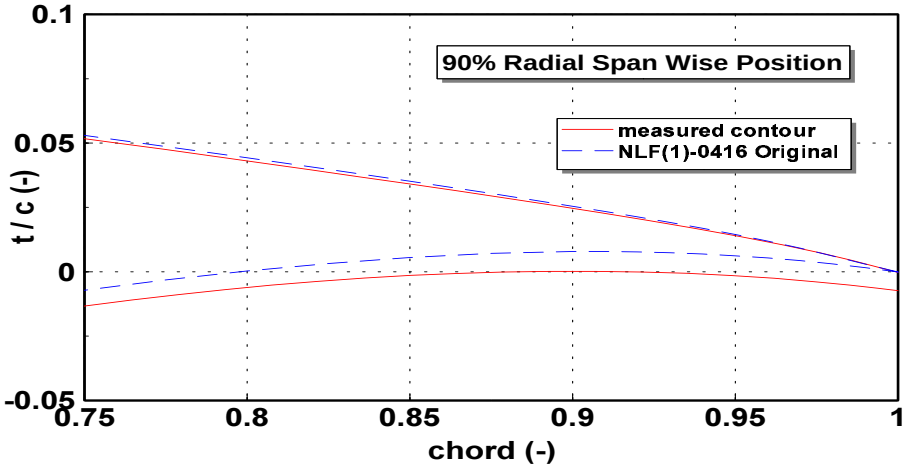

Figure H.12 *DUT: Comparison of the measured contour of the 90% radial spanwise section with the original contour, trailing edge part*

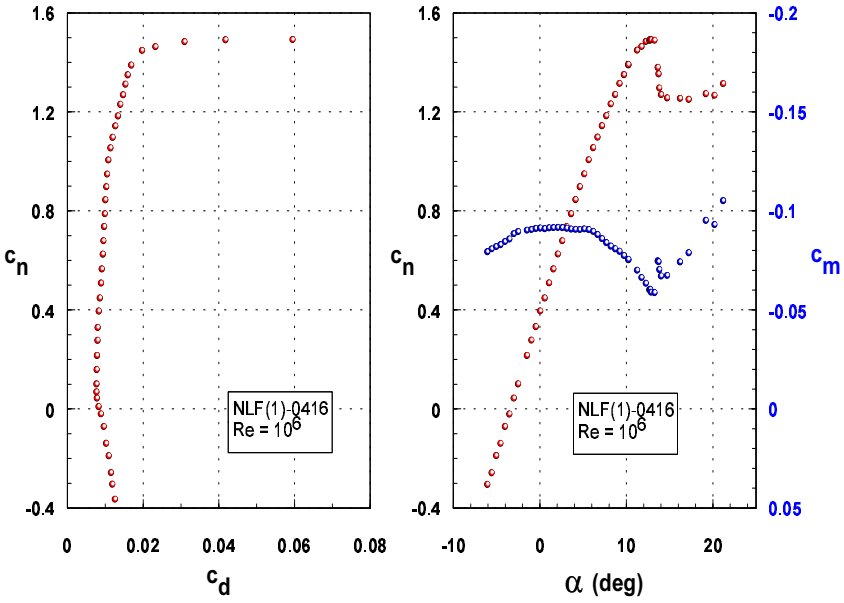

Figure H.13 *Characteristics of the NLF(1)-0416 airfoil, 70% radial spanwise position, measured in the wind tunnel at R=10^6*

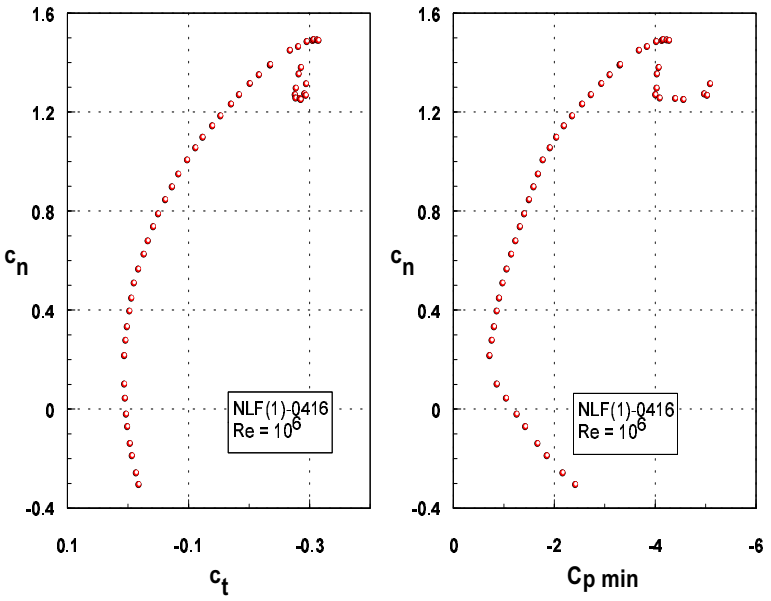

Figure H.14 *Characteristics of the NLF(1)-0416 airfoil, 70% radial spanwise position, c_n as function of c_t and $c_{p,min}$ measured in the wind tunnel at R=10^6*

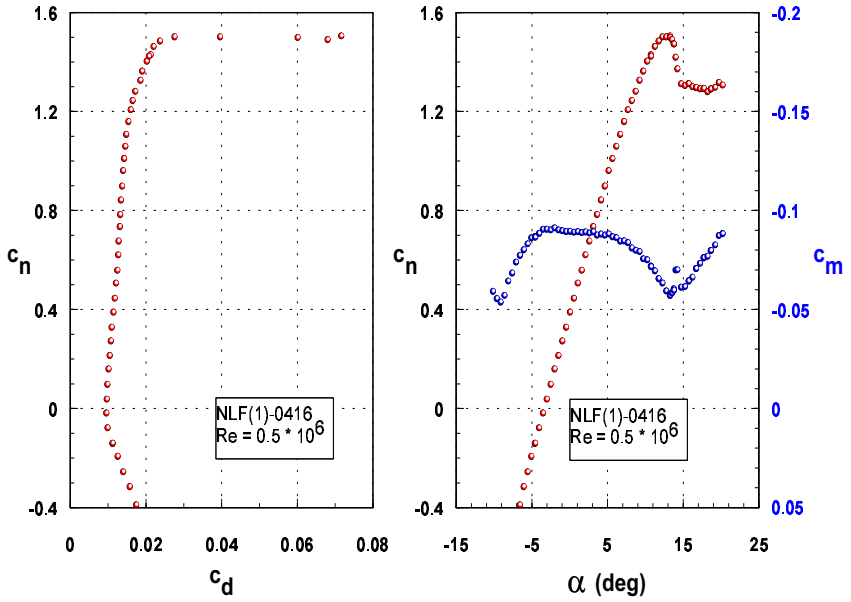

Figure H.15 *Characteristics of the NLF(1)-0416 airfoil, 70% radial spanwise position, measured in the wind tunnel at R= 0.5 10^6*

H.2.3 Structural Properties

- Rotor mass (including hub, root and electronics): 271 kg
- Hub mass (excluding the rotor): 60 kg
- Blade material: Glass fiber reinforced
- Mass of the blade outside root: 66 kg
- Span wise mass distribution: uniform approximately
- Centre of gravity from the blade root 2 m
- Centre of gravity from the rotor centre 2.6 m
- Centre of gravity chord wise: 0.19 m (= 38% chord)
- First edgewise eigenfrequency (estimated): 12 Hz
- First flatwise eigenfrequency
  - instrumented blade 1: 1.85 Hz
  - non instrumented blade 2: 2.25 Hz
  - rotor system not mounted on nacelle: 2.6 Hz
  - higher harmonic: 16 Hz
- Torsional eigenfrequency (roughly)
  - Instrumented blade 1: 22 Hz
  - Non instrumented blade 2: 28 Hz
- EI (determined from static load experiment)
  - Instrumented blade 1: 65262 N m^2
  - Non instrumented blade 2: 84050 N m^2
- E (approximately)
  - Instrumented blade 1: 2.4 1010 N/m^2
  - Non instrumented blade 2: 3.1 1010 N /m^2

H.3 Power train

H.3.1 Layout

The low speed shaft is coupled to the high speed shaft via a gearbox. The high speed shaft is coupled to a motor/generator. The safety brake is positioned on the low speed shaft. The torque meter, the 360 deg pulse and the 6 deg azimuth pulses are on the low speed shaft. The tacho meter is mounted on the generator.

H.3.2 Transmission

- Transmission ratio: 1:8.9142
- System : parallel two-stage
- Coupling to rotor shaft: direct
- Transmission capacity: 35 kW

H.3.3 Braking systems

- fast shaft, parking brake: mechanical laminate
- Low speed, shaft safety brake: hydraulic disc with oil-pump

H.3.4 Electrical system

- Generator/motor: direct current 32 kW electronic field regulation
- Inverter system: Ward Leonard system, single speed, direct connection. 3 phase 380V/50Hz 44 kW asynchronous generator/motor converted to direct current

H.3.5 Characteristics

- Rotor inertia: 1250 kg m^2
- Polar blade inertia moment (Ip = 1/3 M R^3): 550 kg m^2
- Inertia of rotating system, referring to low speed shaft: 1300 kg m^2
- Gearbox ratio : 1:8.9142
- Gearbox inertia: N/A
- Gearbox stiffness: N/A
- Gearbox suspension stiffness: N/A
- Gearbox suspension damping: N/A
- High speed shaft inertia: N/A
- High speed shaft stiffness: N/A
- Generator inertia
  - (in respect to low speed shaft): 35 kg m^2
  - (in respect to high speed shaft): 0.45 kg m^2
- Generator slip: not relevant
- Generator time constant: N/A
- Frequency of drive train: 37 Hz
- Power train efficiency
  - Loss of torque in gearbox
    - constant part: N/A
    - part proportional to rotor speed: N/A
  - Gearbox: N/A
  - Generator: N/A
- Size of mechanical brake
  - Max. torque: 2300 Nm
  - Min. torque: 0 Nm

H.4 Tower

H.4.1 Main Characteristics

- Tiltable tower with tilt hinge at: 6 m
- Basic description: cylindrical
- Tower material: steel
- Rotor axis height: 15.3 m
- Length tiltable tower tube: 14.7 m
- Support towers: 2* 6 m
- Tower diameter base: 0.6096 m + 2* 0.6096 m
- Tower diameter top: 0.6096 m
- Inner diameter support of both towers: 0.5842 m
- Inner diameter tiltable tower tube: 0.597 m
- Tower mass (balance weights included): 7184 kg
- Tower head mass
  - nacelle only: 1716 kg
  - nacelle without rotor: 1894 kg
  - complete, rotor and contra weights: 2165 kg
- Position centre of gravity tower head
  - nacelle only: 0.105 m forward of tower centre
  - nacelle without rotor: 0.205 m backward of tower centre
  - complete, rotor and contra weights : 0.192 m forward of tower centre

- Bending spring constant of tower at tilt hinge (k_1): 1.047 10^7 N / m
- Polar inertia moment of tower, Ip = $\pi/32(d^4 - d_1^4)$: 1.09 10^9 mm^4
- Bending inertia moment of tower, Ix = $\pi/64(d^4 - d_1^4)$: 5.43 10^8 mm^4
- Torsional stiffness: not determined
- Inertia of nacelle around tower axis:
  - 5426 kg m^2 (without rotor)
  - 7865 kg m^2 (rotor included)
- First tower bending eigenfrequency
  - perpendicular to both support towers: 1.27 Hz (x-direction)
  - parallel to both support towers: 1.56 Hz (y-direction)
- First higher order tower eigenfrequency: 25 Hz
- First tower torsion eigenfrequency: not determined

H.5 Control System

H.5.1 Power Control

Electronic control with thyristor. The rotor speed is adjustable to desired speed and kept constant within a couple of rpm. The generator switches automatic motor operation if necessary (Ward-Leonard circuit). The blade pitch is adjustable when turbine is lowered at the ground.

H.5.2 Yaw Control

Manual.

H.5.3 Remaining Control Systems

None.

Table H.1 *Blade geometric distributions*

distance from root (m)	chord (m)	twist (deg)	thick (%)	airfoil section
0.0	0.5	0	16	NLF(1) − 0416
0.0 − 4.4	0.5	0	16	NLF(1) − 0416
4.4	0.5	0	16	NLF(1) − 0416

Table H.2 *Measured blade profile coordinates 30% radial section*

x/c	y/c	x/c	y/c	x/c	y/c	x/c	y/c
1.00000	.004803	.441794	.097340	.000674	.004319	.413316	−.054311
.994919	.006731	.428492	.098528	.000182	.002042	.426548	−.053495
.988607	.008893	.415323	.099637	.000000	−.000035	.439747	−.052589
.980645	.011207	.402331	.100602	.000174	−.002133	.452909	−.051587
.970944	.013715	.389307	.101428	.000647	−.004354	.466064	−.050478
.959765	.016387	.376248	.102136	.001382	−.006724	.479257	−.049268
.947663	.019131	.363235	.102716	.002388	−.009218	.492492	−.047968
.935092	.021856	.350275	.103158	.003809	−.011751	.505716	−.046591
.922257	.024529	.337386	.103449	.005740	−.014296	.518890	−.045132
.909244	.027146	.324554	.103574	.008227	−.016835	.532087	−.043577
.896081	.029723	.311738	.103528	.011329	−.019348	.545279	−.041949
.882808	.032277	.298942	.103314	.015141	−.021800	.558351	−.040243
.869492	.034808	.286198	.102925	.019847	−.024169	.571355	−.038427
.856178	.037308	.273520	.102351	.025710	−.026529	.584381	−.036491
.842874	.039768	.260861	.101579	.032952	−.028944	.597445	−.034448
.829571	.042188	.248189	.100616	.041650	−.031419	.610500	−.032313
.816272	.044563	.235527	.099468	.051660	−.033890	.623508	−.030087
.802948	.046900	.222899	.098136	.062692	−.036285	.636488	−.027756
.789573	.049226	.210321	.096620	.074426	−.038557	.649499	−.025311
.776233	.051548	.197815	.094916	.086601	−.040680	.662617	−.022757
.762916	.053827	.185415	.093019	.099051	−.042647	.675894	−.020128
.749509	.056086	.173130	.090915	.111699	−.044464	.689273	−.017483
.736093	.058331	.160950	.088591	.124480	−.046142	.702643	−.014843
.722735	.060532	.148872	.086039	.137299	−.047677	.715915	−.012239
.709361	.062698	.136905	.083255	.150167	−.049059	.728999	−.009722
.695973	.064834	.125075	.080242	.163165	−.050313	.741909	−.007340
.682618	.066928	.113440	.076999	.176303	−.051469	.754723	−.005105
.669296	.068969	.102087	.073529	.189475	−.052540	.767432	−.003033
.655936	.070963	.091006	.069788	.202585	−.053505	.779999	−.001157
.642513	.072932	.080114	.065748	.215675	−.054351	.792420	.000492
.629094	.074872	.069506	.061456	.228778	−.055079	.804736	.001887
.615690	.076773	.059400	.056981	.241900	−.055692	.817033	.003021
.602287	.078637	.049950	.052350	.255075	−.056198	.829407	.003909
.588888	.080462	.041170	.047547	.268268	−.056608	.841861	.004570
.575501	.082243	.033255	.042714	.281424	−.056911	.854372	.005008
.562126	.083976	.026437	.037963	.294592	−.057102	.866946	.005234
.548751	.085660	.020634	.033231	.307822	−.057193	.879571	.005258
.535373	.087296	.015746	.028561	.321077	−.057196	.892212	.005087
.521989	.088883	.011726	.024068	.334256	−.057108	.904821	.004720
.508600	.090422	.008481	.019857	.347413	−.056903	.917348	.004150
.495217	.091910	.005883	.016039	.360640	−.056597	.929799	.003358
.481826	.093348	.003861	.012648	.373799	−.056201	.942244	.002345
.468411	.094741	.002371	.009632	.386891	−.055681	.954623	.001152
.455066	.096081	.001356	.006879	.400072	−.055043	.966570	−.000161
						.977532	−.001490
						.987048	−.002716
						.994444	−.003679
						1.00000	−.004398

Table H.3 *Measured blade profile coordinates 50% radial section*

x/c	y/c	x/c	y/c	x/c	y/c	x/c	y/c
1.00000	.002804	.406921	.099292	.000417	.003729	.391695	−.057747
.994474	.004793	.393293	.100368	.000049	.001404	.405476	−.057171
.988055	.006844	.379790	.101310	.000014	−.000883	.419199	−.056492
.980056	.008977	.366379	.102112	.000140	−.003145	.432838	−.055705
.969977	.011415	.353030	.102769	.000471	−.005353	.446431	−.054798
.958422	.014037	.339796	.103279	.001118	−.007492	.460063	−.053766
.945812	.016755	.326768	.103620	.002132	−.009552	.473779	−.052614
.932520	.019515	.313922	.103776	.003457	−.011608	.487548	−.051358
.918959	.022229	.301173	.103734	.004986	−.013669	.501286	−.050005
.905025	.024936	.288447	.103492	.006790	−.015648	.514942	−.048554
.890822	.027658	.275710	.103051	.008953	−.017535	.528561	−.046992
.876639	.030342	.262949	.102415	.011548	−.019362	.542225	−.045312
.862476	.032979	.250167	.101587	.014638	−.021211	.555907	−.043527
.848234	.035586	.237402	.100573	.018301	−.023141	.569534	−.041643
.833880	.038184	.224699	.099375	.022597	−.025155	.583100	−.039657
.819498	.040768	.212082	.097989	.027653	−.027203	.596684	−.037554
.805153	.043321	.199566	.096413	.033732	−.029319	.610266	−.035346
.790843	.045840	.187172	.094645	.041041	−.031538	.623735	−.033042
.776541	.048323	.174933	.092683	.049647	−.033840	.637168	−.030614
.762247	.050772	.162866	.090523	.059512	−.036183	.650832	−.028025
.747937	.053186	.151016	.088168	.070431	−.038507	.664957	−.025275
.733531	.055587	.139451	.085620	.082093	−.040748	.679296	−.022478
.719072	.057981	.128198	.082873	.094265	−.042863	.693582	−.019711
.704651	.060349	.117285	.079922	.106868	−.044851	.707865	−.016956
.690231	.062694	.106740	.076763	.119780	−.046716	.722005	−.014232
.675783	.065023	.096536	.073372	.132819	−.048440	.735683	−.011645
.661354	.067330	.086579	.069714	.145915	−.050013	.748754	−.009293
.647022	.069596	.076795	.065769	.159080	−.051435	.761528	−.007181
.632727	.071817	.067284	.061598	.172356	−.052715	.774298	−.005261
.618421	.074004	.058220	.057284	.185786	−.053869	.787103	−.003521
.604259	.076129	.049770	.052914	.199348	−.054908	.799861	−.001968
.590178	.078176	.042088	.048580	.212972	−.055835	.812535	−.000621
.576016	.080175	.035230	.044332	.226622	−.056650	.825204	.000524
.561886	.082118	.029207	.040217	.240267	−.057350	.837999	.001481
.547816	.083986	.024032	.036279	.253887	−.057930	.850897	.002266
.533696	.085794	.019595	.032456	.267509	−.058389	.863722	.002869
.519530	.087550	.015759	.028701	.281176	−.058729	.876523	.003279
.505356	.089251	.012469	.025037	.294918	−.058957	.889292	.003504
.491188	.090894	.009682	.021468	.308727	−.059082	.901847	.003528
.477031	.092477	.007327	.017997	.322568	−.059108	.914310	.003327
.462934	.093991	.005322	.014658	.336407	−.059035	.926842	.002909
.448909	.095425	.003612	.011567	.350253	−.058862	.939392	.002284
.434827	.096788	.002223	.008761	.364093	−.058591	.951908	.001466
.420757	.098090	.001157	.006166	.377901	−.058220	.964163	.000491
						.975644	−.000566
						.985782	−.001616
						.993830	−.002548
						1.000000	−.003306

Table H.4 *Measured blade profile coordinates 70% radial section*

x/c	y/c	x/c	y/c	x/c	y/c	x/c	y/c
1.00000	.002128	.424263	.095615	.000322	.003214	.405172	−.058556
.994701	.004225	.410581	.096753	.000029	.000989	.418660	−.057882
.988301	.006486	.396977	.097804	.000038	−.001165	.432176	−.057098
.980570	.008808	.383534	.098749	.000271	−.003377	.445710	−.056213
.971261	.011256	.370267	.099558	.000706	−.005669	.459218	−.055231
.960420	.013826	.357147	.100211	.001475	−.008004	.472696	−.054144
.948354	.016510	.344148	.100692	.002482	−.010397	.486175	−.052948
.935636	.019205	.331206	.100991	.003802	−.012770	.499661	−.051650
.922547	.021856	.318323	.101110	.005566	−.015058	.513128	−.050248
.909206	.024455	.305562	.101048	.007798	−.017282	.526633	−.048736
.895702	.027006	.292812	.100777	.010535	−.019494	.540180	−.047128
.882084	.029509	.279952	.100320	.013797	−.021746	.553723	−.045433
.868389	.031970	.267011	.099679	.017738	−.023994	.567217	−.043659
.854621	.034390	.254079	.098859	.022549	−.026329	.580599	−.041804
.840761	.036785	.241224	.097865	.028354	−.028805	.593812	−.039862
.826809	.039167	.228442	.096700	.035249	−.031364	.606792	−.037816
.812774	.041550	.215688	.095356	.043355	−.033953	.619586	−.035623
.798715	.043934	.202941	.093825	.052702	−.036568	.632343	−.033242
.784664	.046310	.190250	.092106	.062956	−.039125	.645216	−.030656
.770644	.048672	.177646	.090199	.073761	−.041478	.658375	−.027863
.756657	.051012	.165167	.088103	.085111	−.043605	.671794	−.024955
.742722	.053322	.152883	.085824	.097008	−.045541	.685167	−.022096
.728799	.055598	.140818	.083356	.109422	−.047318	.698408	−.019366
.714885	.057842	.129072	.080707	.122270	−.048981	.711646	−.016753
.700947	.060057	.117734	.077881	.135291	−.050523	.724822	−.014266
.686973	.062253	.106909	.074866	.148413	−.051926	.738056	−.011899
.672986	.064429	.096472	.071560	.161632	−.053200	.751223	−.009647
.659006	.066585	.086166	.067882	.174932	−.054347	.764349	−.007552
.645067	.068708	.075957	.063866	.188346	−.055382	.777470	−.005576
.631119	.070799	.066016	.059604	.201842	−.056318	.790426	−.003776
.617204	.072859	.056569	.055197	.215347	−.057155	.803315	−.002159
.603337	.074871	.047864	.050745	.228870	−.057884	.816183	−.000723
.589474	.076839	.039989	.046264	.242447	−.058515	.829064	.000534
.575631	.078762	.032927	.041765	.256044	−.059054	.841968	.001619
.561861	.080625	.026709	.037321	.269643	−.059498	.854840	.002529
.548163	.082411	.021333	.032985	.283271	−.059847	.867639	.003253
.534444	.084124	.016786	.028802	.296918	−.060108	.880335	.003779
.520664	.085782	.012980	.024746	.310543	−.060283	.892927	.004086
.506895	.087383	.009813	.020858	.324101	−.060362	.905509	.004167
.493146	.088915	.007201	.017207	.337615	−.060332	.918117	.004037
.479390	.090381	.005056	.013862	.351110	−.060193	.930677	.003702
.465633	.091780	.003333	.010845	.364606	−.059941	.943091	.003162
.451842	.093115	.002001	.008092	.378133	−.059581	.955246	.002417
.438023	.094396	.000994	.005564	.391667	−.059120	.966888	.001493
						.977579	.000451
						.986739	−.000608
						.994182	−.001613
						1.00000	−.002477

Table H.5 *Measured blade profile coordinates 90% radial section*

x/c	y/c	x/c	y/c	x/c	y/c	x/c	y/c
1.000000	−.000267	.370632	.102382	.017519	−.020093	.633260	−.035781
.993944	.001736	.356298	.103130	.023754	−.023204	.647520	−.033073
.985890	.004382	.341852	.103661	.031477	−.026408	.662097	−.030140
.975971	.007409	.327398	.104001	.040819	−.029614	.676884	−.027123
.964281	.010518	.312961	.104139	.051652	−.032727	.691679	−.024144
.951155	.013719	.298578	.104068	.063705	−.035659	.706432	−.021232
.937348	.016869	.284260	.103774	.076701	−.038393	.721062	−.018431
.923123	.019930	.270017	.103242	.090339	−.040941	.735584	−.015780
.908642	.022902	.255827	.102459	.104350	−.043306	.750054	−.013294
.893981	.025805	.241667	.101418	.118562	−.045464	.764489	−.010977
.879208	.028652	.227528	.100120	.133065	−.047471	.778869	−.008849
.864378	.031442	.213408	.098570	.147677	−.049349	.793227	−.006921
.849478	.034184	.199345	.096771	.162347	−.051082	.807560	−.005196
.834491	.036901	.185365	.094718	.177040	−.052669	.821842	−.003694
.819464	.039606	.171471	.092399	.191621	−.054113	.836085	−.002429
.804452	.042287	.157666	.089814	.206169	−.055406	.850319	−.001410
.789466	.044930	.144000	.086964	.220745	−.056534	.864559	−.000632
.774469	.047535	.130532	.083851	.235358	−.057495	.878772	−.000099
.759432	.050114	.117401	.080476	.250011	−.058311	.892936	.000176
.744364	.052679	.104682	.076782	.264709	−.058998	.907063	.000183
.729318	.055224	.092240	.072676	.279463	−.059543	.921132	−.000078
.714283	.057733	.079977	.068164	.294270	−.059942	.935078	−.000613
.699221	.060218	.068149	.063353	.309102	−.060219	.948788	−.001431
.684129	.062687	.056968	.058264	.323946	−.060390	.962050	−.002526
.669024	.065144	.046537	.052911	.338770	−.060446	.974401	−.003837
.653925	.067589	.037067	.047415	.353578	−.060378	.985117	−.005208
.638877	.070008	.028856	.041890	.368392	−.060180	.993665	−.006407
.623894	.072374	.021858	.036293	.383200	−.059852	1.000000	−.007317
.608897	.074690	.016017	.030762	.397996	−.059399		
.593910	.076963	.011347	.025521	.412783	−.058821		
.578963	.079176	.007779	.020673	.427559	−.058117		
.564044	.081315	.005043	.016275	.442341	−.057284		
.549103	.083387	.003002	.012466	.457141	−.056331		
.534168	.085395	.001680	.009046	.471970	−.055266		
.519273	.087324	.000888	.005949	.486822	−.054089		
.504393	.089157	.000370	.003170	.501667	−.052794		
.489439	.090911	.000028	.000741	.516487	−.051384		
.474415	.092612	.000110	−.001565	.531292	−.049860		
.459350	.094268	.000732	−.003940	.546076	−.048225		
.444290	.095889	.001875	−.006413	.560808	−.046477		
.429394	.097428	.003513	−.008981	.575475	−.044609		
.414543	.098850	.005804	−.011578	.590103	−.042603		
.399703	.100175	.008803	−.014300	.604687	−.040474		
.385037	.101381	.012623	−.017144	.619070	−.038225		

Table H.6 *Original blade profile coordinates NLF(1)-0416 airfoil section*

x/c	y/c	x/c	y/c	x/c	y/c	x/c	y/c	x/c	y/c
1.00	−.00006	.290	.10381	.00500	.01425	.130	−.04541	.750	−.00715
.990	.00292	.280	.10341	.00400	.01259	.140	−.04662	.775	−.00318
.980	.00609	.270	.10290	.00300	.01077	.150	−.04772	.800	.00031
.970	.00914	.260	.10228	.00200	.00867	.160	−.04873	.825	.00324
.960	.01193	.250	.10156	.00100	.00604	.170	−.04965	.850	.00555
.950	.01449	.240	.10071	.00075	.00520	.180	−.05048	.875	.00712
.940	.01688	.230	.09975	.00050	.00422	.190	−.05124	.900	.00783
.930	.01913	.220	.09867	.00025	.00296	.200	−.05191	.910	.00784
.920	.02129	.210	.09745	.00000	.00000	.210	−.05252	.920	.00770
.910	.02339	.200	.09611	.00025	−.00275	.220	−.05306	.930	.00738
.900	.02543	.190	.09463	.00050	−.00377	.230	−.05354	.940	.00688
.875	.03039	.180	.09300	.00075	−.00450	.240	−.05395	.950	.00621
.850	.03515	.170	.09123	.00100	−.00509	.250	−.05431	.960	.00536
.825	.03976	.160	.08929	.00200	−.00679	.260	−.05462	.970	.00432
.800	.04426	.150	.08717	.00300	−.00804	.270	−.05487	.980	.00308
.775	.04866	.140	.08487	.00400	−.00906	.280	−.05506	.990	.00163
.750	.05296	.130	.08237	.00500	−.00996	.290	−.05521	1.00	−.00006
.725	.05716	.120	.07966	.00600	−.01078	.300	−.05531		
.700	.06128	.110	.07671	.00700	−.01154	.310	−.05536		
.675	.06532	.100	.07351	.00800	−.01226	.320	−.05536		
.650	.06926	.095	.07180	.00900	−.01295	.330	−.05532		
.625	.07311	.090	.07001	.01000	−.01362	.340	−.05523		
.600	.07685	.085	.06814	.01250	−.01517	.350	−.05511		
.575	.08049	.080	.06618	.01500	−.01658	.360	−.05493		
.550	.08400	.075	.06413	.01750	−.01788	.370	−.05472		
.525	.08737	.070	.06198	.02000	−.01910	.380	−.05447		
.500	.09057	.065	.05971	.02500	−.02136	.390	−.05417		
.475	.09360	.060	.05733	.03000	−.02340	.400	−.05383		
.450	.09641	.055	.05482	.03500	−.02527	.410	−.05345		
.440	.09746	.050	.05215	.04000	−.02699	.420	−.05303		
.430	.09847	.045	.04932	.04500	−.02859	.430	−.05256		
.420	.09942	.040	.04631	.05000	−.03008	.440	−.05205		
.410	.10031	.035	.04307	.05500	−.03147	.450	−.05149		
.400	.10113	.030	.03957	.06000	−.03277	.475	−.04992		
.390	.10187	.025	.03576	.06500	−.03401	.500	−.04806		
.380	.10253	.020	.03154	.07000	−.03517	.525	−.04590		
.370	.10310	.0175	.02924	.07500	−.03628	.550	−.04334		
.360	.10357	.015	.02678	.08000	−.03733	.575	−.04016		
.350	.10394	.0125	.02412	.08500	−.03832	.600	−.03623		
.340	.10419	.0100	.02121	.09000	−.03927	.625	−.03163		
.330	.10433	.0090	.01995	.09500	−.04017	.650	−.02657		
.320	.10436	.0080	.01864	.10000	−.04103	.675	−.02137		
.310	.10428	.0070	.01726	.11000	−.04263	.700	−.01632		
.300	.10410	.0060	.01580	.12000	−.04408	.725	−.01155		

H.6 Blade structural distributions

Table H.7 *Structural properties*

Distance from root(m)	mass (kg/m)	edgewise stiffness (Nm^2)	flatwise stiffness (Nm^2)
r> 1.5 m	20.7	not determined	65262 (instrumented blade 1) 84050 (non-instrumented blade 2)

- Center of gravity rotor blade
  - 2 m (from blade root)
  - 0.19 m (= 38% chord, from leading edge)
  - 50% (of blade thickness, estimated)

APPENDIX I. MODEL DESCRIPTION OF MIE TURBINE

I.1 Basic machine parameters

- Easy tiltable tower
- Number of blades: 3
- Rotor diameter: 10 m
- Hub height: 13.3 m
- Type of rotor: fixed hub
- Rotational speed: fixed at approx. 90 rpm
- Cut-in wind speed: 3 m/s
- Cut-out wind speed: 12 m/s (load limits dictated by generator)
- Rated power: 8 kW (electrical)
- Tilt: 0 deg
- Cone: 0 deg
- Location of rotor: upwind
- Rotational direction: anticlockwise (view from upwind)
- Rotor overhang: 1 m
- Power regulation: rotor speed kept constant with pitch control

I.2 Rotor

I.2.1 Geometry

- Blade type: Mie in house
- Root extension: 0.433 m
- Blade length: 4.567 m
- Blade pitch set angle: variable between -7 and +30 deg in operation
- Pitching axis line position: 25% chord
- Blade profile: combination of DU91-W2-250 and DU93-W-210 airfoils
- Blade taper, chord, twist and thickness: see Table I.1 and Figs. I.1 to I.3

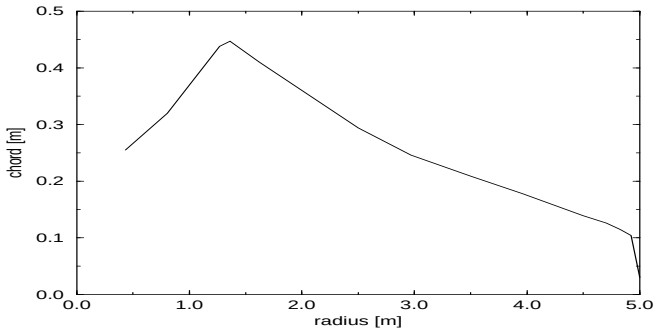

Figure I.1 *Measured chord length*

Note that this blade configuration is referred to Aerpac's APX 40. However, the pitching axis is different from the original. Also, the thickness of blade tip region is different from the original due to the layout of pressure measurement tubing.

radius from rotor center	chord	twist	thickness
m	m	deg	
0.433	0.255	12.8	105.4
0.804	0.320	12.8	78.8
1.269	0.438	12.8	29.2
1.361	0.447	11.8	26.6
1.625	0.410	10.0	25.5
2.500	0.294	5.0	23.5
2.970	0.246	2.6	22.2
3.500	0.209	1.8	22.2
3.960	0.178	1.0	23.0
4.500	0.139	0.0	23.0
4.703	0.126	0.0	20.3
4.827	0.115	0.0	17.3
4.923	0.104	0.0	17.5
5.000	0.030	0.0	17.5

Table I.1 *Measured chord length, thickness and twist*

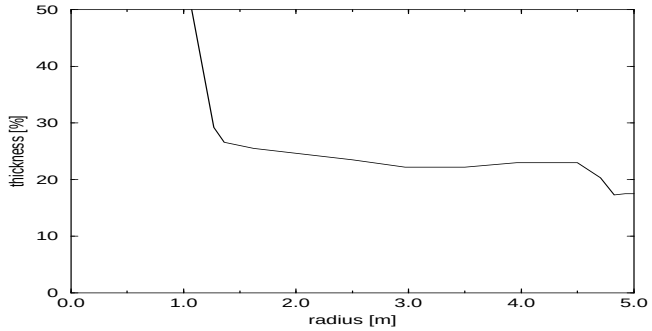

Figure I.2 *Measured thickness*

I.2.2 Aerodynamics

See Figs. I.4 and I.5.

I.2.3 Structural properties

- Rotor mass (including hub, root and electronics): 223.2 kg
- Hub mass (excluding root): 166.5 kg
- Blade material: Grass fiber reinforced polyester
- Mass of the blade outside root (total of three blades): 136.5 kg
- Center of gravity from the blade root: 1.19 m
- Center of gravity from the rotor center: 1.623 m
- First flapwise eigenfrequency: 3.21 Hz
- The mass and stiffness distribution of the blades are unknown.

I.3 Power train

The principal layout of the power train is shown in Fig. 5.44. The low speed shaft is coupled to the high speed shaft through two-stage timing belt and gearbox with 4 speed transmission. The transmission ratio of the timing belt is 9.0. The

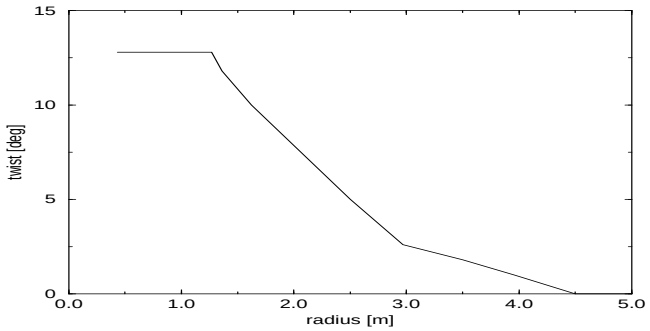

Figure I.3 *Measured twist*

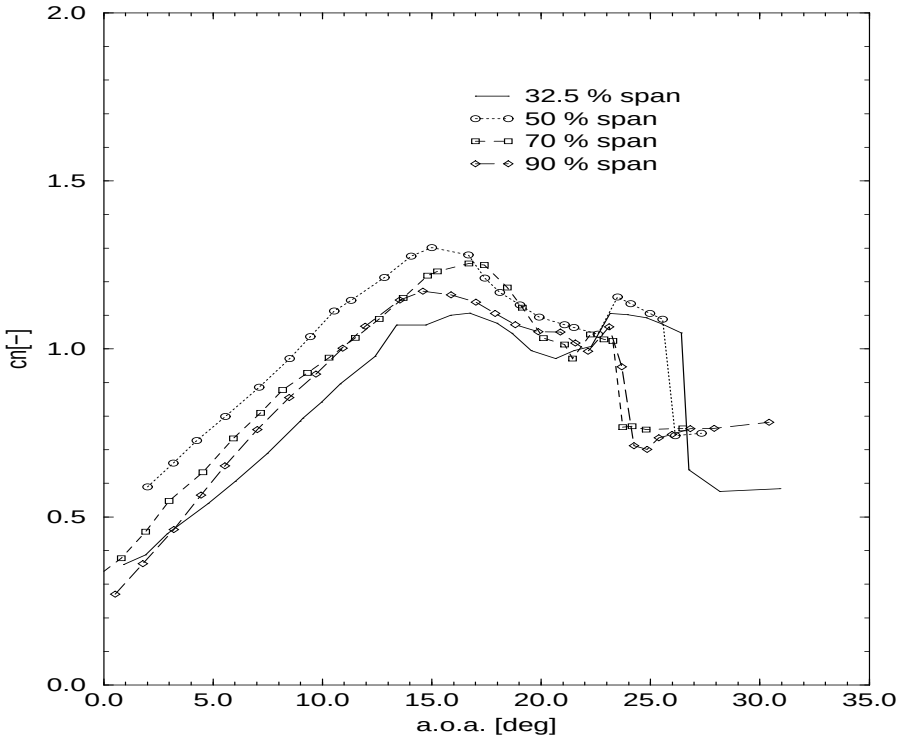

Figure I.4 $c_n - \alpha$ *curves of measurement stations, measured in the Goetingen type wind tunnel with the open test sections at V = 15 m/s*

transmission ratios of the gear box can be changed to 1.00, 1.65, 2.56 and 4.11. In the IEA Annex XVIII experiments, the transmission ratio of the gear box is fixed at 1.00. The high speed shaft is coupled to an induction generator of 8-pole 3 phase 200V/60Hz 8kW. The safety magnetic disc brake is positioned on the middle shaft. The 360 deg pulse and the azimuth pulses are on the low speed shaft. An encoder for detecting rotor speed is mounted on the middle shaft.

I.4 Tower

- Tiltable tower with tilt hinge at 3.0 m high

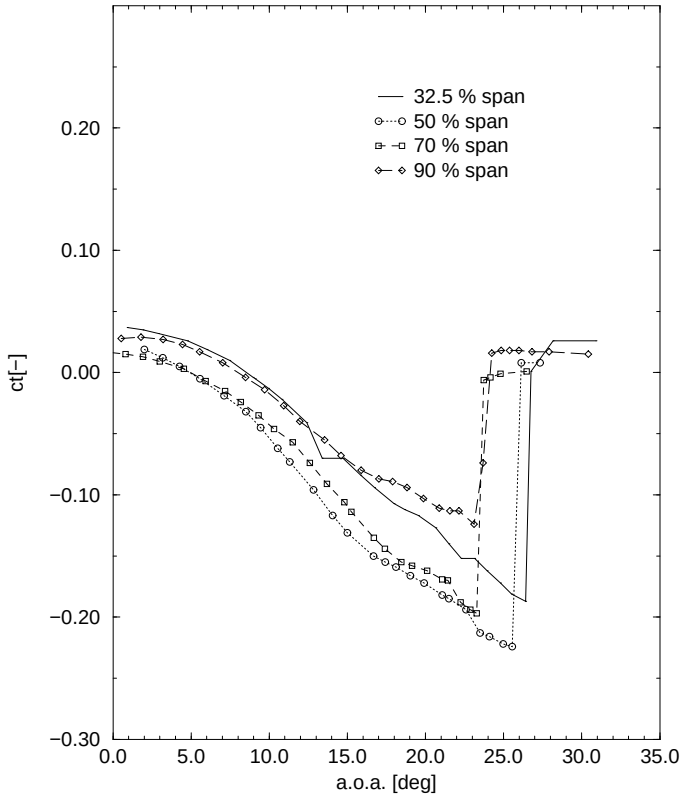

Figure I.5 $c_t - \alpha$ *curves of measurement stations, measured in the Goetingen type wind tunnel with the open test sections at V = 15 m/s*

- Tilt power: hydraulic cylinder with oil pump
- Basic description: cylindrical with ribs
- Tower material: steel
- Rotor axis height: 13.3 m
- Length of tiltable tower pole: 12.045m
- Support towers: 2*3 m
- Tower diameter: 0.457 m
- Tower mass (balance weights included): 5425 kg
- Tower head mass (nacelle without rotor): 1600 kg
- Concrete base mass: 51840 kg

I.5 Control Systems

I.5.1 Power control

Power control is provided by means of electric capacitor excitation system. The turbine is operated at the balance point of electrical capacitor, voltage and current. The blade pitch is variable in operation and turbine can be run from 80 rpm to 100 rpm.

I.5.2 Yaw control

The nacelle has a forced electrical manual yaw control.

I.6 Measurements at turbine operation

I.6.1 Power curve

The power curver is presented in figure I.6.

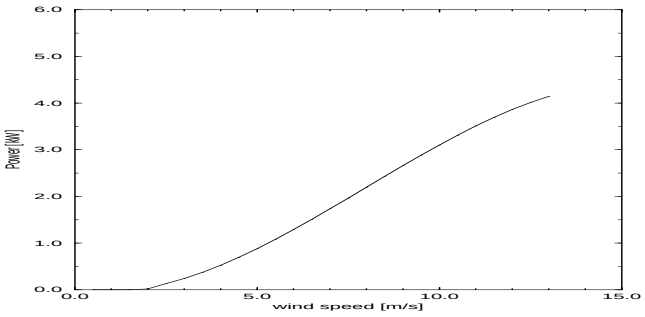

Figure I.6 *Measured electrical power curve*

I.6.2 Profile data

See Table I.2, I.4, and Figs. I.7 to I.10.

	32.5%		50%	
tap nr.	x/c [-]	y/c [-]	x/c [-]	y/c [-]
1	0.000000	0.000000	0.000000	0.000000
2	0.002850	0.010639	0.001394	0.012358
3	0.012085	0.025244	0.004719	0.020555
4	0.019229	0.032420	0.011036	0.029443
5	0.024940	0.038013	0.016804	0.036507
6	0.033212	0.043971	0.023229	0.041782
7	0.041965	0.049211	0.032271	0.048991
8	0.049402	0.054089	0.038976	0.053721
9	0.072293	0.066009	0.048223	0.059707
10	0.098393	0.077763	0.071687	0.073175
11	0.148522	0.095861	0.095899	0.084159
12	0.197370	0.108735	0.146292	0.102305
13	0.245889	0.118686	0.194438	0.115732
14	0.298222	0.125893	0.243990	0.126428
15	0.348215	0.130076	0.295700	0.133453
16	0.400371	0.131343	0.344243	0.136721
17	0.448150	0.129367	0.397220	0.136745
18	0.499767	0.124766	0.447522	0.134328
19	0.551964	0.118058	0.496541	0.129656
20	0.601769	0.109956	0.551687	0.121549
21	0.601769	0.109956	0.595996	0.113122
22	0.653063	0.099942	0.648917	0.102009
23	0.682125	0.093948	0.684705	0.094029
24	0.721730	0.085249	0.721224	0.084937
25	0.751560	0.078108	0.749809	0.078456
26	0.804083	0.064863	0.800150	0.065748
27	0.846520	0.053488	0.846297	0.053856
28	0.900461	0.037972	0.900830	0.038790
29	0.946880	0.023444	0.946128	0.025451
30	0.979883	0.010946	0.978186	0.014805
31	1.000000	-0.000001	1.000000	0.000000
32	0.981566	-0.002581	0.974633	-0.006052
33	0.953204	0.001283	0.945066	-0.002203
34	0.898711	0.006453	0.893224	0.001759
35	0.855152	0.005852	0.850254	0.000778
36	0.798363	-0.000610	0.797473	-0.005097
37	0.751092	-0.011792	0.744762	-0.014924
38	0.698231	-0.029225	0.698368	-0.026491
39	0.650041	-0.046959	0.645215	-0.041754

Table I.2 *Measured profile geometry and position of pressure taps at 32.5% and 50% stations*

	32.5%		50%	
tap nr.	x/c [-]	y/c [-]	x/c [-]	y/c [-]
40	0.595289	-0.064516	0.591423	-0.056601
41	0.546852	-0.079089	0.546629	-0.067663
42	0.495778	-0.092519	0.494988	-0.078639
43	0.444724	-0.103961	0.445119	-0.087586
44	0.395242	-0.111856	0.394105	-0.094518
45	0.341541	-0.117796	0.340708	-0.098266
46	0.293672	-0.118789	0.292697	-0.098336
47	0.246203	-0.116501	0.246966	-0.096435
48	0.190153	-0.111024	0.189955	-0.089661
49	0.139841	-0.101079	0.139609	-0.080038
50	0.083069	-0.082887	0.082521	-0.063312
51	0.065664	-0.074592	0.063683	-0.055530
52	0.049432	-0.066032	0.049602	-0.049655
53	0.038760	-0.058943	0.040223	-0.044654
54	0.031109	-0.053572	0.032818	-0.040390
55	0.022351	-0.046240	0.024962	-0.035561
56	0.012942	-0.036539	0.021224	-0.032225
57	0.006220	-0.028986	0.014629	-0.026852
58	0.003210	-0.021546	0.008564	-0.019824
59	0.000846	-0.013983	0.005148	-0.015153
60	0.000079	-0.007328	0.001625	-0.006870

Table I.3 *Measured profile geometry and position of pressure taps at 32.5% and 50% stations, Ctd*

	70%		90%	
tap nr.	x/c [-]	y/c [-]	x/c [-]	y/c [-]
1	0.000000	0.000000	0.000000	0.000000
2	0.002043	0.006584	0.011414	0.015607
3	0.007916	0.017500	0.012838	0.017032
4	0.011297	0.022335	0.014261	0.020320
5	0.017195	0.029422	0.020349	0.025782
6	0.024498	0.035951	0.027524	0.030531
7	0.029535	0.040454	0.035061	0.035284
8	0.038534	0.047368	0.041879	0.039669
9	0.046751	0.053128	0.057318	0.048455
10	0.053430	0.057061	0.079951	0.059826
11	0.076887	0.070104	0.103666	0.071207
12	0.100435	0.080510	0.154018	0.089661
13	0.154620	0.099730	0.205488	0.103797
14	0.205372	0.113160	0.250498	0.113911
15	0.252809	0.122948	0.305253	0.123384
16	0.303439	0.129926	0.355027	0.125942
17	0.352902	0.133142	0.400088	0.128500
18	0.400508	0.133112	0.445194	0.127071

Table I.4 *Measured profile geometry and postion of pressure taps at 70% and 90% station*

	70%		90%	
tap nr.	x/c [-]	y/c [-]	x/c [-]	y/c [-]
19	0.453466	0.130390	0.500051	0.124279
20	0.556373	0.118178	0.555663	0.117526
21	0.608004	0.108832	0.608049	0.108220
22	0.660973	0.097736	0.653208	0.100297
23	0.697380	0.089959	0.690074	0.091945
24	0.728011	0.081548	0.728013	0.084684
25	0.756562	0.074449	0.763078	0.075956
26	0.805581	0.061182	0.806464	0.064411
27	0.847049	0.049773	0.844787	0.054267
28	0.904998	0.033614	0.902993	0.039238
29	0.953951	0.019155	0.946409	0.024086
30	0.984276	0.009564	0.981847	0.013919
31	0.999680	-0.005890	1.000000	0.000000
32	0.976717	-0.010109	0.962193	-0.008611
33	0.946653	-0.008667	0.931927	-0.013191
34	0.891389	-0.008688	0.882535	-0.016848
35	0.840163	-0.013479	0.832424	-0.020871
36	0.790964	-0.020537	0.785623	-0.032443
37	0.743620	-0.028656	0.733404	-0.043338
38	0.692605	-0.038244	0.680801	-0.051350
39	0.642306	-0.047872	0.634005	-0.063643
40	0.589144	-0.057340	0.581406	-0.072016
41	0.539150	-0.065789	0.532049	-0.080001
42	0.489474	-0.072821	0.478358	-0.087301
43	0.441071	-0.078488	0.431139	-0.092021
44	0.387500	-0.082431	0.384632	-0.095654
45	0.336170	-0.084824	0.330893	-0.097182
46	0.289332	-0.083880	0.286166	-0.097914
47	0.238574	-0.080325	0.232000	-0.093503
48	0.182742	-0.073375	0.175703	-0.089091
49	0.136768	-0.065542	0.125115	-0.079048
50	0.082011	-0.052193	0.069473	-0.068687
51	0.060642	-0.045018	0.049207	-0.060919
52	0.049407	-0.040562	0.034366	-0.054909
53	0.039127	-0.036159	0.026770	-0.052448
54	0.030251	-0.032314	0.016625	-0.047120
55	0.018912	-0.025459	0.008256	-0.038532
56	0.012672	-0.021522	0.003167	-0.033884
57	0.010885	-0.019269	0.002414	-0.030995
58	0.005441	-0.013941	0.001662	-0.026321
59	0.000330	-0.002650	0.000895	-0.015893
60	0.000078	-0.001325	0.000128	-0.015511

Table I.5 *Measured profile geometry and postion of pressure taps at 70% and 90% station, Ctd*

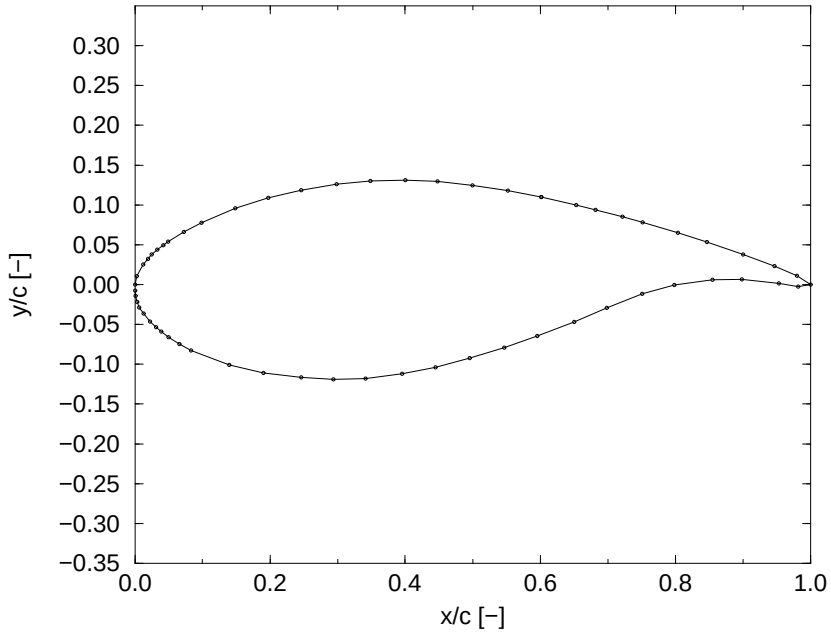

Figure I.7 *Mie: Measured profile geometry and position of pressure taps at the 32.5% radial station*

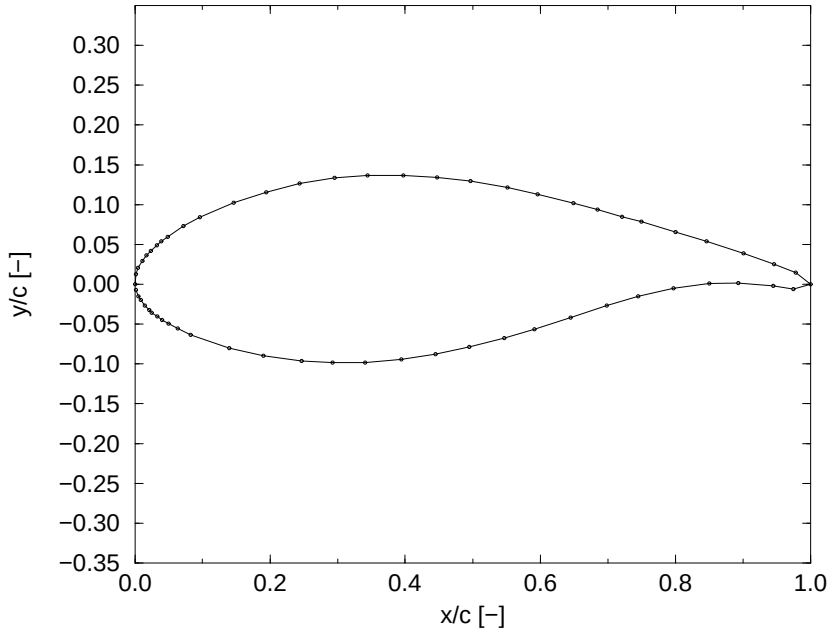

Figure I.8 *Mie: Measured profile geometry and position of pressure taps at the 50% radial station*

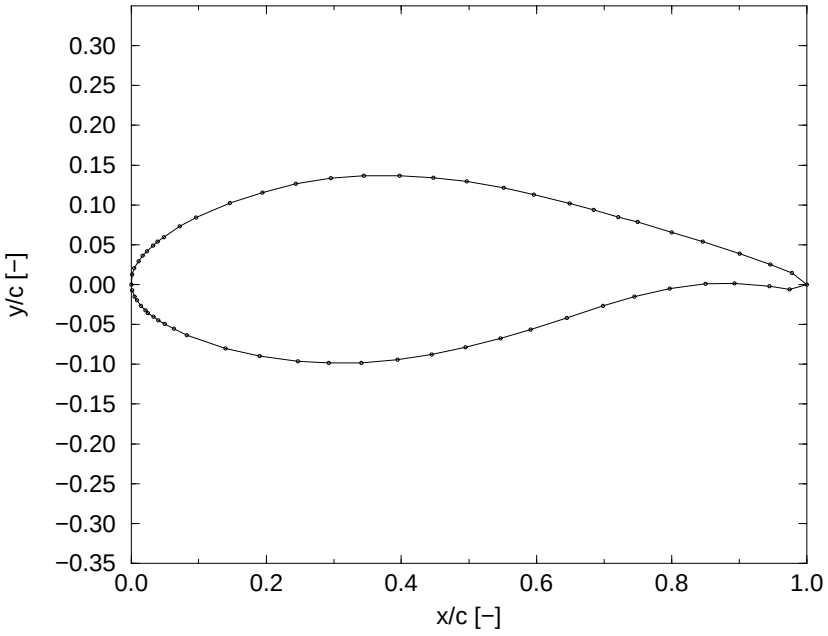

Figure I.9 *Mie: Measured profile geometry and position of pressure taps at the 70% radial station*

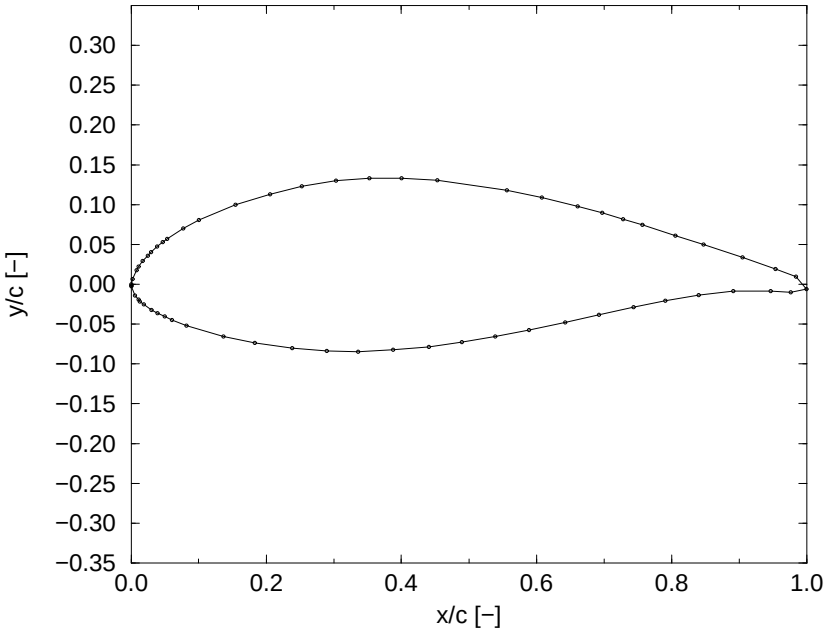

Figure I.10 *Mie: Measured profile geometry and position of pressure taps at the 90% radial station*

APPENDIX J. COMPARISON OF ANGLE OF ATTACK METHODS FOR NREL MEASUREMENTS

J.1 General

In this section, the inverse b.e.m. method, the power method, and the stagnation methods, see section 6.1 are mutually compared on basis of two NREL measurement time series. In the NREL measurement time series, the angle of attack is measured with a flag and corrected for 2D (windtunnel) upwash effects, see section 5.3. One campaign is at below stall conditions (campaign ny-rot-nu-001) and one campaign is at above stall conditions (campaign ny-rot-nu-005). For the description of these campaigns, reference is made to Appendix C. Note that for these campaigns, the profile aerodynamics have been measured at 30%, 63% and 80% span (the instrumentation at the 47% span location was malfunctioning).

J.2 Comparison of NREL power curve with b.e.m. calculations

Two angle of attack methods (inverse b.e.m. method and power method) rely on b.e.m. calculations. In order to facilitate the interpretation of the results of these methods the power curve was calculated with a b.e.m. method and compared with the measured power curve.

The aerodynamic model of the turbine is based on the machine description supplied by NREL. Figure J.1 and J.2 show the lift and drag curves respectively for the S809 profile which is used on the NREL blade.

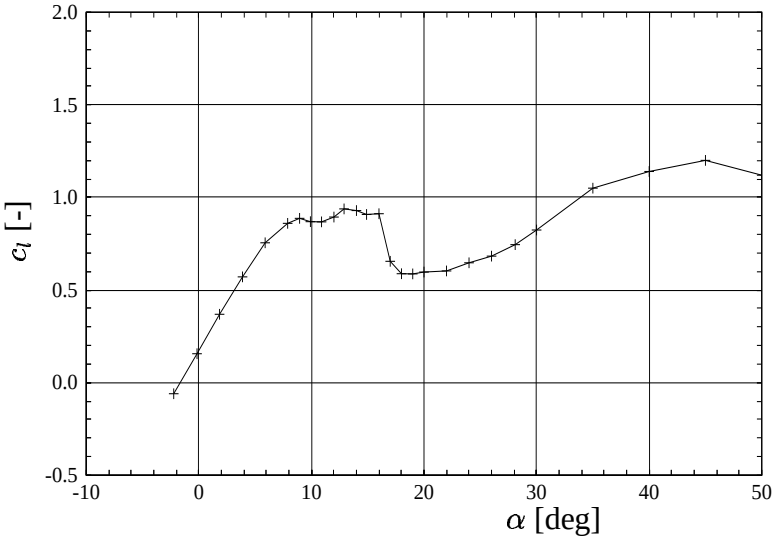

Figure J.1 $c_l - \alpha$ *curve S809 profile*

The power curves have been calculated with the ECN programme PVOPT, see [64]. The aerodynamic model of this program is based on the standard blade element momentum method with Prandtl tip correction and turbulent wake model from Wilson. Note that an air density of 0.9793 kg/m^3 was used as recommended

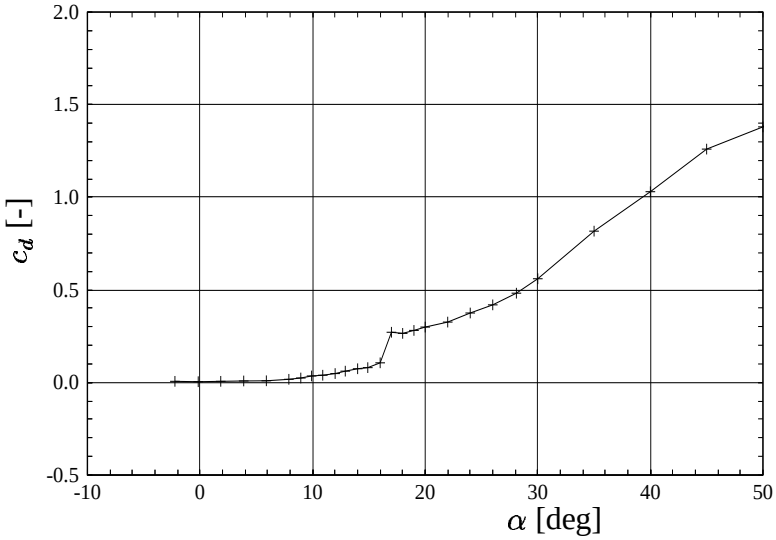

Figure J.2 $c_d - \alpha$ *curve S809 profile*

by NREL, because of the altitude of the site. The drive train efficiency was supplied by NREL.

The results of the power curve are given in figure J.3.

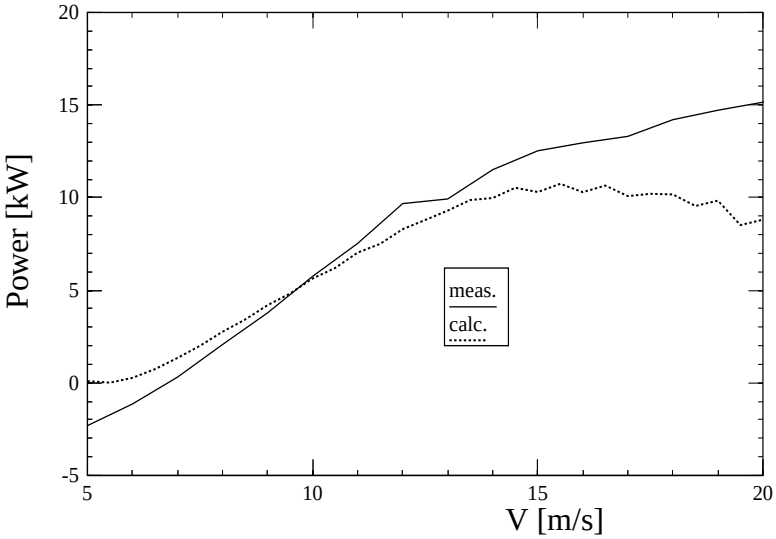

Figure J.3 *Measured and b.e.m. calculated power curve; NREL test turbine; axisymmetric conditions are assumed*

The following observations can be made:

- At high wind speeds, the calculated power curve underestimates the power considerably. This is a result of three dimensional effects in stall, which are not accounted for (the 2D profile data from the figures J.1 and J.2 are used).
- At moderate wind speeds there is a reasonable agreement between calculated and measured power curve
- At low wind speeds the agreement is rather poor, possibly because of inaccuracies in the curve fit for the drive train efficiency.

J.3 Results obtained with inverse b.e.m. method

The blade element momentum method equations have been manipulated and the resulting equation is expressed in terms of the inflow angle, ϕ.

$$4\cos(\phi)\sin(\phi) - \sigma c_t - 4\lambda_r \sin^2(\phi) - \sigma\lambda_r c_n = 0. \tag{J.1}$$

For axial induction factors a > 0.38 an empirical turbulent wake formula according to Wilson is applied:

$$C_{D.ax} = 0.96a + 0.5776 \tag{J.2}$$

By combination of equation J.2 with the blade element equations, the following relation is derived:

$$(4.96\cos(\phi)\sin(\phi) - 1.24\sigma c_t)^2 - 15.36\lambda_r \sin^3(\phi)\cos(\phi) \tag{J.3}$$

$$+3.84\lambda_r \sin^2(\phi)\sigma c_t - 16\sigma\lambda_r^2 c_n \sin^2(\phi) = 0.$$

Note that for reasons of simplicity, the effects of tower, cone angle, tilt angle, (mean) yaw and wind shear are excluded. In [65] the derivation of equation J.1 and J.3 is given in more detail.

From equation J.1 (or if necessary equation J.3), the inflow angle can easily be determined from the measured normal force coefficient c_n and the tangential force coefficient c_t. In the figures J.4 to J.7 the results are presented, for the campaigns described above. The figure J.4 and J.6 show the results for the entire measurement period and the figures J.5 and J.7 show the results for the first 15 seconds. The y_{min} and y_{max} are presented right from the picture. The dotted lines refer to the inverse b.e.m. method results; the solid lines refer to the angle of attack flag measurements which are supplied by NREL. As mentioned previously, the NREL flag data were corrected with 2D windtunnel upwash measurements.

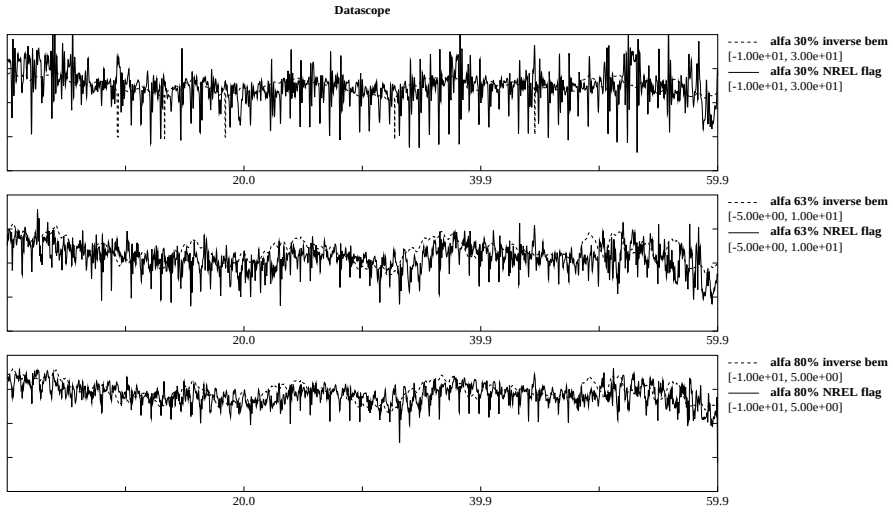

Figure J.4 *Comparison of NREL flag a.o.a. and inverse b.e.m. method a.o.a. for campaign ny-rot-nu-001 (low wind speed), entire period*

The following observations can be made:

- The NREL angle of attack at the inner section at the high wind speed, figure J.6 is limited to a maximum value of 40 degrees. The real angle of attack may exceed this value.

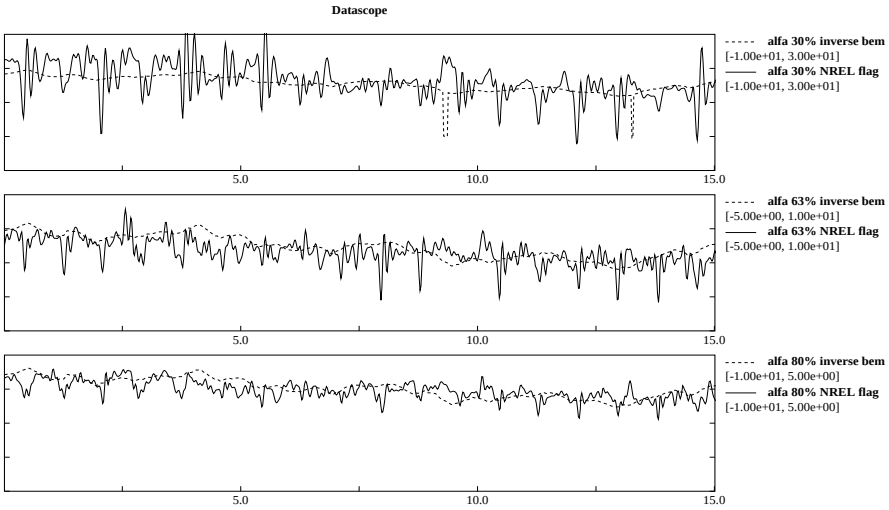

Figure J.5 *Comparison of NREL flag a.o.a. with inverse b.e.m. method a.o.a. for campaign ny-rot-nu-001 (low wind speed), first 15 seconds*

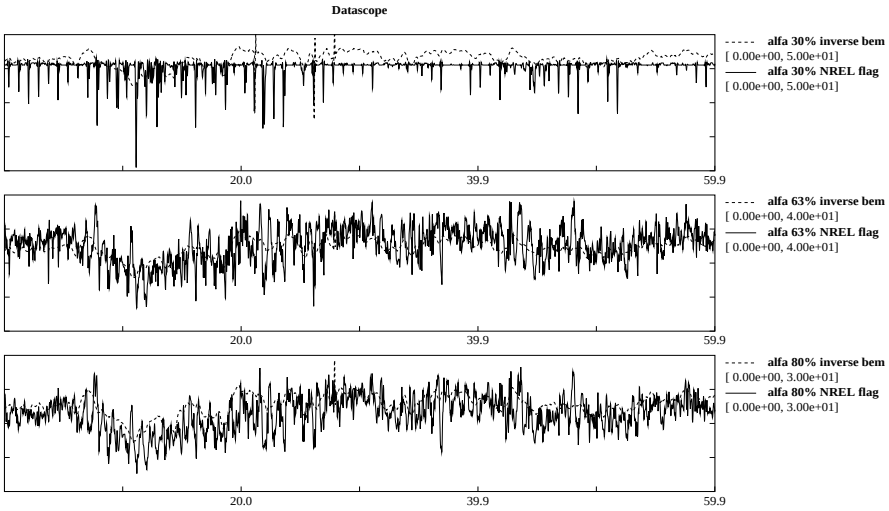

Figure J.6 *Comparison of NREL flag a.o.a with inverse b.e.m. method a.o.a. for campaign ny-rot-nu-005 (high wind speed), entire period*

- Comparison of the mean level of the inverse b.e.m.-method angle of attack (tables J.1 and J.2) with the NREL measured angle of attack shows an excellent agreement.
- In the NREL measured angle of attack, 'high frequency fluctuations' are apparent, which are not present in the angle of attack from the inverse b.e.m. method. The figures J.8 to J.12 show the APSD of the NREL measured angle of attack and the inverse b.e.m. angle of attack. It can be observed that the low frequency fluctuations (until ≈ 0.6 Hz) are predicted well. Dominant frequencies in the NREL measured angle of attack are at 1P and multiples of 1P. It must be noted however, that in the 'inverse b.e.m. method' angle of attack, the effects of yaw, tower and wind shear are excluded. These effects will add 1P (and multiple of 1P) fluctuations. Hence inclusion of these effects will probably improve the correlation. Although the inclusion of these effects is relatively simple, this task was not performed due to the limited time available to finish this study. It must also be noted that the structural dynamic effects are excluded. These

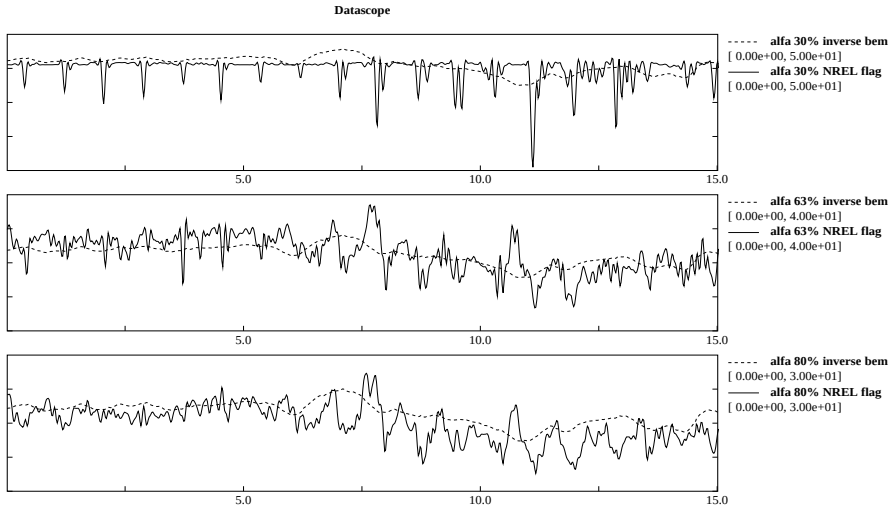

Figure J.7 *Comparison of NREL flag a.o.a. with inverse b.e.m. method a.o.a. for campaign ny-rot-nu-005 (high wind speed), first 15 seconds*

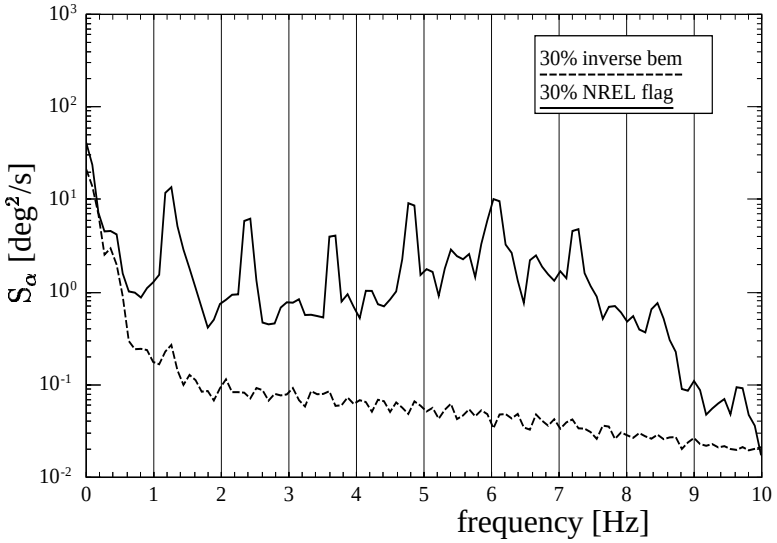

Figure J.8 *Comparison of APSD of NREL flag a.o.a. with inverse b.e.m. a.o.a. for campaign ny-rot-nu-001 (low wind speed)*

effects will be relatively difficult to implement into equation J.1.

- Due to the neglect of tower shadow, windshear etc. the standard deviation of the inverse b.e.m. angle of attack is (considerably) underestimated, see table J.1 and J.2.
- The 'frequency resolution' of the present method will always be poorer than for the other methods. As a consequence the method may not give useful results for studies, in which high frequency fluctuations should be investigated.

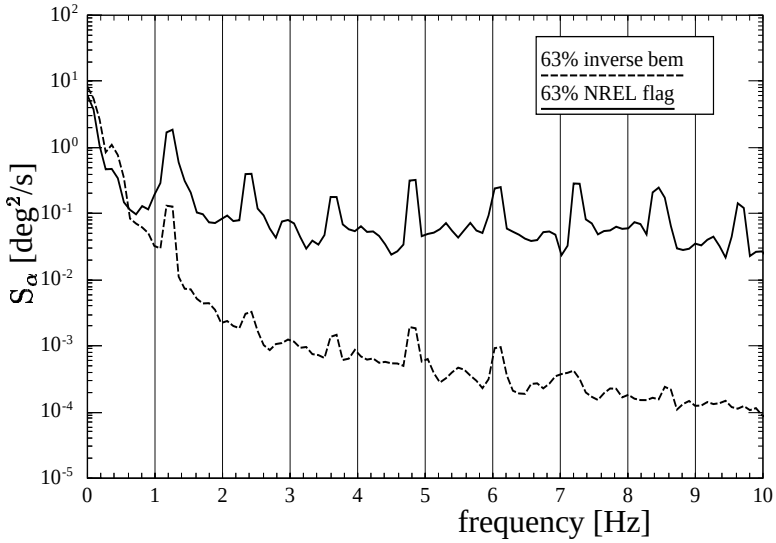

Figure J.9 *Comparison of APSD of NREL flag a.o.a. with inverse b.e.m. a.o.a. for campaign ny-rot-nu-001 (low wind speed)*

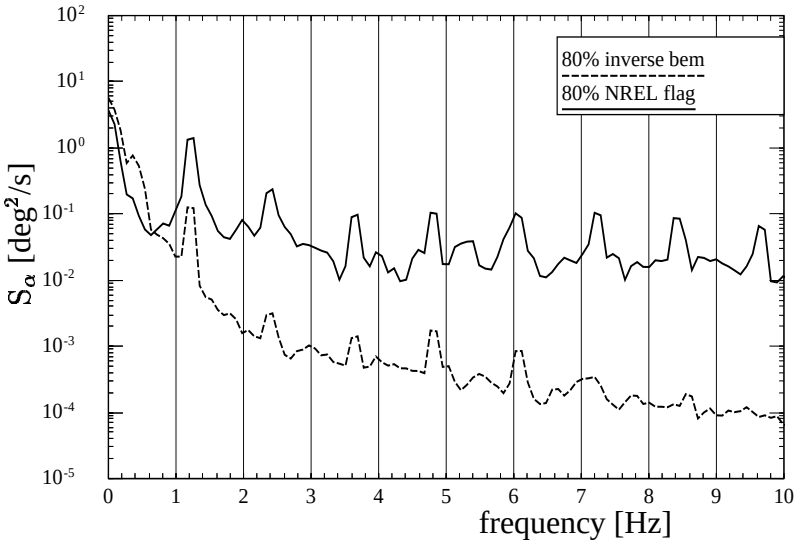

Figure J.10 *Comparison of APSD of NREL flag a.o.a. with inverse b.e.m. a.o.a. for campaign ny-rot-nu-001 (low wind speed)*

Table J.1 *Mean and standard deviation of angles of attack (inverse b.e.m. and NREL flag) for campaign ny-rot-nu-001 (low wind speed)*

	mean		std. dev.	
section	b.e.m [deg]	NREL [deg]	b.e.m. [deg]	NREL [deg]
30%	14.896	14.570	2.071	4.868
63%	3.820	3.044	1.194	1.462
80%	0.993	0.625	0.995	1.094

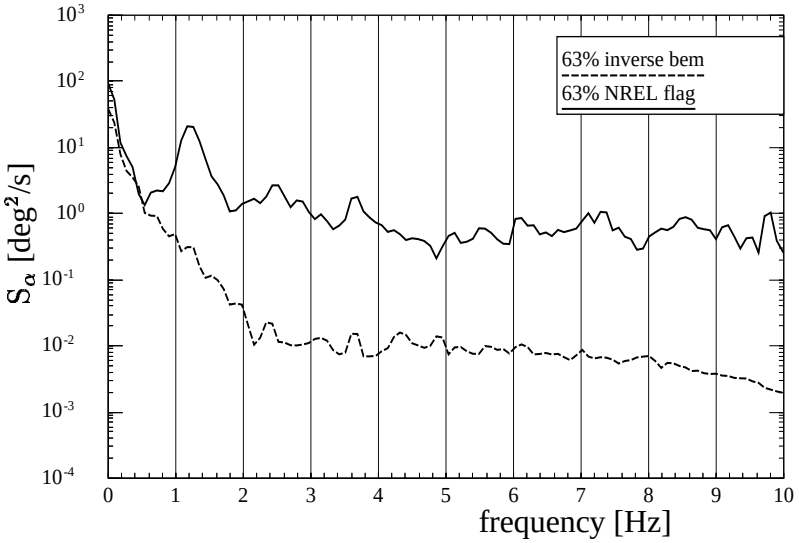

Figure J.11 *Comparison of APSD of NREL flag a.o.a. with inverse b.e.m. a.o.a. for campaign ny-rot-nu-005 (high wind speed)*

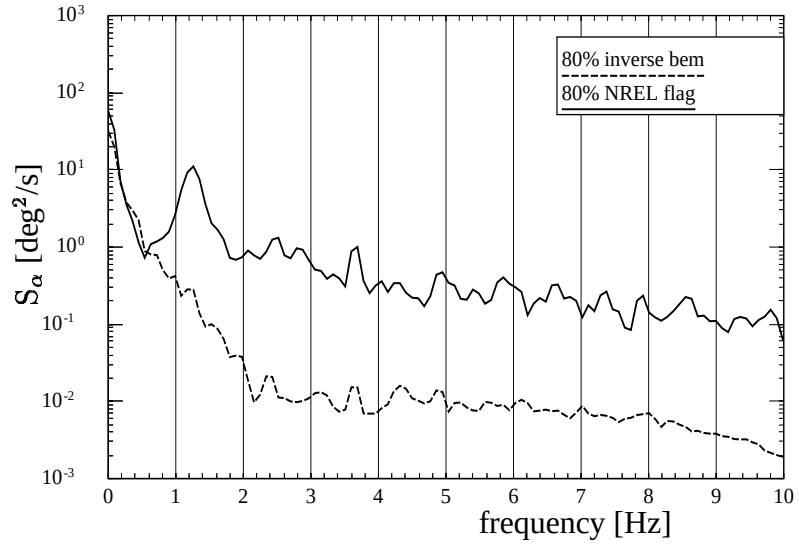

Figure J.12 *Comparison of APSD of NREL flag a.o.a. and inverse b.e.m. a.o.a. for campaign ny-rot-nu-005 (high wind speed)*

Table J.2 *Mean and standard deviation of angles of attack (inverse b.e.m. and NREL flag) for campaign ny-rot-nu-005 (high wind speed)*

	mean		std. dev.	
	b.e.m	NREL	b.e.m.	NREL
section	[deg]	[deg]	[deg]	[deg]
30%	41.063	37.967	2.732	3.180
63%	24.549	25.330	2.514	5.243
80%	19.088	17.125	2.312	3.829

J.4 Results obtained with power method

Figure J.13 to J.15 present the calculated and measured power as a function of angle of attack, for the 3 radial stations. A 2nd order polynomial is fitted through the results. It can be observed that in figure J.14 (63% span), at large angles of attack there are two power levels. The explanation for this is not found, but there are suspects about the quality of the measured data. For this reason the polynomial was fitted until α = 25 degrees only. The calculation is based on the power curve from figure J.3. Two measured curves are plotted, both based on the power curve from figure J.3:

- The measured power versus the uncorrected angle of attack as measured with the NREL flag;
- The measured power versus the angle of attack, corrected according to the wind tunnel method.

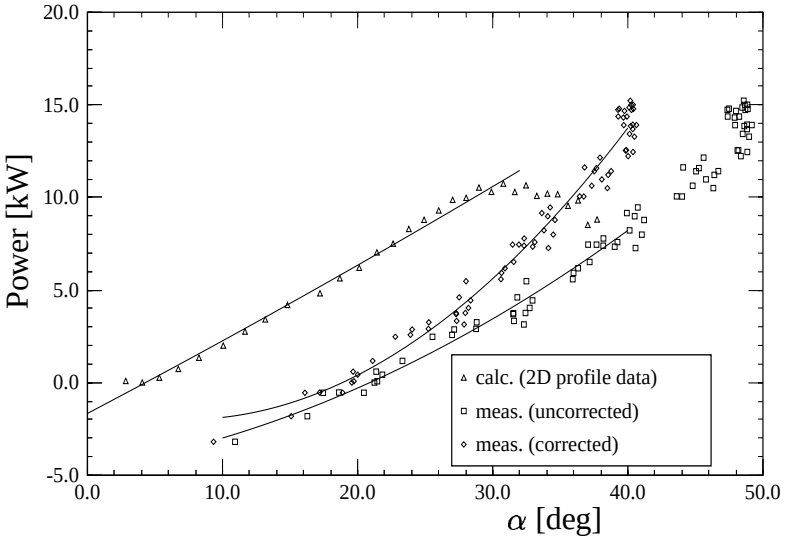

Figure J.13 *Calculated and measured power as function of α at 30% span*

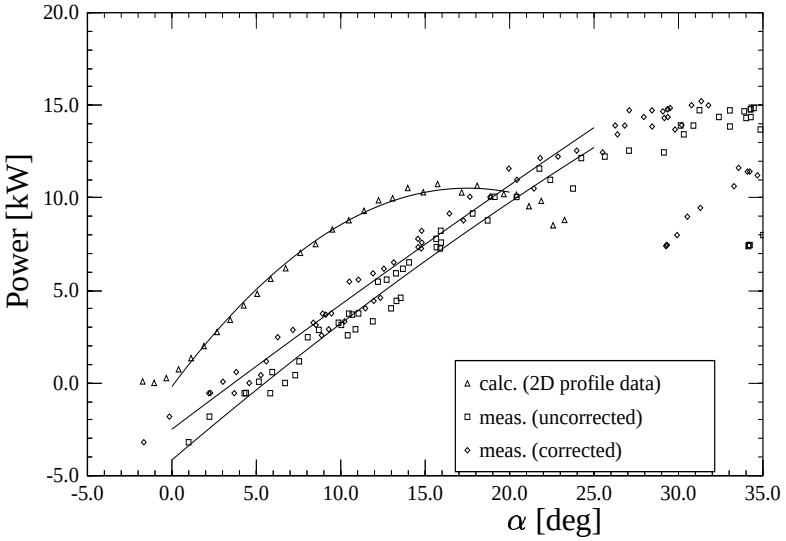

Figure J.14 *Calculated and measured power as function of α at 63% span*

The following observations can be made:

- The Risø power method assumes that there is a constant off-set between the 2D calculated angle of attack and the measured uncorrected angle of attack. For

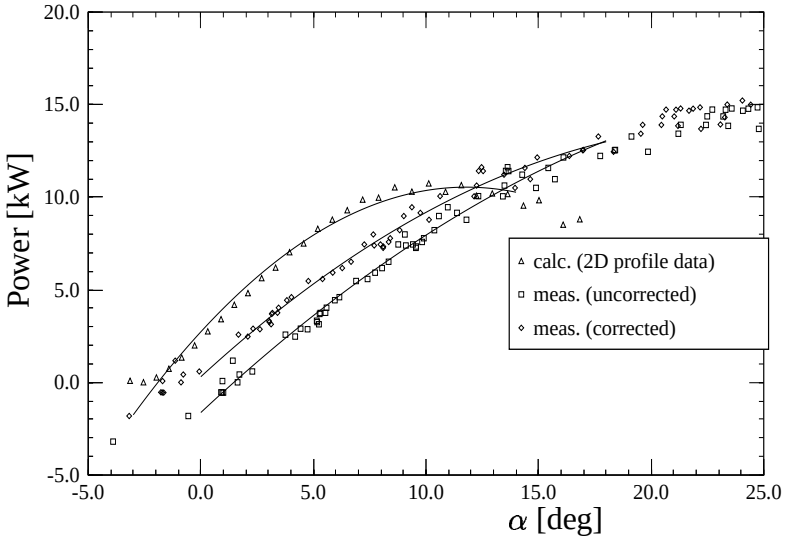

Figure J.15 *Calculated and measured power as function of α at 80% span*

the NREL measurements this constant off-set is difficult to detect.
Furthermore the power should be a unique function of angle of attack which is not the case for the 63% station at high angles of attack. This makes the interpretation of the results difficult.
Nevertheless, the off-sets are determined by fitting straight lines through the curves presented in the figures J.13 to J.15. The resulting off-set for the 30% station is 18.5^0, for the 63% station the off-set is about 7^0 and for the 80% station the off-set is about $4\ ^0$.
Probably it would make sense the make the off-set a function of the angle of attack. Due to the limited time available to finish this study, this is not attempted.

- In general the b.e.m. calculated angle of attack, using 2D profile coefficients is lower than the NREL measured angle of attack (assuming the same power level).

The power method has been applied by substracting the off-sets mentioned above from the uncorrected flag data. The time series are presented in the figures J.16 to J.19. The dotted lines represent the results from the power method and the solid lines are the NREL flag data. The y_{min} and y_{max} values are shown right of the figure. The following observations can be made:

- As stated previously, the NREL angle of attack at the inner station of the high wind speed case, is cut-off at 40 degrees. No further discussion on these results will take place.
- The differences in mean level are larger than for the inverse b.e.m. method, see the tables J.4 and J.5. Generally, the agreement becomes better for larger angle of attack and larger radial position.
  This is also found from the tables J.3, in which the upwash from the power method is compared with the 2D wind tunnel upwash for the three radial stations at α = 5 degrees and α = 15 degrees. The discrepancy is largest at α = 5 degrees, 30% span ($\Delta\ \alpha \approx 15$ degrees).
- The variations in angle of attack agree reasonably well, see also the APSD's which are presented in the figures J.20 to J.24. This could be expected because the variation in both the NREL angle of attack and the power method angle of attack follow the variation from the raw flag measurements to a large extent.

However, it can be observed from table J.3 that in contrast to the NREL angle of attack, the power method yields an upwash correction which is a function of the radial position. On the other hand, the NREL upwash function is no function of radial position.
In particular for the low wind speed campaign this leads to a standard deviation from the power method angle of attack which is considerably higher than the standard deviation of the NREL angle of attack (in the order of 40%), see the tables J.4 and J.5).

Table J.3 *Upwash correction (in degrees, from power method and NREL 2D wind tunnel)*

section:	30%		67%		80%	
α(deg)	windtunnel upwash(deg)	power upwash(deg)	windtunnel upwash(deg)	power upwash(deg)	windtunnel upwash(deg)	power upwash(deg)
5	3.8	18.5	3.8	7	3.8	4
15	$\approx$ 11	18.5	$\approx$ 11	7	$\approx$ 11	4

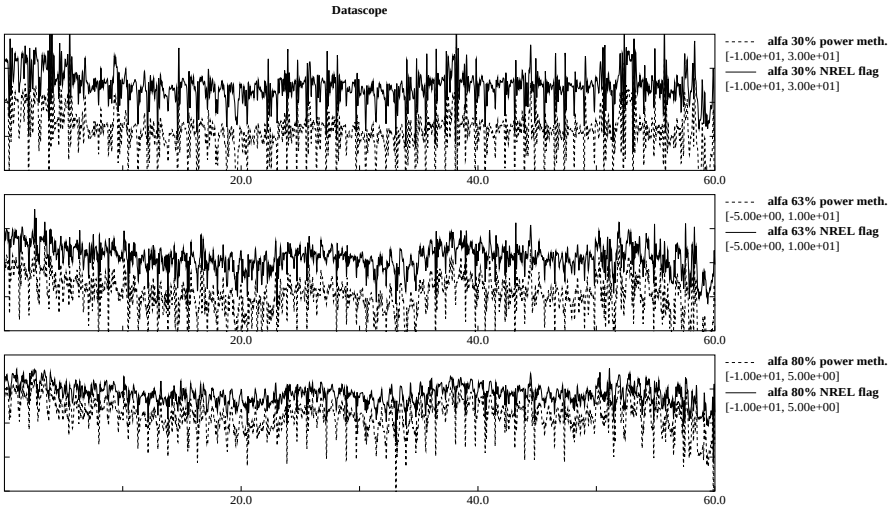

Figure J.16 *Comparison of NREL flag a.o.a. and power method a.o.a. for campaign ny-rot-nu-001 (low wind speed), entire period*

Table J.4 *Mean and standard deviation of angles of attack (power method and NREL) for campaign ny-rot-nu-001 (low wind speed)*

	mean		std. dev.	
section	power [deg]	NREL [deg]	power [deg]	NREL [deg]
30%	1.294	14.570	6.067	4.893
63%	-1.130	3.044	2.147	1.461
80%	-1.742	0.625	1.726	1.095

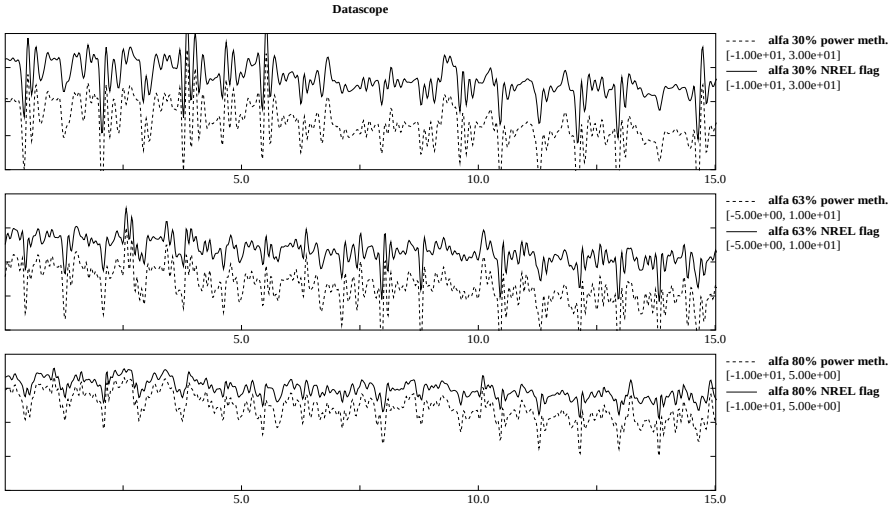

Figure J.17 *Comparison of NREL flag a.o.a. with power method a.o.a. for campaign ny-rot-nu-001 (low wind speed), first 15 seconds*

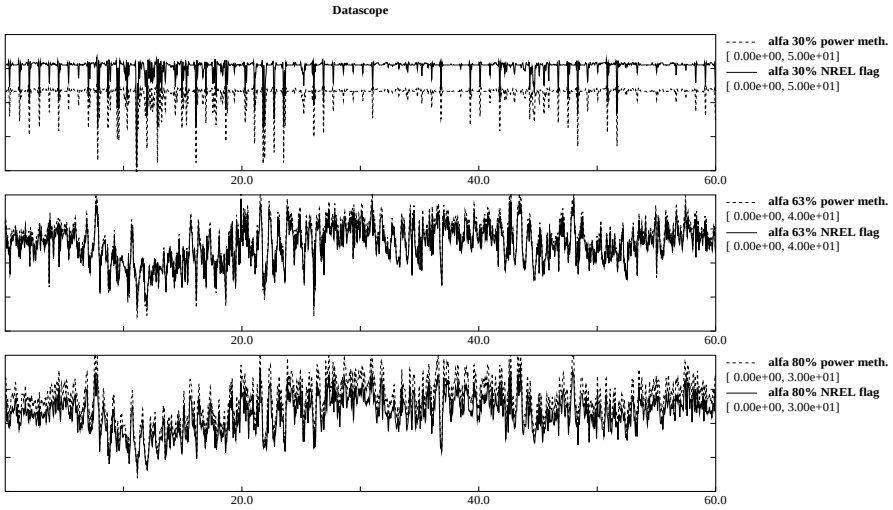

Figure J.18 *Comparison of NREL flag a.o.a. with power method a.o.a. for campaign ny-rot-nu-005 (high wind speed), entire period*

Table J.5 *Mean and standard deviation of angles of attack (power method and NREL) for campaign ny-rot-nu-005 (high wind speed)*

	mean		std. dev.	
	power	NREL	power	NREL
section	[deg]	[deg]	[deg]	[deg]
30%	28.173	37.967	3.627	3.186
63%	26.421	25.330	6.007	5.239
80%	19.951	17.125	4.583	3.829

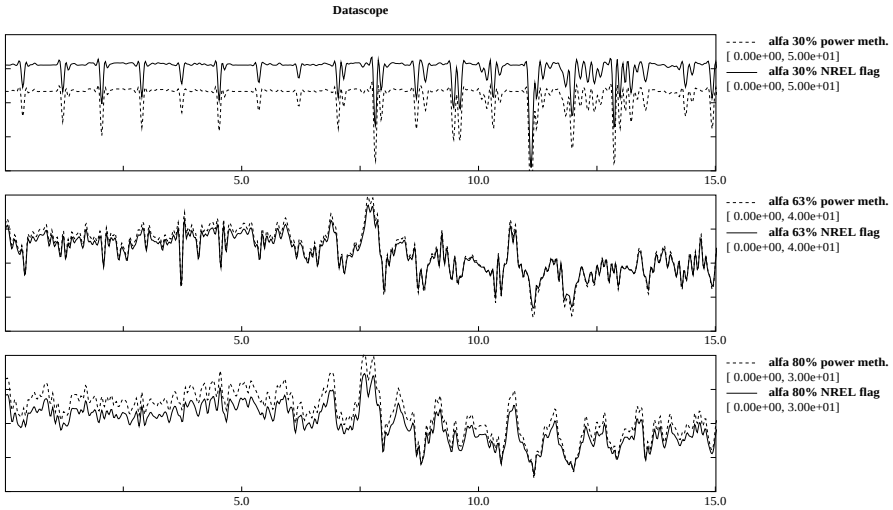

Figure J.19 *Comparison of NREL flag a.o.a. with power method a.o.a. for campaign ny-rot-nu-005 (high wind speed), first 15 seconds*

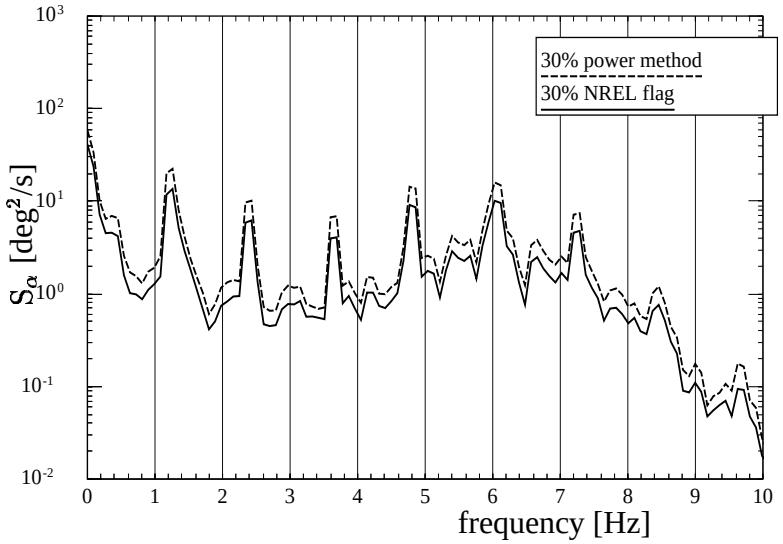

Figure J.20 *Comparison of APSD of NREL flag a.o.a. with power method a.o.a. for campaign ny-rot-nu-001 (low wind speed)*

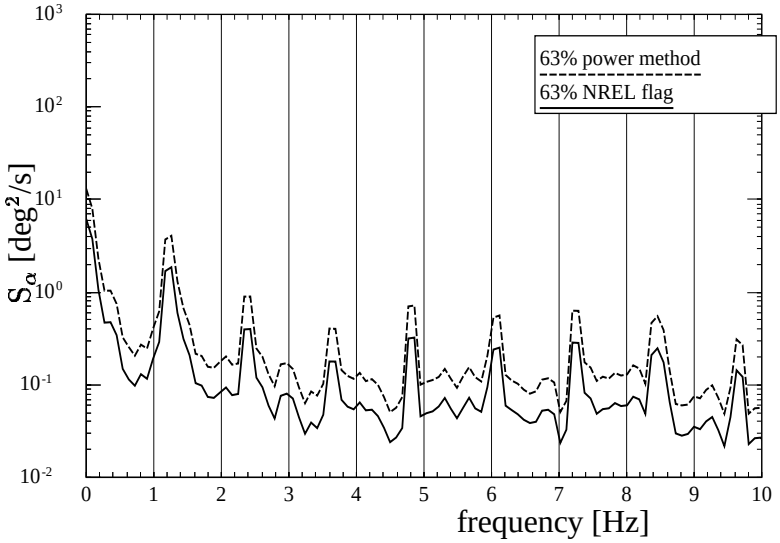

Figure J.21 *Comparison of APSD of NREL flag a.o.a. with power method a.o.a. for campaign ny-rot-nu-001 (low wind speed)*

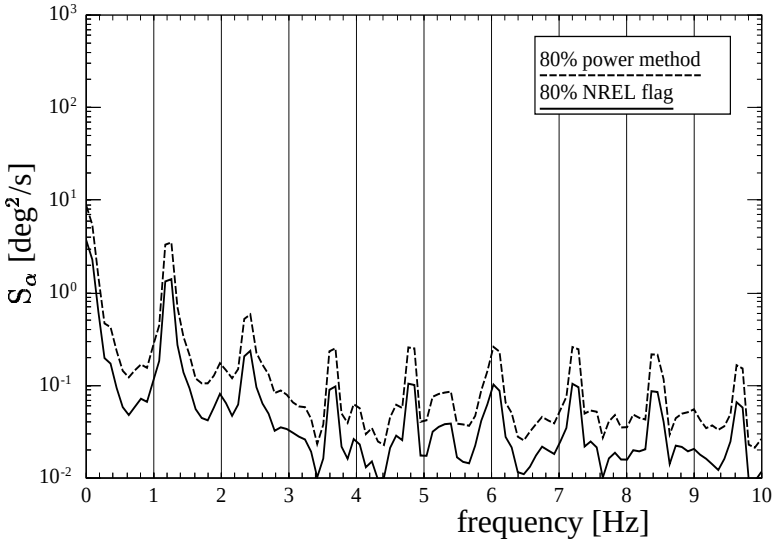

Figure J.22 *Comparison of APSD of NREL flag a.o.a. with power method a.o.a. for campaign ny-rot-nu-001 (low wind speed)*

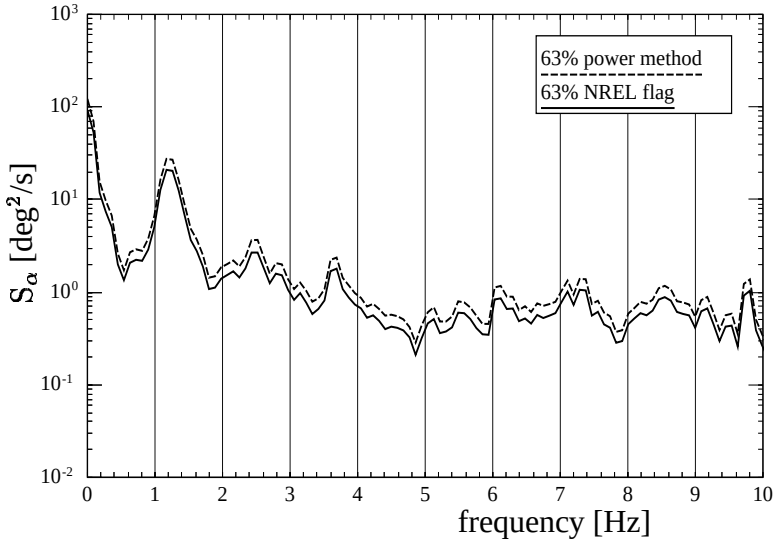

Figure J.23 *Comparison of APSD of NREL flag a.o.a. with power method a.o.a. for campaign ny-rot-nu-005 (high wind speed)*

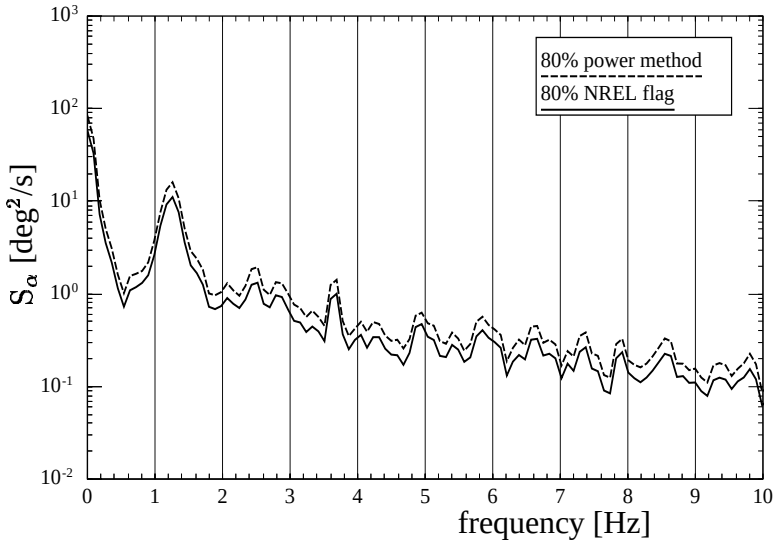

Figure J.24 *Comparison of APSD of NREL flag a.o.a. with power method a.o.a. for campaign ny-rot-nu-005 (high wind speed)*

J.5 Results obtained with the stagnation (XFOIL) method

The position of the stagnation point has been determined from the S809 profile geometry with the design code XFOIL, [33]. Results were available from α = -8^o to α = 22^o. For larger angles of attack, XFOIL did not give a converged solution.

Table J.6 *Determination of intersection point from XFOIL results*

α	$x_{stagnation}/c$ [-]	$y_{stagnation}/c$ [-]	x_m/c [-]
-8.0	0.01322	0.01717	0.13541
-6.0	0.00925	0.01365	0.13911
-4.0	0.00436	0.00899	0.13299
-2.0	0.00080	0.00536	0.15434
0.0	0.00006	0.00457	∞
2.0	0.00176	-0.00316	0.09212
4.0	0.00636	-0.00735	0.11149
6.0	0.01413	-0.01381	0.14548
8.0	0.02138	-0.01920	0.15799
10.0	0.02898	-0.02430	0.16678
12.0	0.03644	-0.02882	0.17203
14.0	0.04375	-0.03287	0.17558
16.0	0.05171	-0.03690	0.18038
18.0	0.05905	-0.04032	0.18313
20.0	0.06549	-0.04313	0.18398
22.0	0.06984	-0.04493	0.18106

Table J.7 *Mean value of intersection point*

α	mean $\overline{x_m}/c$ [-]	$\sigma x_m/c$ [percentage of mean value]
< 0	0.140462	6
> 0	0.159093	19

The results are presented in table J.6. In this table the resulting intersection point (x_m) is given also. The mean values of the intersection point are given in table J.7 together with the standard deviation relative to the mean value.

In the ECN stagnation method a constant value for x_m was assumed. This assumption was based on results for the NACA 44 geometry. The tables J.6 and J.7 show that also for the S809 geometry, the position of the intersection point is a rather weak function of the angle of attack. Nevertheless the variation is larger than for the NACA 44 geometry. For positive angles of attack the method is refined by taking into account the variation of the angle of attack. The situation of negative angles of attack was considered to be of less practical importance. In this situation the intersection point was assumed to be constant at x_m/c = 0.140, see table J.7.

Then the angle of attack is found iteratively from the position of the stagnation point, and $f_{intsec}(\alpha)$ according to:

$$\alpha_1 = \mathrm{atan}\left(\frac{-y_{stag}}{x_{m,1} - x_{stag}}\right)$$

$$x_{m,2} = f_{intsec}(\alpha_1)$$

$$\alpha_2 = \text{atan}\left(\frac{-y_{stag}}{x_{m,2} - x_{stag}}\right)$$

$$etc$$

In the figures J.25 to J.29, the results of the angle of attack obtained with the stagnation(XFOIL) method is compared with the NREL angle of attack. Since XFOIL did not yield a solution for $\alpha > 22$ degrees, the method is not used for the high wind speed case.

The stagnation(XFOIL) angles of attack are shown as dotted lines, and the NREL a.o.a.'s by the solid lines. The y_{min} and y_{max} values are presented right of the figures. Figure J.25 shows the time series for the entire measurement period, and figures J.26 time series for the first 15 seconds.

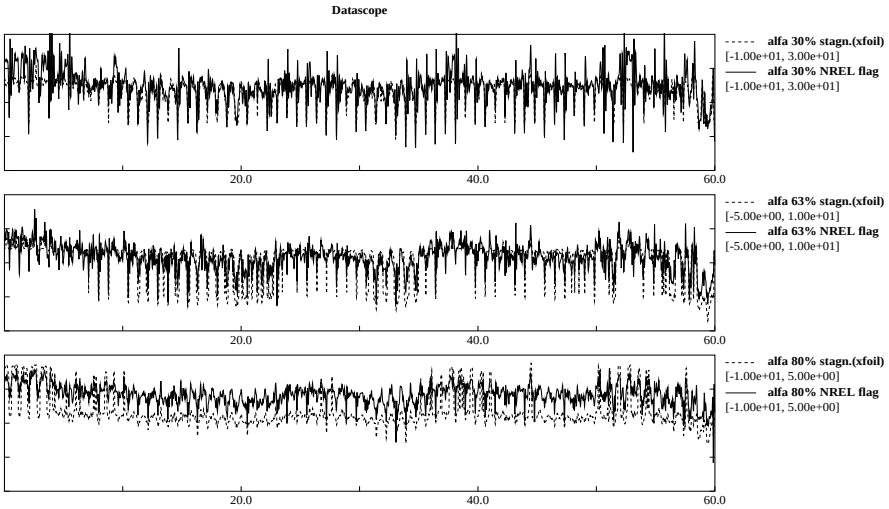

Figure J.25 *Comparison of NREL flag a.o.a. with stagnation(XFOIL)-method a.o.a. for campaign ny-rot-nu-001 (low wind speed), entire period*

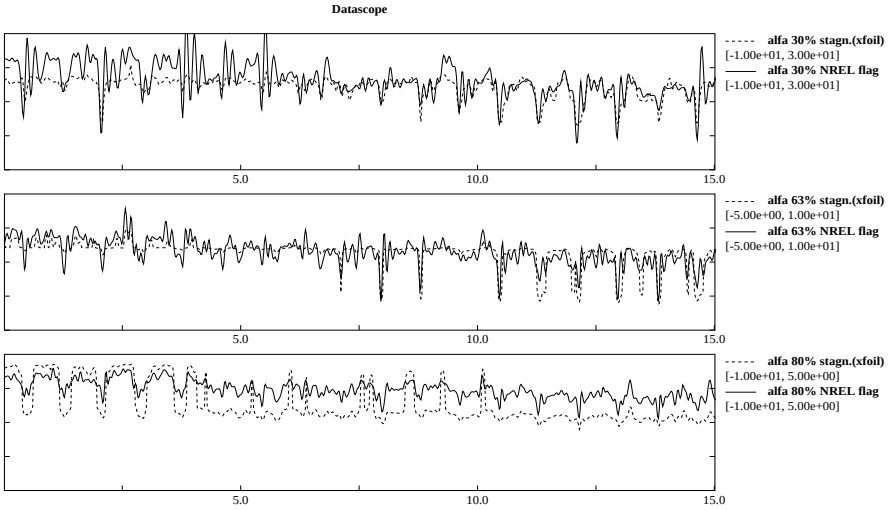

Figure J.26 *Comparison of NREL flag a.o.a. with stagnation(XFOIL)-method a.o.a. for campaign ny-rot-nu-001 (low wind speed), first 15 seconds*

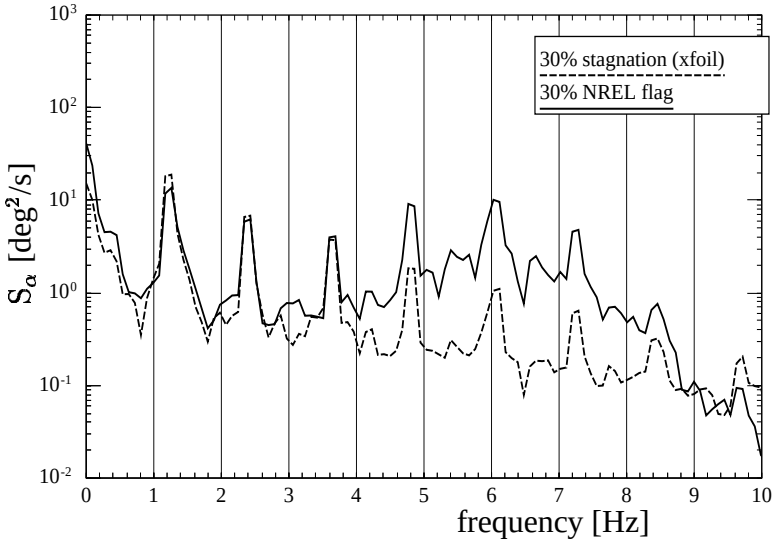

Figure J.27 *Comparison of APSD of NREL flag a.o.a. and stagnation(XFOIL) a.o.a. for campaign ny-rot-nu-001 (low windspeed), 30% section*

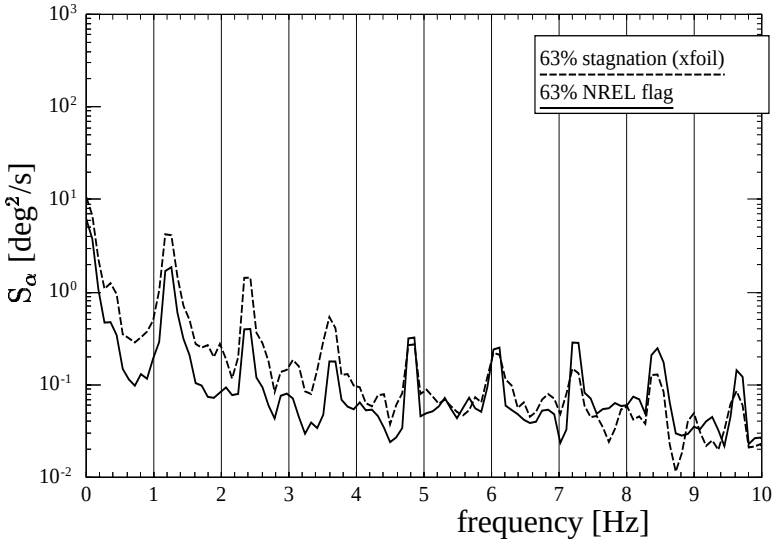

Figure J.28 *Comparison of APSD of NREL flag a.o.a. and stagnation(XFOIL) a.o.a. for campaign ny-rot-nu-001 (low wind speed), 67% section*

It can be observed that the agreement between the stagnation angle of attack and the NREL angle of attack for the low wind speed case ny-rot-nu-001 is very good in terms of the mean value, see also table J.8. The 'jumps' in angle of attack are a result of the discontinuity in intersection point at $\alpha = 0$ degrees. In the figures J.27 to J.29 the APSD's of the stagnation(XFOIL) angle of attack and the NREL angle of attack are presented. Table J.8 shows that the mutual difference in standard deviation is in the order of 40%. However the standard deviaton of the stagnation angle of attack for the 63% and 80% station agrees excellent with the values which are found for the power method, compare table J.8 and J.4. However this is only true for these two stations. The difference at the 30% station is very large.

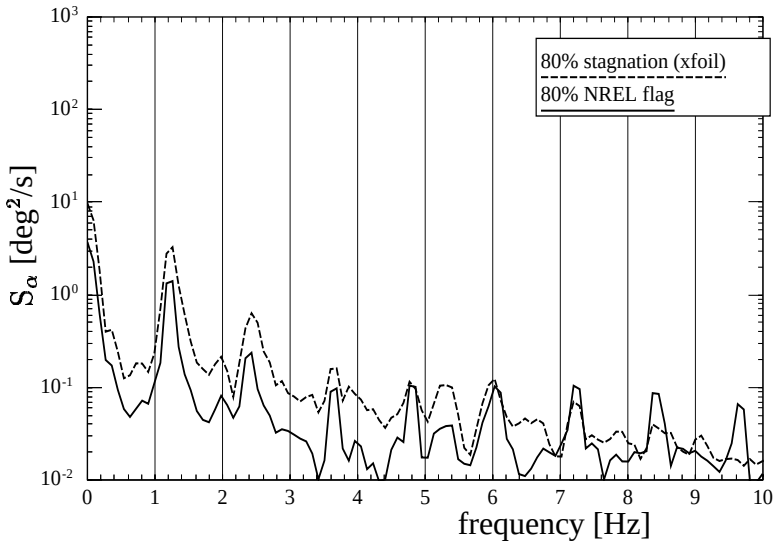

Figure J.29 *Comparison of APSD of NREL flag a.o.a. and stagnation(XFOIL) a.o.a. for campaign ny-rot-nu-001 (low wind speed), 80% section*

Table J.8 *Mean and standard deviation of angles of attack (stagnation (XFOIL) method and NREL) for campaign ny-rot-nu-001 (low wind speed)*

	mean		std. dev.	
	stagn.	NREL	stagn.	NREL
section	[deg]	[deg]	[deg]	[deg]
30%	13.517	14.570	3.545	4.893
63%	2.895	3.044	2.057	1.461
80%	-1.345	0.625	1.727	1.095

J.6 Results obtained with the stagnation(windtunnel) method

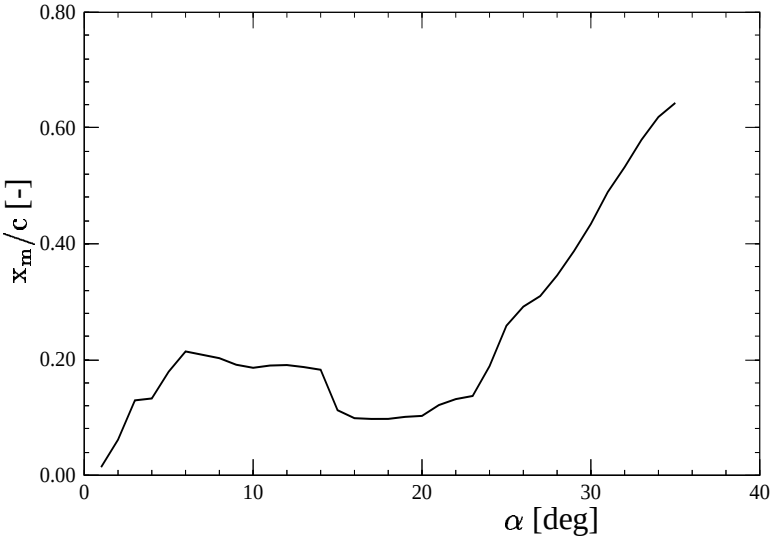

Figure J.30 *Position of intersection point from wind tunnel measurements*

Figure J.30 shows the position of the intersection point as function of angle of attack, as derived from 2D wind tunnel measurements on an S809 profile from [11]. Measurements were available from α = 2 degrees up to α = 35 degrees. For negative angle of attack, no measured data were available and therefore the same procedure as for the stagnation(XFOIL) method was applied: The intersection point is at a constant position of x_m/c = 0.140462, see table J.7.

The results for the low wind speed are given in figure J.33 for the entire period and in figure J.34 for the first 15 seconds. The dotted line represent the a.o.a.'s from the stagnation(windtunnel) method and the solid lines are the NREL angles of attack. The scaling of the lines is presented right from the figures. The figures J.35 to J.37 show the APSD's. The mean values and the standard deviations are presented in table J.9. The mean values and the standard deviation of the angle of attack obtained from both stagnation methods agree very well, compare the values given in table J.9 with the values from table J.8. This could be expected because both methods rely on the same principle. Obviously the differences between the angles of attack from both methods should only be attributed to the fact that the stagnation point position predicted by XFOIL does not fully coincide with the stagnation point measured in the wind tunne.

As a result the level of agreement between the stagnation(wind tunnel) angle of attack and the NREL angle of attack is approximately similar as found for the stagnation(XFOIL) method.

Because the intersection point curve of figure J.30 is no unique function of the angle of attack, considerable numerical problems occured at determining the angle of attack at the high wind speed case.

Although several trics have been attempted to solve the numerical problems, no useful results could be obtained. For this reason the high wind speed case results are not presented. It should be noted that even if the numerical problem would have been solved, the angles of attack which are found from this method would be low compared to the angles of attack from the other methods. This can be explained from the figures J.31 and J.32. Figure J.31 shows the stagnation point location for campaign ny-rot-nu-005 as a function of time. It can be observed

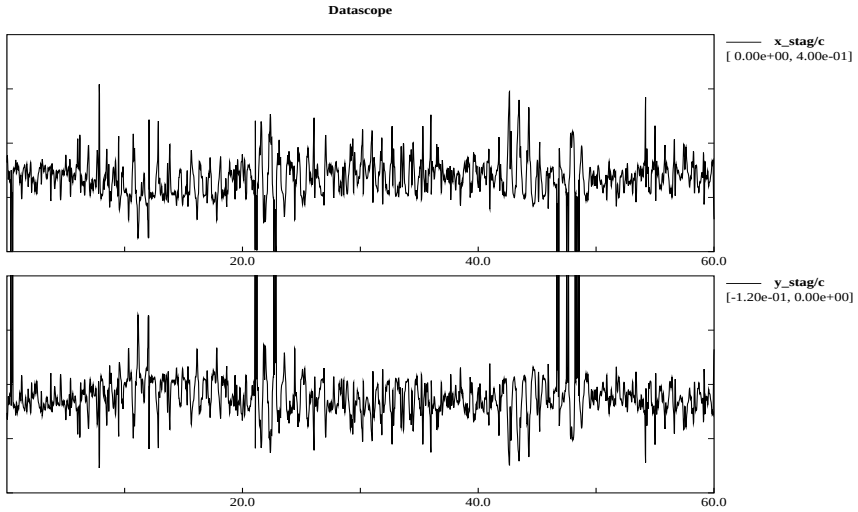

Figure J.31 *X and y coordinate of stagnation point for root section of campaing ny-rot-nu-005 (high wind speed)*

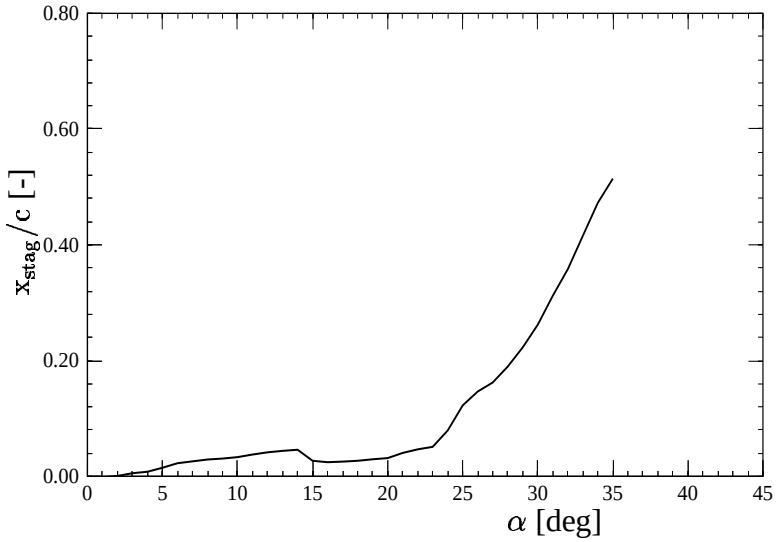

Figure J.32 *Position of stagnation point from wind tunnel measurements*

that x_{stag}/c is on the average ≈ 0.15. Figure J.32, shows the stagnation point as a function of attack from the wind tunnel measurements. In this figure, a value of $x_{stag}/c \approx 0.15$ yields angles of attack which are smaller than ≈ 25 degrees. If the NREL measured angle of attack of ≈ 35 degrees would be assumed to more realistic, the stagnation point x_{stag}/c should be ≈ 0.5. These results indicate that the position of the stagnation point in the wind tunnel differs considerably from the position in the rotating experiment (at least in stalled conditions).
On basis of these results it is concluded that the stagnation (windtunnel) method cannot be used at high angles of attack and no further analysis on these results will take place. It must be emphasised that the above mentioned statements are only valid under the assumption that the stagnation point wind tunnel measurements are reliable. Furthermore the observations do not necessarily be true for other profiles.

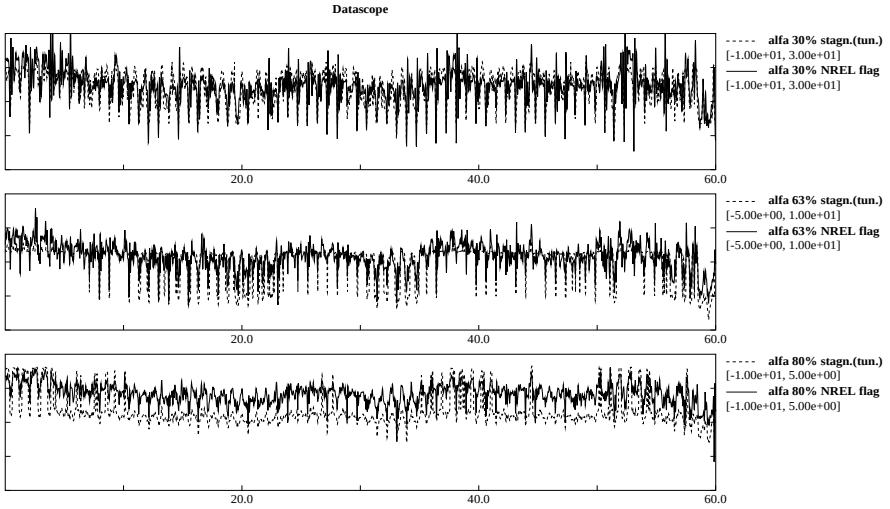

Figure J.33 *Comparison of NREL flag a.o.a. with stagnation(windtunnel)-method a.o.a. for campaign ny-rot-nu-001 (low wind speed), entire period*

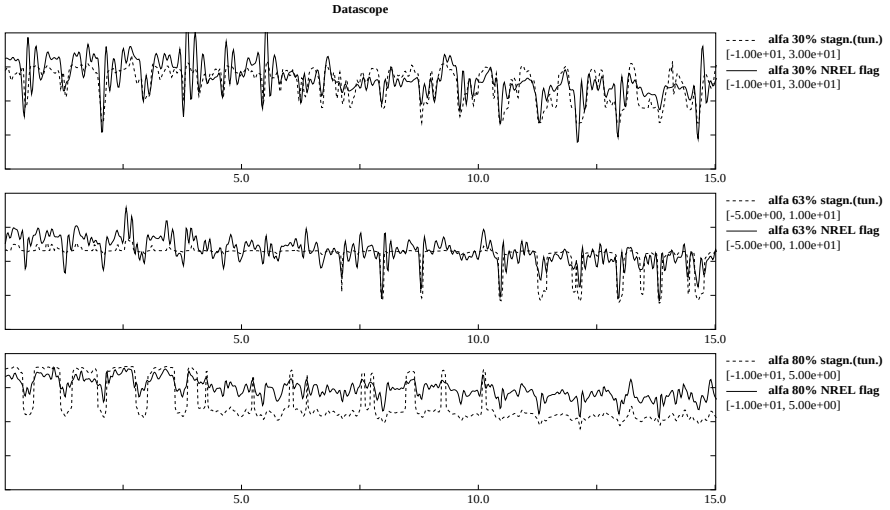

Figure J.34 *Comparison of NREL flag a.o.a. with stagnation(windtunnel)-method a.o.a. for campaign ny-rot-nu-001 (low wind speed), first 15 seconds*

Table J.9 *Mean and standard deviation of angles of attack (stagnation (windtunnel) method and NREL) for campaign ny-rot-nu-001 (low wind speed)*

	mean		std. dev.	
	stagn.	NREL	stagn.	NREL
section	[deg]	[deg]	[deg]	[deg]
30%	13.924	14.570	5.098	4.893
63%	2.647	3.044	1.922	1.461
80%	-1.356	0.625	1.694	1.095

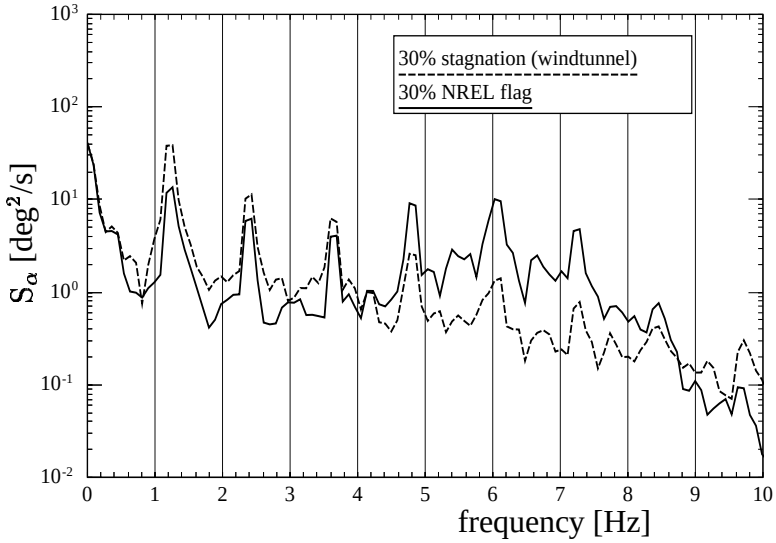

Figure J.35 *Comparison of APSD of NREL flag a.o.a. and stagnation(windtunnel) a.o.a. for campaign ny-rot-nu-001 (low windspeed), 30% section*

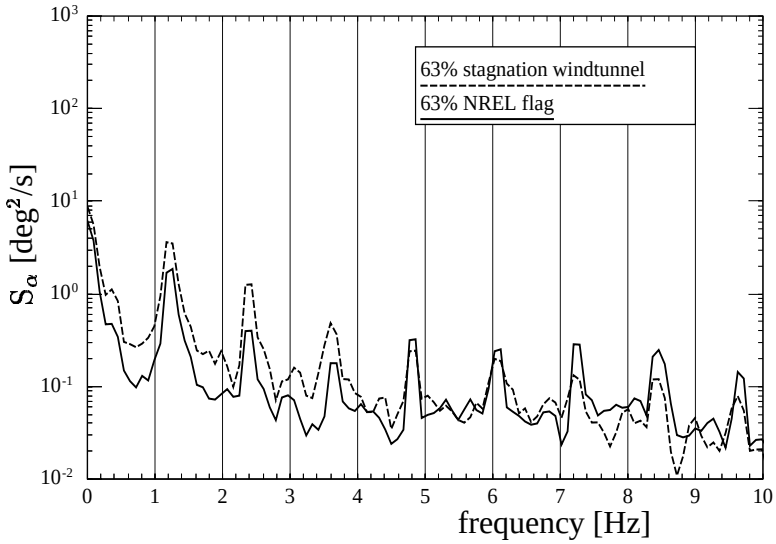

Figure J.36 *Comparison of APSD of NREL flag a.o.a. and stagnation(windtunnel) a.o.a. for campaign ny-rot-nu-001 (low wind speed), 67% section*

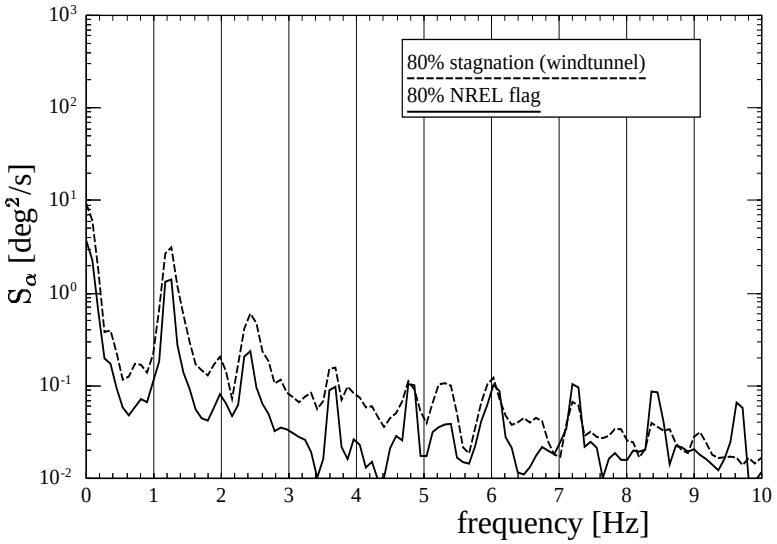

Figure J.37 *Comparison of APSD of NREL flag a.o.a. and stagnation(windtunnel) a.o.a. for campaign ny-rot-nu-001 (low wind speed), 80% section*

J.7 Recommendation on methods

In order to assess the several methods which are described above, selection criteria are introduced. The following criteria are thought to be of importance.

- Is a device needed to measure the inflow angle? This requires additional instrumentation. Furthermore it implies that the measurement of the inflow angle is performed at a different position than the measurement of profile aerodynamics and/or the risk of disturbance from the probe on the profile aerodynamics is introduced.
- Are windtunnel measurements required? This will yield additional costs.
- Are pressure measurements needed or do section forces provide sufficient information?
- What is the degree of complexity of the method?
- Are theoretical models required which were supposed to be verified? For example, if the purpose of the investigation is to verify b.e.m. methods, the use of the inverse b.e.m. method introduces uncertainties which should be investigated.
- Can numerical(convergence) problems occur?
- Note that it is not known how the values of the angles of attack are related to the 'real' angle of attack, because the latter one is a hypothetical quantity according to section 6.1. Hence the criterium 'accuracy' cannot be introduced.

In table J.10 all methods are assessed on basis of the criteria. Note that the 'panel method', see section 6.1 has not been investigated in this appendix. The main conclusion from table J.10 is that no method can be selected which is the 'best'. This is even more true, because the accuracy of the methods cannot be assessed. Actually the 'best method' may depend on the purpose of the investigation, i.e. an analysis of time averaged 3D effects may require another method than the analysis of stall hysteris loops. Furthermore, the most **suitable** method will be related to practical items like availability of wind tunnel facilities, inflow devices, available budgets etc. and therefore may be different for every participant.

Although the results of the methods cannot be compared with the 'real' angle of attack, a mutual comparison has taken place. An encouraging conclusion is that the agreement in mean angles of attack for most cases is reasonable (< 4 degrees). For low angles of attack the agreement is often excellent (< 1 degree).

The exceptions are the power method at low wind speed (difference ≈ 4 degrees, at the root much more) and the stagnation methods at high angle of attacks. Actually the stagnation methods cannot be applied for the NREL S809 profile at high angles of attack, due to the non-uniqueness of the stagnation point curve: XFOIL did not yield a solution for large angles of attack and the the stagnation (windtunnel) method suffered from numerical problems.

Table J.10 *Advantages and disadvantages of the several methods*

method	device	windtunnel	pres. meas.	complexity	model.	convergence
inverse b.e.m.	++	++	++	+	- -	+
windtunnel	- -	- -	++	++	++	++
stagnation(XFOIL)	++	++	- -	-	- -	+
stagnation(windtunnel)	++	- -	- -	-	++	- -
power	- -	++	++	++	- -	+
panel	- -	++	++	- -	-	?

The mutual agreement in the standard deviation of the angles of attack was only moderate: Differences in the order of 40% often occurred.

The methods which are investigated in this appendix are based on the methods applied in the IEA Annex XIV project. Then as a final conclusion it can be stated that the different methods applied in the IEA annex XIV project yield angles of attack which generally show a good mutual agreement in mean values, but only a moderate agreement in variations.